Thèse de doctorat

NNT : 2020UPASS090

université PARIS-SACLAY

GaAs-on-Si solar cells based on nanowire arrays grown by molecular beam epitaxy

Thèse de doctorat de l'université Paris-Saclay

École doctorale n°575: electrical, optical, bio physics and engineering (EOBE)

Spécialité de doctorat: Electronique et Optoélectronique, Nano- et Microtechnologies

Unité de recherche: Université Paris-Saclay, CNRS, Centre de Nanosciences et de Nanotechnologies, 91120, Palaiseau, France

Référent: Faculté des sciences

Thèse présentée et soutenue à Palaiseau, le 12/06/2020 par

Romaric de Lépinau

Composition du Jury

Mathieu KOCIAK Directeur de recherche, LPS, CNRS, Université Paris-Saclay, France	Président
Gregor KOBLMUELLER Chercheur Priv.-Doz., Walter Schottky Institut, Technical University of Munich, Allemagne	Rapporteur & Examinateur
Olivier DURAND Professeur, Institut FOTON, INSA-Rennes, France	Rapporteur & Examinateur
Teemu HAKKARAINEN Chercheur, Tampere University of Technology, Finlande	Examinateur
Sébastien PLISSARD Chargé de recherche, LAAS, CNRS, Toulouse, France	Examinateur

Stéphane COLLIN Chargé de recherche, C2N, CNRS, Palaiseau, France	Directeur de thèse
Fabrice OEHLER Chargé de recherche, C2N, CNRS, Palaiseau, France	Co-Encadrant
Andrea CATTONI Chargé de recherche, C2N, CNRS, Palaiseau, France	Co-Encadrant

Acknowledgments – Remerciements

C'était il y a maintenant plus de 4 ans que, fraichement débarqué de Suède, je discutais avec Stéphane et Andrea d'un sujet de stage sur les cellules solaires ultraminces, et d'une potentielle thèse. Dans quoi m'étais-je engagé : une épopée quotidienne vers la bourgade de Marcoussis, puis entre Paris, Palaiseau et Bezons, des journées passées à m'occuper d'un bout de semiconducteur de quelques cm^2 en espérant qu'il en sorte quelque chose, un labo qui déménage, un autre qui sort de terre, et pour finir en beauté, une pandémie pour ma soutenance! C'est rocambolesque, on pourrait presque en faire un film ! Voire plusieurs ??

Le bon, la brute et le truand

Après avoir erré plus d'une heure, je ne suis plus très loin de Marcoussis. Le vent souffle sur le site de Data 4, pas de signe de vie. Au loin, le labo du LPN et j'aperçois trois silhouettes en cache-poussière...

Stéphane, tu tiens sans aucun doute le rôle du Bon. Ton enthousiasme est communicatif, tu es à l'écoute de chacun d'entre nous, et tu as toujours voulu suivre au plus près ma thèse et mon travail. Tu étais là quand j'étais confronté à des problèmes démotivants ou quand je me laissais aller à un certain pessimisme (chronique?). Ton ambition pour mener une telle variété de projets est inspirante, je te souhaite de toujours emmener l'équipe Sunlit plus loin, plus haut, plus fort !

Vient ensuite la Brute, et c'est vers Fabrice que je me tourne ! Ne le prends pas mal, ici ça se rapporte à ta franchise qui te fait souvent dire les choses sans détours, ce qui peut être déstabilisant mais permet aussi d'avancer vite et efficacement. Tu t'es efforcé de me transmettre beaucoup de choses que ce soit ton expertise en épitaxie ou la rigueur et l'exigence que tu mets dans l'analyse des résultats. Tu as souvent placé la barre haut et ça a été aussi une source de motivation pour moi.

Il reste le Truand, c'est donc Andrea qui tient ce rôle. Je cite : 'Moi j'habite place d'Italie et pour venir au LPN, je mets 50 min, en fait il suffit de prendre les bons bus'. Il faut croire que je n'ai jamais trouvé les bons bus, parce que je mettais plus de temps en habitant plus près ! Plus sérieusement, j'ai eu de la chance d'avoir des encadrants très complémentaires et tu apportais souvent les nouvelles idées, les propositions inattendues de pistes auxquelles on n'avait pas forcément pensé. J'ai apprécié nos conversations autour de problèmes épineux, et ton entrain inarrêtable quand tu veux tester une idée originale.

12 hommes en colère

Ce sont tous des hommes (hasard malheureux du script), ils ont lu le rapport et écouté la plaidoirie du prévenu. A sa comparution, ils l'ont assailli de questions pour le pousser dans ses retranchements. Ils se sont maintenant retirés dans une salle pour décider de son sort.

Merci à vous, Gregor Koblmueller et Olivier Durand qui avez passé de longues heures en confinement à lire mon manuscrit, je ne sais pas si c'était si égayant. Merci à Mathieu Kociak,

qui s'est déplacé à l'IPVF dans un contexte un peu particulier et contraignant. Et merci à l'ensemble du jury avec Sébastien Plissard et Teemu Hakkarainen, pour les échanges riches et stimulants de la session de questions. Merci d'avoir joué le jeu de la soutenance en visioconférence partielle, qui s'est finalement déroulée sans accroc.

Star Wars

Il y a longtemps, bien longtemps, dans une ville de l'Essonne lointaine, très lointaine, un groupe de jedis s'était rassemblé sous le nom de l'ordre de SUNLIT. Le plus vénérable d'entre eux s'appelait Maitre Yoda...

... Non pardon, Maitre Andrea Scaccabarozzi. Tu as été un parfait mentor, j'ai beaucoup appris de toi : épitaxie, PV, fab, avec rigueur et force de travail (et bonne humeur), c'était un exemple inspirant ! Inspirants aussi, les maitres jedis qui m'ont si bien accueilli quand j'arrivais en stage au LPN : Julie, Hung-Ling, Jérôme, Clément. Merci Julie pour ton enthousiasme inébranlable, et toute ta maitrise des technos de fab, carac ou de simulations dont tu m'as transmis une partie. Hung-Ling, qui arrive à faire de la magie avec les nanofils que je sortais péniblement de la MBE, tu as souvent forcé mon admiration par ta force de travail et ta rigueur d'analyse. Louis, Thomas et Amadéo, on a mené ce périple ensemble, on s'est entraidé et réconforté (ralé ensemble quoi) face aux épreuves, et il va bientôt arriver à son terme pour nous tous. Il faudra fêter ça avec une paasta. Merci aux autres jedis, qu'ils soient partis ou encore là : Amaury, Ahmed, François, Daniel, Joya, Linh, Maxime, Benoit. Et bienvenue aux padawans ! Federico, tu as fait un super stage avec nous, tu as bien mérité ton premier sabre laser pour affronter ta thèse. Bérengère, Salim, bon courage pour votre propre aventure, et aussi Capucine, j'espère que j'ai réussi à t'indiquer quelles planètes éviter et vers lesquelles il te sera intéressant de voyager !

Mission : Impossible

Votre mission, si vous l'acceptez, est de développer la nouvelle technologie photovoltaïque permettant d'atteindre une efficacité de plus de 30% en tandem sur silicium. Vous pourrez compter sur une équipe de choc au sein de l'IPVF.

Bon courage pour votre mission agents Olivier, Margot, Emilie, Anatole, Sophie, Arpit, Wei. Vous avez su instiller une si bonne ambiance dans les labos et en dehors, maintenant le plus dur reste à faire. Gardez une pensée pour vos prédécesseurs tombés au champ d'honneur : Karolien, Kathy, Adrien, Harold, Guillaume, Raphaël, Marta, Cécile.

L'IPVF est un beau projet, concrétisé par un bâtiment qui rassemble diverses institutions, mais il repose aussi sur des personnes, qui font en sorte que ça marche et qu'une ambiance saine et bienveillante règne. Merci Bérengère, Christophe, Sonia, Ariana, l'équipe d'Antony qui m'avez vu arriver. Merci aussi Florian, Ariana, Liying, Jennifer, Iris, Alexis, Destin, l'équipe s'est renouvelée et agrandie pour permettre à l'ensemble du laboratoire de se mettre en route. Merci Valérie, Sophie, Thibaud, Samuel, Sébastien, Jessica, Etienne, pour votre soutien quand il a fallu commencer à travailler et trouver mes marques dans les labos. Merci Baptiste et Ombline d'avoir ouvert la voie à de nouvelles caracs optiques pour les cellules solaires à nanofils. Merci Nathanaelle et Shanting pour nos essais d'ALD. Merci à toutes les autres personnes avec qui j'ai interagit autour de sujets scientifiques : Daniel Lincot, Laurent Lombez, Jean-Baptiste Puel, Jean-François Guillemolles et j'en passe.

Le cristal magique

'Il existe un cristal magique, qui a le pouvoir de faire revenir l'eau dans la forêt.'

Bon je vous accorde qu'on est loin d'être sûr que le GaAs a ces propriétés, même en phase Wurtzite, mais ça valait le coup de s'y intéresser quand même. Et j'ai pu compter sur l'aide et l'expertise des pontes du laboratoire du C2N. Gilles, merci pour ces heures passées derrières le TEM à observer les nanofils que je t'apportais régulièrement, et merci pour ta patience quand je venais avec mes questions dans ton bureau ! De même pour celles concernant la physique des nanofils, structure, contraintes, nucléation que je venais te poser, Frank. Merci Laurent, *l'homme qui murmurait à l'oreille des MBE*. Merci également Jean-Christophe, Maria, Federico P, Ludovic et Aristide qui m'avez tous aidé à un moment de ma quête.

Iron Man

Les laboratoires de Stark Industries hébergent des projets incroyables. C'est là qu'a été mise au point l'armure de Tony Stark, mais c'est là aussi que sont conçues les nanotechnologies les plus futuristes, de la photonique quantique à la microfluidique.

Ces laboratoires étaient tout d'abord au LPN à Marcoussis, puis ça a (va ?) continué au C2N à Palaiseau. Merci Christophe, cher vieux technologue, pour m'avoir accompagné et formé à toutes sortes de technos de salle blanche, toujours avec un sourire et une anecdote. Merci à vous tous qui avez partagé avec moi votre savoir-faire en salle blanche ou qui m'avez apporté une aide précieuse : Xavier, Natalie, Stéphane G, Martina, Laeticia, Laurent, Ali, Abdou. Merci Alain, Medhi pour votre expertise IT ! Merci à tout le personnel administratif, du secrétariat aux RH. Merci à Elisa de m'avoir accordé du temps et de l'énergie pour travailler sur des solgels, alors que tu étais déjà en rédaction.

Les temps modernes

C'est une usine dans le Val d'Oise où, toute la journée, on règle la machine, on écoute le ronflement de ses pompes, et surtout on la surveille constamment pour détecter le moindre signe annonciateur d'un problème.

Ce n'était pas une mince affaire d'aller à Bezons à l'usine de Riber pour travailler sur la MBE, mais j'y ai également fait des belles rencontres (en plus d'Ahmed et Amadéo). Merci Patrick pour ton aide et tes conseils précieux, on n'aurait pas fait marcher la MBE dans la durée sans toi. Merci également à Samuel et Mihai. Je salue également Youri, pour nos discussions enthousiastes et tes conseils sur la rédaction de thèse !

La gloire de mon père – Le château de ma mère

Les cigales chantent. Le soleil de plomb cogne les façades de pierres, le mistral soulève des tourbillons de poussière. Ici, c'est le sud (le vrai !).

Je n'oublie pas d'où je viens et je remercie mes parents pour ce qu'ils m'ont transmis. La maison familiale est un havre de paix où je peux vous retrouver avec Erwan et Maÿlis, j'en ai particulièrement profité pendant ces derniers mois un peu spéciaux. Une pensée aussi pour toute ma famille et pour mes amis de longue date, ça faisait longtemps que vous entendiez parler de cette thèse, I did it !

Mr and Mrs Smith

Mr et Mrs Smith forment un couple tout ce qu'il y a de plus banal. Pourtant, Mr Smith prépare une thèse sur les cellules solaires à nanofils, et Mrs Smith, une autre sur la cryptographie post-quantique. Ils vont se rendre compte que, pour mener à bien leurs deux missions, ils vont devoir compter l'un sur l'autre et se soutenir mutuellement...

La salle est maintenant plongée dans le noir. Vous êtes assis bien confortablement dans votre fauteuil en velours rouge et le silence s'installe autour de vous. Un projecteur vient de s'allumer.

Ça commence...

Contents

List of acronyms and symbols

APT ..... Atom-probe tomography
BEP ..... Beam equivalent pressure
BF ..... Bright-field
DF ..... Dark-field
HAADF .. High-angle annular dark-field
CCD ..... Charge-coupled device
CCP ..... Capacitively coupled plasma
CIGS ..... $Cu(In,Ga)Se_2$
CL ..... Cathodoluminescence
EL ..... Electroluminescence
EDX ..... Energy-dispersive X-ray spectroscopy
EBL ..... Electron beam lithography
EQE ..... External quantum efficiency
FF ..... Fill-factor
FFT ..... Fast Fourier transform
FWHM ... Full width at half-maximum
HF ..... Hydrofluoric acid
JV ..... Current-Voltage
ITO ..... Indium-tin oxide (In_2O_3:SnO_2)
LCOE .... Levelized cost of energy
MBE ..... Molecular beam epitaxy
ML ..... Monolayer
MOCVD .. Metal-organic chemical vapor deposition
MOVPE .. Metal-organic vapor phase epitaxy
NIL ..... Nanoimprint lithography
NW ..... Nanowire
PCE ..... Power conversion efficiency
PECVD .. Plasma-enhanced chemical vapor deposition
PL ..... Photoluminescence
PV ..... Photovoltaic
RHEED .. Reflection high-energy electron diffraction
RIE ..... Reactive ion etching

RTA ..... Rapid thermal annealing

SAE ..... Selective area epitaxy

SEM ..... Scanning electron microscopy

SI ..... Semi-insulating

SMU ..... Source measure unit

STEM .... Scanning transmission electron microscopy

TCO ..... Transparent conductive oxide

TEM ..... Transmission electron microscopy

VLS ..... Vapor-liquid-solid

VS ..... Vapor-solid

WZ ..... Wurtzite

ZB ..... Zincblende

III-V ..... Semiconductor crystals with compounds from the columns III and V of the periodic table

All elements are denoted with their symbol. In particular:

Al ..... Aluminum

Ar ..... Argon

As ..... Arsenic

Au ..... Gold

Be ..... Beryllium

C ..... Carbon

F ..... Fluorine

Ga ..... Gallium

Ge ..... Germanium

H ..... Hydrogen

In ..... Indium

N ..... Nitrogen

Ni ..... Nickel

O ..... Oxygen

P ..... Phosphorus

S ..... Sulfur

Sb ..... Antimony

Si ..... Silicon

Sn ..... Tin

Ti ..... Titanium

Zn ..... Zinc

General Introduction

Renewables already cover 26 % of the global electricity generation in 2018 [REN21 2019], and this share is expected to increase to 70–85 % by 2050 [IPCC 2018]. The strong impulse for their development is motivated by the increased awareness regarding the human impact on climate change, and more and more competitive prices relative to fossil fuels, due to continuous technological and industrial development. The international community is committed to limit global warming to 1.5 °C above pre-industrial levels, through the adoption of the Paris agreement.

Solar energy conversion, in particular photovoltaics (PV), occupies an important place among renewables, exploiting a virtually unlimited energy source, sunlight, with limited greenhouse gas emissions. The market of PV for terrestrial electricity production is largely dominated by silicon (Si) wafer-based technologies (95 % of the production). Their power conversion efficiency close to 20 % and their ever decreasing cost allow most recently installed large-scale PV systems to produce electricity at a price competitive with other energy sources, without subsidies. However their power conversion efficiency is fundamentally limited below 30 %. Hence, new technologies are expected to replace them within the next 10 years, presumably based on a combination of several solar cells, stacked in a so-called 'tandem' configuration, which maximizes the use of the solar spectrum.

III-V semiconductors have proven to be the best-in-class materials to fabricate high-efficiency PV cells, notably tandems, though they are limited so far to research or space applications due to their high cost. They represent an excellent platform to explore new concepts for high efficiency PV: nanostructures enhancing light absorption, innovative synthesis techniques, understanding of fundamental concepts like hot carriers, contact formation, passivation *etc.* The knowledge gained through studying advanced solar cell designs based on these materials could also be transferred to other areas of PV development, such as thin-films of micro-crystalline materials where the presence of many grain boundaries at the microscale bears comparison with nanostructured materials.

III-Vs being crystalline materials, they are synthesized by *epitaxy*, which is the growth on a pre-existing crystalline substrate. One way to fabricate a III-V/Si tandem solar cell is to use a III-V substrate to grow a few µm-thick III-V layer (the III-V solar cell), and to peel-it off the substrate to stack it on top of a Si solar cell ('bonding' or 'mechanical stacking'). This approach is not only complex due to the difficult bonding technology for the assembly, but also very costly: the III-V substrate, even reused several times for other thin-film growths, is still extremely expensive. Scenarios estimating the industrial cost of producing such solar cells predict prices per watt one order of magnitude higher than today's technologies.

To avoid the extra cost of the III-V substrate, an alternative would be to epitaxially grow the III-V cell directly on top of a Si cell, which is also crystalline. Unfortunately, the lattice-mismatch between both materials leads to the presence of dislocations in the top III-V cell, inhibiting its performances. Growing III-V nanowires (NWs) is an appealing solution since these nanostructures have a small diameter which allows to relax the mismatch strain, and integrate defect-free III-V material on a Si substrate.

In this thesis, my objective is to fabricate a solar cell from an array of core-shell GaAs NWs grown on Si, as a first step toward a tandem solar cell where the Si substrate is also the

bottom cell. Proofs-of-concepts using NWs on lattice-matched III-V substrates have already demonstrated the potential of NWs for solar cells, with efficiencies up to 15.3 % for bottom-up [Aberg et al. 2016] and 17.8 % [Dam et al. 2016] for top-down fabrication schemes. However solar cells based on direct growth on Si substrates exhibit poor performances: up to 4.1 % efficiency for the sole NW solar cell [Dastjerdi et al. 2016], and 11.4 % in tandem configuration [Yao et al. 2015]. In principle, the vapor-liquid-solid (VLS) growth mode using one of the NW elements to catalyze the growth allows to grow high quality NWs on Si substrate. By reviewing the previous literature, I identify the main issues which need to be addressed to make efficient NW solar cells: (1) a difficult control of the vertical yield of NWs on Si substrates, (2) unoptimized crystal quality with the presence of faults, (3) complex estimation and control of semiconductor doping in such nanostructures, and (4) challenges towards the fabrication of a solar cell from a NW ensemble, especially the contact formation.

My first goals are to tackle these different issues independently, and then to fabricate and fully characterize III-V NW solar cells. The manuscript is organized as follows:

- In the first chapter, I introduce the context of this thesis, I review the state-of-the art of III-V NWs for solar cells, and I present the strategy and the design chosen in this study.
- In the second chapter, I introduce the concepts and methods used in this thesis: physics of carrier separation in solar cells, growth of NWs on patterned Si substrates by MBE, and characterization tools for NWs and solar cells.
- In the third chapter I describe the fabrication of homogeneous arrays of defect-free GaAs NWs on Si, as a baseline for more complex structures. I first review the literature of NW growth in ordered arrays, to then identify why growth on Si appears more challenging. I optimize the vertical yield on patterned Si substrates with different NW architectures. Finally, I present my work to limit the number of crystal defects in NWs.
- In the fourth chapter, I focus on core-shell heterostructures and junctions. I first study the NW shell growth of GaAs and wider bandgap III-V materials, then I investigate the mechanisms of core and shell doping in GaAs NWs using cathodoluminescence spectroscopy. Finally I examine composition inhomogeneities in $GaAs_{1-x}P_x$ NWs.
- In the fifth chapter, I fabricate and characterize complete GaAs NW solar cells. I choose specific architectures for the NW devices, then present the development of a fabrication process, in particular the optimization of a transparent front contact. Finally I present the full characterization of core-shell GaAs homojunction devices, and of novel heterojunction devices.

This three-year project was conducted between two institutes in France, starting in April, 2017. Most of my experimental work was realized at the CNRS laboratory *Centre de nanosciences et de nanotechnologies* (C2N). The lab was formerly the *Laboratoire de photonique et de nanostructures* (LPN), located in Marcoussis, until the labs moved to Palaiseau, in August, 2018. I also worked at the *Institut photovoltaïque d'Ile-de-France* (IPVF), a joint research institute gathering academics and industrial, and whose labs were launched in 2018. In 2018-2019, I had access to a MBE machine located in the factory of the equipment manufacturer *Riber*, in Paris area.

The development of NW solar cells is the object of my PhD thesis, but is of course the result of a team work, and many people in the lab were involved in different aspects of the project. Here, I want to clarify my contributions, as well as the ones of the colleagues who worked with me.

I conducted the NW and thin-film growths, using two different MBE machines (Riber 32 and Compact21). This includes most NWs serving the studies in chapters 3 and 4, the solar cells in chapter 5, and the planar layers used as doping references, for which I also performed Hall measurements. I had the chance to work with Andrea Scaccabarozzi (previously post-doctoral researcher at C2N and IPVF), who in particular trained me to the NW growth at my beginning, and who fabricated a few samples presented in this thesis (in Section 3.2, Section 4.2 and Section 5.5).

I performed the fabrication processes in the cleanroom: the Si substrate preparation and mask fabrication, as presented in Chapter 2, the preparation of samples for CL and TEM, the planarization of NW arrays, and the fabrication of full NW solar cells using photolithography, contact evaporation and sputtering. I developed the transparent top contacts by growing and fabricating thin-film samples with localized contacts, and performing electrical measurements. I studied different planarization schemes for NW solar cell fabrication with Andrea Scaccabarozzi. I later transferred and re-developed the fabrication process at IPVF in 2019. The parts I could not handle were the mask patterning using electron beam lithography, and the HF chemistry, for which I was helped by Andrea Cattoni.

As for the characterizations, I took the SEM images of NW ensembles, and performed the analysis of the vertical yield. I participated in all TEM experiments with Gilles Patriarche (researcher at C2N) and I analyzed the images and EDX data. The cathodoluminescence (CL) experiments were realized by Hung-Ling Chen (former PhD student C2N) and Thomas Bidaud (PhD student C2N). I performed all opto-electrical characterizations of NW solar cells: JV, EQE, and their analysis (I was helped by Capucine Tong, PhD student at IPVF, for the last sample fabrication and characterization in Section 5.5). I performed the hyperspectral PL measurements (Section 5.4) with the help of Baptiste Bérenguier and Amaury Delamarre, and I did the analysis in term of Fermi level. The EL measurements (Section 5.5) were realized by Ombline Lafont (Research engineer at EDF) during a previous campaign.

Chapter

1 Introduction

> “*Des rayons qui accompagnent les rayons les plus réfrangibles de la lumière solaire, font éprouver à des lames métalliques plongées dans un liquide, une action telle, qu'il en résulte des effets électriques auxquels on ne peut attribuer une origine calorifique.* ”
>
> Becquerel 1839

Chapter content

1.1 Context of the thesis

1.1.1 Outlook of the energy market and the place of photovoltaics

Climate change

Since the pre-industrial period (1850-1900), human activities have caused approximately 1.0 °C of global warming (Figure 1.1). 186 states and the European Union have ratified the Paris agreement during the COP21, in 2015, through which they commit to reduce their greenhouse gas emissions in order to limit the global temperature rise to 1.5 °C above pre-industrial levels. Limiting global warming to 1.5 °C is possible only if CO_2 emissions are drastically reduced. The United Nations intergovernmental panel on climate change (IPCC) considers that a linear decrease of the global CO_2 emissions from above 40 Gton/year in 2020 to zero in 2040 (Figure 1.1b) is required, with similar efforts to decrease other contributions to the greenhouse effect(Figure 1.1d). Even in this scenario, which assumes important efforts by the consumers, the policy makers and the industrials, important consequences are still expected on biodiversity, on a number of ecosystems, and directly and indirectly to humans [IPCC 2018].

Among others, the sector of energy production needs to undergo deep transformation in order to maintain global warming below 1.5 °C. The share of electricity in the energy mix needs to increase to satisfy the energy needs but without using fossil fuels which are the main contributors to CO_2 emission. Consequently, renewables energies ('renewables') are projected to supply 70 % to 85 % of electricity in 2050, supported by a factor 4–10 increase of investments in low-carbon energy and energy efficiency technologies [IPCC 2018].

Moreover, all pathways that limit global warming to 1.5 °C with limited overshoot project the use of carbon dioxide removal on the order of 100–1000 Gt CO_2 over the 21st century [IPCC 2018]. Such processes also require high amounts of clean energy, increasing the demand for renewables.

The place of renewables

Today's energy market is still dominated by non-renewable energy sources, in particular fossil fuels such as coal, oil and gas, which amount for 79.7 % of the energy consumption in 2018 (Figure 1.2a). Modern renewables comprise the energy sources used for electricity generation (solar, hydropower and wind power mainly), as well as for biofuels, and for heating (biomass, thermal solar, geothermal energy), and amount for only 10.6 % of the global energy consumption [REN21 2019]. They exclude the traditional use of biomass as an energy source by humans, mostly wood for fire, agricultural residues, *etc.*, which are still dominating the energy use in many developing countries.

However, modern renewables are already a mainstream source of electricity, with an estimated share of 26 % of the global electricity generation in 2018 [REN21 2019]. They are developing at a fast rate (Figure 1.2b) with a global annual investment of 289 billion USD in 2018, and, since 2015, the net capacity additions for renewable have been higher than for fossil fuels and nuclear combined [REN21 2019]. Europe in particular is actively working on replacing fossil fuels by renewables, which represented 35 % of its electricity production in 2019 [Agora-Energiewende and Sandbag 2020].

The PV market

In particular, a fast development of photovoltaics (PV) over the past 20 years has led to a global installed capacity of 512.3 GW at the end of 2018, as monitored by the international energy agency photovoltaics system program (IEA-PVPS), see Figure 1.3. The growth rate is faster than other renewables as more than half of the production capacity was installed during the last

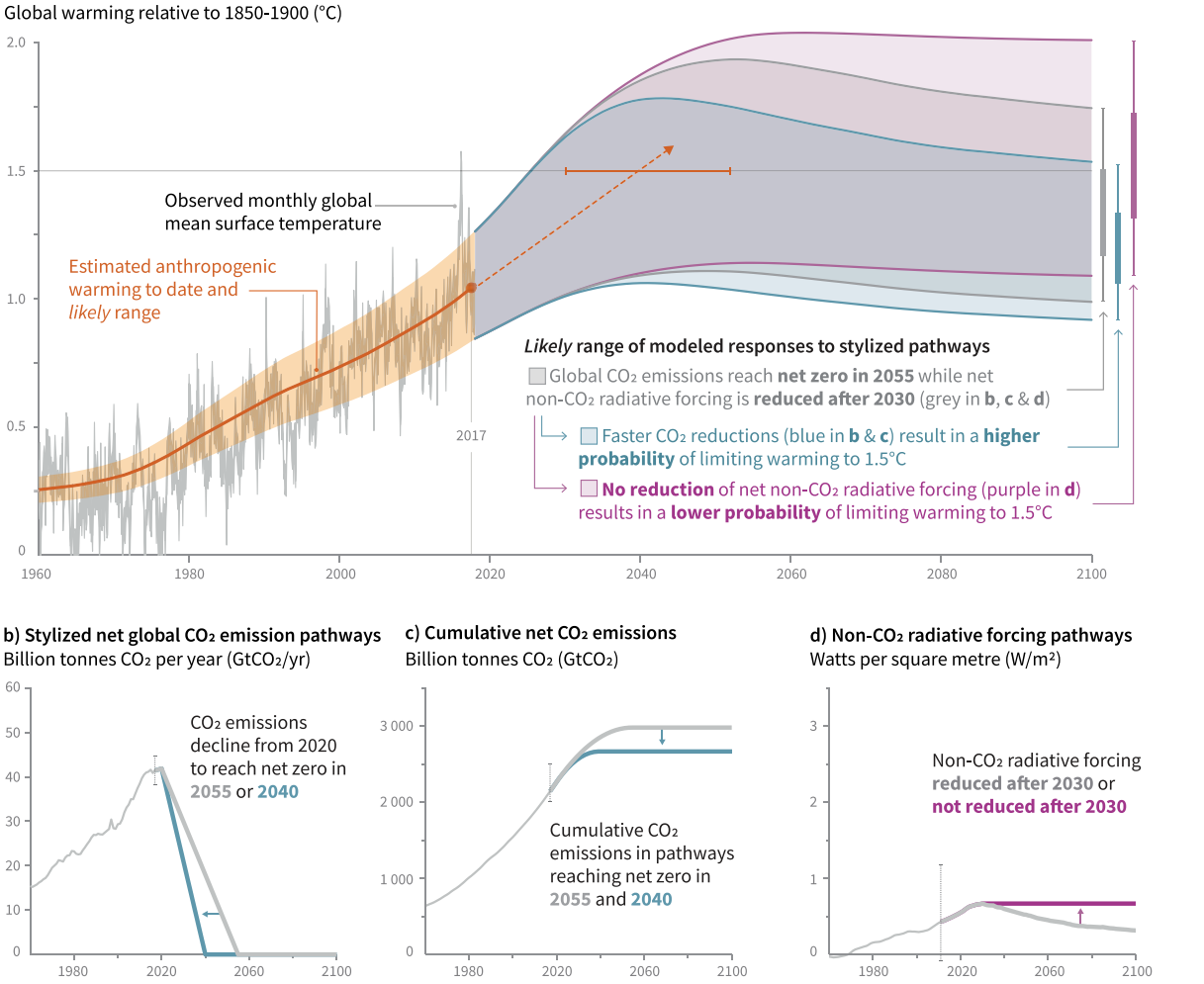

Figure 1.1: *(a) Observed monthly global mean surface temperature (grey line up to 2017) change and estimated anthropogenic global warming (solid orange line up to 2017, with orange shading indicating assessed likely range). Orange dashed arrow and horizontal orange error bar show respectively the central estimate and likely range of the time at which* 1.5 ℃ *is reached if the current rate of warming continues. The grey plume on the right of panel a shows the likely range of warming responses, computed with a simple climate model, to a hypothetical future in which net* CO_2 *emissions (grey line in (b) and (c)) decline in a straight line from 2020 to reach net zero in 2055 and net non-*CO_2 *radiative forcing (grey line in (d)) increases to 2030 and then declines. The blue plume in (a) shows the response to faster* CO_2 *emissions reductions (blue line in (b)), reaching net zero in 2040, reducing cumulative* CO_2 *emissions (c). The purple plume shows the response to net* CO_2 *emissions declining to zero in 2055, with net non-*CO_2 *forcing remaining constant after 2030. The vertical error bars on right of (a) show the likely ranges (thin lines) and central terciles (33rd - 66th percentiles, thick lines) of the estimated distribution of warming in 2100 under these three stylized pathways. Vertical dotted error bars in (b,c,d) show the likely range of historical annual and cumulative global net* CO_2 *emissions in 2017 (data from the Global Carbon Project) and of net non-*CO_2 *radiative forcing in 2011 from AR5, respectively. Vertical axes in (c) and (d) are scaled to represent approximately equal effects on GMST. From [IPCC 2018]*

(a) *Share of different energy sources to the global consumption (2018).* **(b)** *Global energy production by modern renewables.*

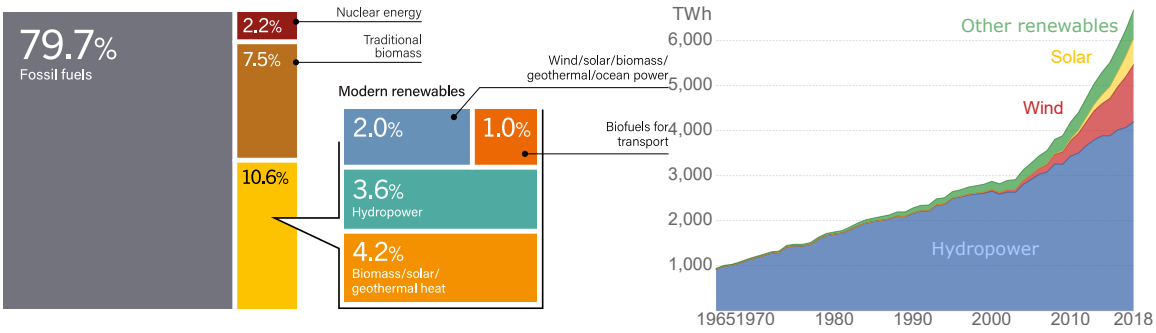

Figure 1.2: *(a) Yearly global primary energy production by sources. From [REN21 2019]. (b) Evolution over the past 50 years for renewables. Data from [BP 2019], chart from* `ourworldindata.org`.

three years. While the market was once led by Europe, it is now in Asia that most PV systems are installed, with more than 50 % in China and India in 2018 (see inset in Figure 1.3).

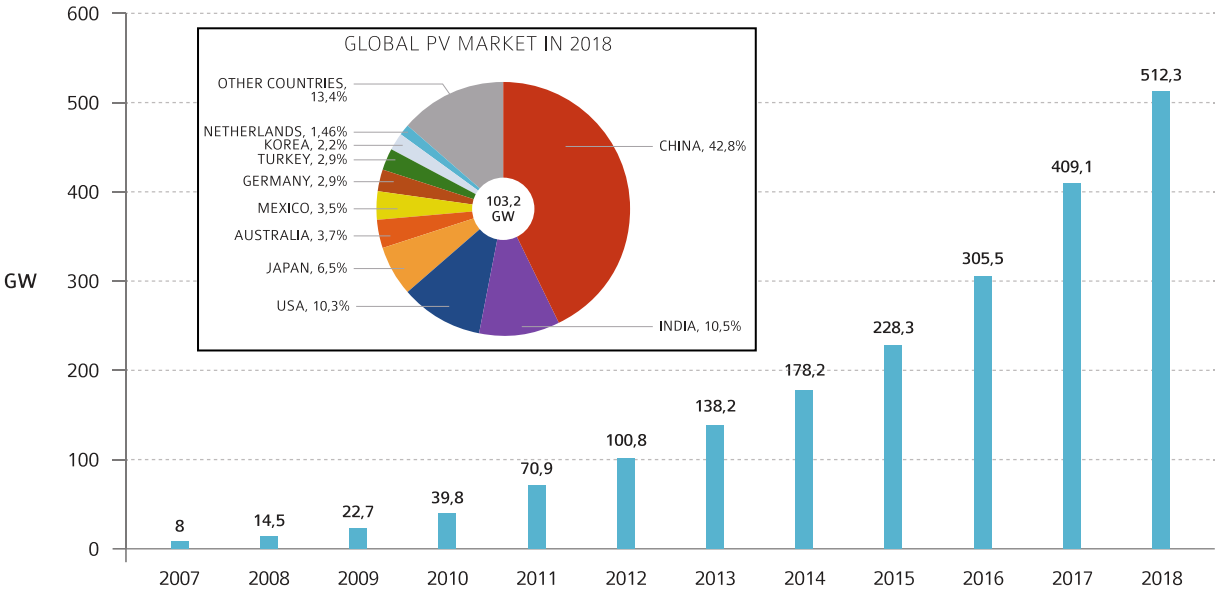

Figure 1.3: *Evolution of cumulative PV installation worldwide. In dark blue are the countries participating in the IEA-PVPS programme. Inset : PV installations in 2018, by country. From [IEA PVPS 2019].*

PV consists in the direct conversion of the radiation energy from the sun into electricity. The potential is enormous, as the Earth surface receives in one hour the same amount of energy as humanity consumes in one year.

Standard PV panels are called 'modules', consisting of several 'cells' connected together. They are essentially made of glass and silicon. Recycling schemes are in place (PV CYCLE in Europe[1]) where the cost of recycling is already included when the panel is sold. In France, an Al-framed silicon panel can be recycled up to 94.7 %. The energy payback time, which is the time needed for the PV system to yield more energy than what was required for its fabrication, ranges typically from 1.5 years to 2.5 years in Europe [ISE 2019], much shorter than its guaranteed lifetime (25 years).

The PV market is dominated by the Si wafer-based technology (95 % of the total production

[1] `pvcycle.org`

in 2017), which has continuously improved over the past decades and whose prices have steadily decreased down to below 0.30 €/Wp in 2018 (Figure 1.4).

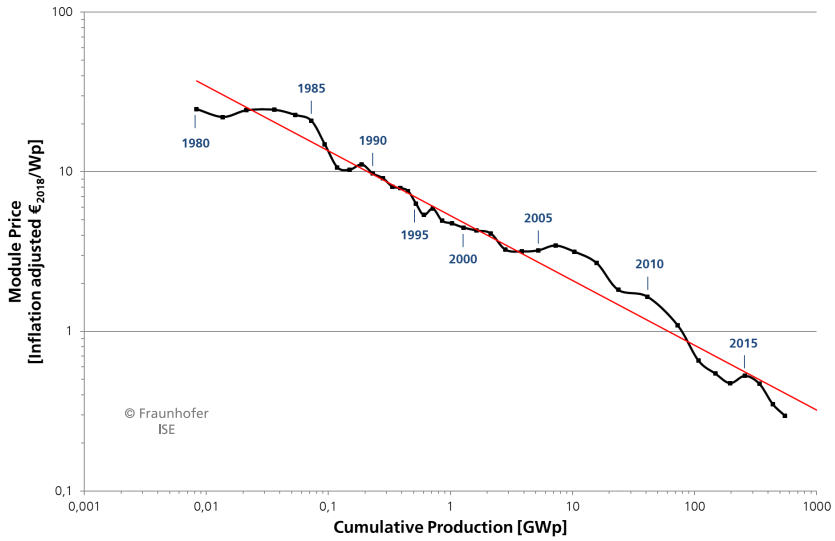

Figure 1.4: *'Learning curve' of the price of PV modules, as a function of the cumulative production. From [ISE 2019].*

For a comparison of the price of electricity produced using PV or other sources, the levelized cost of electricity (LCOE) is defined as the average price of each kWh produced over the lifetime of a PV system, including its manufacturing, installation and end-of-life. Since 2017, many solar projects reach LCOE below 5 c$ per kWh, reaching grid parity in many countries, which means that the cost of electricity is lower than the price at which the local consumer buys it [IEA PVPS 2019]. The prices are now competitive with other traditional energy sources and the PV market is no longer driven by subsidies.

A need for high efficiency PV

Because the price of the PV modules has continuously decreased, it is not the main contribution to the cost of many PV systems. For rooftop installations in Germany for example, the module makes for less than half of the price, the rest comprises the installation labor and the balance-of-system, which is the cost of all electronic components (mostly inverters) needed to connect the system [ISE 2019]. The importance of these additional costs (the module frame and materials, the land, the mounting frames and tracking systems, the balance-of-system) make further reduction of the PV cell cost less impactful. To further decrease the LCOE of PV, improving the power conversion efficiency is now more important as most of these additional costs are fixed and scale with the PV system surface rather than its power output.

The market of renewables and PV in particular has shown remarkable growth over the last decade and they are now a mainstream source of electricity. Future growth and technological development is expected, as ambitious measures are needed to constrain global warming. With the drop of PV module prices, increasing the conversion efficiency is now central in the development of new PV technologies.

1.1.2 Basics of photovoltaics

1.1.2.1 Light absorption

Basic principles. The schematic of a typical solar cell is shown in Figure 1.5. Incident photons are absorbed in the active region, usually a semiconductor. In a semiconductor, the electron energies are constrained within bands; the partially occupied ones are called *valence band* and *conduction band* (Figure 1.5b). The distance between the top of the valence band and the bottom of the conduction band, where electrons cannot exist, is called *energy gap* (E_g), or *bandgap* and is characteristic of the material. A photon is either transmitted if its energy $h\nu < E_g$ (red in Figure 1.5b), or absorbed if $h\nu > E_g$ (green, blue), in which case an electron is excited from the valence band into the conduction band, creating an *electron-hole pair*. The excess energy is lost as heat (blue). The quasi-Fermi levels E_{Fc} and E_{Fv} characterize the electron and hole energy distributions, respectively, when the semiconductor is continuously illuminated and the charge carrier populations stabilize.

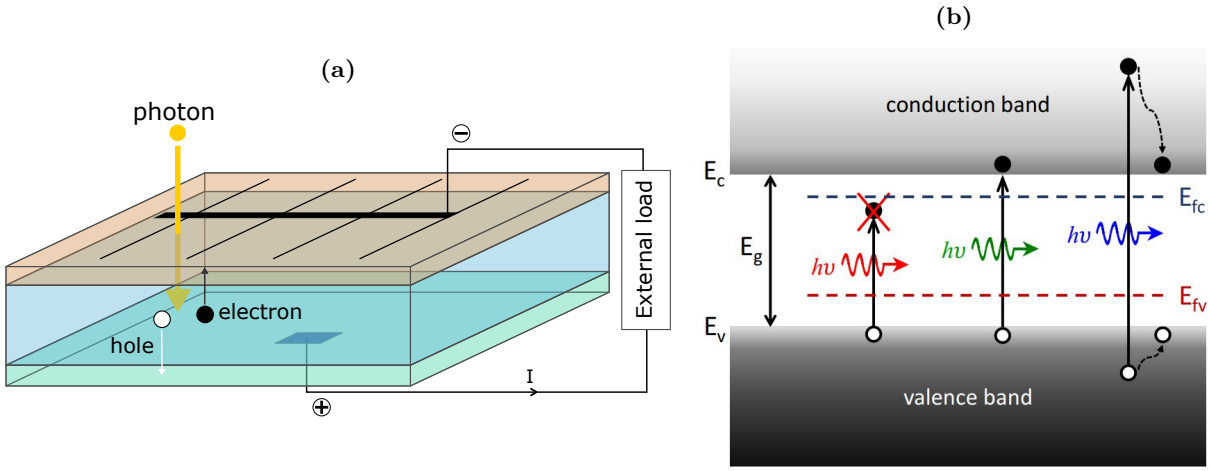

Figure 1.5: *(a) Typical solar cell structure. (b) Energy band diagram of a semiconductor, and interaction with incident photons. From [Chen 2018].*

Once an electron-hole pair is generated inside the solar cell active layer, the presence of selective layers ensures that electrons and holes are collected at opposite sides of the device (orange and green layers in 1.5). The current is then collected by metallic contacts, and can power an external load.

The solar spectrum. Seen from the earth, the sun is basically a disk which occupies an angular diameter of 0.53° in the sky, so that the incidence of sunrays is normal to a solar cell oriented towards it. The reference AM1.5G is the sun spectrum after one pass through the atmosphere with an incidence angle corresponding to temperate terrestrial latitudes (41.8°), the solar spectrum is close to the one of a black-body at 5800 K, minus the absorption of different molecules present in the atmosphere (O_2, O_3, CO_2, H_2O *etc.*) (Figure 1.6). The standard testing conditions of solar cells for terrestrial applications consist in illumination at normal incidence, with the spectrum AM1.5G normalized to a power density of 1000 W m^{-2}.

Due to the trade-off between thermalization losses and transmission losses (Figure 1.5b), some materials are more adequate than others to make solar cells. The theoretical limit for a single junction solar cell was derived by Shockley and Queisser in 1961, taking into account the transmission and thermalization of photons with energy below or above the bandgap, as well as the loss by radiative recombination of carriers and by isothermal dissipation of heat [Guillemoles et al. 2019]. The limit is 30 % for silicon (Si) which has a bandgap of 1.14 eV (1088 nm) at room-temperature [Shockley and Queisser 1961].

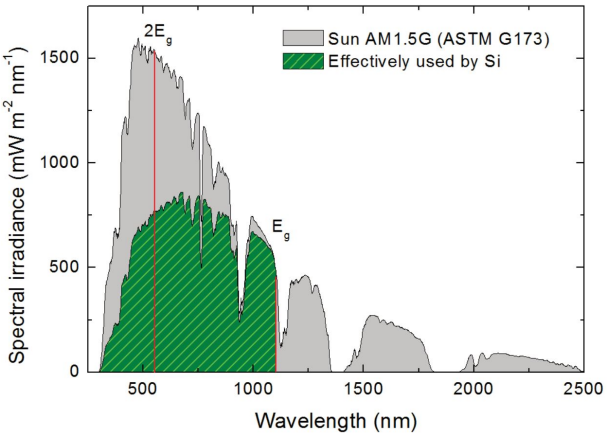

Figure 1.6: *Solar spectral irradiance after 1.5 pass through the atmosphere, as tabulated by the norm AM1.5G. An upper limit for the fraction of the power usable in crystalline Si is represented in the filled area. From [Balestrieri 2014].*

1.1.2.2 JV characteristics

A solar cell is often realized with a p-n semiconductor junction, for which the current density-voltage (JV) characteristic, in the absence of light, is:

$$J(V) = J_0 \left[\exp\left(\frac{qV}{kT}\right) - 1 \right] \tag{1.1}$$

where q is the elementary charge, k the Boltzmann constant, T the temperature (297 K unless specified otherwise). The current density J is the total current normalized by the junction surface area, which in the general case, is considered equal to the contact area and the illuminated area, although it is different in NWs. The *recombination parameter*, J_0, is a term representing the recombination current in equilibrium. In a real solar cell, one must account for the constant photogeneration current J_{ph}, for eventual resistive losses, and current leaking, or *shunt*. Therefore, a solar cell is often modeled according to the schematic in Figure 1.7a, with a diode in parallel with a current source and a resistance, and in series with another resistance. The corresponding JV characteristic is described by:

$$J(V) = J_0 \left[\exp\left(\frac{q(V - JR_s)}{kT}\right) - 1 \right] + \frac{V - JR_s}{R_{sh}} - J_{ph}, \tag{1.2}$$

The corresponding JV characteristic is represented in Figure 1.7, in the dark ($J_{ph} = 0$) or under illumination ($J_{ph} > 0$). The electrical power density generated by the solar cell is the product $P = J \times V$, and is maximized at a point called MP. This maximum power can be related to three quantities which are important metrics for PV performances: the open-circuit voltage (V_{oc}), the short-circuit current (J_{sc}) and the fill-factor (FF), which is defined as the ratio of the maximum power of the cell to the product $J_{sc}V_{oc}$. By evaluating Equation 1.2 at $V = 0$ and $J = 0$, and neglecting R_s and R_{sh}, a useful relation can be found for J_{sc} and V_{oc}:

$$V_{oc} = \frac{kT}{q} \ln\left(\frac{J_{sc}}{J_0}\right) \tag{1.3}$$

The *power conversion efficiency* ('PCE', or η) or simply *efficiency* of the solar cell is the maximum fraction of the incident light power which can be converted into electrical power, and can be written as:

$$\eta = \frac{P_{MP}}{\Phi} = \frac{J_{sc}V_{oc}FF}{\Phi} \tag{1.4}$$

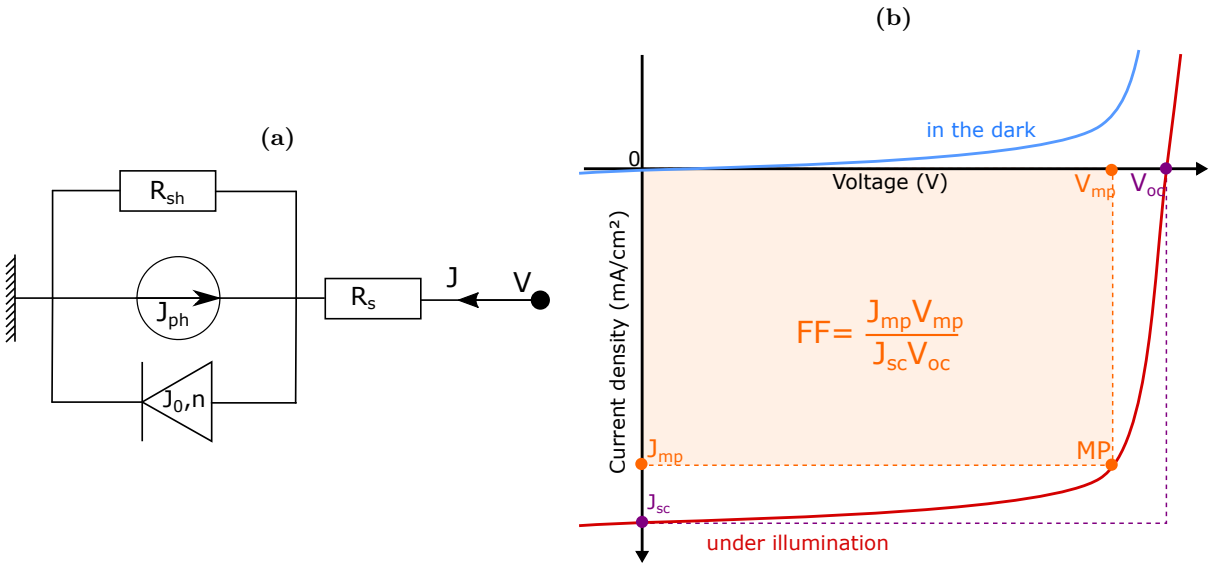

Figure 1.7: *(a) Electrical circuit equivalent to a solar cell under illumination. (b) Current-voltage (JV) characteristic of a solar cell, in the dark (blue) and under illumination (red). MP is the maximum power point*

where $\Phi = 1000\,\mathrm{W\,m^{-2}}$ is the solar irradiance.

The basic principles of photovoltaics were introduced. In particular, the power conversion efficiency is the main figure of merit to compare the performances of different solar cells.

1.1.3 Existing PV technologies for high efficiency and their limitations

1.1.3.1 Silicon solar cells

As stated earlier, the main PV technology consists in poly- or single-crystal-Si wafer based solar cells. The typical efficiency of commercial single-crystal Si modules is 19 % to 20.5 %, an improvement related to the previous years due to the increased industrial production of a new iteration of this technology: the passivated emitter and rear cell (PERC), where both sides are passivated to prevent losses through the non-radiative recombination of electrons and holes (Figure 1.8b). In the laboratories, the highest cell efficiency is 26.7 % for a heterojunction cell with amorphous Si (HJC) and interdigitated back contact (IBC), which further improves the surface passivation and increases the amount of light collected, since all contacts are placed on the cell backside to avoid shading and reflecting the incident light (Figure 1.8b, [Yoshikawa et al. 2017]).

The efficiency limit for Si solar cells is 30 % as derived by Shockley and Queisser [Shockley and Queisser 1961]. However, when taking into account the actual refractive index of Si, the existence of Auger recombination, the bandgap narrowing effect and the new standard solar spectrum, it was shown that 29.4 % was the maximum achievable for Si solar cells [Richter et al. 2013].

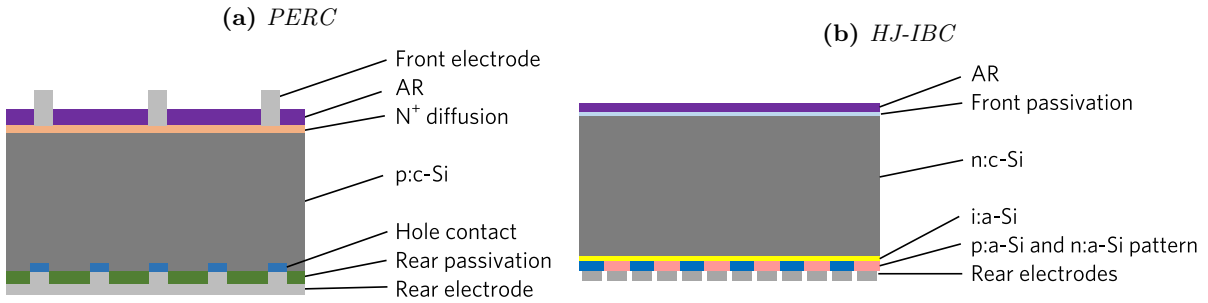

Figure 1.8: *Si wafer-based solar cells. (a) Typical PERC solar cell, commercially available in* 20 % *efficiency modules. (b) Current highest-efficiency lab solar cell, based on a heterojunction with amorphous Si, and an interdigitated back-contact. The front side texturing is not indicated. From [Yoshikawa et al. 2017]*

The maturity of Si PV and the robustness and reliance of its bulk crystalline material have made it the dominant technology suited for large-scale production, and iterative improvement has led to high performances, though they are ultimately limited below 30 %. Next generation PV technologies are therefore expected to build upon the Si cell to increase its efficiency while benefiting from the expertise of manufacturers and the well-established production lines.

1.1.3.2 Polycrystalline thin-films

As an alternative to Si wafer technologies, thin-films represent about 5 % of the global PV module production in 2017 [ISE 2019], essentially shared between two materials: CdTe and $Cu(In,Ga)Se_2$ (CIGS). Despite their lower maturity they present several benefits compared to Si-wafer based solar technologies:

- They are made of direct bandgap materials, for which few-µm-thick layers suffice to absorb most of the incident sunlight, whereas Si wafers (indirect bandgap) are about a hundred times thicker.
- They can be deposited on cheap transparent substrates (glass) or even on flexible ones, well-suited for use in building-integrated photovoltaics for example.
- The module costs are potentially three to four times cheaper than for Si (adjusted per Wp) [ISE 2019]. However the actual price is not cheaper today, mostly due to a much lower cumulative production as compared to Si wafer technologies which have more commercial maturity.
- The carbon footprint of thin-films PV is approximately two to four times lower than that of Si PV since they avoid the energy-demanding purification of Si and semiconductor processing steps [De Wild-Scholten 2013].
- Emerging thin-film materials based on perovskites have recently emerged and shown impressive high power conversion efficiencies (25.2 %[2]), though these performances are achieved for small area devices and they face important stability issues yet preventing their commercialization.

[2]Up-to-date data on record cells for each PV technology is found at https://www.nrel.gov/pv/cell-efficiency.html

Polycrystalline thin-films present several advantages over Si technologies, but have not established themselves as a mainstream technology for terrestrial PV. The rise of perovskites may change the situation, but so far highly efficient (>30 %) and reliable solar cells based on this technology have not been demonstrated.

1.1.3.3 III-V solar cells and multijunctions

III-V solar cells advantages. 'III-V' designates materials consisting of elements from the column III of the periodic table, such as aluminium (Al), gallium (Ga) and indium (In), combined with elements from the column V, such as phosphorus (P), arsenic (As) and antimony (Sb). GaAs, or AlInP are typical III-Vs. They present key advantages for PV:

- Most III-V materials feature a direct bandgap which permits excellent absorption above the bandgap (more than 90 % for a 2 µm thick GaAs solar cells in [Bauhuis et al. 2009])
- III-V solar cells are fabricated by direct growth on a crystalline substrate (epitaxy), which permits extreme control over the thickness and the impurity concentration (doping), so that the carrier concentration and conductivity can be precisely tuned with little compromise.
- The group III (or V) elements are interchangeable so that the composition can be tuned into a wide range of materials, with different optical properties. This allows the direct integration of optimal layers of a solar cell structure (window layer, back surface field, current spreading layer) in a single stack.
- As the layers are typically a few µm thick, they can be removed from their substrate and integrated in flexible, lightweight devices, well suited for space applications or integration onto vehicles or buildings for example.
- An understated advantage for space applications is also their ability to resist harsh space conditions better than other technologies, namely radiation and extreme temperatures ([Bett et al. 1999]; [King et al. 2006]).
- For terrestrial applications, III-V cells also perform better than their Si counterparts under low illumination and high temperature making them even more adequate in non-ideal locations [Silverman et al. 2013]. For a given nominal conversion efficiency, the LCOE of III-V is thus lowered since more energy is generated in non-nominal conditions (cloudy days, morning and evening, *etc.*).

The efficiency record for a single-junction solar cell under one-sun illumination is currently detained by a III-V solar cell made of GaAs, with 29.1 % power conversion efficiency. Like for Si, III-V single junction conversion efficiencies are also ultimately constrained by the Shockley-Queisser limit (33.7 % for a bandgap of 1.34 eV).

But the main advantage of III-Vs is that cells of different bandgaps can be easily integrated together into 'multi-junction' structures, able to exploit more efficiently the solar spectrum and overcome this efficiency limit.

Multi-junctions. In a multi-junction, several solar cells with different bandgap energies are stacked onto each other, each absorbing a part of the incident solar spectrum, which minimizes the thermal and transmission losses. An example of a multi-junction using III-Vs is shown in Figure 1.9, where the cell with the highest energy gap is placed on top (a), so that it is transparent to the light below its bandgap which is transmitted and absorbed by the cells below (b).

III-V multi-junctions have been used to fabricate the world's most efficient solar cells (47.1 % under concentrated illumination, [Green et al. 2019]).

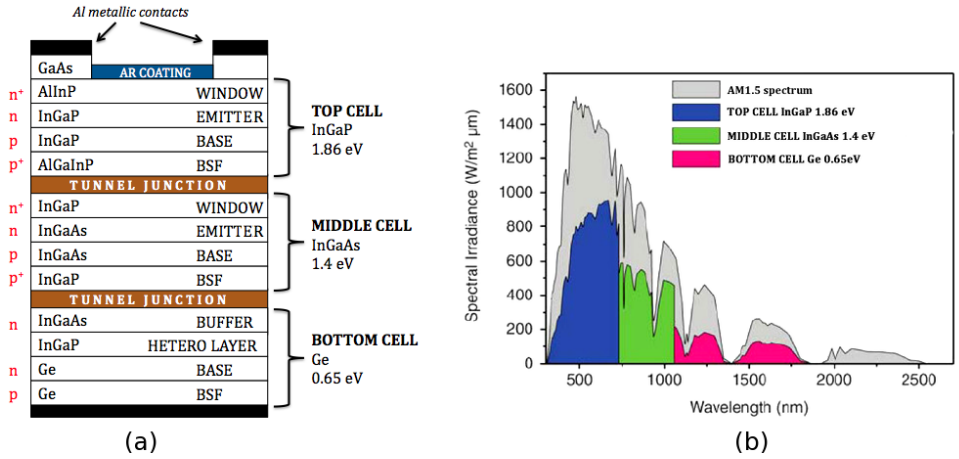

Figure 1.9: *(a) Schematic of a typical III-V triple-junction, grown on a Ge substrate. (b) Fraction of the spectral irradiance collected by each subcell of such structure. From [Yastrebova 2007]*

1.1.3.4 High costs: the problem of III-Vs

Cost and applications. III-V solar cells are not used directly for terrestrial large-scale production due to their high cost. Current module prices often exceed \$150/W [Horowitz et al. 2018], which is roughly 500× the current prices for mainstream c-Si solar (Figure 1.4). While roadmaps for potential cost reductions of III-V PV were realized, proposing to use fast deposition techniques (Hybrid vapor phase epitaxy, HVPE) and substrate reuse (through epitaxial lift-off, ELO), the prices still remain too high mostly due to the expensive III-V substrate ([Ward et al. 2016]; [Horowitz et al. 2018]).

An alternative cost-efficient use of III-V for large-scale electricity generation is the *concentrated PV*, where sunlight is focused on a small area, high efficiency cell using mirrors or Fresnel lenses. Despite the use of an expensive solar cell and a complex tracking system to follow the sun position, it is believed that this technology is viable for terrestrial applications, since the low cell surface area mitigates its cost, and the systems can reach excellent conversion efficiencies [ISE 2015]. However, concentrated PV suffers from a high dependence on ideal conditions (clear sky with direct solar illumination) and from high maintenance needs to compete with standard Si PV systems as of today.

Combinations with Si solar cells. For standard large-scale applications consisting of solar panels without concentration, an attractive way to use III-V is to combine them with Si in order to avoid the extra cost of the III-V substrate and to directly fabricate multi-junction solar cells where the Si substrate serves as the bottom cell, in a so-called 'tandem' architecture.

The cost of such solar cells, if they were industrially produced, was modeled by [Essig et al. 2017]. They considered a technology where a GaInP/GaAs dual-junction is grown on an external substrate and peeled-off the substrate which can be reused for a later epitaxy. The layer is then stacked onto a Si subcell to form a multi-junction (technique detailed in the next paragraph). They envision a near-term price of 4.85 \$/W (Figure 1.10), roughly 15 times higher than today's Si PV. Most of the cost is represented by the III-V deposition method, and the III-V substrate cost, despite optimistic estimations of wafer reuse (50 times, with chemical-mechanical polishing every 10 reuse). In order to decrease the cost, the deposition method envisioned is hybrid vapor phase epitaxy, which allows for extremely fast deposition rates (up to $300\,\mu m\,h^{-1}$ vs $15\,\mu m\,h^{-1}$ for metal-organic chemical vapor deposition, MOCVD), and already proved relevant for III-V solar cells [VanSant et al. 2019]. Using thinner layers can help save material and improve performances, while light-trapping schemes can be employed to preserve high absorption ([Chen et al. 2019]; [Cariou et al. 2018]). More importantly, further decrease of the cost requires that a

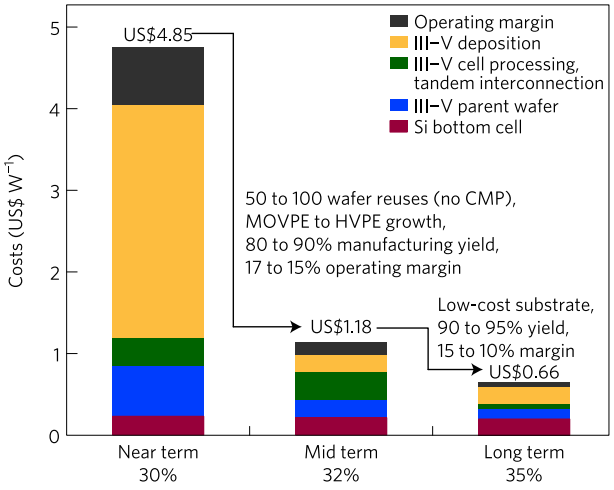

Figure 1.10: *Modelled cost of III-V solar cells on Si, produced industrially, in a scenario where the cost further decreases due to industrial scaling and technological improvements, while the efficiency increases. From [Essig et al. 2017]*

substrate as cheap as Si is used for the epitaxial growth of the III-V, and that a 35 % efficiency be reached in a two-junction (GaInP//Si) design (Figure 1.10). This appears as a challenge as most III-V are incompatible for growth on Si or other cheap substrates.

> III-Vs are today the only materials capable of highly efficient (>30 %), stable solar cells, especially when combined into multi-junctions. Their development for large-scale terrestrial energy production is however hindered by high costs, orders of magnitude higher than Si solar cells. Their integration on Si as tandem solar cells is a possible way to overcome this issue.

1.1.4 III-V/Si tandem solar cells

1.1.4.1 Report of III-V layers on Si

Today's best performing III-V-on-Si solar cells are achieved by fabricating both solar cells separately, on a Si and a III-V substrate, respectively, and joining them in a later step (Figure 1.11).

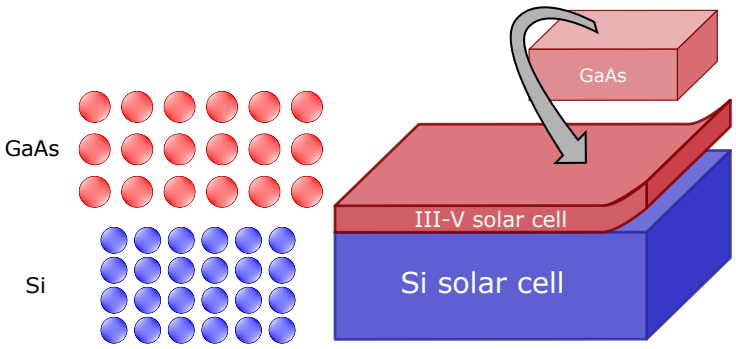

Figure 1.11: *Integration of III-V on Si for a tandem solar cell, by growth of the III-V cell on a III-V substrate, followed by layer peeling and report onto a Si subcell.*

Room-temperature wafer bonding can be used, which consists in creating a monolithic interface where both cells are atomically joined and connected by a tunnel junction. A conversion efficiency of 34.1 % has been reached ([Cariou et al. 2018]; [Green et al. 2020]), and the simple

electrical integration of two-terminal solar cells into modules enables industrial scaling. However, the surface must be polished and activated by removing all oxides and impurities with an ion-beam process in a cleanroom environment, and high pressures (2.5 kN) have to be applied to ensure an interface exempt of voids and with high bonding strengths. These steps are technologically demanding and can mechanically stress the materials. Alternative, low-cost bonding techniques are investigated [Makita et al. 2020].

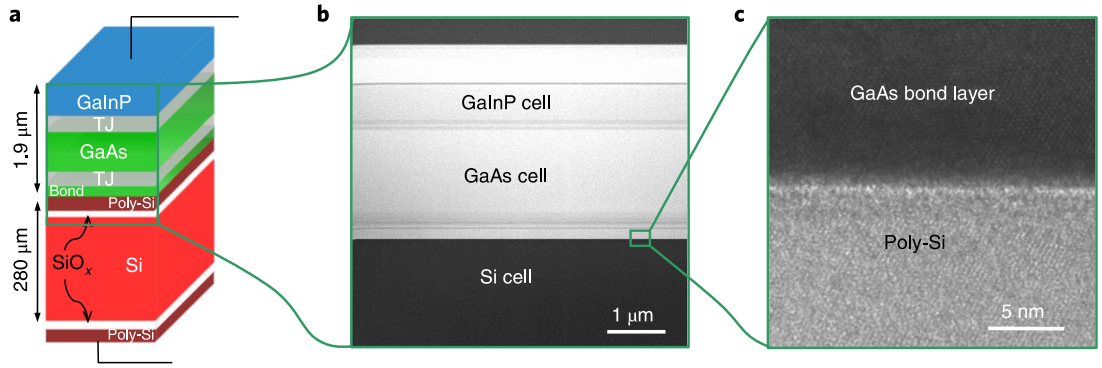

Figure 1.12: 33.3 % *efficient GaInP/GaAs//Si tandem solar cell, fabricated by wafer bonding. The GaInP/GaAs top double-junction was previously grown on a III-V substrate and is then bonded onto the Si bottom cell. (a) Structure of the tandem cell. (b) Cross-section scanning electron microscope (SEM) view of the stack, with real dimensions. (c) Zoom-in on the Si/GaAs, atomically flat, bonding interface. From [Cariou et al. 2018].*

Another method is the mechanical stacking of the cells with transparent electrodes in between, so that the resulting device has a four-terminal configuration. This relieves the constraints on the interface quality and cleanness, and the independent control of the cells enables higher conversion efficiencies, up to 35.9 % [Essig et al. 2017].

Efficient tandem solar cells on Si are fabricated by growing the III-V layer on an external substrate and transfer on Si. In addition to the costs (including the III-V substrate), the complex integration of a 4-terminal device into standard PV panels, or the highly sophisticated technology required for wafer bonding are other limitations to their development.

1.1.4.2 Direct growth of III-Vs on Si

III-Vs are crystalline materials, and the III-V solar cells are fabricated by epitaxy, a deposition process where newly formed layers retain the crystal structure of the underlying substrate.

Anti-phase domains. Contrary to the Si crystal, III-Vs are polar, meaning that the group III and group V atoms are not interchangeable in the lattice. As a consequence, anti-phase boundaries are formed where III-V domains of different polarity coexist and coalesce. But solutions exist to solve this problem, through the formation of biatomic steps at the Si surface, achieved with chosen surface orientations and pre-growth thermal treatment [Kroemer 1987]. Nowadays, better understanding of growth initiation has been reached [Lucci et al. 2018] and with optimized Si surface preparation and growth initiation, all defects related to the heteroepitaxy of GaP on Si could be avoided, first using molecular beam epitaxy (MBE) [Grassman et al. 2009] then MOCVD [Grassman et al. 2013].

Lattice- and thermal-mismatch. A more serious issue is the difference of the inter-atomic distance (lattice parameter) between both crystal materials. It differs by 4 % between Si and

GaAs. This mismatch is relaxed plastically by the introduction of dislocations in the III-V layer, which break the crystal continuity (Figure 1.13). Further stress can arise from the difference in thermal expansion coefficient between the materials, leading to further dislocation generation during cooldown from the growth temperature (typically 600 °C). High density of dislocations, above 10^8 cm^{-2} for GaAs/Si solar cells, result in poor device performances as they act as recombination centers [Dimroth et al. 2014]; [Feifel et al. 2018]. A lot of work has been done towards reducing this density, through annihilation by annealing cycles, or confinement in few µm thick graded buffer layers. Efficiencies close to 20 % have been demonstrated for AlGaAs/Si double-junction [Umeno et al. 1998] and GaAs/Si two-junction, three terminal device [Soga et al. 1996]. With the optimization of Si/GaP interfaces, GaInP/GaAs/Si triple-junction have received more attention [Ringel et al. 2013], and benefit from the use of GaAsP buffers whose high bandgap lets photons reach the Si unabsorbed. Efforts were dedicated to prevent degradation of the Si cell during III-V growth, and to further confine dislocation [Feifel et al. 2018], leading to a recently reported 24.3 % efficiency solar cell [Green et al. 2020].

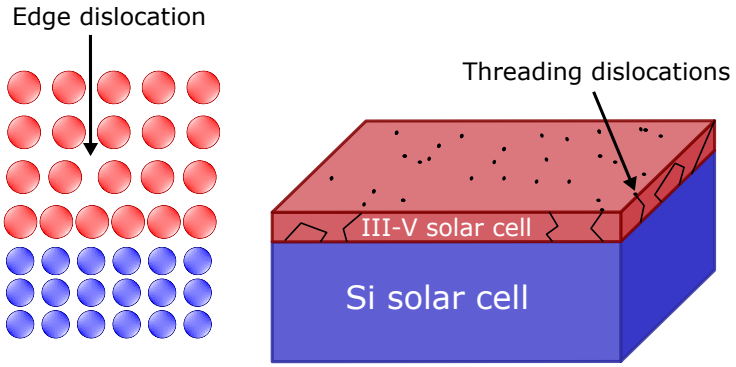

Figure 1.13: *Direct growth of III-V layer on Si, with the corresponding arrangement of atoms at the interface.*

Thermal budget. Strategies to limit dislocations often rely on thermal cycles, and the III-V layer growth itself is performed at high temperatures (up to 700 °C by MOCVD) for several tens of minutes. Such high thermal budget can activate diffusion processes in the underlying Si solar cell, in particular dopants can diffuse from one region to another, annihilating the electronic properties of the solar cell. This is especially critical for the thin, highly doped tunnel junctions, and special care must be paid to limit the growth temperatures.

The direct growth of planar III-V layers on Si is limited by the problem of the interchangeable III-V polarity, of the high thermal budget applied on the Si cell during III-V growth, and most of all, by the dislocations induced by the growth of lattice-mismatched materials.

1.1.4.3 Nanowires: a potential solution?

What are nanowires? *Nanowires* (NWs) typically designates elongated structures, with a diameter of the order of several nm up to tens of nm and more, and with a high aspect ratio (long structures). They can be made of several materials including semiconductors, which opens opportunities for opto-electronic devices ([Dasgupta et al. 2014]; [Barrigón et al. 2019]), among which photo-detectors, transistors, light-emitting diodes, and solar cells ([Garnett et al. 2011]; [Lapierre et al. 2013]; [Otnes and Borgström 2017]). In this work, I extend this definition to designate columnar structures with diameters of several hundred nanometers, and aspect-ratio

below 10, which could be better termed as *nano-* or *micro-pillars*. III-V NWs present several advantages toward the realization of III-V/Si tandem solar cells.

Solving the lattice-mismatch. NWs offer a solution to the lattice-mismatch and thermal-expansion-coefficient-mismatch issues preventing the direct growth of III-V on Si. Indeed, due to their small diameter, they have a small surface in contact with the Si substrate, and the strain in the crystal lattice can be elastically relaxed into the NW without the creation of dislocations (Figure 1.14). Indeed, in GaAs/Si axial NW heterostructure, the mismatch strain was estimated to be relieved for NW diameters up to 100 nm([Cirlin et al. 2009]; [Ye and Yu 2014]).

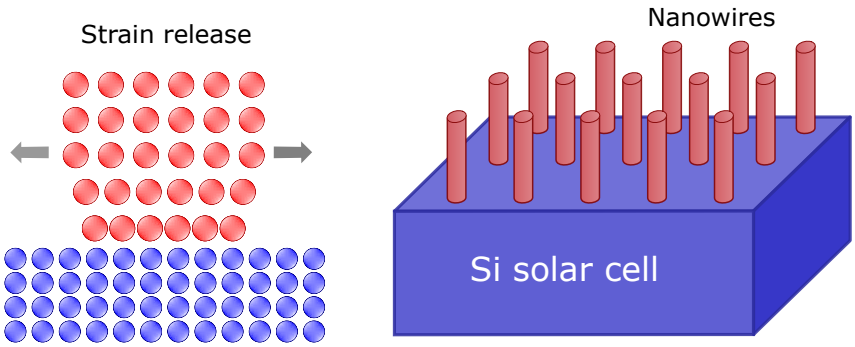

Figure 1.14: *Schematic of a NW-on-Si tandem solar cell. The crystal lattice relaxes elastically above the interface with the Si substrate thanks to the finite NW diameter.*

Light-trapping and equivalent thickness. Due to their small size, light-absorption by NWs cannot be treated using ray optics. They behave like antennas, concentrating the incoming light in their small volume [Krogstrup et al. 2013]. Resonant absorption mechanisms occur in NW arrays such as Fabry-Pérot modes, or waveguide modes, which results in enhanced anti-reflection properties, and light-trapping into the NW array. Depending on its geometrical parameters (NW height, diameter, array pitch), the reflection can be minimized and effective broadband absorption can be reached, which was studied theoretically ([Garnett and Yang 2010]; [Diedenhofen et al. 2011]; [Kupec and Witzigmann 2009]; [Anttu and Xu 2013]; [Huang et al. 2012]; [Azizur-Rahman and LaPierre 2015]; [Anttu 2019b]) and experimentally ([Ghahfarokhi et al. 2016]; [Dam et al. 2016]). For example, 97 % absorption was measured in an InP NW array on an InP substrate (and 80 % absorbed in the NW array alone according to calculations) [Diedenhofen et al. 2011]. The array approximative dimensions (diameter 100 nm, length 3 µm and square pitch of 513 nm) result in an equivalent thin-film thickness of about 100 nm, whereas several µm are typically needed for absorption in planar layers.

High absorption even for large incident angles ([Diedenhofen et al. 2011]; [Dam et al. 2016]) makes them attractive to collect diffuse light in solar cells.

Bottom-up fabrication. An enhanced light absorption in a small volume can result in important cost savings if small amounts of material are used to fabricate the NWs, as a ten-fold reduction of volume compared to planar layer can still result in a similar absorption in a GaAs NW array [Chen 2018]. These potential cost savings are only possible if the NWs are fabricated by addition of material onto the substrate (bottom-up approach) instead of etching away pre-existing material to shape a bulk layer into nanowires (top-down approach). Hopefully, several techniques allow for the localized and unidirectional growth of semiconductor structures. The most famous and employed one is the so-called vapor-liquid-solid mode, where the NW growth is catalyzed by a particle at its top [Wagner et al. 1964], allowing for fast localized growth with efficient use of material.

Cost-efficient tandem on Si. Like for their planar counterparts, high efficiencies are expected for NWs-on-Si tandem solar cells, up to 33.8 % according to calculations [LaPierre 2011a]. The development of NW solar cells is still at a research level and requires the use of expensive methods incompatible with industrial production (growth by MBE, cleanroom fabrication processes, *etc.*). However, going back to the cost analysis of future planar GaAs//Si tandem solar cells (Figure 1.10), one can see that NWs already permit to save the III-V parent substrate cost by using the Si subcell directly as a low-cost substrate. Fast growth of NWs with low-cost deposition techniques like HVPE is possible [Ramdani et al. 2010] and could lead to similar cost reduction of the III-V deposition as in this roadmap, especially considering that less material is deposited for NWs thanks to their efficient light-trapping. If the cost of the substrate preparation (patterning) before NW growth is kept low, by choosing scalable techniques such as nanoimprint lithography for example, a similar target as in Figure 1.10 could be realistically attained, namely below 1 $/W tandem solar cells close to 35 % efficiency.

Nanowires appear as a solution to realize tandem-on-Si since they can alleviate the lattice-mismatch-induced defects, and could also lower the material costs due to their light-trapping properties.

1.2 State-of-the-art and aim of the thesis

1.2.1 Nanowire solar cells: state-of-the-art

III-V NWs for solar cells have been investigated for two decades and several reviews provide a comprehensive overview of what has been achieved with different materials and technologies ([Garnett et al. 2011]; [Lapierre et al. 2013]; [Otnes and Borgström 2017]; [Barrigón et al. 2019]; [Chen and Roca i Cabarrocas 2019]). In particular, several solar cells have been demonstrated with GaAs or InP NW arrays grown on GaAs and InP substrates, or directly etched down from pre-existing bulk structures.

Aside from these promising demonstrations, there is a specific challenge for GaAs NW solar cells on Si. Here, I want to review the main results of the literature and identify the major blocking points towards high efficiency devices. In Table 1.1, I summarize the recent and best literature results regarding III-V NW solar cells with a particular focus on the direct growth on Si for tandems.

1.2.1.1 Patterned or unpatterned substrate?

NW growth can be realized in ordered arrays, where the NW positions are localized in order to arrange them into periodical patterns. This can be done by selective deposition of Au nanoparticle, or by drilling holes in a mask onto which growth is inhibited. Conversely, without such substrate preparation, unordered NW growth can be realized, where catalyst particles are randomly dispersed on the substrate. This can be done for example by using aerosol sprays of nanoparticles [Ohlsson et al. 2001], by metal layer deposition and plasma treatment to form droplets [Misra et al. 2013], or by exploiting the formation of pinholes in the Si native oxide layer, where the catalyst atoms preferably coalesce, localizing the epitaxial growth on the underlying crystalline substrate ([Matteini et al. 2014]; [Matteini et al. 2016]).

Organized growth is preferred for optimal performance of a nanowire array solar cell. Besides the advantage of tuning the light-trapping in the NW device, controlling the NW inter-distance (array pitch) also permits uniform and reproducible growth. Indeed, in a NW array, the equidistant spacing ensures that each NW surroundings are identical during growth, and because the NW growth rate, crystal structure and doping levels are most often controlled by the local material supply, it results in more homogeneous properties among the NWs. These parameters are critical to control as millions of NWs are to be connected together into mm^2 devices.

However, is the extra step and cost of patterning worth the possible gain in reliability and performance?

Unordered growth was successfully used to fabricate Si NW solar cells with relatively high power conversion efficiency (8.14 % in [Misra et al. 2013], 12.9 % in [Togonal et al. 2016] with a top-down approach). However, similar approach with III-V NWs lead to low efficiencies (0.7 % in [Mikulik et al. 2019], for example). This is probably due to the higher sensitivity of III-Vs on surface recombination and depletion, especially GaAs. Consequently, all reported III-V NW solar cells were grown in ordered arrays, with the exception of the example above. Low-cost patterning techniques such as nanoimprint lithography, nanosphere lithography, block copolymers or laser interference lithography, have been used to localize NW growth, and could be compatible with the industrial manufacturing of cost-efficient cells.

> Patterned substrates are preferred, as the NW array uniformity is critical for III-V NW solar cells.

Table 1.1: *Recent NW array solar cell performances for various fabrication technologies.* [a]*Best performing GaAs planar solar cell also indicated for comparison. Two tandem-on-Si NW solar cells are also reported. All junction geometries are p-(i-)n following the NWs growth direction, except for* [b] *which are n-p. Adapted and actualized from ([Lapierre et al. 2013]; [Otnes and Borgström 2017]; [Barrigón et al. 2019]).*

Reference	Material	Structure	Substrate	Growth method	Surface passivation	PCE (%)	FF (%)	J_{sc} (mA cm^{-2})	V_{oc} (V)
[Kayes et al. 2011][a]	GaAs	planar	GaAs	VS (MOCVD)	–	29.1	86.7	29.78	1.127
[Boulanger et al. 2016]	GaAs	radial	p-Si	Self-catalyzed	AlInP	3.3	46.5	18.2	0.39
[Dastjerdi et al. 2016]	GaAs	radial	p-Si	Self-catalyzed	AlInP	4.1	40.0	22.8	0.45
[Mikulik et al. 2019]	GaAs	radial	p-Si (unpatterned)	Self-catalyzed	PDMS	0.7	–	10	0.2
[Mariani et al. 2013b]	GaAs	radial	n-GaAs	SAE	GaInP	7.43	69	18.9	0.57
[Yao et al. 2014]	GaAs	axial[b]	n-GaAs	SAE	none	7.58	63.65	21.08	0.565
[Aberg et al. 2016]	GaAs	axial	p-GaAs	Au-catalyzed	AlGaAs	15.3	79.2	21.3	0.906
[Borgström et al. 2018]	GaAs	axial	Peel-off (GaAs)	Au-catalyzed	AlGaAs	3.5	59	6.8	0.860
[Gao et al. 2019]	InP	axial	p-InP	SAE	none	9.23	75.0	22.5	0.55
[Wallentin et al. 2013]	InP	axial	p-InP	Au-catalyzed	SiO_x	13.8	72.4	24.6	0.779
[Otnes et al. 2018]	InP	axial	p-InP	Au-catalyzed	SiO_x:Al	15.0	77.0	26.64	0.730
[Yoshimura et al. 2013]	InP	radial	p-InP	SAE	AlInP	6.4	59.6	23.4	0.46
[Dam et al. 2016]	InP	axial	p-InP	Etch down	SiO_x	17.8	79.4	29.3	0.765
[Yao et al. 2015]	GaAs/Si	Tandem axial[b]	Si n-p	SAE	none	11.4	57.8	20.64	0.956
[Wood et al. 2017]	GaAsP/Si	Tandem radial	Si p-n	self-catalyzed	AlInP	3.51	39.6	7.65	1.16

1.2.1.2 Best proofs-of-concept and limitations

Top-down fabrication. As a proof-of-concept to illustrate the potential of the NW array geometry, several groups have fabricated it by etching away the material from a pre-existing bulk Si ([Garnett and Yang 2010]; [Togonal et al. 2016]) or III-V [Cho et al. 2011]; [Dam et al. 2016] solar cell. This leads to uniform arrays of NWs, typically tapered into cones, which is beneficial for light absorption [Diedenhofen et al. 2011]. The III-V NW solar cell with the highest efficiency reported was fabricated in this manner, by etching an InP planar solar cell [Dam et al. 2016]. A remarkable improvement of the absolute photoluminescence (PL) compared to the equivalent planar solar cell suggests that higher V_{oc} are attainable in the NW geometry, due to light concentration and lower photon escape probability [Cui et al. 2016], which illustrates the potential and interest of the NW geometry for efficient light trapping. It also indicates that enhanced surface recombination alone do not justify why NW solar cells fabricated in the bottom-up fashion still perform much less than their planar counterparts (Table 1.1), but that other growth-related issues still need to be solved.

Au-catalyzed growth on III-V substrate. Historically, the VLS growth of III-V NWs was first performed using gold (Au) nanoparticles as catalysts. This approach allows for independent tuning of growth fluxes and parameters, which permits to optimize the growth with high reproducibility. It has been developed to maturity in particular by the groups at Lund University, where the best bottom-up InP ([Otnes et al. 2018]) and GaAs ([Aberg et al. 2016]) NW solar cells were fabricated (see Table 1.1).

However, Au-catalyzed growth suffers from important drawbacks for the perspective of tandem solar cells on Si.

1. The Au nanoparticle cannot be removed *in situ*, so that an extra post-growth processing step is required to etch it away. Indeed, leaving it on the NWs would lead to degraded

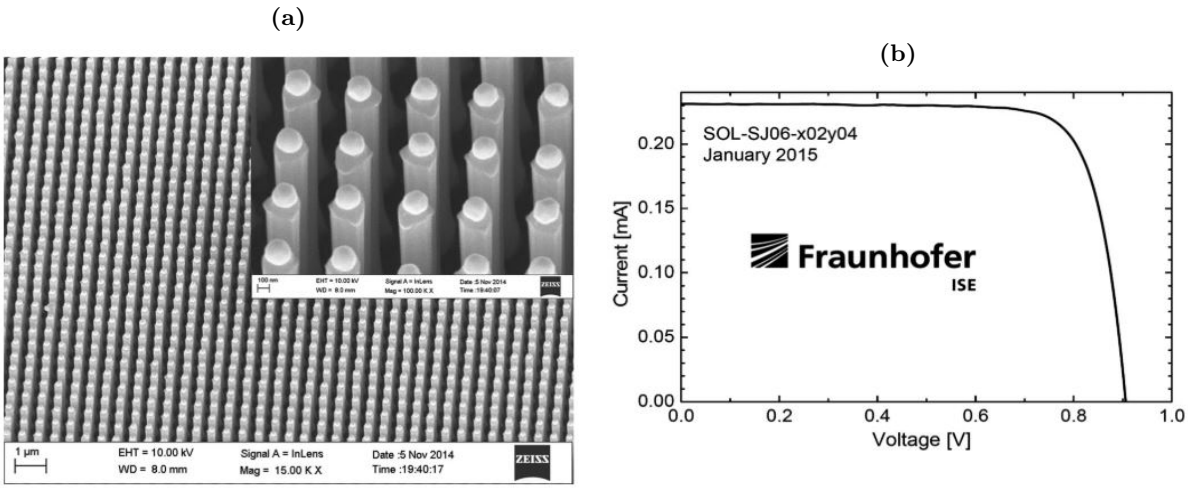

Figure 1.15: *(a) SEM overview of a Au-catalyzed GaAs p-n NW array grown on GaAs substrate, and (b) JV characteristic of the final device. From [Aberg et al. 2016].*

performance due to important parasitic light absorption in the metal [Hu et al. 2012].

2. Au was reported to incorporate in III-V NWs during the VLS growth, to the order of 10–100 ppm ([Perea et al. 2006]; [Bar-Sadan et al. 2012]). Au is known to form deep-states in III-V compounds, which can act as traps or recombination centers and impede the minority carriers lifetime in NWs [Breuer et al. 2011]. Despite this issue, the current best efficiency solar cells are grown in this manner (Table 1.1), and later studies reported reasonably high carrier lifetimes (about 1 ns) for Au-catalyzed GaAs NWs ([Jiang et al. 2013]; [Joyce et al. 2014]; [Aberg et al. 2016]). While it suggests that the presence of Au might not be too detrimental, the performances are still too far from ideal to say that Au-induced defects will not limit the ultimate performances of NW solar cells.

3. If the extent of the detrimental effect of Au incorporation in III-V is still debated, Au is notoriously incompatible with Si as it creates deep recombination centers, and readily diffuses in bulk Si even at moderate temperatures. This would result in very degraded performances of the Si subcell in a tandem configuration. Moreover, Si can alloy with Au in the droplet catalyst in large quantities, resulting in important non-intentional dopant incorporation in Au-catalyzed NWs.

   Solutions to combine the Au-catalyzed NW growth with integration on Si have been sought for. Growth of the NW array on a III-V substrate followed by embossing in a polymer film allows in theory to peel it off the substrate and integrate it on Si. The III-V substrate could be reused. However, efficiencies are degraded during this process which needs further development (Table 1.1).

   Another promising technology is to grow the NWs without employing any substrate, only using Au catalysts flowing inside a modified MOCVD chamber [Heurlin et al. 2012]. This so-called Aerotaxy process has been developed at SolVoltaics[3] with Lund University (Sweden) and produces III-V NWs including heterostructures and junctions ([Metaferia et al. 2016]; [Barrigón et al. 2018]). They developed a technique to vertically align the NWs onto a substrate in a later step [Borgström et al. 2018], which is then embossed into a film compatible with integration on Si for tandem. Despite its potential, this ambitious technology needs a lot of technological development, and due to a lack of further funding the company SolVoltaics filed for bankruptcy in 2019.

[3] solvoltaics.com

NW array solar cells have been fabricated with already high conversion efficiencies, proving the potential of the geometry for high efficiency applications. However, the techniques employed for such results are not compatible with integration on Si for tandem cells.

1.2.1.3 Growth on Si by selective area epitaxy

The direct growth of III-V NWs on Si is more attractive than the above-mentioned techniques for tandem solar cells. However, due to the constraints of the heteroepitaxy on Si and the impossibility to use Au catalysts, the growth is hard to control and the solar cell performances are not yet on par with growths on III-V substrates (Table 1.1).

In particular, several groups have used selective area epitaxy (SAE) to grow NW ensembles, where holes in an inert mask on the growth substrate enable nucleation only in certain locations. Carefully chosen growth conditions lead to faceted nanowires formation at these locations, and the difference in nucleation energy on the different facets ensures continued one-dimensional growth [Otnes and Borgström 2017].

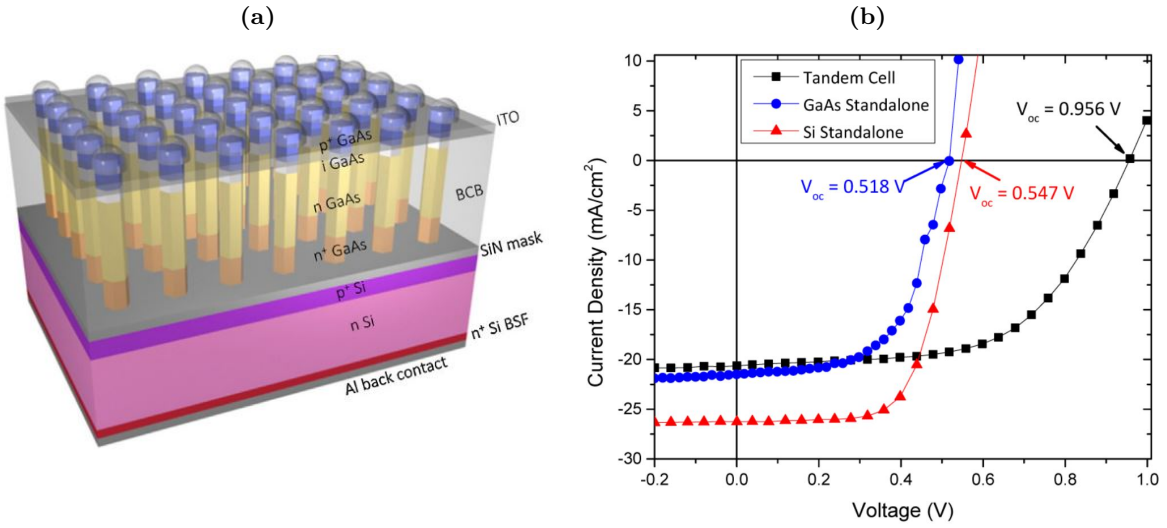

Figure 1.16: *(a) Schematic and (b) JV characteristic of a tandem solar cell made of GaAs NWs grown by SAE-MOCVD on a Si subcell. Current matching and voltage addition are demonstrated. From [Yao et al. 2015].*

The group of Fukui *et al.* drove the development of this technique for solar cell applications, with first demonstrations of NW solar cells at 6.35 % efficiency using InP ([Goto et al. 2009]; [Yoshimura et al. 2013]), 4.01 % with GaAs [Nakai et al. 2013], and 7.14 % with InGaAs [Nakai et al. 2015].

Subsequent development of this technique for solar cells was carried out by two separate groups both at Los Angeles (USA): University of California and University of Southern California. They both reported in one year GaAs NW solar cells with a similar efficiency about 7.5 % ([Mariani et al. 2013b]; [Yao et al. 2014]). Interestingly, the NW junction geometries were different as Mariani *et al.* used a n-i-p core-shell structure, with a GaInP passivation to limit surface charge and recombination, whereas Yao *et al.* employed an n-i-p axial junction without any surface passivation but still reaching a similar efficiency, suggesting that this geometry is more robust to attain high efficiency. Building upon their control of the NW top-cell, Yao *et al.* realized a tandem solar cell by direct growth on Si substrate [Yao et al. 2015]. This tandem cell included a tunnel heterojunction through the p^+-Si/n^+-GaAs interface, allowing the current matching of the two cells and the voltage addition up to 956 mV [Yao et al. 2015]. Their device

is still limited in performance since they did not use a state-of-the-art Si bottom cell (which needs to be (111)-oriented), nor any shell passivation of the GaAs top-cell.

SAE typically suffers from high crystal defect densities compared to catalyzed growth, possibly limiting the best performances attainable ([Tomioka et al. 2008]; [Madaria et al. 2012]; [Haas et al. 2013]; [Bologna et al. 2018]; [Ruhstorfer et al. 2020]). It is also typically performed at high temperature (up to 750 °C), which might be detrimental to the Si bottom junction, especially if the tunnel junction is already implemented in the substrate as the dopants can diffuse at such temperatures. The need for very specific conditions to promote unidirectional growth makes the technique hard to optimize, especially when dopants are supplied, which modify the growth dynamics [Barrigón et al. 2019].

SAE is a promising technique for direct growth on Si and has allowed the fabrication of devices including tandem solar cells, although the growth of doped heterostructures, the crystal quality and the thermal budget are subjects of concern.

1.2.1.4 Growth on Si by self-catalyzed VLS epitaxy

Using self-catalyzed VLS growth, it is possible to grow NWs at 600 °C. MBE has been the most commonly used growth technique [Barrigón et al. 2019]. The fabrication of advanced core-shell structures is possible since the catalyst is made of one of the NW elements and can be removed *in situ*.

Due to the strong potential of this method, several groups have published extensive research results covering the various fundamental and experimental aspects towards working devices. Here, I select some groups who have been working for several years on self-catalyzed GaAs NW growth by MBE on Si for tandem solar cells, and I highlight the mains issues that they have been facing.

Lapierre's group at McMaster University (Canada) has been working on MBE-grown GaAs and GaAsP NWs for solar cells for more than a decade. They aim at growing GaAsP NWs on Si for tandem cells, by taking advantage of the high bandgap of $GaAs_{1-x}P_x$ (1.7 eV for $x \approx 0.25$). They addressed some issues related to the device: modeling and optimizing the growth of core-shell structures [Gibson and LaPierre 2014]; [Mohseni et al. 2007]; [Czaban et al. 2009]; [Gibson et al. 2013]; [Gibson and Lapierre 2013], optimizing the top-contacts of NW solar cells by using an In/ITO bilayer contact ([Tajik et al. 2011]; [Zhang et al. 2014b]), opto-electronic modeling of NW solar cells to study the influence of the surface depletion ([Chia and Lapierre 2012]; [Chia and Lapierre 2013]), or to calculate optimal solar cell performances ([Hu et al. 2012]; [LaPierre 2011a]; [LaPierre 2011b]). Regarding the growth of the NWs, they primarily use a gas-source MBE and Te as an n-type dopant, whereas Si is more standard. They tackled several issues related to the control of the crystal quality [Dastjerdi et al. 2016], or the study of doping, especially with Te which has a surfactant effect modifying the growth dynamics and which showed limited incorporation in NWs ([Yee et al. 2012]; [Chia et al. 2013]; [Chia et al. 2015]; [Dastjerdi et al. 2017]; [Goktas et al. 2018]). They showed that ex-situ surface passivation was possible using sulfur chemicals [Tajik et al. 2011], but they later transitioned toward a scheme where an AlInP shell is grown around the NW and later etched to directly contact the underlying GaAs shell [Boulanger et al. 2016].

They have fabricated GaAs NW array solar cells on Si with very limited performances as compared to other growth techniques (0.9 % at 2.6 sun in [Czaban et al. 2009], 3.3 % in [Boulanger et al. 2016], 4.1 % in [Dastjerdi et al. 2016]), and GaAsP-on-Si tandem solar cell with very degraded performances compared to the subcell alone (3.51 % where the Si alone was 9.33 %). They attribute their low device performances to crystal defects in the top of the NWs limiting

the J_{sc} through recombination losses, and to a too low doping level in the shell limiting the V_{bi} and V_{oc}, as characterized using off-axis electron holography [Dastjerdi et al. 2017].

Fontcuberta i Morral's group at EPFL (Switzerland) has also worked on GaAs NW arrays, for solar cell applications among others. They conducted pioneering research about the self-catalyzed growth of GaAs NWs ([Colombo et al. 2008]; [Fontcuberta I Morral et al. 2008]), in particular focusing on the crystal quality ([Zardo et al. 2009]; [Spirkoska et al. 2009]; [Heiss et al. 2011]; [Conesa-Boj et al. 2014]) and the nucleation on Si substrate which are critical as the self-catalyzed growth on Si is very hard to optimize ([Bauer et al. 2010]; [Uccelli et al. 2011]; [Matteini et al. 2014]; [Russo-Averchi et al. 2015]; [Zamani et al. 2018]; [Vukajlovic-Plestina et al. 2019]). They also focused very early on the doping of GaAs NWs, highlighting the possibility to use Si as a p-type dopant in the VLS grown core and a compensated, n-type dopant in the shell, and investigating Be as a p-type dopant, suggesting that it preferably incorporates through the NW sidewalls rather than by VLS through the droplet ([Ketterer et al. 2010]; [Dufouleur et al. 2010]; [Spirkoska et al. 2011]; [Ketterer et al. 2012]; [Casadei et al. 2013]).

After studying the PV properties of single NWs ([Colombo et al. 2009]; [Krogstrup et al. 2013]), they also struggle to obtain efficient GaAs NW solar cells [Mikulik et al. 2019].

Liu's group at University College, London (United Kingdom) has been focusing on the ternary alloy GaAsP, grown as NW arrays on Si by MBE and optimal for tandem applications. They also dedicated studies to investigate the nucleation on Si substrates ([Zhang et al. 2013]; [Zhang et al. 2014b]; [Zhang et al. 2016]), the NW doping [Zhang et al. 2018] and crystal structure ([Zhang et al. 2017b]; [Sanchez et al. 2017]; [Sanchez et al. 2018]; [Gott et al. 2019]). More specifically, since they use GaAsP alloy they also investigated the composition inhomogeneities in NWs ([Zhang et al. 2013]; [Zhang et al. 2015]; [Zhang et al. 2016]).

Summary of unsolved issues. These works highlight the importance of addressing at least three growth-related issues commonly assumed to be the most limiting for solar cell device performances:

1. The homogeneity of NW ensembles grown on Si
2. The measurement and control of NW doping levels and doping homogeneity
3. The crystal quality and the presence of defects in NWs

More generally, from a photovoltaic point of view, if light absorption enhancement in NW arrays has been demonstrated, the carrier separation and collection still need to be fixed by addressing these growth issues, as well as questions related to the device fabrication: ohmic contact formation, shunt control, stress-free encapsulation, *etc.*

> Several groups have worked on self-catalyzed NW growth on Si for years but the performances are still very limited. It confirms the relevance of working on this approach as there is still room for improvement without any fundamental limitation identified.

1.2.2 Aim of the thesis: a GaAs-based nanowire solar cell on Si

The present project aims at fabricating a solar cell by growing self-catalyzed NWs directly on a Si substrate. Several aspects regarding the techniques used, the designs, the materials and the strategy are now discussed, to finally propose a design for the NW top-junction.

1.2.2.1 MBE or MOCVD?

Molecular beam epitaxy (MBE) is an ultra high vacuum (typically 10^{-10} Torr) epitaxial technique. A chamber comprises several elemental sources thermally evaporated so as to emit a flux

of atoms or molecules, ballistically towards the substrate. It is a technique privileged in many research laboratories for its fine control over the material purity and its ability to control with precision the amount of material deposited, below an atomic layer.

Metal-organic vapor phase deposition (MOCVD), or metal-organic vapor phase epitaxy (MOVPE) is an epitaxial technique which relies on chemical reactions of gas precursors to bring the atoms at the substrate surface sites. Contrary to MBE, the technique does not require ultra-high vacuum but operates close to atmospheric pressure by injection of gases mixed into a reactor. It has been elected by the industry of opto-electronic components for its high throughput.

NWs have been synthesized using both methods, but typically, SAE is better realized using MOCVD probably due to the isotropic nature of the precursor fluxes. On the other hand, MBE is the technique of choice for self-catalyzed VLS growth, where it is necessary to control the presence of a group III droplet at the top of the NW.

MBE is chosen as a development tool for studying self-catalyzed NW growth, but cost-efficient alternatives could be used for industrialization.

1.2.2.2 Radial or axial junction?

Advantages of radial structures. The two main designs for NW heterostructures are the axial and radial configurations, presented in Figure 1.17. In 2005, Kayes *et al.* compared the relevance of both approaches for the realization of solar cells.

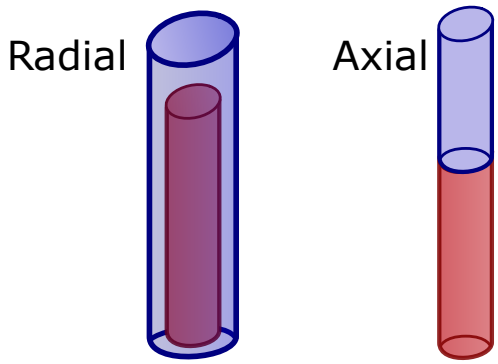

Figure 1.17: *Illustration of the radial and axial NW heterostructures. The colors may represent different materials, or the same materials with different dopants. The radial geometry typically comprises an additional top segment due to the growth modes.*

The main advantage of the radial configuration lies in the fact that the direction of light absorption (along the NW axis) is orthogonal to the one of carrier separation (along the radius), which allows to tune both aspects independently [Kayes et al. 2005]. In a planar solar cell or a NW axial junction, a certain film thickness or NW length is necessary to absorb a sufficient amount of the incoming light, but at the same time the solar cell must be kept thin enough to allow minority carriers to diffuse to the junction, setting a limit to the total thickness of the device [Otnes and Borgström 2017]. In a radial junction, the small NW radius of the order of 100 nm is lower than the carrier diffusion length even with the presence of recombining defects which allow for efficient carrier separation and collection (internal quantum efficiency). This unique property makes the radial geometry more robust to bulk defects decreasing the minority carrier lifetimes, and allows for high efficiencies with lower materials quality than in an axial geometry. While this is very important for indirect band-gap materials for which long NW are needed to absorb most of the incoming light, it is not as essential for III-V NW which can absorb light within µm-long NWs.

Surface recombination are in any case extremely detrimental to the solar cell operation, but even more in the axial configuration where the surface-to-volume ratio is generally higher, and where free surfaces encompass all the regions of the p-n junction [Christesen et al. 2012].

From a device fabrication perspective, the radial junction permits an easier top contact fabrication, as a conducting material can be deposited conformally on the NW array, without risking shunting the device, whereas the contact must be formed only at the top of an axial junction NW. In addition, since ohmic contacts on n-type GaAs are difficult to obtain, the enhanced contact surface area of a conformal contact should be highly beneficial.

Advantages of axial structures. The radial geometry, however, increases greatly the area of the junction, where the n- and p- regions are in contact, with two negative consequences [Otnes and Borgström 2017]:

1. If the doping levels are not sufficiently high (and this is a typical problem in NWs), the depletion volume greatly extends into the core and the shell, possibly depleting one side of carriers, with dire consequences on the V_{oc} (through a lowered V_{bi}), the majority carrier conduction, and the contact formation ([Chia and Lapierre 2012]; [Boulanger et al. 2016]). The axial junction is therefore more tolerant to doping variations.
2. The radial geometry is more sensitive to defects in the depletion region. In particular, a larger junction area results in a larger J_0 (enhanced recombination), and thus a lower V_{oc} through Equation 1.3 ([Christesen et al. 2012]; [Liang et al. 2013]; [Wallentin et al. 2013]). For a fixed density of defects, I later discuss the V_{oc} change for different NW dimensions.

Controlling the crystal defect and doping densities in core-shell NW is thus critical for efficient PV devices.

Moreover, despite the benefits of radial designs for NW single-junctions, axial junctions present the advantage of an easier multi-junction implementation where several materials with alternating dopants are successively stacked on top of each other, including tunnel junctions, without interrupting the VLS growth.

Improving the V_{oc} of radial junctions. The best experimental devices for both geometries can be compared in Table 1.1. While radial devices ([Yoshimura et al. 2013]; [Mariani et al. 2013b]) can reach J_{sc} comparable to the best axial ones ([Otnes et al. 2018]; [Aberg et al. 2016]), their V_{oc} and FF are significantly lower, leading to less than half of the best PCE. Thus, any benefits of the radial structure in terms of charge carrier collection has until now been masked by other dominating factors, probably related with shell growth, but which are not yet fully determined [Otnes and Borgström 2017]. Although the VS growth of shells around 3D structures could be considered straightforward at first glance, due to the similarity with the well-known 2D growth processes, there are actually major issues related to dopant incorporation on the rather unusual sidewall facets, which can lead to important alterations of the growth dynamics, and very low and inhomogeneous carrier densities [Hilse et al. 2010]; [Chen et al. 2017]; [Goktas et al. 2018].

Moreover, the growth conditions for the shell often lead to undesired parasitic deposition of material on the mask in between the NWs [Dimakis et al. 2012], possibly forming an extended recombining surface with the underlying substrate.

This work focuses on the radial configuration, which presents several key advantages facilitating the fabrication of solar cells, but which is still not on par with the performances attained with axial junctions, probably due to issues related to the shell growth. Nonetheless, the core-shell design should allow for high efficiency GaAs NW solar cells (27.3 % efficiency as calculated by [LaPierre 2011a]) and GaAsP/Si tandem cells (33.8 % calculated in [LaPierre 2011b]).

1.2.2.3 Array geometry

As shown above, the NW array solar cells grown on Si are not impeded by unoptimized light absorption, but still suffer mostly from issues which prevent efficient carrier separation and collection. A wide parameter range is compatible with absorption enhancement in a NW array, and the fine tuning of the resonance modes can be the object of another study, after the device growth and fabrication have been fully developed and optimize. Consequently, I chose a range of parameters for the array and NW geometries which should ensure reasonable absorption even with parameter fluctuations, but I do not optimize the structure.

Choice of a pattern. A hexagonal array is chosen as it allows for a wider NW inter-distance (pitch), at a given NW surface coverage. Lower pitches are undesirable from a growth perspective, as issues such as flux shading, adatom out-diffusion or coalescence can arise. The influence of the array geometry is in all cases very low as calculated by different groups ([Mariani et al. 2013a]; [Chen 2018]; [Anttu 2019b]).

Lateral dimensions. The NW diameter has an important influence on the absorption, since it determines the number and position of the resonant modes inside individual NWs. Optimal diameters have been calculated for various materials, in particular by tuning the location of strong resonance peaks close to the energy gap where the absorption is the weakest [Anttu and Xu 2013]. It allows for choosing a diameter rather independently of the rest of the array geometry.

Tapered NWs with a conical shape have the advantage of a varying diameter allowing for a continuum of modes to coexist and overlap, thus enhancing absorption ([Fountaine et al. 2014]; [Gibson et al. 2019]). However, using MBE self-catalyzed VLS growth, achieving such shapes is too challenging.

The choice of the array pitch is closely linked to the NW diameter since together they govern the surface filling ratio:

$$\mathcal{F} = \frac{S_{NW}}{S_{\text{unit-cell}}} = \frac{\pi D_{NW}^2}{4p^2 \sin(60°)}, \tag{1.5}$$

with S_{NW} the surface section of a vertical NW seen from the top, D_{NW} its diameter, $S_{\text{unit-cell}}$ the surface of the hexagonal array unit-cell, p the array pitch. Large filling ratios lead to high absorption independently of the pitch, however the maximum is often found for the lower values, as there is a trade-off to find between promoting a large number of resonance modes in the NWs (large NW diameter), while restricting the number of modes propagating the light outside the array, towards the substrate or the air above (through reducing the array pitch) [Sturmberg et al. 2014].

Here, rather than aiming at the optimal absorption, I prefer to set the array parameters in a range where absorption is less sensitive to fluctuations of the geometrical parameters and refractive indices, as I later investigate different growth modes leading to different dimensions, in sometimes imperfect arrays, and varying the NW material. For a pitch between 400 nm and 600 nm, and keeping a filling ratio close to 30 %, the absorbed photocurrent in an array of 1 µm long GaAs nano-cylinders on top of a Si substrate remains above 20 mA cm^{-2}, as calculated in [Chen 2018] as well as in [Benali et al. 2014].

Moreover, aside optical considerations, large filling ratios are preferred to maximize the surface area of the usually poor electrical contact between the NWs and the top electrode. But a too large filling ratio nullifies one advantage of the NW geometry which is to absorb more light using less material than planar layers. From a growth perspective, low pitches increase competitive effects between neighboring NWs, due to shading or group III atom diffusion [Rudolph et al. 2014].

Accounting for all these aspects, an array pitch of 500 nm is chosen, aiming at diameters of 280 nm. As multiple arrays can be patterned on one sample, other dimensions can be tested, especially a pitch of 1000 nm for which less proximity effects are expected to affect the NW growth.

NW height. Typically, the absorption increases with the NW length with a weak dependence on the diameter, and in relation with the absorption coefficient of the NW material. In GaAs, the absorption is already close to 80 % for 1.3 µm long NWs [Mariani et al. 2013a]. The NW height influences the light transmission towards the underlying Si substrate. As the envisioned device is a tandem solar cell, the light transmitted to the Si is not lost and can be collected by the bottom cell. Ultimately, the NW height will serve as a tuning parameter to match the current through the tandem cell. Consequently, I do not aim at maximizing the absorption in the NW array but limit the length to about 2 µm.

Aside optical considerations, increasing the NW length also increases the depletion volume of the p-(i-)n junction (see [Kayes et al. 2005] for example). Under the assumptions that:

- The dark current is governed by non-radiative recombination of injected carriers in the space-charge region, possibly assisted by deep defects
- The recombination rate in the space-charge region scales with the developed area of the p-i-n junction.

The macroscopic (solar cell) recombination parameter then writes:

$$J_0 = \frac{J_0^* \times S_{\text{junction}}}{S_{\text{illum.}}} \tag{1.6}$$

Where the current density due to recombination across the p-n junction J_0^* is normalized by the junction area and distinguished from the macroscopic quantity J_0, normalized by the total solar cell area (illuminated area). Increasing the NW length will linearly increase S_{junction} and J_0, resulting in a logarithmic decrease of the V_{oc} through Equation 1.3. Therefore, a reduced V_{oc} could be expected compared to a planar junction simply due to recombination in the enhanced area of the space charge region. Assuming that J_0^* is the same in all geometries (radial and axial NW, and planar), and that NWs are 2 µm long and 250 nm wide in a 500 nm pitch hexagonal array, the axial configuration yields a V_{oc} enhancement of 38 mV, whereas the radial configuration (for a given p-n interface location) leads to a −33 mV loss.

This indicates that although the chosen geometry is adequate for the early solar cell development, it should be optimized to reach the best device performances, in particular through reducing the NW height and displacing the radial junction closer to the core.

A hexagonal array of 500 nm pitch is chosen inside which 2 µm long and 280 nm wide NWs should lead to absorption above 20 mA cm^{-2}, with small sensitivity to geometrical variations.

1.2.2.4 Choice of materials

Several III-V alloys permit to reach a bandgap of 1.7 eV, optimal for tandem-on-Si, such as $GaAs_{0.75}P_{0.25}$, $In_{0.6}Ga_{0.4}P$ and $Al_{0.2}Ga_{0.8}As$ (Figure 1.18).

The VLS growth mode does not ensure that the crystal composition is governed by the ratio of precursors provided. Indeed, for example with Au-catalyzed growth, even though the droplet is mostly made of Au, only very little is incorporated into the NW. Similarly, some group-III constituents of the droplet do not incorporate as well as others into the NW. Our group reported very limited incorporation of In relative to Ga in GaInAs and GaInP NWs, making these alloys unsuited for VLS growth [Scaccabarozzi et al. 2020]. Growth of Al-containing alloys by VLS is also challenging due to undesired interaction with the Si substrate [Vettori et al. 2018].

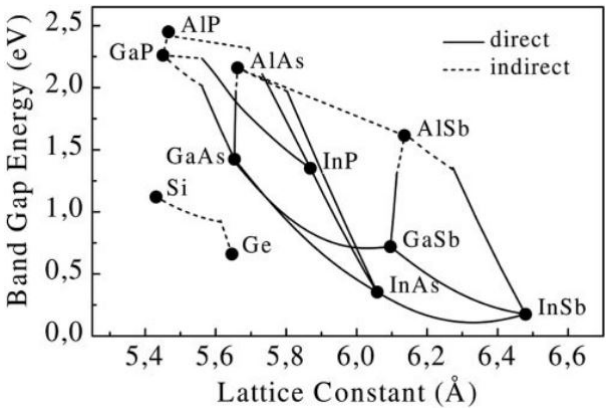

Figure 1.18: *Bandgap energy and lattice parameter of various III-V binary (dots) and ternary compounds (lines), along with Si and Ge. From [Bett et al. 1999].*

As a consequence, I prefer to use an alloy with a unique group III element and a mix of group V compounds. $GaAs_{0.75}P_{0.25}$ is close in composition to GaAs, which has been one of the most studied material for self-catalyzed NW growth. GaAsP has been employed by several groups and the compositions appears to be tunable over a wide range ([Sun et al. 2015]; [Himwas et al. 2017]; [Zhang et al. 2013]).

I study GaAs NWs as a baseline towards GaAsP NWs, which permit to reach the optimal bandgap of 1.7 eV.

1.2.2.5 Short-term goal: a GaAs(P) NW top-cell

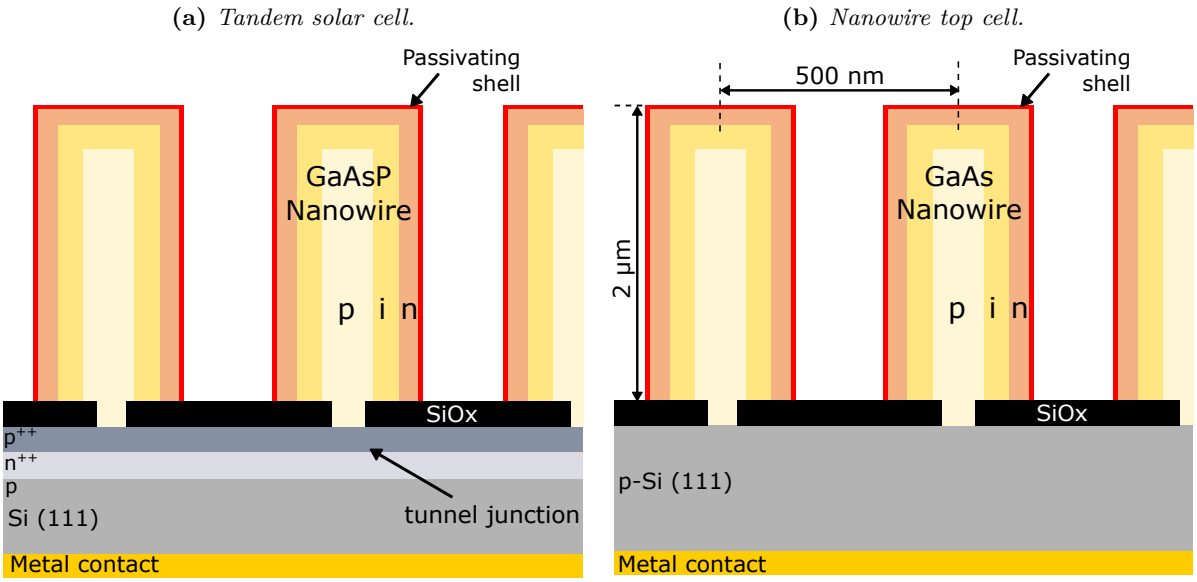

Figure 1.19: *(a) Envisioned tandem structure combining a GaAsP NW array top-cell directly grown on a (111)-oriented Si solar cell, including a tunnel junction. (b) Short-term goal: the sole NW top-cell made of GaAs in a core-shell structure, grown on inactive p-type Si(111) substrate. Not at scale.*

The tandem NW solar cell structure envisioned in this project is shown in Figure 1.19a. The bottom cell is a p-n Si solar cell on a (111) substrate, terminated by heavily doped n^{++}-p^{++} layers to form a tunnel junction. This can be realized by a combination of spin-on doping and proximity rapid thermal diffusion for example, a technique which enabled efficient tunnel

junctions fabrication with a simple, industry-compatible process [Fave et al. 2017]. The top junction is made of GaAsP p-core/n-shell NWs passivated by a wide bandgap shell such as GaInP or AlInP, which can then be contacted using a transparent conductive layer. The doping is arbitrary proposed as p-to-n from bottom to top, but it is studied in a dedicated section of this thesis.

Because a two-terminal tandem solar cell requires a perfect current matching of the subcells, the top NW cell must be reliably efficient and yield a high current, otherwise it simply acts as a parasitic absorber which results in a degraded tandem cell performing worse than the initial Si cell, such as in [Wood et al. 2017].

In this thesis, I therefore dedicate my efforts towards the fabrication of the top NW cell alone, grown on an inactive, uniformly doped Si substrate, as depicted in Figure 1.19b. The baseline is a GaAs NW core-shell junction passivated with a wide bandgap alloy (AlGaAs or GaInP).

1.2.3 Issues to address: plan of the thesis

Chapter 2: Tools and methods

The next chapter serves to introduce the physics needed to understand the processes in semiconductor solar cells, and the growth of nanowires by molecular beam epitaxy, as well as the introduction of the fabrication and characterization methods employed in this thesis.

The following chapters are dedicated to presenting my efforts towards the fabrication of an efficient NW-based solar cell, addressing the different topics identified in this state-of-the-art section.

Chapter 3: Growth of Defect-free GaAs NW Arrays on Si

The growth of an array of GaAs NWs with homogeneous dimensions and good crystal quality is a prerequisite for all NW array-base applications. Consequently, my first chapter is dedicated to the study and optimization of such array.

The homogeneity of the NW array is of prime importance for fabricating devices, which is one reason to use a patterned substrate. However, even using a regular template for the growth, it is a tough task to obtain an array with perfect homogeneity and vertical alignment of all NWs without optimization, and there is room for improvement especially regarding the growth on Si. The state-of-the art of the growth of NW arrays is presented in Section 3.1 where different NW synthesis techniques are compared.

Then, I present the optimization of the NW vertical yield on patterned Si substrates with specific designs, growth conditions and substrate preparation (Section 3.2).

Several groups have worked on the control of the crystal quality, in particular the presence of *stacking faults* and *twins* in the NWs. In Section 3.3, I investigate and reduce the occurrence of such defects in the NWs, in particular during the last step consisting in removing the catalyst *in situ*.

Chapter 4: GaAs(P) Core-Shell Nanowire Structures

In the fourth chapter, I study the fabrication of NW core-shell structures for practical use in solar cells: shell growth, doped junctions, tuned alloy compositions.

For efficient surface passivation and carrier separation, shells have to be grown around the NW core, possibly with ternary compounds. Section 4.1 is dedicated to the presentation of such cell growth, and the study of a GaInP passivating shell.

Researchers have been studying doping in NWs for years but nanoscale characterization is challenging, and the incorporation mechanisms not well understood. In Section 4.2, I present our lab team effort toward developing a robust cathodoluminescence-based method to measure doping in single NWs, and the study of carrier concentrations under various growth conditions.

Ideal monolithic III-V-on-Si tandem solar cells include a top cell with a bandgap of 1.7 eV for a perfect current matching. Using GaAsP, it is possible to reach this value, but composition inhomogeneities are to be expected within the NW volume. In Section 4.3, I investigate such inhomogeneities and present strategies to avoid them.

Chapter 5: Nanowire Solar Cell Fabrication and Characterization

Fabricating a solar cell from a NW array is complicated and a certain process has to be chosen and developed in the lab.

In Section 5.1, I define the strategy adopted for the solar cell fabrication, in light of previous literature works, and I present the processing steps in Section 5.2.

The front contact of the n-doped III-V shell with transparent conductive oxides is notoriously complicated as our materials are prone to Fermi-level pinning. The optimization of a front-contact using planar stacks is the object of Section 5.3.

Finally, the NW solar cells that I fabricated and characterized are presented in Section 5.4 and Section 5.5. In particular, I relate the opto-electrical characteristics of the cells to various phenomena identified in the previous studies, and propose new designs to alleviate the identified issues.

Chapter

2 Theory and Methods

Chapter content

In this chapter I start by explaining key concepts in semiconductor solar cells which need to be implemented in order to fabricate efficient devices: the losses by recombination, adequate designs to separate carriers of both types, concepts about semiconductor interfaces for conductive electrical contacts. I choose to have a general approach (1D) without particular focus on a given NW geometry, to later apply it when choosing specific NW junction architectures.

I then focus on the synthesis of NWs, first by describing the crystal structure of III-V semiconductors, and the basics of their vapor-solid epitaxial growth by MBE. In particular, I compare two MBE setups used during this project. I introduce two models describing the NW growth by vapor-liquid-solid (VLS), which will serve to explain the morphology and crystal structure found in the NWs, and point out the efficient use of precursor materials using this technique. I then present our baseline process for the fabrication of patterned substrates, and for the growth of core-shell NWs.

Finally, I introduce the most advanced techniques employed here to characterize NWs and NW solar cells: transmission electron microscopy, cathodoluminescence spectroscopy, quantum efficiency measurements and hyperspectral photoluminescence imaging.

2.1 Charge carrier separation and collection in semiconductor solar cells

Solar cells are often made of crystalline semiconductor into which photons are converted into charge carriers as introduced in Figure 1.5 (page 12), but the principles driving the separation of electrons and holes to result in an electrical current were left unexplained. The terminology following the book [Würfel and Würfel 2016], the section is based on considerations of semiconductor physics which can be found in [Sze and Ng 2006], for example.

2.1.1 Carrier motion

The average motion of electrons and holes inside the conduction and valence band is driven by two distinct processes. First, as free particles, they tend to equilibrate their spatial distribution through their individual random motion. They flow from regions where they are numerous towards regions where they are scarce. As electrons are charged, their average motion can be expressed as a charge current density J [mA cm^{-2}], following the spatial variation of their chemical potential, μ_e^*:

$$J_{diff}^e = -\frac{q\,n}{k_B T} D_e \,\mathrm{grad}\,\mu_e^* \tag{2.1}$$

where D_e is the diffusion coefficient of electrons. This is also valid for the current caused by the diffusion of holes, replacing $-n$ by p and using the hole diffusion coefficient.

Then, as charged particles, electrons and holes are affected by the electric field $E = -\mathrm{grad}\,V$ (V is the electric potential). On average, after multiple collisions due to the random thermal motions of carriers, they drift by following the electric potential, resulting in a current:

$$J_{drift}^e = -\mu_e n \;\mathrm{grad}\,(qV) \tag{2.2}$$

where μ_e is the mobility of the electrons. It is the same expression for holes using p instead of n, and μ_h instead of μ_e.

Four relations allow to write these currents in a compact form:

- Einstein relation relates the diffusion coefficient D to the mobility μ: $\frac{\mu}{D} = \frac{q}{kT}$
- The electrochemical potential combines the electrical and the chemical potential of carriers: $\eta = \mu^* + qV$
- In out-of-equilibrium semiconductors, charge carrier populations are described by their quasi-Fermi energies ε_{Fc} and ε_{Fv}, which equal the electrochemical potentials: $\varepsilon_{Fc} = \eta_n$ and $\varepsilon_{Fv} = \eta_p$
- The electrical conductivity of electrons is defined as $\sigma_e = n\,q\,\mu_e$. For the holes it is: $\sigma_h = p\,q\,\mu_h$.

Overall, after summing both current contributions, for electrons and for holes, the total charge current can be written:

$$J_{tot} = \underbrace{n\,\mu_e \,\mathrm{grad}\,\varepsilon_{Fc}}_{\text{electron current}} + \underbrace{p\,\mu_h \,\mathrm{grad}\,\varepsilon_{Fv}}_{\text{hole current}} \tag{2.3}$$

Any current flow thus results from a gradient of the hole and electron Fermi energies, and depends on the conductivity for both carriers.

2.1.2 Carrier separation

In a solar cell, the difference in the Fermi energy levels that arises between left and right contacts results in a voltage between both terminals:

$$\varepsilon_{F,right} - \varepsilon_{F,left} = qV \tag{2.4}$$

Let us consider a solar cell made of a semiconductor p-n junction under illumination, but not connected to an external load ($V = V_{oc}$, black in Figure 2.1). Electrons in the n-doped semiconductor and holes in the p-doped semiconductor are called *majority carriers*, and their concentration does not vary significantly with the addition of photogenerated carriers (low-injection regime). The quasi-Fermi levels of holes and electrons merge at both contacts. As no total current flows at V_{oc}, the majority and minority carrier currents compensate each other in Equation 2.3.

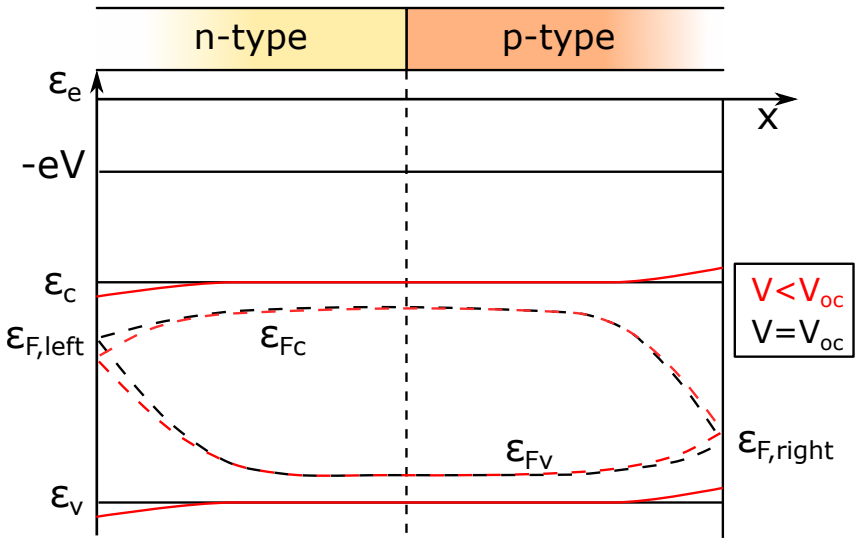

Figure 2.1: *Band structure of a simple p-n junction with finite surface recombination velocities, under illumination without applied bias. Adapted from [Würfel and Würfel 2016].*

If the cell is biased slightly below V_{oc} (red in Figure 2.1), the majority (minority) carrier quasi-Fermi level gradient slightly increases (decreases). This results in a net current flow in the solar cell, extracting photogenerated carriers.

2.1.3 Recombination processes

Not all carriers can be extracted at the selective contacts, as electron and holes recombine after a lifetime spent in the material. Recombination can occur from one band to the other, or through a defect at an intermediate energy level, by emission of a photon or not.

Radiative recombination

Similar to how a photon can be absorbed and create an electron-hole pair, electrons and holes can interact from their respective bands and emit a photon:

$$e + h = \gamma \tag{2.5}$$

This process is more likely to happen with increasing electron or hole concentrations. The rate R_{rad} $[cm^{-3}]$ at which it occurs is thus described by:

$$R_{rad} = B\, n\, p \tag{2.6}$$

where B is the *radiative recombination coefficient*.

Under illumination, in a n-type region, $n = n_0 + \Delta n \approx n_0$ and $p = p_0 + \Delta p \approx \Delta p$, so that Equation 2.6 becomes:

$$R_{rad} = B\, n_0\, \Delta p = \frac{\Delta p}{\tau_{rad}} \tag{2.7}$$

where $\tau_{rad} = 1/(B\,n_0)$ is the minority carrier radiative lifetime, here, a hole in the n-region. It varies with the doping and is typically 10^{-8} s in p-GaAs doped to $p = 10^{18}\,\mathrm{cm}^{-3}$ [Nelson and Sobers 1978].

It is sometimes convenient to express light emission, or *luminescence* of a semiconductor using the Fermi levels. In non-degenerate semiconductors, when the Fermi levels remain inside the band gap, a few kT away from the band edges, the carrier populations can be described by a Boltzmann statistics instead of a Fermi statistics, and Equation 2.6 becomes then:

$$R_{rad} = B\,n_i^2 \exp\left(\frac{\varepsilon_{Fc} - \varepsilon_{Fv}}{k_B T}\right) \tag{2.8}$$

However, an exact derivation of light emitted by recombination in one hemisphere above the flat surface of a semiconductor, $\phi(\hbar\omega)$ (in units of photons $\mathrm{m}^{-2}\,\mathrm{s}^{-1}\,\mathrm{eV}^{-1}$), yields what is known as the *generalized Planck law* [Würfel and Würfel 2016]:

$$\phi(\hbar\omega) = \frac{A(\hbar\omega)}{4\pi^2\hbar^3c^2}\frac{(\hbar\omega)^2}{\exp\left(\frac{\hbar\omega-(\varepsilon_{Fc}-\varepsilon_{Fv})}{k_BT}\right)-1}, \tag{2.9}$$

where $\hbar$ is the reduced Planck constant, c the speed of light in vacuum, $\hbar\omega$ the photon energy, and $A(\hbar\omega)$ the absorptivity of the solar cell material.

These radiative processes are intrinsic properties of ideal solar cells, and determine a lower limit for the recombination parameter J_0.

Shockley-Read-Hall recombination

When impurities are incorporated in the crystal lattice, the new bonds they form with the atoms may change the band structure and introduce new energy levels deep inside the bandgap. The recombination of an electron with a hole through this new level is typically non-radiative (energy dissipation). The electron (or hole) emission rate is proportional to :

- The density of trap states, N_t $[cm^{-3}]$
- The capture cross-section of each trap state (an area σ which represents its ability to capture efficiently nearby carriers)
- The concentration of each type of carriers (some defects behave preferentially as acceptors, or donors)
- The thermal velocity of the carriers, v_{th}.

Then the electron-hole recombination rate is [Würfel and Würfel 2016]:

$$R_{SRH} = \frac{n\,p - n_i^2}{\frac{n+N_C\exp[-(\varepsilon_C-\varepsilon_{imp})/kT]}{n_{imp}\,\sigma_h\,v_{th,h}} + \frac{p+N_V\exp[(\varepsilon_v-\varepsilon_{imp})/kT]}{n_{imp}\,\sigma_e\,v_{th,e}}} \tag{2.10}$$

The recombination rate is higher when the defect level is close to the middle of the energy gap : $\varepsilon_{imp} - \varepsilon_v \approx E_g/2$, so that the deepest defects are the most detrimental. In a uniformly n-doped region, under low injection, it can be simplified to :

$$R_{SRH} = (p - p_0)\,n_{imp}\,\sigma_h\,v_{th,h} = \frac{p - p_0}{\tau_{nr}} \tag{2.11}$$

where τ_{nr} is the non-radiative lifetime of holes in the n-doped region. The non-radiative recombination lifetime due to impurities in GaAs is typically 10^{-9} s.

Lifetimes and diffusion lengths

Each of these recombination process lifetimes contributes to the total minority carrier lifetime:

$$\frac{1}{\tau} = \frac{1}{\tau_{nr}} + \frac{1}{\tau_{rad}} \tag{2.12}$$

Through the diffusion equation, a characteristic length is associated with the recombination of carriers after their lifetime τ. This *diffusion length* is (for electrons):

$$L_e = \sqrt{D_e \, \tau_e} \tag{2.13}$$

It is important, when designing a solar cell, to ensure that the minority carriers have to travel less than L to reach their selective contact, the region where they are no longer minority carriers. This is particularly critical for NWs where defects tend to lead to small lifetimes and diffusion lengths.

Surface recombination

The surface of III-Vs can be either intentionally covered with a metal contact or an oxide, but even a free surface, upon exposure to air, forms a native oxide at its surface. A certain density of defect states forms at these interfaces, due to the interruption of the tetrahedral atom bonding prevailing in the bulk, resulting in dangling bonds, or due to new bonds with adsorbed foreign atoms at the surface, or due to As and Ga segregation induced by the presence of adsorbed species ([Spicer et al. 1980]; [Freeouf and Woodall 1981]). The resulting high density of defect levels within the bandgap typically form a continuum, as depicted in Figure 2.2. Similar to bulk defects, this type of recombination can be treated by summing the contribution of defects from all energy levels through Equation 2.10, knowing their capture cross-section, density, *etc.*:

$$R_{\text{surf}} = R_{\text{surf},e} = \underbrace{\sigma_{s,e} \, v_e \, n_{\text{surf},h}}_{v_{\text{surf},e}} \, n \tag{2.14}$$

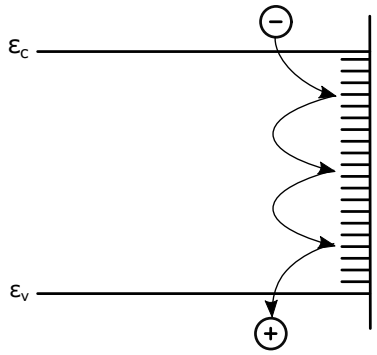

Figure 2.2: *Schematic of the energy distribution of defects responsible for surface recombination. From [Würfel and Würfel 2016]*

However, the density of unoccupied surface states $n_{\text{surf},h}$ is hard to calculate for all levels, and these defects are thus generally treated more simply, by empirically determining the proportionality factor called the *surface recombination velocity*, v_{surf}, in $\text{m}\,\text{s}^{-1}$. Note that R_{surf} is now in cm^{-2} and thus cannot be combined with the bulk recombination rates to deduce a bulk lifetime. The surface recombination velocity of an unpassivated GaAs surface increases with the doping level, and can be as high as $10^6 \, \text{cm}\,\text{s}^{-1}$ ([Aspnes 1983]; [Brillson 2010]). It is generally lowered in devices, by chemical treatment with sulfides, or by growing lattice-matched high-bandgap compounds which prevent carriers to reach the surface.

While radiative recombination processes are intrinsic to semiconductors and cannot be avoided, non-radiative recombination is detrimental to the device operation, as it can prevent the photogenerated carriers to reach their selective contact. Their presence or density should therefore be minimized in our material.

2.1.4 p-n and p-i-n junctions

The most common way to make a selective contact is by joining a p-type semiconductor with an n-type one, forming a p-n junction. It is either a hetero-junction when the materials are different, or homo-junction when they are identical. Here, I focus on p-i-n homojunctions to examine the influence of an intrinsic region. For heterojunctions the calculation is similar but the different permittivities must be taken into account in the electric field expression, and the different electron affinities for the built-in potential.

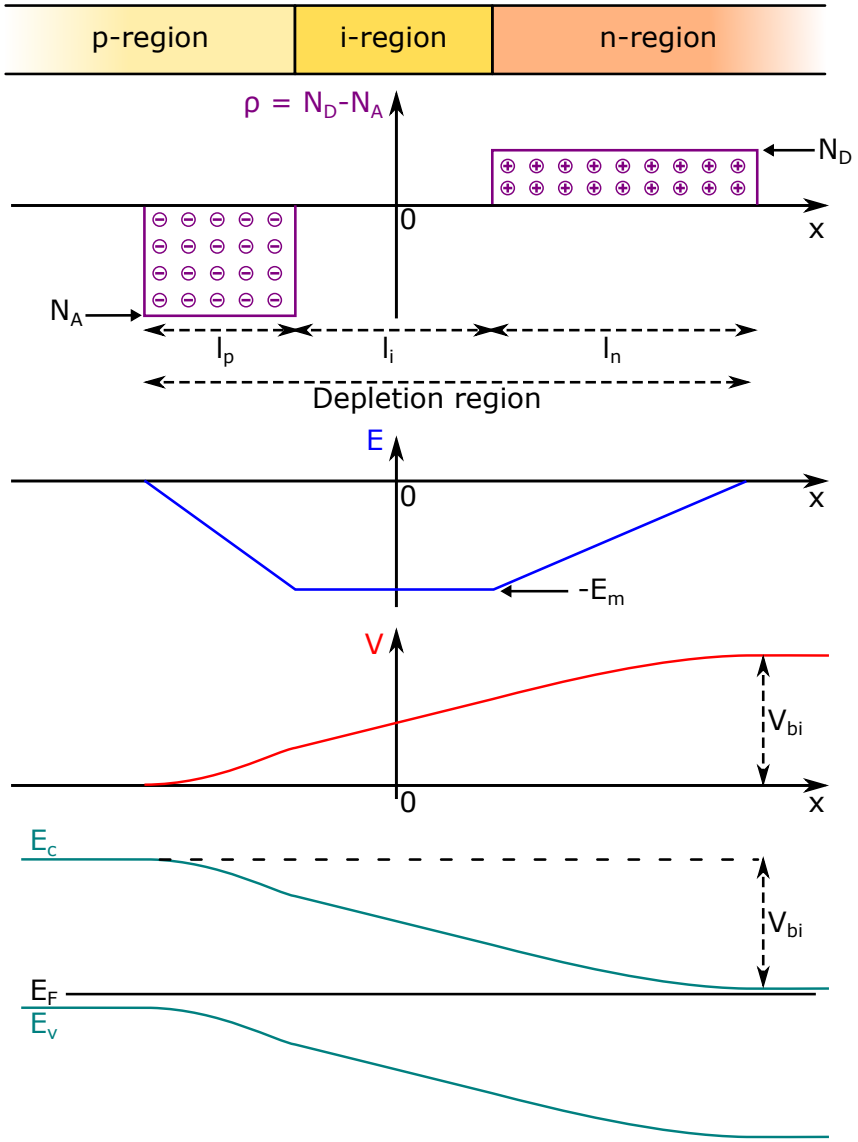

Figure 2.3: *p-i-n junction in thermal equilibrium. Violet: space-charge distribution, l_i is the width of the intrinsic region, l_n and l_p the extent of the depletion region in the n- and p- domains. Blue: electric field distribution Red: electric potential distribution, V_{bi} is the built-in potential. Green: energy band diagram.*

Depletion region

When a p-type semiconductor is put in contact with an n-type semiconductor, the majority carriers flow towards the other region due to diffusion. While the electrons and holes can diffuse spatially in the material, the cores of the impurity atoms occupy fixed position. Each electron or hole diffusing to the opposite side thus leaves one ionized impurity behind, either a donor or

an acceptor (Figure 2.3). These ionized impurities then give rise to an electric field that opposes the diffusion of electrons and holes. At equilibrium, the drift compensates the diffusion, i.e. $J_{tot} = 0$. As a first approximation, the depletion zone has abrupt boundaries, so that the charge inside is uniformly $\rho = +N_D$ (n-side) or $\rho = -N_A$ (p-side).

The charge conservation yields:

$$l_n N_D = l_p N_A \tag{2.15}$$

Solving Maxwell-Gauss equation ($\nabla \cdot \mathbf{E} = \frac{\rho}{\varepsilon}$, with ε the permittivity in the material) in 1-D gives a trapezoidal profile for the electric field (blue in Figure 2.3), with a plateau at E_m in the intrinsic region (length l_i):

$$\begin{aligned} E_m &= -\frac{qN_D l_n}{\varepsilon} = -\frac{qN_A l_p}{\varepsilon} \\ &= -\frac{N_D N_A}{N_D + N_A}\frac{q}{\varepsilon}W \end{aligned} \tag{2.16}$$

where $W = l_n + l_p$.

The electric potential distribution V(x) is then determined by integration of E (red in Figure 2.3). The potential difference across the junction is called the *built-in potential* V_{bi} and is:

$$V_{bi} = \frac{1}{2}E_m\, W + E_m\, l_i \tag{2.17}$$

Note that the electro-chemical potential (or Fermi level) is flat everywhere in the p and n materials (equilibrium), even far from the interface. Thus, V_{bi} must be the difference between the Fermi levels in the p- and n- materials, prior to contact:

$$\begin{aligned} V_{bi} &= E_g - E_{F_n} - E_{F_p} \\ &\approx \frac{k_B T}{q} ln\left(\frac{N_D N_A}{n_i^2}\right) \end{aligned} \tag{2.18}$$

Combining Equation 2.18 and Equation 2.17, W is the solution to a 2nd degree equation:

$$-\frac{V_{bi}\,(N_D + N_A)\,\varepsilon}{N_A N_D q} + l_i W + \tfrac{1}{2}W^2 = 0 \tag{2.19}$$

Benefits of p-i-n junctions

Solving Equation 2.19 for given doping levels N_D and N_A (Figure 2.4a), it is visible that the extension of the depleted zone in the p- and n-regions is greatly reduced by the insertion of an intrinsic region, from $W = 45\,\text{nm}$ without intrinsic region ($l_i = 0$) to $W = 20\,\text{nm}$ with $l_i = 40\,\text{nm}$. This could be one reason to prefer a p-i-n junction for NW core-shell junctions, where the doped regions are thin and thus more prone to depletion.

As it is shown in the next chapters of this thesis, a p-core/n-shell design is privileged, but doping of the n-shell is typically limited. To further investigate the effects of l_i, N_D and N_A on the extent of the depletion on each side of the junction, several curves are plotted in Figure 2.4b where the doping level in the p-side is fixed and the one in the n-side is varying. If the doping in the n-side is below $10^{18}\,\text{cm}^{-3}$, the depletion l_n is several tens of nm wide, hence, possibly entirely depleting thin n-doped shells of carriers. This is partially alleviated by inserting an intrinsic shell ($l_i = 60\,\text{nm}$), which typically lowers the l_n by a factor 2 in this doping range.

P-doping of the core to at least $N_A = 2 \times 10^{18}\,\text{cm}^{-3}$ do not lead to depletion larger than $l_p = 20\,\text{nm}$ in these conditions (dashed lines). However, the depletion in the cylindrical core

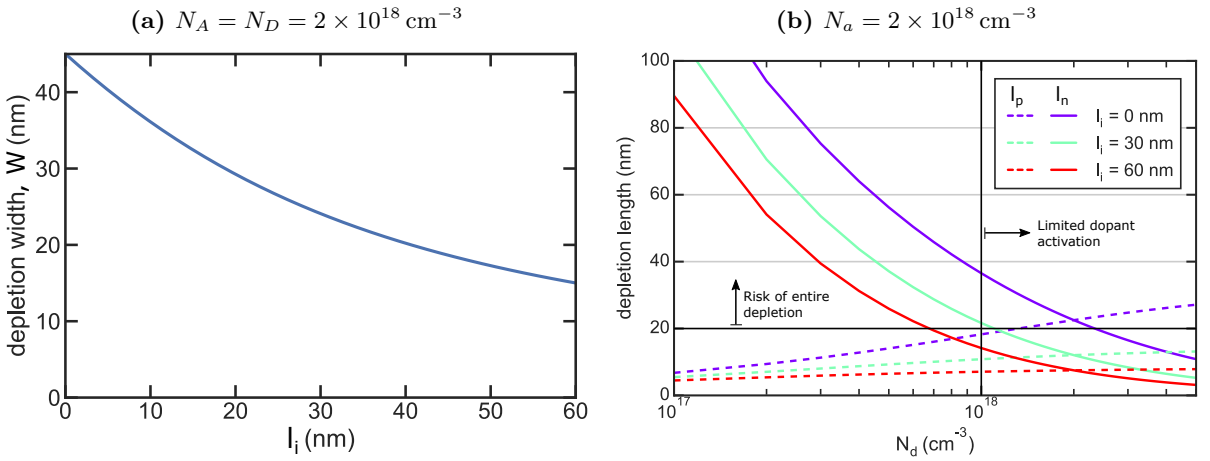

Figure 2.4: *(a) Extent of the depletion in the doped regions ($W = l_n + l_p$) for a 1D p-i-n homojunction where both regions are evenly doped to $2 \times 10^{18}\,\mathrm{cm}^{-3}$. (b) Extent of the depletion in the n-region (l_n, full lines) and the p-region (l_p, dashed lines) for a varying doping level on the n-side and for different lengths of the intrinsic region.*

is expected to be larger than in this simple 1D geometry calculation. The NW core radius are typically 50 nm, doping to $2 \times 10^{18}\,\mathrm{cm}^{-3}$ appears to be a lower limit to ensure that it is not depleted.

If large doping levels are attainable in the core and the shell of NWs, the problem of the depletion is avoided but another issue might arise: an enhanced recombination current due to tunneling across the junction. The p-i-n design offers yet another advantage to mitigate this problem, as it spatially separates the highly-doped regions so that carriers can no longer tunnel through their interface.

Finally, in extremely defective materials, where the minority carriers have short diffusion lengths due to high SRH recombination rates, the carriers generated in the depletion region can still be effectively separated and contribute to the photocurrent for two main reasons:

- SRH recombination is very low in the depletion region since carrier concentrations are close to 0, therefore the diffusion length of both carriers is much higher than in the quasi-neutral regions, allowing them to diffuse to the regions of their type.
- Even though the cell in working conditions (under illumination and at the maximum power point) is forward biased, there still exists a small electric field E inside the depletion region, contributing to separate the carriers.

P-i-n junctions allow to collect more carriers than p-n junctions in defective materials, as the depletion region occupies a larger fraction of the total volume.

> P-n junctions are a simple implementation to fabricate selective contacts with semiconductor crystals. However, a p-i-n junction provides some advantages to avert total depletion and to circumvent an eventual poor carrier lifetime.

2.1.5 Contacts on semiconductors

In a p-i-n homo or heterojunction, once the excess carriers have reached the region of their polarity (n or p), they need to be extracted to an external circuit, usually made of metal wires. In an ideal implementation, they would do so without any loss or barrier at the semiconductor-metal interface, however this is not the case in practice. Ohmic contacts, *i.e.* metal-semiconductor contacts with a negligible junction resistance relative to the total resistance of the semiconductor

device, are complicated to implement. This is particularly the case for n-GaAs which is the main example here, as it is a likely candidate material for the n-shell of the NW junction.

Surface depletion and Schottky barriers

Surface and interface states introduced in Figure 2.2 (page 41) not only act as recombination centers for excess carriers, but can also trap majority carriers. Due to this displacement of carriers from the semiconductor to the interface states, a depletion region forms within the first few nm of the semiconductor, and the associated field induces an electrical potential gradient which equilibrates the chemical potential gradient toward the surface states, similarly to the p-n junction space-charge-region. The Fermi level typically pins at a position inside the energy gap, which can be independent of the nature of the metal or oxide (including the native oxide) in contact, like it is the case for GaAs. Thus, the extent of the depletion at a surface or interface depends only on the doping type and doping level of GaAs as depicted in Figure 2.5, for planar n- and p-GaAs. The Fermi level in n-GaAs is generally pinned 0.75 eV above the valence band maximum, close to the middle of the bandgap, making it very prone to surface depletion.

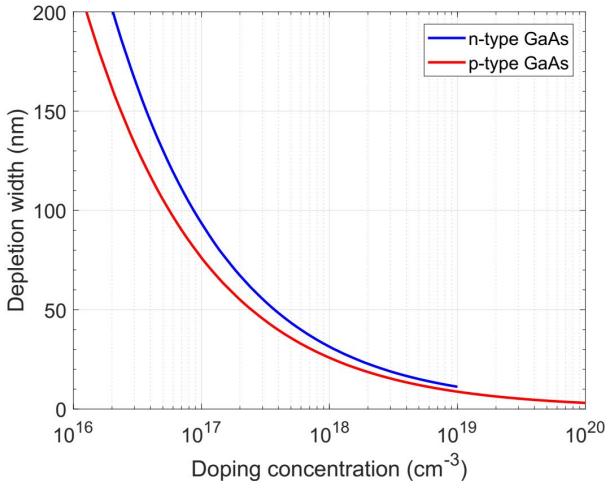

Figure 2.5: *Calculated surface depletion in GaAs, assuming Fermi-level pinning* $-0.75\,\mathrm{V}$ *and* $-0.55\,\mathrm{V}$ *above the valence band maximum for n- and p-GaAs, respectively. From [Chen 2018].*

Another consequence of the Fermi level pinning and the associated interface depletion is that it effectively results in a barrier for the majority carriers crossing the interface. The typical barrier for electrons from n-GaAs to a metal is thus $\Phi_B \approx 0.8\,\mathrm{eV}$.

Contacts to n-GaAs

Two main mechanisms exist that allow a particle to cross an energy barrier, which lead to the choice of certain strategies to form an ohmic contact on n-GaAs ([Rideout 1975]; [Brillson 2010]).

The first mechanism is thermionic emission, which relies on the fact that a small part of the carriers have a thermal energy higher than the barrier, due to their exponential energy distribution (Boltzmann distribution), and can thus pass through it (Figure 2.6a). Under a bias V, the current across the barrier is then given by:

$$J_{th} = A^* T^2 \exp\left(\frac{-q\,\Phi_B}{k_B T}\right)\left[\exp\left(q\frac{-\Phi_B + V}{k_B T}\right) - 1\right] \tag{2.20}$$

where $A^* = \frac{4\,\pi\,q\,m^*\,k_B^2}{h^3}$ is the Richardson constant, with m^* the particle effective mass. This equation is similar to the diode equation describing the transport across a p-n junction. Another

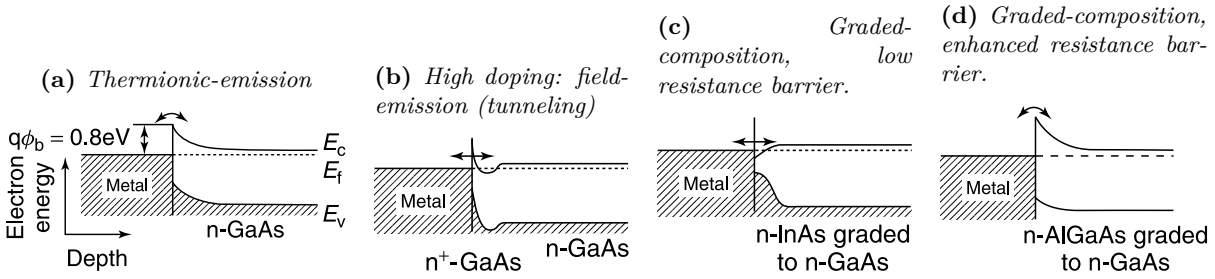

Figure 2.6: *Schematic band diagrams illustrating different n-GaAs/metal contacts (a) without or with strategies to (b,c) lower or (d) increase the effective barrier height. From [Brillson 2010].*

mechanism is the tunneling of particles through the barrier (field emission). This quantum mechanical process results in a current [Rideout 1975]:

$$J_{tunnel} \propto \left(\frac{q\,V}{E_{00}} \right) \tag{2.21}$$

where $E_{00} = \frac{q\,h}{4\pi}\sqrt{\frac{n}{m^*\,\varepsilon}}$, with ε the permittivity of the material and $n = N_D$, the electron concentration in the semiconductor bulk (for n-type conduction). This tunneling contribution relative to the thermionic one increases with $\frac{E_{00}}{k_B T}$, so with $\sqrt{N_D}$. Pure field emission governs the electron transport only at very high doping ($N_D > 10^{19}\,\mathrm{cm}^{-3}$), whereas a combination of thermionic emission and field emission exist in the range $N = 10^{18} - 10^{19}\,\mathrm{cm}^{-3}$, where the effective barrier height for thermionic emission is lowered since its upper part is thin enough to be crossed by tunneling.

Hence a strategy to enhance the current across a barrier consists in increasing the doping concentration N_D near the interface, either by *in situ* incorporation of dopant during epitaxial growth, or by *ex situ* deposition and interdiffusion by annealing for example (Figure 2.6b). I try this strategy for the front contact fabrication on the n-GaAs shells in Section 5.3.

Another strategy to make ohmic contacts is to change the semiconductor composition to obtain a material which does not make a Schottky barrier with a metal. For example, the Fermi level in n-InAs is pinned within the conduction band which allows for low-barrier electron contacts (Figure 2.6c). In Section 5.3, I insert an n-InGaAs layer to try to improve the top contact on n-GaAs. Conversely, if the chosen material has a larger bandgap or a deeper Fermi-level pinning, it results in an enhanced barrier at the interface (Figure 2.6d).

Other strategies exist to obtain low-resistance contacts, for example by introducing many defect levels in the bulk, close to the interface with the metal Figure 2.7. Indeed, an amorphous material, for example, presents a lot of midgap states due to the non-periodicity of its atomic bonds. Particles can effectively pass the barrier by successive tunneling through the many defect states (*trap-assisted tunneling*, or *hopping*).

Note that a similar situation could be expected when linearly increasing the dopant concentration way above $10^{19}\,\mathrm{cm}^{-3}$ near the semiconductor-metal interface (as I try in Section 5.5). Indeed, the impurities can then incorporate in different lattice sites, or even alter the crystal structure of the semiconductor, which could lead to a graded transition towards a disordered contact layer similar to Figure 2.7b, very beneficial for current extraction.

Due to the presence of interface states, the surfaces of III-V materials, especially of GaAs, are prone to surface depletion, and generally make a Schottky barrier altering the electrical contact with metals. Strategies exist to improve the contact with n-GaAs, through high doping, graded material transition, or the introduction of a defective contact layer, and will be investigated in Chapter 5.

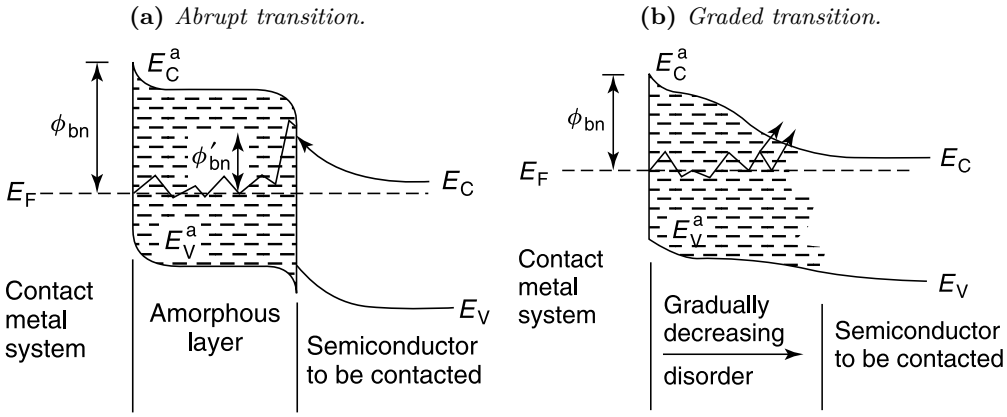

Figure 2.7: *Schematic band diagrams illustrating the use of a defective amorphous layer sandwiched at the interface between n-GaAs and a metal. The current is enhanced by electron tunneling via the numerous defect states in the amorphous layer. From [Brillson 2010].*

2.2 Molecular beam epitaxy of nanowires

Knowing the important processes at stake in solar cells, and the parameters that need special care to ensure functioning devices, I now introduce the theory behind the epitaxial growth of nanowires, and describe the procedure for their synthesis by MBE.

2.2.1 III-V semiconductor epitaxy

Crystal structure of III-V materials

Many III-V semiconductor bulk or planar layer crystals exhibit a cubic Zinc-Blende (ZB) lattice (Figure 2.8a), described by the $F\bar{4}3m$ crystallographic space-group (216). There are 4 atoms of each type per crystal unit-cell, each bonded to 4 atoms of the other type in a tetrahedral configuration. The lattice dimensions are determined by the length called *lattice parameter*, denoted a, which varies between compounds (see Table 2.1). The intentional substitution of an atom in the lattice by an impurity atom can be used to dope the material and tune its electrical properties.

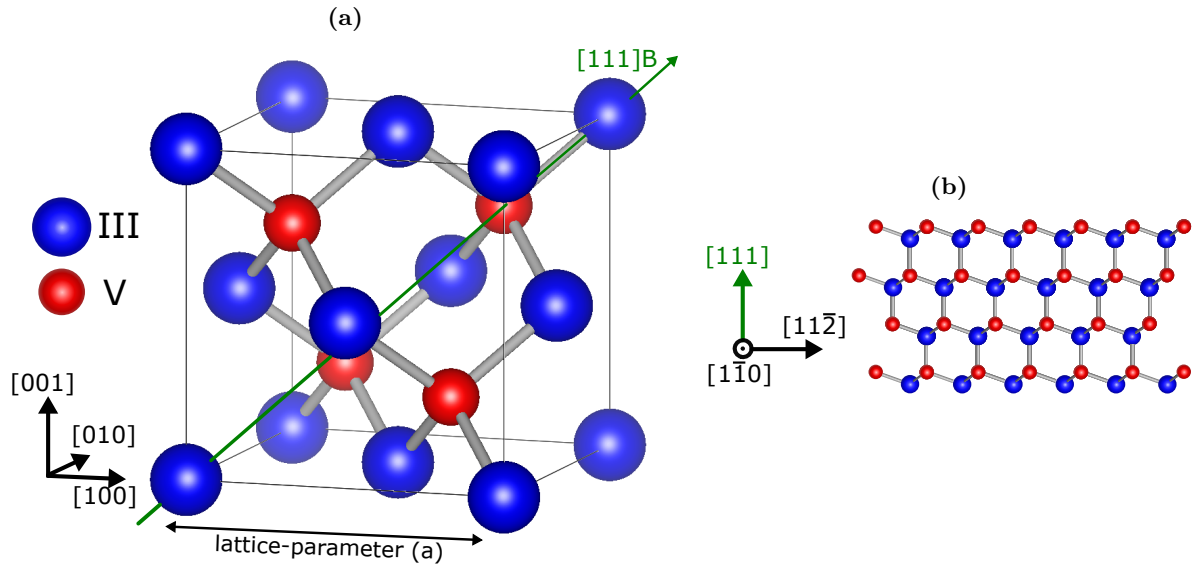

Figure 2.8: *Schematic of the atomic structure of the cubic Zinc-Blende (ZB) unit cell. The* $\langle 100 \rangle$ *(black, common for planar layer epitaxy),* $\langle 111 \rangle B$ *(green, typical NW growth direction) directions are indicated by arrows. (b) Crystal structure viewed along the* $[1\bar{1}0]$ *direction.*

Table 2.1: *Lattice-parameter at* 300 K *for some cubic crystals employed in this thesis.*

Si	GaP	$GaAs_{0.75}P_{0.25}$	GaAs $Al_xGa_{1-x}As$ ($x < 0.5$) $Ga_{0.51}In_{0.49}P$
5.43 Å	5.45 Å	5.60 Å	5.65 Å

Epitaxial processes

Epitaxy, from the greek 'taxis': 'arrange', and 'epi': 'on top', describes the technique by which thin crystal films are synthesized, generally employing a *seed* or *substrate* made of a pre-existing crystal, and onto which material precursors are brought and solidified, following the underlying crystal structure.

Figure 2.9 describes the processes at a III-V surface during vapor-solid (VS) epitaxial growth. The surface is not perfectly flat but presents steps of atomically flat domains called 'terraces', which follow the eventual tilt of the surface from its nominal crystal direction, or its macroscopic roughness. The atoms are supplied to the surface either through a beam of atoms or molecules, or through a gas of chemical precursor that release the desired atoms at the surface with a chemical reaction. The different technologies are discussed later. Atoms are then adsorbed onto the surface where they can migrate in 2D, a process called 'adatom diffusion'.

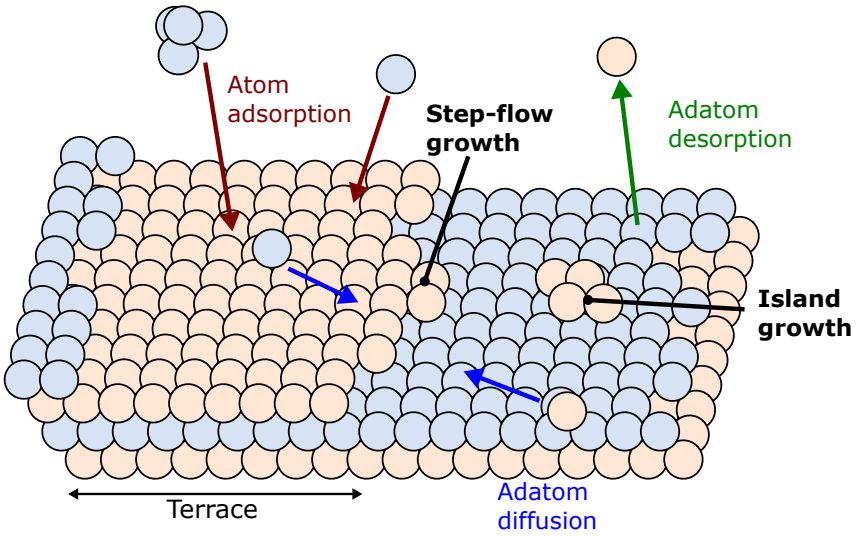

Figure 2.9: *Schematic of a III-V surface during epitaxial growth.*

Adatoms can incorporate into the lattice, and they preferably do so at the step edges, more favorable energetically. Epitaxial growth can thus occur with a continuous influx of atoms extending the terraces, the so-called 'step-flow' regime. However, it is also possible that they incorporate in the middle of a plane, and start clustering into a new island. This 'island growth' process becomes more favorable when the diffusion length of adatoms is reduced, by changing the temperature or the group-V flux for example. Finally, the adsorbed atoms can also migrate and then evaporate. Typically, group V adatoms have short residence time and diffusion length, and readily evaporate from the surfaces, whereas group III elements are generally assumed to have a unity sticking coefficient, so that adatoms diffuse until they either incorporate into the crystal, or coalesce into droplets.

Vapor-solid epitaxial processes typically govern the growth of the NW shells, which takes place in the same conditions as thin-film growth.

2.2.2 Molecular beam epitaxy

MBE principle and components

A solid-source MBE (Figure 2.10) consist in a chamber kept in ultra-high vacuum conditions (background pressure of 10^{-10} Torr), where materials are heated and evaporated from effusion cells. In the absence of obstacle, the evaporated molecules flow ballistically toward the substrate holder placed in the middle of the chamber, and contribute to the epitaxial growth, hence the name 'molecular beam epitaxy'. Controlled shutters are used to stop the fluxes individually. The substrate holder is equipped with a rotator to ensure uniform coating.

A combination of high-vacuum pumps are needed at such low pressures, which consist mainly in traps for residual molecules (ionic and cryogenic pumps). As the atoms travel in a ballistic

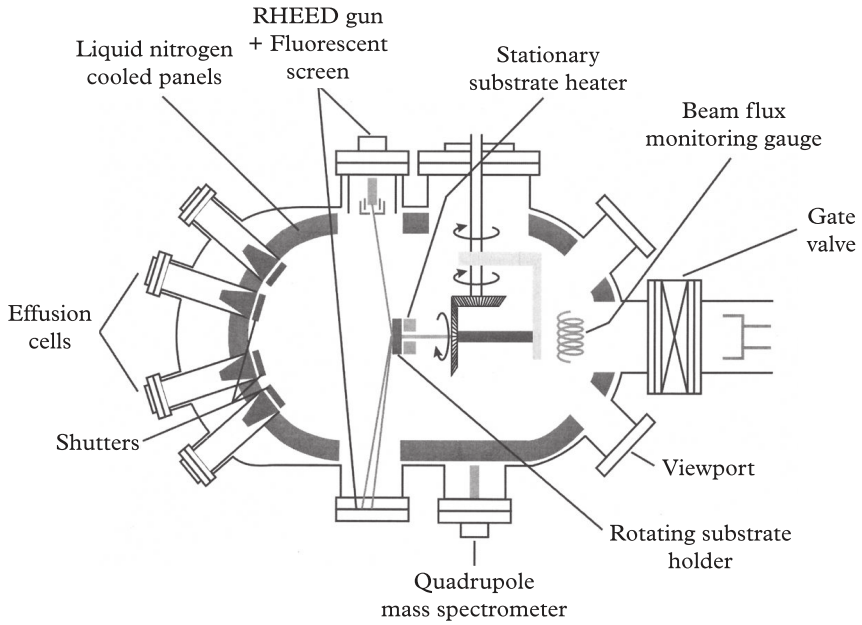

Figure 2.10: *Schematic of the growth chamber of an MBE. From [Orton and Foxon 2015].*

regime in the chamber, the sidewalls must capture all incoming molecules to prevent re-emission. The final pumping component consists therefore in hollow panels surrounding the sample holder, and filled with liquid N_2 flowing from an external circuit, keeping them close to $-196\,°C$. This way, the incident molecules condensate on the walls and do not have enough thermal energy to re-evaporate. To gain further insight on the residual elements in the chamber, it is equipped with a quadrupole mass spectrometer, able to detect the presence of elements and their molecular configuration.

To monitor the cell fluxes, two complementary tools are also needed. First, several flux gauges (Bayard-Alpert gauges) are placed inside the chamber, in particular just before the sample holder in the path of the beams. They work by ionizing gas molecules with a heated filament, and collecting the ions within a biased grid. The resulting electric current is related to the incident atom flux with their ionization cross-section, the temperature, and a gauge geometrical factor. But in general, such gauges are calibrated to give the equivalent pressure of a gas of N_2 molecules (beam-equivalent pressure, BEP). To make this value meaningful for another gas, it should be multiplied by a relative sensitivity factor, which is in first order the ratio of the ionization cross-section of the new specie to the one of N_2. However, for the gauge placed right across the flux, the hypothesis of an isotropic gas does not hold and this value, though expressed in Torr, is not representative of a physical pressure. Therefore, the BEP is used as a value proportional to the molecular beam flux. As the proportionality coefficient can drift over time due to gauge ageing, the absolute flux has to be calibrated by other means.

This brings us to the electron gun facing a fluorescent (phosphorus) screen, constituting together the *reflection high-energy electron diffraction* (RHEED) characterization setup. Electrons are accelerated towards the sample surface at grazing incidence and diffract on the first few atomic layers of its crystal lattice. The diffraction pattern displayed on the screen gives some insight on the surface arrangement of atoms. In particular, from the change of RHEED intensity during growth, it is possible to determine with precision the moment when a new monolayer is completed (for a complete introduction to the technique, see for example [Orton and Foxon 2015]). The continuous monitoring of the diffracted intensity allows thus to precisely calibrate the growth rate of a planar crystal layers. This value in monolayer/s can be expressed in unit length per unit time, knowing the crystal lattice parameters, or even in a number of atoms per unit time per unit area (flux).

An actual MBE setup with all these elements is shown in Figure 2.11.

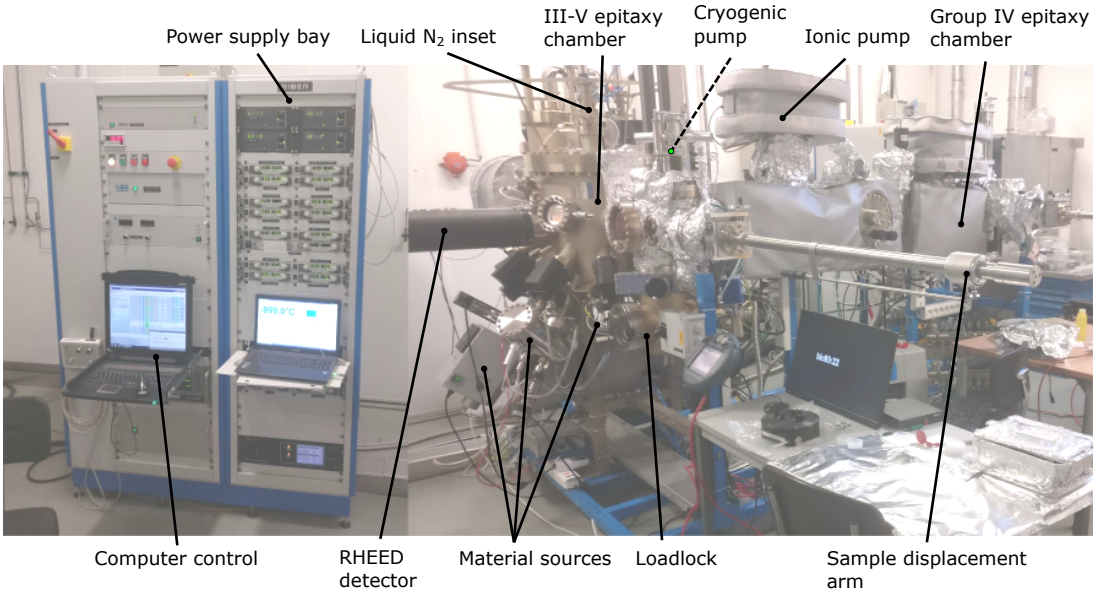

Figure 2.11: *Photograph of an MBE setup used in this project (IPVF's Compact21 MBE).*

MBE setups used in this project

C2N: MBE Riber32. During the first year of my thesis, I used a Riber32 MBE, located in the C2N labs in Marcoussis (previously Laboratoire de Photonique et Nanostructures, LPN). This MBE is smaller and more compact than the one described in Figure 2.11. The source cells are disposed on two rows on one side of the machine, facing the substrate holder (Figure 2.12a). In this configuration, the angles of incidence of the cells relative to the substrate normal are not identical. They are summarized in Table 2.2. Some molecular beams like P or Be are much closer to the substrate normal than others such as As or Si. It is important to consider for NWs, which, as 3D structures, are affected by the flux incidence angles.

IPVF: MBE Compact 21. Another MBE was used the last year of the project, a Riber Compact21 shown in the photograph Figure 2.11.

Table 2.2: *Summary of the cell incidence angles relative to the substrate normal in the Riber32 and Compact21 MBEs.*

	As, Si	P, Al	Ga, In	Be
Riber32	35°	17°	32°	16°
Compact21	40°	40°	40°	40°

The main differences expected from the change of setup are:

1. A different sample temperature. In both systems, the temperature is measured with a pyrometer pointed towards the center of the sample holder, but the incidence angle, the distance to the sample, and possibly the solid angle of optical collection are not identical. The molybdenum holders used are also different so their contributions to the radiated power are also expected to be different. The temperature measured by the thermocouple at the rear side of the wafer is not reproducible either, due to the unpredictable contact

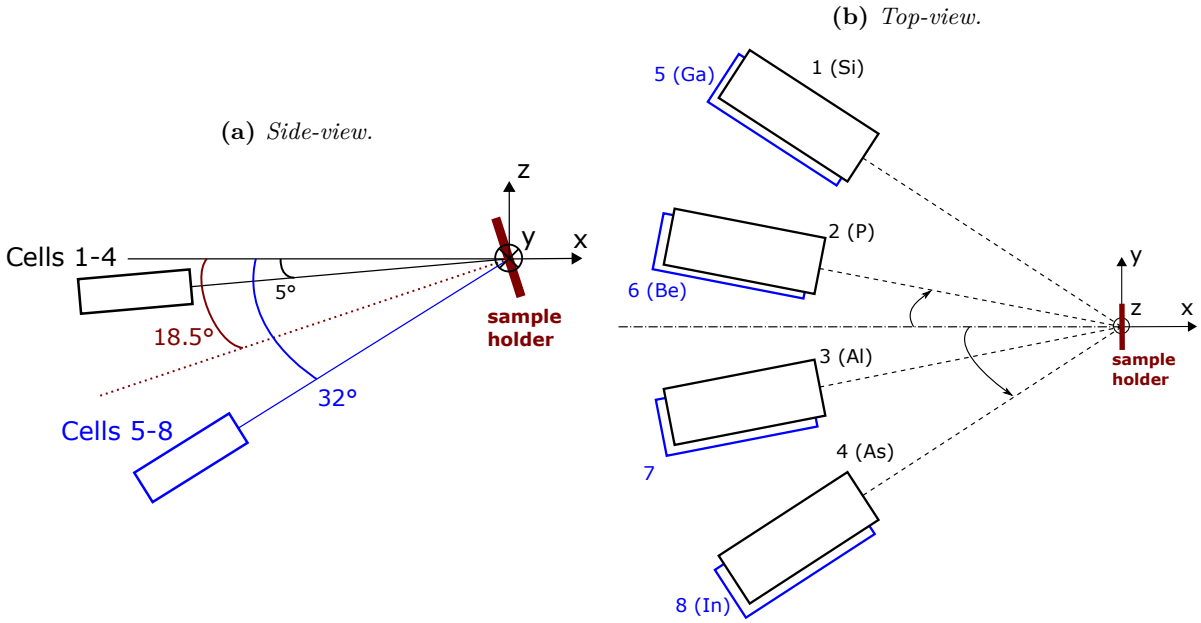

Figure 2.12: *Source cells geometrical configuration in the Riber32 setup. The cells are disposed on two rows facing the substrate holder.*

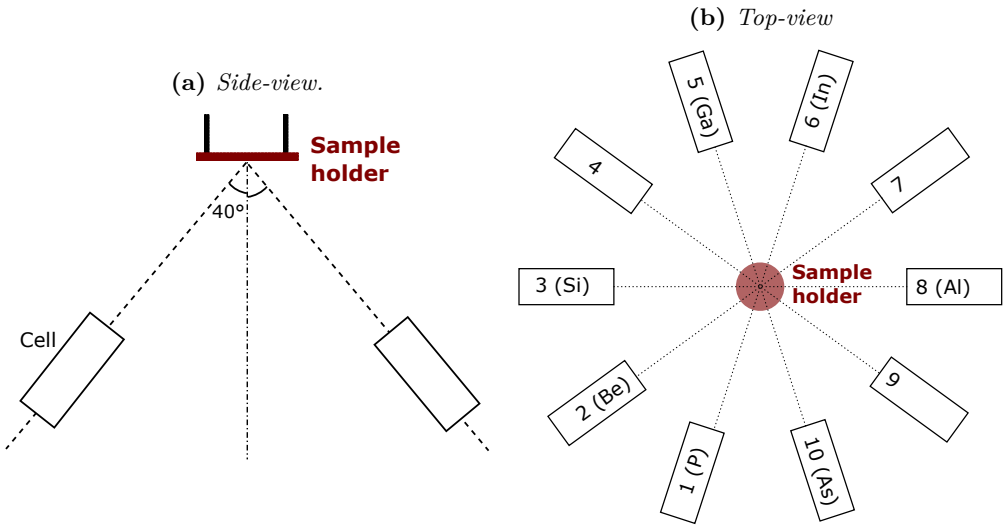

Figure 2.13: *Source cells geometrical configuration in the Compact21 setup. The cells are disposed on a ring under the substrate holder.*

mismatch between the 1/6 2” sample and the molybdenum holder, which can alter the thermal equilibrium.

2. In this equipment the cells are arranged along a ring at the bottom of the chamber, facing the substrate holder which is lying on top of them. All cells make a 40° angle with the substrate normal, which is larger than in the Riber32, and uniform among the cells (Figure 2.13 and Table 2.2). In addition, the sequence of the cells, as seen from one NW sidewall, is different. These differences may result in different growth dynamics especially for the NW shells.

3. The residual impurities inside the chamber might differ, this new chamber was only used for the growth of AlGaAs and GaInP compounds for solar cells, whereas the Riber32 system was used for many years for NW (including Au-catalyzed) and planar III-V growth.

Two MBE setups were used for this thesis project, and special attention must be paid to differences between the machines which can affect the NW growth.

Growth rate calibration by RHEED oscillations

The source cell fluxes are calibrated using RHEED oscillations on planar III-V layers [Orton and Foxon 2015].

For the group III elements Ga and Al, a GaAs(100) substrate is used, and growth is carried out at 580 °C under an excess of As (typically $V/III = 10$). For In, it is an InAs(100) substrate, and the substrate temperature is typically 480 °C to 530 °C. The growth rate is measured using RHEED oscillations for different temperatures of the cell, and is fitted with an Arhenius law (Figure 2.14a). The BEP corresponding to each cell temperature is then recorded to get a calibration law of the flux as a function of the BEP (linear, Figure 2.14b). The atomic flux of the cell is thus expressed in unit of the corresponding growth rate of a GaAs(100) layer, either in monolayers per second (ML/s) or in Å s^{-1}.

(a) *Growth rate vs Ga cell temperature.*

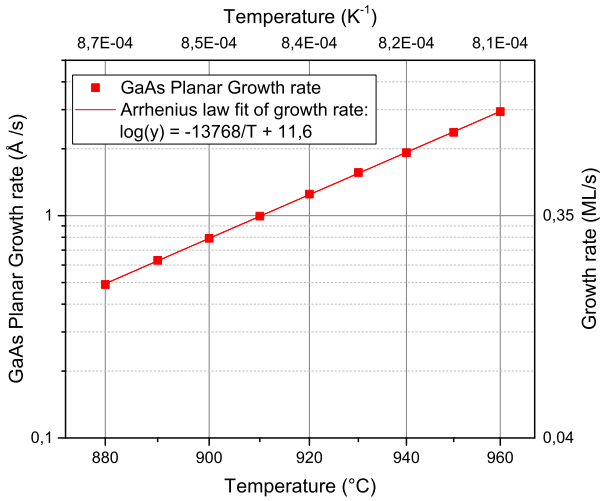

(b) *Growth rate vs BEP.*

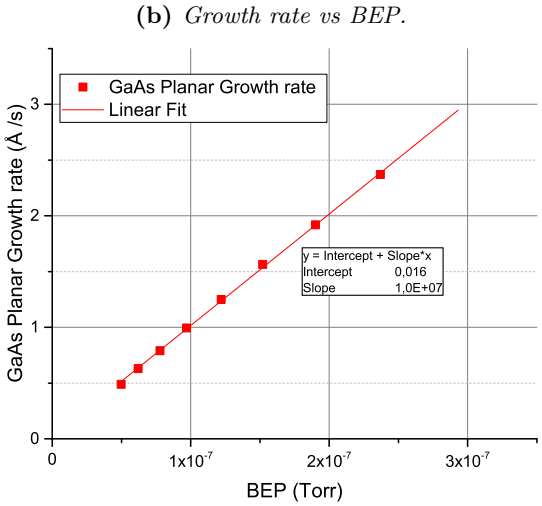

Figure 2.14: *(a) Growth rate of a GaAs(100) thin-film measured by RHEED oscillations, for different temperatures of the Ga cell in the Riber32 MBE. The data is fitted to an Arhenius law. (b) Linear relationship between BEP and growth rate. The BEPs were measured for the different Ga cell temperatures after the growth rate measurements.*

For the group V element As, a GaAs(100) substrate is used. The substrate temperature and Ga growth rates are typically 580 °C and 2 Å s^{-1}, respectively. The As flux is modulated

by adjusting the cell valve opening. The absolute flux is deduced from the linear interpolation of the growth rate measured by RHEED oscillations for As fluxes below $2\,\text{Å}\,\text{s}^{-1}$, as described in [Ramdani et al. 2013], Supplementary. This method is also applied to calibrate the P flux, using a GaP(100) substrate. The BEP is then recorded for each valve opening value, to get a calibration law of the flux vs BEP, like for group III fluxes.

Doping flux calibration by Van der Paw measurement

To calibrate each dopant flux as a function of the crucible temperature, 3 GaAs samples are grown on semi-insulating (SI) substrates at different dopant crucible temperatures, but using the same growth rate.

The carrier concentration inside each layer is measured by Hall effect using a Van der Pauw setup [Van der Pauw 1958]. Specifically, 5×5mm square pieces are contacted at all 4 corners with In dots rapidly annealed at 400 °C to form ohmic contacts, as verified from IV curves. The measured carrier concentrations are assumed to correspond to the number of dopants arriving at the surface during the layer growth. This implies two assumptions:

1. The sticking coefficient of Si and Be on GaAs(100) surfaces during epitaxial growth is unity, meaning that atoms do not re-evaporate.
2. The dopant activation is also unity, meaning that atoms systematically incorporate in the lattice where they act as donors (Si in Ga sites for n-type) or acceptors (Be in Ga sites for p-type).

Thus, to ensure complete dopant activation even for doping levels $[Si] > 5 \times 10^{18}\,\text{cm}^{-3}$, the substrate temperature is typically lowered to 550 °C, which minimizes As desorption and prevents Si atoms to incorporate in As lattice sites where they would behave as acceptors [Tok et al. 1998]. The carrier concentrations corresponding to different crucible temperatures are then fitted with an Arhenius law, and normalized with the layer growth rate to obtain a calibration law of the dopant flux as a function of the crucible temperature (see for example Figure 2.15 for the Be cell calibration in the Riber32 MBE).

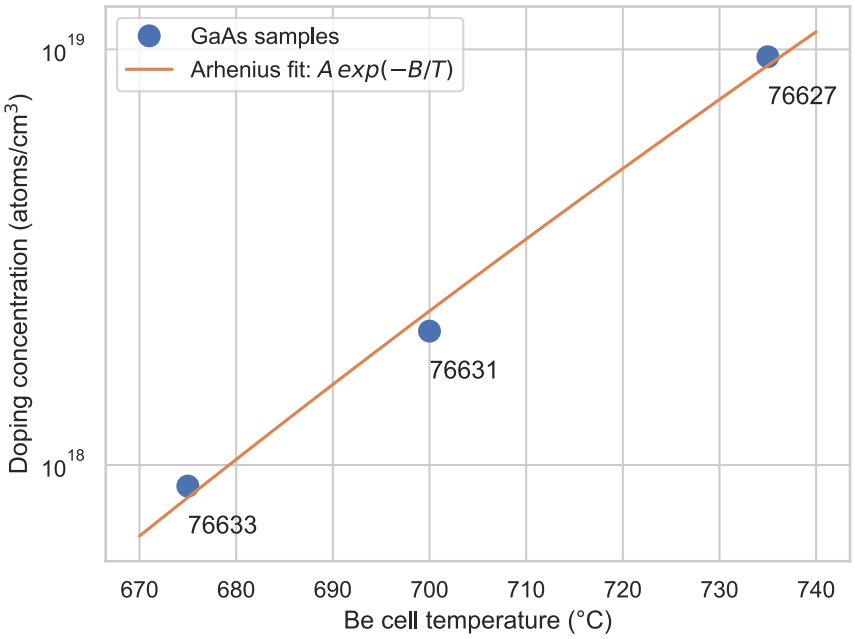

Figure 2.15: *Doping concentration (logscale) in three GaAs thin-films doped with Be in the Riber 32 MBE setup, using different Be cell temperatures. The growth rate was* $2\,\text{Å}\,\text{s}^{-1}$ *in all cases. Doping concentrations were measured by Hall effect in a Van der Pauw setup. The curve is fitted with an Arhenius law of parameters* $A = 2.3 \times 10^{35}\,\text{cm}^{-3}$ *and* $B = 3.81 \times 10^{4}\,\text{K}$. *[76633, 76631, 76627]*

Two MBE setups were used in this project. Here I have presented their principle and their specificities, and described the flux calibration methods.

2.2.3 Vapor-liquid-solid growth of nanowires

Aside the widely used MBE and MOCVD, liquid phase epitaxy (LPE) is another growth technique where crystals are precipitated from a high-temperature melt of precursors, close to thermodynamic equilibrium. Vapor-liquid-solid (VLS) growth is basically a combination of these techniques, where one species, dissolved in a liquid phase with the other compound (the typical solubility of As in liquid Ga at 600 °C is 1 %), is constantly replenished from the vapor phase. Metal-catalyzed NWs are grown this way, though the term 'catalyzed' is generally inappropriate. Although in MOCVD the hot liquid phase enhances the chemical decomposition of the metalorganic precursors into the growth elements and therefore acts as a catalyst, in general (in MBE), the droplet is merely a reservoir of atoms, and the preferential incorporation at this growth front results from the imbalance of the chemical potential there and at the NW sidewall or on the mask.

As early as in 1964, Wagner and Ellis proposed the VLS growth to explain how Au-catalyzed NWs are formed [Wagner and Ellis 1964]. Here, I present some models proposed to explain the VLS growth of III-V NWs independently of the catalyst (a foreign metal such as Au, or a group-III constituent of the NW, such as In or Ga), or the technique (MBE or MOCVD). [1]

2.2.3.1 Polytypism in NWs: simplified nucleation model

Elaborating a complete thermodynamic model quantitatively explaining NW growth is difficult since most of the processes happen outside equilibrium, complex nucleation events are involved and many material parameters like surface energies are unknown in the considered growth conditions. In 2007, Glas, Harmand and Patriarche proposed a model based on nucleation to explain the NW growth. This model was the first to satisfyingly explain an important peculiarity of NWs: they can adopt the cubic ZB crystal phase as well as the hexagonal Wurtzite (WZ) phase, whereas the former should be energetically favored and is the only one encountered in planar crystal growth.

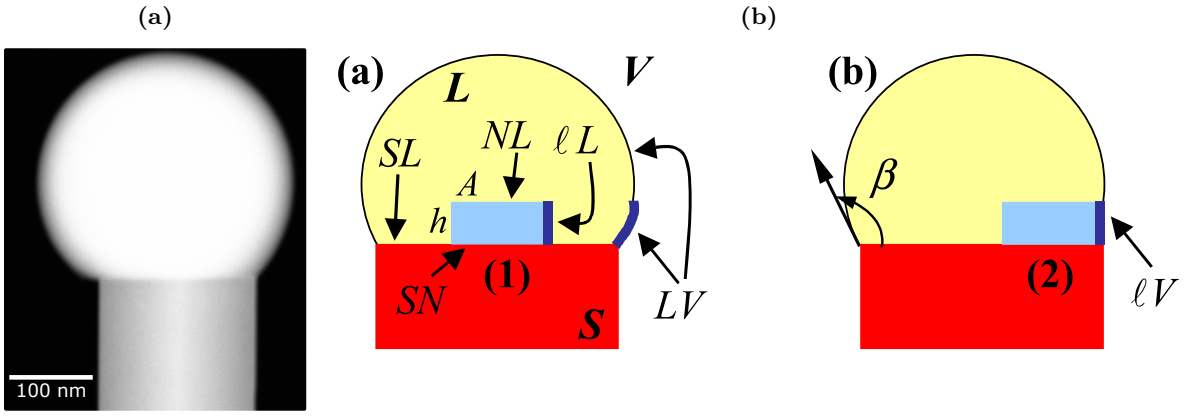

Figure 2.16: *(a) TEM image of the top of a GaAsP NW, later presented in Section 4.3. (b) Schematic of the nucleus of a new monolayer in VLS-grown NWs, with the interfaces of interest, in the hypothesis of (b.(a)) nucleation away from and (b.(b)) at the triple-phase-line. From [Glas et al. 2007]*

[1] To better appreciate self-catalyzed VLS growth, I encourage the reader to watch short videos of *in situ* observations of NW growth, at https://pubs.acs.org/doi/10.1021/acs.nanolett.9b04808

The chemical potential of group III-group V pairs per unit volume of crystal (μ) must be higher in the liquid droplet than in the solid crystal below, as the droplet is supersaturated with group V atoms supplied from the vapor phase:

$$\Delta\mu > 0 \tag{2.22}$$

However, forming a small nucleus of crystal which will then make a new atomic layer and therefore extend the crystal, is not necessarily favored as it results in new surfaces and interfaces which may increase the overall energy. Moreover, depending on whether the nucleus forms inside the droplet, or at the edge (triple-phase-line), different surfaces are formed, with different surface energies. The change of free enthalpy associated with a nucleus formation inside the droplet (Figure 2.16ba), can be expressed :

$$\Delta G = -A\,h\,\Delta\mu + P\,h\,\gamma_{lL} + A\,\gamma_{SN}, \tag{2.23}$$

where γ_{lL} is the energy per unit area of the lateral interface between the liquid and the nucleus, γ_{SN} the energy per unit area of the solid-nucleus interface, A is the top area of the nucleus, P its perimeter, and h its height (one atomic layer). The critical enthalpy change ΔG^* is the maximum value of ΔG for any size of nucleus (A), and represents the energy barrier to overcome to form a new monolayer.

A nucleus of given shape is identical in ZB and WZ, apart from its position on the underlying crystal. Thus, the ΔG can be directly compared, and $\Delta\mu$ and γ_{lL} are identical. However, $\gamma_{SN}^{WZ} > \gamma_{SN}^{ZB}$ (the cohesive energy of WZ is higher than of ZB), resulting in a lower ΔG for ZB and a preferred nucleation in this phase. In conclusion, nucleation away from the TPL results in ZB phase.

Conversely, considering nucleation at the TPL (Figure 2.16bb), a portion α of the nucleus perimeter is now exposed to the vapor phase, whereas the total droplet surface has diminished by an area proportional to the exposed nucleus area through a factor named τ. The free enthalpy change is then:

$$\Delta G = -A\,h\,\Delta\mu + P\,h\,\left[\alpha(\gamma_{lV} - \tau\,\gamma_{LV}) + (1-\alpha)\,\gamma_{lL}\right] + A\,\gamma_{SN} \tag{2.24}$$

Geometrical calculations yield $\tau = \sin(\beta)$. ΔG is in this case dependent on the type and position of the nucleus, and the kind of lateral facets which are exposed. Arguing that the lateral surface energy of a WZ nuclei is smaller than the one of ZB: $\gamma_{lV}^{WZ} < \gamma_{lV}^{ZB}$, the authors show that for high enough supersaturation $\Delta\mu$, a WZ nucleus is favored. Thus, nucleation at the TPL makes WZ nucleation at least possible, if not certain.

Finally, the difference between Equation 2.24 and Equation 2.23 yields the following condition for the nucleation to occur at the TPL:

$$\gamma_{lV} - \gamma_{lL} - \gamma_{LV}\sin(\beta) < 0 \tag{2.25}$$

As a result, nucleation at the TPL is preferred for a given droplet contact angle range, centered at 90°.

For an intermediate range of droplet contact angles, nucleation occurs at the TPL and the WZ phase is likely preferred. For higher or lower contact angles, nucleation occurs inside the droplet and results in ZB phase. Experimental observations qualitatively agree with the model, as a ZB phase is observed at high and low contact angles, and WZ in between (Figure 2.17, or [Priante et al. 2013]).

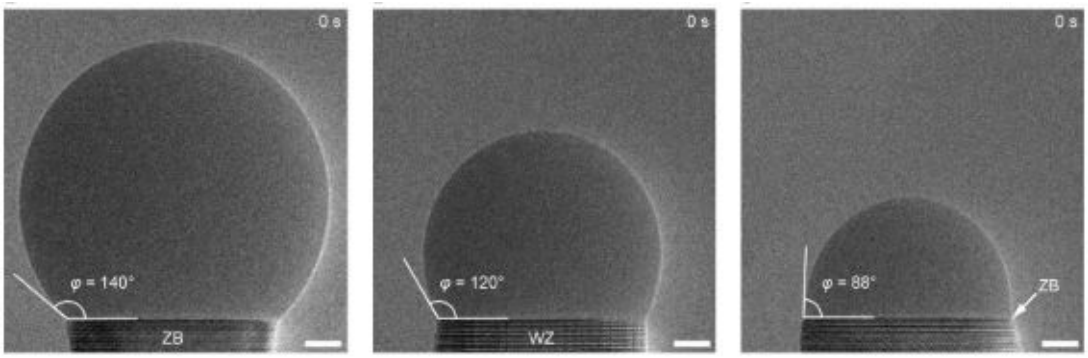

Figure 2.17: *In situ transmission electron microscope (TEM) images of a NW with 3 different droplet contact angles, which correlates with the growth of ZB at large and small angles, and WZ at intermediate angles. From [Panciera et al. 2020]*

2.2.3.2 Truncated and tilted facets: total surface energy considerations

Since 2007, new experimental results have become available, in particular, growth inside a transmission electron microscope (TEM) allows to follow the growth dynamics with unprecedented spatial and temporal resolutions ([Wen et al. 2010]; [Jacobsson et al. 2016]; [Harmand et al. 2018]; [Panciera et al. 2020]). It was evidenced that the NW corners are periodically truncated during the VLS growth of ZB Si [Wen et al. 2011], Ge [Gamalski et al. 2011] or GaAs NWs [Jacobsson et al. 2016], which seems like a general effect occurring after or during monolayer completion. Moreover, NWs are often widening or narrowing during growth depending on the droplet geometry. In addition, the droplet contact angle appears to be the sole parameter controlling the crystal phase, but the range for WZ formation is actually not centered around 90° [Jacobsson et al. 2016]. The previous model needs to be revamped to explain why these different configurations exist.

Recent calculations do not actually consider nucleation but rather compare the total surface energy between a given morphology, which can exhibit tapered sidewalls and even truncated edges under the droplet, and the reference state having vertical sidewalls and 90° edges at the TPL ([Jacobsson et al. 2016]; [Kim et al. 2018]; [Panciera et al. 2020]). Panciera *et al.* calculated these terms using surface energies from the literature, except for the ones at the solid-liquid interfaces (including a truncated facet at a given angle), which are fitted with the *in situ* observations. The resulting configuration diagram is shown in Figure 2.18, and can explain the different situations encountered in the experiments: narrowing ZB segments for low contact angles, straight WZ sidewalls for intermediate, and truncated ZB facets in the droplet for large contact angles, with widening sidewalls.

Controlling the contact angle is possible during growth, since increasing the V/III ratio leads to an increased axial growth rate and a reduction of the droplet volume, and consequently, of its contact angle. Conversely, decreasing the V/III ratio allows to inflate the droplet and increase the contact angle. Thus, crystal phase control is possible.

Despite its ability to predict the NW crystal structure, the absence of nucleation considerations in this model might be lacking for a complete picture. Indeed, given that a non-zero duration elapses before each monolayer initiation [Harmand et al. 2018], there must be a nucleation step which should govern the new monolayer configuration.

> Considerations of the total surface energy of the NW facets in different configurations suffice to explain the remarkable transition between different NW morphologies and crystal structures for some determined values of the contact angle.

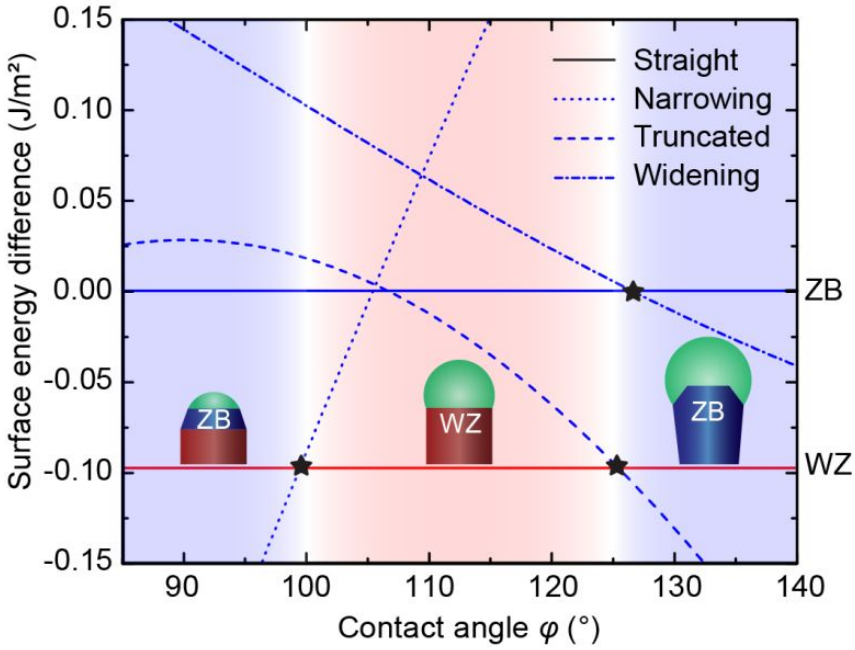

Figure 2.18: *Favorable VLS growth configurations as a function of the droplet contact angle, considering the total surface energy of the sidewall and wetted facets. Blue zero-level line corresponds to vertical (110) ZB facets and the red horizontal line to vertical* $(1\bar{1}00)$ *WZ facets. At small contact angles, the structure is ZB and the sidewalls are narrowing. Above* 100 °*, the WZ phase is preferred, with vertical sidewalls. Beyond* 125 ° *the ZB phase is once again favored with truncated wetted facets and vertical sidewalls. Only a few degrees higher, widening sidewalls are more favored (still with truncated wetted ZB facets. From [Panciera et al. 2020].*

2.2.3.3 Enhanced material collection

A NW ensemble should, in principle, only collect a small portion of the incident flux, most of it impinging the mask or the NW trunks instead of the NW droplet. However, the VLS growth of NW ensembles can actually lead to similar material consumption as planar growth, through various means. Here I focus in particular on considerations for molecular beam epitaxy (MBE). In particular, there are important flux shading effects in dense NW arrays.

- **V/III ratio close to unity.** As the VLS growth is generally group-V-limited, V/III flux ratios from 1 to 2 are typically employed. On the other hand, planar growth requires important group V overpressures and the V/III ratio is typically 10, meaning that 90 % of the supplied group V material is lost by re-emission.

- **Group V re-emission.** The droplet is replenished of group V atoms from the gas phase, not only from the direct flux from the source cell, but also by an indirect flux caused by re-evaporation of As atoms that primarily intercepted the surrounding NW sidewalls, or the mask surface. Indeed, the surface diffusion length of As adatoms is negligible. This secondary flux can amount for twice the direct flux. [Ramdani et al. 2013].

  Note that the group V atoms inside the droplet do not necessarily end up in the crystal but may evaporate back to the vapor phase. This flux becomes negligible close to the typical VLS growth temperatures (580 °C [Glas et al. 2013]), so this loss channel could be minimized.

- **Group III diffusion and re-emission.** Group III atoms that intercept the NW sidewalls may either:

  1. Diffuse to the NW droplet and participate to the VLS growth.

2. Evaporate back to the vapor phase.
3. Incorporate into the NW sidewalls by VS epitaxy, contributing to the NW formation. This effect is particularly sensitive to the temperature and the type of group V molecule in the precursor flux [Sartel et al. 2010], and is further investigated in this thesis when dealing with ternary alloys (Section 4.3).

As for the atoms impinging the mask surface, they readily re-evaporate into the gas phase and have another chance to reach the NW sidewalls or droplet ([Plissard et al. 2011]; [Oehler et al. 2018]).

Overall, once steady-state growth is attained in arrays of long NWs, diffusion and re-emission effect results in the incorporation of more than 90 % of the Ga from the incident flux into the crystal [Oehler et al. 2018]. On the negative side, the amount of Ga stored in the droplet at the end of the growth is not used, except if an *in situ* droplet consumption method is employed that permits to fully crystallize it into a useful extra NW segment.

Many factors contribute to use a significant amount of the incident material for the NW growth. The group III usage can reach 90 %, lower than for planar growth which incorporates 100 % of the incident atoms. However, the group V usage benefits from low V/III flux ratio, and important re-emission effects in NW arrays, and could be tuned to overcome the usage in planar epitaxy, where only 10 % of the flux is typically incorporated. This is particularly attractive given that arsenic is more expensive than gallium and indium.

2.2.4 Patterned substrate fabrication

All patterned wafers were fabricated in C2N laboratories in Marcoussis. Here, I describe their fabrication process, and then the baseline procedure for MBE growth.

Table 2.3: *Electrical characteristics of the Si wafers used as substrates for the growth of NWs. The doping level is estimated from the resistivity following an empirical relationship [NSM (Ioffe) 2019].*

Wafer	Resistivity	Doping level
$\mathbf{p}^{+}$	10—20 mΩ cm	$4—9 \times 10^{18}$ cm^{-3}
$\mathbf{p}^{++}$	0.8—1.2 mΩ cm	1×10^{20} cm^{-3}

Two-inch Si wafers are used, to fit the MBE holders. They are ⟨111⟩-oriented to follow the preferred NW growth direction. They are p-doped as p-core/n-shell devices are pursued, which, in a tandem configuration, have to grow on a p(bottom)/n(top) silicon subcell, terminated by a n+/p+ tunnel junction. The wafers are supplied by Siltronix. They are grown by Czochralski process, doped with boron, oriented (111) ± 0.5°, and 250—300 µm thick. Their electrical characteristics are summarized in Table 2.3.

After fully deoxidizing the wafers in hydrofluoric acid (HF) diluted in water to 5 % concentration, a silica layer about 30 nm thick is deposited via plasma-enhanced chemical vapor deposition (PECVD).

Electron Beam lithography patterning

The substrates are coated with an electron-sensitive resist (495PMMA, 2 %) and patterned in a Vistec EBPG 5000+ electron beam lithography machine, operating at 100 kV.

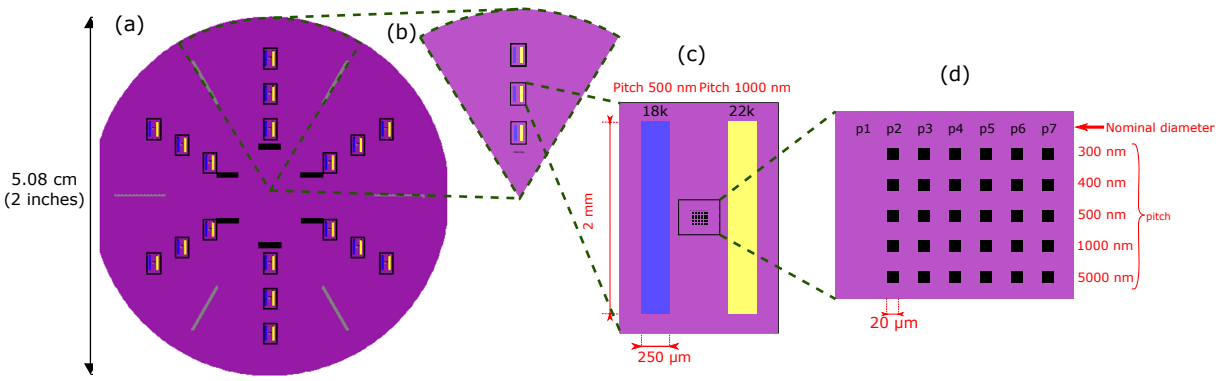

Figure 2.19: *(a) Schematic of a patterned 2" silicon substrate. (b) The substrate is then cleaved into 6 similar samples. 3 patterned zones are located at the sample tip, middle, and closer to the wafer curved edge. (c,d) Details of the patterned zones. (c) Two large rectangular areas (blue and yellow), visible with bare eye, are hexagonal arrays of pitch* 0.5 µm *and* 1 µm*, written with EBL by single-shot exposure at the middle of each hole. (d) A small matrix contains hexagonal arrays of different pitches and hole dimensions, defined by standard multiple-exposure EBL. Indications in red provide information about the dimensions and are not part of the EBL patterning.*

The patterns typically used are summarized in Figure 2.19. Large rectangles up to 2 mm long are patterned by electron beam lithography (EBL), by injecting a single dose at the center of each hole. The dose is expressed in $\mu C\,cm^{-2}$ and corresponds to the density of injected charge if the holes were 10 nm × 10 nm. For example, 20 000 $\mu C\,cm^{-2}$ corresponds to 2×10^{-8} µC/hole. On the pattern shown in Figure 2.19c, there are two large-area patterned zones, but some designs contain up to 8 zones (4 for pitch 500 nm and 4 for pitch 1000 nm). The hole size is determined empirically after the etching steps.

The design also includes a small matrix of arrays with different pitches and hole diameters (Figure 2.19d). There, the holes are written by EBL pixel-by-pixel, with a beam step size of 1 nm to ensure that small circles can be defined. The dose here is typically 2500 $\mu C\,cm^{-2}$, which for a single hole of 50 nm diameter corresponds to a charge of 4.9×10^{-8} µC/hole. This is comparable to the previous value for the single-shot exposed patterns. The hole dimension and edge definition is much better controlled using pixel-by-pixel writing, and the yield of vertical NWs is typically higher than in the 'single-shot' patterns. However, it is very slow to write the patterns this way, so it cannot be used for the large areas needed for the fabrication of devices

Note that the design of the patterns was adapted for some sample series. In particular for the growth on full 2" substrates, a unique large square pattern (1 cm to 2 cm wide) is defined at the center by single-shot exposure.

Pattern transfer

The following fabrication steps are described in Figure 2.20. The sample with patterned PMMA is placed in a capacitively coupled plasma-reactive ion etching (CCP-RIE) chamber. The pressure is stabilized to 7 mTorr, as SF_6 and CHF_3 gases are provided with a flow rate ratio of 8:20, and the bias voltage is about 190 V. The etch rate was previously calibrated on planar SiO_x layers deposited in the same conditions as our mask, etched for different durations, and whose thicknesses were measured by fitting their normal reflectance to a SiO_x–on–Si model. Special attention is paid not to etch all the way down to the bottom of the holes so as to leave about 4 nm of SiO_x (nominally). This way, plasma-induced damage to the Si is avoided, in particular any possible amorphization.

The PMMA resist is removed by successive immersion in trichloroethylene and acetone (with sonication), then rinsed with IPA. To ensure complete removal of organic residues, the sample is then subject to an oxygen plasma cleaning by CCP-RIE.

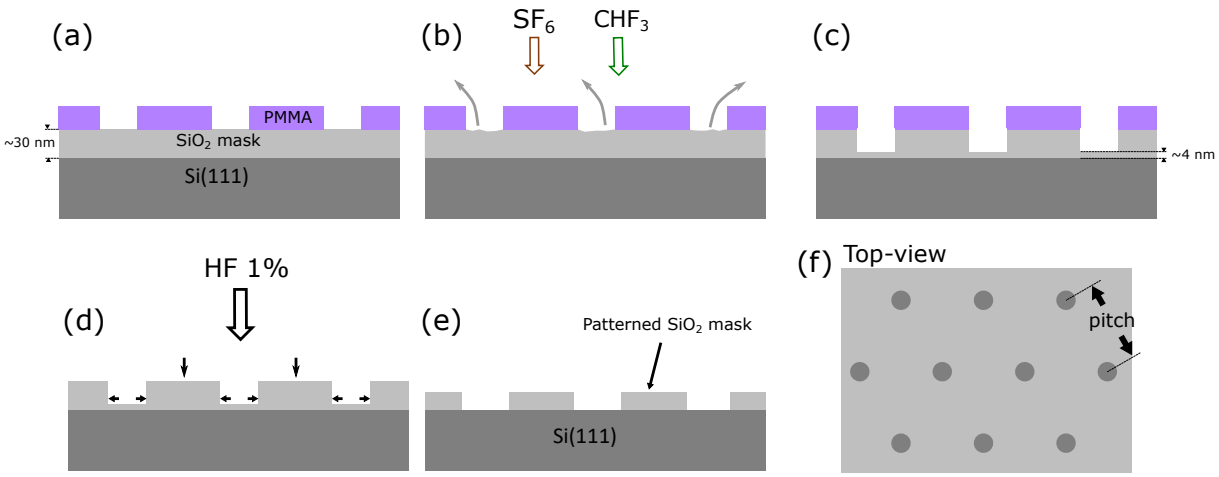

Figure 2.20: *(a-e) Schematic of the patterned substrate fabrication. (a) Initially, PMMA patterned by EBL into a hexagonal array of holes lies on a* $\approx 30\,\text{nm}$ *thick* SiO_x *layer, coating a p-Si(111) substrate. (b) The holes are transferred into the* SiO_x *layer by CCP-RIE. (c) The holes are not etched down to the bottom, to avoid amorphization and damage to the first Si layers. (d) After resist stripping and sample cleaning, a last dip is performed in HF diluted in water at a concentration of* $1\,\%$*. (e) Due to the isotropy of this etching method, the mask is thinned and the holes are enlarged.(f) A top-view of the patterned substrate showing the hexagonal geometry of the pattern and the inter-hole distance (pitch).*

The remaining SiO_x is removed by a dip in a $1\,\%$ HF solution (diluted in water), for a typical duration of 30 s, and under dimmed light to prevent any light-induced modification of the etching process. Due to the isotropy of HF wet etching, the holes are enlarged and the mask is thinned during this step. After rinsing with de-ionized water and drying with N_2, the sample is quickly loaded into the MBE (within 5 minutes), to prevent Si re-oxidation inside the holes.

During the second half of this thesis, while it was not possible to realize this HF dip at the MBE facility, the sample was stored overnight in a container flushed two timed with N_2, and inserted in the MBE the following day. Parasitic deposition on the mask seems enhanced in these conditions, but with careful pre-growth thermal treatment it can be prevented.

2.2.5 Baseline procedure for the nanowire growth by MBE

The morphology of the sample during the different steps of the NW growth is schematically described in Figure 2.21, along with illustrating SEM images.

Pre-deposition

The patterned substrate is outgassed at 500 °C in the MBE system to desorb water, and then introduced inside the growth chamber on a rotating holder (at typically 10 rpm). The substrate temperature is monitored with a pyrometer (IRCON 0.9 µm) and stabilized at 600° for at least 10 min before the growth.

The growth procedure is initiated with the catalyst pre-deposition, during which only a Ga flux is provided to form liquid droplets inside the holes of the mask. Some experimental studies suggest that, at this temperature, Ga evaporates from the mask so that only the direct flux impinging the holes contribute to the droplet formation ([Plissard et al. 2011]; [Oehler et al. 2018]).

Core growth

Without stopping the Ga flux, a flux of group V molecules is provided to initiate the VLS growth. The V/III flux ratio is close to stoichiometry as the VLS growth is group V limited, typically

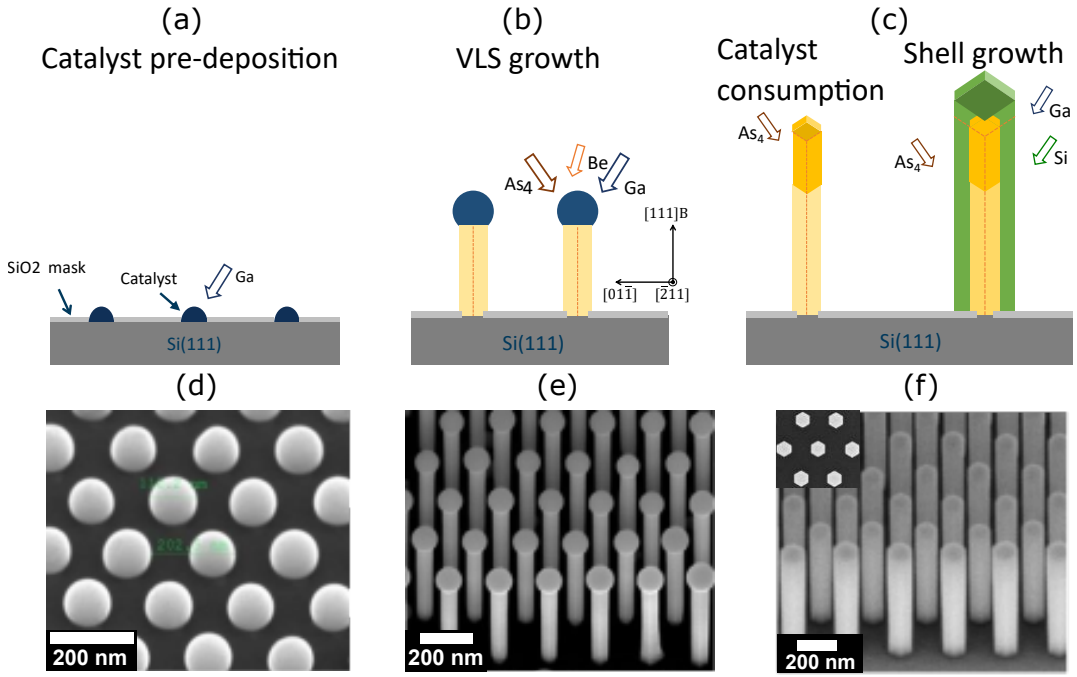

Figure 2.21: *Schematic of the growth sequence for core-shell NWs in the MBE chamber. (a) Ga droplets are formed in the holes of the patterned wafer by supplying only Ga. (b) VLS growth of GaAs NWs is initiated by supplying an As flux. (c) Catalyst consumption can be realized by supplying only an As flux, thus crystallizing the liquid Ga into GaAs. A shell can be grown by supplying Ga with an excess of As. (d,e,f) SEM images corresponding to the different steps are also provided. The stable facets for a GaAs made of ZB phase are the* {110}*, as represented on the drawings.*

around 1.5. A Si or Be flux can be provided during core growth (starting from the beginning of the pre-deposition) to incorporate them as dopants. The incorporation and activation of such impurities in the NW core are investigated in Chapter 4. If the sample needs to be taken out right at the end of the axial growth, all fluxes are stopped abruptly, while the heating oven is switched off to quickly cool the sample down. The typical NW diameter at the end of this step is between 85–105 nm. Otherwise, the droplet can be consumed by switching off all group III fluxes while maintaining the group V fluxes, which crystallizes the remaining liquid Ga into an extra GaAs segment.

Shell growth

For shell growth, the conditions are similar to planar III-V layers, and a group V flux is provided in excess, while the group III flux determines the growth rate. The typical V/III ratio used for GaAs shell growth is 7. The substrate rotation is maintained throughout the shell duration at rather high speed (preferably 20 rpm), to promote a uniform coating of the NW sidewall facets. Switching from a shell with As compounds to P compounds necessitates to gradually turn down the As flux while at 450 °C, then turning the P flux on, to avoid intermixing of P and As at the interface.

The fabrication of a solar cell from the epitaxial NW array was developed and optimized during this thesis work, and is presented separately, in Section 5.2.

2.3 Characterization of nanowires and nanowire solar cells

After the growth, NW arrays are systematically observed using a standard scanning electron microscope (SEM). The acquisition of the JV characteristics of complete NW solar cells in the dark and under an AM1.5G solar simulator is also always performed. However, more advanced characterization techniques were used to characterize individual NWs or complete NW solar cells, which I briefly describe in this section.

2.3.1 Transmission electron microscopy and energy-dispersive X-ray spectroscopy

TEM Imaging

Transmission electron microscopy (TEM) at room-temperature is used to investigate the crystal structure of individual NWs at the atom scale. The tool is a FEI Titan THEMIS operating at 200 kV. Following the epitaxial growth, individual NWs are mechanically transferred on a TEM grid, transparent to the electron beam. They are observed from their lateral side.

Operation in TEM mode along the $\langle 1\bar{1}0 \rangle$ zone-axis of the NWs allows to distinguish the WZ and ZB crystal phases in the selected area diffraction patterns, as well as acquiring low-resolution bright- and dark-field (BF or DF) images to identify twins and stacking faults in the NWs. By selecting specific spots of the diffraction pattern, dark-field images can be reconstructed which highlight the WZ and/or one of the WZ phases.

High-resolution pictures are taken in scanning mode (STEM), allowing to distinguish atom columns and to identify the polarity of the crystal. High-angle annular diffraction (STEM-HAADF) allows to get some insight on the chemical composition from the image contrast, as heavier atoms have a higher chance of scattering the incident electrons to high angles.

More insight on their chemical composition is gained when using X-rays detectors to perform energy-dispersive X-ray spectroscopy measurements (EDX), using a Brucker Super X detector.

Core-shell composition measurement by EDX

The quantification of the chemical composition in the NW from the X-ray spectrogram is automatically performed by the software ESPRIT[2], specifying a nominal thickness of 100 nm to take photon reabsorption into account.

This allows to characterize NWs where the core and the shell composition differ, as in Figure 2.22a for example. The EDX analysis is actually performed along the $\langle 11\bar{2} \rangle$ zone-axis of an entire NW, so the shell apparent signal does not need further correction, see Figure 2.22b. As for the core, its apparent EDX composition is corrected by weighing the signal with the thickness of the core and shell along the electron beam direction:

$$x_{app} \times (t_{core} + 2t_{shell}) = x_{core} \times t_{core} + x_{shell} \times 2t_{shell} \tag{2.26}$$

where x_{app} is the apparent core composition, x_{shell}, the shell composition, t_{core} and t_{shell} the effective thicknesses of the core and shell along the beam path. The shell thickness t_{shell} is measured between two facets from EDX mappings, with an eventual error term to account for the variation of the shell thickness among facets, typically 1 nm to 2 nm. Error bars are calculated from the standard error on the EDX measurement, and the uncertainties on the different thicknesses. This method is used in this thesis to characterize GaInP shell (Section 4.1), or slight core-shell composition inhomogeneities in GaAsP NWs (Section 4.3).

[2] https://www.bruker.com/fr/products/x-ray-diffraction-and-elemental-analysis/eds-wds-ebsd-sem-micro-xrf-and-sem-micro-ct/esprit-2/spectrometry-functions/esprit-imaging.html

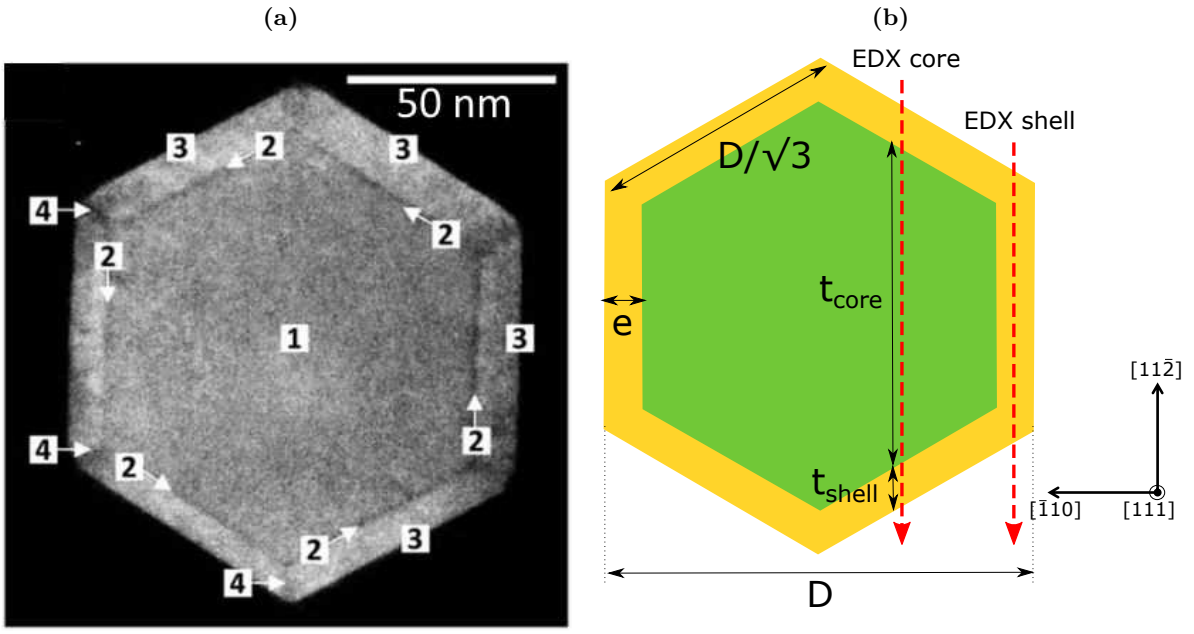

Figure 2.22: *(a) TEM micrograph of a GaAsP NW, viewed along its cross-section. A shell of different alloy composition is visible. From [Himwas et al. 2019]. (b) Geometry of a core-shell NW cross-section. The red dashed lines represent the possible electron beam paths when observing the NW from the side in STEM, through the NW core and shell. Orientation along a* $\langle 11\bar{2} \rangle$ *direction permits a direct and accurate determination of the alloy composition in the shell.*

2.3.2 Cathodoluminescence

Cathodoluminescence (CL) consists in the excitation of a semiconducting material with a focused electron beam, generating multiple electron-hole pairs in a small volume. After thermalizing to the band edges, defect levels, or excitonic states, electrons and holes may recombine radiatively and the emitted photons are collected and spectrally dispersed using a spectrometer.

The setup at C2N is a quantitative cathodoluminescence microscope manufactured by *Attolight* (*Allalin 4027 Chronos*[3]). It can perform time-resolved measurements, but only the continuous operation mode configuration is presented here (Figure 2.23). The sample is placed on a piezo-electric control stage with nanopositioning ability, cooled down to the 10 K to 20 K range with a He cryostat.

Electron optics

A Schottky field emission gun using a ZrO coated tungsten tip generates the electron beam. It can be operated in steady-state mode (continuous wave, CW) by heating the tip, or in pulsed mode by photoemission with a pulsed laser focused at the tip (not described here). After being directed through a positively charged extractor, the electron beam is then controlled by an electromagnetic lens called gun lens, which determines its spread onto an aperture. Diameters of 100 µm, 50 µm, 30 µm and 25 µm can be used for the aperture. The electron beam is then focused through the second electromagnetic lens (objective lens) onto the sample surface where the final spot size is about 10 nm of less (nominally 3 nm at 10 keV).

Light collection and detection

The light emitted from the sample is collected with an ensemble of mirrors, with a design similar to Cassegrain reflectors. The resulting objective is achromatic from 180 nm to 1600 nm, with a

[3] https://attolight.com/chronos/

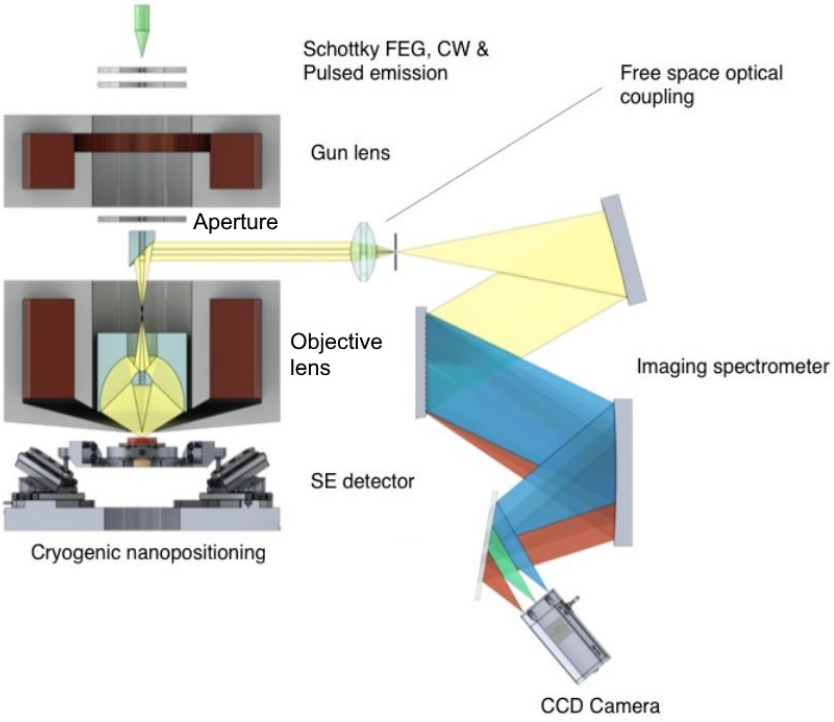

Figure 2.23: *Detailed picture of the CL chamber in the configuration used for doping study, showing the electron gun, the electromagnetic lenses, the cryogenic sample stage, the electron detectors and the light collection optics. Adapted from https://attolight.com/.*

numerical aperture of 0.71, and nominally collects 30 % of the photons emitted by a Lambertian emitter (constant over the whole field of view of up to 300 µm).

The light is dispersed with a Horiba iHR320 monochromator grating with 150 grooves/mm. The spectra are recorder on an Andor Newton Si charge-coupled device (CCD) camera (1024 × 256 pixels, pixel width 26 µm, spectral dispersion: 0.53 nm/pixel). Luminescence spectra are corrected for the diffraction efficiency of the grating and the sensitivity of the CCD camera. The typical spectral resolution is 2 nm.

Spatial resolution

For the acquisition of hyperspectral CL maps, the electron beam scans a rectangular region of interest, and a full spectrum of the luminescence is collected at each pixel. While the electron beam spot size is only about 10 nm, the volume of interaction between the electrons and the sample is larger. Using the program CASINO (v. 2.51[4]), electron trajectories can be simulated and the volume where electrons lose energy due to collisions can be estimated (detailed explanations in ref. [Drouin et al. 2007]). For example, 75 % of the energy of a 6 kV electron beam absorbed in a GaAs slab is dissipated in a cylinder-like volume, about 70 nm-deep and 20 nm-wide (see Figure 2.24).

Moreover, while the excitation is localized, light is collected from the entire sample, which means that electro-generated carriers can diffuse in the material and recombine radiatively somewhere else. The resolution is thus in general governed by the carrier diffusion lengths, which can be up to several µm in high-quality, well-passivated III-V materials. However, in NWs the high surface/volume ratio and the presence of defects (impurities and stacking faults) limit the carrier diffusion, especially at low temperature. While this is undesired from a device perspective, it is paradoxically beneficial to improve the CL spatial resolution.

[4] https://www.gel.usherbrooke.ca/casino/index.html

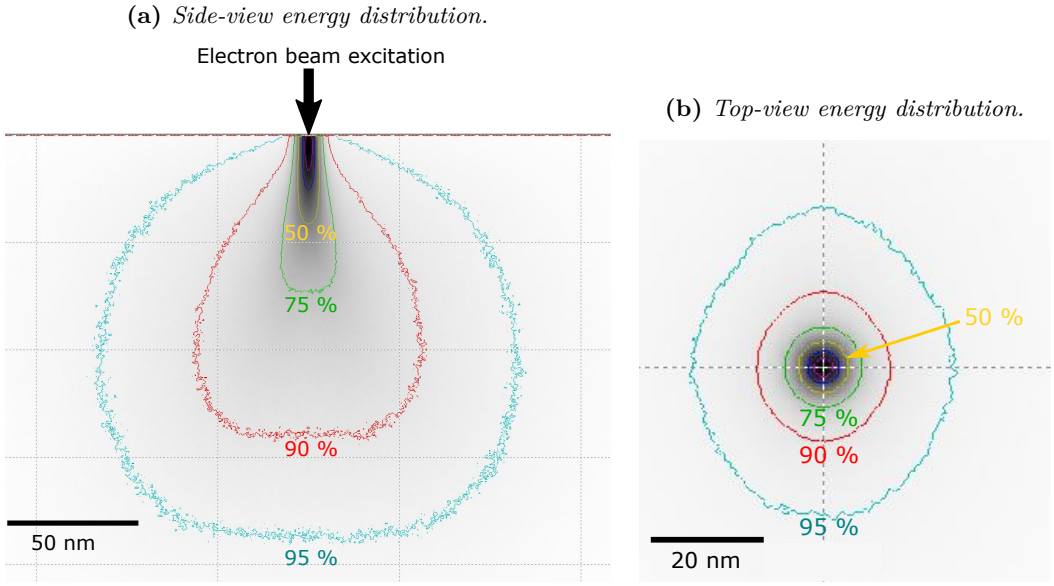

Figure 2.24: *Contour plot of the energy dissipation in a GaAs slab exposed with a* 6 kV *electron beam with a* 10 nm *spot size, calculated in (a) side-view and (b) top-view. The percentages indicate the proportion of the energy that is dissipated within the corresponding contour. Realized with the software CASINO. 800000 electron trajectories were simulated, a density of* 5.32 mg cm^{-2} *was used for GaAs and the energy distribution was calculated with 700 divisions on each axis.*

Cathodoluminescence is used in Section 4.2, to evaluate the doping levels in single GaAs NWs.

2.3.3 External quantum efficiency of solar cells

The external quantum efficiency (EQE) measures the probability for a solar cell to collect a photogenerated electron at a given wavelength:

$$EQE(\lambda) = \frac{\text{Collected electrons}}{\text{Incident photons}} \tag{2.27}$$

This allows for the calculation of the experimental J_{sc} by integration with the AM1.5G spectrum, supposing that the response of the cell is independent from the power it receives:

$$J_{sc} = q \int_0^\infty EQE(\lambda)\, \varphi_{AM1.5G}\, \mathrm{d}\lambda \tag{2.28}$$

where $\varphi_{AM1.5G}$ is the AM1.5G spectral photon flux, in photons $\mathrm{s}^{-1}\,\mathrm{m}^{-2}\,\mathrm{nm}^{-1}$.

EQEs are measured with a home-built set-up at C2N. The light emitted by a xenon lamp is filtered using a grating monochromator and guided to the setup optical axis with an optical fiber. The photon flux over the spectral range of interest (300 nm to 1000 nm for GaAs) is first calibrated with reference GaAs and Si solar cells with known responsivity. Then, the sample is subject to the same illumination conditions, while the current at its terminals is collected at zero bias with a Keithley 2600 source measure unit. The EQE is then deduced from the photon flux and the collected current, using Equation 2.27. An example of the EQE of an actual NW solar cell is presented in Figure 2.25, with the value of the integrated J_{sc}.

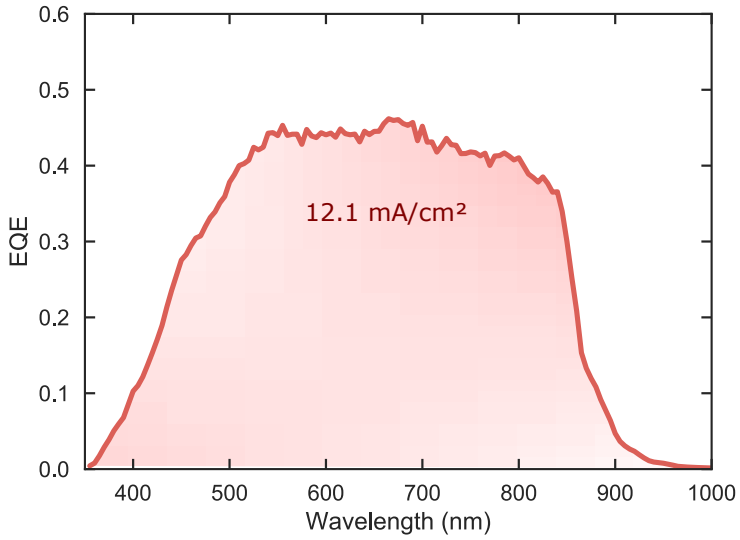

Figure 2.25: *EQE of a NW solar cell. The J_{sc} is calculated using Equation 2.28. [76838]*

2.3.4 Hyperspectral photoluminescence mapping

To characterize NW solar cells with spatial resolution, a hyperspectral imager setup developed at IPVF was used, which yields spectrally-resolved Photoluminescence (PL) images in absolute units. PL is similar to CL but the excitation consists of photons, usually from a monochromatic laser source. The photogeneration of carriers also translates into a quasi-Fermi level splitting $\Delta\varepsilon_F = \varepsilon_{Fc} - \varepsilon_{Fv} \neq 0$, and to emission of light according to the generalized Planck law Equation 2.9.

Hyperspectral imager setup

As sketched in Figure 2.26, the excitation source is a green laser, whose beam is spread through a diffuser to ensure wide-field illumination, and focused on the sample surface. As for the emitted

light (red in the schematic), it is collected from the sample through the same objective as the excitation, and selectively transmitted upwards using a beam splitter.

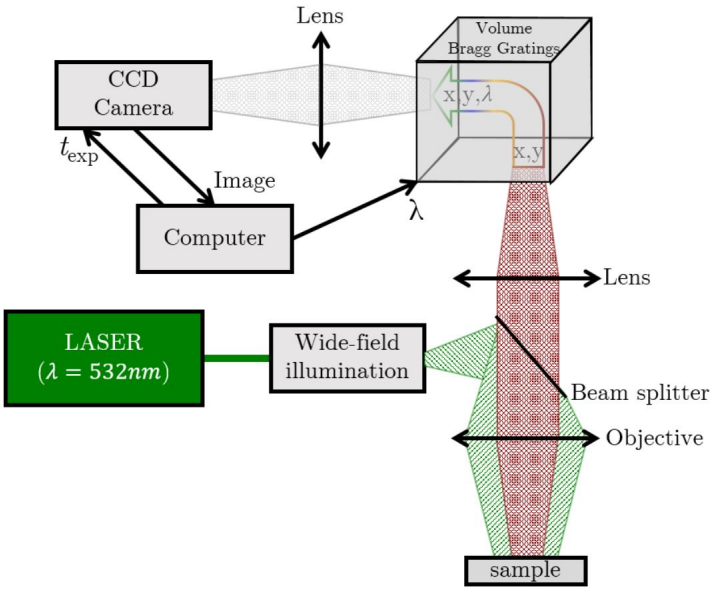

Figure 2.26: *Sketch of the hyperspectral PL imaging setup. The sample is here supposed to emit red luminescence. From [Bercegol 2019].*

In order to separate the spectral components of the signal, a 2D spectral filter based on volume Bragg grating is used[5], which forms a 2D image where the y-axis corresponds to one spatial direction, while the x-axis contains a combination of the other spatial direction, as well as the spectral information. This image is acquired by a CCD camera (Si detector). Specifically, each pixel row along the x-axis corresponds to the luminescence of this x-coordinate, at a given wavelength (in an interval $\delta\lambda = 1\,\text{nm}$, the grating bandwidth). The wavelength range spans the entire x-axis and is arbitrarily centered. By multiple acquisition of the convolved image for different central wavelengths (grating controlled by a computer), a data cube is obtained. A numerical treatment allows to deconvolve x and λ and to obtain a x-y-λ data cube of the luminescence intensity, the *raw image*.

The solar cells themselves are used as power-meters to measure the intensity of the exciting light. For a given laser illumination, knowing the quantum efficiency of the solar cell, its J_{sc} is a direct measurement of the incident photon flux. This flux is preferably expressed as an equivalent number of *suns*, one sun corresponding to the flux at which $J_{sc}{}^{\text{laser}} = J_{sc}{}^{1\text{ sun}}$.

Calibration to absolute units

The system needs to be calibrated in order to measure the luminescence in absolute units (photons $\text{s}^{-1}\,\text{m}^{-2}\,\text{eV}^{-1}\,\text{sr}^{-1}$). To do so, several parameters need to be determined:

- **Solid angle**: Only the light emitted within a given solid angle is collected by the system, as defined by the microscope objective numerical aperture (NA): $\Omega = \pi\, NA^2$
- **Spectral accuracy** of the grating is verified by shining two lasers of known wavelengths (1062.2 nm and 783.6 nm) into the objective.
- **Spectral response**: a calibrated white lamp with a known spectrum is placed in an integrating sphere at the sample position, which ensures uniform light emission along the x- and y- axes. The spectral response is a cube with the ratio of the recorded (CCD camera)

[5] http://www.photonetc.com/fr/

and reference intensity for each position and wavelength: Spectral response$(x, y, \lambda) = \frac{\text{recorded luminescence}(x,y,\lambda)}{\text{reference luminescence}(x,x,\lambda)}$

- **Total transmitted power**: a laser is placed at the sample position and directed towards the objective. The laser photon flux is first deduced from its power, measured with a powermeter. Then the total power measured by the hyperspectral imager is obtained by integrating the cubes. The power transmission ratio is then the ratio of the photons emitted by the laser to the ones collected by the imager, over a duration dt: $I_R = \frac{counts}{\Phi_{laser}\,\mathrm{d}t}$
- **Pixel size**: Knowing the sample characteristic dimensions (diameter of one diode for example), the surface of each pixel of the CCD camera can be estimated from the images (S_{pix}).

Then, the acquired luminescence cubes can be expressed in absolute units through:

$$\text{Absolute luminescence}(x, y, \lambda) = \frac{\text{raw luminescence}(x, y, \lambda)}{\text{spectral response}(x, y, \lambda)} \times \frac{1}{S_{pix}\, I_R\, \delta\lambda\, \Omega} \tag{2.29}$$

I use this setup to characterize NW solar cells and gain more insight about their internal quasi-Fermi level splitting and spatial inhomogeneities (Chapter 5).

2.4 Summary of Chapter 2: Theory and methods

In this chapter, I first briefly described the physics behind the separation and collection of charge carriers in semiconductor solar cells. In particular, I looked into the role of the electrochemical potential, the importance of recombination processes, the advantage of a p-i-n structure for NWs, and the issues toward making ohmic contacts, with a particular focus on GaAs.

As the NWs are to be grown by molecular beam epitaxy, I introduced the basic principles of crystal growth and our MBE setups. I then presented two models for the NW growth by VLS, which relate the observed morphology and crystal structure to growth parameters, in particular through the droplet contact angle. This growth regime also promotes an efficient use of precursor materials. I then described the patterned substrate fabrication process, and the baseline procedure for the growth of core-shell NWs by MBE.

Finally, I presented several advanced characterization techniques employed in this thesis. Transmission electron microscopy and cathodoluminescence spectroscopy are used to investigate the properties of individual, as-grown NWs, in particular their crystal structure, composition, and carrier distribution. External quantum efficiency and hyperspectral photoluminescence imaging, on the other hand, allow to characterize fully processed solar cells.

Chapter

3 Growth of Defect-free GaAs Nanowire Arrays on Silicon

Chapter content

The central step towards the fabrication of a NW solar cell is the epitaxy of the NW array. This array should be homogeneous, with limited NW to NW variation in term of growth morphology and crystal quality.

In this chapter, I first make a historical overview of the different techniques employed to fabricate arrays of GaAs NWs, focusing on the homogeneity of the NW ensemble. I then turn to the self-catalyzed VLS growth of GaAs NWs by MBE, and on the origin of defects in the array, to then optimize the vertical yield with specific growth conditions, NW design and substrate preparation. Finally, the crystalline quality of the NWs is investigated, in particular regarding the defects created during the *in situ* consumption of the catalyst.

3.1 State-of-the-art of nanowire growth in ordered arrays

The homogeneity of NW arrays is of prime importance. Growth should only occur at the desired locations of the patterned substrate and all NWs must share a similar geometry (height, diameter, etc.). Imperfections, such as tilted NWs, polycrystalline non-NW growth, or the absence of growth, hinder the performances of the final device. While NW arrays can be tailored to maximize light absorption using the multi-resonant properties of periodic nanostructures, optical calculations showed that the introduction of disorder leads to a reduced absorption [Loiko et al. 2018], despite experimental results reporting limited impact of disorder on absorption [Madaria et al. 2012]. Moreover, the electrical properties of the solar cell are also altered if defective growth occurs in place of NWs, as it can provide a leakage path for the carriers generated in the rest of the array. Individually, the NWs are single solar cells connected in parallel, up to $5 \times 10^8\,\mathrm{cm}^{-2}$ in a 500 nm pitch hexagonal array, which makes it crucial to control their homogeneity.

In the following I denote *vertical yield* or simply *yield*, the ratio of the number of vertical NWs with regular morphology to the total number of holes in the array. NW arrays whose yield approaches 100 % are called *homogeneous*. This yield can be optimized, but it strongly depends on the growth mode, the technique employed to localize the NWs, and the substrate used. It is not always explicitly mentioned in the NW literature, but the published SEM images allow some estimates. Best performing NW array solar cells systematically exhibit yields close to 100 % ([Aberg et al. 2016]; [Dam et al. 2016]; [Wallentin et al. 2013]), and the company Solvoltaics which produced NWs by aerotaxy, had to develop a technique to vertically align the NWs on an external substrate, until they achieved 99 % alignment yield [Borgström et al. 2018].

In this state-of-the-art review, I focus on III-V NWs fabricated in a bottom-up fashion such as VLS growth or selective area epitaxy, because this approach is of technological and industrial relevance in the perspective of low-cost fabrication of arrays of nanostructures. I review the historical developments of the most encountered NW growth techniques, shown in Figure 3.1: (a) Au-catalyzed, (b) self-catalyzed, and (c) catalyst-free III-V NW growth on Si.

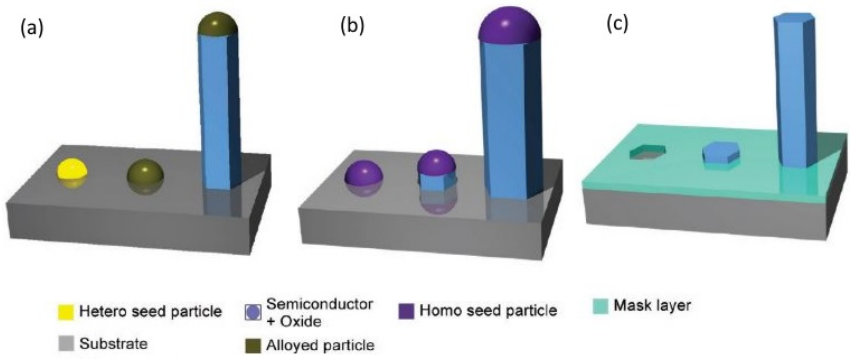

Figure 3.1: *Schematic representation of the three most encountered NW growth techniques. (a) gold-catalyzed VLS growth, (b) self-catalyzed VLS growth, (c) Selective Area Epitaxy (SAE). Adapted from [Mandl et al. 2010].*

Patterning techniques

Several techniques were explored to pattern a selective mask for NW growth in ordered arrays, such as block copolymers [Fan et al. 2006], nanosphere lithography ([Fuhrmann et al. 2005]; [Madaria et al. 2012]), laser interference lithography [Kauppinen et al. 2016], and focused ion beam (FIB) lithography ([Detz et al. 2017]; [Mosberg et al. 2017]; [Bahrami et al. 2020]). But the versatility and reliability of electron-beam lithography (EBL), and to a lesser extent, of nano-imprint lithography (NIL), make them the preferred choices for NW array research studies

which are often at the stage of the proof-of-concept where the cost of the techniques employed is not a stringent constraint. Therefore, most of the NW arrays reported in the literature and the ones in this thesis are patterned using EBL.

3.1.1 Gold-catalyzed nanowire arrays

Growth on III-V substrates

The pioneering works on regular NW arrays on III-V substrates involved the deposition of gold particle catalysts on the substrate prior to VLS growth, as represented Figure 3.1. As early as 1994, Sato *et al.* demonstrated the localized growth of NWs by MOVPE on GaAs(111)B substrate [Sato et al. 1995] (Figure 3.2a). They used an electron beam lithography (EBL)–patterned double layer silica mask to obtain localized gold pads after gold deposition and lift-off. They demonstrated selectivity of the NW growth (MOVPE) which only took place inside the patterned holes. But the homogeneity of the growth was not good as many NWs grew at each site, due to the large hole size (200 nm to 1000 nm wide squares).

(a) *Localized GaAs NWs. [Sato et al. 1995] (1994)*

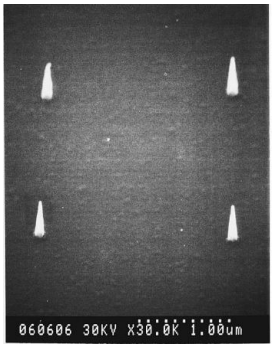

(b) *InAs NW array. [Jensen et al. 2004] (2004)*

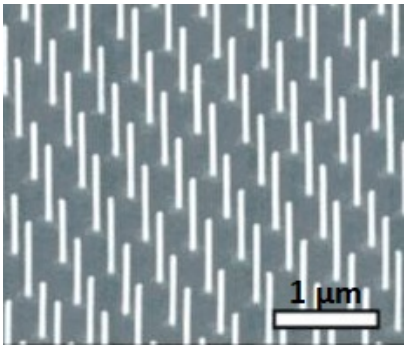

(c) *InP NW array. [Otnes et al. 2016] (2016)*

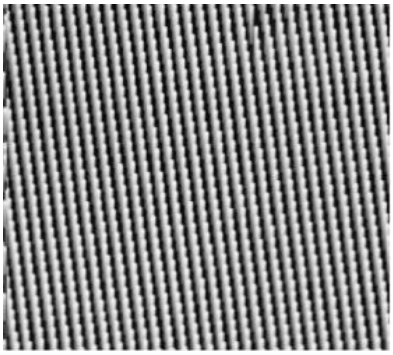

Figure 3.2: *Examples of gold-catalyzed NW arrays grown by MOVPE on III-V substrates.*

In 2002, Wu *et al.* demonstrated the first growth of organized arrays of GaAs NWs (MBE). An anodized aluminum template with well-ordered enlarged nanopores was bonded to the GaAs(111)B substrate, serving as a mask for the localized deposition of gold particles [Wu et al. 2002]. This array was not yet homogeneous though, and the technique had to be perfected.

The following development was then mostly driven by Lars Samuelsson group at Lund University. At first in 2001 they were using aerosol gold particles randomly located at the surface of GaAs(111)B substrates, for the growth of GaAs NWs [Ohlsson et al. 2001]. It was in 2003 that they demonstrated the first homogeneous arrays of gold-catalyzed InP NWs by MOVPE (Figure 3.2c), followed by InAs NW arrays with similar excellent yield [Jensen et al. 2004] (Figure 3.2b). They used EBL-patterned resist to localize the gold particles, but then proved that such homogeneity was achievable using low-cost and large-scale compatible nanoimprint processes ([Mårtensson et al. 2004]; [Otnes et al. 2016]). In 2016, they reported the fabrication of a 15.3 % GaAs NW solar cell, and the SEM images show a perfectly homogeneous NW array (Figure 1.15a in the introduction, page 25), which confirms that they also have excellent control over the yield of GaAs NWs [Aberg et al. 2016].

Growth on silicon substrates

In 2006, Roest *et al.* demonstrated the localized growth of GaAs NWs on Si(111) with a low yield: NWs were growing tilted along either of the 4 possible ⟨111⟩ directions [Roest et al. 2006]. In 2010 homogeneous arrays of InAs NWs were reported but this growth process involved the

epitaxy of an epitaxial InAs thin film on the Si(111)substrate prior to gold catalyst deposition and NWs growth [Ghalamestani et al. 2012].

However, the research on gold-catalyzed III-V NWs on silicon substrates was not intensely pursued over the past few years. Gold is notably incompatible with silicon technologies because it incorporates in this material and introduces mid-gap defect states, very detrimental to devices.

Au-catalyzed VLS NWs paved the way toward homogeneous arrays, though mostly on III-V substrates. On Si substrate, there are fewer results due to the notable incompatibility of Au with Si for device applications (deep traps).

3.1.2 Catalyst-free nanowire arrays

Growth on III-V substrates

Another conventional NW growth method on III-V substrates is the Selective Area Growth (SAG) that takes place in the Vapor Solid growth regime (VS). It is most commonly done with MOVPE and the epitaxial growth is restricted to certain locations defined using a patterned dielectric mask. This technique demonstrated as early as 1996 highly homogeneous arrays of GaAs NWs using a SiO_2 mask [Hamano et al. 1997]. After this precursor work, there are few reports on this technique but later there was a renewed interest for the technique. Fukui and coworkers demonstrated many important results towards homogeneous arrays grown in this fashion using a SiO_2 mask patterned by EBL : InP ([Mohan et al. 2005]; [Mohan et al. 2006]) (Figure 3.3a) and GaAs [Noborisaka et al. 2005] (Figure 3.3b) NWs in 2005, and InAs NWs in 2006 [Tomioka et al. 2007]. The vertical yield attained with this technique is impressive as large-view SEM images attest. Other groups later obtained similarly high yields by MOVPE ([Zhong et al. 2016]; [Heurlin et al. 2015]; [Farrell et al. 2015]), even when using NIL-defined arrays [Haas et al. 2013] (Figure 3.3c). III-V alloys were also grown by this method ([Hertenberger et al. 2012]; [Farrell et al. 2015]; [Berg et al. 2017]; [Ren et al. 2017]), allowing the growth of high-bandgap NW arrays, best suited for tandem solar cells.

(a) *InP NW array. [Mohan et al. 2005] (2005)*

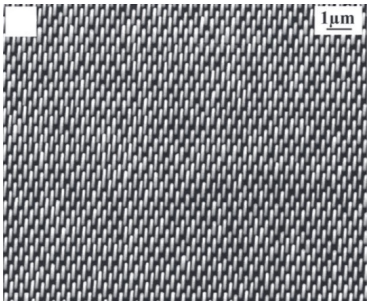

(b) *GaAs NW array. [Noborisaka et al. 2005] (2005)*

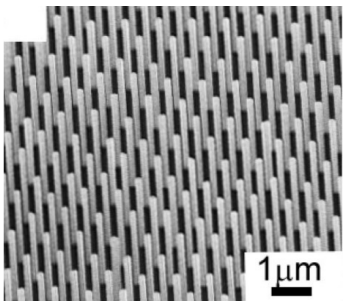

(c) *GaAs NW array. [Haas et al. 2013] (2013)*

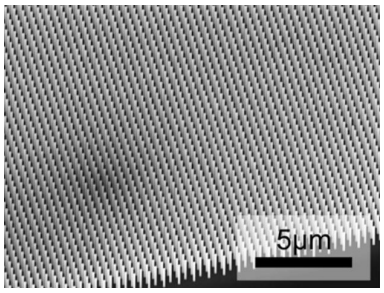

Figure 3.3: *Examples of highly homogeneous NW arrays grown by selective area epitaxy (MOVPE) on III-V substrates.*

Growth on silicon substrates

Similar to the epitaxy on III-V substrates, SAE of NWs was also investigated on silicon substrates. Fukui's group grew InAs NWs on silicon in 2008 [Tomioka et al. 2008]. They could tune the ratio of NWs growing vertically in the [111]B orientation via a pre-treatment of the surface,

and demonstrated homogeneous arrays[1].

Similar yields were later reported by MBE with EBL– [Hertenberger et al. 2010] or NIL– [Hertenberger et al. 2012] defined arrays of In(Ga)As NWs, but more homogeneous arrays were obtained using MOVPE for the growth of InP [Nakai et al. 2015] or GaAs [Yao et al. 2015] NWs. Although MOVPE has been the preeminent technique for SAE, MBE can also be employed to growth GaAs nanocrystals [Molière et al. 2017] or NW arrays [Rudolph et al. 2011] with high homogeneity (>98 % in [Ruhstorfer et al. 2020]).

Highly homogeneous arrays of GaInP NWs on silicon were recently demonstrated [Bologna et al. 2018], paving the way towards high bandgap material integration on silicon.

Catalyst-free growth of NW arrays is possible, especially using the SAE technique. High control over the homogeneity of NW ensembles has been demonstrated, though this technique is mostly employed in MOVPE growth.

3.1.3 Self-catalyzed nanowire arrays

3.1.3.1 Self-catalyzed nanowire arrays on III-V substrates

Besides gold-catalyzed and catalyst-free growth, a few groups started to investigate alternative catalyzed growth methods without using gold particles, using instead some of the NW constituents as catalyst. Catalyst-free growth of InAs NWs was first reported by MOCVD for InP NWs by Novotny and Yu [Novotny and Yu 2005] followed by demonstrations of InAs NWs and arrays on different substrates [Mandl et al. 2006] (Figure 3.4a), and InP NWs on silicon(111)[Mattila et al. 2007]. After some discussion over the results, it was suggested that the mechanism was self-catalyzed VLS growth. Novotny and Yu employed a pre-annealing step to decompose the InP substrate and form liquid In droplets at the surface. The other experiments cited above highlighted the importance of a thin SiO_x layer (typically 1 nm) deposited on the substrate surface which leads to preferential In droplet formation in the oxide pinholes that later catalyze the NW growth [Mandl et al. 2010]. The native oxide on Si(111) substrates can also play this role [Mattila et al. 2007]. The droplets are often not seen on these NWs after the growth but this does not settle the debate since it is very likely that they were crystallized during the sample cooldown under group V precursor flux.

(a) *InAs NW array on InP(111)B substrate. [Mandl et al. 2006]*

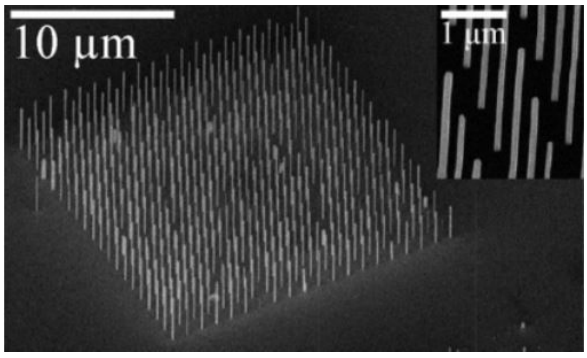

(b) *GaAs NW array on GaAs(111)B substrate. [Bauer et al. 2010]*

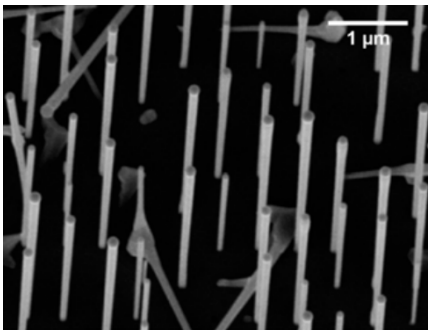

Figure 3.4: *Examples of self-catalyzed NW arrays on III-V substrates, using (a) MBE or (b) MOVPE*

In 2008, A. Fontcuberta i Morral *et al.* reported the self-catalyzed growth of GaAs NWs

[1]Such procedure is not directly transferable to self-catalyzed GaAs NWs grown by MBE but shows that carefully chosen growth parameters can favor vertical growth along [111]B, which is particularly relevant for our approach in the next section.

by MBE [Fontcuberta I Morral et al. 2008]. They outlined the importance of the SiO_2 layer deposited on the substrate for the control of the NW density and morphology. The oxide layer must be thin enough (<30 nm) so that the holes that form inside of it prior to the growth reach the substrate surface, which ensures an epitaxial relation between NW and substrate. The first organized arrays of self-catalyzed NWs on III-V substrates was reported soon after [Bauer et al. 2010] (Figure 3.4b). This NW array is not homogeneous which suggests that self-catalyzed NW growth is harder to control than gold-catalyzed, even on the same substrate.

3.1.3.2 Self-catalyzed nanowire arrays on silicon substrates

Most of the following developments of self-catalyzed growth were focused on the heteroepitaxy on silicon substrate, typically using a patterned SiO_x layer to localize the droplet.

GaAs nanowires The growth of self-catalyzed GaAs NWs on Si was reported in 2008 [Jabeen et al. 2008], soon after the pioneering work of Fontcuberta i Morral *et al.*. Two years later, the first reported arrays of self-catalyzed GaAs NWs on silicon were not homogeneous, with a lot of parasitic bulk growth, non-vertical NWs and multiple NWs per hole [Plissard et al. 2010]. Since then many groups worked on optimizing the yield, as summarized in Table 3.1. It was found that:

- The interactions between the droplet and the hole are of prime importance, and the hole dimensions and droplet size must thus be optimized. In particular, the aspect-ratio of the holes is supposed to strongly influence the NW stem growth through the positioning of the Ga droplet ([Plissard et al. 2011]; [Munshi et al. 2014]; [Vettori et al. 2018]; [Vukajlovic-Plestina et al. 2019]). The nucleation of the first GaAs seed was recently reported to happen preferentially in a 3-D fashion, at the hole periphery [Vukajlovic-Plestina et al. 2019]. While NIL-defined arrays offer few degrees of freedom on the hole dimensions, rather homogeneous arrays can be obtained by the sole optimization of the Ga droplet volume [Munshi et al. 2014]. The alloying of the Ga droplet with the underlying oxide or alternatively with amorphous silicon was also reported to play a role [Russo-Averchi et al. 2015].

- The V/III ratio and the temperature during the growth have a moderate influence on the yield, and most groups use temperatures below or close to 630 °C [Munshi et al. 2014] and V/III growth rate–equivalent–ratio around 2 [Küpers et al. 2018].

- Finally, a pre-growth annealing step improves the yield by removing the traces of SiO_x inside the holes before the growth ([Zhang et al. 2014b]; [Munshi et al. 2014]; [Russo-Averchi et al. 2015]; [Küpers et al. 2018]). Vettori *et al.* recommend a modified pre-growth treatment only 15 °C above the growth temperature [Vettori et al. 2018].

Some of these groups report high vertical yields nearing 90 %, and even up to 95 % after thorough optimization for [Plissard et al. 2011] (Figure 3.5). However, there is a lack of large-field SEM picture proving >90 % yield over a large ensemble of NWs, like it is the case for patterns obtained by selective area epitaxy for example (see Figure 3.3). Many groups working on the self-catalyzed growth of GaAs on patterned silicon report yields still well below 90 % [Gibson et al. 2013]; [Gibson and Lapierre 2013]; [Küpers et al. 2018].

GaP nanowires GaP NW arrays were less investigated than GaAs because this material has less technological interest. Its indirect bandgap makes it unsuitable for most optoelectronic applications, in particular photovoltaics. However, there were reports of hexagonal phase (Wurzite) GaP NW arrays with light emission in the visible range [Assali et al. 2013].

Table 3.1: *Growth conditions for self-catalyzed GaAs NWs on patterned silicon(111) from the literature. The Ga flux is indicated in monolayers (ML) per second (for a GaAs(100) layer). The In blue are the parameters that were optimized in the corresponding reference. In [(a)], the Ga flux was started even before the pre-growth annealing. In [(b)], the material is GaAsP with 30 % P in the group V vapor phase. No absolute measure of flux was indicated.*

ref	wet etch	mask material	mask thick.	pitch	hole diam.	V/III (or As BEP)	Ga flux	pre-dep. duration	growth temp.	pre-growth annealing	
	—	—	nm	µm	nm	— (or Torr)	ML/s	s	°C	°C	min
[Plissard et al. 2011]	HF 1 % 1 min	SiO_x therm.	10	0.5, 1	60	1.8	1	45	630	—	—
[Munshi et al. 2014]	BOE	SiO_x therm.	<40 (pre-HF)	1	100	$<5 \times 10^{-6}$	0.6	50	630	690	5
[Russo-Averchi et al. 2015]	BHF 7:1 12 s	SiO_x therm.	20 (pre-HF)	0.2–2	90 (pre-HF)	2×10^{-6}	0.35	>1800[(a)]	630	770	30
[Vettori et al. 2018]	HF 1 % 25 s	SiO_x PECVD	19	0.3–0.5	50	2.3	0.5	216	600	615	5
[Küpers et al. 2018]	HF 1 % 60 s	SiO_x therm.	15–20 (pre-HF)	1	50	2.2	0.5	90	630	680	10
[Vukajlovic-Plestina et al. 2019]	HF 1 % 60 s	SiO_x therm.	10	0.2–2	45	2×10^{-6}	0.35	600	635	—	—
[Zhang et al. 2014b]	HF 5 % 120 s	SiO_x therm.	30	1	50	—[(b)]	—	60	630	900	20

(a) *GaAs NWs. [Munshi et al. 2014] (2014).*

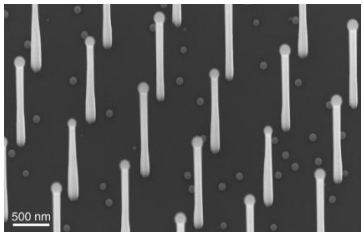

(b) *GaAs NWs. [Russo-Averchi et al. 2015] (2015).*

(c) *GaAs NW array on Si(111) substrate. [Plissard et al. 2011]*

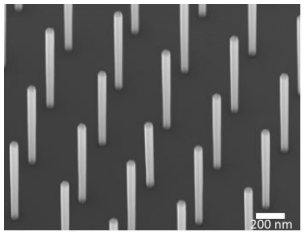

Figure 3.5: *Examples of self-catalyzed GaAs NW arrays on silicon using MBE.*

The few reports of self-catalyzed GaP NW array growth tend to show reproducible reasonably high yields in the 80 % range without optimization [Oehler et al. 2018][Kuyanov et al. 2017]. Some wires are very short in [Kuyanov et al. 2017] due to the consumption of the Ga droplet during the growth, showing that the growth conditions still need to be optimized.

3.1.3.3 Indium catalysis of GaAs nanowires

A recent work from our team at C2N reports high yields (80 % to 90 % with high reproducibility, see Figure 3.6a,b) of (In)GaP or (In)GaAs when In is used alongside Ga as liquid catalyst. The yield enhancement may be attributed to the lower contact angle formed by the liquid catalyst on the NW. They report a 95° contact angle for In-catalyzed GaP whereas it is typically 130° for standard Ga-catalyzed GaP grown under the same conditions. Contact angles close to 90° were reported to be the optimum for the vertical yield ([Russo-Averchi et al. 2015]; [Matteini et al. 2016]). Despite its presence in the catalyst, In is barely incorporated in GaP NWs as can

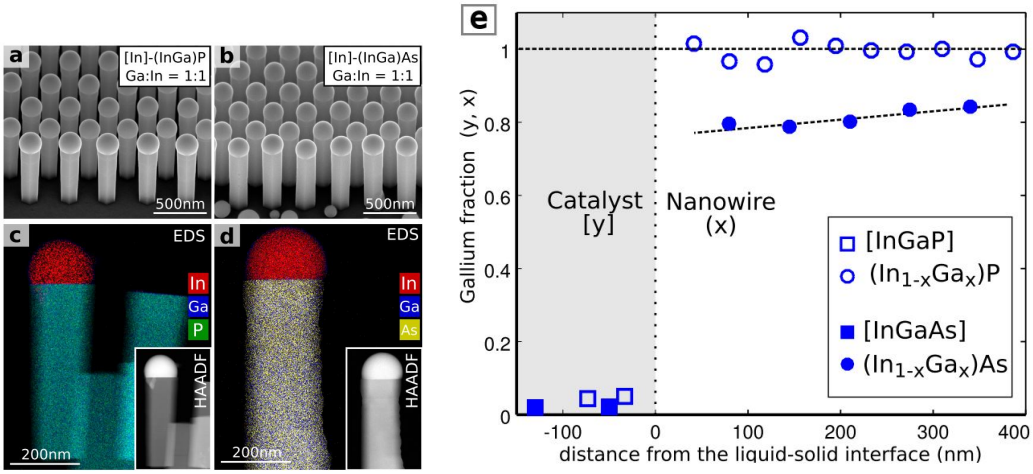

Figure 3.6: *(a,b) Tilted SEM views of In-catalyzed (In)GaP and (In)GaAs NWarrays. (c,d) Corresponding STEM-EDX maps of individual NWs. (e) Plot of the Ga content along the longitudinal axis of the InGaP and InGaAs NWs, extracted from the EDX maps. From [Scaccabarozzi et al. 2020].*

be seen on the EDX map Figure 3.6c, where the In signal (red) is not visible in the NW bulk. This is confirmed by the EDX linescan along the NW growth axis (Figure 3.6e) where the In signal is below the detection limit of the EDX measurement. On the other hand, a fraction of In is incorporated in (In)GaAs NWs (up to 20 % of the group III elements, Figure 3.6e).

This is coherent with the phase diagram of the solid-liquid equilibrium of InGaAs (or InGaP), as shown in Figure 3.7. A fraction of liquid Ga as low as 0.01 inside an In droplet, leads to a Ga concentration of nearly 100 % in (In)GaP (black curves). The same is found for (In)GaAs

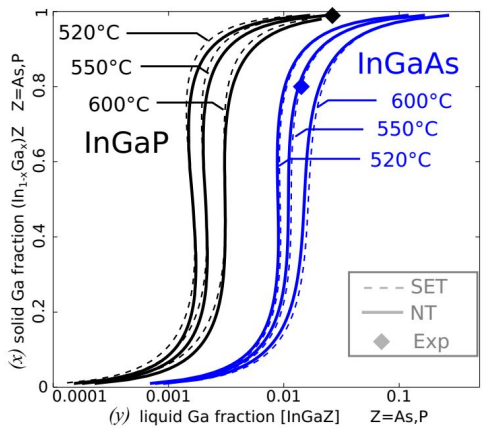

Figure 3.7: *Pseudo-binary distribution coefficient of [InGaP] (black) and [InGaAs] (blue) liquids respectively in contact with $In_{1-x}Ga_xP$ and $In_{1-x}Ga_xAs$ solids at three different temperatures. Nucleation theory (NT) is compared with standard equilibrium (SET) and experimental data (Exp). From [Scaccabarozzi et al. 2020].*

at larger Ga concentration in the droplet (0.1). One can see in Figure 3.6e that the Ga content in (In)GaAs NWs is not constant over 400 nm under the catalyst.

As it is challenging to control the fraction of Ga and In incorporated in such NWs, In-catalysis does not seem suitable to grow well-controlled GaAs or GaAsP NWs with a specific bandgap. A composition gradient can also lead to charge accumulation or depletion in critical parts of the structure. Moreover, these NWs exhibited many twin planes and stacking faults, which suggests that it is hard to optimize the crystal quality and grow pure cubic phase. For these reasons, I choose not to use In catalysts for the solar cell devices.

Self-catalyzed VLS growth of NW arrays is possible in MOVPE and in MBE on Si substrates, it is the method employed in the current thesis. However, the control of the yield is challenging and there is still room for improvement over the array homogeneity. Catalysis with liquid In along with Ga is an effective way to promote high yield, at the cost of poor control over the alloy composition.

3.2 Control of the vertical yield in nanowire arrays

I have shown that even though self-catalyzed growth of ordered NW arrays by MBE is a promising technique for III-V integration on Si, optimization is required to attain high homogeneity in the NW ensemble. In this section, I first investigate the parameters leading to the occurrence of non-vertical growth in NW arrays, then I study the yield of GaAs-based NW arrays grown on Si according to some growth parameters. The substrate preparation and growth parameters of the NW arrays are summarized in Table 3.2 and the Riber32 MBE was used for all growths, apart from the samples in subsection 3.2.3 which were grown in Riber Compact21 MBE system.

Table 3.2: *Summary of the substrate characteristics and growth conditions for the studies on the GaAs NW yield. The fluxes are indicated as the equivalent growth rate of planar GaAs(100)* ($1\,\mathrm{ML_{GaAs(100)}/s} = 2.83\,\mathring{A}/\mathrm{s}$).

Mask thickness	30 ± 3	nm
Thickness left inside holes after RIE	3 ± 1	nm
Last wet etch duration	30 ± 5	s
Growth temperature	600 ± 10	°C
Ga flux	1.5 to 2	$\mathrm{Å\,s^{-1}}$
Ga pre-deposition	32	ML
V/III ratio	1.3 ± 0.1	
Hole diameter for pitch 500 nm	50–60	nm
Hole diameter for pitch 1000 nm	60–80	nm

3.2.1 Defective nanowire growth

3.2.1.1 Examples of unoptimized GaAs nanowire arrays

Figure 3.8 provides examples of typical occurrences of irregular NW growth. One can see many tilted NWs in various directions, in particular in the $[11\bar{2}]$ direction towards which the SEM view is tilted (NWs that appear as vertical). Apart from these tilted NWs, one can also see 'crawling' NWs, which touch the mask. Finally, there can be 'crystallites' that are not elongated structure but still show defined facets. These sometimes bear a catalyst droplet in contact with them, or not.

Looking closer at a typical 'crawling' NW, Figure 3.8b, a clearly defined facet can be seen, indicated with a white arrow. The rest of this object does not have as well-defined facets but the VLS growth has continued. The determined orientation of the initial facet, which is observed on most of these defective NWs, suggests an epitaxial relation with the substrate, followed by an event leading to a change of the growth direction by VLS. Most of the other undetermined NW shapes or crystallites also look like crawling NWs after multiple changes of growth direction and thickening by VS growth. In the following I start by investigating tilted NWs, for which an epitaxial relationship between the VLS growth direction and the substrate seems to have been preserved throughout the growth.

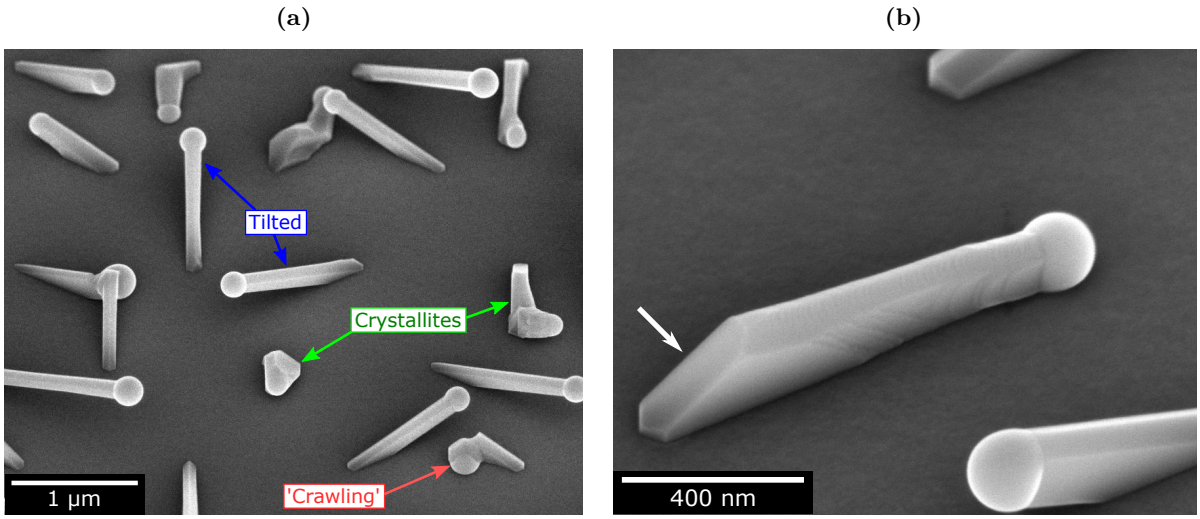

Figure 3.8: *(a) Tilted SEM image of a NW array showing a variety of irregular or non-vertical NWs. The view is tilted at 45° in the $[11\bar{2}]$ direction. (b) Detailed view of a single 'crawling' NW. The arrow indicate a flat facet corresponding to a typical orientation of the tilted NW facets. [76731]*

3.2.1.2 [111]A vs [111]B

As shown in Figure 3.9a, epitaxial growth in free space above a (111) substrate can either follow the [111] direction or 3 directions of the $\langle 11\bar{1}\rangle$ family. To verify that the tilted NWs indeed grow along the $\langle 111\rangle$ directions, I observed NWs in cross-section and measured their angle with the substrate. In Figure 3.9b one can see that the top facets of crawling NWs make the 19.5° angle with the substrate surface, expected from the $\langle 1\bar{1}1\rangle$ orientations.

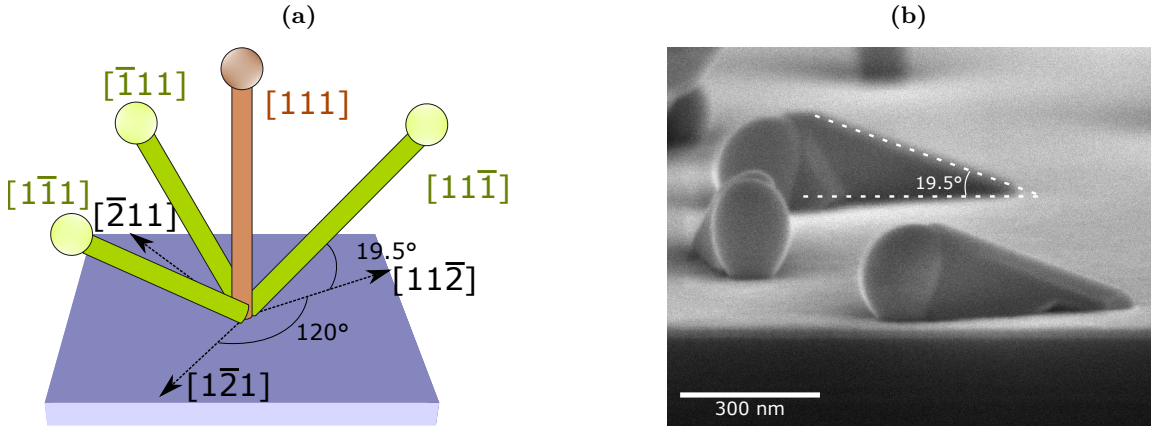

Figure 3.9: *(a) Schematic of the geometrical relationship between NWs grown along the* [111] *and* $\langle 1\bar{1}1\rangle$ *directions in epitaxial relation with a (111) substrate. If the vertical (orange) NW is* [111]*A, the tilted (green) ones are* $\langle 111\rangle$*B, and* vice versa*. (b) Tilted GaAs NWs on Si viewed by SEM at an 85° angle from the substrate normal. The top facet makes a 19.5° angle with the substrate. [76890]*

The {111} planes are not equivalent in the ZB structure of III-V materials due to the orientation of the group III–group V atoms tetrahedra. The 2 configurations are commonly named [111]A and [111]B, if the double-layers are terminated by group III atoms or group V atoms, respectively (Figure 3.10). It was widely observed in the literature that [111]B is the preferred direction for NW growth. MOVPE Au-catalyzed [Sato et al. 1995]; [Hiruma et al. 1995], MBE Au-catalyzed [Piccin et al. 2007] and MBE self-catalyzed [Fontcuberta I Morral et al. 2008] GaAs NWs were reported to grow tilted along the $\langle 111\rangle$B directions when (100) or (110) substrates are used, on the contrary they grow vertically on GaAs (111)B substrates. A more systematic

study of Au-catalyzed InAs NWs grown by MOVPE on a variety of substrates with different orientations confirmed that they always grow along the [111]B direction[Hiruma et al. 1995]. Remarkably, [Wang et al. 2013] reported the growth of [100]-oriented InP NWs by MOVPE with intentional changes of the growth direction, and more recently, regular gold-catalyzed GaAs and GaAsSb NW arrays growth along [111]A were also reported [Yuan et al. 2015]. Those examples are Au-catalyzed growth, in which the composition of the catalyst can be changed by pre-loading it with Ga or Sb, which provides additional degrees of freedom for the control of the equilibrium of the surface energies, to find conditions that favor [111]A VLS growth. [111]B orientation is thus still expected for self-catalyzed GaAs NWgrowth.

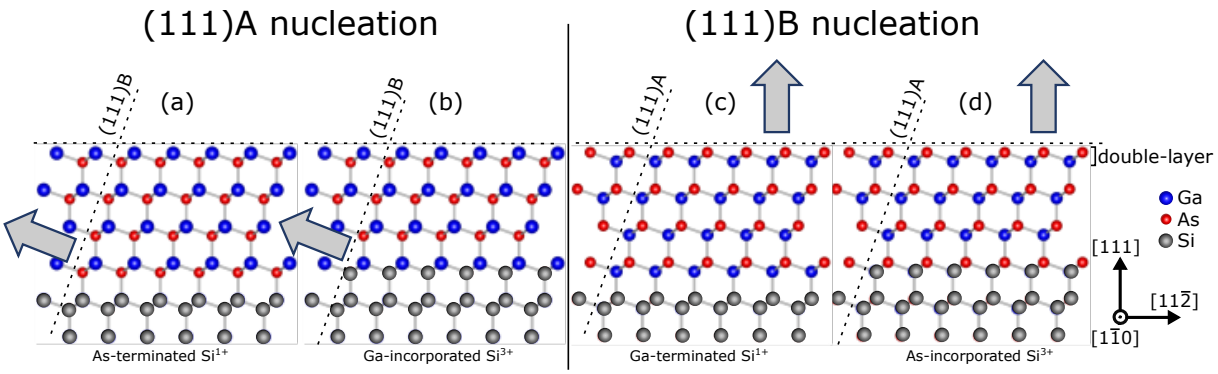

Figure 3.10: *Representation of the atomic structure of (a,b) ⟨111⟩A– and (c,d) ⟨111⟩B–oriented GaAs, viewed along ⟨1$\bar{1}$0⟩ zone-axis. The NW growth direction (⟨111⟩B), is indicated with a grey arrow. The 4 configurations differ with the arrangement of the first GaAs double-layer at the heterointerface with the Si(111) substrate. There is either (a,c) a complete Si double-layer (Si^{1+}) with As or Ga monolayer termination, or (b,d) a half Si double-layer (Si^{3+}) with the incorporation of As or a Ga monolayer. Inspired from [Tomioka et al. 2008]*

.

If the NWs observed in the arrays grow along the [111]B direction, it implies that for tilted wires, it is the [111]A direction which is aligned with the substrate normal. This suggests that they first nucleate on Si substrate as (111)A atomic planes (Figure 3.10a,b), and then the VLS growth occurs along a [111]B direction to follow the preferred growth direction. On the other hand, vertical NWs nucleate as (111)B (Figure 3.10c,d) and thus continue growing vertically. 4 different interface configurations are possible between the Si substrate and the GaAs seed, depending on the arrangement of the atomic planes at the interface, as illustrated in Figure 3.10. I aim at configurations with either (c) a Ga-terminated Si^{+} surface or (d) an As-incorporated Si^{3+} surface, both configurations leading to a GaAs(111)B seed.

3.2.1.3 In-plane twinning

From the top-view SEM image in Figure 3.11b, most tilted NWs seem to grow at discrete in-plane angles, 30° relative to each other. If only NWs in continuous crystal relation with the substrate were present, only three ⟨111⟩ directions would be allowed, with an in-plane angle separation of 60° as shown in Figure 3.9a. The 30° angle distribution is explained by the typical occurrence of rotational twins in ZB GaAs NWs.

Rotational twins are commonly observed in our NWs. As shown in Figure 3.11a, it is equivalent to having 2 adjoined ZB crystals, one rotated by 60° relative to the other, along the ⟨111⟩ direction. As a result, a new set of 3 ⟨111⟩B directions is permitted after one twin, at 60° relative to the previous directions. After two twins, the crystal is back in its original configuration, thus only two configurations exist. As some twins occur at the beginning of the growth, the orientation of the top monolayer at the moment when the NW tilts can be in either phase of the twin. Similar amounts of NWs are present in both ZB phase orientation, highlighted

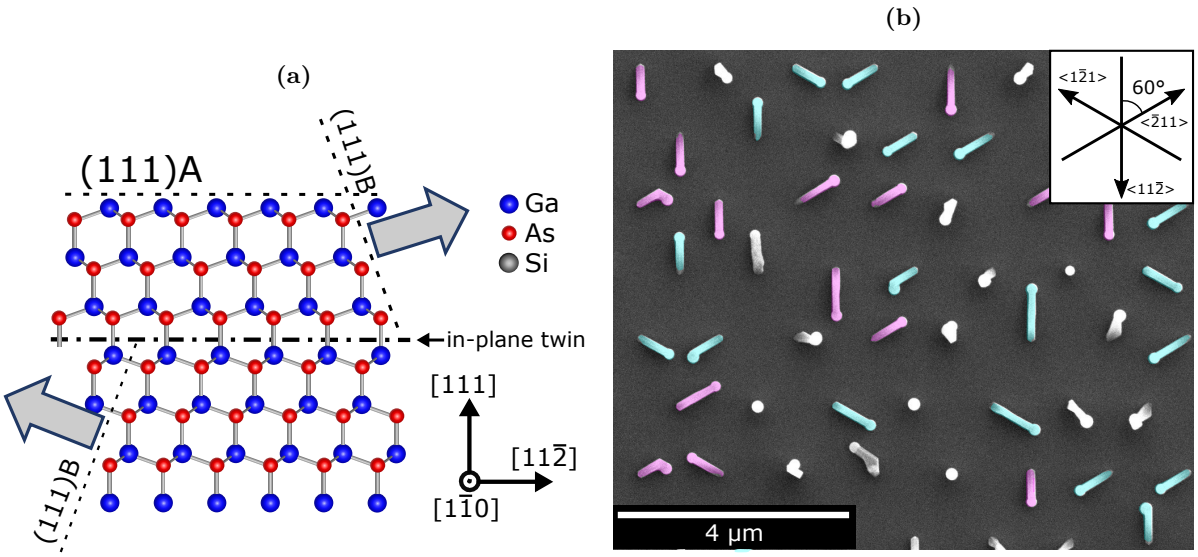

Figure 3.11: *(a) Representation of an in-plane twin in a GaAs(111)A ZB crystal, which is equivalent to a 60° rotated crystal above the twin plane. The ⟨111⟩B directions are also rotated by 60° above the twin. (b) Top-view of a GaAs NW array showing the angle distribution of tilted NWs. The ⟨1$\bar{2}$1⟩ directions (the in-plane projections of the ⟨1$\bar{1}$1⟩) are indicated in inset. The NW orientations after an even and an odd number of in-plane twins are highlighted in different colors. [76890]*

in color in Figure 3.11b, which is consistent with a large number of twins at the beginning of the growth.

3.2.1.4 3D-twinning

The preference for [111]B direction for VLS growth associated with nucleation in (111)A suffices to explain the angle distribution observed in the NW arrays previously shown. However, occasional tilted wires can grow along other angles. In particular, crawling NWs or crystallites show multiple facets which suggest that they experienced several changes of direction during the growth.

New directions can be explained if the epitaxial relation with the substrate is more complex. In particular, this is the case when 3D–twinning occurs inside the NW [Uccelli et al. 2011]. The difference with the previous 'in-plane' twinning is that the twin planes can be the other {11$\bar{1}$} planes, not aligned with the initial NW growth direction. An example of a crystal with one 3D-twinning event is shown in Figure 3.12. Such twinned crystal has a new set of ⟨111⟩B directions along which the NW can grow. Considering multiple successive twinning events, a whole set of growth directions can be computed. The top-view angles made by NWs growing along these new ⟨111⟩B directions are reported in Table 3.3 for up to two twinning events in the seed.

These new orientations are not visible on top-view SEM images of typical GaAs NW arrays (Figure 3.11), which confirms that most NWs seed in the [111]A direction. However, NW in-plane orientations different from 60° can be noticed for some samples for which the growth conditions were optimized and which thus exhibit a high vertical yield (see Figure 3.13). Angles of 19.11° from the ⟨11$\bar{2}$⟩ directions are measured, which correspond to the expected direction of a NW after one twinning event in a (111)B seed (see Table 3.3). As most of the NWs of this sample are growing vertically, most seeds must nucleate in the [111]B direction, making it more likely to observe this angle. However, only a few out of the 800 NWs of the image grow along these directions, so it is still a marginal effect in our conditions. New angles are permitted after two twinning events but, in our conditions, no tilted NWs follow these angles.

From this, I conclude that the 3D twinning effect is quite unlikely especially for 2 or more

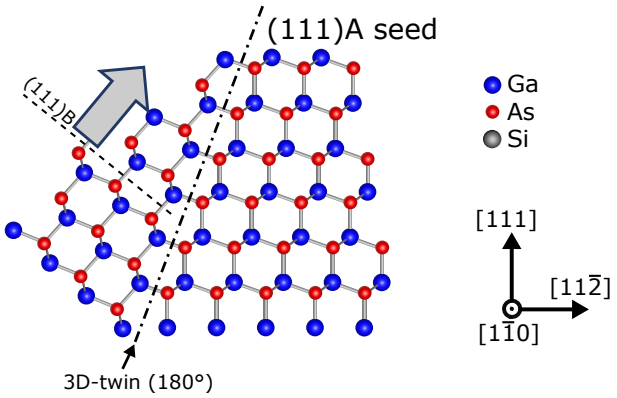

Figure 3.12: *Representation of the atomic structure of a secondary crystal with one twin plane with respect to a GaAs(111)A seed crystal (3-D twinning). The new* [111]*B direction is indicated.*

Table 3.3: *Possible directions for the NW growth considering the nucleation polarity and 3D-twinning in the seed. The in-plane angle is the projection of the new* ⟨111⟩*B directions to the* $\langle 1\bar{2}1 \rangle$ *directions. Note that considering the possibility of in-plane twinning before 3D twinning, 6* $\langle 1\bar{2}1 \rangle$ *directions are possible, spaced by* 60°*. Adapted from [Uccelli et al. 2011].*

Number of twins	**In-plane angles to** $\langle 1\bar{2}1 \rangle$ **(modulo 60°)**	
	(111)A seed	(111)B seed
0	0°	— (vertical)
1	0°	±19.11°
2	±33°	±36.59°
	±5.21°	±40.89°
	±13.90°	0°

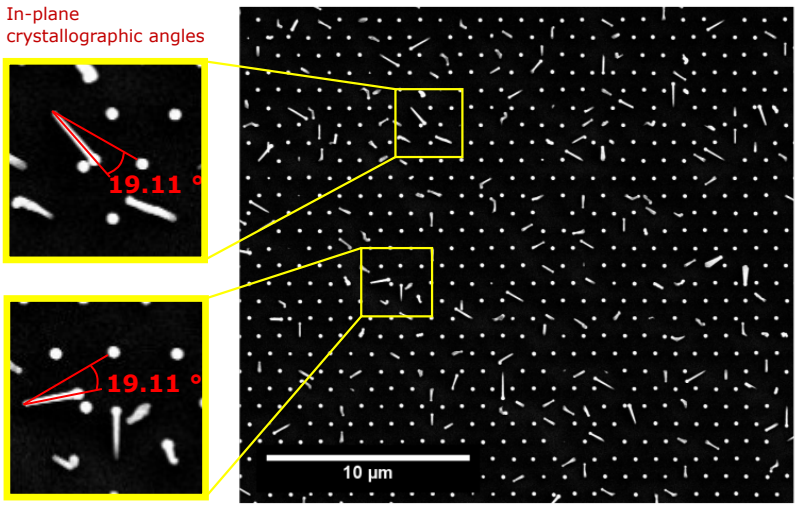

Figure 3.13: *Top-view SEM image of an optimized GaAs NW array. The NW growth was initiated under a V/III ratio of 0.3, and the vertical yield on this image is* 74 %*. The inset shows tilted NWs growing at in-plane angles different from* ±60°*, which is consistent with a GaAs(111)B nucleation with one twinning event in the seed (see Table 3.3). [76771]*

twinning events, or that it typically destabilizes the droplet and favors the formation of a crawling NW, or a 'crystallite', for which it is hard to determine which crystallographic relationship they have with the substrate. For this reason, I focus my efforts toward finding conditions that force GaAs nucleation as (111)B over (111)A on the Si(111)surface, and treat 3D-twinning as a second order problem.

Overall, defective growth can be explained by a sequence of seed configurations throughout the early stages of the growth, as described in Figure 3.14. Nucleation as GaAs(111)A is assumed, without certainty about the seed location, either (a) at the hole periphery, or (b) completely filling the hole. Eventual 3D-twinning may happen at this stage. The VLS growth continues along the ⟨111⟩B direction, and (c) as the droplet exits the hole it can either (d) continue in free space following the ⟨111⟩B direction, thus leading to a 'tilted' NW, or (e) stay in contact with the mask surface and lead to a 'crawling' NW. (f) As the growth continues by VLS, new growth facets are formed to satisfy the constraint of the contact between the droplet and the mask. This may lead to 3D-twinning, changes of direction, and VLS along non-(111) planes, altering the facet morphologies of 'crawling' NWs.

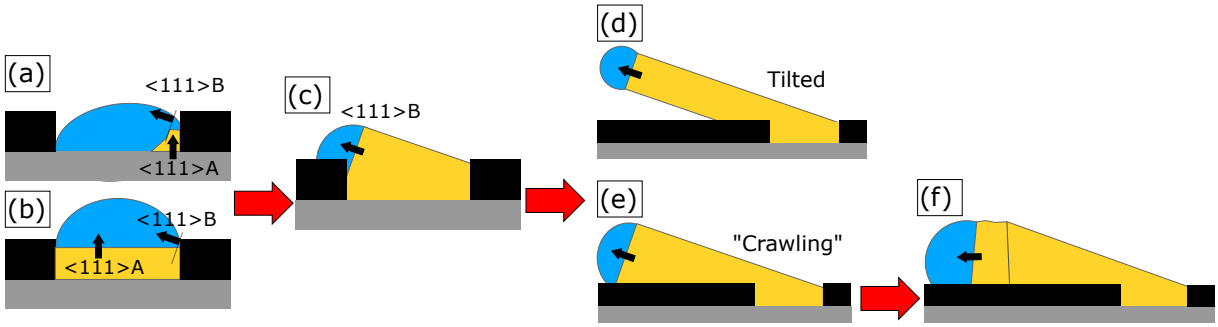

Figure 3.14: *Illustration of hypothetical seed configurations which lead to non-vertical VLS growth, after first nucleation along (111)A. Initially the seed could present (a) a 3D nucleus at the hole edge, or (b) a completed (111)A facet. (c) Growth preferentially occurs along the tilted ⟨111⟩B direction. Depending on the droplet position, the growth can (d) continue as standard tilted VLS NW, or (e) as a crystal 'crawling' by VLS on the mask surface, until (f) the growth facets become too large and a change of growth direction occurs.*

According to this simple model, the morphology of the emerging (111)B facet depends a lot on the aspect-ratio of the hole (Figure 3.14c).

> Defective growth on Si(111) is primarily associated with growth initiation of GaAs(111)A seeds which then tilts to follow the favored ⟨111⟩B directions. 3-D twinning can also occur in the seed, though in marginal proportion in our conditions, and explain in-plane angles different from ±60°.

3.2.2 GaAs nanowire yield optimization

Since growth conditions may influence the seed polarity [Tomioka et al. 2008], I investigate the variation of the vertical yield according to various parameters, while keeping the others as indicated in Table 3.2 (page 81) unless otherwise specified.

3.2.2.1 Yield quantification

The yield is determined from representative top-view SEM images where typically 200 NW sites are visible, and up to 800 as on the top-view image in Figure 3.15a. Using the freeware ImageJ [Schneider et al. 2012], a threshold is applied to the image, to filter only the bright zones

corresponding to GaAs in contrast of the dark background of the SiO_x mask (Figure 3.15b). Finally, individual shapes are sorted and counted to keep the ones within a certain range of size and circularity, corresponding to vertical NWs. The yield is the ratio of this number by the number of sites in the hexagonal array.

(a) *Top-view SEM image of a NW array.*

(b) *Thresholded image.*

(c) *NWs placement determination from their contour.*

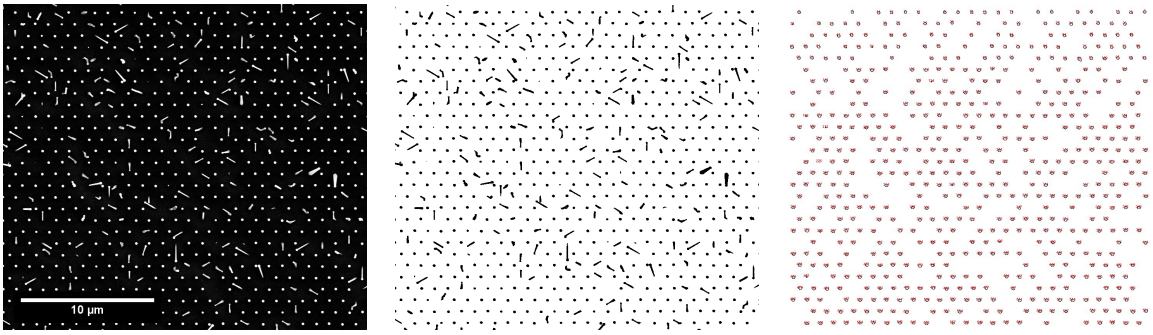

Figure 3.15: *Steps to quantify the yield from a top-view image.(b) A threshold is applied to the SEM image (a) to distinguish the NWs from the mask, and (c) the contours of the NWs are determined, filtering them according to their size and circularity to exclude the non-vertical NWs. [76771]*

There are uncertainties and errors due to the finite size of the image, and due to the difficulty to identify if NWs are well-grown from the SEM image, especially if a shell was grown around the cores. It is typically about $\pm 2\,\%_{\text{absolute}}$.

3.2.2.2 Dependence on the absolute Ga flux

The absolute Ga flux is reported to have an influence on the NW nucleation. Zamani *et. al.* report a trend for NW growth along the ⟨111⟩A directions preferably to the ⟨111⟩B at higher Ga flux and low As/Ga flux ratio [Zamani et al. 2018], for NWs on Si(100) substrates.

In the present study, 4 different Ga fluxes were employed, keeping the same V/III ratio at 1.4. The yields at different patterned zones of each sample are reported in Figure 3.16.

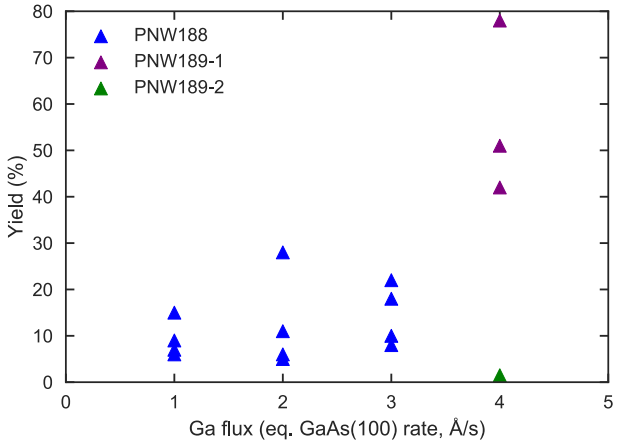

Figure 3.16: *Yield of vertical NWs for different Ga fluxes. Each color represents a series of samples grown from the same patterned substrate (legend) and identically prepared. Each triangle represents the yield in a specific zone of the pattern (specific array pitch, hole size/ebeam dose, pattern placement). Each color represents samples from a unique patterned wafer, prepared identically (wafer label in legend). [76712, 76713, 76714, 76740, 76732]*

It seems that in our conditions, the Ga flux has only a moderate impact, if any, on the vertical yield. There seems to be an important effect of the wafer preparation, as the sample on

the substrate PNW189-1 (purple marks) shows an improved yield (up to 75 % on one pattern), whereas another sample grown on the substrate PNW189-2 (same wafer processed another day: different hole etching duration, different operator) exhibits a yield close to 0 % (green mark). This wafer-to-wafer variation is discussed later.

To understand if the Ga droplet volume changes significantly due to the Ga flux when the As flux is started, the duration of the incubation before the first GaAs double-layer is formed can be estimated. Considering that 32 ML of Ga were deposited, that the growth is initiated at a V/III ratio of 1.3, the incubation time is then 0.5 s for the As atomic concentration inside the droplet to reach 1 %, which is typically the concentration at which NW growth happens [Glas et al. 2013]. This is very short compared to the pre-deposition duration and the effect of the Ga flux should not have modified the droplet volume by this time. This considered, rather than the initial Ga flux, I expect the Ga droplet initial volume to play a more significant role on the nucleation of the first monolayer.

3.2.2.3 Dependence on the Ga droplet pre-deposition

For this series, the Ga flux was set to 2 Å s^{-1}. Despite large yield fluctuations between different patterns of the same sample, there is a clear trend showing an increased yield from 28 $ML_{GaAs(100)}$ to 212 $ML_{GaAs(100)}$ (Figure 3.17).

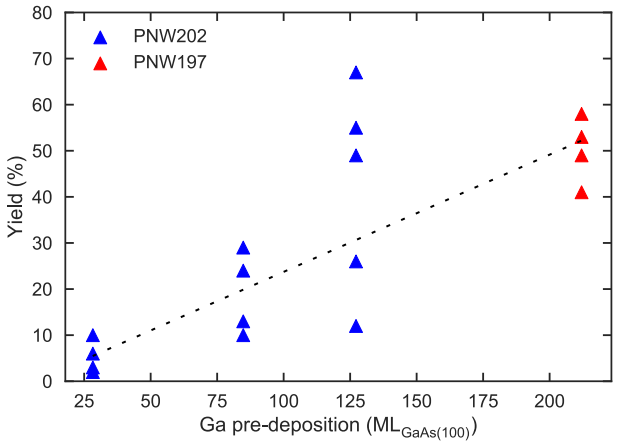

Figure 3.17: *Yield of vertical NWs for different Ga pre-deposition volumes. Each color represents a series of samples grown from the same patterned substrate (legend) and identically prepared. Each triangle represents the yield in a specific zone of the pattern (specific array pitch, hole size/ebeam dose, pattern placement). The black dashed line is a guide for the eye. [76885, 76907, 76902, 76927]*

The first benefit of the Ga pre-deposition is the droplet positioning [Plissard et al. 2011], if the droplet wets the inside of the hole in a conformal manner, the growth initiation is expected to occur in a stable way. In particular, it was reported that growth initiation when the droplet contact angle with silicon is close to 90° promotes verticality [Matteini et al. 2016]. The volume of Ga deposited in each hole can be estimated through Equation 3.1.

$$V_{Ga} = t_{Ga} \times S_{collection} \tag{3.1}$$

In a first approximation only the Ga impinging the silicon surface at the bottom of the hole contributes to the droplet formation, consistently with the fact that at these temperatures the Ga readily evaporates from SiO_x surfaces ([Plissard et al. 2011]; [Vettori et al. 2018]; [Oehler et al. 2018]), so $S_{collection} = \pi \frac{D_{hole}^2}{4}$ is the surface area of the hole.
The thickness of liquid Ga deposited, t_{Ga}, can be converted from the resulting thickness of

GaAs(100), t_{GaAs} (the unit used in epitaxy for convenience), through the formula:

$$t_{Ga} = \underbrace{\frac{m_{Ga}}{\rho_{Ga}}}_{cm^3/\text{Ga atom}} \times \underbrace{\frac{4t_{GaAs}}{a^3_{GaAs}}}_{\#(\text{Ga atom})/cm^2} \tag{3.2}$$

Where m_{Ga} is the atomic mass of Ga. Considering a Ga pre-deposition of $t_{GaAs} = 212\,\text{ML}$ (red data in Figure 3.17), the hole needs to be as large as $D_{hole} = 80\,\text{nm}$ for a droplet with a contact angle $\alpha = 90°$ to fully occupy it. From the image in Figure 3.18a, that the hole diameter at the bottom of a hole can be as low as 30 nm when they are not well opened (and wider at the top to the enlargement from the HF dip and the liquid Ga). The diameter of well-opened holes is most likely between 30 nm and 80 nm [Vettori et al. 2018]. Thus, in our conditions, the droplet is expected to wet the entire hole with a contact angle either close to or above 90°.

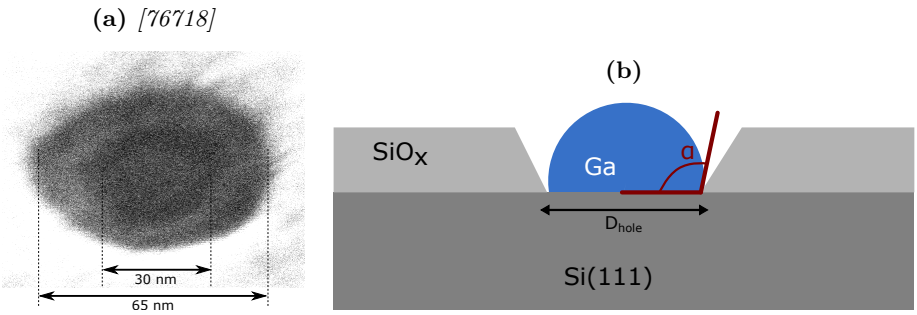

Figure 3.18: *(a) SEM image of a hole in a large pattern of pitch* 1000 nm *(dose 22k), viewed with a* 45° *tilt and with enhanced contrast. An internal ring suggests a conical shape with a smaller base. Most holes surrounding this particular hole had a NW grown in them, suggesting that the etching time was just enough to reveal the silicon in some holes but left a few monolayers of oxide in others. (b) Schematic of the section of the hole with a deposited Ga droplet. Not at scale.*

In this case, the yield should decrease with longer pre-deposition than $212\,\text{ML}_{\text{GaAs(100)}}$ of Ga. It could be interesting in future experiments to observe if this estimation holds true.

Moreover, the liquid Ga could induce self-cleaning of the silicon surface by reducing the residual SiO_x [Wright and Kroemer 1980]. It was reported that they can help enlarge the SiO_x holes[Vettori et al. 2018]. In this sense, it is fulfilling a similar role as the pre-growth high-temperature annealing for removing oxide residues [Zhang et al. 2014b].

3.2.2.4 Dependence on the initial As flux

The V/III ratio is often set close to 1.5 because it is typically what preserves the NW shape (no tapering, droplet not consumed before the end) and crystalline quality (fewer stacking faults and twin planes). However, the V/III ratio allowing a maximum yield may differ from this. In this study, I changed the As_4 flux during the first 15 s of the growth and observed the effect on the yield (Figure 3.19). For the sake of reproducibility, the growths were realized on 5 pieces of the same patterned wafer, and special attention was paid to the initial pre-growth conditions: the samples were kept at growth temperature for at least 30 min before the growth start, waiting for the residual BEP in the chamber to be below 1×10^{-9} Torr (PNW 191). The Ga flux was set to $1.5\,\text{Å}\,\text{s}^{-1}$ for this series. Because I previously observed a lot of variation in the GaAs NW yield under identical conditions, the growths at the highest and lowest initial V/III ratios were repeated on another piece of the same patterned wafer. The yield was consistent between these growths (Figure 3.19), so variations due to inhomogeneous surface roughness or oxide thickness over the 2-inch wafer area can be ignored.

The yield is severely limited for an initial V/III ratio of 5.4, while it is above 70 % for lower ratios. Growths on other patterned wafers at low V/III ratios show much lower yields, below

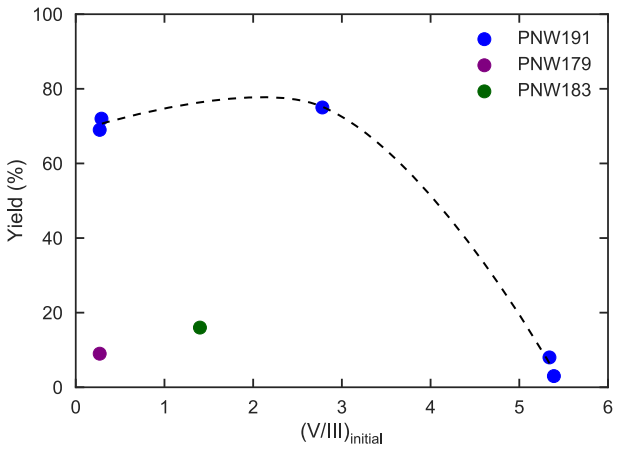

Figure 3.19: *Yield of vertical NWs for different V/III ratios at the beginning of the growth. Each color represents a series of samples grown from the same patterned substrate (legend) and identically prepared. Each dot corresponds to a single growth run and the yield is calculated on the large arrays of pitch* 1000 nm *(dose 22k). The black dashed line is a guide for the eye. [76771,76778,76779,76780,76784,76791,76694]*

20 %. The low yield samples exhibit non-vertical growth along the ⟨111⟩ directions (not shown), similar to the samples described in the previous section.
This trend for better yield at lower V/III ratios is consistent with what other groups observed ([Munshi et al. 2014]; [Küpers et al. 2018]). A high As flux promotes VS growth which may destabilize the VLS ⟨111⟩growth front and hinder the VLS growth[Munshi et al. 2014]. The yields are similarly high at V/III ratios of 0.3 and 2.8, which suggests that there is a wide window of suitable ratios.

A significant batch effect is also visible in this study, as the samples from the patterned wafers PNW179 and PNW183 (purple and green dots) exhibit a much lower yield.

3.2.2.5 Holder inhomogeneity

There is an important dispersion of the yield at different locations of each 1/6 2" samples as already seen in the figures 3.16, 3.17, 3.19. Figure 3.20 shows the yield at the tip, middle and close to the edge of various samples. In particular, there does not seem to be any trend towards one sample edge to the other.

There could be at least two explanations to this phenomenon:

- The temperature might be highly inhomogeneous over the sample. The sample is heated from the rear side with a radiating oven. The mismatch between the silicon and molybdenum emissivities can lead to different equilibrium temperatures for the sample and the holder. The uneven mechanical contact at the sample edge, with the 1/6 2" molybdenum imprint then leads in turn to temperature inhomogeneities over the sample.

- Contamination could occur during the last HF dip before sample loading. Special care is taken with the contamination and dedicated beakers and tweezers are used, but there could be contamination originating from the tweezers, the environment, or inhomogeneous re-oxidation of the bare silicon during the sample rinsing and drying.

3.2.2.6 Wafer-to-wafer reproducibility

While consistent trends could be identified for samples grown from the same substrate (Those in identical colors in the figures 3.16, 3.17, 3.19), they are not reproducible on samples from other substrates (identified with different colors), despite all growth conditions being kept the

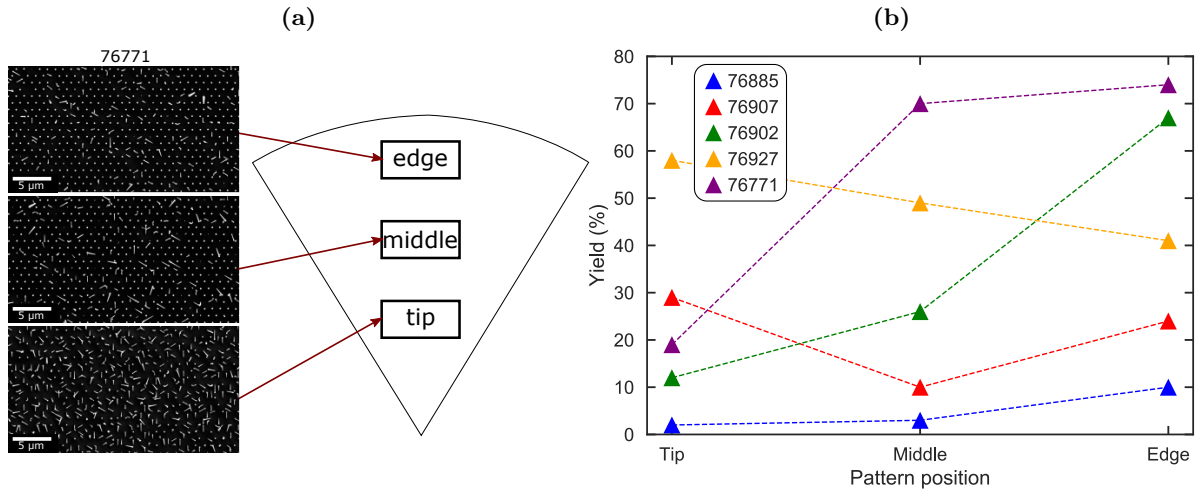

Figure 3.20: *(a) Schematic of the different possible pattern locations on a 1/6 2"" sample, along with representative top-view SEM images of different* 1000 nm *pitch patterns from sample 76771. (b) NW yield at the different pattern locations. Each color represents a single GaAs NW sample. Each symbol represents the yield at a pattern of pitch* 1000 nm *(single-dose exposure), at a given location on the 1/6 2" sample.*

same. This suggests that at least two other parameters could have a more important influence on the yield:

- The patterned substrate preparation. The thickness of the PECVD–deposited SiO_x is not homogeneous between different wafers and the RIE etching duration always has to be manually adjusted, so as to leave (3 ± 1) nm of SiO_x inside the holes (As described in Chapter 2, Figure 2.20, page 61). Variations could also arise from the last dip in the 1 % HF solution which is done by hand by different people.

- The pre-growth conditions in the chamber. While the growth of the samples from the wafer PNW191 in Figure 3.19 was initiated at a carefully controlled background pressure and after being kept a long time at growth temperature, the other samples did not follow such procedures.

Different growth conditions were investigated in hope to favor nucleation of GaAs(111)B. While there is a benefit of increased Ga pre-deposition, a wide range of V/III ratio seems adequate, and there is no clear benefit of an increased Ga flux. Overall, the yield never overcomes 80 %, and is often inhomogeneous over the sample surface. Moreover, while samples prepared identically from one wafer are consistent, important wafer-to-wafer variations were observed. Alternative designs or techniques are needed, to improve the yield and its robustness.

3.2.3 Yield improvement of GaAs nanowires with GaP stem

In our conditions, GaP NW arrays systematically present better yields than GaAs ones, as shown for example in Figure 3.21 where GaAs and GaP NWs were grown in short succession on identically prepared pieces of the same patterned wafer. All growth parameters were kept identical and the V/III ratio is around 1.4 in both cases.

For this reason, I decide to initiate the growth of GaAs NWs with a GaP stem, by growing GaP during 30 s, enough to nucleate the first monolayers and then switch to GaAs NW growth

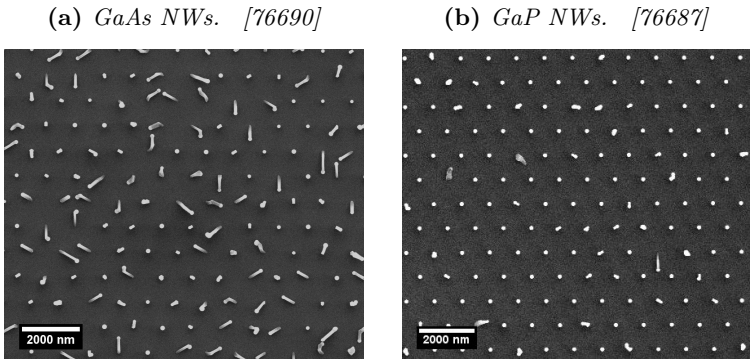

Figure 3.21: *SEM overview of unoptimized GaAs and GaP NW arrays grown under similar conditions on identically prepared substrates from the same wafer.*

(see flux sequence in Figure 3.22). Using this technique, I now focus on improving the wafer-to-wafer yield reproducibility and the yield itself, to consistently reach high levels.

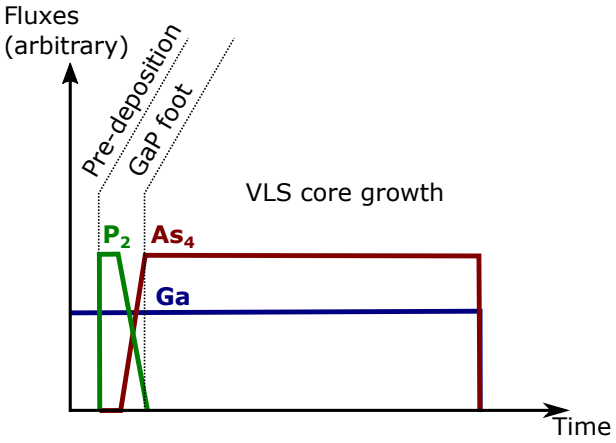

Figure 3.22: *Flux sequence during the growth of GaAs NWs with a GaP stem.*

3.2.3.1 Substrate preparation: improved wafer-to-wafer reproducibility

Considering the low reproducibility between different wafers, a cleaning recipe was developed for the silicon wafers prior to mask fabrication. It consists of 3 cycles of oxidation/etching similar to the one described by Madaria *et al.* [Madaria et al. 2012] for the MBE growth of III-V on silicon. First a 4 min oxygen plasma by CCP-RIE is performed to ensure that remaining carbon impurities are burned, and to oxidize a few nanometers of silicon at the surface, trapping impurities inside. Then the sample is immersed in a 5 % HF solution which removes the oxide and eventual impurities trapped inside. After 2 cycles, [Madaria et al. 2012] did not notice further improvement. We prefer to perform 3 cycles to ensure maximum NW yield.

Core-shell NWs initiated with a GaP stem were grown on 2" substrates, with or without this specific wafer cleaning procedure (Figure 3.23). As I look into wafer-to-wafer reproducibility, the design used here is a full $1.5 \times 1.5\,\mathrm{cm}^2$ square entirely patterned with a hexagonal array at the center of a 2" wafer. This way, the wafer-to-wafer differences are examined while the effect of surface inhomogeneity can be neglected.

One can see a significant yield improvement from the cleaning procedure, as it is close to 95 % for all samples, and systematically above 90 %. Moreover, the yield is high all over the pattern surface, whereas the samples without the cleaning procedure can exhibit inhomogeneous yields (not shown).

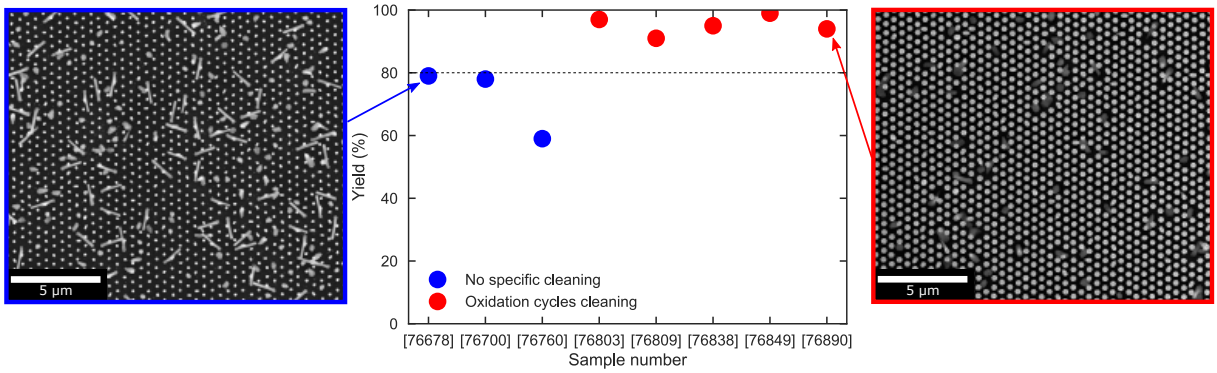

Figure 3.23: *Influence of wafer cleaning on the yield. Various samples were grown with a similar GaP foot, on patterned wafers cleaned with a simple HF dip (blue) or with a cleaning procedure consisting of 3 cycles of plasma oxidation and HF etching (red). The vertical yield is estimated at the middle of the* $1.5 \times 1.5\,\mathrm{cm}^2$ *arrays located at the center of 2" wafers. SEM top-view images of two representative samples for each condition are shown. The different morphologies come from different shell thicknesses.*

While excellent yields are obtained at the center of 2" wafers, it is typically limited below 90 % on 1/6 2" samples prepared with this procedure, especially close to the tip. This could be due to a better thermal homogeneity over 2", as well as a lower level of contamination which often comes from the edges due to tweezers manipulation, rinsing and drying steps, contact with the molybdenum holder at high temperature, *etc.* For the following studies, 1/6 2" samples are still used for convenience, but a new pattern design is used with larger zones only at the middle of the 1/6 sample, where the yield is the most reproducible (Figure 3.24).

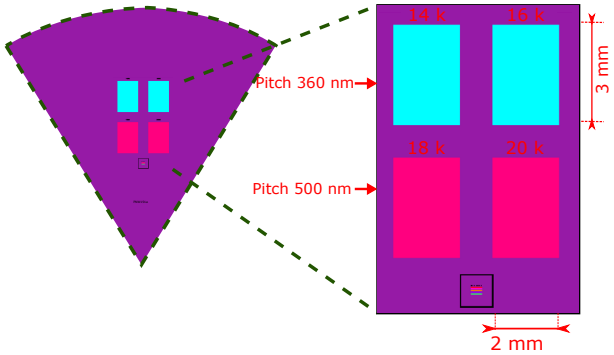

Figure 3.24: *Schematic of the new pattern design on 1/6 2" wafers. On the detail of the patterned zone, two large rectangular areas (red) are hexagonal arrays of pitch* 500 nm*, written with EBL by single-shot exposure at the middle of each hole, at different electron doses. Similar zones of pitch* 360 nm *(cyan) are not considered here due to poor EBL patterning.*

Though this cleaning procedure allows to reach yields above 90 % when the NW growth is initiated with a GaP stem, the growth of pure GaAs NW still lacks reproducibility and the yields are often very low, as shown in Figure 3.25.

A specific wafer cleaning procedure based on oxidation/etching cycles is found to greatly improve the yield of NWs with a GaP stem, and to ensure wafer-to-wafer reproducibility. The yield can reach 95 % in the middle of full 2" substrates, while it is closer to 90 % on 1/6 2" samples. This cleaning procedure is not as beneficial for pure GaAs NWs.

(a) *GaAs NWs. [76885]* **(b)** *GaAs NWs with GaP stem. [76891]*

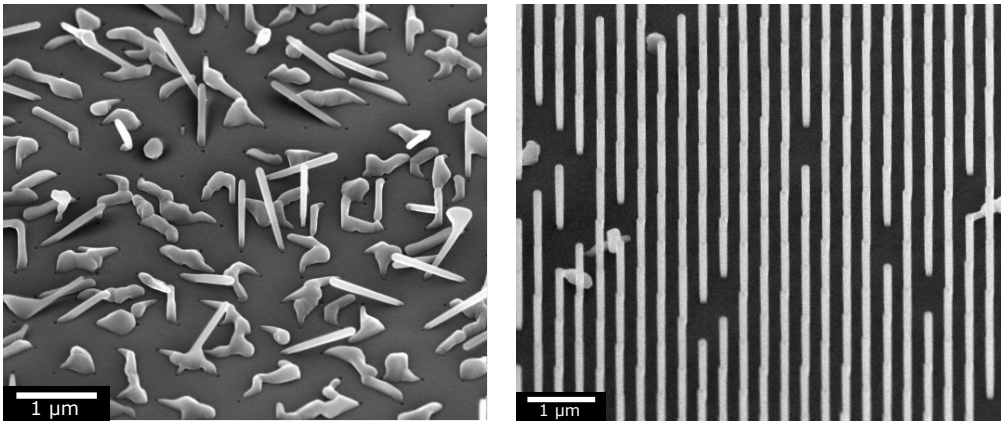

Figure 3.25: *SEM overview of GaAs NW arrays on 1/6 2" patterned substrates, with 3 cycles of plasma oxidation/HF etching before mask deposition. Both samples were grown the same day on the same patterned wafer, in similar conditions. The droplet was consumed at the end of the axial growth.*

3.2.3.2 Robustness to different growth conditions

GaP-initiated NWs grown on substrates prepared with the specific cleaning procedure described in the previous paragraph are very reproducible and homogeneous in term of vertical yield. For this reason, the substrates are considered identical even between separate preparation batches. The Compact21 MBE was used for these growth experiments, with growth conditions described in Table 3.2. Due to the lack of chemical facilities at the machine location, the final HF dip was performed one day before the growth, and the substrates were transported in a container filled with nitrogen gas. After opening the container, the substrates are immediately placed in ultra-high vacuum (UHV) inside the MBE. The yields were measured on representative SEM images of 500 nm-pitch 'single-shot' arrays, at the middle of the 1/6 2" samples.

Table 3.4: *Summary of the substrate characteristics and growth conditions for the studies on the GaAs NW yield with a GaP stem, in the Compact21 MBE system. The fluxes are indicated as the equivalent growth rate of planar GaAs(100)* ($1\,\mathrm{ML_{GaAs(100)}/s} = 2.83\,\text{Å/s}$).

Mask thickness	37.5 ± 1.0	nm
Thickness left inside holes after RIE	5 ± 1	nm
Last wet etch duration	40	s
Growth temperature	620 ± 5	°C
Ga flux	2	$\text{Å}\,\text{s}^{-1}$
Ga pre-deposition	84	ML
As/Ga ratio	1.2 ± 0.1	
GaP stem duration	20 s GaP & 30 s GaAsP	

As seen in Figure 3.26a, the yield does not change substantially with the temperature in the 50 °C temperature range investigated. From 600 °C to 625 °C, the yield is consistently between 80 % and 90 % and only at a much higher temperature close to 650 °C does the yield drop below 80 %. Similarly, the volume of pre-deposited Ga only has a minor influence on the yield (Figure 3.26b) and is above 80 % in the investigated range. The fact that there is little yield variation confirms that:

1. The calibration for 1/6 2" sample temperature measurement in the Compact21 MBE setup is compatible with that of the Riber 32 setup.

2. The procedure combining substrate cleaning and GaP stem is robust over 25 °C temperature change, and droplet deposition thickness from 0 $ML_{GaAs(100)}$/s to 85 $ML_{GaAs(100)}$/s.

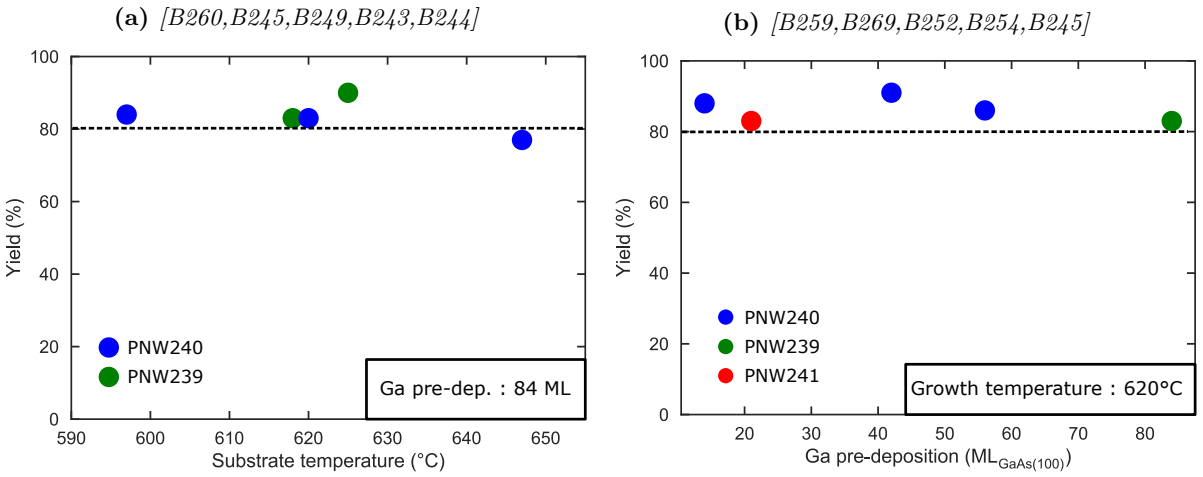

Figure 3.26: *Yield of vertical NWs for (a) different growth temperatures and (b) for different volumes of pre-deposited Ga. Each color represents a series of samples grown from the same patterned substrate (legend). The yields are calculated on a* 500 nm *pitch pattern written by single-shot exposure at the middle of 1/6 2" samples. The dashed line is a guide to the eye.*

This robustness relieves the constraints on the temperature control and the droplet positioning.

It also appears that any trend for the yield versus these growth parameters is hard to decorrelate from the sample-to-sample fluctuations, especially when the substrate was stored overnight in a box after the HF dip.

> The yield of GaP-initiated NWs is found to be relatively insensitive to the substrate temperature and Ga pre-deposition in a wide range, which confirms that the growth procedure is robust.

3.2.3.3 Benefit of substrate pre-annealing

The benefit of a pre-growth annealing was widely reported in the literature (see Table 3.1). On the Riber 32 MBE setup, the oven does not permit to reach higher temperatures than 700 °C (measured with the pyrometer). Our typical procedure on this MBE includes a pre-annealing up to 700 °C for 5 min to 10 min, without significant improvement to the yield. On the other hand, the oven in the Compact21 setup allows to reach higher temperatures, up to 800 °C as measured with the pyrometer.

Three samples from the same wafer were prepared identically and annealed *in situ* just before the growth in the Compact21 MBE, for a duration of 10 min, at up to 800 °C as measured with the pyrometer (Figure 3.27). Without pre-annealing or with a pre-annealing at 690 °C, the yield is found to be rather inhomogeneous from one patterned zone to the other, ranging from 70 % to 87 % (Figure 3.27a and Figure 3.27b), whereas increasing the pre-annealing temperature to 800 °C allows to improve the yield above 90 % and to keep it homogeneous between patterns (Figure 3.27c).

> An 800 °C *in situ* annealing of the substrate prior to the growth is very beneficial to the yield of GaP-initiated NWs and in particular to its homogeneity over 1/6 2" samples.

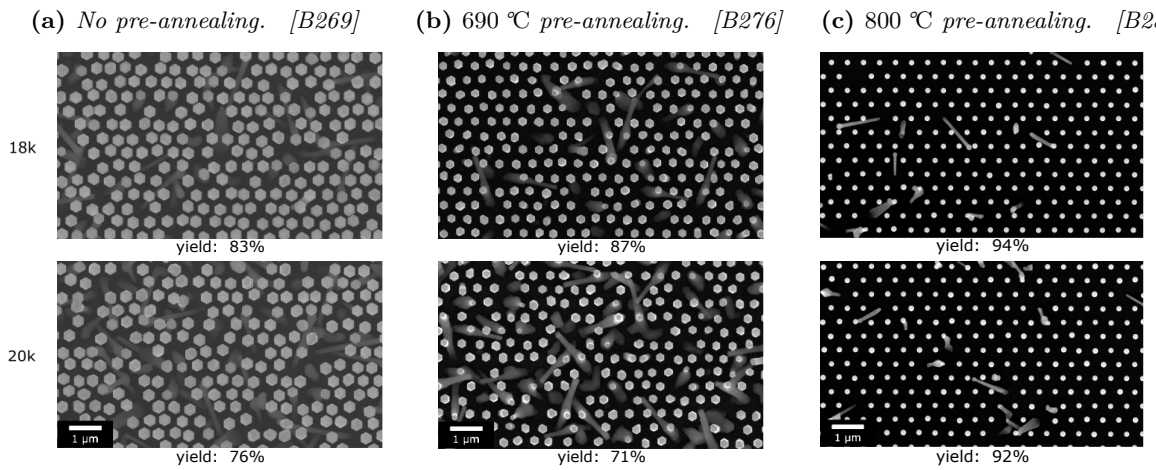

Figure 3.27: *Influence of the pre-growth* in situ *annealing on the vertical yield in GaAs NW arrays with GaP stem. Top-view SEM images are taken at* 500 nm *pitch patterns with two different EBL exposure doses (hole size). In (a,b), core-shell NWs were grown, explaining the different morphology and image contrast.*

3.2.4 Conclusion

Section: Control of the vertical yield in NW arrays

I investigated the origins of defective growth in self-catalyzed GaAs NW arrays grown by MBE, in particular the importance of a (111)B polarity for the initial NW seed.
While I showed that the yield of pure GaAs NWs depends on some growth parameters, this simple growth scheme is not robust and lacks homogeneity and reproducibility.

A robust growth design was developed through the use of GaP stems at the start of NW growth and with a specific wafer cleaning procedure, allowing to reach 95 % yield in the center of 2" wafers. A high temperature *in situ* pre-treatment prior to growth is also beneficial to the yield homogeneity over 1/6 2" samples. Full 2" wafers are preferred for the growth of solar cell devices such as in Figure 3.28 where the high yield in the main pattern (>90 %) is confirmed by the excellent diffraction as seen with naked eye at specific angles-of-view (Figure 3.28a). The yield reaches 100 % in the small patterns written 'pixel-by-pixel' (Figure 3.28c) due to the better control over the hole size and edge definition with this exposure method.

Such NW arrays with excellent homogeneity make a suitable baseline for the fabrication of core-shell devices, provided that the GaP foot does not alter the electric properties, and that the NW crystal quality is sufficient.

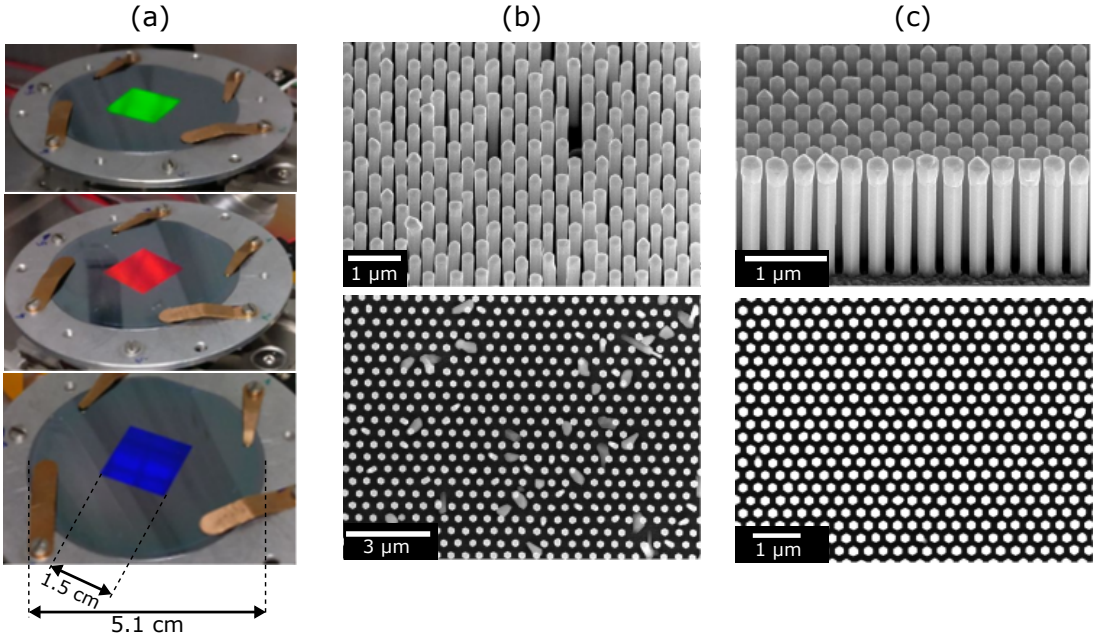

Figure 3.28: *(a) Photographs of a 2" Si wafer patterned with a* $1.5\,\mathrm{cm} \times 1.5\,\mathrm{cm}$ *array at the center. The periodic NW ensemble diffracts the white light in the room at different angles and colors. (b) SEM overview at the middle of the NW array at a* $45°$ *tilt (top) and in top-view (bottom). The yield is above* $90\,\%$*. (c) SEM overview at a pattern written 'pixel-by-pixel' (*$300\,\mathrm{nm}$ *pitch, diameter P2 in the design described in Figure 2.19). The yield is* $100\,\%$*. [76838]*

3.3 Crystal quality in GaAs nanowires

NWs grown on Si have the potential to form perfect mono-crystals with low density of recombining defects, suited for solar cells. However, their bottom-up fabrication process can induce crystal imperfections which might result in recombining defects at the bulk and surfaces (especially since the surface-to-volume ratio is enhanced). In this section, I focus on the crystallinity of GaAs NWs and on the typical defects that are found in self-catalyzed NWs: presence of twins, of stacking faults, or inclusion of WZ phase in otherwise ZB NWs.

3.3.1 Crystal defects in nanowires

3.3.1.1 Typical defects: stacking faults, twin planes and polytypism

Stacking faults and twins. Self-catalyzed GaAs NWs consist mostly of ZB phase. In this structure, the atomic planes positions along the [111]B direction respect the sequence *A,B,C,A,B,C, etc.* (Figure 3.29a). The regularity of this sequence can be interrupted with stacking faults for example, which represent a shift of the atomic planes : $A, B, C, \underline{B}, C, A, B, C$ *etc.* Rotational twin, as already introduced in Section 3.2 (page 84), are also commonly found in ZB NWs and represent an inversion of the atomic plane sequence order : $A, B, C, \underline{A}, C, B, A, C$ *etc.* (Figure 3.29a). The plane sequence can be accurately determined from high-resolution STEM images of NWs along the $[1\bar{1}0]$ direction, and the crystal structure (twins, WZ phase) can thus be readily identified (Figure 3.29b). In Figure 3.29b, the Fourier transform of selected areas from the STEM image are displayed (with matching color frames) and the diffraction spots corresponding to both ZB orientations and to the WZ phase are labeled. Analyzing the selected-area diffraction pattern is thus another way to quickly identify the crystal phase of a NW.

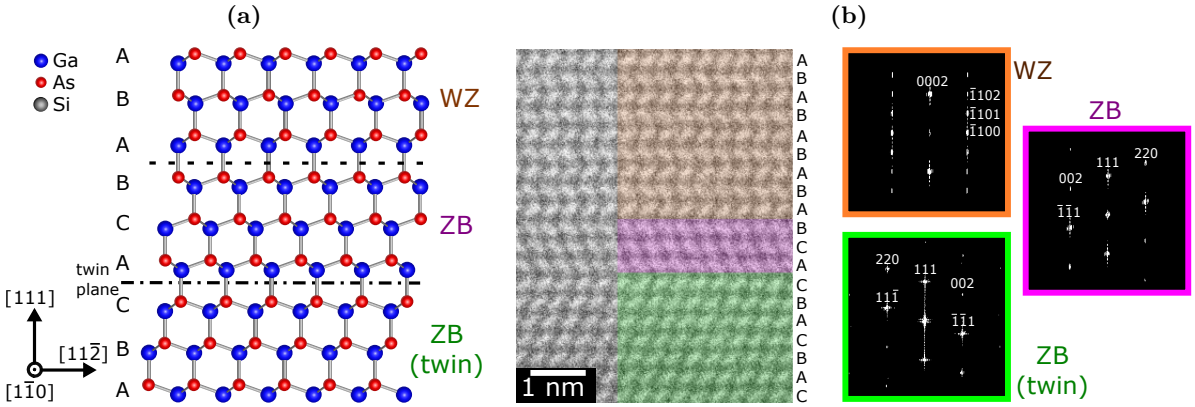

Figure 3.29: *(a) Representation of the atomic structure of a GaAs crystal with three different crystal structures along the* [111]*B direction: WZ, ZB, and twinned ZB. The sequence of atomic planes is indicated with letters. (b) High-resolution STEM-HAADF images of a NW exhibiting such crystal structure, viewed along the* $[1\bar{1}0]$ *zone-axis (*$[11\bar{2}0]$ *for WZ). Each crystal phase is highlighted in a different color, and its Fourier transform is also indicated with labelled diffraction spots. [76659]*

The formation of a stacking fault or the growth of the first planes of a twinned crystal during the axial growth of a ZB NW correspond to the same sequence as the formation of a new WZ plane in a WZ NW. In all cases, the last 3 atomic planes are A,B,A or equivalent. It is then reasonable to assume that the nucleation barrier for the formation of a twin in ZB is similar to the one of a stacking fault, or a new WZ bilayer. Thus, the growth conditions favoring WZ should also favor twins and stacking faults in ZB, namely low droplet contact angles (close to 110° for pure WZ).

From a growth perspective, the presence of twin boundaries at the sidewall facets can change the dynamics of adatom diffusion and epitaxial incorporation, and disturb shell growth or dopant

incorporation. There are reports of faceting of the $\{1\bar{1}0\}$ sidewalls into $\{111\}$ facets ([Xiong et al. 2006]; [Algra et al. 2008]; [Caroff et al. 2009]), which result in variable core diameter. With high Be doping during shell growth on faulted core, Zhang *et al.* reported local overgrowth rings centered at the stacking faults positions ([Zhang et al. 2017b] mention a 'kabob-like' morphology),

From an electronic perspective, since the atoms at the twin plane are still bonded to the surrounding atoms as tetrahedra, the band structure should remain largely unchanged, without creation of deep non-radiative recombination centers for the photo-generated carriers. However, the surface electronic states at the $\{1\bar{1}0\}$ sidewall facets might be changed more significantly by the presence of twins. In ref [Brown et al. 2015], recombination rates orders of magnitude higher than for pure $\{1\bar{1}0\}$ surface were calculated at the sidewalls of twinned GaAs NWs, assuming a high twin density leading to faceting of the sidewalls into $\{111\}$ facets. While this surface effect can kill the luminescence of twinned regions of the NWs studied by cathodoluminescence (as in the next chapter), it should not be too detrimental in the devices where a passivating shell is systematically added, which confines carriers into the NW bulk where twins have little effect [Chang et al. 2012]. On the other hand, the charge carrier transport can be affected by scattering of the charge carriers and strain from the presence of twin planes [Shimamura et al. 2013]. In Ref. [Qian et al. 2015], the effect of twin boundaries on the mobility was investigated using density functional theory and Green's function method, and was not important even at high twin density (hole mobility of $500\,\mathrm{cm^2\,V^{-1}\,s^{-1}}$ for an average twin spacing below 2.4 nm, similar to high quality GaAs layers). Some experimental results tend to show degraded intrinsic carrier mobilities in defective NWs although the amount of twins is controlled by changing the growth conditions, which might introduce other defects also affecting the mobility [Parkinson et al. 2009]. Other reports do not correlate degraded conductivity with the presence of stacking faults and twin planes [Thelander et al. 2011].

Polytypism. Polytypism designates the coexistence of both crystal structures (ZB and WZ) in a single NW. While in most III-V bulk crystals, only the ZB phase is possible, the specific nucleation mechanisms at stake during VLS makes the formation of WZ possible in NWs. In WZ phase, the atomic plane sequence is A,B,A,B, etc. along the growth direction, as shown in Figure 3.30b. The different crystal symmetry (hexagonal unit cell whereas ZB is cubic) results in a different band structure for WZ GaAs. While WZ GaAs was reported to have the same bandgap (within ±1 meV to ±10 meV) as ZB GaAs ([Ketterer et al. 2011]; [Vainorius et al. 2014]; [Chen 2018]), the band-alignment differs and PL data supports the hypothesis of a type-II band-alignment between ZB and WZ GaAs, with the WZ conduction band 115 meV higher than the ZB as depicted in Figure 3.30c [Vainorius et al. 2015].

Polytypism in NWs is reported to greatly increase the resistivity in InAs NWs, by up to two orders of magnitude [Thelander et al. 2011]. The presence of both crystal phases in GaAs NWs should also be avoided as ZB and WZ are believed to form a type II heterostructure [Vainorius et al. 2015] which could confine carriers in each phase (holes in WZ and electrons in ZB). Such offsets in the conduction and valence bands may also hinder the mobility of the carriers along the NW (effect number 1 in Figure 3.30c). Moreover, spatially indirect recombinations could occur below the bandgap [Heiss et al. 2011] (effect number 2 in Figure 3.30c).

Other defects. Other crystal defects can arise during the NW VLS growth, such as three-monolayer step facets, which is supposedly strongly recombining [Sanchez et al. 2017]. However, their occurrence seems unlikely as it requires two simultaneous nucleation events at the top (111) plane, and it was not observed in TEM images.

During shell growth, new sidewall atomic layers grow epitaxially on the core and thus preserve the crystal structure. Stacking faults and twin boundaries are thus propagated inside the shell.

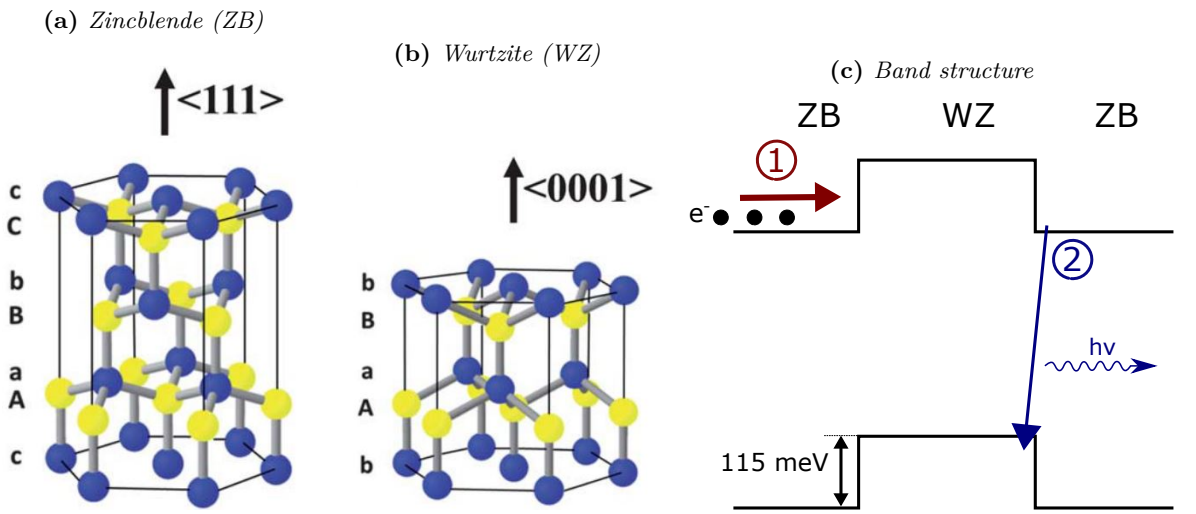

Figure 3.30: *Ball-and-stick representation of the (a) ZB and (b) WZ structures, showing the sequence of atomic planes along the* [111] *direction (*[0001] *for WZ). (c) Band diagram of a ZB/WZ/ZB heterostructure (not at scale), using an identical bandgap for both phases and the offset from [Vainorius et al. 2015]. Two detrimental mechanisms are highlighted: (1) the carrier confinement or degraded carrier transport due to band offset, and (2) the spatially indirect recombinations at energies lower than the bandgap.*

Threading dislocations due to lattice-parameter misfit between core and shell are also very detrimental and are discussed in the next chapter.

> Twin planes, stacking faults and polytypism are typical defects encountered in self-catalyzed NWs. They form during the VLS core growth and extend into the shell. They should be avoided not only to preserve the opto-electronic quality of the core, but also because they can disturb shell growth and alter its quality.

3.3.1.2 NWs with minimized twin density

The defect density in GaAs NWs was optimized empirically in previous work at C2N laboratory by choosing an adequate V/III ratio close to 1.4, sufficiently high to result in large droplet contact angles (typically 130°), which promotes the formation of long ZB segments separated by few twin planes.

Faults in the foot. Figure 3.31 presents the dark-field TEM image of a representative core-shell NW (for each TEM experiment, at least three NWs are characterized), reconstructed from selected diffraction spots, which results in this image where the WZ phase and one of the ZB orientations are highlighted. A high density of stacking faults is visible from the TEM contrast in the first 200 nm of the NW.

High twin plane density and WZ inclusions at the foot of self-catalyzed GaAs NWs is often reported ([Jabeen et al. 2008]; [Krogstrup et al. 2010]). It could be explained by a too low droplet contact angle at the beginning of the growth, as the VLS growth has not yet reached its steady state. The initial influx of Ga is limited to the directly impinging flux at the droplet, which is later reinforced by the flux collected by the NW sidewalls, and re-emitted from the substrate [Schroth et al. 2019]. Thus, the local V/III ratio is probably higher at the initial stage of the growth.

While such high density of stacking faults is undesired, it is not as critical as in other parts of the NW:

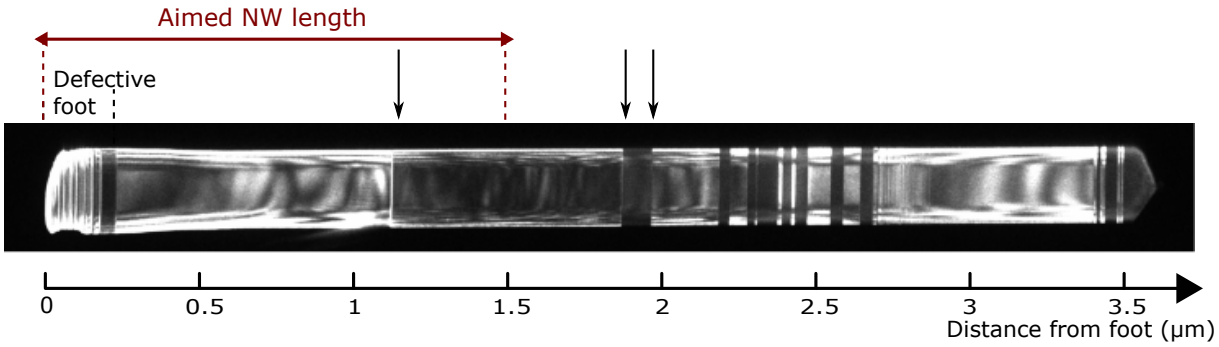

Figure 3.31: *TEM-DF micrograph of a long GaAs core-shell NW (>3.5 µm, viewed along the $\langle 1\bar{1}0 \rangle$ zone-axis. One ZB phase and the WZ phase are highlighted, the other ZB phase appears as dark zones. The NW foot with a high density of stacking faults is indicated. Three twin planes are seen in the first 2 µm of the main axial segment of the NW, indicated with arrows. [76769]*

- In NW array solar cells, most of the light absorption is localized in the middle or upper part of the NW due to the resonant mechanisms, especially for shorter wavelengths ([Anttu 2019a]; [Chen 2018]). If these stacking faults at the foot induce many recombining defects, it would not be as detrimental to solar cell performance.
- They could hinder the majority carrier transport from the core towards the substrate. However, as mentioned in the previous section their influence on the mobility in the bulk is not significant, and the presence of heterostructures between the GaAs NW, the GaP foot and the Si substrate with high band offsets are expected to be more impactful on the transport. Moreover, if it is possible to dope the core to high levels ($p > 10^{18}\,\mathrm{cm}^{-3}$), it would compensate a low mobility and result in sufficient conduction.

Due to the additional complexity of employing a GaP foot in the NW devices, the optimization of the crystal quality in the foot was not part of my thesis work.

Towards pure ZB axial segments. Looking at the rest of Figure 3.31, many twin planes and stacking faults are visible along the 3.5 µm long NW, with varying densities. However, such long NWs are not needed for solar cells and light absorption can be achieved with lengths below 1.5 µm [Chen 2018]. Our conditions lead to the occurrence of only one twin plane within the first 1.5 µm of the wire (first black arrow). Therefore, in the following, I limit myself to the growth of 1.5 µm long NWs and focus on limiting the defect density in the tip, resulting from droplet consumption.

A high density of defects is present after 2.5 µm, which is a consequence of the droplet consumption method and is tackled in the next section.

Noteworthy, the crystalline structure is preserved between the shell and the core, and the twin planes extend through the shell until the NW sidewall facets. Controlling the defect density in the core is thus of prime importance. No dislocations are visible on this NW though dislocations and 3D-twins were occasionally seen in the tip of other NWs.

Our growth conditions lead to NWs with a high density of twin planes or stacking faults near the foot. Short NW can be grown almost defect-free above the foot, as the first 1.5 µm consist of pure ZB with an occasional twin plane, but the droplet consumption needs to be optimized.

3.3.2 Droplet consumption optimization

After self-catalyzed axial VLS growth, the Ga droplet can be consumed *in situ*. This can be done, for example, by providing an As flux while shutting the Ga flux, so that an extra segment of GaAs is formed, as illustrated in Figure 3.32.

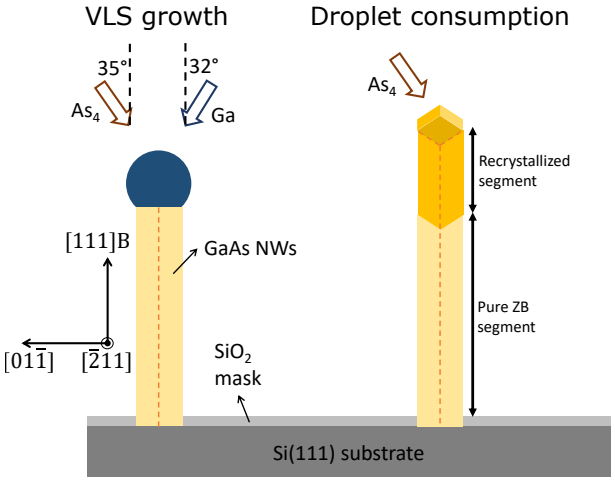

Figure 3.32: *Overview of the NW droplet consumption. Ga-catalyzed NW cores are grown by VLS. Ga liquid droplets are consumed at the end of the VLS growth. Subsequently, shell growth can be conducted (vapor-solid, VS growth) for surface passivation or to create a core-shell junction. The incident angles of molecular beams with respect to the substrate normal are indicated. Adapted from [Chen et al. 2020a].*

The objective is to find a droplet consumption method that generates the fewest twin planes and WZ inclusions, ideally zero. On the other hand, the morphology of the tip does not necessarily need to be accurately controlled since, as I show in the next chapter, the subsequent shell grown at 580 °C forms a set of flat $\{1\bar{1}0\}$ facets, independently of the core morphology.

3.3.2.1 Crystal structure with unoptimized droplet consumption

TEM characterization of a core-shell NW. GaAs NWs were grown as in Section 3.2 (see Table 3.2, page 81), but after the axial VLS growth the temperature was decreased to 500 °C with an As_4 flux of 7 Å s^{-1} (BEP = 5.5×10^{-6} Torr) for 25 min in order to consume the Ga droplet (Figure 3.32). A GaAs shell was then grown at 580 °C.

NWs from a 500 nm pitch pattern were reported on a TEM grid and studied by TEM. The bright-field (BF) TEM image (Figure 3.33a) shows a 2 µm long and 250 nm thick NW. As most NWs typically show a 100 nm core before the droplet consumption, I infer that the shell is 75 nm thick here. The dark-field (DF) TEM image (Figure 3.33b) gives more insight on the crystalline structure: the NW is mostly ZB, in particular its main segment is a 1300 nm-long pure ZB phase. A 490 nm-long WZ segment is present near the NW top, along with zones of mixed ZB and WZ phases, which are clearly identified from the Fourier transforms of the TEM images (Figure 3.33c). The topmost mixed phase segment ('tip') is expected to have been formed during the shell growth. This tip segment is 220 nm-long, whereas it could be expected to be 475 nm-long by considering the Ga flux and the cell orientation. Additional diffusion mechanisms may enhance the growth on the sidewall facets and lead to this relatively low tip length. Figure 3.33d,e shows high-resolution TEM micrographs which confirm the presence of both WZ and ZB in alternation at the locations where mixed phases were identified.

Origin of the WZ segment. The WZ segment is believed to form during the droplet consumption step, as explained in Figure 3.34b.

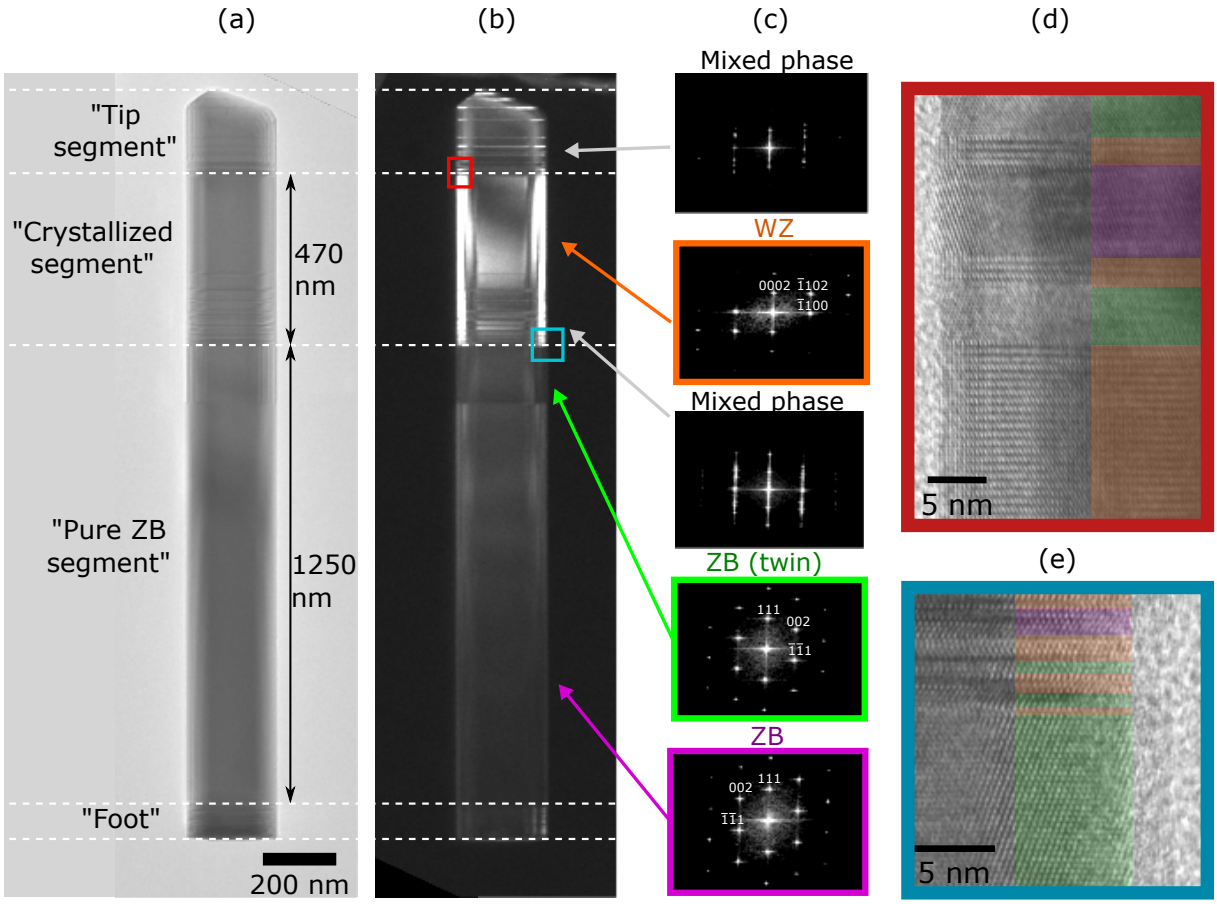

Figure 3.33: *(a) TEM-BF micrograph of a GaAs NW whose catalyst was consumed after the axial growth and with a GaAs shell grown around its core. View along the* $\langle 1\bar{1}0 \rangle$ *zone-axis. (b) TEM-DF micrograph highlighting the WZ phase. Above the NW foot, several segments can be identified from the crystal phase. (c) The corresponding Fourier transforms (FFT) are shown to the right. (d,e) High resolution TEM-BF images at the locations indicated by colored squares, showing the cubic zinc-blende (ZB) twinned crystals (green and pink color) and the hexagonal wurtzite (WZ) phase (orange color). [76709]*

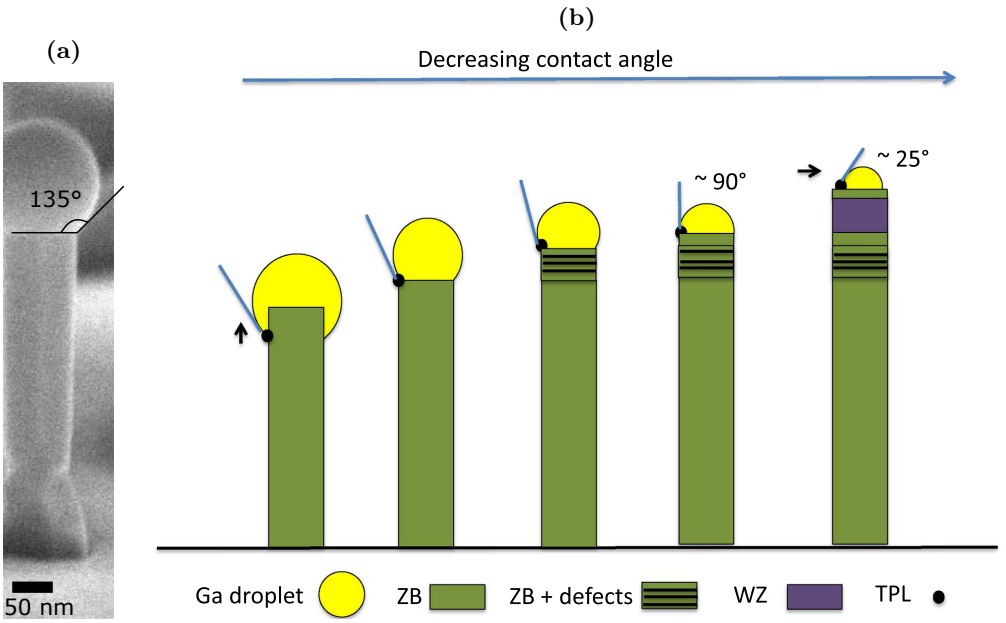

Figure 3.34: *(a) Typical contact angle at the end of the axial growth in our conditions, measured on a 80° tilted SEM image of a NW. [76690] (b) Schematic of the hypothetical droplet consumption evolution. The gallium droplet contact angle decreases as more GaAs crystal is formed. At lower contact angles, defects and WZ inclusions begin to appear in the ZB phase, followed by the formations of a pure WZ segment. The tip segment is ZB again as the contact angle goes well below 90°. At the end, the droplet can still be seen if the As flux was too low or the step duration too short. Figure reproduced from [Scarpellini et al. 2017].*

At 500 °C, the evaporation rate of arsenic from the gallium droplet is negligible [Glas et al. 2013], so the incoming arsenic is expected to be entirely contributing to the consumption of the gallium droplet through the growth of extra GaAs material. The Ga droplet contact angle is expected to decrease as it is consumed under As flux. As seen in Chapter 2, the formation of WZ is favored when the droplet contact angle decreases below 125° (see Figure 2.17). Past this WZ segment, the contact angle is further reduced and a last ZB segment is expected at the end of the consumption, when the contact angle drops well below 100°, but unfortunately it cannot be distinguished from the tip segment unintentionally formed during shell growth. Similar extended WZ segments sandwiched between ZB sections have been reported during the catalyst consumption of self-catalyzed GaAs NWs in the literature ([Priante et al. 2013]; [Heon Kim et al. 2012]; [Scarpellini et al. 2017]).

Lowering the sample temperature to 500 °C and providing a high As flux effectively consumes the droplet and creates an extra GaAs segment, characterized by a ZB/WZ/ZB sequence, expected from canonical VLS growth models.

3.3.2.2 Improved droplet consumption procedure: low As flux

Following the procedure described by Dastjerdi *et al.* in [Dastjerdi et al. 2016], droplet consumption was performed at the same substrate temperature as during the axial growth (595 °C), and under an As_4 flux of $BEP = 2.45 \times 10^{-7}$ Torr, 15 % of the flux that was used during the NW growth.

GaAsP markers were inserted during the growth to keep track of the axial growth dynamics. They were formed by pulsing P in addition to Ga and As, during 20 s, every 3 min (growth sequence schematically described in Figure 3.35). The P BEP was 15 % of the As BEP, which

should give a low P percentage in the solid, so the markers can be distinguished from STEM contrast, but do not disturb the growth conditions too much.

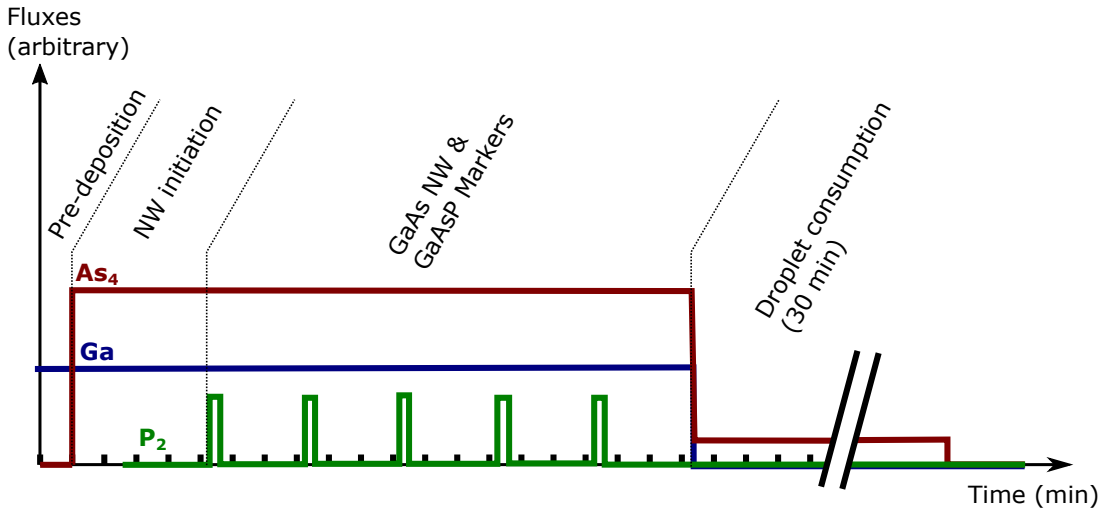

Figure 3.35: *Schematic of the flux sequence during the growth of NWs with markers. The As flux during the first* 15 s *of the NW initiation was also varied independently between experiments, which should not alter the state of the NW at the droplet consumption.*

Two NW samples, with and without droplet consumption, are presented in Figure 3.36.

In the first sample (Figure 3.36a), the droplet was not consumed and the growth was terminated by shutting down the As flux while quickly decreasing the substrate temperature. The droplet is still well visible at the NW top, and the NWs are slightly reverse-tapered (their diameter increases towards the top). The STEM-BF image below reveals all 5 markers (the first one is visible with an enhanced contrast).

Interestingly, the last segment, which should nominally be as long as the previous ones, is about 20 % shorter. This could be an indication that despite the quick temperature drop at the end of the growth, the NW stayed long enough at a temperature sufficiently high to allow VLS re-dissolution of the solid GaAs into the droplet. The NW studied by STEM was probably not aligned along the $\langle 1\bar{1}0 \rangle$ zone-axis, because no stacking faults or twin planes are seen by STEM contrast, even in the foot where they are systematically present.

The second sample (Figure 3.36b) shows NWs for which the droplet was consumed. They exhibit a particular morphology, with a regrowth at the tip, as seen by SEM. The re-growth at the tip is showing a uniform phase from the STEM-DF contrast, whereas about 10 twin planes or stacking faults are visible in the rest of the NW. The markers are also seen after careful examination of the image contrast. They can be distinguished from twin planes since their transitions are not as sharp. The last segment is 90 nm longer than the previous ones, suggesting that extra GaAs was created during the droplet consumption. However, this is much shorter than the 470 nm-long mixed WZ segment on the NW with the droplet consumption at low temperature and high As flux (Figure 3.33), which suggests that this procedure leads to less GaAs regrowth.

A droplet consumption scheme at 595 °C and using a low As flux is used. Using periodic markers along the NW growth axis, I show that this procedure results in shorter GaAs regrowth at the tip. It suggests that it is possible to consume the droplet while creating only small amounts of extra GaAs.

(a) *No Be, no droplet consumption. [76771]*

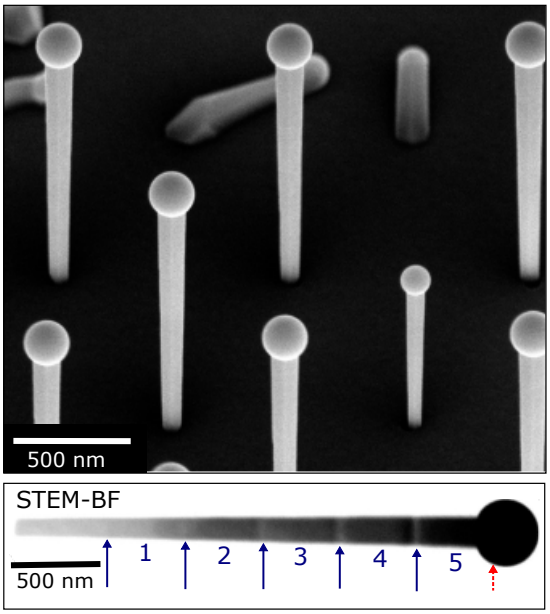

(b) *No Be, droplet consumed. [76780]*

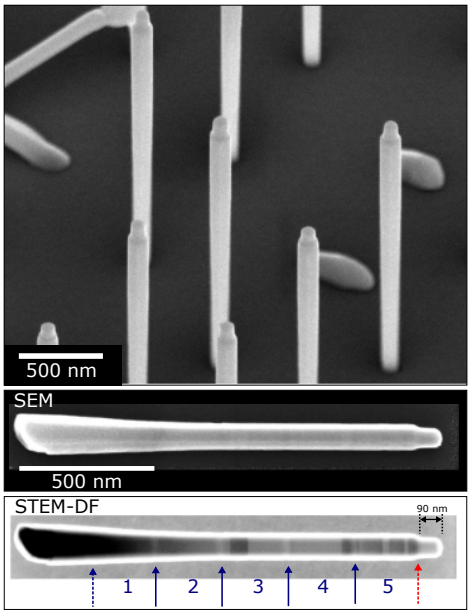

Figure 3.36: *NW morphology and crystallinity before and after droplet consumption at* 595 ℃ *and under low As flux (*15 % *of that during axial growth). For both samples an SEM image with a* 45° *tilt gives insight on the exterior morphology of the NWs. SEM and STEM (DF or BF) micrographs of single NWs are shown below, with the 5 GaAsP marker positions indicated by blue arrows and numbered. When the marker is not visible from STEM contrast, its assumed position is indicated by a dashed arrow. The red arrow indicates the expected position of the droplet by the end of the axial growth*

3.3.2.3 Influence of Be doping

In the core-shell devices, a doping level in the core in the $10^{18}\,\mathrm{cm}^{-3}$ range is desired. Since the NW axial growth rate (typically $12\,\mathrm{Å\,s}^{-1}$) is much higher than standard planar growth rates (typically $1.5\,\mathrm{Å\,s}^{-1}$), a high Be flux is needed to reach those doping levels, typically what would yield planar doping levels in the $10^{19}\,\mathrm{cm}^{-3}$ range. Such strong flux of Be can influence the NW growth, particularly during droplet consumption ([Hilse et al. 2010]; [Zhang et al. 2017a]).

Two other NW samples were grown and the droplet consumed with the same procedure as previously (at growth temperature, and under a low As flux), with a Be flux during the axial growth. For one of them, the Be flux was maintained during droplet consumption. The Be flux used was very high (it would result in a $6 \times 10^{19}\,\mathrm{cm}^{-3}$ Be concentration in planar GaAs(100) grown at $1.5\,\mathrm{Å\,s}^{-1}$) in order to exacerbate any eventual effect.

The NWs whose droplet was consumed under a Be flux present a very different morphology (Figure 3.37a) compared to the previous intrinsic NWs. While some of them occasionally show a regular, straight morphology (like one at the upper left corner of the SEM overview), most of the tips exhibit a high amount of lateral overgrowth, which do not present well-defined crystalline facets. The markers are identified from the STEM-BF image and the overgrowth at the tip occurs where another GaAs segment was expected. This observation could mean two things:

- The high Be content may have led to growth destabilization before the end of the axial growth, right after the last GaAsP marker.
- The axial growth happened undisturbed but during the droplet consumption step, some re-dissolution of the NW took place, followed by extreme GaAs material overgrowth.

The NWs presented in Figure 3.37b were exposed to the same Be flux but not during the droplet consumption. They present a varying morphology as seen on the SEM overview: Some grow straight with or without a small regrowth at the tip, and some present the same large tip

(a) *High Be flux during growth and droplet consumption. [76778]*

(b) *High Be flux during growth but not during droplet consumption. [76784]*

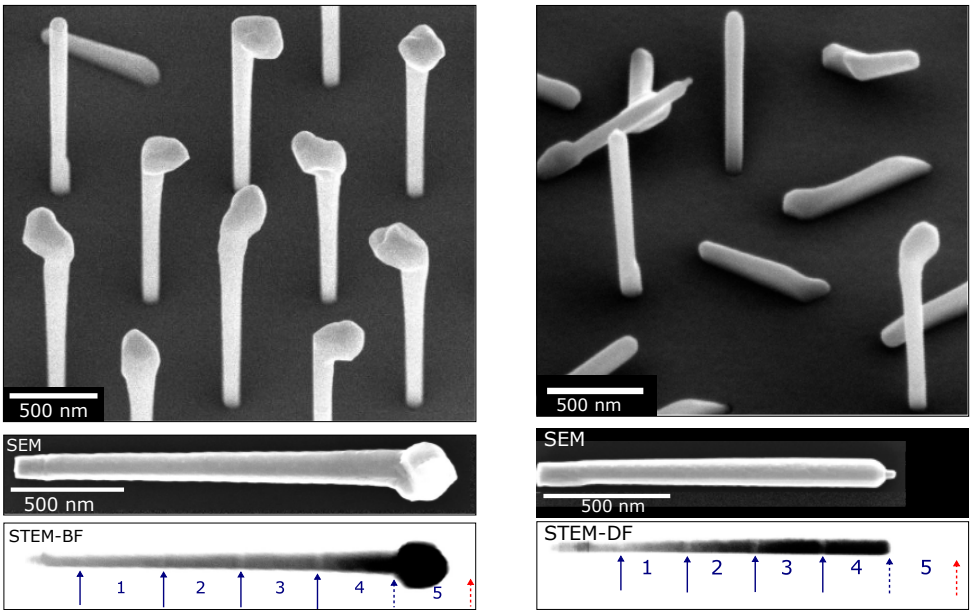

Figure 3.37: *NW morphology and crystallinity after droplet consumption, presented as in Figure 3.36. A high Be flux was employed (equivalent to a* $6 \times 10^{19}\,\mathrm{cm}^{-3}$ *in planar GaAs(100) grown at* $1.5\,\mathrm{\AA\,s}^{-1}$*).*

overgrowth as previously seen. But overall, the morphology has improved by stopping the Be flux during droplet consumption. The STEM-DF image of such NW presents 4 markers. Like before, an entire GaAs segment is missing, which suggests that re-dissolution of GaAs occurred during the droplet consumption, followed by the small tip regrowth.

A degraded tip morphology under high Be flux was already reported in [Hilse et al. 2010], without droplet consumption. This tip morphology is also similar to NWs in [Zhang et al. 2017a], although they did not observe it after core growth, but after shell growth of heavily Be-doped GaAs onto an intrinsic GaAs core already presenting stacking faults. Overall, Be acting as a surfactant at the GaAs sidewalls [Harris et al. 1991] may destabilize the adatom diffusion and the growth dynamics.

As for GaAs:Be NW re-dissolution, it was observed in a similar experiment [Dastjerdi et al. 2016]. They suggest that re-dissolution takes place at the beginning of the droplet consumption due to a lack of As in the droplet, before growth is resumed to form the NW tip. Throughout the growth, one can assume that Be accumulates inside the droplet, up to levels where it could lower the supersaturation in the droplet, which may lead to a regime inhibiting GaAs VLS growth and promoting dissolution instead.

Interestingly, for both samples the STEM contrast reveals many stacking faults or twin planes near the foot but not in the rest of the NWs, contrary to the undoped NWs where many were observed (Figure 3.36b). There are reports of Be dopant having a beneficial effect on stacking faults suppression during core growth, most likely due to accumulation of Be into the Ga droplet ([Zhang et al. 2018]; [Rizzo Piton et al. 2019]). Alloying with dopants may indeed lower the supersaturation and the droplet surface energy, resulting in a higher nucleation barrier for WZ relative to ZB ([Algra et al. 2008]).

A NW segment is dissolved during droplet consumption under a high Be flux. A degraded tip morphology with uncontrolled lateral overgrowth is observed, especially when the Be flux is also provided during droplet consumption. However, GaAs regrowth at the tip can be smaller than for undoped NWs. Be also seems to have a suppressing effect on the formation of twins in the core.

3.3.2.4 Characterization of nanowires with improved droplet consumption

To avoid morphology degradation, a reduced Be flux is used during the axial growth, which corresponds to a doping concentration of $1.5 \times 10^{19}\,\mathrm{cm}^{-3}$ in a planar GaAs(100) layer grown at $1.5\,\text{Å}\,\mathrm{s}^{-1}$. It is shut down during the droplet consumption to avoid uncontrolled lateral overgrowth as seen previously. While this could lead to the creation of an intrinsic or lightly p-doped GaAs segment at the tip, it is not a problem in core-shell devices, as it would be located in between the p- and n-sides, effectively forming a p-i-n junction.

Figure 3.38 shows the TEM characterization of a nanowire collected from a 1000 nm-pitch pattern on this sample. The TEM-BF image (Figure 3.38a) shows a 1250 nm–long NW with a relatively thin diameter (100 nm), which is consistent with the fact that no shell was grown around the core. The faulted foot segment, also visible on the TEM-DF image, is 200 nm-long and consists of twinned ZB and WZ inclusions. Above the faulted foot, a 1160 nm-long pure ZB segment is obtained, which reinforces the hypothesis that Be is beneficial for the growth of a pure ZB core. A remarkable overgrowth is visible at the tip of the NW, a 50 nm long segment with a smaller diameter (50 nm). The analysis of the crystal phases by TEM-BF and STEM-HAADF (Figure 3.38(c,d)) reveals a characteristic ZB/WZ/ZB structure, this time the topmost ZB segment is well visible.

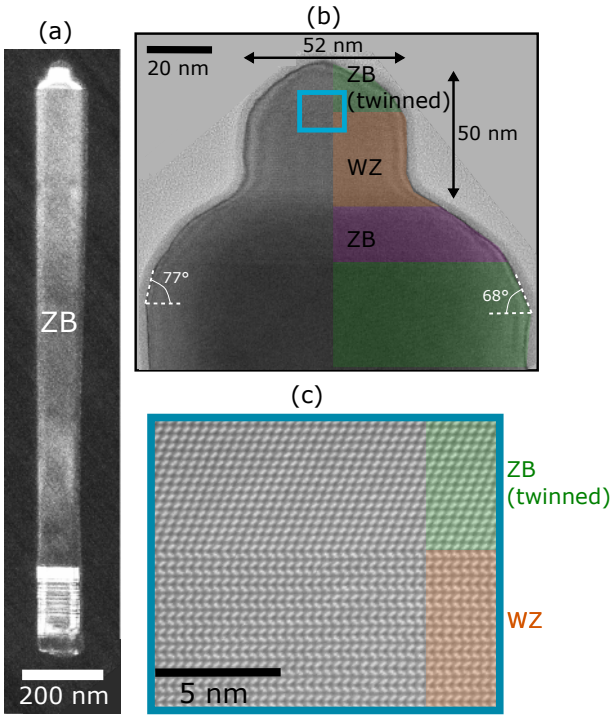

Figure 3.38: *(a) TEM-DF micrograph of a GaAs NW from a* 1000 nm *pitch pattern), whose catalyst was consumed at* 600 ℃ *and under low As_4 flux. No shell was grown after catalyst consumption. The zone-axis is $\langle 1\bar{1}0 \rangle$, and the WZ and one ZB phase are selected. (b) TEM-BF detail of the NW tip, with the 3 different crystal phases highlighted in color. (c) High-resolution STEM-HAADF image of the WZ/ZB transition at the zone marked with a blue square. [76791]*

As for the diameter, a first tapering is observed while still in the main (green) ZB segment (inward angle from 68° to 77°). Above this, the diameter is reduced quickly, and stabilizes at 50 nm, at the onset of the WZ segment. After the last transition to ZB, the diameter finally decreases quickly down to zero. This observation allows to refine the simple sequence introduced in Figure 3.34b when observing the previous NW after unoptimized droplet consumption.

This reduction of the ZB NW diameter under low group V flux is compatible with calculations of the total surface energy, already introduced in Section 2.2 (see Figure 2.18, page 58). The configuration of a droplet sitting on top of narrowing facets, without wetting them, is only favored in term of total surface energy at contact angles below 100°. Therefore, the ZB segment with reducing diameter below the WZ segment (purple in Figure 3.38b) must have formed while the droplet contact angle was already low. A transition must have occurred from angles $> 125°$ to angles $< 100°$ in the ZB segment before that, *without actually introducing a WZ segment*, but possibly causing the formation of the single twin plane observed at this location.

As the growth continues, the most likely scenario is that the NW diameter keeps lowering faster than the droplet volume, leading to an increase of the contact angle until it reaches 100°, where WZ is favored instead of ZB. Contrary to ZB, the WZ segment appears to maintain a constant diameter in Figure 3.38b, in agreement with previous reports ([Kim et al. 2018]; [Priante et al. 2013]; [Heon Kim et al. 2012]) and consistently with the hypothesis used by Panciera *et al.* in their model. This might be because non-wetted vertical WZ facet have a lower surface energy than most other interfaces, making this configuration the most stable.

As the droplet volume decreases and the contact angle gets back below 100°, ZB is once again promoted. During the last ZB segment, the droplet volume may decrease faster than the NW diameter, resulting in a stable ZB phase until droplet consumption.

This specific termination sequence is very similar to that described by [Kim et al. 2018], where the reduction of the NW diameter and its consequence on the droplet contact angle lead to WZ/ZB alternation in thin GaAs NWs.

An optimized droplet consumption procedure employing a moderate Be flux permits to limit the re-growth to a 50 nm protrusion, whose shape is consistent with a model from the literature. Only 3 twin planes were observed in otherwise pure ZB NWs down to the foot segment.

3.3.2.5 Is the droplet consumption procedure robust?

Influence of the pitch. It is already visible on Figure 3.39 that the WZ/ZB regrowth at the tip of the NW grown inside a 500 nm pitch pattern presents different dimensions from the one at the tip of the NW from a 1000 nm pitch pattern, about twice as small. Moreover, the position of the twin planes in the ZB part before the ZB/WZ/ZB sequence differs from the 1000 nm pitch NW (verified on two NWs from this pattern, not shown).

This sensitiveness to the pitch could originate from different group V flux re-emission from the surrounding NWs due to the different array densities, which could affect the effective As_4 flux impinging the droplet. A similar effect during the axial growth could also have led to a different droplet volume at the end of the axial growth, which could modify the droplet consumption dynamics.

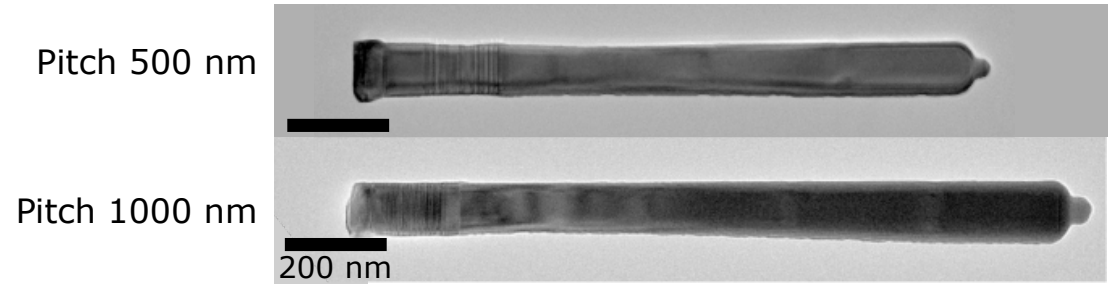

Figure 3.39: *TEM-BF micrograph of nanowires with optimized growth consumption. They were grown simultaneously but come from patterns with different pitches. [76791]*

Sample-to-sample reproducibility and homogeneity. Other NW samples were grown to optimize the droplet consumption in the conditions used for device fabrication: The Ga flux was increased from 1.5 Å s^{-1} to 2 Å s^{-1} (and the As flux accordingly adjusted), the Be flux was lowered to avoid the extreme effects observed with high flux, and the temperature was set to 610 °C. The growth parameters could be slightly different from one growth to the other, and the NW tip morphologies were observed by SEM. Figure 3.40 shows various NW head morphologies observed for different samples but also within the same sample at different pitches or even between neighboring NWs.

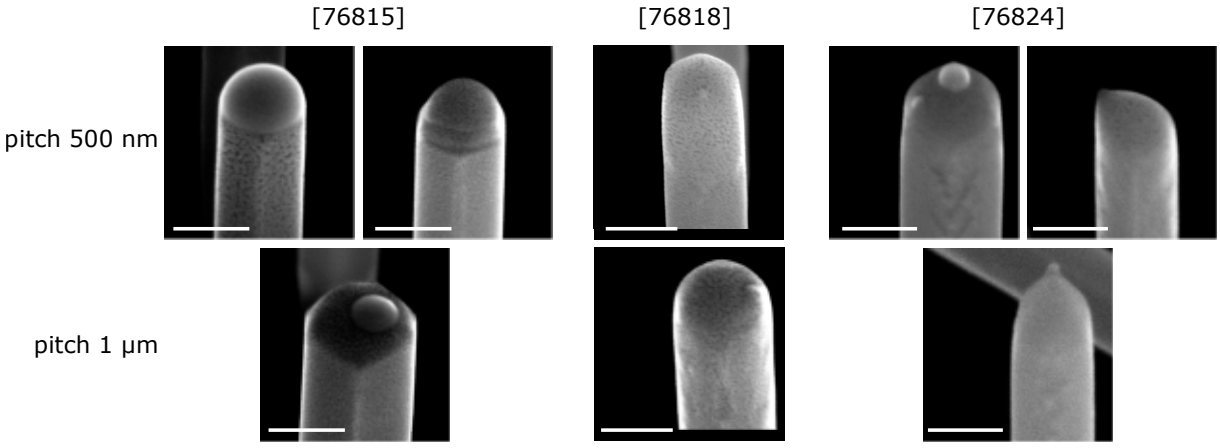

Figure 3.40: *SEM details of NW tips, after droplet consumption under an As flux of* 17 % *of its value during axial growth. NWs from different samples and different pitches are shown. The scale bar is* 100 nm *on all images. [76815,76818,76824]*

On some NWs the droplet is still present at the tip after 30 min. It can either wet the entire top surface, or partially when its volume is already too low. On some samples the NWs have a completely consumed droplet, and they can either present a regular morphology, or a pointy regrown tip, similar to the one characterized by TEM in Figure 3.38.

The balance between temperature, Be concentration and As flux must be precisely tuned to obtain this perfect catalyst consumption. Indeed the discrepancy between the NWs in Figure 3.40a shows that the slight variations occurring between different growth runs and over one sample surface are sufficient to disturb the processes and either leave some gallium, or lead to the regrowth of an extra GaAs segment. In particular, the growth conditions leading to perfect droplet consumption in the Riber32 MBE, were reproduced in the Compact21 MBE. In this other system, significant GaAs regrowth of mixed ZB and WZ phases could not be avoided, including a >100 nm-long pure WZ segment. This suggests that a parameter was not accurately reproduced in this MBE, probably the substrate temperature, or the local flux of As since the source cells arrangement is different.

Perfect droplet consumption. I observed the NWs for which the tip morphology after consumption is homogeneous (sample 76818 in Figure 3.40) by STEM-BF (Figure 3.41). No twin planes are seen above the foot, which indicates that the crystallinity is preserved up to the topmost layer. The absence of a last ZB/WZ/ZB sequence indicates that in our conditions, there is no regrowth at the tip and a fault-free droplet consumption was achieved. Out of 3 NWs observed from this sample, only one had a single twin plane above the foot up to the tip.

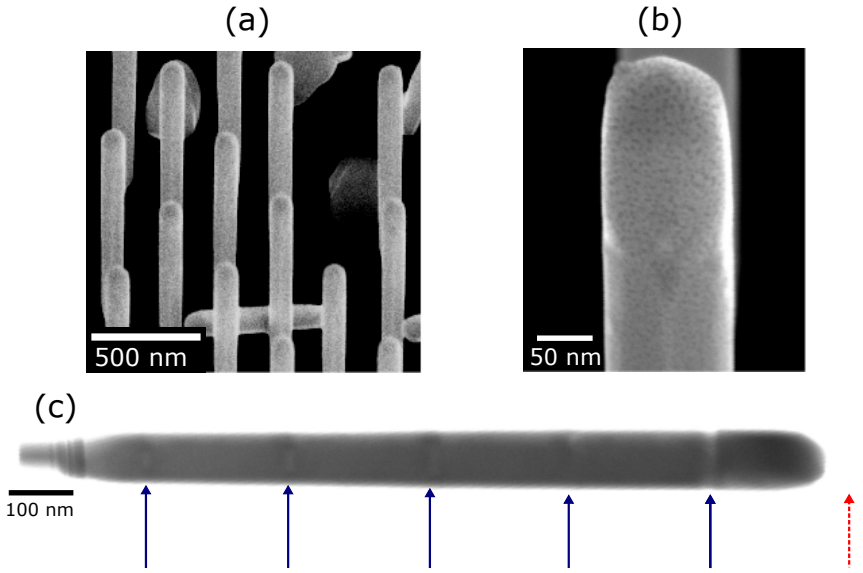

Figure 3.41: *(a) SEM overview of a NW array with optimized droplet consumption. (b) Detail of a NW tip showing no re-growth or liquid Ga. (c)STEM-BF image of a NW. The blue arrows indicate the positions of the GaAsP markers, the red arrow indicates the expected position of the droplet by the end of axial growth. [76818]*

The GaAsP markers also indicate here that some GaAs dissolution took place.

Inhomogeneities of the tip morphology from NW to NW are seen on the same sample, and between samples grown in similar conditions, in particular with residual, unconsumed liquid droplets, or sharp regrown tips. Arrays of NWs with satisfying tip morphology were obtained, without any twin planes above the foot and until the tip termination. Tuning the growth conditions to obtain perfect droplet consumption is thus possible, but seems non-reproducible in our conditions.

3.3.3 Gallium pathways during droplet consumption

Gallium crystallized at the tip

The amount of Ga stored in the droplet by the end of the axial growth is very high. Considering a Ga droplet with a diameter of 195 nm, on top of a NW with a diameter of 115 nm (which corresponds for example to the NWs in Figure 3.36a, page 106), one can evaluated the length of GaAs that could be formed using only the droplet as Ga reservoir. Assuming that Ga occupies an entire sphere (which is a reasonable approximation considering the large contact angle), and using the densities of liquid gallium and solid GaAs, an extra GaAs segment of 850 nm could be grown during the consumption. This is already much longer than the extra segment created during the consumption of the droplet on intrinsic NWs (about 90 nm in Figure 3.36b, page 106). As for Be-doped NWs (Figures 3.38 and 3.37b, pages 108 and 107), an entire GaAs segment is missing after droplet consumption, which is a significant amount of Ga.

Even for the first NW whose droplet was consumed at low temperature and under a high As flux (Figure 3.33), the length of the WZ segment was only 470 nm, much lower than the 850 nm expected from full crystallization of the liquid Ga. There must be other pathways for Ga to escape from the droplet during consumption.

Gallium evaporation

Up to about 630 °C GaAs surfaces are expected to evaporate congruently ([Heyn and Jesson 2015]; [Spirina et al. 2018]; [Chatillon and Chatain 1995]). Considering the surface chemical potential of Ga at a GaAs surface, μ_s, and the surface chemical potential of liquid Ga, μ_L, congruent evaporation implies that $\mu_s < \mu_L$. Indeed, if it were not the case, Ga would preferentially form droplets at the surface instead of evaporating, resulting in a higher sublimation rate for As relative to Ga, which is not compatible with congruent evaporation. In this regime, Ga droplets are not stable on GaAs surfaces and shrink through losing Ga to the surrounding surface, and evaporation ([Chatillon and Chatain 1995]; [Heyn and Jesson 2015]; [Tersoff et al. 2009]). In our procedure, the temperature is about 600°, so that droplet shrinkage should be expected in the absence of incoming As flux, if the mechanism is similar to that on planar GaAs(100). *In situ* TEM experiments have shown that the droplet can shrink without NW VLS growth nor re-dissolution, by reducing the fluxes at a specific temperature [Panciera et al. 2020].

Interestingly, droplet shrinkage is often associated with GaAs re-dissolution in the so-called *local droplet etching* (LDE) mechanism, where Ga droplets are deposited on GaAs(100) surfaces, and which, upon annealing, form nano-holes by etching the underlying GaAs while evaporating Ga and As species ([Wang et al. 2007]; [Heyn et al. 2009]). A parallel can be made between my experiment which combines reverse-VLS of self-catalyzed NWs with Ga escape from the droplet, and the LDE on GaAs(100) surfaces realized in a single-step at 600 °C by Heyn *et al.*, [Heyn et al. 2015] during which GaAs is etched by the Ga droplet, while the droplet is dried.

Gallium diffusion and sidewall re-incorporation

The Ga adatoms diffusing out of the droplet could also incorporate as GaAs at the sidewalls, since an As flux is provided. Thermal decomposition of GaAs was already observed in NWs, and re-incorporation at the tip or sidewalls lead to elongation or tapering of the NWs [Ilkiv et al. 2020]. The latest models of LDE also consider that Ga adatom mainly detach from the droplet to diffuse and crystallize as GaAs evenly on the substrate surface, and to this purpose, maintaining a low flux of As was shown to be critical [Heyn et al. 2015].

The volume created around the 1500 nm-long NWs if all the Ga from the droplet was crystallized would be equivalent to an 8 nm thick extra shell, which is compatible with the typical sample-to-sample variation on the diameter measurement.

During droplet consumption, the first step is a re-dissolution where Be seems to play an important role. A significant amount of liquid Ga is not incorporated as GaAs, and could have either evaporated or diffused to be incorporated at the sidewalls as GaAs, consistently with the expected behavior on planar GaAs(100) surfaces. This could happen concurrently with GaAs re-dissolution, in agreement with recent results from the LDE literature.

3.3.4 Conclusion

Section: Crystal quality in GaAs NWs

I have shown that, in our conditions, many stacking faults or twin planes are formed inside the foot, but they might not be as detrimental there as in the rest of the structure. Carefully chosen conditions lead to a maximum of one twin plane inside the main 1.5 µm-long core segment above the foot. Therefore, I have focused on controlling the density of faults at the very top of the NW, arising during the droplet consumption step.

Unoptimized consumption at 500 °C under a high As flux leads to the formation of a 470 nm extra WZ segment, which is expected from canonical models, as the droplet contact angle decreases during the consumption.

An elaborate consumption scheme inspired from the literature was employed, to limit the length of the re-grown segment to 90 nm, as shown by periodic GaAsP markers inserted inside the NWs. High Be fluxes cause morphology degradation and uncontrolled overgrowth at the NW tip and should be avoided, especially during droplet consumption. The presence of Be also induces the re-dissolution of part of the GaAs NWs during the droplet consumption. With moderate Be doping, the morphology is preserved and the re-growth is limited to a 50 nm long protrusion at the tip, with only 3 twin planes in the whole NW apart from the foot. The origin of the ZB/WZ/ZB alternation is shown to be more complicated than a simple continuous decrease of the contact angle, consistently with recent models considering surface energies.

By fine-tuning the growth conditions, I could obtain NWs without regrowth, which exhibit no twin planes from the foot to the tip, but I also show that in these conditions, the droplet consumption mechanism is very sensitive to growth parameter variations, leading to either unconsumed Ga staying at the tip, or GaAs re-growth.

Large quantities of Ga are not incorporated in the NW via VLS. Consistently with the literature on *local droplet etching*, dissolution of the GaAs by the Ga droplet followed by droplet drying through Ga out-diffusion and re-incorporation at the sidewalls is a possible explanation.

3.4 Summary of Chapter 3: GaAs nanowire arrays on silicon

After reviewing the state-of-the art of NW array growth in Section 3.1, I looked into the verticality in self-catalyzed GaAs NW arrays grown by MBE in Section 3.2.

I investigated the occurrence of non-verticality in self-catalyzed GaAs NW arrays grown by MBE and highlighted different causes, in particular the importance of the polarity of the initial NW seed. While there is a dependence of the yield of pure GaAs NWs on various growth parameters, it still lacks homogeneity and reproducibility with this simple growth scheme.
On the other hand, I showed that it is possible to consistently reach yields higher than 90 % with careful preparation of the wafer surface before mask processing, and by initiating the GaAs NW growth with a GaP stem. Other procedures are beneficial for the yield, such as using 2" substrates to limit edge effects or applying a high temperature *in situ* pre-treatment before initiating the growth.

In Section 3.3, I studied the crystal defects in NWs, in particular those formed during the Ga catalyst consumption, using TEM and atomic-resolution STEM. Consumption at low temperature under a high As flux leads to the formation of an extra WZ segment which is expected as the droplet contact angle decreases during the consumption. An elaborate consumption scheme inspired from the literature was employed, which permits to limit the GaAs regrowth to a 50 nm segment with only 3 twin planes from the foot to the tip, only if a moderate Be flux is provided during axial growth, whereas high Be fluxes lead to uncontrolled overgrowth at the tip. I also show that in these conditions, the droplet consumption mechanism is very sensitive to growth parameter variations, leading to either unconsumed Ga staying at the tip, or GaAs re-growth. Using GaAsP markers helped to evidence the re-dissolution of part of the GaAs NWs during the droplet consumption, when a Be flux is provided during the axial growth. A significant amount of Ga is missing after the consumption, either through evaporation or through diffusion and crystallization at the sidewalls.

Overall, these combined results demonstrate the possibility to grow homogeneous (95 % yield) GaAs NW arrays over 1.5 cm×1.5 cm on 2" Si substrates, without crystal defects above the foot and up to the tip after droplet consumption. Such NW array is a convenient platform to investigate core-shell structures for photovoltaic devices, which is the object of the next chapter.

Chapter

4 GaAs(P) Core-Shell Nanowire Structures

Chapter content

The homogeneous growth of high-quality GaAs NWs in ordered arrays is not sufficient to make solar cell devices suited for tandem-on-Si.

Here, the aim is to fabricate core-shell junctions in every NW, the individual solar cells which are later combined into a device. To do so, it is important to effectively incorporate dopants to form a p-n junction, to passivate the core-shell junction with a wide-bandgap shell, and in the perspective of an optimal tandem configuration, to control the axial growth of high bandgap III-V alloys.

In this chapter, I focus first on the growth of GaAs shells around GaAs NW cores by MBE toward core-shell junctions, but also the shells made of other high bandgap materials, for passivation purpose. I then study the dopant incorporation of Si and Be in the core and in the shell, in the perspective of radial junctions, using cathodoluminescence to measure carrier concentrations at the nanoscale. Finally, in the perspective of making high-bandgap NW array absorbers, best suited for tandem solar cells, I study the growth mechanisms at stake in GaAsP NWs, in particular the spatial homogeneity of the alloy.

4.1 Growth of nanowire shells

Following the growth of ordered arrays of NW cores and catalyst consumption (Chapter 3), I now go into detail about the shell growth, leading to the formation of core-shell structures and devices.

4.1.1 Core-shell growth

A schematic of the NW structure at each step of the growth is illustrated in Figure 4.1, and the corresponding flux sequence is represented in Figure 4.2. The core growth procedure is similar to the one described in the previous chapter unless otherwise specified. It consists in GaAs axial growth during 20 min by VLS under a Ga flux equivalent to 2 Å s^{-1}, and without GaP stem. The droplet is consumed using the unoptimized recipe, a procedure which leads to the creation of an extra >300 nm-long GaAs segment with mostly WZ phase (as shown in Chapter 3, on page 103). The shell is grown in similar conditions as planar GaAs layers, with an excess of As, and a growth rate determined by the limiting Ga flux. The substrate temperature may be set to a lower value before starting the shell growth, and dopants may be provided.

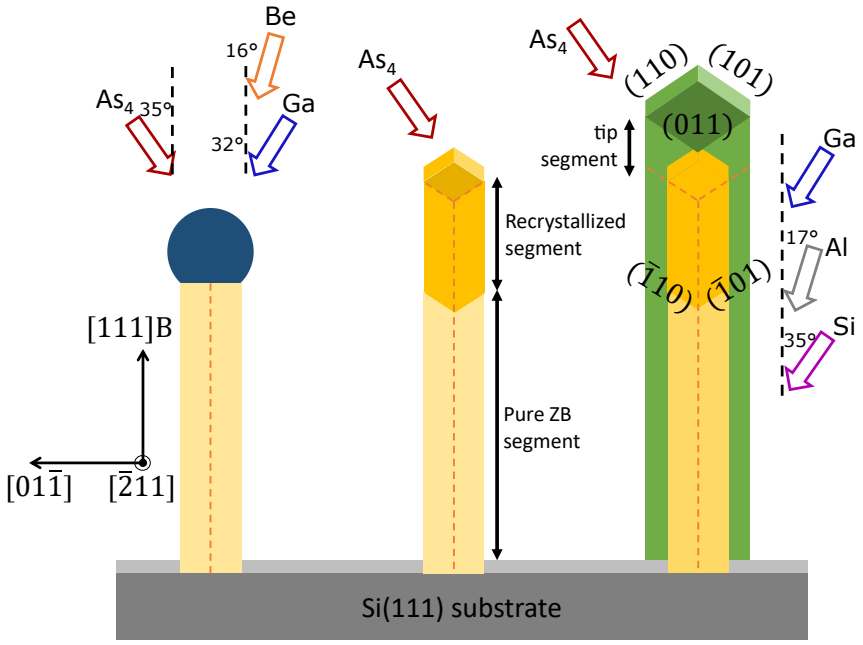

Figure 4.1: *Schematic of the growth sequence for core-shell NWs, in the case of p-doped GaAs core and n-doped AlGaAs shell. The cell incidence angles in the Riber32 MBE setup are indicated.*

GaAs shell growth conditions. GaAs shells are typically grown using a low Ga flux (0.8 Å s^{-1}) and a flux of As_4 in large excess to promote Si incorporation in Ga sites (V/III ratio of 16). The substrate rotation is set to a relatively high value (20 rpm) in order to promote a uniform coating of the sidewalls.

4.1.1.1 Shell growth rate estimation

Due to the source cell angles of incidence, a thicker layer is expected at the NW top than at the sidewalls (Figure 4.3). The growth rate at the top relative to the growth rate at the NW vertical sidewalls is given by Equation 4.1, where α is the angle of incidence of the source cell to the substrate normal, and v, the growth rate. The factor π is here to account for the sample

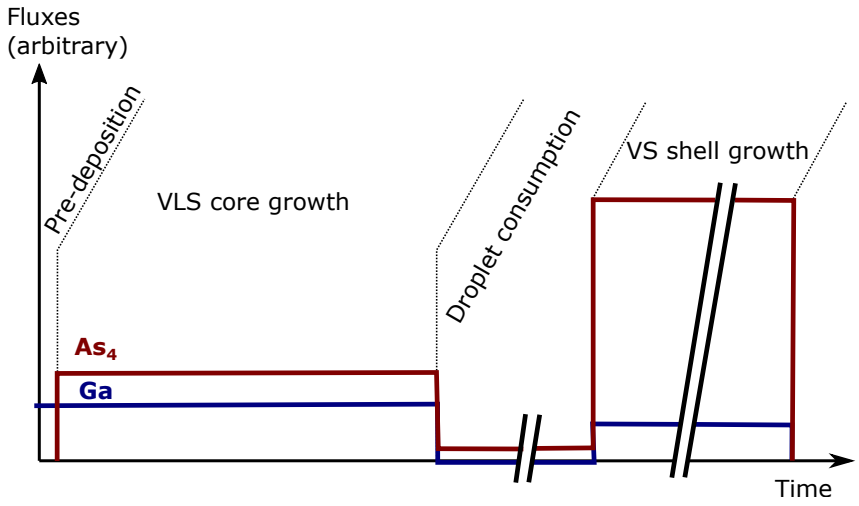

Figure 4.2: *Schematic of the flux sequence during the growth of core-shell NWs.*

rotation, as the NW sidewall facets are not always exposed to the flux.

$$\frac{v_{planar}}{v_{shell}} = \text{cotan}(\alpha) \times \pi \tag{4.1}$$

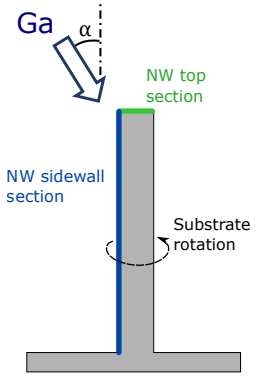

Figure 4.3: *Schematic of the flux incidence angle relative to the NW sidewall in an MBE. Due to the substrate rotation and the vertical facets, the effective flux cross-section is different between the NW top and the sidewalls.*

In the Riber 32, this ratio is 5.0 for Ga and In and 10.3 for Al, so that significant composition inhomogeneities are expected in AlGaAs alloys simply due to the geometry, with more Al incorporated at the top than at the sidewalls of the NWs.

In the Compact21 the cells are all at a 40° incidence to the substrate normal, so the ratio is 3.1 for all cells. While this implies that in the Compact21, the thickness at the tip will be closer to the one at the sidewalls, more important effects of flux shading between neighboring NWs are also expected.

This estimation only considers directly impinging fluxes on a vertical facet. However, the shell growth processes are complex and there are possibly additional group-III adatom contributions from the mask by diffusion or by re-emission [Oehler et al. 2018]; [Plissard et al. 2011], which means that the actual amount of material formed on the sidewalls might be underestimated.

4.1.1.2 Shell morphology improvement with growth temperature

Sample description. I investigated the influence of the growth temperature on the NW array morphology by growing 3 similar samples with a Si-doped GaAs shell around a GaAs core, only

changing the temperature during shell growth.

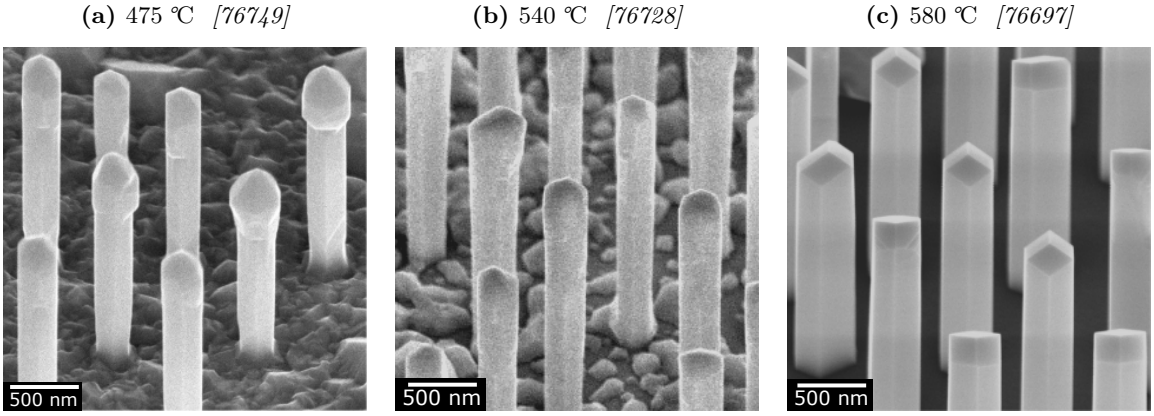

Figure 4.4: *SEM overviews of core-shell GaAs nanowire arrays, with the Si-doped shell grown at different substrate temperatures, and under a Si flux corresponding to a doping level of* $7 \times 10^{18}\,\mathrm{cm}^{-3}$ *in planar thin-films grown in the same conditions.*

At 475 °C (Figure 4.4a), the NWs exhibit a degraded morphology. The top can be thicker than the rest of the core over 300–500 nm, which could correspond to shell growth around the WZ segment formed during Ga consumption. The shell sidewalls are not completely smooth and some step edges can be seen near the NW feet. A continuous layer of material without apparent crystal facets is present in between the NWs.

Increasing the temperature to 540 °C (Figure 4.4b), one can see an improvement of the NW morphology, with less lateral overgrowth at the tip. The material deposition in between the NWs is no longer continuous, and the SiO_x mask surface can be seen underneath.

Finally, at 580 °C (Figure 4.4c), all NWs present smooth facets only consisting of {110} planes, at the sidewalls and at the tip. In addition, there is no more parasitic material deposition on the mask. These NWs are thicker than those grown at lower temperatures, and present more thickness inhomogeneity between NWs, and between different facets of one NW, leading to irregular hexagonal cross-sections.

Enhanced Ga adatom diffusion. Si-doped shells grown at 580 °C seem to benefit from increased Ga adatom diffusion or evaporation rate on the mask, which prevent the formation of parasitic material there. The additional contribution of Gallium diffusing or evaporating from the mask towards the NWs could also explain the increased NW thickness at high temperature. At lower temperature, the Ga adatom diffusion (or evaporation) on the mask is inhibited and nucleation of GaAs becomes favored under the high As_4 flux, which leads to this parasitic, multi-crystalline GaAs layer.

At the NW sidewall facets, an enhanced Ga adatom mobility at 580 °C promotes growth in a layer-by-layer fashion which results in smooth {110} planes. It could also result in inhomogeneous sidewall growth and irregular NW cross-section if, besides an increased Ga adatom diffusion length, some mechanisms favor GaAs nucleation at some facets relative to others. Such mechanism could be a local imbalance of impinging As flux due to complex shadowing effects and re-emission in NW arrays ([Ramdani et al. 2013]; [Oehler et al. 2018]), especially since the yield is not optimized in these arrays, which modifies the local environment of each NW.

As for planar layer MBE growth, lowering the temperature favors island nucleation instead of step-flow [Orton and Foxon 2015] which leads to irregular facet surface morphology. In particular, the NWs are thinner close to the foot which could be due to shading of the incident Ga flux by neighboring NWs, resulting in fewer material reaching this zone by direct incidence. The thicker NW tip at low-temperature (Figure 4.4a) could result from the higher exposure of the NW top to the Ga flux (5 times more exposed than the sidewalls, see Equation 4.1),

associated with a short diffusion length toward the sidewalls. Another possibility could be that Ga adatoms incorporate faster at WZ facets compared to ZB. On the positive side, a reduced Ga adatom diffusion length before nucleation implies that the NWs are more likely to retain a regular hexagonal cross-section shape.

An optimal temperature for the NW facet morphology would lie in between 540 °C and 580 °C, at which parasitic deposition on the mask is completely prevented, while the shell thickness homogeneity is still preserved. However, the shell doping in these conditions needs to be evaluated.

4.1.2 Wide-bandgap alloy shells

As GaAs is prone to surface depletion, a passivating layer is generally grown around the NWs, using ternary III-V materials which can be lattice-matched with GaAs. In general, I use the properties of group III-V alloys from the book [Adachi 2009], which offers a comprehensive set of relatively recent results and data on these materials.

4.1.2.1 Possible material candidates

AlGaAs. With a bandgap ranging from 1.43 eV to 2.2 eV, $Al_xGa_{1-x}As$ is a material of choice, widely employed for GaAs thin-film passivation, especially since it is closely matched to GaAs at any Al fraction (mismatch $< 0.143\,\%$). Moreover, above 2 eV ($x = 45\,\%$) the minimum of the conduction band is the X-valley, which results in an indirect bandgap, well suited for solar cell window layers due to its low absorption.

In our typical growth conditions, Al and Ga are provided with an excess of As, in conditions that would lead to a planar $Al_xGa_{1-x}As$ layer with an Al content $x = 40\,\%$. Considering only the incident fluxes in the Riber32 MBE, a 10 times thinner shell is expected at the sidewalls compared to what would be obtained on a planar layer or at the NW top (Equation 4.1).

Al is known to be more reactive than Ga and bond more strongly to As, which results in low diffusion lengths and atomically rough interfaces [Orton and Foxon 2015]. In addition, due to this low diffusion length, to the lower temperatures employed during n-shell growth (<500 °C) and to the low Al cell incidence angle in the Riber32 MBE (17°), a thick parasitic layer is expected to form on the mask surface in between the NWs (10 times thicker than at the NW sidewalls according to Equation 4.1). Al is also very reactive with oxygen and the Al-O bonds introduce deep levels, detrimental to the carriers' lifetime ([Akimoto et al. 1986]; [Amano et al. 1988]).

A GaAs capping shell (typically equivalent to a 30 nm planar layer, so that 6 nm expected at the sidewalls) is systematically grown afterwards, in order to avoid oxidation of the last Al-containing shell when the sample is exposed to air. However, parasitic light absorption in this capping layer, especially at the top where it is thicker, do not contribute to the photocurrent generated in NW devices and is a net loss.

A major issue with AlGaAs for NWs grown on Si is its low diffusion length, even on selective masks, which systematically leads to parasitic crust of Al oxides and AlGaAs in between NWs [Vettori et al. 2018].

GaInP. $Ga_xIn_{1-x}P$ is also widely used for GaAs passivation, although the Ga fraction in the alloy needs to be contained near $x = 51\,\%$ to match the GaAs lattice constant (with $E_g = 1.9$ eV). It presents the advantage over AlGaAs to be less prone to oxidation and do not necessitate a capping layer. Very low recombination velocities at the interface between GaInP and GaAs can also be attained ($S < 1.5\,cm\,s^{-1}$), two orders of magnitude lower than that of $Al_{0.4}Ga_{0.6}As$ on GaAs [Olson et al. 1989]. Moreover, In has long diffusion lengths contrary to Al, which could

help maintain the atomic flatness of the facets. However, GaInP is prone to periodical spatial segregation of Ga and In in the lattice of epitaxial thin-films, an effect known as 'ordering' [Gomyo et al. 1986], which can lower the effective bandgap of the material.

Other materials. GaP has been employed to passivate GaAsP NWs, which presents the advantage of being Al-free and has a high (2.26 eV), indirect bandgap, suitable for window layer without parasitic absorption. However, it is lattice-mismatched with GaAs and GaAsP, with a critical thickness before relaxation of the order of 5 nm [Himwas et al. 2017].

AlInP is a suitable ternary material widely used to passivate high bandgap III-V cells due to its high indirect bandgap (2.2 eV) at the composition where it is lattice-matched with GaAs. However, it contains Al and does not present significant advantages compared to AlGaAs to passivate GaAs NWs, while introducing the constraint of bandgap tuning.

Several III-V compound combinations are adequate for the growth of wide-bandgap shells around GaAs NWs. AlGaAs appears to be convenient due to the lattice compatibility with GaAs, but GaInP is very promising as it is free of Al, and is then further characterized by TEM and EDX.

4.1.2.2 STEM-EDX study of GaInP shells

Core-shell GaAs/GaInP NWs grown in the Compact21 MBE were characterized by STEM and energy-dispersive X-ray spectroscopy (EDX). They are made of a p-doped GaAs:Be core, an undoped GaAs shell and a n-doped GaInP:Si shell, the same structure used for the fabrication of solar cell devices. The aimed composition was $Ga_{0.42}In_{0.58}P$, which is the composition that would be obtained when growing planar thin-films under the same conditions. As I show in the following, the resulting sidewall alloy is in general richer in Ga than the target composition, which is why I target such low Ga fraction instead of the desired $Ga_{0.51}In_{0.49}P$.

Such NW is studied by STEM-EDX in Figure 4.5. The STEM-HAADF micrograph in inset shows a NW with slightly reverse-tapered shape, but with sidewalls relatively straight up to the tip. A (111) flat top facet is clearly identified from the STEM-HAADF micrograph of the tip, which differs from the usual set of $\{1\bar{1}0\}$ facets that typically terminated GaAs NWs.

Elemental EDX maps are acquired at the tip of this NW, which unambiguously show the core-shell heterostructure, with a GaInP shell of even thickness (40 nm) around a 150 nm GaAs core (previously thickened by an undoped GaAs shell). The shell is 5.9 times thicker at the tip than at the sidewalls on this NW, which is higher than the factor 3.1 expected from the cell angles in the Compact21 MBE. Moreover, the relative tip and sidewall thicknesses were found to vary from NW to NW. The NW is outlined on the O map, which indicates the presence of a few nm thick native oxide. The left side of the NW is unexpectedly darker than the right side on the O map, which could be the consequence of shading of the X-rays as discussed in the next paragraph. The In and Ga maps exhibit axial variations with higher In content (brighter and darker stripes) where twin boundaries or stacking faults are visible on the HAADF map. This could indicate that the incorporation dynamics of In are strongly influenced by twin boundaries, and that the In adatoms have a long diffusion length on pure ZB surfaces, whereas they are readily incorporated at crystal imperfections, where they occupy group-III sites before Ga atoms.

The segment close to the foot of this NW was also analyzed (Figure 4.5b). While the shell thickness was about 40 nm on both sidewalls observed close to the top, it is now thinner, and differs from one side to the other (20 nm and 12 nm). A thinner shell can be due to shading of the incident fluxes by the surrounding NWs in the array. It is even thinner close to the bottom, maybe due to the presence of twin boundaries or stacking faults (white mark) inhibiting adatom diffusion there. The difference in thickness from left to right could be a consequence of the

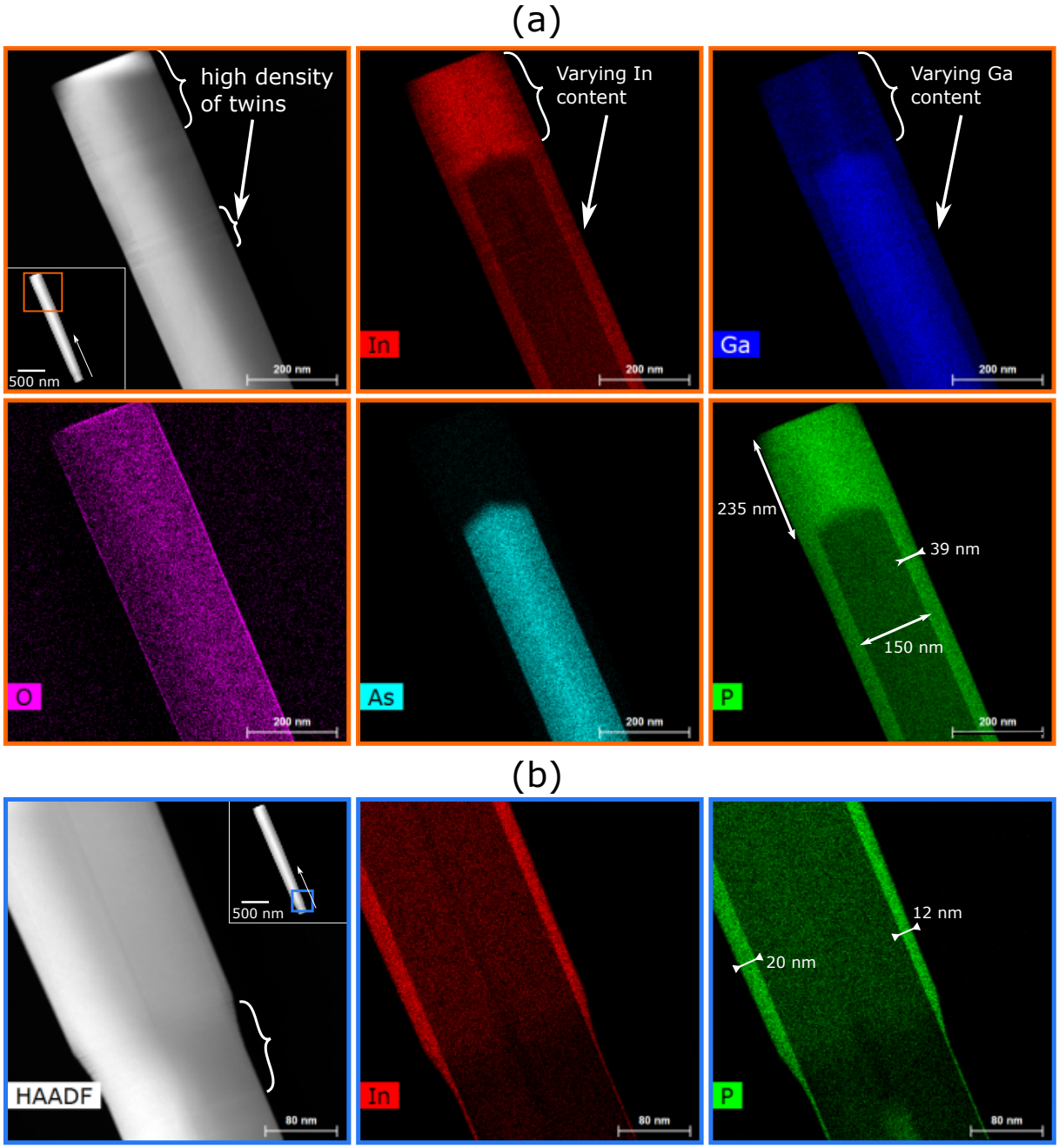

Figure 4.5: *(a) STEM-HAADF and EDX elemental maps of the tip of core-shell undoped GaAs-GaInP NWs, showing the core-shell heterostructure. Viewed from the $\langle 11\bar{2} \rangle$ zone-axis. In the inset is the full NW, the arrow indicates the growth direction. (b) Same analysis close to the foot of the NW, only displaying the P and In elemental maps. [B276]*

inhomogeneity of the NW array. As the local environment is not the same from one facet to the other, the flux shading is not the same from one side to the other, and neither is the collection of group-III adatoms by surface diffusion.

Quantitative composition measurement by EDX. In order to gain more insight on the composition of the shell, quantitative EDX analysis was performed. An EDX linescan was performed through the shell, along the growth direction, as described in Figure 4.6a, and the EDX acquisition software automatically computes the atomic fraction of each element from the average spectra with the adequate material corrections. The Ga fraction in $Ga_xIn_{1-x}P$ is calculated from the In and Ga fractions as $x = \frac{x_{Ga}}{x_{Ga}+x_{In}}$, It appears that it is constant along most of the NW at $x = (39 \pm 2)\,\%$, and increases up to about 50 % over the last 600 nm. Many composition fluctuations are also seen closer to the top, which seems to correlate with NW segments with a high density of twin boundaries or stacking faults.

The quantification can also be performed from the previously acquired EDX maps, by regular sampling over rectangular areas to obtain a local averaged EDX chemical composition (Figure 4.6b,c). The Ga content is calculated with an error within $\pm 4\,\%_{abs.}$, due to the low signal-to-noise ratio when integrating over small rectangles. Close the foot and away from the stacking faults (Figure 4.6b), The Ga fraction is about 35 % on the right sidewall shell and from 33 % to 41 % on the left. A measurement artifact cannot be excluded, since, due to the geometry of the TEM, X-rays emitted from one sidewall shell may need to pass through the NW to reach the detector and be reabsorbed. In particular, on these two maps, the P content on the left side was systematically underestimated (44 % to 47 % instead of 50 %), which is indicative of absorption of the low-energy X-rays from the $K\alpha$ emission line of P (2.01 keV). However, the emission lines of In ($L\alpha = 3.29$ keV) and Ga ($K\alpha = 9.25$ keV) are at higher energies and the influence of re-absorption should not be significant. Thus, this small discrepancy between right and left could originate from the difference in the NW surroundings which influence the flux shading. The same effect is observed at the NW tip (Figure 4.6c) where there is also on average more Ga in the left sidewall shell than in the right.

Focusing on the right sidewall, the Ga content is lower close to the foot (35 %, Figure 4.6b) than in the main section of the sidewall measured from the linescan (39 %, Figure 4.6a), and than close to the head (about 50 % on average, Figure 4.6a,c)). In particular, it fluctuates a lot close to the top (from 39 % to 56 %), and the highest Ga fraction (56 %) is found at a location where many twin boundaries are present. In the tip shell segment on top of the NW, it also varies significantly, between 33 % and 52 % (Figure 4.6c).

Alloy composition inhomogeneities. In order to obtain more information about the incorporation inhomogeneities in GaInP shells, two samples are compared, which were grown with identical GaInP shells except for the Ga fraction in the flux. Two representative NWs from each sample were characterized by EDX as described above, and the compositions in different parts of the shells are reported and summarized in Table 4.1. Shell sidewalls for which significant X-ray shading is suspected were discarded from the analysis.

From these values of the Ga content and the analysis of EDX maps and linescans from Figure 4.6, several comments can be made.

- The 230 nm long shell tip segment which was formed during the growth of the GaInP shell by VS and not during the VLS growth, is full of crystal defects. As the final facet is a flat (111)B plane, GaInP was likely growing along such facet, which is consistent with the fact that twin planes are easily formed along this growth direction. From this perspective, although this trend of GaInP to stabilize on flat (111)B facets leads to NWs with a better aspect, it might not be desired for the sake of crystal quality.
- The presence of crystal defects both inside the tip segment and in the segment from droplet crystallization seems to greatly disturb the incorporation kinetics of Ga and In, as

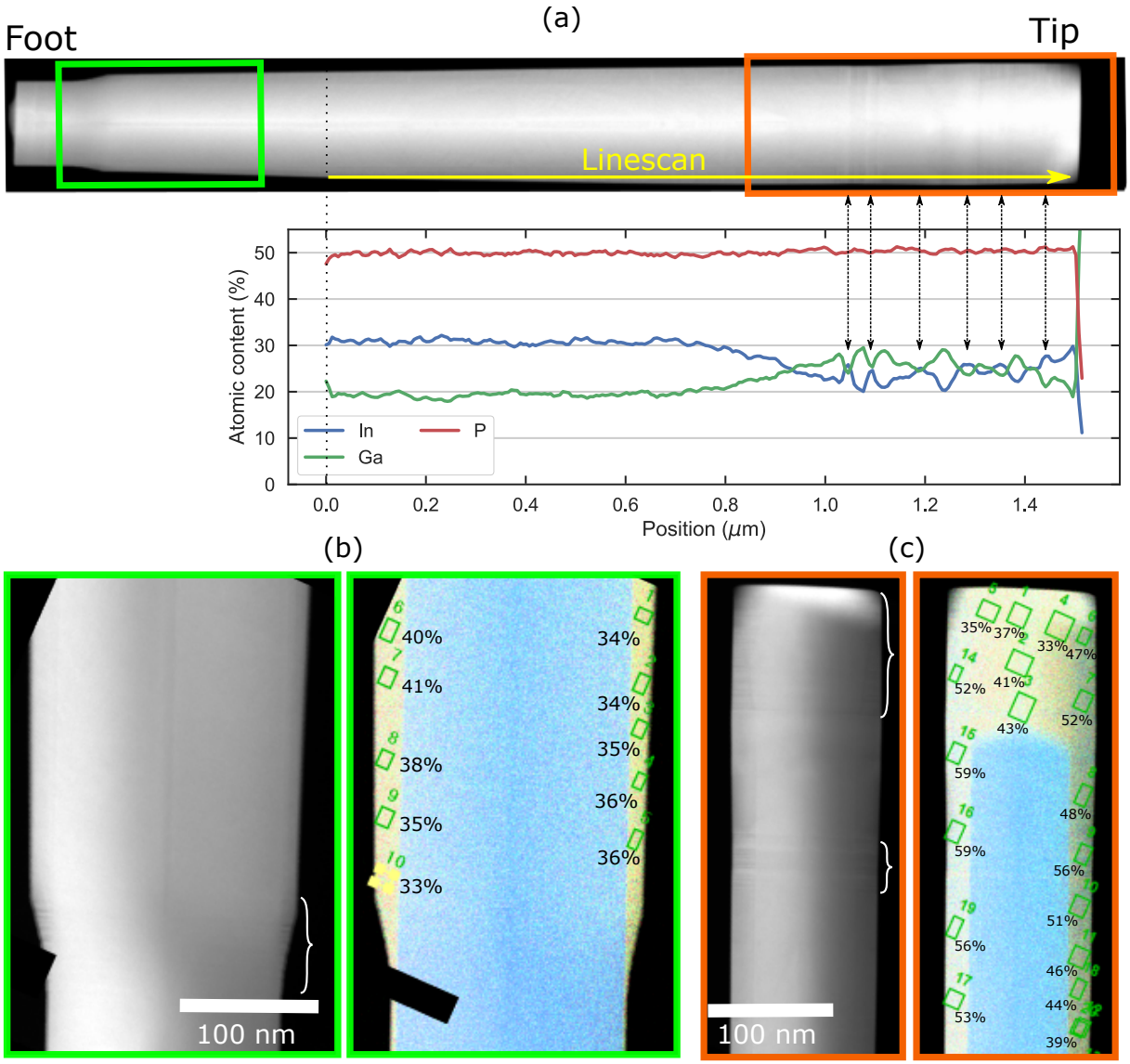

Figure 4.6: *Quantification of the EDX signal. (a) Atomic content of each element in the shell along the growth axis of the NW, computed from an EDX linescan along the line shown on the STEM-HAADF micrograph. The NW is the same as in Figure 4.5. The position of the peak in In content are related to the crystal structure seen by STEM with black arrows. (b) STEM-HAADF (left) and EDX map (right) close to the foot, with the zones of high twin density indicated by white markers, and the superimposed colors from all studied elements on the EDX map. Each green square corresponds to a region where the composition was quantified from EDX and the Ga fraction is indicated, with a precision of ±4 %. (c) Similar analysis close to the NW tip. [B276]*

Table 4.1: *Ga content in $Ga_xIn_{1-x}P$ shells. The vertical yield is also reported, as it changes each NW's surroundings, resulting in different re-emitted fluxes and shading. The error is estimated from the precision of the EDX measurement and the spread of the measurements inside one zone of interest. For the zones with large composition fluctuations, a range of values of x is given.*

Sample	B265		B276	
Vertical yield	30 %		70 %	
Aimed Ga fraction	51 %		42 %	
NW	NW 1	NW 2	NW 1	NW 2
Ga fraction (head)	45–60 %	55-65 %	35–50 %	40–50 %
Ga fraction (sidewall close to head)	50–65 %	55-65 %	44–56 %	46–57 %
Ga fraction (main sidewall)	(62 ± 2) %	(59 ± 2) %	(39 ± 2) %	(45 ± 2) %
Ga fraction (sidewall close to foot)	(56 ± 3) %		(35 ± 2) %	(41 ± 3) %
Average Ga fraction (main sidewall)	(60 ± 3) %		(42 ± 4) %	

important composition fluctuations are observed along the shell sidewall, correlated with the positions of the faults (the topmost 600 nm in Figure 4.6).

- The Ga fraction in the main part of the shell sidewalls is pretty constant although there is a non-negligible variation from NW to NW. It is in general higher than the aimed value, which means that more Ga is incorporated than anticipated.
- For both NWs from sample B276, there is on average more Ga in the shell sidewall close to the top than below, which is not the case for B265 which exhibits the same average Ga fraction. Since the yield is much higher for B276 (70 %) than B265 (30 %),a more important effect of shading of the incoming flux by neighbouring NWs is expected. This results in the first 400 nm to 600 nm of the NWs being more exposed to the direct flux (Figure 4.7). As In adatoms typically have longer diffusion lengths than Ga adatoms, they can diffuse and incorporate further down the NW sidewalls. This might explain why the Ga fraction is lower near the foot (35 %) compared to the main part (39 %) and the top part ($\approx$ 50 %) of the NW (NW1) in Figure 4.6.

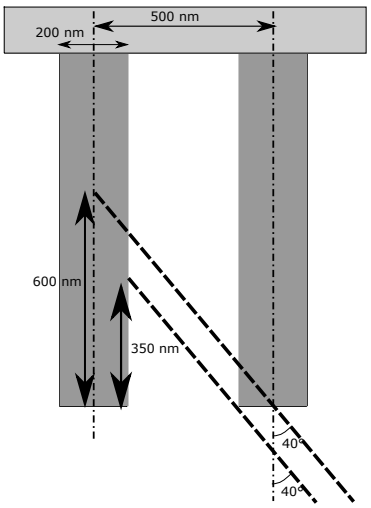

Figure 4.7: *Schematic of the shading by adjacent NWs in a typical array, using the cell geometry of the Compact21 MBE.*

4.1.2.3 Dislocation in lattice-mismatched GaInP shells

As the average measured Ga fraction (39–45 %) is much lower than 51 % in the main section of the GaInP shell at the sidewall of the GaAs core NWs from sample B276, a significant lattice-mismatch is present. The expected lattice-mismatch is 0.9 % for a $Ga_{0.39}In_{0.61}P$ shell around a pure GaAs core.

Expected dislocations. The core-shell misfit has both a longitudinal component and an 'in-plane tangential' component (normal to the axis and tangent to the sidewalls). In order to fully relax the strain, two types of simple edge dislocation (burger vector normal to line directon) are required ([Raychaudhuri and Yu 2006]; [Glas 2015]):

- Line dislocations, which travel along the NW axis and relax the tangential strain. In a realistic cubic crystal (not a cylinder), we can propose a simple picture in which we remove one of the $(11\bar{2})$ plane in the shell and the resulting Burger vector is along [11-2] (i.e. perpendicular to the NW axis, Figure 4.8a)
- Loop dislocations around the core, also called 'prismatic loops' (*i.e.* Burger's vector perpendicular to the loop plane), which relax the longitudinal strain, resulting in the removal of one (111) plane in the shell (Figure 4.8b). The Burger's vector is then along [111] (the NW axis).

(a) *Straight edge dislocation.* **(b)** *Edge dislocation loop.*

Figure 4.8: *Illustration of 2 kinds of pure edge dislocations (red lines) which can relieve the longitudinal and tangential strain in mismatched core-shell NWs, with their corresponding Burger's vector.*

In practice, dislocation lines are more complex : they can form half-loops in the shell [Perillat-Merceroz et al. 2012], and are most often tilted inside $1\bar{1}1$ glide planes [Dayeh et al. 2013]. Although they are expected to thread near the core-shell interface, where they relax the strain the most effectively, they can also form in the shell close to the core interface, in the case of weak mismatch [Perillat-Merceroz et al. 2012].

However, in our case the TEM observation conditions are imposed by the NW geometry, and only the $\langle 1\bar{1}0 \rangle$ zone-axis was explored. We did not look for conditions allowing the systematic characterization of dislocations, nor their density. Instead, we focus on determining whether or not they are present in the NWs. The presence of the dislocations is determined by the observation of strain fields from dark-field TEM images, where it can be decorrelated from other effects, such as equal-thickness fringes (on the side facets, parallel to the NW longitudinal axis).

Critical strain and lattice-mismatch for dislocations. Figure 4.9 presents the DF-TEM micrograph of a NW from sample B276, with a slight tilt from the $\langle 1\bar{1}0 \rangle$ direction. Dislocations induce some strain which can locally align the crystal zone-axis, creating a bright contrast. Note that the bright lines aligned with the NW growth direction are fringes of equal thickness,

a dynamic effect in TEM, only seen in Bragg's conditions. The other bright artifacts and tilted lines are the signature of dislocations.

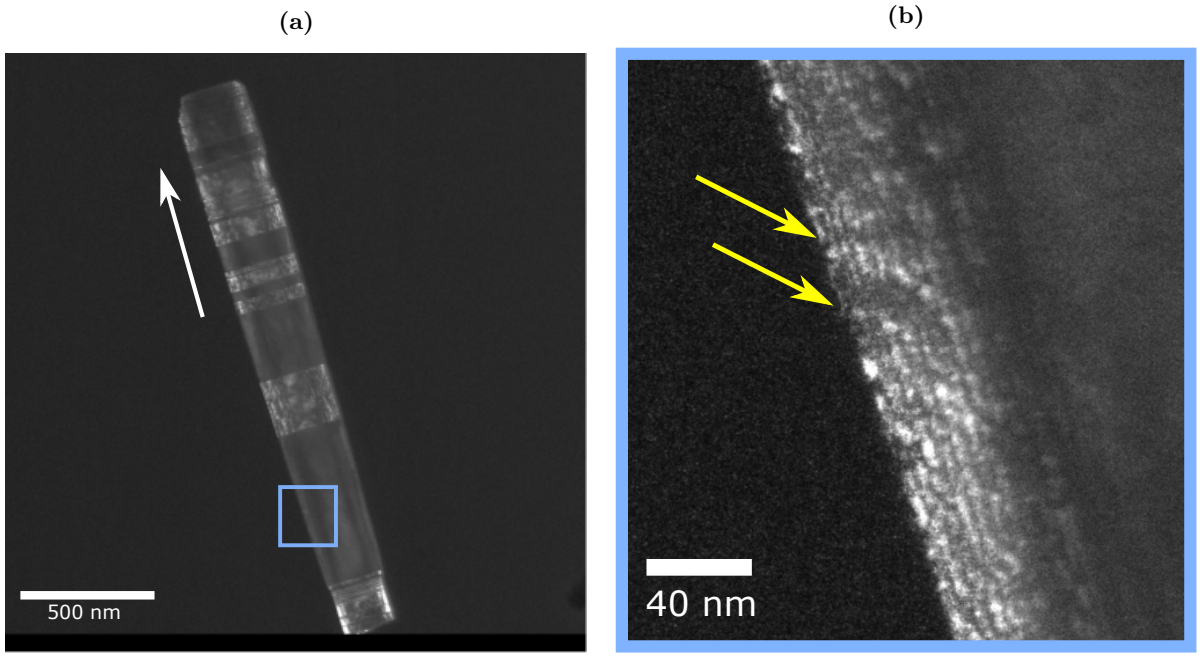

Figure 4.9: *(a) DF-TEM micrograph of another NW from the same sample as Figure 4.5, highlighting one ZB and the WZ phase (220 diffraction spot). The growth direction is indicated with a white arrow. (b) Zoom-in of the NW sidewall, with another ZB phase highlighted. The beam direction is slightly misaligned from the $\langle 1\bar{1}0 \rangle$ zone-axis (weak-beam dark-field conditions) to highlight the strain field around dislocations, visible as white artifacts (indicated with yellow arrows). [B276]*

In order to calculate the critical dimensions or the critical mismatch beyond which plastic relaxation occurs, the contributions of the elastic strain and of the dislocations must be estimated, which is a difficult task owing to the complex nature of the dislocations, and considering that their presence modifies in turn the strain fields [Glas 2015]. This complexity may explain the large discrepancies between the predictions from different literature models (see Figure 4.10).

Calculations in [Raychaudhuri and Yu 2006] anticipate line dislocations to form before loop dislocations. For a misfit close to 1 % on a 75 nm-radius GaAs core, the critical shell thickness is lower than 10 nm. In the present case where the shell is 40 nm-thick close to the top and 20 nm-thick close to the bottom (red dots in Figure 4.10), line dislocations are expected at both locations.

Calculations in [Salehzadeh et al. 2013] (dashed line in Figure 4.10) indicate that for a very important misfit (3.2 %), a 10 nm shell can already elastically relax on a 75 nm core. This selected misfit value is about three times higher than that of our B276 sample. Even if our InGaP shells are thicker (20-40nm), it may be possible to remain in the elastic domain. However, their predictions of the critical core radius before plastic relaxation are rather optimistic compared to the rest of the literature, and do not agree with some experimental observations of dislocations [Glas 2015].

Following [Raychaudhuri and Yu 2006]'s calculation, in order to avoid plastic relaxation, a combination of 20 nm-thick shell on a 75 nm-radius core is possible with a misfit below 0.5 %. Following the calculation by [Haapamaki et al. 2012] (dash-dotted line in Figure 4.10), a mismatch of 1 % does not allow realistic combinations of core and shell dimensions that would allow to relax the strain elastically. However, their predictions of critical thicknesses are very pessimistic compared to the rest of the literature [Glas 2015]. Aifantis *et al.* also studied the critical shell thickness on a mismatched core although with a radius fixed to 40 nm, which allows

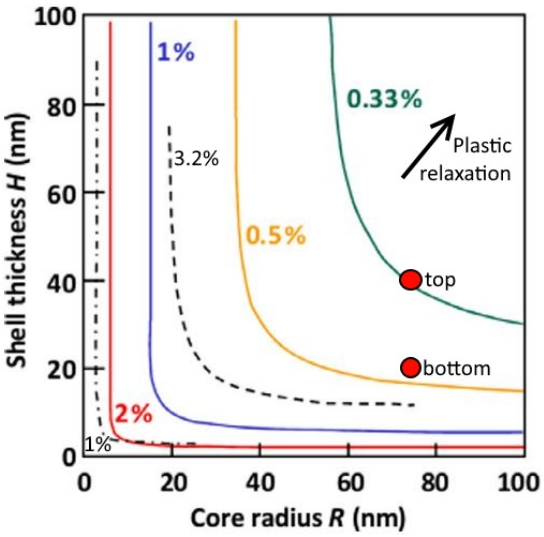

Figure 4.10: *Calculations of the critical shell thickness on a mismatched core for different radiuses. Each curve corresponds to a different relative misfit between core and shell, and separates the domain of elastic relaxation at the bottom-left from the domain of plastic relaxation (misfit dislocations) at the top-right. Full lines: calculations for GaN/AlGaN core-shell by [Raychaudhuri and Yu 2006], dashed lines: The same for WZ InAs/InP by [Salehzadeh et al. 2013] and dash-dotted lines: WZ InAs/AlInAs by [Haapamaki et al. 2012]. The red dots are the data points for sample B276. Adapted from [Glas 2015].*

15 nm-thick shells for 0.4 % mismatch [Aifantis et al. 2007].

Based on the trend among these calculations, plastic relaxation could be avoided if uniformly thick (15 nm) shells can be grown and if their composition can be maintained within ±5 % of $Ga_{51}In_{49}P$ (misfit < 0.4 %). This thickness is sufficient to ensure that, for the solar cell structure, the shell still acts as a selective contact. As for such control over the composition, it could be attained in a future work, by optimization on NW arrays with robust, high vertical yield to ensure reproducibility.

While it is true that dislocations in the shell or at the core-shell interface can act as electronic defect centers, this detrimental effect is tempered by the fact that the GaInP shell is not the absorber in the device architecture, and recombination in this part is not critical, except at the interface with GaAs, where photo-generated carriers might not have been separated yet.

The composition of GaInP shells was investigated by STEM-EDX and shows important variations between the tip segment and the sidewalls at different heights, and the In and Ga incorporation seem greatly affected by the presence of crystal defects. Inhomogeneous shading of the incident fluxes by neighboring NWs may also lead to a vertical gradient and inhomogeneities of the Ga content. The GaInP shells are usually richer in Ga than anticipated which can lead to the presence of dislocations, as expected from theoretical models from the literature.

4.1.3 Conclusion

Section: Growth of NW shells

After axial VLS growth and droplet consumption, core-shell structures can be readily fabricated by changing the growth conditions to grow a shell in VS mode. Due to the geometry of the molecular beams in the chamber, the estimates of fluxes and thicknesses at the NW sidewalls must be corrected. GaAs shells show an improved morphology at higher growth temperature (from 475 °C to 580 °C) with the additional benefit of the suppression of parasitic material deposition on the mask.

Wide-bandgap alloy shells are needed to passivate the GaAs NWs and fabricate selective contacts. Among the available III-V alloys, GaInP is promising due to its good passivating properties and the absence of Al. GaAs/GaInP core-shell NWs were investigated by STEM and EDX, and the GaInP is Ga-rich compared to the aimed composition. Important variations of the Ga content were evidenced, depending on the In/Ga flux ratio employed, the presence of crystal defects, and the effect of shading by neighboring NWs. In particular the tip GaInP shell segment formed on top of the NW is faulted and exhibits large composition variations.

Significant core-shell misfit induced by the uncontrolled GaInP composition is responsible for the presence of dislocations in the shells, which is consistent with theoretical works. However, according to the same references, a fairly realistic control over the GaInP atomic composition (limited to ±5 % variations) should place the system in the elastic domain and avoid the formation of the dislocations.

4.2 Doping control in GaAs nanowires

Achieving controlled and reproducible doping is essential for the fabrication of core-shell p-i-n devices. Due to their low dimensions, NWs have higher requirements on doping levels. Indeed, for doping levels below $10^{18}\,\mathrm{cm}^{-3}$, the surface of p- and n-GaAs is typically depleted of carriers over a few tens of nm (see Figure 2.5, page 45), as well as the bulk near the p-n junction (see Figure 2.4b, page 44). This is precisely the order of magnitude of typical NW shell thicknesses, which may therefore become completely depleted of carriers. Moreover, high doping levels are generally necessary to fabricate good ohmic contacts, as introduced in subsection 2.1.5 (page 44). It is thus necessary to study and to understand the doping processes during NW growth, and to evaluate the attainable doping range.

Here, luminescence is used to evaluate the carrier concentrations in GaAs NWs. Ternary alloys such as GaInP or AlGaAs are of prime importance for photovoltaic devices since their bandgap can be tuned with their composition, allowing for wide-bandgap absorbers optimized for tandem-on-Si, or passivating shells. However, to avoid possible interplay of the effects of the composition and of the doping on the spectral lineshape, I choose here to focus on determining carrier concentrations in GaAs, and eventually extrapolate the findings to ternary materials such as $GaAs_{1-x}P_x$, close in composition to GaAs for $x \approx 0.2$.

As the doping was studied alongside the yield optimization, some of the NWs characterized here do not come from perfectly homogeneous arrays (but rather from 10 % to 80 % yield). The general trends and estimations should still be significant, but sophisticated effects relative to the local NW environment (shadowing, diffusion, re-evaporation), might lead to different quantitative results compared to perfectly homogeneous NW arrays

4.2.1 Nanowire doping measurement with cathodoluminescence

4.2.1.1 Relevance of CL compared to alternative techniques

Due to their small size, it is complicated to evaluate the dopant concentration in NWs as compared to planar thin-films. A number of techniques have been employed to evaluate the dopant and carrier concentrations and their spatial distribution in single NWs or NW ensemble. A comprehensive overview of techniques used before 2011 can be found in ref [Wallentin and Borgström 2011]. Here, I present the advantages and limitations of the most important ones, and put them in perspective with our technique based on CL spectroscopy.

Electrical contact measurements. Individual NWs can be reported on an external substrate and contacts defined by EBL along their axis, which allows to estimate the conductivity along the axis ([Gutsche et al. 2009]; [Dufouleur et al. 2010]). Optimized metal stacks need to be used along with a post-annealing to ensure good contact, though using a 4-point measurement helps to limit the negative impact of non-ohmic contacts. Under specific assumptions regarding the surface depletion in the NW, and assuming a charge carrier mobility, the doping concentration can be estimated ([Gutsche et al. 2009]; [Casadei et al. 2013]). But this technique is more adequate to retrieve qualitative information about the spatial distribution of dopants along the NW axis [Rizzo Piton et al. 2019].

Hall effect measurement can also be realized on single NWs by deposition of localized contacts on the NW sidewalls ([Blömers et al. 2012]; [Storm et al. 2012]). Precise charge carrier concentrations can be obtained but the sample preparation is even more sophisticated and requires very precise EBL alignment.

Raman spectroscopy. Low-temperature resonant Raman spectra can exhibit Local Vibrational Mode (LVM) peaks due to Si occupying either Ga or As sites in the GaAs lattice. In strongly compensated n-type or even p-type GaAs:Si, the Si_{As} ($399\,\mathrm{cm}^{-1}$) and Si_{As}–Si_{As}

($393\,\mathrm{cm}^{-1}$) peaks are visible, whereas only the $\mathrm{Si_{Ga}}$ ($384\,\mathrm{cm}^{-1}$) is expected in uncompensated n-GaAs:Si ([Hilse et al. 2010]; [Dimakis et al. 2012]), which permits to retrieve qualitative information on the compensation level in GaAs:Si NWs.

With increasing p-carrier concentration, the GaAs LO phonon mode is found to decrease and broaden in forward Raman scattering, due to phonon-plasmon coupling. The plasma frequency can be estimated from the fit of the room-temperature Raman spectrum, and a carrier concentration value can be accessed ([Ketterer et al. 2012]; [Goktas et al. 2018]; [Rizzo Piton et al. 2019]). In any case, the spatial resolution is limited by the exciting light beam spot size, typically 1 µm wide.

Mass spectrometric methods. Atom Probe Tomography (APT) allows to reconstruct the 3D distribution of dopant atoms with excellent resolution (typically 1 nm), by evaporating the NW constituents with a pulsed laser. However, there is no information about the dopants activation, which can be a limitation in the case of an amphoteric dopant such as Si. It was used to evaluate Be-doping concentrations in GaAs NWs in the range of $10^{18}\,\mathrm{cm}^{-3}$ [Zhang et al. 2018] and can reveal spatial segregation of dopants inside the NW radial structure [Connell et al. 2013]. However, this technique is sophisticated and relatively slow, in particular each characterized NW needs to be mounted and sharpened into thin (<100 nm) tips, which represents extensive sample preparation with focused ion beam (FIB).

Secondary Ion Mass spectroscopy (SIMS) also allows to retrieve quantitative values of the atomic concentration but with lower spatial resolution than APT. Large numbers of standing NWs are analyzed simultaneously as the etching beam is about 60 µm wide, and the NWs need to be planarized with a filling polymer to prevent any etching of the substrate. With the good depth resolution (<100 nm), information about the dopant concentration profile along the NW axis is retrieved [Chia and Lapierre 2013]. However, it was later shown that dedicated reference NW ensembles have to be used to calibrate the measurement instead of standard thin-films, due to the NW array geometry and the influence of the polymer [Chia et al. 2015].

Electron holography. Off-axis electron holography in a TEM is a technique where an object electronic wave that passes through the sample interferes with a reference wave that passes through vacuum. From the interference pattern (known as electron hologram), an amplitude and phase image of the specimen can be reconstructed. The phase is related to the crystal potential, or mean inner potential. The built-in potential of a p-n junction can be determined from the phase contrast.

It has emerged as a powerful technique to investigate dopant inhomogeneities in NWs. It was first applied to Si NWs [Den Hertog et al. 2009] and only recently to GaAs NWs [Darbandi et al. 2016]. Electron holography on NW hexagonal sections gives insight on dopant inhomogeneities [Dastjerdi et al. 2017], and p-n junction activation [Boulanger et al. 2016], although quantitative doping level determination is complicated due to the effects of surface depletion, or of damage induced during sample preparation (FIB cut) [Goktas et al. 2018].

PL and micro-PL. Photo-luminescence (PL) can be performed at room- or low-temperature on NW ensembles, similar to thin-films, to retrieve information about the carrier concentration from the spectrum lineshape or from the luminescence decay [Arab et al. 2016]. Such large-area measurements may be hindered by the contribution from parasitic material growth on the mask during NW shell growth, and the inhomogeneities of the NW ensemble which can contribute to broaden the spectrum. For this reason, micro-PL is more commonly used for NW characterization, which makes use of a localized excitation with a focused laser beam to excite single NWs ([Wang et al. 2015]; [Goktas et al. 2018]).

The PL lineshape of semiconducting material can be analyzed in term of peak position and broadening, due to changes to the absorption near the bandgap, and variable Fermi-level po-

sitions. In highly doped material, enhanced overlap of impurities wavefunctions results in the broadening of their energy levels into impurity bands, which can eventually merge with the valence or conduction band and lower the effective bandgap ('bandgap narrowing'). Exponential tails under the bandgap (Urbach tail) result from fluctuations of the potential or the local strain, induced by the disordered ionized dopants. They also contribute to smear the band edges and lower the effective bandgap. In p-type GaAs, the peak energy broadens and redshifts as a consequence. Conversely, in n-type GaAs the peak blueshifts with increasing electron concentration above the degenerative threshold of about $4 \times 10^{17}\,\mathrm{cm}^{-3}$, due to conduction band filling by electrons, the effective density of states being relatively low in this material, $5 \times 10^{17}\,\mathrm{cm}^{-3}$. This so-called Burstein-Moss effect counteracts and overcomes the redshift of the energy peak due to bandgap narrowing.

Cathodoluminescence spectroscopy. Cathodoluminescence (CL) also allows to study luminescence spectra (see Section 2.3, page 64). The principles for the analysis of carrier concentrations from CL spectroscopy are similar to that of PL spectroscopy, as presented above.

Compared to the techniques previously presented, CL presents several key characteristics:

- The main advantage compared to most techniques mentioned above is the high spatial resolution of the tool. With an electron spot focused within 10 nm, the resolution is mainly limited by the interaction volume (from 10 nm to 100 nm depending on the acceleration voltage), and by the diffusion length of charge carriers. It allows to retrieve details about dopant homogeneity in NWs.
- In contrast with methods based on electrical contacts, or mass spectrometry, there is no need for sample fabrication, individual NWs can be simply reported on an external substrate.
- It is a contact-less method, allowing to probe the NW properties without being hindered by contact or surface issues, and with a relatively high throughput. Spectra can be acquired either at room- or low-temperature (typically 10–20 K).
- Charge carrier concentrations are estimated, but not atomic dopant concentration. While this is very relevant for optoelectronic devices, as it directly gives information on the electrical properties, it does not permit to directly measure the quantity of impurity atoms incorporated in the material.

CL is an adequate tool for NW characterization, but its specific use for doping level estimation in III-V NWs is relatively new [Chen et al. 2017]. Our team at C2N has demonstrated a rigorous method for the quantitative assessment of p-type and n-type carrier density in GaAs thin-films using CL in ref [Chen et al. 2020b], and applied it to GaAs NWs in ref [Chen et al. 2020a], based on the PhD thesis work of Hung-Ling Chen [Chen 2018].

A variety of techniques have been employed in the literature to characterize doping in single NWs or NW ensembles, for example through optical, electrical or mass spectrometric means. Determination by CL spectroscopy is advantageous since, unlike other techniques, it combines a high spatial resolution, quantitative estimation of carrier concentrations, and a simplicity of sample preparation associated with fast contact-less analysis.

4.2.1.2 Fit of luminescence spectra with a generalized Planck law

The fit of GaAs luminescence spectra with the generalized Planck law is explained by Chen *et al.* in refs ([Chen et al. 2017]; [Chen et al. 2020b]), based on the derivation of the law in [Wurfel 1982]. Here the key results are summarized to apply this technique to doping measurement in NWs in the next subsections.

The generalized Planck law is the expression of the luminescence spectrum $\phi(\hbar\omega)$ (in units of photons $\mathrm{m}^{-2}\mathrm{eV}^{-1}$) of a semiconductor under steady-state excitation:

$$\phi(\hbar\omega) = \frac{A(\hbar\omega)}{4\pi^2\hbar^3c^2}\frac{(\hbar\omega)^2}{\exp\left(\frac{\hbar\omega-(\varepsilon_{Fc}-\varepsilon_{Fv})}{k_BT}\right)-1}, \tag{4.2}$$

where $\hbar\omega$ is the photon energy, $A(\hbar\omega)$ the absorptivity, and ε_{Fc} and ε_{Fv} the quasi-Fermi levels of electrons and holes, respectively.

If the photon energy is several k_BT larger than the separation of the quasi-Fermi levels, the -1 term in the denominator can be neglected. In this condition, the spectral irradiance of a black-body is $\phi_{\mathrm{bb}} \approx \frac{(\hbar\omega)^2}{4\pi^2\hbar^3c^2}\exp\left(\frac{-\hbar\omega}{k_BT}\right)$, and Equation 4.2 can be simplified to:

$$\phi(\hbar\omega) = A(\hbar\omega)\phi_{\mathrm{bb}}(\hbar\omega)\exp\left(\frac{\varepsilon_{Fc}-\varepsilon_{Fv}}{k_BT}\right) \tag{4.3}$$

The absorptivity in a homogeneous slab of thickness d is:

$$A(\hbar\omega) = (1-R)\left[1-\exp\left(-\alpha(\hbar\omega)\,d\right)\right] \tag{4.4}$$

R is the reflectivity on the front surface, which should have minor impact on the luminescence lineshape as compared to the absorption drop near the bandgap.
$\alpha(\hbar\omega)$ is the absorption coefficient of the material. In GaAs, it can be expressed as:

$$\alpha(\hbar\omega) = \frac{1}{2\gamma}\int_{E_g}^{\infty} \underbrace{14800\sqrt{\frac{\mathcal{E}-E_g}{1.6-E_g}}}_{\text{ideal semiconductor}} \times \underbrace{\exp\left(-\frac{|\hbar\omega-\mathcal{E}|}{\gamma}\right)}_{\text{Urbach tail}} d\mathcal{E} \times \underbrace{(f_v-f_c)\,(\hbar\omega)}_{\text{Joint probability of occupation}} \tag{4.5}$$

In the above expression, the absorption coefficient for an ideal pure semiconductor is modeled by a parabolic band with realistic values for GaAs. It is convoluted with an Urbach tail which is a low-energy exponential decay representing sub-bandgap absorption. The joint probability of occupation is here to take into account the probability of finding available states in the conduction and valence band that match the energy $\hbar\omega$, which is lowered when many carriers occupy the bands, in the case of high doping for example. It is described by the electron and hole Fermi distributions, which depend on the electron and hole quasi-Fermi levels:

$$(f_v-f_c)(\hbar\omega) = \frac{1}{\exp\left(\frac{\varepsilon_h-\varepsilon_{Fv}}{k_BT}\right)+1} - \frac{1}{\exp\left(\frac{\varepsilon_e-\varepsilon_{Fc}}{k_BT}\right)+1} \tag{4.6}$$

In Equation 4.6, the excess kinetic energy $\hbar\omega - E_g$ is transferred in part to the electron and in part to the hole, according to w, the weighing parameter of the hole effective mass ($0.50m_0$) relative to the electron effective mass ($0.063m_0$), which is $\frac{m_h}{m_h+m_e} = 0.89$ for GaAs:

$$\varepsilon_e - \varepsilon_{Fc} = w(\hbar\omega - E_g) \tag{4.7}$$

$$\varepsilon_h - \varepsilon_{Fv} = (1-w)(\hbar\omega - E_g) \tag{4.8}$$

The lineshape of the luminescence spectrum of GaAs can be fitted to a generalized Planck law with 5 parameters: E_g, the Urbach tail parameter γ, the temperature T, ε_{Fc} and ε_{Fv}.

4.2.1.3 Determination of carrier concentrations in p-GaAs thin-films by CL

To fit the spectrum lineshape of p-type doped GaAs luminescence spectra, 3 parameters are fixed:

- The temperature is set to 300 K
- Since GaAs is usually not degenerate for p-doping up to the $10^{19}\,cm^{-3}$ range, both quasi-Fermi levels are set to a value within the bandgap, several k_BT away from the band edges, so that they do not contribute to the spectrum lineshape through Equation 4.6.

Thus, only γ and E_g are fitted.

Figure 4.11a shows the CL spectra of 6 GaAs:Be thin-films whose doping levels were previously determined by Hall measurement. One can see a red-shift of the peak energy as well as an enlargement with increasing doping level, which indicates that the dopant impurities merge with the valence band, resulting in an effective bandgap narrowing (BGN). The generalized Planck law is fitted to the spectra and the position of E_g is indicated. The effect of BGN is confirmed as the position of E_g shifts significantly with the doping level. The bandgap narrowing is simply $BGN = E_{g0} - E_g$, where $E_{g0} = 1.424\,eV$ is the bandgap of undoped GaAs.

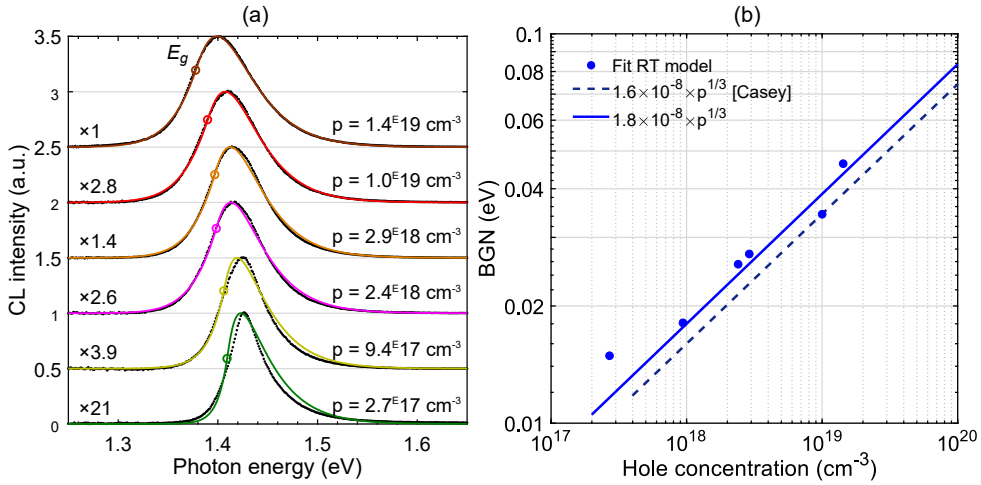

Figure 4.11: *CL spectra of p-GaAs:Be thin films measured at RT (black dots) and the fitted generalized Planck's law (colored lines). The CL normalization factors are indicated. Open circles superimposed on the CL spectra mark the bandgaps determined from the fits. (b) BGN as a function of hole concentration p. Blue dots are bandgaps obtained with a parabolic absorption model combined with Urbach tails (RT model), the blue dashed curve is the empirical relation from Casey and Stern [Casey and Stern 1976] (Equation 4.10), and the blue solid curve is the fit of the data (Equation 4.9). Adapted from [Chen et al. 2020b].*

From Figure 4.11b, the BGN can be fitted with a power law of the doping level:

$$BGN(RT) = 1.8 \times 10^{8} \times p^{1/3} \tag{4.9}$$

This power law dependence is similar to the one determined by Casey and Stern[Casey and Stern 1976], who determined the bandgap by fitting the absorption measurements for three p-GaAs thin films with hole concentrations from $1.2 \times 10^{18}\,cm^{-3}$ to $1.6 \times 10^{19}\,cm^{-3}$, and found the following relationship:

$$BGN(RT) = 1.6 \times 10^{8} \times p^{1/3} \tag{4.10}$$

A wide range of p-type doping levels ($2.7 \times 10^{17}\,cm^{-3}$ to $1.4 \times 10^{19}\,cm^{-3}$) can be reliably estimated in GaAs:Be thin-film samples, using a power-law relationship with the BGN, extracted from the fit of room-temperature CL spectra with the generalized Planck law.

4.2.1.4 Determination of carrier concentrations in n-GaAs thin-films by CL

Fit with the generalized Planck law. The lineshape of n-type doped GaAs luminescence spectra is fitted as previously with E_g and γ, but with ε_{Fc} as an additional fitting parameter to account for the conduction band filling with electrons, which modifies the lineshape through Equation 4.6.

Figure 4.12b shows the CL spectra for 6 GaAs:Si thin-films whose doping levels were previously determined by Hall measurement. For higher doping levels in the $10^{18}\,\mathrm{cm}^{-3}$ range, a blueshift and a broadening of the peak are observed, as expected from the Burstein-Moss effect: electrons fill the conduction band which shifts the Fermi level inside the conduction band, which in turns shifts the absorption edge to higher energies (Figure 4.12a). Such effect is more common in n-type GaAs owing to the relatively small effective density of states in the GaAs conduction band ($N_c = 4.2 \times 10^{17}\,\mathrm{cm}^{-3}$) ([Burstein 1954]; [Moss 1954]). The curves are fitted with the generalized Planck law, and circles and squares on each CL spectrum indicate the bandgaps and electron Fermi levels extracted from the fits, respectively. For the two samples with lowest doping ($n < 5 \times 10^{17}\,\mathrm{cm}^{-3}$), accurate electron Fermi levels cannot be easily extracted from the luminescence analysis. For the highly doped sample ($n = 1.4 \times 10^{19}\,\mathrm{cm}^{-3}$), luminescence from deep levels is deconvoluted with a Gaussian term. The electron Fermi levels extracted from the

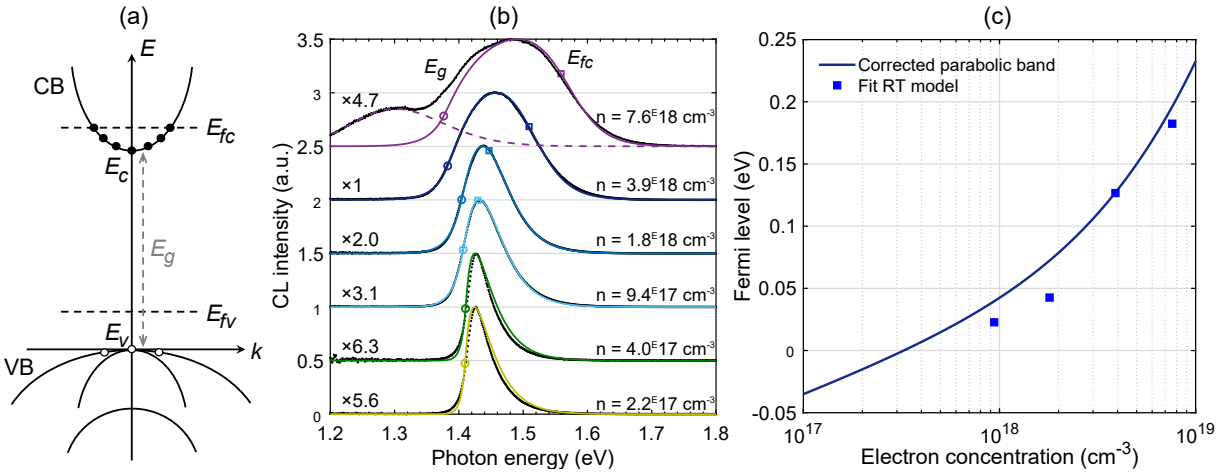

Figure 4.12: *(a) Schematic band diagram of a degenerate n-type III-V semiconductor. Under excitation, excess carriers are characterized by two separate quasi-Fermi levels. (b) CL spectra of n-GaAs:Si thin films measured at RT (black dots) and the fitted generalized Planck law (colored lines). The CL normalization factors are indicated. Circles and squares mark the fitted bandgaps and electron Fermi levels, respectively. (c) Electron Fermi level obtained from the fit of CL spectra (circles) and theoretical curves calculated by assuming a parabolic conduction band (dashed line) and non-parabolicity correction (solid line). Adapted from [Chen et al. 2020b].*

fit of the 4 samples with higher doping are reported in Figure 4.12c against the electron concentration. The blue curve represents a theoretical relation between the electron concentration and the Fermi energy in GaAs, corrected for the non-parabolicity of the band ([Chen et al. 2020b]; [Blakemore 1982]). The Fermi levels of highly doped samples ($n > 3 \times 10^{18}\,\mathrm{cm}^{-3}$) are in good agreement with the model, but they are lower than expected for lower electron concentrations.

N-type doping levels above $3 \times 10^{18}\,\mathrm{cm}^{-3}$ in GaAs:Si can be accurately predicted from the electron quasi-Fermi level extracted from the fit of room-temperature CL spectra with the generalized Planck law. However, the quasi-Fermi level cannot be reliably extracted to evaluate lower electron concentrations, for which another technique has to be used.

Empirical doping determination from the low-temperature FWHM. CL spectra of the same n-type GaAs:Si thin-films were acquired at low temperature (20 K, Figure 4.13a). Similarly to room-temperature measurements, the spectra broaden and the peak energy shifts to higher energies with increasing electron concentrations.

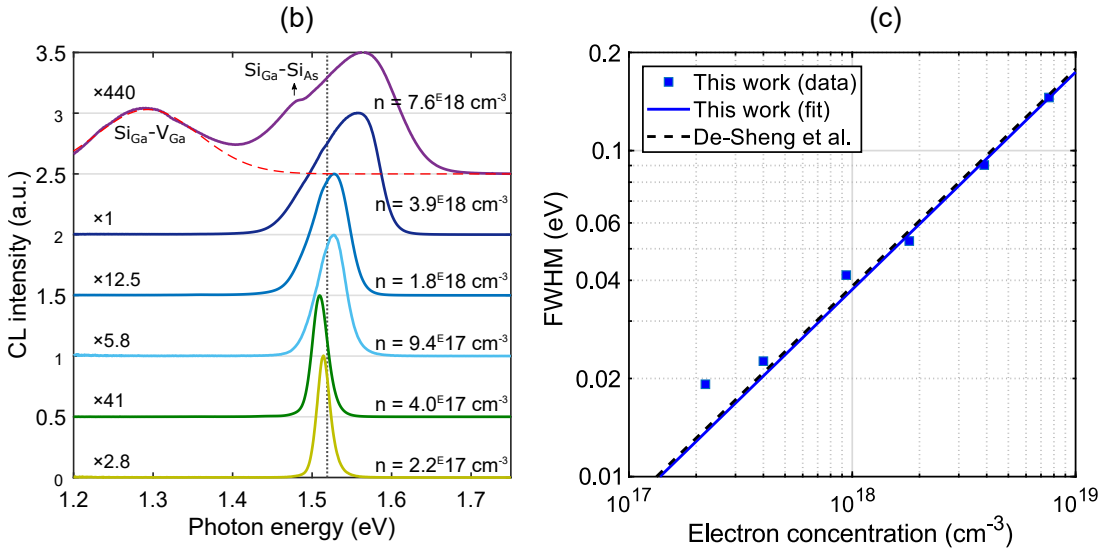

Figure 4.13: *CL spectra of n-GaAs:Si thin-films measured at low temperature (20 K). The CL normalization factors are indicated. The vertical dashed line marks the bandgap of undoped GaAs at 20 K (1.519 eV). Adapted from [Chen et al. 2020b].*

The electron concentration n can be related to the full width at half maximum (FWHM) of luminescence spectra measured at LT when thermal broadening is practically suppressed. De-Sheng et al. first established, from low-temperature PL spectra of n-GaAs:Te, a 2/3 power function of the FWHM with n [De-Sheng et al. 1982]. In Figure 4.13b, experimental FWHM values are fitted with:

$$FWHM(\text{eV}) = 3.75 \times 10^{-14} \times n^{2/3} \tag{4.11}$$

This is very close to the relation of De-Sheng *et al.* which is also indicated in Figure 4.13b with a dashed line.

An empirical relation between LT FWHM and the electron concentration n can be used to determine the electron concentration in a wide range (from 4×10^{17} cm^{-3} to 1×10^{19} cm^{-3}), which complements the doping estimation from the fit of room-temperature CL spectra.

4.2.1.5 CL probing of individual NWs

Experimental details. An advantage of NW growth in ordered arrays is the homogeneity of the ensemble, which should limit any NW-to-NW variation. For this reason, the CL maps were always acquired on single NWs, and at least 3 NWs were studied to rule out the possibility of studying only one extraordinary NW. In order to probe the luminescence properties along the axis of a NW, the CL maps were acquired on NWs lying on their side. A small (5 mm × 5 mm) p-Si(100) wafer piece, previously deoxidized in HF 1%, is gently pressed on a pattern of interest and displaced with tweezers. This is sufficient to transfer some NWs from the pattern to the Si slab surface, where they lie on one sidewall.

The typical electron beam acceleration voltage is 6 kV while the current ranges from 0.3 nA to 0.7 nA. In these conditions, the maximum excess carrier density generated by the electron

beam in GaAs thin-films was estimated to be below $8 \times 10^{15}\,\mathrm{cm}^{-3}$ [Chen et al. 2020b], which corresponds to a low-injection regime since doping concentrations above $10^{17}\,\mathrm{cm}^{-3}$ are studied here. The luminescence spectrum lineshape should therefore not be affected by the injected current.

Estimate of the probed NW shell volume in the typical operating conditions. It is important to ensure that only the region of interest is probed when performing CL, especially when studying doped shells, which are systematically grown on intrinsic cores. Indeed, depending on the interaction volume of the incident electrons in the NW, carriers may be generated in the depleted layer near the surface (especially for n-type GaAs NWs where the depletion can be several tens of nm thick [Chia and Lapierre 2012]), or in the core where carrier concentrations are low but not negligible compared to the shell due to free electron diffusion.

I consider here an infinitely long NW representative of NWs studied in the next subsections, with an intrinsic core and a 90 nm-thick shell doped to $n = 4 \times 10^{18}\,\mathrm{cm}^{-3}$ (Figure 4.14a). Taking into account the electron depletion near the surface and their diffusion to the core, the electron distribution was calculated, using the software ATLAS by Silvaco Group Inc.[1]), as represented in Figure 4.14b. To simulate the ≈ 15 nm thick surface depletion, a Gaussian distribution of deep acceptor electronic defects was implemented at the NW periphery, with a defect density of $10^{13}\,\mathrm{cm}^{-2}\mathrm{eV}^{-1}$ centered 0.7 eV below the conduction band, in agreement with surface defect models for GaAs ([Spicer et al. 1979]; [Aspnes 1983]). It is clear that electrons diffuse from the doped shell into the intrinsic core, which is thus extrinsically doped by free carriers to $n > 10^{17}\,\mathrm{cm}^{-3}$, as seen in orange color in Figure 4.14b. Luminescence from the core would then yield wrong information about doping.

(a) *Nominal electron distribution.*

(b) *Electron distribution at equilibrium & expected e-beam interaction volume.*

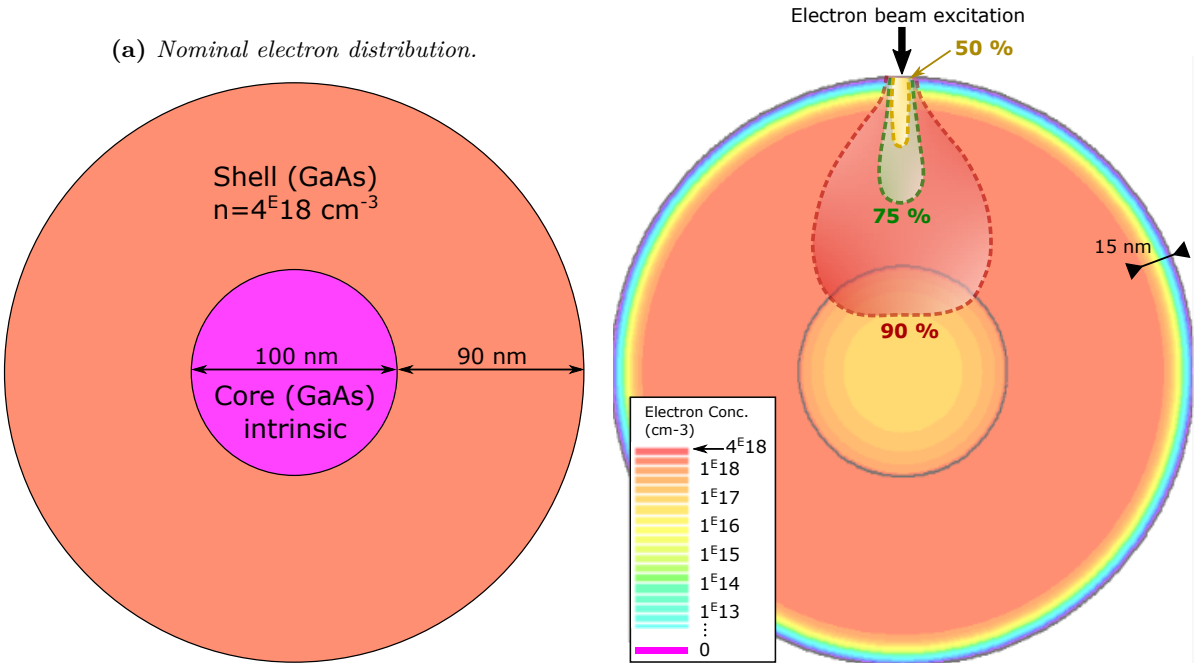

Figure 4.14: *(a) Doping distribution in an infinitely long NW with an intrinsic core (100 nm wide) and an n-doped shell ($N_D = 4 \times 10^{18}\,\mathrm{cm}^{-3}$, 90 nm-thick). (b) Electron distribution in the NW, considering surface defects (deep acceptors) with a Gaussian energy distribution centered 0.7 eV below the conduction band, and a peak defect density of $10^{13}\,\mathrm{cm}^{-2}\mathrm{eV}^{-1}$ (integrated density $8 \times 10^{12}\,\mathrm{cm}^{-2}$). Calculated using the software ATLAS. The electron beam interaction volume is superimposed for scale comparison.*

[1] https://www.silvaco.com/products/tcad/device_simulation/atlas/atlas.html

To get more insight on whether we are indeed probing the doping concentration in the shell, I evaluated the interaction volume in the typical working conditions: e-beam acceleration voltage of 6 kV and impinging current from 0.3 nA to 0.7 nA (see subsection 2.3.2, page 64). In Figure 4.14b, I superimposed the volumes where most electron-hole pairs are generated, and the simulated electron distribution in the NW. A significant proportion of the carriers are generated sufficiently deep not to be affected by surface depletion (mostly in the green and red areas, about 50 % of the dissipated energy), while they are not generated inside the core either. In addition, owing to the charge accumulation, an internal field exists in the core and at the depleted surface, which tends to separate electrons and holes generated there, resulting in a reduced chance of radiative recombination.

Consequently, the n-doped shell should be the main source of luminescence, and the CL spectra yield information about the carrier concentration in the shell.

4.2.1.6 Determination of carrier concentrations in NWs by CL

CL maps of GaAs NWs. Figure 4.15 shows the example of a NW with a GaAs:Si shell grown around a GaAs core, studied by CL at room-temperature (297 K) and low-temperature (20 K). The map of the integrated CL intensity allows to identify zones with high densities of defects and non-radiative recombination, whereas the maps of the peak position of the FWHM give insight into the crystal structure or the doping homogeneity in the NW. In particular, three segments are distinguishable from these maps at low-temperature, which correspond to the main ZB axial segment (A), the WZ segment crystallized during catalyst consumption (B), and the tip segment formed during shell growth (C). This specific structure was already analyzed by TEM on a NW with an identical core growth procedure (Figure 3.33, in Chapter 3, on page 103) and the segment lengths identified from the CL at low temperature are in very good agreement with the ones measured from the crystal structure. The integrated CL intensity reaches a maximum inside the pure ZB part, and is at least an order of magnitude lower close to the WZ segment. This can be related to the high density of crystal defects formed during droplet consumption, which may act as non-radiative recombination centers.

The analysis of the WZ crystallization segment is not relevant here since pure ZB phase is desired for core-shell devices, and I showed in the previous chapter that it was possible to inhibit its formation. For this reason, the CL spectra analyzed in this section were all extracted from the middle of the main ZB axial segment, within the first 1/3 of the total NW length from the foot (black dashed square area in the LT integrated CL map of Figure 4.15).

N-doped NWs. Once the spectrum is extracted from a zone of interest of a n-type Si-doped NWs, either of the two techniques described in subsubsection 4.2.1.4 are employed to determine the carrier concentration

The room-temperature fit of the CL spectrum with the generalized Planck law yields reliable doping level values from the electron quasi-Fermi level for concentrations above $3 \times 10^{18}\,\mathrm{cm}^{-3}$. However, in the rest of this section, doping levels mostly remain in the $10^{17}\,\mathrm{cm}^{-3}$ range. Consequently, the empirical relationship relating the electron concentration with the FWHM of CL spectra acquired at low-temperature is preferably used. In Figure 4.16, an average spectrum was extracted from the low-temperature CL map of Figure 4.15. The FWHM can be extracted from the CL spectrum (Figure 4.16a), and the electron concentration is accessed through the power law relationship with the FWHM (Figure 4.16b).

P-doped NWs. Similarly to n-type NWs, the CL map of a p-type NW is shown in Figure 4.17. Here the core is doped and a passivating AlGaAs:Be shell is then grown to prevent surface depletion is these thin NWs. The pure ZB part and the segment crystallized during droplet consumption are again well identified from the peak position and FWHM maps. An average

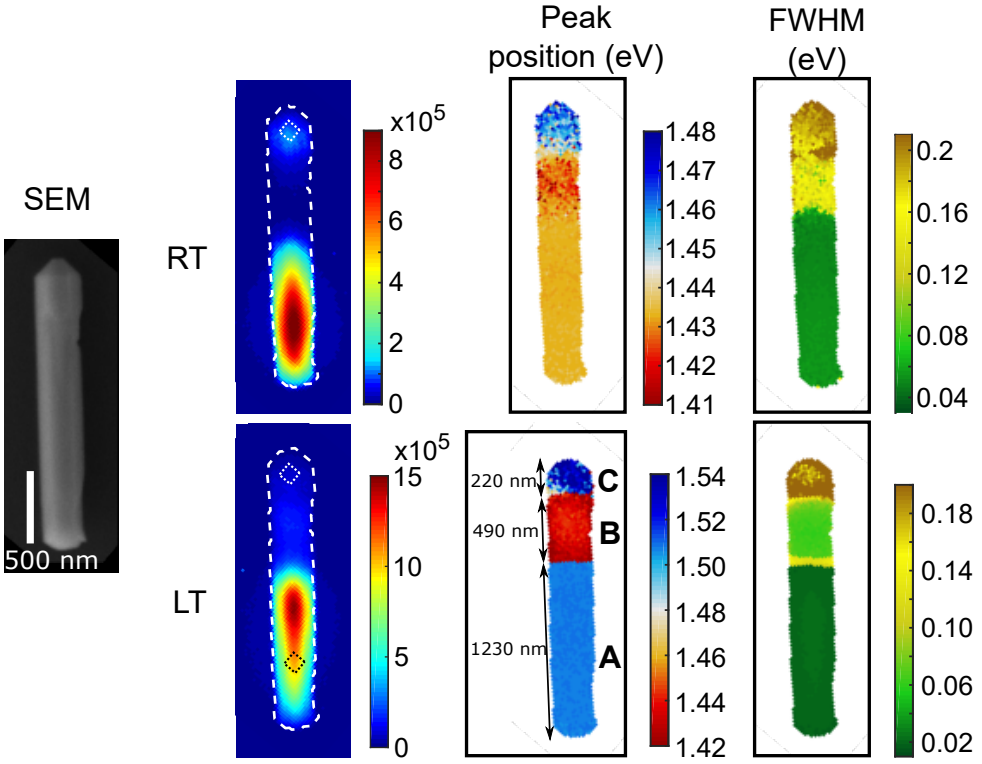

Figure 4.15: *Room- and low-temperature CL maps of a GaAs NW with a Si-doped shell grown around an intrinsic core. From left to right, the SEM micrograph, the CL maps of the integrated CL intensity, of the peak position, and of the FWHM, all aligned with the NW vertical growth direction. The main ZB segment created during axial VLS growth is denoted A, the WZ segment crystallized during droplet consumption, B, and the tip shell segment, C. Adapted from [Chen et al. 2020a]. [76749]*

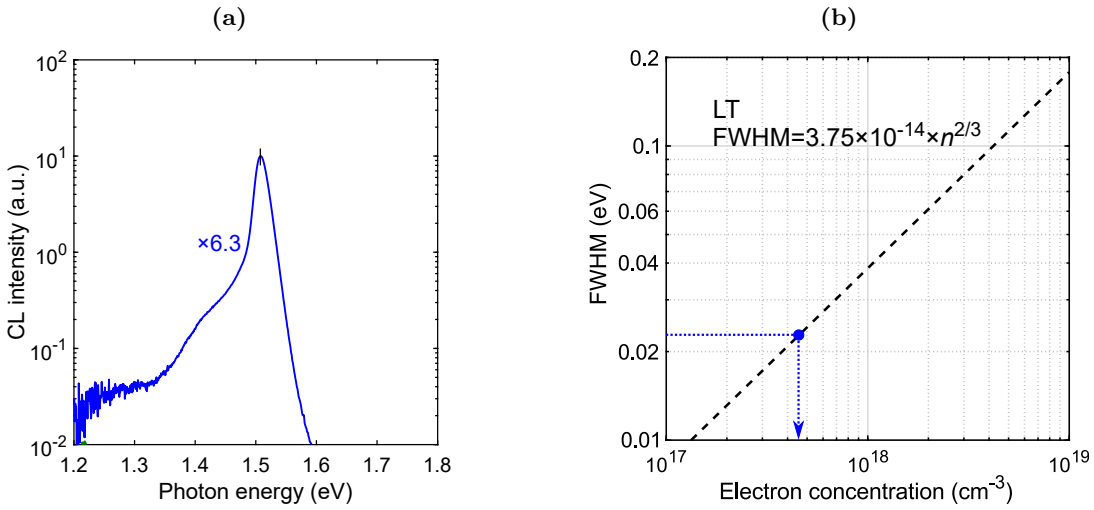

Figure 4.16: *(a) Low-temperature CL spectrum of a Si-doped GaAs NW (b) Empirical relation used to access the electron concentration from LT FWHM of CL spectra (Equation 4.11). Adapted from [Chen et al. 2020a] [76749]*

spectrum is extracted from the pure ZB part of p-type NWs (dashed square), and plotted in Figure 4.18a.

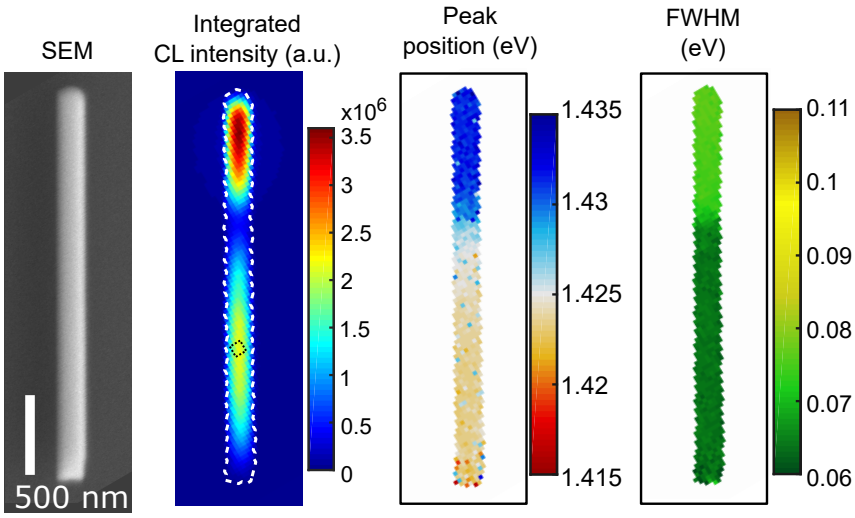

Figure 4.17: *Room-temperature CL map of a GaAs NW with a Be-doped core passivated with an AlGaAs:Be shell. The dashed rectangle indicates the region from where an average luminescence spectrum is extracted. Adapted from [Chen et al. 2020a]. [76847]*

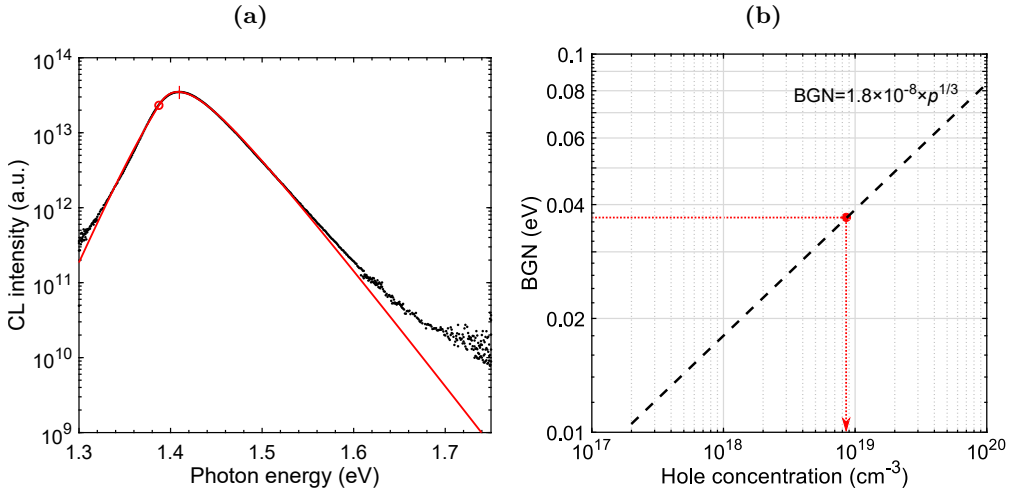

Figure 4.18: *(a) Room-temperature CL spectrum of a Be-doped NW, along with the fit to the generalized Planck law. The position of the bandgap (dot) and of the Fermi-level (vertical dash) are indicated. (b) Hole concentration deduced from the BGN, using the empirical relationship of Equation 4.9. Adapted from [Chen et al. 2020a]. [76741]*

The hole concentration is then estimated by fitting the room-temperature CL spectrum (black dots in Figure 4.18a) with the generalized Planck law (colored curve in Figure 4.18a), allowing to determine the bandgap energy level. A hole concentration is determined from the BGN value (Figure 4.18b), using the empirical relation previously determined on planar thin-film samples (Equation 4.9).

The methods developed with GaAs thin-films for the doping estimation from CL measurement can be applied to GaAs NWs. CL mappings allow the identification of the NW crystal structure, and CL spectra are extracted from the main ZB axial segment. P-type doping can be evaluating from the BGN extracted from the fit of room-temperature CL. N-type doping are better evaluated using the relation with the FWHM of low-temperature CL spectra.

4.2.2 Control of GaAs nanowires p-type doping from CL measurements

In this section I use the method just presented to determine hole concentrations in different NWs, in order to study the incorporation of Be as a p-type dopant in GaAs NWs, both in the core and the shell.

4.2.2.1 State-of-the-art

Here I focus on MBE-grown self-catalyzed NWs, with p-type doping either in the shell or in the core.

Doping during core growth. Beryllium (Be) is often present in MBE systems due to its good incorporation and activation up to $10^{19}\,\mathrm{cm}^{-3}$ in III-V thin-films under a wide range of growth conditions. It was thus employed by many groups for the self-catalyzed growth of GaAs NWs and was shown to behave as a p-type dopant in the NW core and shell [Czaban et al. 2009]. In particular, while Be was shown to occupy interstitial sites when extremely high fluxes are provided, it mostly substitutes Ga in the lattice up to the 10^{18} range, suggesting a very good dopant activation in this range [Hilse et al. 2010].

Starting in 2013, the incorporation mechanism of Be during VLS growth has been debated. Casadei *et al.* compared electrical resistivity measurements between GaAs:Be NWs and found enhanced conductivity in NWs with a doped shell grown under the same Be flux as the core, compared to simple core NWs [Casadei et al. 2013]. They deduce that Be incorporates through the GaAs NW sidewalls, and that incorporation via VLS is negligible. However, as the VLS axial growth rate is much faster than the VS shell growth rate, dopants are expected to be much more concentrated in the shell. Moreover, their model relies on the diffusion of Be from the NW sidewall surfaces into the core, using a Be diffusion coefficient extrapolated from measurements between 700 °C and 900 °C[Masu et al. 1983], which are several orders of magnitude higher than similar literature as discussed in the next paragraph.

In 2017, using off-axis electron holography, Dastjerdi *et al.* unraveled a 3-fold symmetry of hole concentration in the NWs cross-section, perpendicular to the growth direction [Dastjerdi et al. 2017]. Measurements along the NW axis suggest incorporation of Be through truncated 112A facets under the droplet during the VLS growth. The presence of truncated facets under the droplet during the growth of ZB NWs was already reported [Jacobsson et al. 2016]. From the hole concentration profile and a Be diffusion model, a diffusion coefficient of $3.8 \times 10^{-16}\,\mathrm{cm}^2\mathrm{s}^{-1}$ at 600 °C is deduced. However, in 2018, using APT, Zhang *et al.* reported homogeneous Be concentration in NW cross-sections of about $10^{19}\,\mathrm{cm}^{-3}$ [Zhang et al. 2018]. They attested the absence of Be segregation at or near the sidewalls, and suggest that the Be accumulates in the droplet and incorporates via VLS.

Very recently, Piton *et al.* reported p-type core doping of GaAs:Be NWs in the $10^{18}\,\mathrm{cm}^{-3}$ range by Raman spectroscopy [Rizzo Piton et al. 2019]. They also measured the resistivity at different locations along the NW growth axis, using electrical contact measurements. Interestingly, they observed that with low Be flux the dopant concentration decreases towards the NW tip, while for high Be flux the gradient is opposite. These results suggest: (a) that the Be dopants

incorporate predominantly via VS growth at the NW sidewalls with low Be flux, since freshly created facets near the tip have received less Be flux, and (b) that the relative contribution of the VLS mechanism becomes more significant when the Be flux is increased, which could be due to increasing accumulation over time of Be inside the droplet, at the VLS growth front.

As there is yet no consensus about the incorporation mechanism, I consider both hypothesis when analyzing the measured hole concentrations.

Diffusion of Be during growth. Due to its small atomic size, Be is prone to diffusion and redistribution inside III-V lattices. In our case, diffusion of Be during VLS axial growth is not a problem since a homogeneous dopant distribution in the core is desired. However, it could be a problem during the subsequent shell growth.

Most studies on the Be diffusion in GaAs were conducted by MBE or LPE, at temperatures close to 800 °C, and a wide range of values are reported for the Be solid diffusion coefficient: $<1 \times 10^{-15}\,\mathrm{cm^2 s^{-1}}$ [Ilegems 1977], $1 \times 10^{-15}\,\mathrm{cm^2 s^{-1}}$ (at 825 °C) [Tejwani et al. 1988], $3.5 \times 10^{-14}\,\mathrm{cm^{-2} s^{-1}}$ [Enquist et al. 1985]. These values are two to three orders of magnitude below $2.5 \times 10^{-12}\,\mathrm{cm^2 s^{-1}}$ at 800 °C [Masu et al. 1983]. Moreover, the diffusion coefficient is found to be extremely dependent on the Be concentration, and only significant above $1 \times 10^{19}\,\mathrm{cm^{-3}}$ [Enquist et al. 1985]. Let us consider a typical diffusion coefficient of $5 \times 10^{-15}\,\mathrm{cm^2 s^{-1}}$ at 800 °C, as a middle point between most literature results. One can extrapolate a Be diffusion coefficient at lower temperature through an Arrhenius law with two parameters:

$$D(T) = D_0 \exp\left(\frac{-E_0}{kT}\right), \tag{4.12}$$

Using the least favorable activation energy among the aforementioned papers, ($E_0 = 1.6\,\mathrm{eV}$ from [Tejwani et al. 1988]), and the maximum temperature at which the NW shells presented here are grown (580 °C), I find $D(580\,^\circ\mathrm{C}) = 5.8 \times 10^{-17}\,\mathrm{cm^2 s^{-1}}$, which is below the value estimated from the Be profile distribution in ref [Dastjerdi et al. 2017]($3.8 \times 10^{-16}\,\mathrm{cm^2 s^{-1}}$), but realistically close.

Considering a shell growth duration $\tau = 1\,\mathrm{h}$, the diffusion length of Be can be determined as $l = \sqrt{D \times \tau}$. It is 4.6 nm at 580 °C and only 0.6 nm at 450 °C, temperature at which most of the n-shells are grown after the p-core. This is small compared to the typical shell thickness of 50 nm which means that Be diffusion from the core into the shell should not be a problem in our conditions. Moreover, a p-i-n design was chosen, which makes it even less likely for Be atoms to reach the n-shell.

Alternative dopants. Other dopants were used during the VLS growth of NWs such as Zn, or even Si which, as an amphoteric dopant, lead to n-type or p-type doping of GaAs depending on whether it replaces Ga or As in the crystal lattice [Wallentin and Borgström 2011]. P-type GaAs:Si was obtained by providing Si during the VLS growth of self-catalyzed NWs ([Colombo et al. 2009]; [Dufouleur et al. 2010]; [Ketterer et al. 2010]). However, an optimized set of growth conditions (temperature, As and Ga fluxes, dopant flux) seems necessary to ensure the desired level of compensation, and the different incorporation mechanisms between core VLS growth and simultaneous shell VS growth may lead to undesirable core-shell structures.

Be has been used successfully to dope self-catalyzed MBE-grown GaAs NWs. However, the Be incorporation mechanisms are still largely debated.

4.2.2.2 Core p-type doping

Sample description. In this study, the Be flux during the core growth is varied between two NW samples, and a Be-doped AlGaAs passivating shell is grown around the core to maximize

CL intensity. A 15 nm-thick shell is expected at the sidewalls, considering only the directly impinging fluxes. The Be cell was kept at the same temperature used for the core, thus leading to high doping in the AlGaAs shell, equivalent to, respectively, $1 \times 10^{19}\,\mathrm{cm}^{-3}$ and $7 \times 10^{19}\,\mathrm{cm}^{-3}$ (planar layer equivalent) in each sample.

The NWs final morphology is shown in Figure 4.19. They are straight with three well-defined $\{1\bar{1}0\}$ facets at the tip. The tapering at the base is attributed to group-III adatoms diffusion during the growth of the AlGaAs shell, as more material is deposited on the mask due to the low incidence angle of the Al cell.

(a) *Lower Be flux. [76847]*

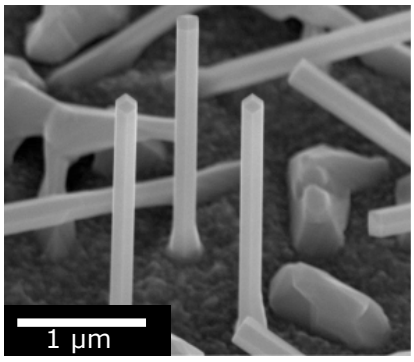

(b) *Higher Be flux. [76741]*

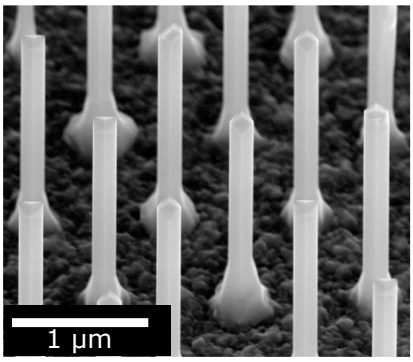

Figure 4.19: *SEM details of GaAs NWs with direct Be doping during axial VLS growth. The droplet was consumed and an AlGaAs shell grown around the NWs. Viewed with a 45° degree tilt.*

Be flux capture section. The Be dopant concentration can be estimated from the planar dopant flux, calibrated on GaAs(100) thin-films, by rescaling the incoming flux to the NW capture cross-section, and dividing by the NW growth rate. The growth rate is the length of the segment created during axial growth, divided by its duration. To account for the extra segment created during droplet consumption, and during shell growth, it is assumed that 2/3 of the total NW length correspond to the segment created during the core growth, in agreement with TEM and CL observations (see Figure 4.17).

As for the effective capture section for the incident Be flux, different surfaces can be considered.

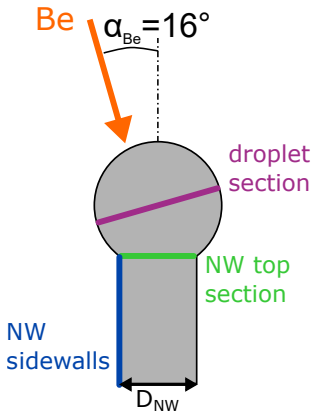

Figure 4.20: *Schematic of the hypothetical sections for the effective capture of the incident Be flux, either the NW top section (in green), the droplet section (in purple), and the sidewall section (blue). The 16° cell incidence angle must be accounted for.*

1. **The NW hexagonal top section.** Here the droplet is completely ignored, so that the

NW growth is thus treated similarly as the growth of a nanopillar with a flat top facet. Considering $\mathcal{F}_{Be}$, the Be flux on planar surfaces as calibrated on GaAs(100) thin-films, and v_{axial}, the experimental axial growth rate deduced from the measured length, the Be concentration in the NW is:

$$[Be] = \frac{\mathcal{F}_{Be}}{v_{\text{axial}}} \tag{4.13}$$

2. **The NW droplet.** Assuming large contact angles so that the droplet is assimilated to an entire sphere, the Be flux must be rescaled with the Be cell incidence angle, as described in Figure 4.20. The Be concentration is then:

$$[Be] = \frac{\mathcal{F}_{Be}}{v_{\text{axial}}} \times \frac{D^2_{droplet}}{\cos(\alpha_{Be}) D^2_{NW}}, \tag{4.14}$$

where α_{Be} is the angle of incidence of the Be cell (see Figure 4.20), D_{NW} is the NWcore diameter and $D_{droplet}$ is the droplet diameter, which may vary during the growth although in this calculation it is set to the typical value of 200 nm.

3. **The NW sidewalls.** There might also be collection, then incorporation via the sidewalls, or diffusion to the droplet and VLS incorporation. In this case, I assume a linear growth rate and integrate the amount of Be atoms captured at the exposed sidewall, diluted into the final core volume:

$$[Be] = \mathcal{F}_{Be} \times \tan(\alpha_{Be}) \times \frac{S \times \tau}{V}, \tag{4.15}$$

where τ is the core growth duration, $V = L \times \pi \frac{D^2}{4}$ is the volume of the NW core, L is the length of the pure ZB core, and S is the section of the NW sidewalls to the incident Be flux. Assuming a constant axial growth rate, $S = \frac{L}{2} \times D_{NW}$.

Table 4.2: *Description of Be-doped (core) GaAs NW samples. NW length is obtained by examining tilted-view SEM images, with a typical variation of ±0.1 µm. The duration of the core VLS growth is indicated. The dopant flux was calibrated using GaAs reference thin films and is given with respect to the substrate normal. Nominal Be concentrations are calculated from the dopant flux and the NW axial growth rate, with a typical relative error within ±10 %. Different sections are considered for the capture of impinging Be flux, corresponding to the colored sections in Figure 4.20. Experimental hole concentrations are obtained from the BGN values from the fit of CL spectra from the pure ZB segment of the NW, with the generalized Planck law.*

	Length	Duration	Be flux	Be conc. (top)	Be conc. (droplet)	Be conc. (sidewall)	Hole conc. (Fit BGN)
	µm	min	$s^{-1}\,cm^{-2}$	cm^{-3}	cm^{-3}	cm^{-3}	cm^{-3}
76847	2.5	20	1.5×10^{11}	1.0×10^{18}	4.4×10^{18}	3.3×10^{18}	1.3×10^{18}
76741	1.8	20	8.8×10^{11}	8.1×10^{18}	3.4×10^{19}	1.9×10^{19}	8.5×10^{18}

Hole concentration measurement. In Table 4.2, the results of hole concentrations measured by CL are presented, and compared to the expected values considering the different incorporation mechanisms.

Doping levels as high as $8.5 \times 10^{18}\,cm^{-3}$ were measured (Table 4.2, second sample), a value that is typically compatible with core-shell NW devices (no core depletion).

Consistency with estimated Be concentrations.

1. **Top section.** The carrier concentrations in the core measured by CL, are in very good agreement with the expected concentration with the dopant flux rescaled by the NW growth rate, *i.e.*, using the NW top section for the Be capture (Table 4.2). The slightly higher measured hole concentrations could originate from inhomogeneous dopant concentration in the NW. Indeed, Be is suspected to incorporate through 3 truncated $\langle 11\bar{2} \rangle$ corners at the top facet [Dastjerdi et al. 2017], which could lead to higher local Be concentrations in the NW.

   However, a carrier concentration level higher than the calculated dopant concentration is still rather surprising and implies that, in addition to the aforementioned phenomenon of local Be concentration, the dopant activation is near 100 %, and that all the Be atoms were incorporated in the GaAs crystal, *i.e.*, there is no Be in the droplet, which seems rather unlikely considering the vertical incidence of the Be molecular flux, right towards the droplet.

2. **Droplet.** On the other hand, the expected concentration using the section of a 200 nm diameter droplet is 3 to 4 times higher than the measured hole concentration. This strong overestimation could be due to the fact that the droplet inflates during the growth, and actually collects less flux at the beginning. More importantly, this overestimation is also compatible with the likely presence of Be in the droplet at the end of the core growth, which was not incorporated in the GaAs core segment. Assuming that the extra amount of Be is still diluted inside the droplet, it corresponds to a Be concentration in liquid Ga of, respectively, 0.02 $\%_{\text{atom.}}$ and 0.11 $\%_{\text{atom.}}$ in both samples. Little is known about the solubility of Be in Ga, but this value is reasonably low compared, for example, with the As concentrations in liquid Ga near supersaturation(1 $\%_{\text{atom.}}$).

3. **Sidewalls.** Regarding the possibility of Be incorporation through the NW sidewalls, the expected Be concentration is about twice the measured carrier concentration. However, if this was the main pathway for the dopant, a carrier concentration gradient should be expected along the NW axis, as the sidewalls at the NW base are exposed to the flux for a longer duration than the freshly grown GaAs at the top. This gradient should even go to zero at the NW tip, as the new segment created below the droplet never received a Be flux. No such gradient is present on the CL maps[2].

   The complete incorporation of Be from the sidewalls is also very unlikely. With realistic Be diffusion coefficient of $3.8 \times 10^{-16}\,\text{cm}^2\text{s}^{-1}$, Dastjerdi *et al.* simulated the diffusion of Be from the sidewalls together with incorporation through truncated facets according to their model, after a duration of 1200 s. They can only explain the profiles measured by electron holography if the incorporation of Be from the sidewall is of the order of 10^{-3} ([Dastjerdi et al. 2017] and supplementary information). Moreover, Be is known to segregate at the surface of heavily doped GaAs thin-films grown by MBE ([Enquist et al. 1985]; [Ivanov et al. 1991]).

   Based on the carrier concentrations measured by CL, and the absence of any gradient of the peak position or FWHM along the NW length, the hypothesis of incorporation by VLS is privileged.

[2] See for example the CL map in Figure 4.17, page 140, where the peak energy remains constant within ±5 meV in the pure ZB segment. Assuming the BGN remains constant within the same error, it leads to a hole concentration within a ±30 % error according to Equation 4.9

P-type doping levels above $8 \times 10^{18}\,\mathrm{cm}^{-3}$ can be reached in the NW core. The measured concentrations are consistent with the hypothesis of a Be flux captured by the droplet and partially incorporated in the NW.

4.2.2.3 Shell p-type doping

Sample description. In this study, the Be dopant flux during shell growth is varied between three different samples.

The GaAs NW core growth differs from the two previous samples:

- No dopant was provided during the growth of the core, which is thus supposedly intrinsic. The Ga flux is also lower than previously ($1.5\,\mathrm{Å\,s}^{-1}$ vs $2\,\mathrm{Å\,s}^{-1}$) but the V/III ratio is kept the same
- The NW growth was initiated by a GaP stem during 40 s. This ensures a higher vertical yield in the NW array but should not impact the cathodoluminescence measurement as it is expected to be shorter than 20 nm.

A Be-doped shell was then grown around the core at 550 °C, with a Ga flux that would lead to a 280 nm-thick planar GaAs layer. Due to the MBE cell angles and the substrate rotation, a 55 nm-thick shell is expected at the sidewalls considering only the contribution of directly impinging Ga flux. Different Be fluxes were used for the 3 different samples. Despite the expected surface depletion, no passivation layer was grown around these NWs. Indeed, contrary to VLS-grown cores, shell thicknesses can be directly controlled through the growth duration, and widths larger than the expected surface-depletion of p-GaAs layers (typically 20 nm at $p = 1 \times 10^{18}\,\mathrm{cm}^{-3}$, see Figure 2.5, page 45) can be attained.

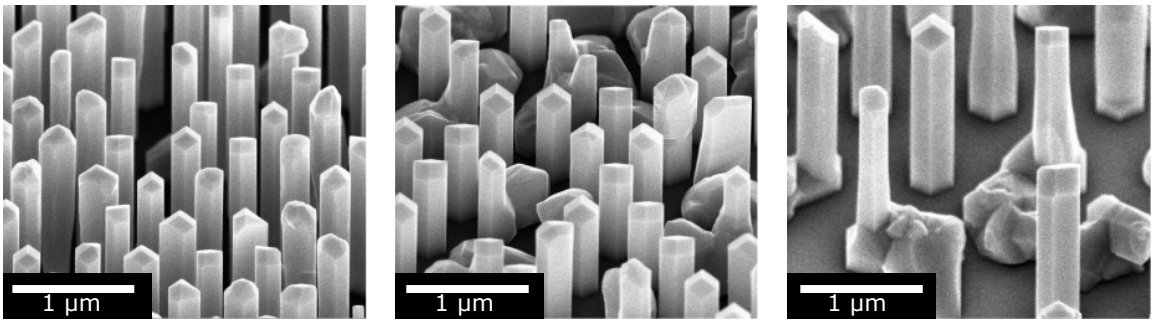

(a) *Lower Be flux. [76720]* **(b)** *Intermediate Be flux. [76718]* **(c)** *Higher Be flux. [76723]*

Figure 4.21: *SEM details of GaAs NWs with an intrinsic core and a Be-doped shell. An increasing Be flux is employed, as reported in Table 4.3*

.

Consistently with the trend identified on GaAs:Si shells grown at different temperatures (see Figure 4.4 on page 119), the GaAs:Be shells grown at 550 °C exhibit smooth and well-defined {110} facets (Figure 4.21). Although there was some parasitic deposition on the mask for Si-doped shells grown at 540 °C (Figure 4.4b), there is no parasitic deposition for these Be-doped shells grown at 550 °C, where the bare mask surface is visible in between the NWs (Figure 4.21b). This suggests that Si atoms could play a role in promoting GaAs nucleation at the mask surface.

Expected Be concentration. The measured shell thickness values (up to 116 nm, see Table 4.3) are much higher than the expected shell thickness (55 nm), which likely results from the diffusion of Ga atoms from the mask to the NWs sidewalls. The fact that thicker NWs are observed where the NW density is lower (from left to right in Figure 4.21) reinforces this

hypothesis. In these conditions, the NW cross-sections are highly irregular due to uneven shell growth.

To evaluate the shell growth rate, the diameter is measured from the SEM images as the distance between two opposing {110} facets. This length is close to the diameter of a disk with identical surface area as the NW hexagonal cross-section, which is conveniently used for the shell volume calculations. The shell thickness is obtained by subtracting the diameter of the core (100 nm as typically observed on axial growths) to the total diameter, and a shell growth rate can be determined after division by the shell growth duration.

Three estimates of the doping concentration are given:

1. **Planar equivalent.** The expected doping concentration in planar GaAs thin-films exposed to the same fluxes, as previously calibrated on (100) thin-films.
2. **Flux on vertical sidewalls.** The nominal doping concentration in the NW sidewalls, rescaling the fluxes to account for the different incidence angles of the Ga cell (32°) and the Be cell (16°).
3. **Flux on sidewalls, empirical growth rate.** The concentration calculated from the Be flux on the facet and rescaled by the shell growth rate experimentally determined by examining SEM images. Due to the large variations of NW dimensions, this method presents a relative standard deviation of about 25 %.

Table 4.3: *Description of Be-doped (shell) GaAs NW samples. The NW shell thickness is obtained by averaging measurements on tilted-view SEM images, but as the dimensions are inhomogeneous on this sample, the standard deviation of the thickness can be up to* ±21 nm. *The dopant flux was calibrated using GaAs reference thin films and is given with respect to the substrate normal. Nominal Be concentrations are either the expected doping in planar GaAs thin-films, or the expected concentration by rescaling the Ga and Be flux directions to the NW sidewalls, or the concentration calculated from the dopant flux and the NW radial growth rate, with a typical error within* ±25 %, *mostly due to the NW diameter variations. Experimental hole concentrations are obtained from the BGN values from the fit of CL spectra from the pure ZB segment of the NW, with the generalized Planck law.*

	Shell thick. (SEM)	Be flux	Be conc. (planar)	Be conc. (vertical sidewalls)	Be conc. (SEM gr. rate)	Hole conc. (Fit BGN)
	µm	$s^{-1}\,cm^{-2}$	cm^{-3}	cm^{-3}	cm^{-3}	cm^{-3}
76720	67	2.1×10^{10}	2.6×10^{18}	1.2×10^{18}	1×10^{18}	3.3×10^{17}
76718	88	1.5×10^{11}	1.9×10^{19}	8.7×10^{18}	5.4×10^{18}	4.6×10^{18}
76723	116	8.8×10^{11}	1.2×10^{20}	5.3×10^{19}	2.5×10^{19}	1.3×10^{19}

Hole concentration measurements. The carrier concentrations in the shell are determined from the fit of the room-temperature CL spectra (Figure 4.22) and reported in Table 4.3. They cover a wide range from $3 \times 10^{17}\,cm^{-3}$ to $1.3 \times 10^{19}\,cm^{-3}$. Being able to reach the $10^{19}\,cm^{-3}$ range is very important for ohmic contact fabrication if a design with an external p-type shell is adopted. The measured carrier concentrations in the 2 samples with higher doping are, respectively, 14× and 39× higher than in the first sample, whereas the Be flux values were, respectively, 7× and 45×. The dopant activation level between the first and last sample seems to be the same, which suggest that no compensation took place. However, the moderately doped sample does not follow the trend and exhibits a lower hole concentration.

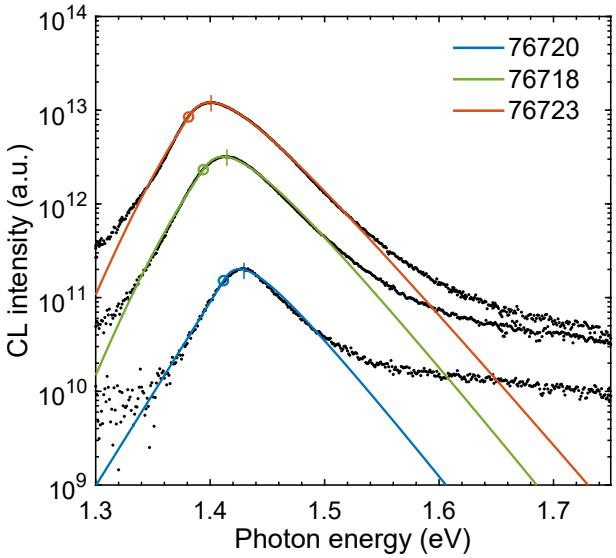

Figure 4.22: *Room-temperature CL spectra extracted from the main core segment of NWs with Be-doped cores, grown with different Be fluxes. Adapted from [Chen et al. 2020a].*

Consistency with estimated Be concentrations.

1. **Planar equivalent.** The measured Be concentrations are almost an order lower than what would be obtained in planar thin-films. This suggests that the actual dopant flux at the NW sidewalls is important to consider, and that a significant contribution of Be diffusing from the mask into the NW is unlikely.
2. **Flux on vertical sidewalls.** The calculated dopant concentration rescaled with the fluxes at the sidewalls is closer to the measured values, but still higher by a factor 2 to 4.
3. **Flux on sidewalls, empirical growth rate.** Finally, using the empirical shell growth rate estimated from SEM images, the calculated doping level is slightly closer to the measurement. This method is thus more trusted, also since it relates to the actual NW dimensions.

For the sample with the lowest doping (76720), the carrier concentration is lower by a factor 3 but its determination from the BGN is less accurate in this range (see Figure 4.18b) and at doping levels near $1 \times 10^{18}\,\mathrm{cm}^{-3}$, the surface depletion can reach 20 nm, which is a non-negligible fraction of the shell which could lead to underestimated carrier concentration measurement.

The sample with intermediate doping (76718) has an estimated dopant concentration rather consistent with the measured carrier concentration.

The sample with the highest doping level (76723) shows an estimated Be concentration twice as large as the measured hole concentration, possibly due to surface segregation of Be, as it is the case for heavily doped GaAs thin films grown by MBE ([Enquist et al. 1985]; [Ivanov et al. 1991]). Little is known about the incorporation on {110} facets, which might be different than the typical (100).

Apart from these hypotheses, the discrepancy between estimation and measurement among all three samples could originate from the significant spread over the NW diameters in our growth conditions, as seen on the SEM image(Figure 4.21c). The diameter then determines the calculated growth rate and estimated Be concentration. If the probed NWs were among the ones with the thickest shell, the dopants would be more diluted and the measurement would yield a lower value.

Overall, the reasonable agreement with the expected values and the high level attained are consistent with what is known of planar GaAs(100) doping with Be: Be incorporates effectively

in the lattice in a wide range of conditions, and doping levels up to $5 \times 10^{19}\,\mathrm{cm}^{-3}$ are attainable without degradation of the material quality [Ilegems 1977].

P-type doping levels as high as $1.3 \times 10^{19}\,\mathrm{cm}^{-3}$ were attained in NW shells, without apparent saturation. Lower measured carrier concentrations than the estimated doping levels may originate from the shell thickness variations, or from an imperfect dopant incorporation and activation in these conditions.

4.2.3 Control of GaAs nanowires n-type doping from CL measurements

In this subsection I use the method presented at the beginning of this section to determine electron concentrations in different NWs, in order to study the incorporation of Si as an n-type dopant in GaAs NW.

4.2.3.1 State-of-the-art

Core-doping with Si. Si is a widely used n-type dopant in MBE thin-film growth, which does not suffer from surface segregation unlike Sn or Te, and is less prone to n-type compensation than Ge [Orton and Foxon 2015] as doping levels up to $6 \times 10^{18}\,\mathrm{cm}^{-3}$ can be attained without any compensation ([Chai et al. 1981]; [Tok et al. 1998]), and in the $10^{19}\,\mathrm{cm}^{-3}$ range with compensation [Köhler et al. 1993]. Its high vapor pressure also prevents re-evaporation from the layer and ensures a unity sticking coefficient. As mentioned previously, its amphoteric nature may lead to p- or n-type behavior. The density of As vacancies at GaAs surfaces decreases with the V/III ratio and increases with the temperature (higher As desorption rate), which promotes Si incorporation at the As sites. The formation of [$\mathrm{Si_{Ga}}$-X] deep acceptor complex at high Si concentration and temperature is also reported, where X is in general attributed to a Ga vacancy $\mathrm{V_{Ga}}$ ([Maguire et al. 1987]; [Domke et al. 1996]; [Hurle 1999]).

Under the droplet, the Ga-rich conditions promote incorporation as acceptor, whereas the (111)B facets are usually more prone to incorporation as donor in planar MBE growth [Pavesi et al. 1993]. Self-catalyzed n- or p-type ([Ketterer et al. 2010]; [Colombo et al. 2009]; [Dufouleur et al. 2010]) GaAs:Si NWs can thus be obtained, but always with a strong level of compensation [Hilse et al. 2010].

Shell doping with Si. The NW shell growth by VS is more comparable to planar thin-film growth. The sidewall facets are {110}-oriented, and Si generally incorporates as donor at these facets ([Pavesi et al. 1992]; [Holland and Stanley 1996]), although with more stringent restrictions on the growth conditions than for (100). Typically, uncompensated n-GaAs:Si(110) layers can be grown at 480 °C with an As/Ga flux ratio of 30 [Tok et al. 1998].

In 2012, Dimakis *et al.* reported the growth of n-GaAs:Si shells without apparent compensation as observed by Raman spectroscopy. To avoid compensation, the temperature must be <490 °C, and the nominal Si concentration should not exceed $1 \times 10^{19}\,\mathrm{cm}^{-3}$ [Dimakis et al. 2012], in agreement with the literature on GaAs thin-films.

Alternative dopants. Several groups have employed Te for n-type doping of GaAs NWs. Te has a high vapor pressure but it is still well-incorporated in GaAs thin-films up to $10^{19}\,\mathrm{cm}^{-3}$, however it is prone to surface segregation [Orton and Foxon 2015]. Lapierre's group have reported partial dopant activation in Te-doped n-GaAs NWs by combining different characterization tools, with carrier concentrations limited to $10^{18}\,\mathrm{cm}^{-3}$, an order of magnitude below the aimed level. In ref [Orrù et al. 2016], higher core doping levels up to $10^{20}\,\mathrm{cm}^{-3}$ were determined using a different method combining transport measurement and Kelvin probe force microscopy, but under different growth conditions. Recent results suggest uncompensated n-GaAs NWs

doped with Te during axial growth, with concentrations of $4 \times 10^{18}\,\mathrm{cm}^{-3}$ measured by Raman spectroscopy and APT close to the top [Hakkarainen et al. 2019]. However, the nominal dopant concentration was $2 \times 10^{19}\,\mathrm{cm}^{-3}$. Important doping inhomogeneities in GaAs:Te NWs were revealed by transport measurement and off-axis electron holography, and attributed to lateral growth of intrinsic GaAs during axial VLS growth, followed by Te diffusion from the core to this unintentional shell [Hakkarainen et al. 2019]. At high concentration, Te could segregate at the surface and lower the Ga adatom diffusion length, which results in enhanced VS radial growth during axial VLS growth ([Czaban et al. 2009]; [Suomalainen et al. 2015]).

N-type doping of GaAs NWs is notably difficult. Even Si, a well known n-type dopant for 2D GaAs(100), is strongly amphoteric in NWs: it is generally p-type when incorporated by VLS and suffers from high degree of compensation. For this reason, I focus on n-type doping of GaAs NW shells, in conditions closer to the ones of planar (110) thin-films.

4.2.3.2 Shell n-type doping: growth at high temperature

I showed in Section 4.1 (page 118) that the morphology of GaAs:Si shells is improved when grown at 585 °C, compared to growth at lower temperatures. Here, I investigate whether the Si dopants are effectively incorporated as donors in shells grown at this temperature.

Sample description. Three samples were grown with an intrinsic GaAs core, and a GaAs:Si shell grown at 585 °C during 80 min (75 nm-thick shell expected from incident Ga flux). Three different Si fluxes were employed during the growth. Unlike with Be, the incidence angles of the Ga cell (32°) and the Si cell (35°) are rather close (see for example Figure 4.1 on page 117), so that a similar dopant concentration is expected in the NW sidewall shell as in planar GaAs thin-films. Thus, this planar dopant concentration is used as an estimate of the nominal doping level in these shells, as reported in Table 4.4.

Room- and low-temperature CL. The samples were analyzed by CL and spectra were extracted from the pure ZB segment at room- (Figure 4.23a) and low- temperature (Figure 4.23b). It should be noted that for these samples the luminescence was very low, and a current of several tens of nA was used to obtain an exploitable signal, instead of the usual 0.7 nA, which is indicative of a very defective material. Instead of the expected blueshift due to electron band-filling, all three samples exhibit a red-shift of the energy peak relative to the bandgap of GaAs (1.52 eV). Moreover, the red-shift is more significant with higher Si doping, reaching 0.04 eV at a Si concentration corresponding to $1 \times 10^{19}\,\mathrm{cm}^{-3}$ in planar thin-films. The low-temperature CL peak position and FWHM are reported in Table 4.4 but without doping estimation due to this unexpected behavior. The absence of blueshift suggests that the Burstein-Moss effect does not take place in these NWs, which indicates n-doping levels below $4 \times 10^{17}\,\mathrm{cm}^{-3}$. The redshift could be a signature of important bandgap narrowing, similarly to p-type doping with Be.

Analyzing further the low-temperature luminescence (Figure 4.23b), Si impurities incorporated as acceptors are expected to have a transition at 1.484 eV, which is consistent with the peak position of the moderately-doped sample 76697 (1.483 eV), and with a remarkable peak below the main one for the lightly-doped sample (76710). The 1.45 eV main peak of the highly-doped sample 76709 could also correspond to this transition but from a lower electron energy, as with high Si concentration, donor levels result in a sub-bandgap tail reaching 40 meV below the conduction band [Kressel et al. 1968]. A broad emission peak around 1.3 eV (Figure 4.23b) is visible for moderate Si concentration level (76697), and is enhanced for the highly doped sample (76709), where it seems to have merge into a continuum with the main peak. This is typically observed in p-type GaAs:Si grown by LPE [Kressel et al. 1968] and in highly Si-doped GaAs

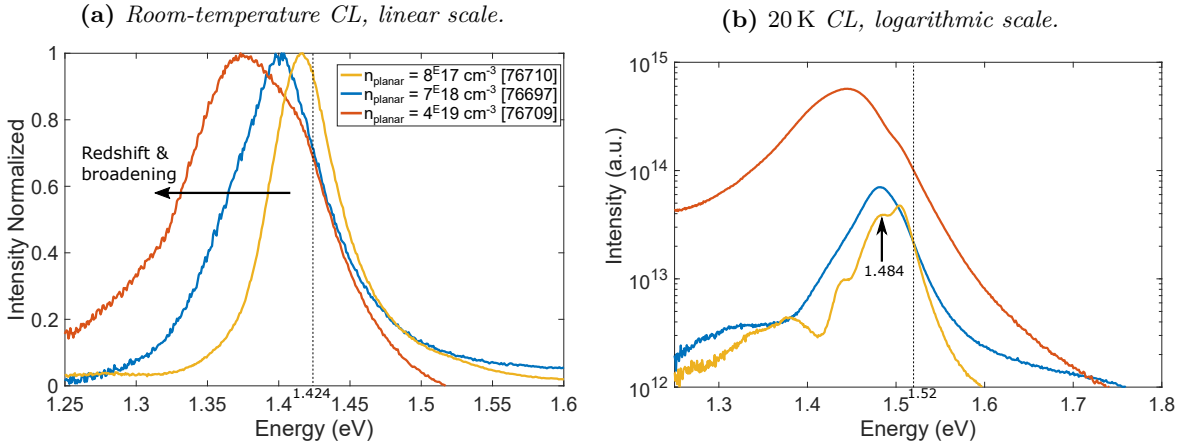

Figure 4.23: *(a) Room- and (b) low-temperature CL spectra of NWs with a Si-doped shell grown at* 585 ℃*, with an increasing Si flux. The nominal doping level corresponding to planar GaAs thin-films grown under the same conditions, is indicated.*

Table 4.4: *Description of Si-doped (shell) GaAs NW sample, grown at* 585 ℃*. Nominal Si concentrations correspond to the doping in planar n-GaAs:Si thin-films grown under the same conditions, calibrated from reference GaAs thin-films. The peak position and FWHM extracted from low-temperature CL are indicated.*

	Substrate T °C	Si conc. (planar) cm^{-3}	Peak energy (LT CL) eV	FWHM (LT CL) eV
76710	585	8.2×10^{17}	1.50	0.06
76697	585	6.5×10^{18}	1.48	0.06
76709	585	3.7×10^{19}	1.45	0.10

after annealing and is attributed to Si_{Ga}-V_{Ga} defects, the combination of a Si atom in a donor site next to a Ga vacancy ([Pavesi et al. 1992]; [Ky and Reinhart 1998]).

While the shell morphology is improved when grown at 580 °C, the CL intensity is low and an unexpected redshifht with increasing Si concentration suggests highly compensated n-type or even p-type doping. The low-temperature CL bears the signature of Si acceptor levels, and of defects commonly found in compensated layers. These growth conditions are thus not adequate for the fabrication of n-type shells.

4.2.3.3 Shell n-type doping: growth at low temperature

The growth temperature is actually expected to play a role on Si compensation, and the electron concentration in GaAs(110) layers was reported to be increased by an order of magnitude when lowering the growth temperature from 520 °C to 440 °C, while maintaining the same Si flux [Tok et al. 1998]. Lowering the temperature reduces the evaporation rate of As adatoms, which effectively increases the V/III ratio and promotes Si incorporation as donor.

Sample description. Core-shell samples were grown in conditions that should promote Si dopant incorporation as donor in the $10^{18}\,cm^{-3}$ range.
The core growth conditions are similar as before. Specifically, for 76749, an intrinsic GaAs core was first grown by VLS, without GaP stem, employing a Ga flux of $2\,Å\,s^{-1}$ during 17 min. A Si-doped GaAs shell is grown with a nominal 75 nm sidewall thickness, considering the directly impinging Ga flux. The temperature was set to 475 °C during shell growth. As before, the shell was not passivated, counting on the sufficiently high thickness to overcome surface depletion.

Another sample (76844) was grown with the shell at even lower temperature (450 °C). The droplet was consumed at high temperature and under low As flux, conditions that limit the extent of the GaAs segment crystallized during droplet consumption. The CL spectra were still acquired in the intense zone in the middle of the pure ZB segment, like for other NWs.

Significant parasitic deposition on the mask can be seen on the SEM images (Figure 4.24), resulting from the low shell growth temperature. The measured shell thickness is 90 nm for 76749 and 80 nm for 76844, which is 20 % and 40 % thicker, respectively, than what was expected from the direct flux at the sidewalls, suggesting that Ga collection from the mask to the sidewalls still takes place at these low temperatures (475 °C and 450 °C), though to a lesser extent than in previous samples at 550–585 °C. The shell thickness is also more homogeneous than on the previous samples, as all facets of a single NW look equally thick. As for samples grown at high temperature, the Si concentration is estimated with the expected concentration in planar films.

Compensation at low growth temperature. The electron concentration in the sidewalls is determined empirically from the CL at low-temperature (Figure 4.25), and is more than an order of magnitude lower than the expected Si concentration in the shell for both samples (Table 4.5). However, in ref. [Tok et al. 1998], doping levels up to $6 \times 10^{18}\,cm^{-3}$ can be attained in GaAs(100) and GaAs(110), if the V/III ratio is maximized.

These elements suggest that NW sidewalls cannot be strictly compared with planar {110} facets for what concerns the incorporation of Si dopants. This could be due to a difference between the local V/III ratio and the V/III flux ratio. Indeed, a NW sidewall facet is vertical and rotating, thus it is not exposed to all 3 fluxes (group V, group III, and Si dopant) all the time, nor simultaneously, during shell growth. In the Riber32 MBE tool, the Ga and As cells are in opposing directions relative to the substrate normal axis, whereas the Si cell is next to the Ga (Figure 4.26a). The exposure of a vertical rotating facet to the different fluxes is schematically described in Figure 4.26b. The typical residence time of As adatoms on a GaAs surface before

(a) 475 ℃ *[76749]* **(b)** 450 ℃, As_4 *[76844]*

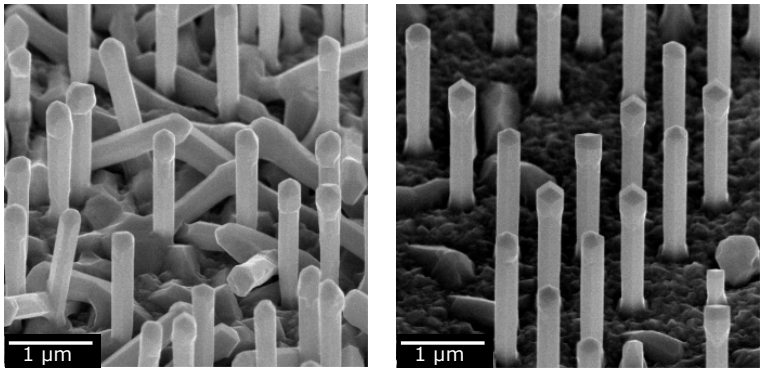

Figure 4.24: *SEM detail of GaAs NWs with an intrinsic core and a Si-doped shell grown at low temperature.*

Table 4.5: *Description of Si-doped (shell) GaAs NW samples. Nominal Si concentrations correspond to the doping expected in planar n-GaAs:Si thin-films grown under the same conditions, calibrated from GaAs(100) reference thin-films. Experimental hole concentrations are obtained from the Electron Fermi level from the fit of CL spectra at the tip segment corresponding to shell growth, with the generalized Planck law. At the pure ZB segment of the NW, the electron concentration is too low and is determined empirically from the FWHM using the relationship in ref [Chen et al. 2020b].*

	Substrate T.	Si flux	Si conc. (planar)	Electron conc. (Fit Fermi level)	Electron conc. (low-T FWHM)
	K	$s^{-1}\,cm^{-2}$	cm^{-3}	cm^{-3}	cm^{-3}
76749 (main)	475	5.5×10^{10}	6.5×10^{18}	–	4.5×10^{17}
76749 (tip)	475	5.5×10^{10}	6.5×10^{18}	5.1×10^{18}	9.2×10^{18}
76844	450	4.3×10^{10}	5.7×10^{18}	–	3.6×10^{17}

(a)

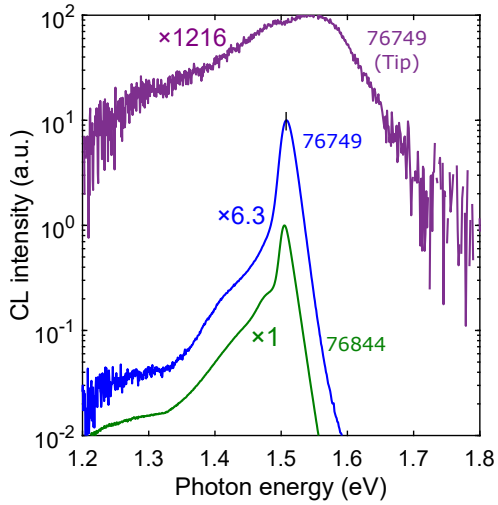

Figure 4.25: *Low-temperature CL spectra extracted from the tip and the pure ZB segment of the NW with a GaAs:Si shell grown at 475 ℃, from the CL maps presented in Figure 4.15 (page 139). The intensity was rescaled with the indicated multiplying factor. [76749]*

re-evaporation is below 10^{-4} s at 300 °C and further decreases with temperature [Foxon et al. 1980]. It is thus much shorter than the period of rotation of the NW (2.5 s). As the NW rotates and the sidewall facet is no longer exposed to As flux, the As-rich surface becomes As-deficient. When the Ga and Si fluxes impinge on the facet, the local V/III ratio is close to zero, which favors Si incorporation as donor.

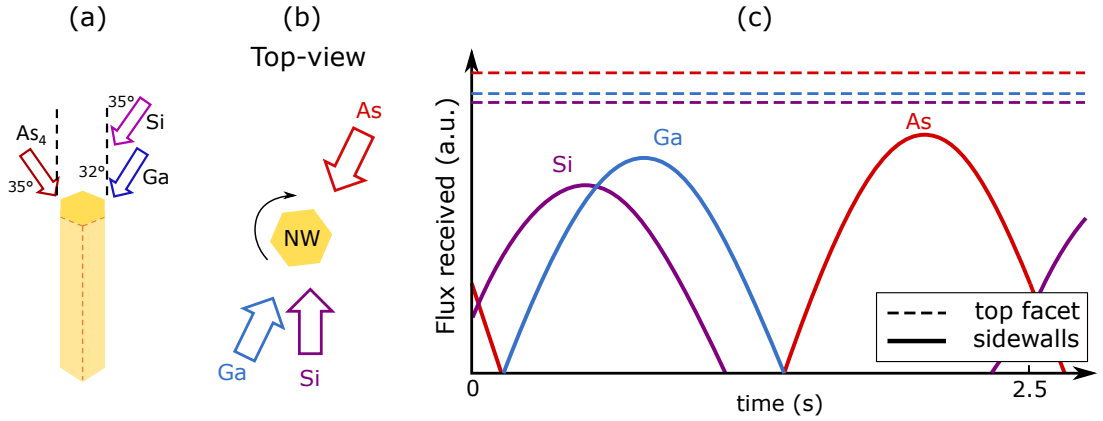

Figure 4.26: *(a) Top-view representation of a vertical NW and the directions of the incoming molecular beams during shell growth, in the Riber32 MBE setup. (b) Schematic of the sequence of incident fluxes on a vertical facet during shell growth, over the course of one substrate rotation.*

Influence of using As_2 instead of As_4. Another sample (not shown) was grown in an identical manner as 76844, but providing As_2 instead of As_4 during shell growth. The measured electron concentration is identical to 76844, within ±10 % (less than the typical NW to NW variation).

It is reported that GaAs(110) layers grown with As_2 instead of As_4 are less compensated ([Sørensen et al. 1995]; [Holland and Stanley 1996]). Similar effects could be expected in NW sidewalls as the Ga adatom diffusion length is lowered under an As_2 flux [Sartel et al. 2010]. Here, however, the carrier concentration is not higher in GaAs:Si shells grown using As_2.

Higher doping concentration in the tip. The CL map of sample 76749 at room- and low-temperature was already presented in Figure 4.15 (page 139). The CL spectrum extracted from the pure ZB segment but also the one from the tip segment formed during shell growth are reported together with the electron concentration determined from the FWHM in Figure 4.25. The tip spectrum, despite an overall lower intensity, presents a remarkable blueshift and broadening. Higher electron concentrations are measured at the tip using either the fit of the room-temperature CL spectrum (9.2×10^{18} cm^{-3}) or the empirical relationship with the low-temperature FWHM (5.1×10^{18} cm^{-3}). This last value may be slightly overestimated due to low-energy luminescence from defects (Figure 4.25a). This measurement is consistent with the Si concentration estimated from the balance of fluxes (7×10^{18} cm^{-3}), suggesting much fewer compensation than at the sidewalls.

In contrast with the sidewalls, a flat top facet (or similarly, a set of {110} facets) receives all fluxes simultaneously independently of the sample rotation (see Figure 4.26). Thus, GaAs growth can occur in similar conditions as for thin-films, with an As_4 overpressure during Si incorporation, conditions that lead to uncompensated n-doped layers [Tok et al. 1998]. Alternatively, since the final morphology of NWs grown at this temperature (475 °C) does not exhibit three well-defined {110} facets at the top (Figure 4.24a), but a rather rough surface suggesting a regime of growth with 3D-nucleation rather than step-edge growth [Orton and Foxon 2015], the growth possibly takes place on other planes than the {110}. Dopant incorporation might be different at these surfaces and less subject to compensation.

Si-doping in the shell sidewalls is limited below $5 \times 10^{17}\,\mathrm{cm}^{-3}$ in our conditions, due to doping compensation on the {110} facets aggravated by the sequential exposure of the NW sidewalls to the fluxes during sample rotation, and independently of the As molecule used. High doping levels are measured at the NW tip segment formed during shell growth, which is consistent with their uninterrupted exposure to fluxes throughout the growth.

4.2.3.4 Shell n-type doping: perspectives to limit compensation

Growth in a different MBE setup. As mentioned earlier, the higher level of compensation in GaAs:Si NW shells, relative to planar thin-films grown under the same conditions, might come from the flux sequence at the sidewall facets, which can lead to Si incorporation in local Ga-rich conditions. In order to investigate this phenomenon, I have grown NWs in another MBE setup (Riber Compact21), where the source configuration is different from the previous Riber32 (as described in the methods, Figure 2.13 on page 52). The sample rotation was inversed between two samples, resulting in different flux sequences as seen from the NW sidewall facet (Figure 4.28b).

The apparent NW morphologies are similar, with a thick NW tip (Figure 4.27). This reverse-tapered (club-like) shape is likely due to low adatom diffusion at this temperature and important shading of the source fluxes in this MBE. Because these patterns only had 500 nm pitch arrays (and not 1000 nm), and because the yield is particularly high, the NWs can be much thinner closer to the foot.

(a) *Rotation 1. [B259]* **(b)** *Rotation 2. [B260]* **(c)** *Delta-doping. [B269]*

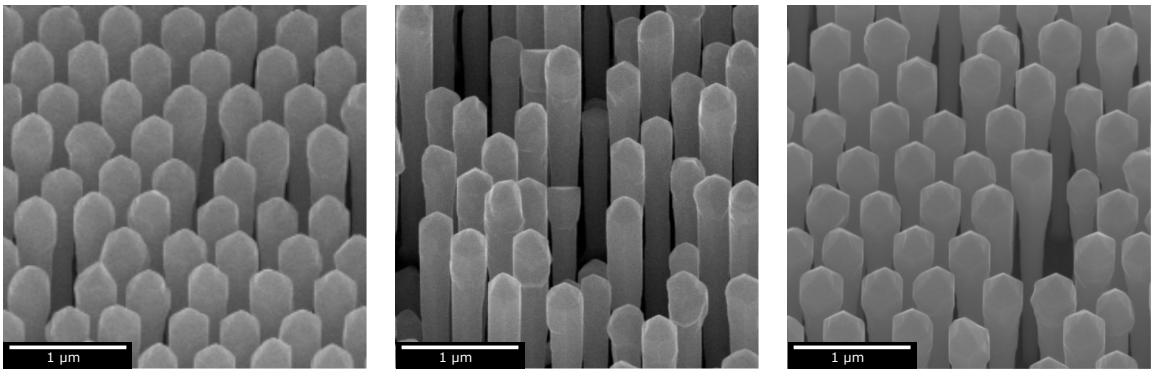

Figure 4.27: *SEM details of GaAs NWs grown in the Compact21 MBE, with an intrinsic core and a Si-doped shell. In (a) and (b), different rotation directions were used during shell growth. In (c), the shell was doped by* delta-doping.

In the second sample, the yield is degraded and the NWs are inhomogeneous in length, which is probably due to the substrate preparation, this particular sample had to be re-cleaved after HF dip and overnight storage, just before introduction into the MBE machine, because it didn't initially fit the substrate holder. Wafer dust contamination and re-oxidation in air might have occurred due to this extra step.

Influence of flux sequence. The new cell orientations relative to the NW sidewall facets are shown in Figure 4.28a. The samples B259 and B260 had a GaAs:Si shell grown in similar conditions, only changing the direction of holder rotation. The low-temperature CL spectra acquired in the pure ZB segment of these samples are shown in Figure 4.29. Table 4.6 summarizes the expected Si concentrations from the balance of fluxes, as well as the measurement of electron concentration by CL using the empirical relationship from the low-temperature FWHM of the CL

spectrum. Due to the presence of a low-energy tail at 1.48 eV in the spectrum of sample B259 and even more in sample B260, a wider uncertainty on the doping estimation is obtained. One can see that no significant improvement has been made on the doping level in these samples, which are still in the $10^{17}\,\mathrm{cm}^{-3}$ range as previous samples. However, the slight blueshift compared to B259, and the disappearance of the low-energy tail in B269 might indicate a decrease of the deep defect level density, and a possible increase of the electron concentration with a slight Burstein-Moss shift. Moreover, while the shell thickness is in general 60 nm-thick, it can be as low as 10–20nm-thick near the base, questioning the depletion of the shell and the fact that the CL indeed probes the shell and not the core.

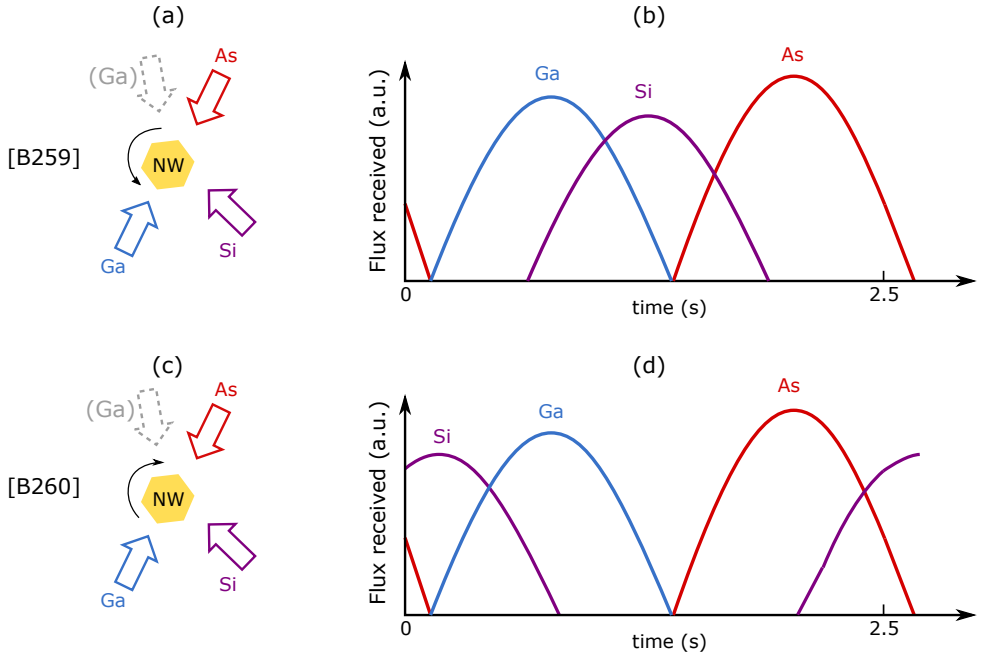

Figure 4.28: *(a,c) Top-view representation of a vertical NW and the directions of the incoming molecular beams during shell growth in the Compact21 MBE setup. (b,d) Schematic of the sequence of incident fluxes on a vertical facet during shell growth, over the course of one substrate rotation. (a,b) and (c,d) represent two different substrate rotation directions.*

Table 4.6: *Description of Si-doped (shell) GaAs NW samples, with similar notation as in Table 4.5. Both rotation directions are called 1 and 2, respectively, and the rotation frequency is* $20\,\mathrm{min}^{-1}$. *The shell thickness is not used for dopant concentration estimation as it is uneven along the NW length due to shading and tip lateral overgrowth during shell growth at low temperature. Instead, as all flux incidence angles are the same, the estimated doping corresponds to the doping of planar GaAs(100) layers grown in identical conditions. The low electron concentrations are determined empirically from the FWHM using the relationship given by Equation 4.11, and the range represents the spread of 3 measured individual NWs.*

Sample	Description	Si flux $\mathrm{s}^{-1}\,\mathrm{cm}^{-2}$	Si conc. (planar) cm^{-3}	Electron conc. (low-T FWHM) cm^{-3}
B259	Rotation 1	5.5×10^{10}	1×10^{19}	4—7 $\times 10^{17}$
B260	Rotation 2	5.5×10^{10}	1×10^{19}	4—9 $\times 10^{17}$
B269	Delta-doping	5.5×10^{10}	1×10^{19}	4—5 $\times 10^{17}$

Let aside these doubts, the doping levels have not significantly improved. it could be that

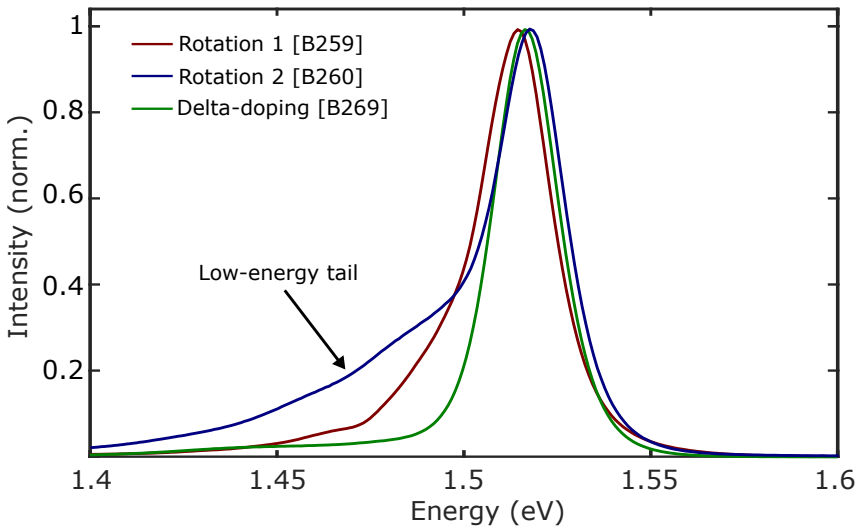

Figure 4.29: *Low-temperature CL spectra extracted from the pure ZB segment of NWs from 3 different samples implementing different Si-doping schemes in the GaAs shell.*

the cell configuration is still not adequate for optimal shell growth doping, as the Ga and As fluxes are also impinging the NW from opposite directions, like in the Riber32 setup. Another Ga source cell exists in the C21 setup which is next to the As cell (dashed arrow in Figure 4.28a) but it was not working when I did my experiments. It would be interesting in future experiments to use it for shell growth, as it would allow for quasi-simultaneous exposure to As and Ga, while ensuring that while a facet receives a Si flux, it is always more exposed to As than Ga.

Delta-doping. Pursuing a similar effect as for the previous samples, *i.e.*, maximizing the local V/III ratio during Si incorporation, another sample was grown with the shell doped using the so-called *delta-doping* or *modulation doping* technique. It consists in confining the dopants inside one or a few atomic planes, and it was initially developed in order to achieve high electron mobilities in MBE-grown GaAs layers, by localizing the dopants in a passivating AlGaAs layer, letting carriers diffuse and extrinsically dope the active GaAs layer [Ploog 1987]. It was used with Si as a n-dopant in multiple works for GaAs/AlGaAs core-shell NWs ([Boland et al. 2015]; [Sladek et al. 2010]; [Morkötter et al. 2015]; [Spirkoska et al. 2011]; [Irber et al. 2017]).

The growth occurs in a sequence where at first, only Ga and As are provided to grow the material, and then As is kept on while the Ga flux is stopped, and Si dopants are provided (see Figure 4.30). This cycle was repeated 120 times, with 8.5 Å of GaAs formed at each cycle (equivalent GaAs(100) growth rate), and a Si concentration of $2.8 \times 10^{11}\,\mathrm{cm}^{-2}$ inside each doped plane. This amounts to the same nominal shell thickness and doping concentration as for the other two samples (see Table 4.6).

This growth scheme did not allow to increase the doping level which is still in the $10^{17}\,\mathrm{cm}^{-3}$ range. The fact that the facet is not subject to a direct As flux throughout the sample rotation implies that the surface may become Ga-rich as soon as the As flux is shaded. Again, this may lead to Si redistribution into the wrong lattice sites, despite the fact that no Ga is provided during this time.

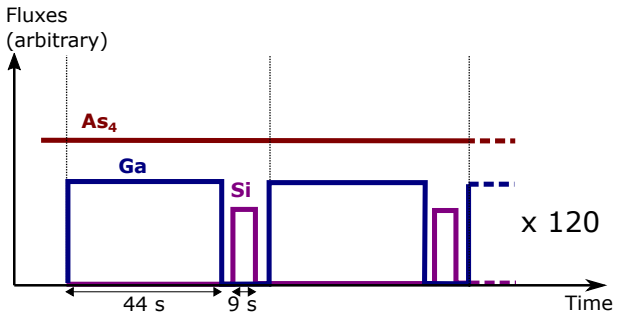

Figure 4.30: *Flux sequence of two cycles of GaAs shell growth with Si delta-doping. The cycle is repeated 120 times to amount for similar GaAs thickness deposited and similar doping levels as for previous samples.*

In order to promote Si incorporation as donor, different sequences of flux impinging the sidewalls during shell growth are tested, by using a new MBE setup and by changing the substrate rotation direction. A similar growth using delta-doping in the shell is also tested with the aim of maximizing the local V/III ratio during Si incorporation. None of these growth schemes showed any n-type doping enhancement, which is probably due to the cell configuration as the As cell is always facing the Ga cell.

4.2.4 Conclusion

Section: Doping control in GaAs NWs

Investigating doping in NWs is challenging and CL spectroscopy appears as a very adequate high-resolution, contactless technique for quantitative carrier concentration measurement.

Our team developed a method based on a fit of the CL spectrum lineshape with a generalized Planck law, to estimate the bandgap narrowing and Fermi-level shift in doped GaAs. Relationships linking these fitted parameters with carrier concentrations were established using calibrated planar GaAs reference thin-films, in agreement with previous literature results. This method yields quantitative values for the electron and hole concentrations, up to $p = 1.4 \times 10^{19}\,\mathrm{cm}^{-3}$ and $n = 3 \times 10^{18}\,\mathrm{cm}^{-3}$, respectively. N-type doping levels up to $10^{19}\,\mathrm{cm}^{-3}$ can also be estimated with an empirical relationship with the FWHM of the luminescence peak at 20 K. CL maps of single NWs allow to identify the crystal structure and to systematically probe the carrier concentration in representative, pure ZB segments.

I have used this method to study the incorporation of dopants in NWs, by growing core- or shell-doped NWs under varying growth conditions and comparing the dopant concentration estimated with a set of assumptions, to the carrier concentrations determined by CL.

Doping with Be appears to be effective even at concentrations close to $10^{19}\,\mathrm{cm}^{-3}$, for both core and shell. An incorporation through the droplet by VLS is inferred from the balance of the fluxes, with possible accumulation of Be in the droplet. As for VS shell growth, carrier concentrations are also in reasonable agreement with Be concentrations estimated from direct fluxes, though systematically below by a factor 1 to 3.

Doping with Si is a more difficult task due to strong compensation effects as it is an amphoteric dopant for III-Vs. Shell doping was investigated, and strong compensation at the {110} sidewalls was systematically observed. At 580 °C, the spectra present signatures of defective, strongly compensated n-GaAs or even p-GaAs. At 450 °C, n-type doping around $5 \times 10^{17}\,\mathrm{cm}^{-3}$ is estimated, an order of magnitude below the target level, without any significant improvement when using As_2 instead of As_4.
Only the NW sidewalls are highly compensated, and doping levels above $5 \times 10^{18}\,\mathrm{cm}^{-3}$ were measured at the NW tip. The sequential exposure of the sidewall facets during shell growth may lead to lower local V/III ratios, which promotes Si incorporation in the wrong lattice sites. I tried new growth schemes to alleviate this effect without success; a different arrangement of the source cells in our MBE setups could be beneficial.

4.3 Alloy composition control in GaAsP nanowires

Compared to the NWs made of binary III-V compounds, ternary NWs offer more potential in term of band gap tuning. In particular, the energy gap of GaAsP NWs can be tuned to 1.7 eV, which provides the best theoretical efficiency for a III-V top cell on silicon tandem [LaPierre 2011a]. To date, only a few teams have reported experimental results with solar devices based on GaAsP NWs ([Holm et al. 2013]; [Tchernycheva et al. 2012]; [Wood et al. 2017]; [Wu et al. 2014]), and a certain number of epitaxial growth difficulties are still to be addressed ([Metaferia et al. 2016]; [Mohseni et al. 2007]; [Zhang et al. 2014b]; [Zhang et al. 2017b]). Among others, the alloy homogeneity of ternary NWs is debated. Composition variations between different NWs grown in the same experiment ([Tchernycheva et al. 2012]; [Zhang et al. 2016]) have been observed, as well as variations within a single NW along the growth axis ([Glas et al. 2010]; [Holm et al. 2013]; [Mohseni and Lapierre 2009]). Compositional changes have also been observed at the corners of the hexagonal cross-section of AlInP ([Sköld et al. 2006]; [Wagner et al. 2010]), AlGaAs ([Mancini et al. 2014]; [Rudolph et al. 2013]), and GaAsP ([Himwas et al. 2017]; [Zhang et al. 2015]; [Himwas et al. 2019]) core-shell NWs. These features have been linked to different diffusion lengths for the species during shell growth.

Beside segregation at the edges during radial growth, it is commonly reported that some unintentional radial growth occurs concurrently to the VLS axial growth. This has been particularly investigated in binary III-V nanowires, for which the concurrent VLS and VS growth results in particular NW shapes ([Colombo et al. 2008]; [Gibson and Lapierre 2013]; [Küpers et al. 2018]; [Munshi et al. 2014]; [Oehler et al. 2018]; [Sartel et al. 2010]). For ternary III-V NWs, the unintentional radial growth creates a core-shell structure, in which the chemical composition of the shell often differs from that of the NW core, as reported for AlGaAs ([Chen et al. 2007]; [Lim et al. 2008]), InGaAs ([Guo et al. 2013]; [Mohseni et al. 2013]), InAsSb [Xu et al. 2012] or GaAsSb [Conesa-Boj et al. 2014] NWs. In GaAsP NWs, alloy variations between the unintentional NW shell and the core were observed independently of the growth method, MOCVD [Sun et al. 2015] or MBE ([Himwas et al. 2017]; [Mohseni et al. 2009]). The presence of such unintentional shell with a different chemical composition compared to the NW core poses problems for the design and fabrication of NW solar cells.

In the following, I study the unintentional shell that forms during the axial growth of self-catalyzed GaAsP NWs by using specific growth designs with well-controlled alloy compositions. The core and shell alloy compositions are accurately determined by TEM using STEM-HAADF imaging and EDX chemical contrast. I also present how compositional differences between core and shell can be controlled and mitigated.

This section's content was published in an article: [Lépinau et al. 2019].

4.3.1 Growth of GaAsP nanowires: parasitic shell during core growth

4.3.1.1 TEM study and evidence of a parasitic shell

To experimentally evidence the formation of the unintentional shell during the growth of ternary GaAsP NWs, a dedicated growth sequence was devised, which alternates three segments of different atomic composition. For this experiment, the Riber32 MBE setup was used, and the substrate temperature was fixed to 600 °C. Figure 4.31a shows this specific growth sequence, which starts with a pure GaP segment (approximately 1 µm long), continues with a $GaAs_{1-x}P_x$ segment with $x \approx 0.4$ (approximately 2 µm long) and finishes with a $GaAs_{1-x}P_x$ segment with $x \approx 0.2$ (approximately 2 µm long). These approximative alloy compositions correspond to experimental atomic flux ratios $\varepsilon_P = \frac{P}{As+P}$ of $\varepsilon_P = 1$, $\varepsilon_P = 0.56$ and $\varepsilon_P = 0.18$, respectively. The actual alloy composition of each NW segment is investigated in detail in the following.

The aspect of the NW array is shown in Figure 4.31f. The overall yield of vertical nanowires is below 50 %. The wires are reverse-tapered from 140 nm in diameter to 180 nm, they are 5 µm

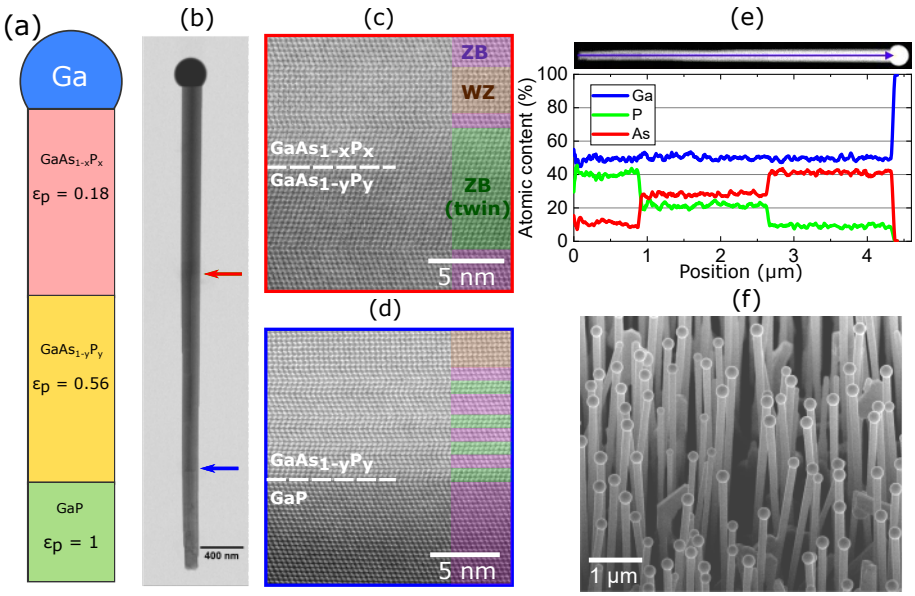

Figure 4.31: *(a) Schematic of the nominal structure of the GaAsP NW, showing the three alloy compositions (not at scale). (b) STEM-BF image of a single NW viewed along the $\langle 1\bar{1}0 \rangle$ zone-axis. (c),(d) High resolution STEM-HAADF images of the upper and lower heterostructures, showing the cubic zinc-blende (ZB) twinned crystals (green and pink color) and the hexagonal wurtzite (WZ) phase (orange color). The white horizontal dashed lines indicate the compositional change ($x \approx 0.2$ and $y \approx 0.4$) at the position of the heterostructure. (e) Chemical composition profile of the NW along the growth direction obtained by using a STEM-EDX line scan. (f) SEM overview of the GaAsP NW array. [76659]*

long and are terminated by a Ga droplet. Most NWs are tilted due to strain from the core-shell unintentional heterostructures, but do not exhibit any kink or specific defect between the three segments. Representative 5 µm long NWs are selected for TEM studies. From the contrast on STEM-HAADF micrographs, Figure 4.31c and Figure 4.31d, each of the three segments can already be distinguished: darker areas correspond to regions with more P, which is lighter than As. The crystal phase of the NWs is mainly cubic ZB with a large number of twins and small segments of hexagonal WZ independently of the alloy composition. The relatively sharp contrast variations in each of the STEM images demonstrate that the transition regions between two segments are only couple of monolayers thick. This indicates that the flux transients in the group V cells are relatively well controlled, even though specific flux switching methods were not used [Priante et al. 2015].

A simple EDX analysis using a line scan along the NW axis, Figure 4.31e, reveals the expected structure: three segments of distinct chemical compositions with increasing As content from bottom to tip. However, the reported composition values are rather unexpected: the bottom segment, nominally pure GaP, appears here as $GaAs_{1-x}P_x$ with $x \approx 0.8$. This clearly demonstrates that the simplistic scheme of Figure 4.31a does not capture the actual structure of the NW.

In Figure 4.32a, an improved schematic of the NW structure is proposed, in which the axial and radial growth modes have been taken into account to represent the actual alloy composition and material volume created at each growth step. The first segment only consists in binary GaP ($\varepsilon_P = 1$), as the volumes created by the axial and radial growth are of the same composition (light green color). The next growth step ($\varepsilon_P = 0.56$) results in the expected $GaAs_{1-x}P_x$ segment by axial growth (yellow) while a $GaAs_{1-x}P_x$ shell is also grown radially (orange). In the final growth step ($\varepsilon_P = 0.18$) the last NW segment is formed by axial growth (light red) together

with an additional shell (dark red). Note that the chemical compositions of the NW core and shell grown in same nominal conditions can differ due to the distinct growth mechanisms and flux geometries.

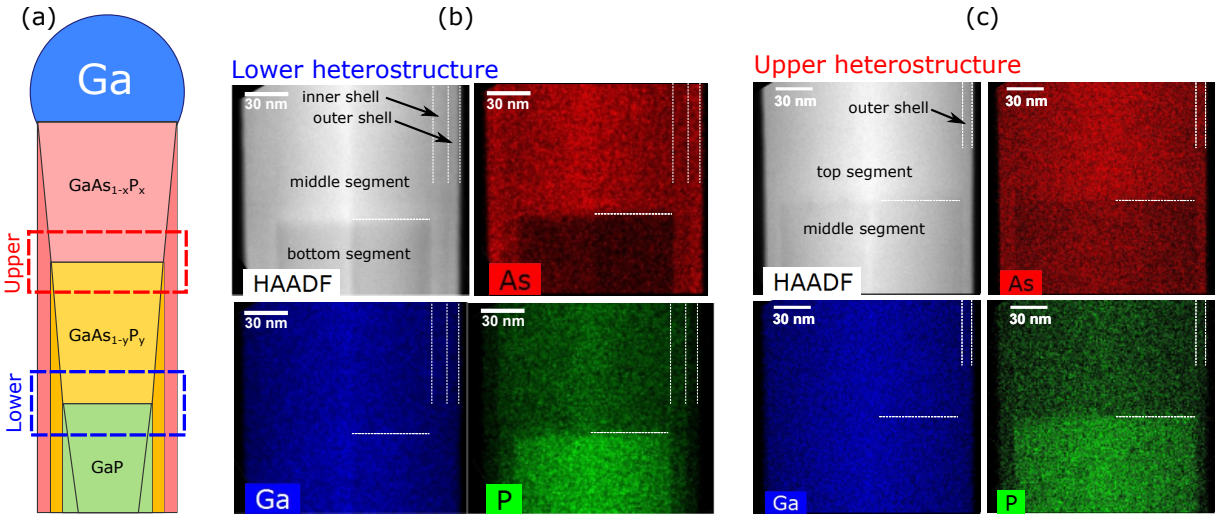

Figure 4.32: *(a) Updated schematic the NW structure, including the radial and axial volumes created at each growth step, which results in a coremultishell structure, depending on the axial position along the wire. (b),(c) STEM HAADF and EDX maps acquired along the $\langle 11\bar{2} \rangle$ zone-axis, which reveal double (b) and simple (c) core–shell structures at the lower and upper heterostructure, respectively. The observed shells are always As-rich (P-poor) compared to the NW core. [76659]*

Figure 4.32b shows a high-resolution chemical map of the lower heterostructure (from $\varepsilon_P = 1$ to $\varepsilon_P = 0.56$) and the corresponding HAADF image acquired along a $\langle 112 \rangle$ zone axis. This specific orientation provides superior details when investigating the possible presence of a NW shell, as discussed below. The Ga elementary map is uniform, as expected, but the As and P composition maps reveal the presence of a shell around the NW core, irrespectively of the axial position of the heterostructure. Detailed analysis reveals that this shell actually separates into two $GaAs_{1-x}P_x$ layers, the inner and outer shells with a larger As content in the outer shell, see white lines in Figure 4.32b. Figure 4.32c presents the analysis of the upper heterostructure, (from $\varepsilon_P = 0.56$ to $\varepsilon_P = 0.18$). Similarly to the lower heterostructure, a core-shell structure is identified, but with a single shell wrapped all around the NW core heterostructure.

The shells seem richer in As than the core onto which they grow, however the EDX signal on the maps is also proportional to the thickness of the material which varies due to the hexagonal shape of the NW section. Precise quantifications of the alloy compositions are needed.

Using a dedicated NW design alternating 3 GaAsP core segments of different composition, the presence of a 10 nm shell formed during each segment growth is attested. This unintentional shell is always present around the nanowires and results from the radial growth operating on the NW sidewall in the VS mode.

4.3.1.2 Shell composition quantification

The presence of an unintentional shell of different composition than the NW core obfuscates the simple line scan analysis presented in Figure 4.31f. The average composition must be carefully deconvolved using the actual hexagonal geometry, core diameter, shell thickness and shell composition to obtain the correct NW core composition, as explained in Section 2.3. At the lower heterostructure of the NW (Figure 4.32b), two shells are present, so the inner shell composition

is corrected before the core composition. Because of the successive corrections, larger error bars are obtained.

Table 4.7 summarizes the corrected chemical compositions for the 3-segment GaAsP NW. Note that the corrected alloy composition of the first segment, $x = 1$, now matches the experimental growth conditions, nominally pure GaP, which confirms the validity of this correction.

Table 4.7: *Core and shell compositions in the 3 segments of the $GaAs_{1-x}P_x$ NW measured by STEM-EDX. The measurements are taken at the lower and upper heterostructure, as indicated in Figure 4.32. The compositions are corrected to account for the surrounding shell. Δx is the composition difference from the core to the shell formed during the same segment growth.*

Segment	Bottom (GaP)	Middle ($GaAs_{1-x}P_x$)	Top ($GaAs_{1-x}P_x$)
$x_{\text{Outer shell}}$	0.20 ± 0.01	0.16 ± 0.01	0.14 ± 0.01
$x_{\text{Inner shell}}$	0.47 ± 0.03	0.41 ± 0.03	–
x_{Core}	1 ± 0.04	0.44 ± 0.025	0.18 ± 0.01
Δx	–	-0.03 ± 0.04	-0.04 ± 0.02

As-rich shells. The unintentional shell grown is As-rich (P-poor), compared to the core formed during the same segment growth ($\Delta x \approx -0.03$ for the middle shell on the middle core segment and for the top shell on the top core segment)(Table 4.7).

Unintentional As-rich shells on MBE-grown GaAsP NWs have been observed on Au-catalyzed NWs [Mohseni et al. 2009] and Ga-catalyzed NWs ([Himwas et al. 2017]; [Himwas et al. 2019]). In addition to the As-rich shell, a P-enrichment at the ⟨112⟩ corners of the shell was also reported by [Himwas et al. 2017] and [Zhang et al. 2015]. Following [Mohseni et al. 2009], the core-shell composition mismatch could be attributed to a P-enrichment of the core due to enhanced P adatom migration on the Si(111) surface towards the VLS catalyst. However other experimental studies have shown that group V diffusion is unlikely on the NW sidewall [Ramdani et al. 2013] and that the migration length of atoms on SiO_x masks, as used here, should be very small ([Oehler et al. 2018]; [Schroth et al. 2019]).

In the following, as I attempt to control the composition homogeneity, I search for alternative explanations to explain such increase of As in the shell.

The exact core and shell composition can be determined from EDX measurements and the shell is found to be As-rich compared to the corresponding core segment.

4.3.2 Control of the core-shell composition homogeneity

4.3.2.1 Influence of the MBE geometry

In a first attempt to explain the different alloy contents between the NW core and shell, the geometry of the Riber32 MBE chamber is first considered. Due to the different incident angles of the P and As cells in our MBE, the geometrical corrections for the direct fluxes impinging the droplet and the sidewalls differ slightly between As and P, see Figure 4.33a. These simple corrections strictly depend on the local configuration of the MBE chamber. Assuming the total incorporation of the group V atoms, the P content in the different solids (NW core, sidewall or planar layers) is plotted in Figure 4.33b as a function of the P content in the total group V flux

(ε_P), taking the planar surface as a reference (Equation 4.16 and Equation 4.17).

$$x_{\text{sidewall}} = \frac{1}{1 + \frac{\tan(\alpha_{P_2})}{\tan(\alpha_{As_4})} \times \frac{1-\varepsilon_P}{\varepsilon_P}} \tag{4.16}$$

$$x_{\text{droplet}} = \frac{1}{1 + \frac{\cos(\alpha_{P_2})}{\cos(\alpha_{As_4})} \times \frac{1-\varepsilon_P}{\varepsilon_P}} \tag{4.17}$$

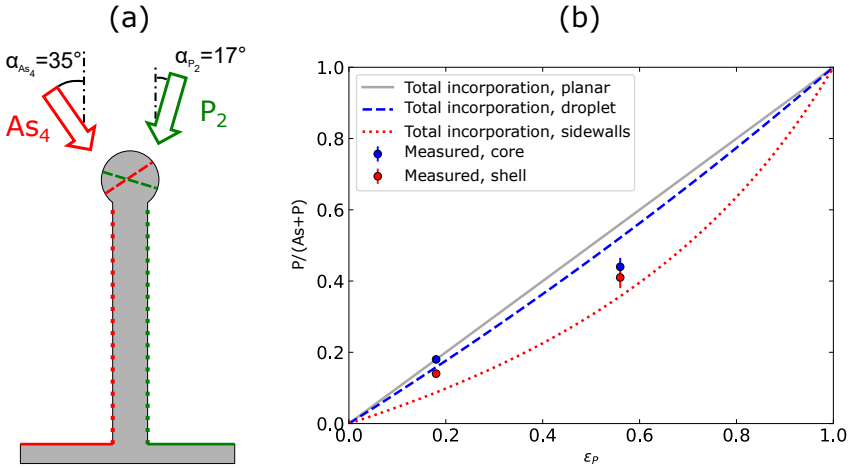

Figure 4.33: *(a) Illustration of the different cell inclinations in the MBE chamber, leading to different effective fluxes on the droplet (dashed line), planar surface (filled line) and NW sidewalls (dotted lines). (b) Effective proportion of P atoms at the different growth fronts relative to the P proportion in the vapor phase, only considering directly impinging fluxes. Filled circles are the composition measurements by STEM-EDX at the upper and lower heterostructures.*

In our configuration, the local arrangement of the group V cells leads to a higher P content in the NW core (blue dashed line) than the shell (red dotted line), which loosely matches the experimental results (dots). However such a simplistic growth model, only based on directly impinging fluxes, is not accurate enough to make compositional predictions if the re-emitted fluxes and shadowing effects are not taken into account ([Dalacu et al. 2009]; [Gibson and LaPierre 2014]; [Kelrich et al. 2013]; [Oehler et al. 2018]). Moreover, the local V/III ratio could be larger than unity on the NW sidewall, so that the radial growth may proceed in the group III-limited (Ga-limited) regime. In that case the final composition does not depend only on the As and P flux values, but also on the V/III ratio and on the actual growth kinetics on the {110} surfaces of the NW sidewalls. Therefore, the local arrangement of the elemental sources is not a likely explanation for the observed compositional change between the NW core and the unintentional shell.

> The incidence angle of the source cells in the MBE chamber could lead to As-rich shells if all incoming group V atoms were incorporated. However, this hypothesis is unlikely and the measured compositions do not fully agree with such model.

4.3.2.2 Influence of the strain

Strain can also alter the composition of an epilayer growing on mismatched substrate, as described by the 'lattice-pulling' effect after Stringfellow et al. [Stringfellow 1972]. Qualitatively, the extra elastic energy is balanced by a change in the chemical potential of the epilayer so that the total energy of the system is lowered. Compared to planar growth in which the strain is mostly contained in the epilayer, the strain in NW heterostructures is shared between the NW

core and shell. In a first approximation, this balance is governed by the ratio of the core and shell volume ([Glas 2015]; [Hestroffer et al. 2010]).

Figure 4.34 presents a detailed chemical analysis of the lower heterostructure shown in Figure 4.32b, focusing on the chemical composition of each shell, inner (orange color) and outer (blue color), across the heterostructure in the NW core. The shells are regularly sampled using rectangular areas to obtain a local averaged EDX chemical composition (Figure 4.34a). Figure 4.34b shows the obtained composition against their position d relative to the core heterostructure.

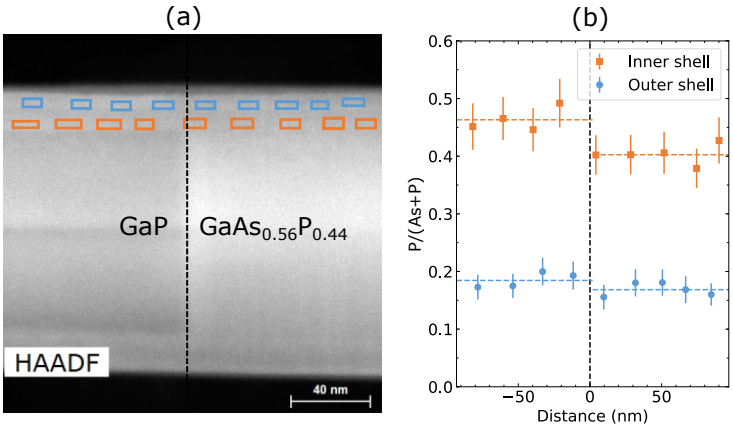

Figure 4.34: *(a) Detailed analysis of the lower heterostructure by STEM-HAADF (⟨112⟩ zone axis). The marked areas are used for the determination by EDX of locally averaged compositions. (b) Composition profile of the outer and inner shells with respect to the distance to the heterostructure. Dashed lines are the average compositions to the left and to the right of the heterostructure.*

The composition of the core has a clear effect on that of the shell. Here, the NW core abruptly changes from pure GaP to $GaAs_{0.56}P_{0.44}$, while the surrounding (inner) shell composition changes from $x = 0.46$ to $x = 0.40$ (Figure 4.34b, orange line). The compositional change of the inner shell is small compared to that of the core, but it is occurring at the same axial position along the NW. At such small scale (a few tens of nanometers) the shells can be considered to be at the same temperature and to receive the same atom flux. The core and shell geometrical parameters are also identical (i.e. same volume ratio and strain balance) so that only the composition of the NW core varies. The GaAsP shell mismatch decreases by one order of magnitude from $e = 2.0 \times 10^{-2}$ on the GaP core, to $e = 1.5 \times 10^{-3}$ on the adjacent GaAsP core. There is a qualitative agreement with the lattice-pulling effect, as the shell is richer in P on the GaP than on the GaAsP core. Yet, even in these rather extreme conditions, more than one decade change in lattice mismatch, the effect on the composition is rather modest, $\Delta x = 0.06$, for typical shell composition $GaAs_{0.6}P_{0.4}$.

The strain in the shell grown on a mismatched core is shown to influence the relative P incorporation in GaAsP, as the shell composition changes from $x = 0.46$ to $x = 0.40$ at the GaP/GaAsP lower heterostructure. However, an important mismatch leads to a small composition variation. Another control parameter is needed to tune the alloy content.

4.3.2.3 Influence of the temperature

Growth of uniform GaAsP NWs at different temperatures. In Figure 4.35, the effect of the substrate temperature on the NW structure and chemical composition is investigated. Here, two $GaAs_{1-x}P_x$ NWs ($x \approx 0.2$) were grown in a single step using the same group III (Ga at the equivalent growth rate of 1.8 Å s^{-1}) and V flux ($\varepsilon_P = 0.24$, $V/III = 1.5$). The first sample, Figure 4.35a-d), was grown at 590 °C, while the second sample, Figure 4.35e-h, was

grown using a higher substrate temperature, 620 °C. To account for the axial growth speed reduction with temperature, the growth duration was increased from 20 min to 40 min. The two experiments were performed in succession to minimize any experimental variation. Both NWs have comparable diameter (190 nm and 170 nm below the droplet).

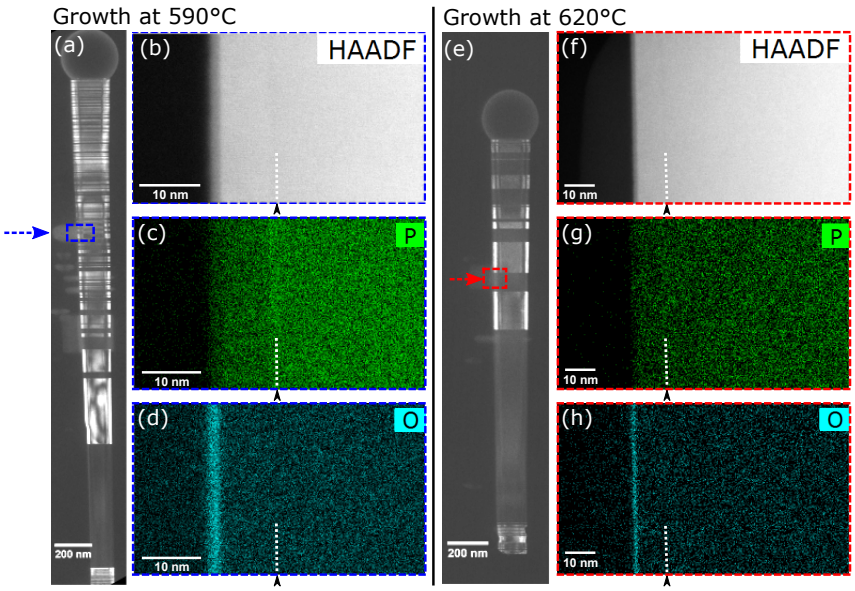

Figure 4.35: *Comparison between GaAsP NWs grown at* 590 ℃ *(a-d) and* 620 ℃ *(e-h), respectively. (a,e) TEM-DF micrographs along the* ⟨110⟩ *zone-axis, highlighting one of the twins in the ZB structure. The blue and red arrows indicate zones further analyzed by EDX. (b-d) Details of the NW shell grown at* 590 ℃*, observed by STEM-HAADF (b) and EDX showing the corresponding P and O chemical maps (c,d). The white dotted line marks the interface between the As-rich (P-poor) shell and the NW core. (e-h) Similar analysis for the NW grown at* 620 ℃*, with no visible change in the chemical composition between core and shell.*

Using conventional TEM, Figure 4.35a and Figure 4.35e, one observes that they still differ in length (2800 nm at 590 °C and 2000 nm at 620 °C) despite the change in growth duration. They both present a cubic structure with several twins, identified by the contrast change in the DF TEM images. In our growth conditions, the lower substrate temperature (590 °C) leads to a more defective structure compared to the higher growth temperature (620 °C). Chemical analysis using STEM-EDX and HAADF (Figure 4.35b-d and Figure 4.35f-h) is extracted from an area situated at approximately the same distance from the NW catalyst (respectively 800 nm and 700 nm). The presence of an As-rich (P-poor) shell around the NW core for the sample grown at 590 °C is clear (Figure 4.35c) and no shell can be distinguished in the EDX map acquired in the same conditions for the sample grown at 620 °C Figure 4.35g. Chemical maps of the O content, Figure 4.35d and Figure 4.35h, confirm that the native oxide on the NW outer surface is limited to the first 2 nm and cannot be confused with the GaAsP shell.

Table 4.8: *Core and shell compositions of the* $GaAs_{1-x}P_x$ *NWs grown at lower (*590 ℃*) and higher (*620 ℃*) temperature as presented in Figure 4.35, measured by STEM-EDX. The measurements are taken at the zones indicated in Figure 4.35a,e.*

Growth temperature	590 °C	620 °C
x_{shell}	0.20 ± 0.01	0.235 ± 0.01
x_{core}	0.29 ± 0.02	0.24 ± 0.02
Δx	-0.09 ± 0.02	-0.005 ± 0.02

Kinetic effects. In the absence of strain-related effect (subsubsection 4.3.2.2) or change in the source positions (subsubsection 4.3.2.1), I must find alternatives to explain the difference in alloy composition between the unintentional shell and core. Typically, a preferred As incorporation relative to P is widely reported for GaAsP layers grown by solid-source MBE ([Arthur and LePore 1969]; [Foxon et al. 1980]; [Matsushima and Gonda 1976]; [Nomura et al. 1991]; [Shu-Dong et al. 2005]; [Woodbridge et al. 1982]) or gas-source MBE ([Hou et al. 1991]; [LaPierre et al. 1996]). However this balance is affected by the temperature and the P content is found to increase with increasing temperature ([Nomura et al. 1991]; [Woodbridge et al. 1982]). The later relates to the increased sublimation of As compounds on the growing surface between 450 °C and 650 °C, while the desorption of P is still negligible in this temperature range. In addition to temperature, the actual growth rate and V/III ratio values are also expected to play a role [Nomura et al. 1991]. The reported increase in P content with the substrate temperature is in agreement with the present results, as the P content in the shell varies from $x = 0.20$ (590 °C) to $x = 0.235$ (620 °C). No study actually considers the growth on {110} surfaces, i.e. the NW side facets, and I extrapolate results obtained on (100) epilayers grown in the group-III-limited regime.

In the NW core, the opposite trend is observed, with a decrease of the phosphorus content in the core from $x = 0.29$ at 590 °C to $x = 0.24$ at 620 °C. This variation occurs despite the use of identical fluxes and geometry. As the VLS growth is group V limited, it is very sensitive not only to the direct group V fluxes but also to the re-evaporation of group V species from the liquid droplet [Glas et al. 2013]. The final chemical composition of the material is obtained by balancing the impinging and re-evaporation fluxes of group V element in the liquid droplet. The actual balance depends on the thermodynamics parameters of each species and compound, which are different for As, P, GaAs and GaP [Ansara et al. 1994]. The specific case of self-catalyzed VLS GaAsP ternary NWs has not yet been modeled theoretically [Dubrovskii 2017] and equilibrium data for the Ga-GaAs-GaP system is only available at much higher temperature (>900 °C) [Panish 1969].

In our growth conditions, the composition of the VLS grown NW core (group-V-limited) shows a decreasing P content with temperature while the VS-grown shell (possibly group-III-limited) has an opposite variation. Therefore, there should exist a growth temperature for which the core and shell composition can be made equal. In general, one could perform this optimization for each group V flux composition, ε_P, by either lowering or increasing the substrate temperature depending on the initial starting point. In this experiment, for a group-V flux composition $\varepsilon_P = 0.24$, a substrate temperature of 620 °C leads to a uniform composition $x = 0.24$ in the core and in the shell.

Presence of a P-rich interface. Interestingly, the GaAsP shell is separated from the NW core by a dark line in HAADF for both samples, independently of the growth temperature; see dotted white line in Figure 4.35b and Figure 4.35f. The chemical map of the sample grown at low temperature, Figure 4.35c, shows that this dark HAADF contrast is associated to a P-rich region. This feature is not visible Figure 4.35g due to the low spatial resolution of this particular EDX map.

To better characterize this P-rich interface, high resolution STEM-HAADF was performed. Figure 4.36a,b presents the details of the core-shell interface of the NW grown at low temperature (590 °C). The dark line between the NW core and shell is well visible. The HAADF intensity profile (Figure 4.36c), reveals that the dark region is about 7 monolayers thick (1.4 nm). Figure 4.36d-f show high resolution HAADF images of the NW grown at high temperature (620 °C). The dark contrast is also well visible in Figure 4.36e,f, which detail upper and lower parts of the NW, respectively. The HAADF profiles, Figure 4.36g, reveal that the P-rich interface is close to the NW outer surface at the top of the NW and that it is buried below an increasingly

thicker shell toward the base of the NW. This correlates with the position of the NW core-shell interface, consistently with the schematic in Figure 4.32a.

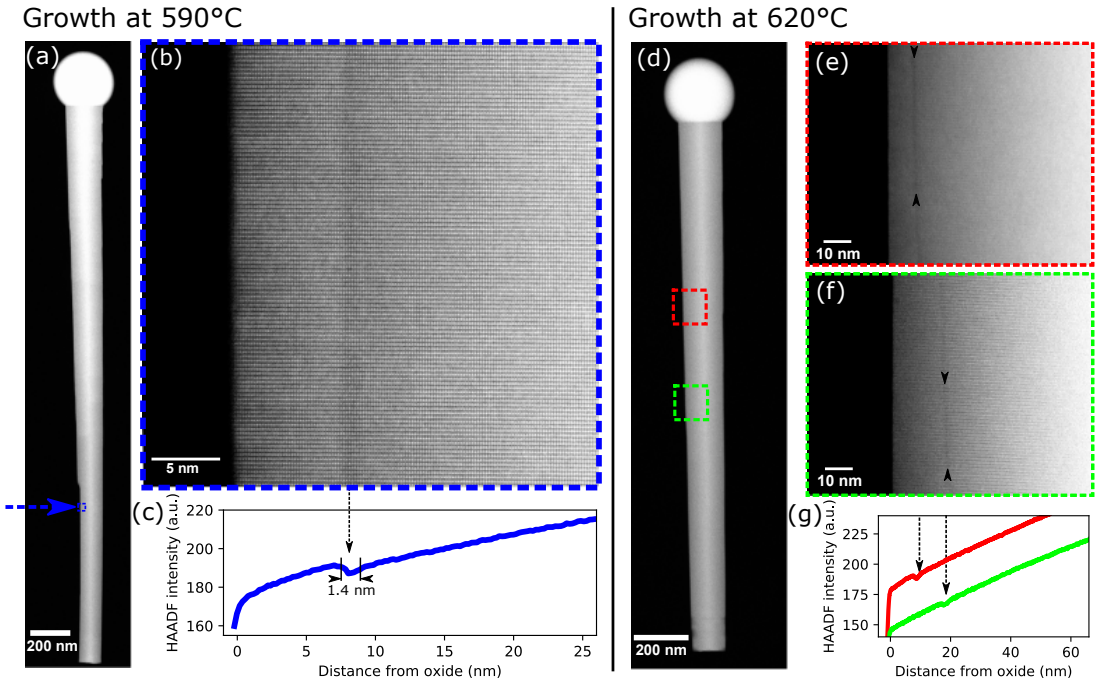

Figure 4.36: *Details of the core-shell interface. (a) Overview of NW grown at* 590 ℃ *using dark field TEM along the* ⟨112⟩ *zone-axis. (b) Atomically resolved STEM-HAADF of the NW shell at the location indicated by an arrow in (a). (c) Corresponding HAADF intensity profile. (d-g) Similar observations for the NW grown at* 620 ℃. *(e-f) Details of the shell observed by STEM-HAADF toward the NW top (red rectangle) and NW base (green rectangle). Black arrows mark the position of the region used to compute the HAADF intensity profiles, in (g): toward the NW top (red line, offset) and NW base (green line).*

Note that this local P enrichment is visible independently of the substrate temperature, between 590 °C and 620 °C, Figure 4.36c and Figure 4.36g. This P-rich material can only form just after or during the VLS growth of the top layer of the NW core, before the VS grown shell covers the NW sidewall. Although the exact origin of this P-rich interface is beyond the scope of this study, I can suggest a few alternatives. First, a very fast reaction of the exposed (110) facet with the vapor phase just after it is formed, *i.e.* P-enrichment after the VLS growth. Second, a local segregation of P at the triple phase line inside the Ga droplet, i.e. P-enrichment during the VLS growth. Some sort of segregation at the triple phase line has been reported in the NW literature ([Connell et al. 2013]; [Hilse et al. 2010]) but limited to inhomogeneities in dopant concentrations, orders of magnitude below the compositional variations observed here.

4.3.3 Conclusion

Section: Alloy composition control in GaAsP NWs

Using a growth scheme where several core alloy compositions are successively grown in $GaAs_{1-x}P_x$ NWs, I showed that an unintentional shell forms during the core axial growth. The P content in this $GaAs_{1-x}P_x$ shell was quantitatively estimated using STEM-EDX and is typically As-rich compared to the core, in our conditions.

This mismatch cannot be only explained by geometrical corrections to the fluxes in the growth chamber, or strain related effect in core-shell heterostructures but it is assigned to the different growth mechanisms: VS for the NW shell and VLS for the NW core. By increasing the substrate temperature, the P content in the shell increases while that of the NW core decreases, so that it is possible to match the chemical composition of the unintentional GaAsP shell with its GaAsP core.

Even in these favorable growth conditions, the interface between the NW core and shell still exhibits a local P-enrichment. While the later permits to precisely localize the position of the core shell interface in my NWs, it is not clear how this P-rich region is formed. Yet the removal of such inhomogeneities is important for NW-based solar cells.

4.4 Summary of Chapter 4: GaAs(P) core-shell NW structures

In Section 4.1, I introduced the method used to grow core-shell NWs by MBE, and showed how the NW array morphology improves when growing GaAs shells at 580 °C instead of lower temperatures. I then compared possible materials to grow wide-bandgap passivating shells and studied InGaP shells by TEM and EDX. The composition in InGaP is found to differ from the nominal composition that would be obtained on planar layers, due to the unique growth mode of NW shells. On average, the GaInP is richer in Ga compared to the expected composition, but large fluctuations of the content are found, which are influenced by the presence of crystal defects and by the shading of adjacent NWs. Misfit dislocations are seen by TEM, in agreement with previous calculations in the literature. According to the same sources, only small adjustments of the shell thickness and composition are needed to reach dislocation-free conditions.

In Section 4.2 the relevance of cathodoluminescence to characterize doping in NWs was first established. Using a technique developed by our team at C2N, CL spectra of doped NWs are acquired and fitted to the generalized Planck law. Empirical relationships which relate features of the spectrum or fitted parameters to the doping level are established using reference GaAs thin-films, and applied to NWs.

Based on this method, I have studied the incorporation of dopants in the core and shell of GaAs NWs.
P-type doping of GaAs NWs with Be was found to be effective both in the core grown by VLS (up to $8 \times 10^{18}\,\mathrm{cm}^{-3}$) and in the shell grown by VS (up to $1.3 \times 10^{19}\,\mathrm{cm}^{-3}$), in agreement with previous literature.
N-type doping with Si was only investigated for GaAs NW shells as previous literature showed incorporation as acceptor (p-type) in NWs grown by VLS. Signature of p-type or heavily compensated n-type GaAs was found for NW shells grown at 580 °C. At lower temperature (450 °C), the shells appear to be of n-type but strong compensation is still suspected as carrier concentration one order of magnitude below dopant concentrations are found. As planar layers grown in the same conditions and in the (110) orientation should not exhibit such high degree of compensation, it seems specific to the NW sidewall geometry. Despite employing advanced growth schemes in order to maximize the local V/III ratio, it seems that electron concentration in the shell is limited to $5 \times 10^{17}\,\mathrm{cm}^{-3}$ in our conditions.

In Section 4.3 I investigated composition inhomogeneities in $GaAs_{1-x}P_x$ NWs, as such alloys can be tuned to higher bandgap, optimal for tandem-on-Si. In particular, I used a specific NW design to evidence the simultaneous growth of a shell during core growth, which was characterized by STEM-EDX. A quantitative estimation of the shell composition can be made and it is found to be As-richer than the core. The directionality of the fluxes in the MBE may have an impact but it does not suffice to explain such effect. The shell composition is shown to depend on that of the underlying core on which it grows, but this effect cannot be used to completely match both compositions. However, the temperature was found to change the P content both in the core and in the shell, which allows to obtain homogeneous $GaAs_{1-x}P_x$ NWs with a 1.7 eV bandgap.
There are still composition inhomogeneities in the NWs as a P-rich layer is always present at the interface between core and shell, for reasons not yet understood.
Due to the required optimization to partially control alloy homogeneity in GaAsP, I decide to focus on GaAs NWs for the fabrication of NW solar cells.

Chapter

5 Nanowire Solar Cell Fabrication and Characterization

Chapter content

In Chapter 3 I have described the development of homogeneous GaAs NW arrays with high yield and low density of crystal defects. In Chapter 4 I presented studies aimed at the realization of core-shell structures, with controlled doping levels and with shells made of wide-bandgap alloys. In this chapter, I detail the fabrication and characterization of complete NW array solar cells.

I first motivate the choice made for the structure of the NW and the fabrication process, in light of previous works in the literature. I then present the technological steps I have developed in our laboratory for fabricating solar cells from an array of NW junctions. Based on experiments on planar layers, I have studied and optimized an ITO contact, which I describe in the third section. Then, I present a complete NW solar cell device, and the analysis of its performances through opto-electrical characterization means. Finally, I introduce a new core-shell heterojunction design and its implementation into devices with improved performances.

The technological process development and transparent contact optimization described in the next sections were carried out at the C2N lab in Marcoussis before it moved at the end of August 2018. Consequently, epitaxial growths were realized in 2017 and 2018, and all processed together in 2018 while the fabrication was being developed. As the MBE was the first equipment to shut down, no new epitaxies were possible and the NW solar cell architectures could not be adjusted from the characterization of the first fabricated devices.

Therefore, I present in section 4 and 5 two selected samples from this first-generation batch: a core-shell homojunction and a core-shell heterojunction.

In November 2018, the NW growths were resumed on the IPVF Compact21 MBE equipment, and devices were fabricated in 2019 at IPVF when the new labs were operational. The last core-shell heterojunction device presented in section 5 comes from this second-generation batch.

5.1 Junction design and device architecture

In Chapter 1 (Section 1.2), I introduced the envisioned architecture for the top junction made of GaAs NWs: a core-shell GaAs junction with a self-catalyzed p-doped core and a n-doped (Si) shell grown by VS mode.

In light of the results of Chapter 3 and Chapter 4, I now present the choices I made for the junction design in more detail. Then, based on previous work in the literature and the specifics of my junction structure, I elect a fabrication strategy to electrically contact the NW array.

5.1.1 Junction design considerations

Here, I present the aimed junction design, as a compromise between what is achievable for NWs based on self-catalyzed growth by MBE, and the parameters we were able to measure (doping, shell quality, array morphology *etc.*).

The baseline NW structure is summarized in Figure 5.1a. As introduced in Section 1.2, I aim at about 2 µm-long and 280 nm-thick NWs, resulting in a surface filling ratio close to 25 % in a 500 nm pitch hexagonal array, for a compromise between efficient light absorption and robustness. A schematic of the band diagram is displayed in Figure 5.1, simplified in one dimension along the NW length and across its shell. The actual material band offsets are used, to get an idea of the barriers existing along the carriers' path.

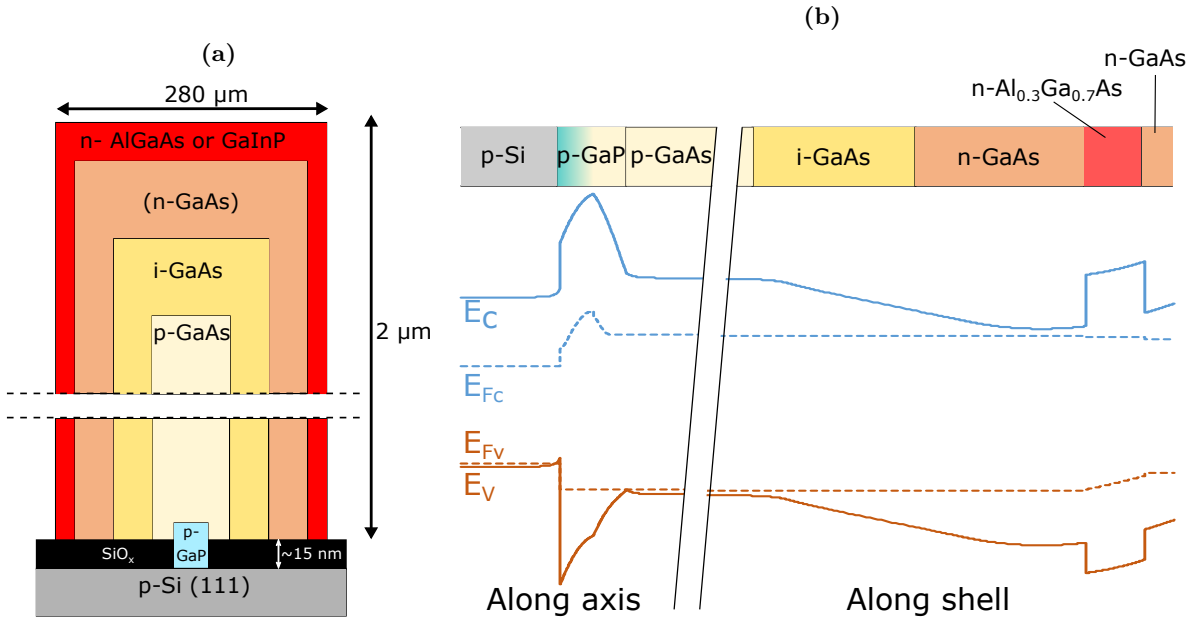

Figure 5.1: *(a) Base NW structure and dimensions for solar cell devices. (b) simplified 1D band structure along the NW axis and shell, calculated at V_{oc} and for a constant photogeneration in all layers. Not at scale.*

Junction material. Despite the bandgap of GaAs (1.4 eV) not being optimal for tandem compared to GaAsP (1.7 eV attainable), it appears to be a simpler material system for the demonstration of a tandem solar cell (which can later be complexified using GaAsP):

- The growth of GaAs does not involve composition variations, which were shown in Section 4.3 to be an issue for GaAsP NWs. Controlling the composition of the core implies important constraints on other growth parameters, the temperature for example. Matching the core and shell compositions looks difficult as well, especially between the tip segment and the sidewalls.

- Although doping levels in GaAsP NWs could be assumed to be similar to GaAs due to a close composition, it is complicated to directly measure them. The analysis of a CL spectrum might be altered by the uncertainty over the exact composition and its local fluctuations, and reference planar layers on which to perform Hall measurement is challenging due to the lattice-mismatch of GaAsP with III-V substrates.

- Due to its lower bandgap (and thus, higher photocurrent), using GaAs could even be beneficial in the short-term to achieve current-matching with the Si bottom cell, as the top-cell current is still unoptimized and limited. Indeed, the current through a two-terminal device is determined and limited by the lowest current in each subcell, and the first demonstrations of III-V NW array solar cells on Si all exhibit poor performances, in particular low currents ([Mariani et al. 2013a]; [Boulanger et al. 2016]). Specifically, [Wood et al. 2017] reported a tandem solar cell using GaAsP NWs grown on Si and despite a remarkable 0.62 V voltage addition to the Si subcell, the device is only 3.51 % efficient due to a very low J_{sc} (7.65 mA cm^{-2}). On the other hand, [Yao et al. 2015] reported a tandem with GaAs NWs on Si at an efficiency of 11.4 % with a current of 20.64 mA cm^{-2}.

p-i-n structure. A p-core, i-n-shell structure is chosen as I showed that the VLS method allows to obtain Be-doped GaAs NWs with carrier concentration $p > 10^{18}$ cm^{-3}.

Furthermore, the addition of an intrinsic layer was shown (Section 2.1) to be beneficial to limit carrier depletion in the doped regions, and to prevent tunneling recombinations [LaPierre 2011a]. It also allows to tune the NW diameter by changing the intrinsic shell thickness. Thus, light absorption can be maximized while the n-shell is kept thin, which limits parasitic growth on the mask and rough and uneven {110} sidewall facets (see Section 4.1).

GaP stem. I choose to initiate the GaAs NW growth with a GaP foot considering the significant yield improvement using this technique (Section 3.2). Despite the eventual barriers arising from the additional heterojunction at the foot (Figure 5.1b), ensuring a high yield seems critical for good device performance ([Yao et al. 2015]; [Aberg et al. 2016]; [Wallentin et al. 2013]), and functioning NW solar cells were already reported with such GaP stem [Boulanger et al. 2016].

Wide-bandgap shell for passivation or heterojunction architecture. Without passivation, the GaAs surface presents many defect states, resulting in surface depletion and recombination (surface recombination velocities up to 10^5 cm s^{-1} were measured in GaAs NWs [Joyce et al. 2013]). While some groups have employed sulphur-based chemical treatment to passivate NWs ([Tajik et al. 2011]; [Cui et al. 2013]; [Hakkarainen et al. 2019]), wide-bandgap lattice-matched III-V are typically more suited for GaAs

For simplicity, I use an AlGaAs passivation shell as a baseline for the first cells, as it is lattice-matched to GaAs independently of the Al content. But I also use InGaP once first devices are demonstrated with AlGaAs, due to its promising properties, as discussed in Section 4.1. Indeed, it is less prone to parasitic deposition on the mask than AlGaAs, it can lead to a simplified design without capping shell, and it is less reactive with O, often resulting in better material quality and GaAs surface passivation. Yet, it comes at the price of composition inhomogeneities and dislocations.

Alternatively to the GaAs p-i-n homojunction design with a passivation, I also made devices without the n-GaAs shell, with a n-GaInP shell directly in contact with i-GaAs, resulting in a core-shell heterojunction. In the last section, the advantages of this architecture and the device performances are discussed and compared with the homojunction.

5.1.2 Planarizing the nanowire array?

Because I choose to grow core-shell NWs, several contacting schemes are possible (Figure 5.2). Namely, I could :

(a) Directly deposit a transparent conductive oxide (TCO), coating all the mask and NW surfaces. Because of the presence of the mask and thanks to the core-shell structure, only the n-shell would be contacted.
(b) Coat the substrate and NW surfaces with a thin insulator and then contact only part of the NWs. Such techniques have been used for GaAs [Tajik et al. 2011] and for InP NW solar cells ([Wallentin et al. 2013]; [Otnes et al. 2018]).
(c) Fully planarize the NW array by embedding it inside an insulator, and only contact the emerging tips of the NWs, which is the main process used in the literature [Otnes et al. 2018].

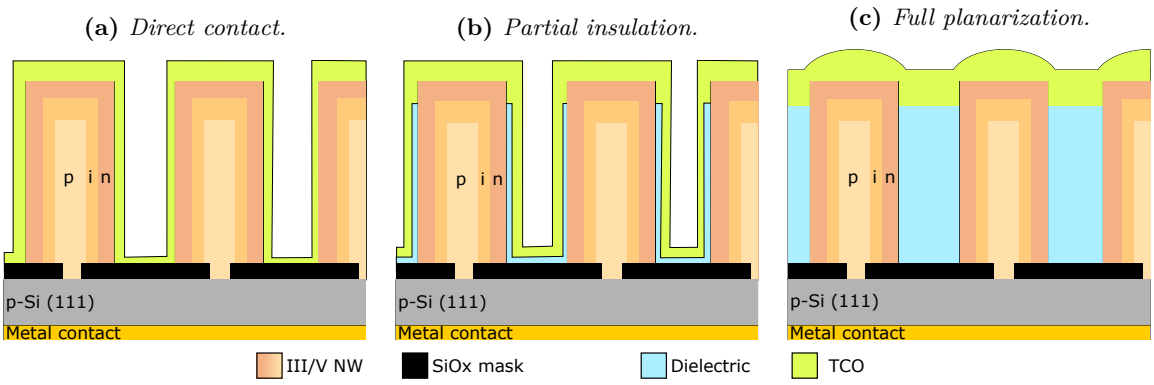

Figure 5.2: *Three possible contacting schemes for the NW arrays.*

We decided to use the method (c), consisting of full planarization, for several reasons.

- **Preventing shunt.** We tried the method (a) by directly depositing a conformal ZnO:Al contact by atomic-layer-deposition (ALD), as described in Chen's thesis [Chen 2018], and found the device to be shunted (highly conductive JV characteristic with low rectification). The SiO_x mask is only 10 nm to 15 nm thick and is exposed to Ga and As fluxes during the NW growth at 600 °C. It might degrade during this step and provide leakage paths, especially since its surface is covered by a poly-n-(Al)GaAs parasitic layer during shell growth.
- **No consequence on contact resistance.** I show in the following that high doping levels are extremely important for the contact quality with a transparent conductive oxide (TCO). The doping level in the NW was characterized in the previous chapter (Section 4.2) and was found to be very low in the shell sidewalls, whereas it might be an order of magnitude higher in the tip. Contacting only the tip then appears as efficient for current extraction as contacting all the NW shell.
- **Mechanical stability.** The as-grown NW array is extremely fragile; for example, it is easy to collect NWs for CL or TEM characterization with a simple gentle touch. Although a thin SiO_x coating followed by TCO deposition was shown to successfully contact InP NWs without shunt [Wallentin et al. 2013], planarization ensures that the contact with the mask during photolithography steps or the electrical probes during measurement does not damage the NWs.
- **Optical losses.** Coating the whole structure with ITO may also increase the fraction of light parasitically absorbed, and is thus unwanted.

5.1.3 Choice of a top-contact

To electrically contact the NWs together, few possible techniques exist. Silver NWs have been used to contact NW-based LEDs by spreading them with a random organization so that they touch every NW in the array [Dai et al. 2015]. However, this is more adequate to help for lateral conduction. Ag does not make an ohmic contact when touching free GaAs surfaces, especially as the contact area is very small.

Transparent conductive oxides (TCO) have been mostly used so far for NW solar cells [Otnes and Borgström 2017], the most common being indium-tin-oxide (ITO), but ZnO:Al (AZO) was also tested with lower performances [Mariani et al. 2011]. A possible advantage of this contact scheme is a concentrating effect of ITO which forms domes at the NW tips, enhancing light concentration ([Mariani et al. 2013b]; [Dam et al. 2016]). The main problem encountered with TCO contact is the high contact resistance with the III-V shell (often n-type), in particular for GaAs which suffers from important mid-gap Fermi level pinning and Schottky barriers. A common solution to improve such contact is to highly dope the III-V layer in contact with the TCO, for example up to $3 \times 10^{18}\,\mathrm{cm}^{-3}$ in the tip segment of the axial junction in ([Aberg et al. 2016]). But reaching high electron concentrations is challenging in GaAs NW shells (see Section 4.2). [Nakai et al. 2015] employed a pulsed-doping technique (MOCVD) to form a highly tin-doped (n) contact layer on InGaAs NWs, similar to modulation doping in MBE. Some groups have improved successfully this contact by inserting few nm-thick Ti ([Mariani et al. 2013a]; [Nakai et al. 2015]) or 25 nm thick In ([Zhang et al. 2014a]) layers between GaAs and ITO to alter the surface chemistry or promote interdiffusion at this interface. Recently, an alternative contacting scheme (for single NWs) was reported which consists in a molybdenum oxide coating wrapping the head of an InP NW which acts as an electrostatic gate due to its ability to trap fixed charges, followed by an ohmic (but recombining) contact at the NW tip [Oener et al. 2018]. The gate effect results in a depletion of minority carriers inside the NW head so that only majority carriers can flow towards the ohmic contact and be collected, without recombination. Such advanced scheme is beyond the scope of this project but illustrates the importance of decoupling charge extraction and carrier selectivity.

I choose to use ITO layers over AZO based contacts after preliminary tests which show that AZO contacts make non-ohmic, lossy contacts on n-GaAs and do not improve upon annealing like ITO. I do not intercalate thin metal layers as the deposition is done in a separate chamber, and the thin metal layers could thus oxidize in an uncontrolled manner upon exposure to air.

Instead, I study the contact of ITO on different III-V planar layers and the effect of various thermal treatments.

Section: Design and motivations

In light of the results from the previous chapters studies, and from past literature results, I focus on a structure consisting in a planarized array of core-shell GaAs NWs, top-contacted with a transparent layer of ITO.

5.2 Nanowire solar cell fabrication process

The technological steps of the NW solar cell fabrication presented here were developed at C2N laboratory. While many groups have already reported fully processed NW array solar cells, there have been few reports on the details of the fabrication process, and adapting a technology in a new laboratory of often a task to be carried out from scratch.

5.2.1 Planarization

Alternative planarization techniques

I tested several methods for NW array planarization.

- **Ormostamp® planarization.** Ormostamp® is an inorganic-organic hybrid polymer, suited for the fabrication of transparent stamps used in nanoimprint lithography[1]. We found spin-coating conditions compatible with its viscosity so that a uniformly thick layer can be obtained after polymer curing, leaving only the first 200 nm of the NWs emerging. While it seems that the NW tips are free of polymer after an HF dip, I did not characterize the surface nor the electrical contact. We faced several issues: chemical incompatibility with our photo-resist solvent (PGMEA in the AZ5214 resist), poor thermal stability of the processed array which cracked after 350 °C annealing, and residual strain after curing which tilts the NWs.

- **Solgels planarization.** SiO_2 sol-gel-derived films were also tested, in collaboration with the *Laboratoire Chimie de la Matière Condensée de Paris*. The spin-coating conditions and the solgel composition were optimized to ensure uniformly thick coating and lower the residual strain. In particular, the use of surfactants allows to relieve the strain in the final layer [Cop et al. 2018], and µm thick layers can be obtained by multi-layer deposition, without thermally stabilizing the solgel in between successive coatings. The NW tips can be cleared with a final diluted HF dip. However, despite our efforts, the strain was never released in our arrays and NWs always tilt under the electron beam irradiation during SEM observation, and after thermal annealing with ITO.

- **SiO_x planarization.** The NW array can be coated with silica using plasma-enhanced chemical vapor deposition (PECVD). It presents the advantage of simplicity and reliability (single-step in a deposition chamber), of resulting in a low-loss dielectric material with limited residual strain, and of easy selective removal with diluted HF. We found that the resulting layer is not conformal, with a thicker deposition rate at the NW top than at the sidewalls, making it hard to completely fill the array, even using multiple cycles of deposition & selective top etching by RIE.

- **BCB planarization.** We also used Cyclotene™ 3022-46, a resin commercialized by Dow Chemicals and derived from B-staged bisbenzocyclobutene (BCB) monomers. It results in a low dielectric constant and low-loss dielectric material, and features low moisture absorption, no out-gassing, low temperature cure and excellent planarization. It was widely used in the NWs community to planarize arrays ([Aberg et al. 2016]; [Boulanger et al. 2016]; [Cui et al. 2013]; [Mariani et al. 2013b]; [Yao et al. 2014]; [Nakai et al. 2015]; [Senanayake et al. 2010]; [Yao et al. 2015]; [Shin et al. 2013]; [Koblmueller and Abstreiter 2013]; [Dimakis et al. 2012]; [Gibson et al. 2019]). However, after embedding of the NWs, it needs plasma-RIE etching to reveal the NW tips, which is an additional processing step and which might induce ion-induced damage in the III-V material.

[1] https://www.microresist.de/sites/default/files/download/PI_OrmoStamp_2015_1.pdf

We decided to employ a scheme combining a BCB planarization with a preliminary SiO_x coating by PECVD, similar to ([Aberg et al. 2016]). The SiO_x protects the III-V from surface damage during the RIE. It is then removed in diluted HF, which does not deteriorate the III-V underneath. This additional coating also enhances the mechanical stability of the NWs.

BCB planarization steps

Here I detail the steps to planarize a NW array with a two-step SiO_x/BCB planarization, while referring to the different stages in Figure 5.3, starting with the as-grown NW array **(a)**. More information about the processing of BCB resin can be found on the documentation sheet[2].

- SiO_x deposition by PECVD, 280 °C, 3 min (nominal planar deposition rate : 15 nm min^{-1}).
- Water desorption on a hotplate: 125 °C, >1 min
- Spin-coating of BCB adhesion promoter (Dow AP3000) at 4000 min^{-1}, 60 s. Dried on a hotplate at 125 °C
- BCB (Cyclotene 3022-46) dispense with a syringe through a 0.2 µm filter.
- Spin-coating at 4000 min^{-1}, 60 s (Nominal resulting planar thickness: 2.6 µm). **(b)**
- Soft-bake on hotplate from 90 °C to 125 °C
- Thermal cure in a tubular furnace oven at 300 °C, 2 hours, under N_2 atmosphere, to reach >98 % polymerization.
- Plasma CCP-RIE etching with a mixture of O_2 and SF_6 gases (50:10 flowrate ratio), at a pressure of 100 mTorr, a power of 50 W and a bias of (150 ± 10) V. The etch rate of planar BCB layers was calibrated using ellipsometry and is 315 nm min^{-1} in these conditions. **(c)**
- Due to different plasma etching dynamics in NW arrays, the etching rate is not linear and does not follow the calibration. Hence, multiple short etching sessions followed by SEM observation are needed to reveal the NW tips everywhere. **(d)**
- The SiO_x coating and eventual BCB residues are chemically removed in HF1 %, for a duration ranging from 1 min to 3 min. **(e)**

BCB planarization limitations

This planarization technique is not yet fully satisfying and suffers from some issues identified from SEM observation.

In some samples, the resulting BCB thickness after etching was not uniform, but presents locally thicker zones (Figure 5.4a), where the NWs don't emerge and as a result are not electrically contacted in the final device. I noted however that such inhomogeneities were correlated with the presence of an unusually long NW at the center (inset). As it emerges from the BCB before the others, it might act as an antenna and concentrate the electric field and the accelerated ions, to the detriment of the surrounding area. The BCB layer is also thinner at the pattern edge, within 50 nm (not shown), which might be due to proximity effects during RIE etching, or BCB reflow by capillarity before its full thermal cure.

Another limitation of this planarization technique is its thermal stability. After ITO deposition (Figure 5.3f), the sample may be annealed to improve the electrical contact, as described in the next subsection. While BCB-planarized layers could be annealed at 400 °C without apparent degradation, at 500 °C cracks in the ITO layer appeared, mostly at the array edges (Figure 5.4b). The glass transition of BCB is specified to be above 350 °C, densification might happen at higher temperatures. The ITO itself might densify upon annealing. If the adhesion to the BCB layer is degraded at high temperature, it might not be able to hold the stressed ITO film and thus let cracks appear.

[2] https://signupmonkey.ece.ucsb.edu/wiki/images/7/72/BCB-cyclotene-3000-revA.pdf

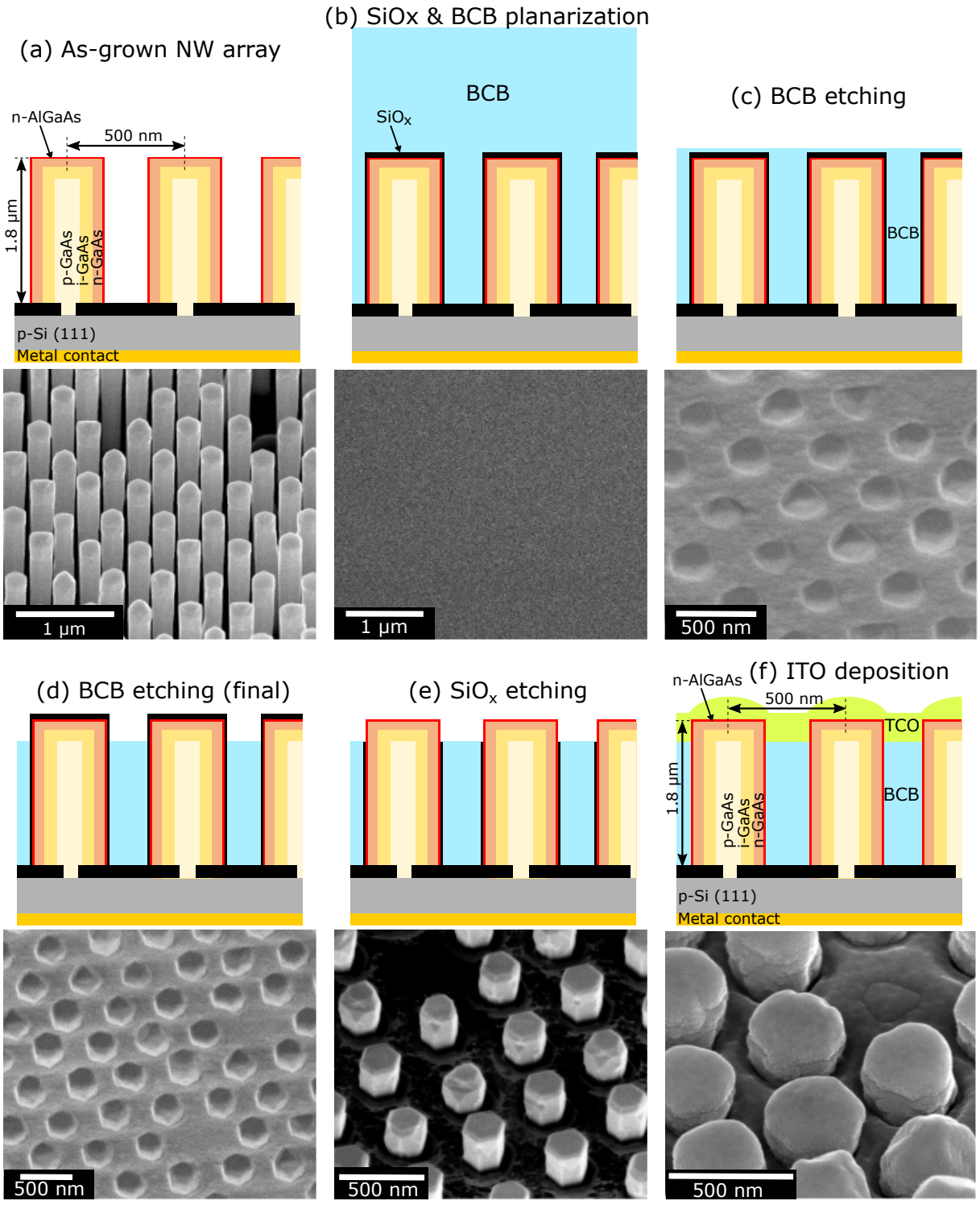

Figure 5.3: *Schematic side-view drawing and tilted SEM images of the NW array at the different stages of the planarization and contact deposition. (a-e): [76838] (f): [76890] after annealing.*

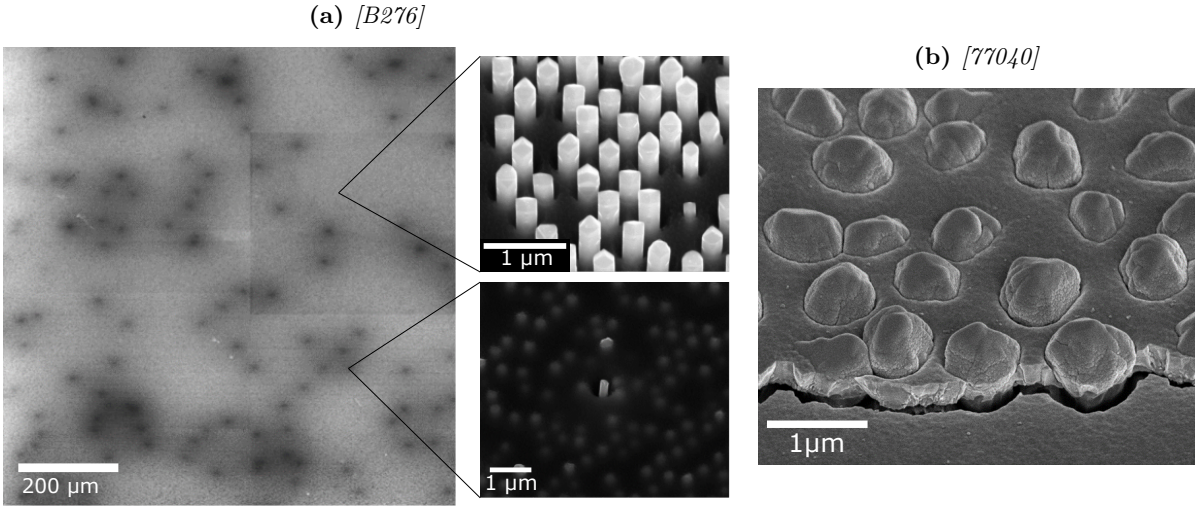

Figure 5.4: *(a)Large-field top-view SEM image of a BCB-planarized NW array after BCB etching. Lighter and darker areas are further investigated with zoomed-in SEM images, showing inhomogeneous BCB etching. (b) SEM overview of a processed NW array after a* 500 ℃ *annealing during* 1 min *in inert atmosphere.*

A planarization technique based on the use of SiO_x and BCB coating was developed. A rapid thermal treatment above 400 °C is found to induce cracks in the processed NW array, thus giving an upper limit for the post-fabrication contact annealing temperature.

5.2.2 Transparent contact deposition

Photolithography

Photolithography is widely used in the semiconductor manufacturing to replicate a mask pattern onto a sample, down to the µm resolution. In the NW solar cell fabrication process, a negative lithography process allows to open disks and rings inside a resist layer. Transparent contacts and metal contacts can then be selectively deposited (see Figure 5.7a).

The photolithography process is similar at C2N and IPVF, and comprises the following steps:

- Water desorption on a hotplate: 125 °C, >1 min
- Dispense of the light-sensitive resist AZ 5214 E (from the supplier MicroChemicals) with a syringe.
- Spin-coating at 4000 min^{-1}, 60 s, for a nominal 1.4 µm thick layer.
- Pre-bake: solvent degassing on hotplate at 125 °C
- First exposure. The mask consists of an opaque Cr pattern at the surface of a glass slab. It is placed in close contact to the sample surface ('soft contact' mode) and UV light from a Hg vapor lamp (filtered below the 405 nm emission line, 23 mW cm^{-2} measured in the setup at IPVF) illuminates the unshaded areas of the resist, to reach an energy density (or *dose*) of 0.2 J cm^{-2}.
- Inversion bake on a hotplate: 125 °C, >1 min. This enables the cross-linking of the resist in the exposed parts, which are later insoluble in the developer solution.
- Flood exposure. The whole sample surface is illuminated with the same lamp (about 1 J cm^{-2}, non-critical), without mask. Since there is no subsequent bake, this illumination makes the exposed resist soluble in a developer solution.
- Development. The sample is immersed in an alkaline solution (AZ826MIF) and manually stirred during 45 s to 60 s. Only the regions exposed only during the flood step are soluble

and get dissolved in the solution.

Photolithography is used to define ITO discs by lift-off, as illustrated in Figure 5.5.

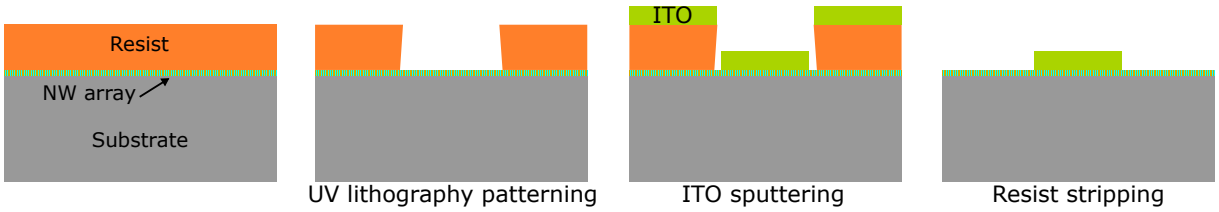

Figure 5.5: *Schematic of the lift-off process.*

Sputtering of ITO

To connect all NWs together and ensure sufficient lateral conduction, a transparent top contact is used. Here I describe the deposition of indium tin oxide (ITO) by sputtering, whereas the choice and optimization of the transparent contact is presented in Section 5.3. After photolithography, the sample is immersed in a 37 % HCl solution diluted in water (1:3) for at least 1 min, to remove the GaAs native oxide before contact deposition. At C2N, ITO deposition is performed in a Plassys MP800S chamber, using an ITO target (composition In_2O_3:SnO_2, 10:90) and under an Ar plasma at a pressure of 3 mTorr and a RF power of 200 W, for a nominal 120 nm thickness. At IPVF, a Plassys MP600 sputtering system is used, with an Ar pressure of 2 mTorr and a power of 200 W (typical bias of 120 V). The different conditions, electrode size and chamber configuration result in a different deposition rate, about 10 times slower than at C2N.

It results in a conformal and continuous layer on the NW tips and the BCB surface (Figures 5.3f and 5.6). The ITO layer exhibits a rough faceted morphology, suggesting a polycrystalline nature. After annealing, the surface morphology is more regular.

(a) *ITO annealed. [76890]*

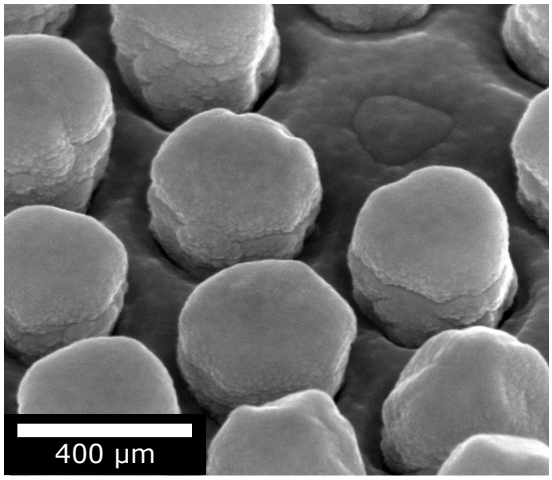

(b) *Extra ITO layer, not annealed. [77033]*

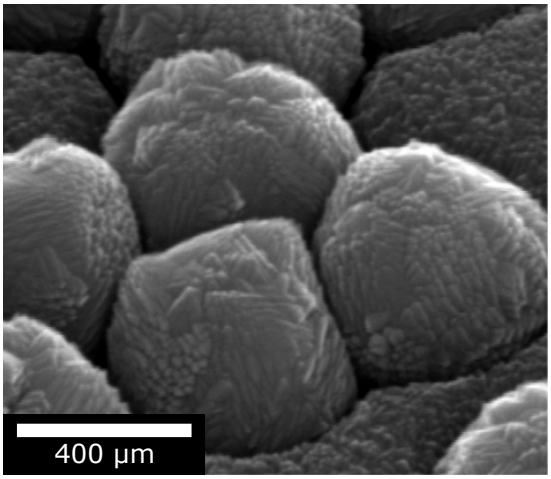

Figure 5.6: *ITO layer deposited on planarized NW arrays. In (a), a* 120 nm *thick ITO layer was annealed at* 400 °C *for* 1 min. *In (b), ITO was deposited in two-steps, and the topmost* 100 nm *thick ITO layer was not annealed. Viewed by SEM with a* 45° *and* 40° *tilt, respectively.*

5.2.3 Metal contacts and annealing

Metal pads deposition

To ensure a good mechanical and electrical contact with the point-probes used for electrical measurements, rings of metal contacts are deposited at the periphery of the ITO contacts (Figure 5.7a). Like for ITO, a negative photolithography step is performed on the sample, to open rings aligned with the ITO disks. Ti and Au are successively evaporated in a Plassys MEB550 SL electron-beam evaporator (20 nm and 200 nm, respectively), followed by lift-off. The resulting metal pads are continuous and conformal on the array of NW tips (Figure 5.7c).

The final device looks like the picture in Figure 5.7b, where more than 300 diodes with independent ITO/metal front contacts are defined by optical lithography from a NW array with a surface area of 1.5×1.5 cm. The blue color is caused by the light diffraction by the periodic array of NWs. The processed NW array was analyzed in cross-section by FIB milling and tilted SEM observation (Figure 5.7d). The NWs are found to be perfectly vertical, which suggests that the residual stress is negligible. The parasitic n-type GaAs/AlGaAs layer deposition on the mask surface is found to be relatively thin (<20 nm), probably due to the important shading in such dense NW array. The BCB layer is conformally filling the space between NWs and the SiO_x coating could not be identified from this SEM observation, though one can suppose that the voids present around the NWs close to the heads correspond to SiO_x etched in diluted HF when the NW heads were revealed. The ITO layer on top of the NWs is about 100 nm thick, thinner than the nominal 120 nm expected on planar layers, which could be due to densification upon annealing .

Annealing and ITO continuity

Finally, after an eventual first round of characterization, the solar cell device can be annealed in order to improve the electrical properties of the ITO/GaAs contact. It is performed in a rapid-thermal-annealing (RTA) oven, under inert atmosphere (Ar and H gas mix) at 400 °C during 1 min to 3 min, because higher temperatures lead to cracks in the BCB and ITO as previously discussed.

It is hard to assert if the ITO layer is continuous after annealing, as the SEM images (tilted view in Figure 5.6a and cross-section in Figure 5.7d) suggest the presence of a gap between the ITO coating the NW tips and the ITO coating the BCB surface, which might be due to the ITO densification upon annealing and crystallization. The NWs in Figure 5.6b were coated a second time with an additional ITO layer, in the IPVF setup which presents the advantage of having an ITO source tilted from the normal, and a rotating substrate holder, which might improve the coating conformity and the interconnection between ITO on top of the NWs and in between them. Electrical measurements before and after this extra step did not show any significant difference, suggesting that each NW was actually connected to the rest of the ITO film.

The planarized NW array can be processed by standard techniques for semiconductor thin-films. Transparent top contacts are defined and deposited through UV photo-lithography and sputtering of ITO, and ring-shaped metal pads are evaporated. The ITO electrical continuity is confirmed despite a change in morphology after annealing.

(a)

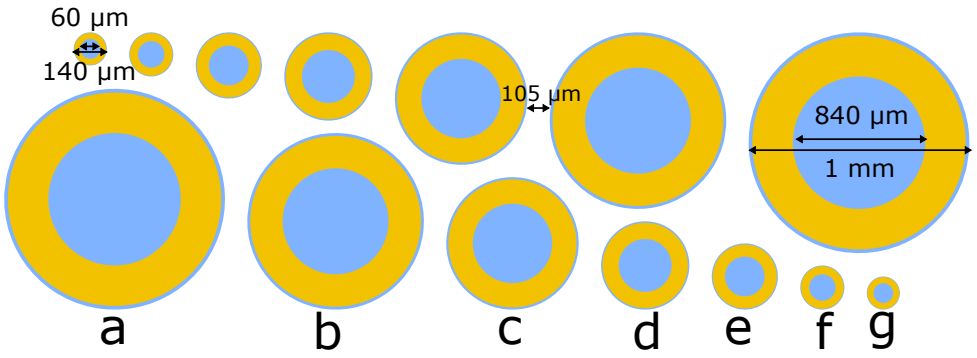

(b) *[76838]*

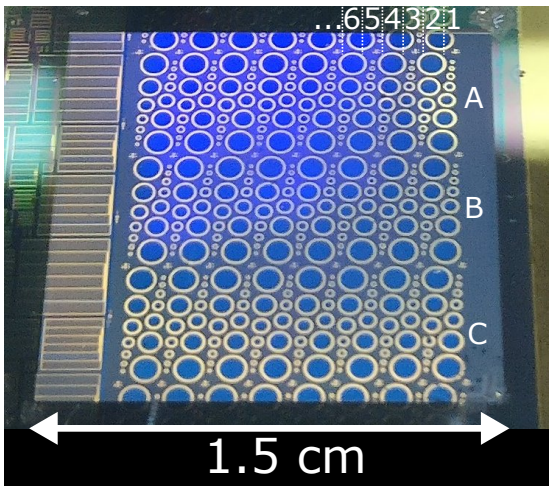

(c) *[76890]*

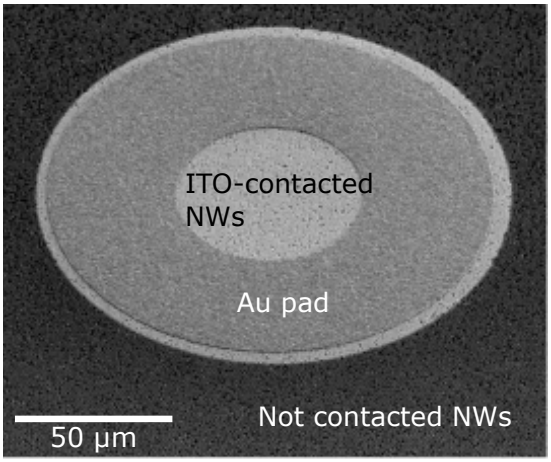

(d) *[76838]*

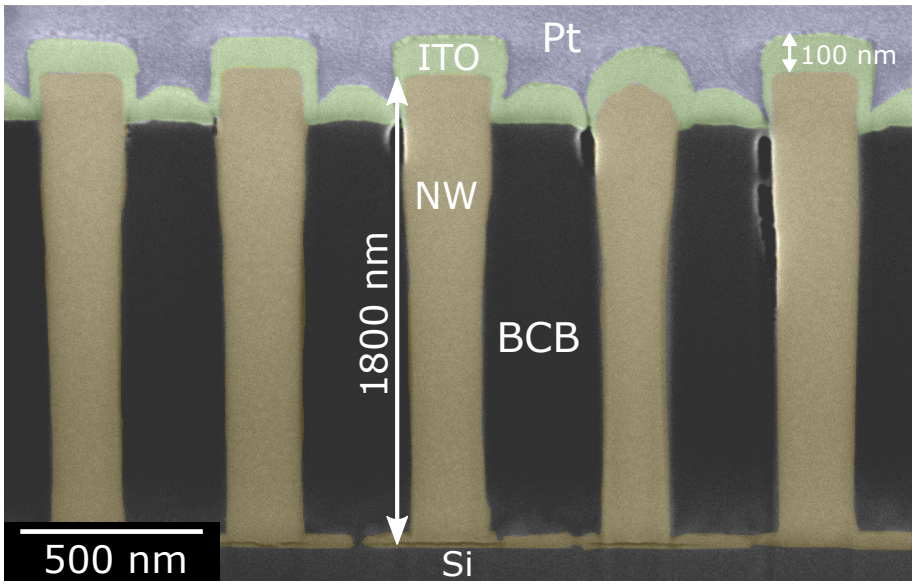

Figure 5.7: *(a) Nomenclature and dimensions of the diodes defined by photolithography. In a first step ITO disks are deposited, which contact NWs together (blue), and in a second step a Ti/Au (20/200 nm) annular pad is deposited to allow easy electrical contact. (b) Image of the fully processed* 1.5×1.5 *cm NW array, in the center of a 2" Si wafer. Each circle is an ITO & Ti/Au contact which delimits an individual diode, as depicted above. Each series of diode is localized with a letter for the column and a number for the row. (c) SEM overview of a NW diode of size g, viewed with a* $45°$ *degree tilt. (d) Cross-section of a fully contacted core-shell solar cell, viewed by SEM with a* $45°$ *degree tilt (colorized). The Pt layer present at the top is not part of the device but was locally deposited for protection during the FIB cross-section. [76838]*

5.2.4 Conclusion

Section: NW solar cell fabrication process

I have shown that a double-step planarization technique based on a thin SiO_x layer deposited by PECVD, followed by embedding in BCB is appropriate to planarize the NW arrays without residual stress, even though this process can be improved in term of thickness homogeneity. Standard thin-film fabrication techniques are then used, photo-lithography and lift-off to localize the contacts, sputtering of ITO to form front transparent contacts and evaporation of Ti and Au to make contact pads suited for electrical characterization with point-probes. The resulting ITO coating is found to be conformal. A thermal annealing is performed to improve the ITO/GaAs contact, but its temperature is limited to 400 °C, above which the BCB is degraded and cracks occur in the processed array.

In 2019, this fabrication process was re-developed and adapted to IPVF facilities and equipment, allowing for the fabrication of a new series of devices in the end of 2019.

In particular, I have fabricated hundreds of functional devices on a 1.5×1.5 cm NW array, ready for opto-electrical characterization.

5.3 Optimization of an indium-tin oxide front contact

ITO (In_2O_3:SnO_2) is a polycrystalline material generally considered as a wide bandgap (<3.75 eV), degenerated semiconductor, with typical electron concentrations of $10^{21}\,cm^{-3}$, and mobilities in the 15-40 $cm^2\,V^{-1}\,s^{-1}$ range [Chopra et al. 1983]. ITO has been used as a transparent contact for thin-film PV materials like perovskites or CIGS. However, it has not been studied as well for the fabrication of contact on III-V layers, for which the epitaxy of a wide-bandgap doped layer (window layer) is a better alternative. Moreover, ITO was shown to form an important Schottky barrier (see Figure 5.8) at the interface with n-GaAs or InGaP ([Parker 1987]; [Bachmann et al. 1979]; [Balasubramanian and Subrahmanyam 1990]; [Morgan et al. 1992]; [Lee et al. 1998]). It was often pointed as an interface limiting the performances of NW solar cells ([Otnes et al. 2018]). In this section, I study and optimize the electrical contact between ITO and n-doped III-V planar layers.

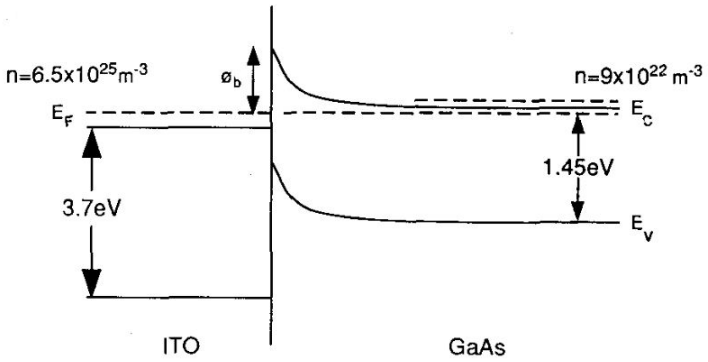

Figure 5.8: *Proposed band structure model for a n-GaAs/ITO contact. From [Morgan et al. 1992].*

5.3.1 Method: planar ITO layers characterization

In order to study the contact resistance between the n-type III-V semiconductor and the ITO, I fabricated planar devices schematically represented in Figure 5.9. I have grown three different III-V semiconductor thin films (GaAs, InGaP (≈ 100 nm-thick) and $In_{0.25}Ga_{0.75}As$ (≈ 5 nm-thick)) in the Compact21 MBE, with two different doping concentrations ($n = 1.5 \times 10^{18}\,cm^{-3}$ and $n = 1.7 \times 10^{19}\,cm^{-3}$), or directly used the n-GaAs substrate (nominally doped to $(1.5 \pm 0.5)\,cm^{-3}$).

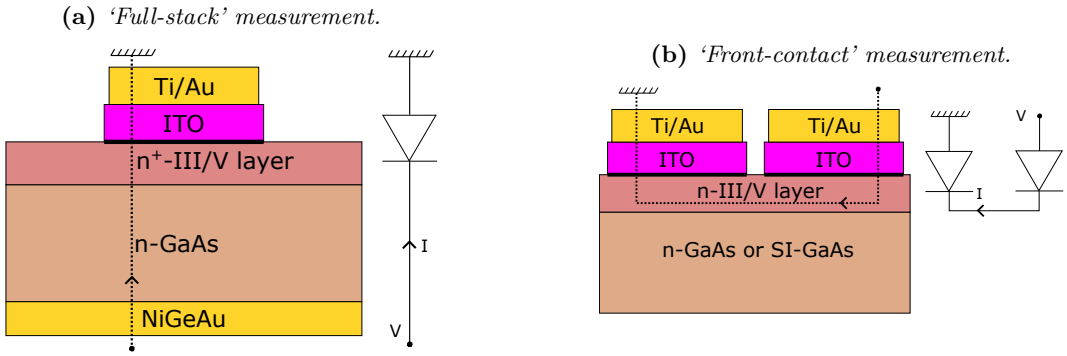

Figure 5.9: *Schematic of the stack configurations used to evaluate the electrical contact between ITO and various III-V layers, and the equivalent electrical circuit, assuming that the ITO/III-V contact dominates other resistances. The first (a) is called* full-stack*, and the second (b) is called* front-contact*, in which the carriers cross two times the interface with ITO, in opposite directions.*

After epitaxy, a Ni/Ge/Au contact is formed on the entire backside, by electron-beam evaporation. On the frontside, circular ITO(150 nm to 200 nm)/Ti(20 nm)/Au(200 nm) contacts with

different diameters (Figure 5.7a) were fabricated by optical lithography and lift-off, using the sputtering tool at IPVF (MP600). The fact that metal evaporation is more directional than ITO sputtering ensures that the metal contact do not spill outside the ITO contact and touch the III-V.

As for the electrical measurement, the first configuration is the 'full-stack' measurement where the III-V/ITO characteristic is directly investigated (Figure 5.9a). Note that the current convention of the NW solar cell structure is used here, and that the Schottky contact forward bias corresponds to $V < 0$. I use the contact resistivity (in $\Omega\,\mathrm{cm}^2$) calculated at $V = 0$ as a figure of merit to characterize the contact. In this configuration, the contact resistivity is defined as :

$$\rho_c = S \times \left.\frac{\mathrm{d}V}{\mathrm{d}I_{\text{full-stack}}}\right|_{V=0} \tag{5.1}$$

with S the surface of the contact, assuming that the ITO/III-V contact dominates the other resistances in the stack.

For front-contact measurements between two top contacts (possibly with different surface areas), it is defined as:

$$\rho_c = S_{\text{eff}} \times \left.\frac{\mathrm{d}V}{\mathrm{d}I_{\text{front-contact}}}\right|_{V=0} \tag{5.2}$$

Where $S_{\text{eff}} = \frac{S_1 S_2}{S_1 + S_2}$ is an effective surface for both contacts.

The assumption that the other resistances are negligible is sensible:

1. The contact with Ti/Au is considered ohmic since ITO is a degenerate semiconductor with a high carrier concentration.
2. For the sample of the *full-stack* structure (Figure 5.9a), at the back contact made of Ni, Ge and Au (which is not fully ohmic before annealing), and at the n-GaAs/n^+-III-V interface (expected to be conductive), the contact area is the whole sample surface, which is large relative to the ITO contact surface area (usually by a factor >10).
3. The n-GaAs substrate resistivity is $(2.0 \pm 0.5) \times 10^{-3}\,\Omega\,\mathrm{cm}$ as specified by the supplier, which amounts to a surface resistivity through a 350 µm thick substrate of $\rho_s^{\text{subs}} = 7 \times 10^{-5}\,\Omega\,\mathrm{cm}^2$, negligible compared to the ITO contact surface resistivity measured below.
4. For the samples with the 'front-contact' structure (Figure 5.9b), the lateral resistance through the III-V layer is imperceptible. This design was initially chosen to make *transmission line measurements* (TLM), but the sheet resistance was found to be negligible compared to the contact resistances, independently of the contact spacing and aspect.

5.3.2 Influence of the doping level on the ITO/III-V contact resistance

In Figure 5.10a, the n-GaAs/ITO characteristics of the different stacks are directly shown, using axis scales consistent with the JV measurement of solar cell devices, to have an immediate information about their detrimental influence on the PV performances. All three layers with high doping ($n^+ = 1.7 \times 10^{19}\,\mathrm{cm}^{-3}$) doped layers appear as fully conductive (vertical dashed lines). For moderate doping ($n = (1.5 \pm 0.5) \times 10^{18}\,\mathrm{cm}^{-3}$), the contact with n-InGaP and n-GaAs is found to be non-ohmic, with a rectifying characteristic in the reverse direction. This is in agreement with [Zhang et al. 2014a] who found an order of magnitude improvement of ρ_c for ITO on n-GaAs:Te NWs, by increasing the dopant concentration by 60 % while in the $10^{18}\,\mathrm{cm}^{-3}$ range.

The contact resistivities were also calculated in the front-contact configuration according to Equation 5.2. The values determined with this measurement (Figure 5.10b) are consistent with the 'full-stack' configuration.

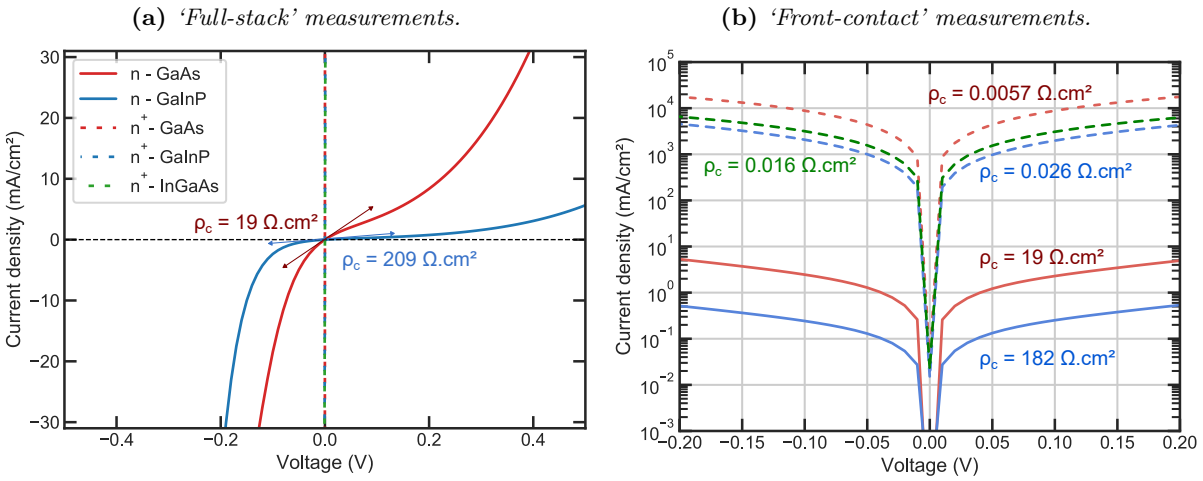

Figure 5.10: *JV characteristic of an ITO contact on different III-V materials doped to* $n = (1.5 \pm 0.5) \times 10^{18}\,\mathrm{cm}^{-3}$ *or* $n^+ = 1.7 \times 10^{19}\,\mathrm{cm}^{-3}$. *For n-GaAs, the substrate is directly used. (a) JV characteristic in linear scale in 'full-stack' configuration. The contact resistivity calculated according to Equation 5.1 is indicated. (b) Same samples measured in the 'front-contact' configuration. The contact resistivity calculated according to Equation 5.2 is indicated for all curves. [c1_b2,B281_b1], B272_b1, B268_b1, B273_b1*

Independently of the doping level, the n-GaAs/ITO contact is more conductive than the n-GaInP/ITO. This suggests the presence of a higher Schottky barrier at the interface with GaInP, consistently with the fact that it has a higher bandgap than GaAs. The n^+-InGaAs layer is also very conductive, but not more than n^+-GaAs, so I choose to avoid InGaAs in our designs and studies, for the sake of simplicity.

Despite these good results using highly doped layers, I know from the study of the doping (Section 4.2) that GaAs NW shells cannot yet be doped above $10^{18}\,\mathrm{cm}^{-3}$, which might also be the case for GaInP. Consequently, I need to focus on the contact to GaInP and GaAs layers doped in the low $10^{18}\,\mathrm{cm}^{-3}$ range, and improve them through other means.

In order to assess quantitatively the effect of such resistive contact on a NW solar cell, the voltage drop at this interface at the device working point can be roughly estimated. The ITO/n-GaAs shell contact area is not the same as the illuminated area. It is, for one NW:

$$S_{\text{NW contact}} = \underbrace{\pi \frac{D_{NW}^2}{4}}_{\text{top facet}} + \underbrace{h_{\text{exposed}} \times \pi D_{NW}}_{\text{exposed sidewalls}}, \tag{5.3}$$

where h_{exposed} is the height of the NWs emerging from the BCB. Conversely, the illuminated area around one NW in a hexagonal array is:

$$S_{\text{unit-cell}} = p^2 \times \sin(60°), \tag{5.4}$$

where p is the array pitch, 500 nm. Using the dimensions estimated from the cross-section SEM image in Figure 5.7d ($D_{NW} = 220\,\text{nm}$ and $h_{\text{exposed}} = 150\,\text{nm}$), the ratio of the ITO/GaAs contact and illuminated surface contact areas is:

$$R_{\text{surf}} = \frac{S_{\text{NW contact}}}{S_{\text{unit-cell}}} = 0.65 \tag{5.5}$$

Assuming that in a GaAs NW tandem solar cell on Si, $J_{sc} = 20\,\text{mA}\,\text{cm}^{-2}$ [Yao et al. 2015], the current across the ITO/shell interface is then $J_{NW} = \frac{-J_{sc}}{R_{\text{surf}}} = -31\,\text{mA}\,\text{cm}^{-2}$. Using the JV characteristic in Figure 5.10a, it results in a voltage loss close to the solar-cell working point of

about −0.16 V and −0.20 V for n-GaAs and n-GaInP, respectively. This is highly detrimental as the V_{oc} is already expected to be low, typically 0.4 V for state-of-the-art NW solar cells on Si.

> The contact between ITO and highly doped III-V layers is perfectly conductive, whereas it has a Schottky characteristic on GaAs and GaInP doped to $n \leq 2 \times 10^{18}\,\mathrm{cm}^{-3}$, which would results into a substantial voltage loss in NW devices. However, since NW shells suffer from doping compensation, the ITO contact on these moderately doped layers must be optimized.

5.3.3 Benefits of annealing the ITO/III-V contact

Improvement of the conductivity

The previous n-GaAs stack was annealed in air at increasingly higher temperatures, each time for a duration of 1 hour, to investigate the influence on the contact resistivity.

In particular, a significant contact resistivity improvement is observed after annealing at 400 °C, as shown in the 'full-stack' forward JV characteristic in Figure 5.11. Besides the overall current increase, there is a change of behavior from an exponential curve, expected for a reverse-biased Schottky diode [Sze and Ng 2006], to a linear (ohmic) one after annealing. Before annealing, the curve can be fitted with a forward diode model with an ideality factor of 8, which is useful to compare with the forward characteristic of our final NW solar cell devices.

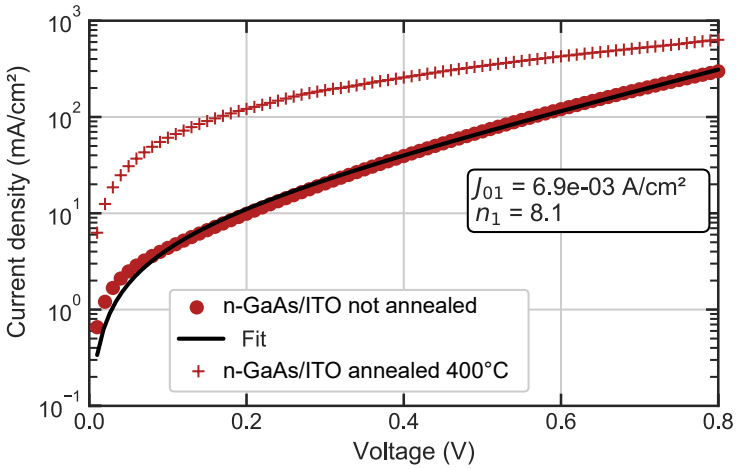

Figure 5.11: *Reverse-current ($V > 0$ in the 'full-stack' configuration) of a typical n-GaAs/ITO contact, plotted in logarithmic scale before and after annealing at* 400 °C *in air for* 1 h. *The curve before annealing is fitted with a diode model in forward bias to extract an apparent ideality. [c1_b2]*

In previous works, the Schottky behavior of n-GaAs/ITO contacts was reported to be altered after annealing, with increased currents and a lowered Schottky barrier height, possibly due to diffusion of Sn forming an n^+ layer in the GaAs [Morgan et al. 1992]. However, with other deposition techniques and annealing conditions, the inter-diffusion of Sn and/or In might not be enabled and lower currents can be obtained after annealing [Balasubramanian and Subrahmanyam 1990].

However, this annealing lacks robustness since:

- I observed some diode-to-diode variation of the JV characteristic over the sample surface.
- Before this transition to an ohmic behavior at 400 °C, the resistivity was following an opposite trend, increasing up to 300 °C

- N-GaAs/ITO contacts from another deposition run but prepared identically as in Figure 5.11 were found to become conductive after annealing above 500 °C instead of above 400 °C (not shown)

Therefore, long annealing in air might not be suited for such sensitive effects, and the optimization should be performed in more reproducible conditions.

Improvement of the transparency

The transmittance of ITO before and after annealing was studied using 200 nm thick ITO layers deposited on a 3 mm thick soda-lime-glass slab. The annealing conditions were not the same as previously as the stack was annealed for a shorter duration (10 min) and at a higher temperature (540 °C) in air.

As seen in Figure 5.12, before annealing, the ITO-on-glass transmittance is affected by parasitic absorption and reaches 80 % at 700 nm, while being as low as 60 % at 500 nm and below. After annealing, the transmittance is greatly improved especially in the low-wavelength region, and remains between 75 % and 90 % from 350 nm to 1000 nm. Compared to the bare glass slab, the only significant transmission loss is a drop at 450 nm and a slight decrease after 700 nm.

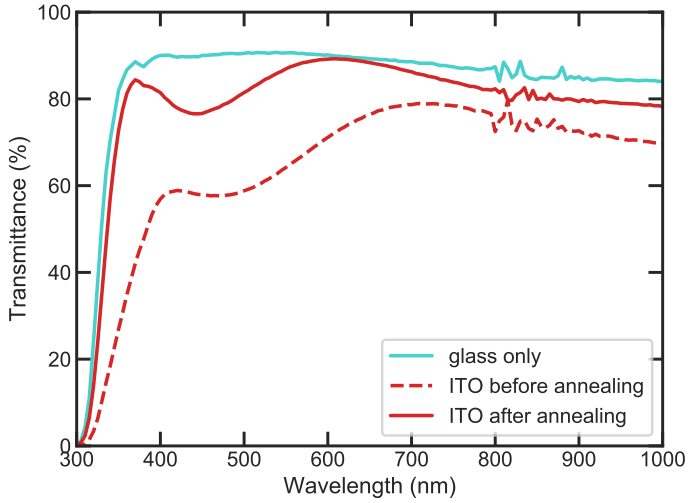

Figure 5.12: *Transmittance of a* 200 nm *thick ITO layer sputtered on a* 3 mm *thick soda-lime glass slab, before (dashed red line) and after (full red line) annealing at* 540 °C *in air during* 10 min. *The transmittance of the bare glass slab is plotted for comparison (cyan). [ITO_200_2; ITO_200_1]*

ITO/n-GaAs contacts becomes ohmic after annealing in air above 400 °C. The transparency of ITO deposited on glass is also found to greatly increase after a 540 °C annealing, with <10 % transmission loss compared to a bare glass slab.

5.3.4 Optimization of the ITO/n-GaAs contact resistance by rapid annealing in inert atmosphere

Annealing of n-GaAs/ITO contact in air seems to improve the contact resistance after 400 °C. However, annealing of BCB in oxidizing atmosphere above 150° leads to its deterioration, so I instead perform the annealing under inert atmosphere (mix of Ar and H_2 gas) in a rapid thermal oven, which should also improve the reproducibility. The presence of O_2 ambient during ITO

annealing was reported to alter its properties [Lee et al. 1998], however in the previous electrical study the ITO was encapsulated under a gold contact and not directly exposed to air, so a similar result is expected after annealing in inert atmosphere.

For this study, epitaxially grown GaAs layers were used ($n = 1.5 \times 10^{18}\,\mathrm{cm}^{-3}$ as measured by Hall effect) on semi-insulating substrate, separated by a 50 nm-thick AlGaAs insulator, and contacts were measured on the front side (*front-contact* configuration in Figure 5.9b). A 200 nm thick ITO layer was deposited by sputtering in the MP800 equipment at C2N.

The resistivity of all contacts steadily decreases up to 350 °C at which point the average contact resistivity strongly decreases until 500 °C, down to below $10^{-2}\,\Omega\,\mathrm{cm}^2$ (Figure 5.13).

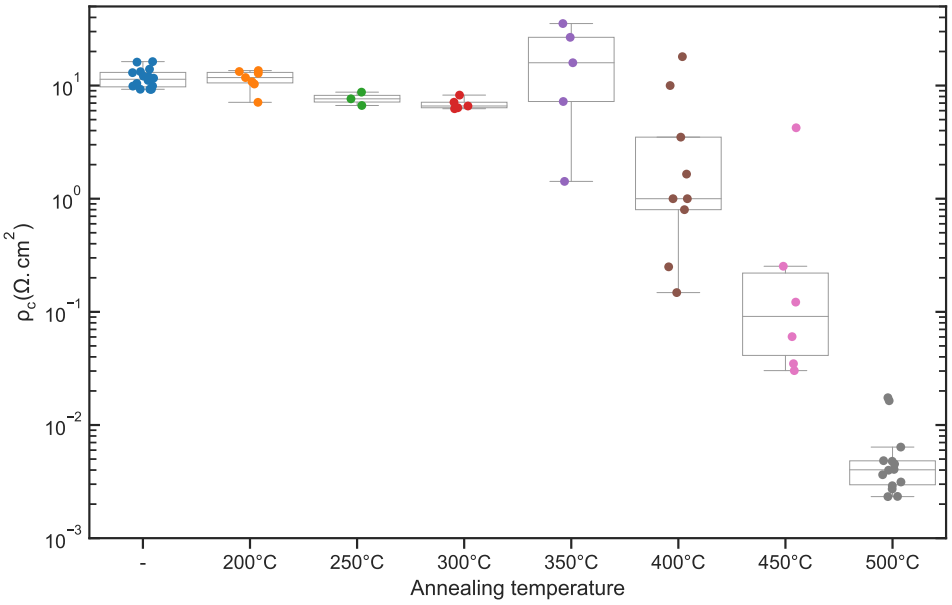

Figure 5.13: *Evolution of the contact resistivity ρ_c of a n-GaAs/ITO contact after successive annealings during* 1 min *in inert atmosphere, plotted in logarithmic scale. For each condition, different contacts (dots) were measured on the same sample. The boxes and the whiskers show the quartiles and the entire extent of the distribution, respectively, excluding outlier points (beyond 1.5 times the interquartile range).*

For ohmic but resistive contacts, a resistivity ρ_c leads to a voltage drop in NW solar cells approximately equal to:

$$\Delta V = \rho_c \times \frac{J_{sc}}{R_{surf}} \tag{5.6}$$

With $\rho_c = 10^{-2}\,\Omega\,\mathrm{cm}^2$ and $J_{sc} = 20\,\mathrm{mA\,cm}^{-2}$, $\Delta V = 0.2\,\mathrm{mV}$ which is not impacting the PV performances.

However, as previously mentioned, the processed NW arrays cannot withstand such high temperature without cracks, due to BCB instability. The NW solar cells are thus annealed at 400 °C, where the contact resistivity varies from $0.1\,\Omega\,\mathrm{cm}^2$ to $10\,\Omega\,\mathrm{cm}^2$. For $\rho_c = 10\,\Omega\,\mathrm{cm}^2$, $\Delta V = 200\,\mathrm{mV}$. This is an upper limit for the voltage loss, as the contact is then still Schottky and not linear like it is assumed for Equation 5.6. Still, such contact should have a noticeable impact on the JV curve of the solar cell.

The fluctuations between different contacts on the same sample, observed after annealing at temperatures between 350 °C and 450 °C may arise from spatial inhomogeneities over the sample surface, for example due to the presence of defects in the epitaxial growth film, or due to an uncontrolled reoxidation of the GaAs at the interface, which may lead to uneven ITO adhesion and contact. Two mechanisms seem to be activated above 300 °C, one increasing the resistivity (as already observed for the samples annealed in air), and one decreasing it (possibly the diffusion of In or Sn into GaAs). The competition between these effects might depend strongly on the

exact interface configuration, and therefore either increase, or lower the resistivity. Above 450 °C, the mechanism lowering the conductivity prevails over the one increasing it.

An ITO/n-GaAs contact can be greatly improved through rapid annealing in inert atmosphere and made suitable for the device working conditions. However, processed NW arrays are restricted to annealing temperatures up to 400 °C, at which the contact is improved on average but with fluctuations.

5.3.5 Conclusion

Section: Optimization of an ITO front-contact

I have studied a contact made of ITO deposited on planar III-V layers. A Schottky contact is observed on III-V layers doped at $n = (1.5 \pm 0.5) \times 10^{18}\,\mathrm{cm}^{-3}$, whereas a conductive ohmic contact is obtained on layers doped at $n = 1.5 \times 10^{19}\,\mathrm{cm}^{-3}$.

Upon annealing at 540 °C in air, the transparency of ITO deposited on glass is found to greatly improve and reach 80 % transmittance. The electrical characteristic of the contact was also found to improve for ITO-on-GaAs.
A reproducible annealing scheme is chosen to optimize a n-GaAs/ITO contact, using rapid thermal annealing in inert atmosphere. The contact resistivity was found to improve above 350 °C down to below $10^{-2}\,\Omega\,\mathrm{cm}^2$ at 500 °C, fully compatible with the NW device working conditions.

However, the processed NW arrays can only be annealed at 400 °C, temperature at which the contact with ITO is not homogeneously improved over the sample surface, which is expected to have a noticeable impact on the solar cell performances.
As the doping level in the external GaAs shell was shown to be compensated n-type, with low electron concentration, the ITO contact on actual NW devices might differ significantly to that measured on planar layers.

5.4 Characterization of a GaAs core-shell homojunction solar cell

Among the 15 to 20 NW solar cell samples fabricated, many were shunted due to processing issues, or showed low performances due to poor yield or sample homogeneity. Here, I present a core-shell homojunction grown on a full 2" wafer, and which exhibited above-the-average performances, probably thanks to a particularly high vertical yield (above 90 %, see Figure 3.28, page 97).

5.4.1 Sample presentation

This *NW homojunction* sample consists in a GaAs p-i-n core-shell structure passivated with an AlGaAs shell, as shown in Figure 5.14. It is the sample presented in the previous section (76838), with 1800 nm long NWs (see Figure 5.7d for example).

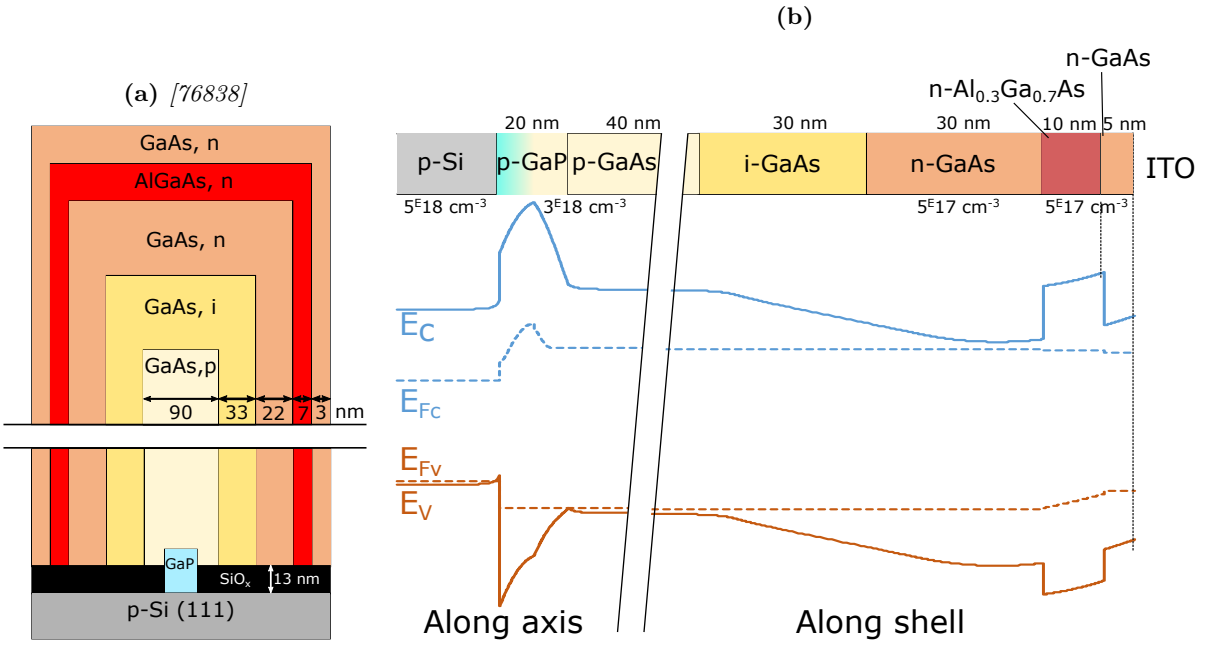

Figure 5.14: *(a) Schematic of the shell dimensions in the core-shell GaAs homojunction with an AlGaAs passivation (sample 76838). (b) 1-D simplified band structure along the NW axis and shell, using the doping concentrations expected by comparison with previous CL measurements, and approximative dimensions. Calculated at the open-circuit voltage and for a homogeneous photogeneration in all layers. Not at scale. The front contact comprising the n-GaAs cap and the ITO is represented by a recombining contact with a Schottky barrier for the electrons.*

Nanowire growth

In the Riber32 MBE machine, the p-type NW core growth was initiated with a 1 min Ga pre-deposition (45 $ML_{GaAs(100)}$) at a substrate temperature of (607 ± 3) °C, without Be flux. The Ga flux during core growth is set to 2.1 Å s^{-1} and a GaP:Be foot is grown during 20 s at a P/Ga flux ratio of 1, before linearly closing the P valve while opening As, over 20 s. The main core segment is grown under an As/Ga flux ratio of 1.3, and a Be flux of 4.6×10^{11} cm^{-2} s^{-1}, during 13 min. The droplet consumption is performed during 25 min at the same temperature by shutting down the Ga flux and using an As_4 flux at 19 % of its value during core growth, which should lead to a minimized re-growth at the tip, and very few crystal defects as shown in Chapter 3. However, the temperature determination by infrared pyrometry might differ for this 2" Si substrate compared

with the 1/6 2" samples used for the droplet consumption optimization. The temperature is then stabilized at 580 °C and an intrinsic GaAs shell is then grown during 30 min at a Ga flux of 0.75 Å s^{-1}, under an excess of As_4. The substrate temperature is finally set to 450 °C for the growth of a n-GaAs:Si shell during 20 min in conditions that would give a doping level of 4×10^{18} cm^{-3} in GaAs(100) thin-films. The shell is terminated by a 5 min n-AlGaAs:Si shell (planar doping level of 2×10^{18} cm^{-3}) followed by a 3 min GaAs capping shell (average planar doping level of about 10^{18} cm^{-3}).

Dimensions and doping levels

The NWs height ($h_{NW} = 1800$ nm) and diameter ($D_{NW} = 220$ nm) can be obtained by examining the SEM images after the growth. The amount of material in the NW array can be expressed as the thickness of an equivalent planar thin-film, using the relation:

$$t_{\text{thin-film}} = h_{NW} \times \underbrace{\frac{\pi D_{NW}^2}{4}}_{S_{1NW}} \times \underbrace{\frac{p_{\text{array}}^2 \sin(60°)}{2}}_{S_{\text{array unit cell}}}, \tag{5.7}$$

where p_{array} is the pitch of the hexagonal NW array. The volume of the absorber (GaAs), is equivalent to a $t_{\text{thin-film}} = 630$ nm-thick GaAs planar device. This allows for a comparison of the performances (notably the light-trapping properties) with ultrathin planar GaAs solar cells (where the absorber can be as thin as 205 nm [Chen et al. 2019]).

As a result of Equation 4.1 (page 118), a shell with composition $Al_{0.30}Ga_{0.70}As$ is expected in the shell sidewalls, using growth conditions that would result in $Al_{0.44}Ga_{0.56}As$ in planar growth.

Finally, the shell thicknesses are estimated by rescaling the expected sidewall growth rates to the actual total shell thickness (subtracting 90 nm for the core, as measured at the end of the VLS growth of NWs grown in similar conditions), and reported in Figure 5.14a. Note that it is only a rough estimate and that significant deviations are expected due to :

1. The diffusion dynamics of group-III adatoms which vary depending on the species, and on the growth temperature. Some shells may collect more material from the mask, or may be more sensitive to the shading by surrounding NWs. NW shells in Section 4.2 (page 146) were found to be between 20 % and 40 % thicker than expected, and up to 100 % thicker for the shells grown at 580 °C, which is the case for the intrinsic shell here.
2. The precision on the NW core estimation, which is found to vary between growth and after droplet consumption (typically within ±10 nm).
3. The NW tapering: the shell is thicker close to the NW head than towards the foot.

The doping levels can be estimated by analogy with the NWs characterized by CL in the previous chapter, taking into account the growth duration and the length of the core (approximately 3/4 of the final length, excluding the shell tip segment and the droplet crystallization segment). I expect $p = 3 \times 10^{18}$ cm^{-3} in the core and $n < 4 \times 10^{17}$ cm^{-3} in the GaAs shells, and also in the AlGaAs shell by extrapolating the doping behavior of GaAs shells to AlGaAs shells.

For the Si substrate, the doping level is estimated from the nominal conductivity (see Table 2.3, page 59).

Band structure

The band structure in such a 3D object is difficult to simulate. It can be represented with a 1D estimate along the path followed by both carriers : from the substrate to the NW core, and from the core to the shell (Figure 5.14b). In this representation, the band structure is plotted for a constant photogeneration along the stack (except the Si and GaP), equivalent to 20 mA cm^{-2}, and at the open-circuit voltage (V_{oc}). The parameters used are taken from Adachi's textbook

[Adachi 2009], and the 1D simulations are realized with SCAPS, a free software developed at the University of Gent (Belgium) and dedicated to solving the drift-diffusion equations in 1-D with additional features adequate for solar cells (defects, etc.) [Burgelman et al. 2013][3]. A doping concentration $p = 5 \times 10^{18}\,\mathrm{cm}^{-3}$ is used for the Si substrate, $p = 3 \times 10^{18}\,\mathrm{cm}^{-3}$ for the GaP foot and GaAs core, and $n = 5 \times 10^{17}\,\mathrm{cm}^{-3}$ for the GaAs and $Al_{0.3}Ga_{0.7}As$ shells.

There are important barriers along the path of carriers at the GaP foot (barrier for extracted holes) and at the GaAs/$Al_{0.3}Ga_{0.7}As$ shells interface (335 meV conduction band offset for extracted electrons). The simulated JV curve corresponding to this structure is plotted in Figure 5.15, with and without the Si substrate.

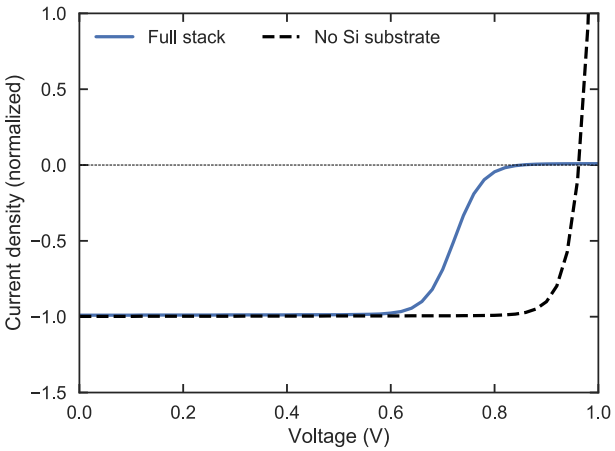

Figure 5.15: *Simulated JV curve under illumination for the 1D structure corresponding to Figure 5.14b, with and without including the p-Si substrate. Simulated in 1D with SCAPS, using a constant generation rate, only in the GaAs junction. The current is normalized to the total photogenerated current.*

The structure which does not include the Si substrate yields the curve of an ideal solar cell, with a V_{oc} close to 1 V, an exponential shape and a perfect collection efficiency, defined as the proportion of photogenerated carriers collected at short-circuit:

$$\eta_{col.} = \frac{J_{sc}}{J_{ph}} \tag{5.8}$$

This indicates that, despite low n-type doping levels ($n = 5 \times 10^{17}\,\mathrm{cm}^{-3}$), a 1D p-i-n GaAs solar cell with such small dimensions is still expected to operate properly.

However, an important departure from ideality occurs for the structure including the Si substrate. At bias above 0.6 V, the current is quenched which results in a lower FF. In the band structure, it can correspond to the GaP foot, fully depleted of carriers due to diffusion to the adjacent Si and GaAs layers with lower bandgaps. This effect should be considered when analyzing the experimental JV curves, however the 3D structure of the NW is more complicated and the carrier diffusion might lead to a different situation. The NW foot is largely unknown, in particular the length of the GaP inclusion and its doping level, as well as the intermixing at the Si interface. If the foot is thin and doped enough, hole tunneling might even be expected at this interface [Boulanger et al. 2016].

Device characterization

On this sample, the diode performances are relatively homogeneous over the 1.5×1.5 cm patterned area, as seen in Figure 5.20 where the compiled results from the JV characteristics of about 20 diodes from the homojunction sample are displayed. In the following, the characterization curves of one representative diode are shown and analyzed.

[3] http://scaps.elis.ugent.be/

A GaAs core-shell homojunction passivated with AlGaAs was grown and processed into individual diodes. A simplified 1-D model of the junction suggests that depletion in the GaP foot could lead to degraded electrical performances, but that the junction should otherwise be functional with the estimated doping levels and dimensions.

5.4.2 External quantum efficiency

The external quantum efficiency (EQE) of the homojunction solar cell diode is presented in Figure 5.16. The overall EQE is quite low, never reaching 50 %, whereas it would be close to unity in the case of perfect absorption and collection. The shape is consistent with expectations for GaAs solar cells, with a sharp decrease close to the GaAs bandgap (871 nm at room-temperature), and a decrease at low wavelengths (below 500 nm) typically due to absorption in the first layers (transparent oxide, window layer) where the carriers recombine without being collected.

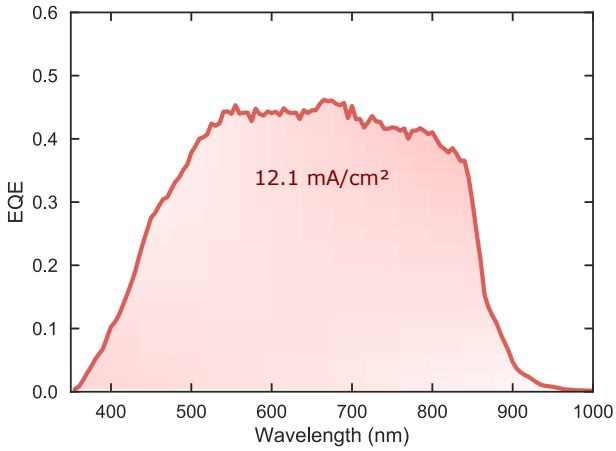

Figure 5.16: *EQE of the NW homojunction. [76838, A16_a]*

The short-circuit current (J_{sc}) can be calculated from the EQE with the relation 2.28 (page 67).

I find $J_{sc} = 12.1\,\mathrm{mA\,cm^{-2}}$, about half as low as what was obtained for ultrathin (200 nm absorber) GaAs solar cells ($J_{sc} = 24.6\,\mathrm{mA\,cm^{-2}}$, [Chen et al. 2019]), despite the three times higher equivalent GaAs thickness, and 2.5 times lower than the best performing GaAs planar solar cell ($J_{sc} = 29.7\,\mathrm{mA\,cm^{-2}}$, ([Kayes et al. 2011]; [Green et al. 2019])).

Due to light scattering, specular reflectivity measurements could not be performed on our NW solar cells that would allow to decorrelate with certainty absorption issues from carrier collection issues. However, with a NW diameter of 220 nm, and our array dimensions, absorption is expected to be close to 80 % for most wavelengths. The imperfect vertical NW yield for this sample (95 %) may lower the overall absorption. Due to the NW length and BCB thickness inhomogeneity, some NWs may also remain buried inside the BCB and not contacted, thereby not contributing to the photogenerated current. The parasitic layer on the mask was found from SEM observation to be very thin (see Figure 5.7d, page 183), so it should not cause major parasitic absorption. Therefore, and since the EQE is quite symmetrical, I infer that it is mainly limited by the carrier collection.

The EQE of a representative diode of the best core-shell GaAs homojunction sample is lower than expected but the shape is consistent with expectations for GaAs. I infer that the low EQE is due to poor carrier collection.

5.4.3 Current-voltage characteristics

JV in the dark and under illumination

The normalized current-voltage (JV) curves in the dark and under a solar simulator illumination are shown in Figure 5.17a. The cell exhibits low performances (1.5 % efficiency) and several departures from ideality. First, the short-circuit current (J_{sc} = 11.8 mA cm^{-2}) is consistent with the one calculated from the EQE measurement (12.1 mA cm^{-2}). The lamp used in the solar simulator is supposed to match the tabulated AM1.5G illumination using a broadband lamp and filters, but it is calibrated on Si cells and small spectral mismatches can lead to noticeable changes in J_{sc} estimation for other solar cell materials with different spectral response. The J_{sc} value from the EQE and the FF and V_{oc} from the JV measurement yield an efficiency $\eta^* = 1.51$ %.

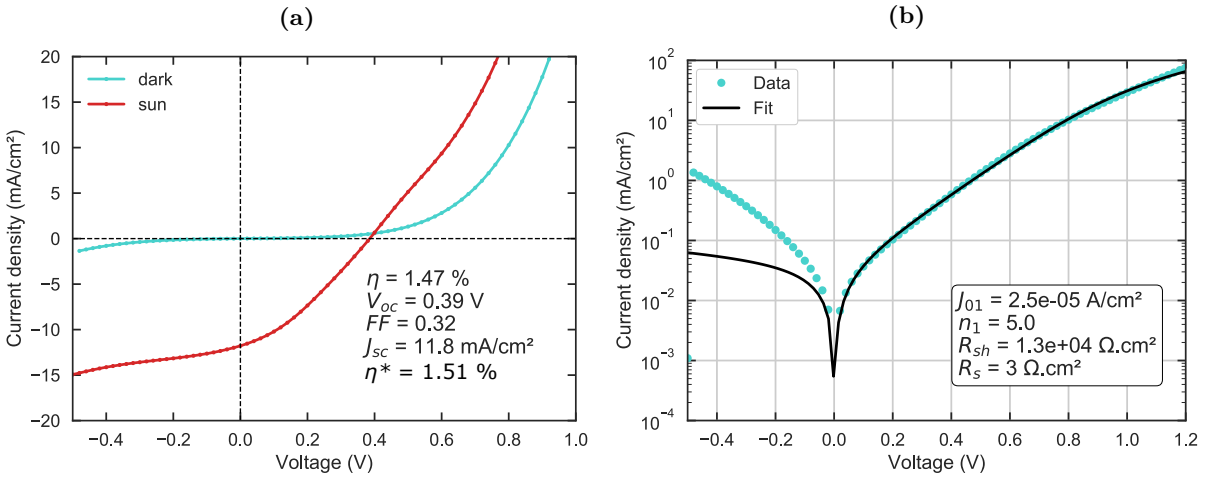

Figure 5.17: *JV curves of a NW solar cell. (a) In the dark and under illumination and (b) in the dark in logarithmic scale, along with a one-diode fit. [76838, A16_a]*

The open-circuit voltage (V_{oc}) is also low, at 0.39 V whereas the best GaAs planar solar cells typically reach 1 V ([Kayes et al. 2011]; [Chen et al. 2019]; [Green et al. 2019]). The fill-factor (FF) is 32 % instead of 85 % in state-of-the-art GaAs cells, mostly due to an unexpected shape of the JV curve under illumination. Indeed, an *S-shape* or *kink* is observed around V_{oc}, which is typical of a barrier for the photocurrent in solar cells [Scheer and Schock 2011]. It is associated with another anomaly: the curve under illumination intersects the curve in the dark (*cross-over*). This should not happen if the total current was a simple superposition of a diode current (forward, curve in the dark), and a photogenerated current (constant term, in reverse). This could be due to a variable photo-current which changes direction at the cross-over point, due to barriers for the carriers, at the GaP foot interface for example.

An insufficient doping level in the n-shell might also lead to its entire depletion, which displaces the electron Fermi level away from the conduction band and results in a lower built-in potential (V_{bi}) across the junction. When a simple p-n junction is biased to $V = V_{bi}$, the bands are flat and the photo-generated carriers do not have any preferred direction, which means that at this bias, the current in the dark is the same as under illumination, thus $V_{\text{cross-over}} = V_{bi}$. While this can explain cross-over at small voltage in p-n homojunction, the presence of heterostructures (the AlGaAs shell and GaP foot in our NWs) and their band offsets contribute to drive photogenerated carriers toward their respective contacts, so this effect should be limited [Moore et al. 2014].

The JV curve in the dark is fitted with a model associating one diode and two resistances in series and parallel, as introduced in Figure 1.7a and Equation 1.2 (page 14), and using the

free program developed by Stephan Suckow [4]. The curve and the fit are plotted in logscale in Figure 5.17b. Only the positive voltage values were fitted since the reverse current exhibits an important reverse-bias current (close to $1\,\mathrm{mA\,cm^{-2}}$ at $-0.5\,\mathrm{V}$), higher than the forward current, and incompatible with the diode fit. Such high reverse-current was also reported for GaAs NW solar cells on Si (about $5\,\mathrm{mA\,cm^{-2}}$ at $-0.5\,\mathrm{V}$ in [Boulanger et al. 2016]), whereas for NWs on GaAs substrate it is much lower ($<10^{-2}\,\mathrm{mA\,cm^{-2}}$ in [Mariani et al. 2013a] and in [Aberg et al. 2016]). This could be due to enhanced recombinations at the Si/(GaP/)GaAs interface, where electrons from the GaAs NW could recombine with holes in the Si substrate. High currents in n^+-GaAs NW / p^+Si substrate heterojunction contacts were demonstrated in ([Yao et al. 2015]), possibly relying on trap-assisted tunneling transport at the heterointerface.

A shunt resistance of $1.3 \times 10^4\,\Omega\,\mathrm{cm^{-2}}$ is fitted, which should not hinder the solar cell operation since the FF is typically affected when $R_{sh} < 10^3\,\Omega\,\mathrm{cm^{-2}}$. On the other hand, the current is found to vary more significantly close to $V = 0$ for the curve under illumination. This could be caused by a voltage-dependent photocarrier collection efficiency ($\eta_{col.}(V)$), or to illumination-dependent shunt paths [Scheer and Schock 2011].

Concerning the diode itself, a recombination parameter $J_0 = 2.5 \times 10^{-5}\,\mathrm{A\,cm^{-2}}$ is fitted, along with an ideality $n = 5.0$. Typical recombinations in GaAs can reach 2 when SRH recombinations at mid-gap defect levels dominate. Above this value, saturation of the dominant recombination processes with increasing voltage bias is sometimes invoked [Scheer and Schock 2011]. Tunneling from one band to the other, possibly through deep-level states, was also shown to lead to excess currents and ideality factors >2 in planar GaAs- [Dumin and Pearson 1965], or GaN-based diodes ([Casey et al. 1996]; [Shah et al. 2003]), however with the presence of the intrinsic shell spatially separating the doped regions, interband tunneling is unlikely.

In our case, one can argue that the current at high voltage bias is not limited by recombination in the GaAs NW but by one of the interfaces or contacts, outside the junction. Indeed, the p-Si/p-GaP/p-GaAs foot structure also creates a barrier for the injection (diode) current: holes flowing from left to right in Figure 5.14b. It was reported that such unipolar heterostructure can lead to ideality higher than 2 which was verified for AlGaN/GaN structures [Shah et al. 2003]. The front ITO layer was also found to form a Schottky contact on n-GaAs even for higher doping levels ($1\,\mathrm{cm^{-3}}$ to $2 \times 10^{18}\,\mathrm{cm^{-3}}$, whereas we estimate it below $4 \times 10^{17}\,\mathrm{cm^{-3}}$ in our NWs), which also leads to higher ideality factors. In Figure 5.11, I found an apparent ideality of 8 for the reverse-biased GaAs/ITO contact.

Comparison with ITO characteristic

Focusing on the GaAs/ITO interface, the previously determined JV characteristic of planar GaAs/ITO contacts can help us understand whether this interface can be responsible for the shape of the solar cell JV curves. A solar cell under illumination is modeled here by a diode and a current source, in series with a GaAs/ITO contact (Figure 5.18a). A realistic ideality factor of 2 and a recombination parameter $J_0 = 1 \times 10^{-6}\,\mathrm{A\,cm^{-2}}$ were used to obtain a JV characteristic with a low V_{oc}, representative of our device (dashed lines in Figure 5.18b, cyan in the dark and red with a photocurrent). For the GaAs/ITO contact, our experimental JV data points for ITO on planar GaAs were used (green dots in Figure 5.18b). The resulting JV characteristics are plotted as full lines in Figure 5.18b. An S-shape is well reproduced and the current at higher bias is indeed limited by the GaAs/ITO contact.

[4] Stephan Suckow, 2/3-Diode Fit (2014). http://nanohub.org/resources/14300

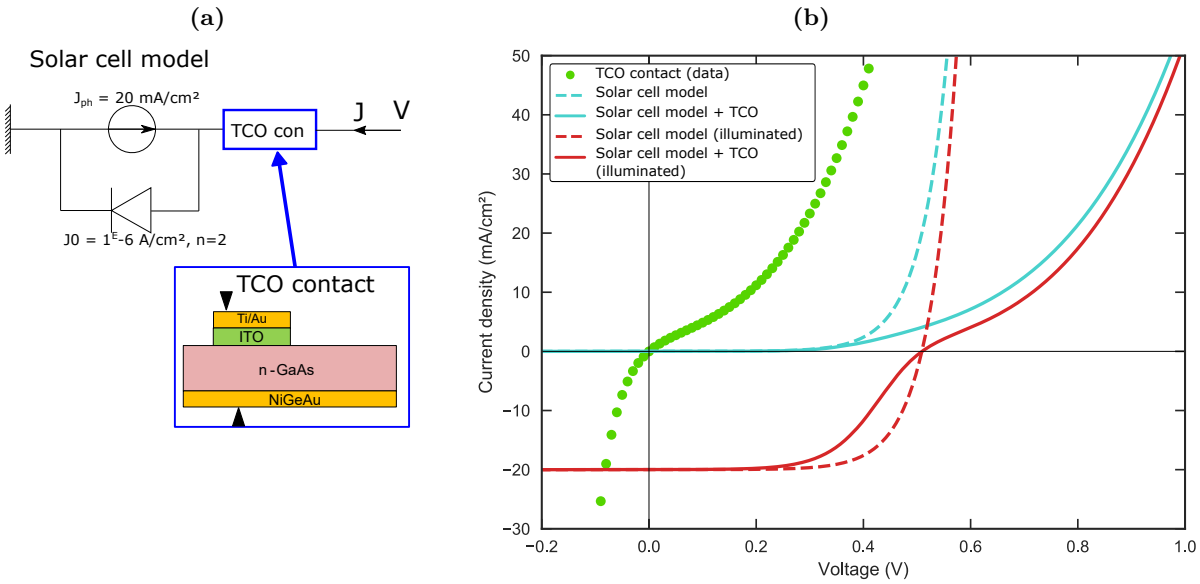

Figure 5.18: *Simulation of an equivalent circuit representing the NW solar cell with non-ideal contact. (a) Schematic of the equivalent circuit, using one diode with $n = 2$ and $J_0 = 1 \times 10^{-6}\,\mathrm{A/cm^2}$, and a photogeneration term $J_{ph} = 20\,\mathrm{mA/cm^2}$, in series with the TCO/GaAs contact characterized experimentally from planar layers (inset). (b) Experimental JV characteristic of the planar ITO/n-GaAs contact (green markers, $n_{GaAs} \approx 1.5 \times 10^{18}\,\mathrm{cm^{-3}}$). Simulated JV characteristics corresponding to the equivalent circuit to the left with the GaAs/TCO contact(full lines), and without it (dashed lines), in the dark (cyan) or with a $20\,\mathrm{mA/cm^2}$ photogeneration (red). [C1B2, A4_a]*

The JV curves of the homojunction diode were analyzed. The solar cell exhibits low performances ($\eta = 1.5\,\%$), and several characteristics point towards a bad collection of the photogenerated carriers. In particular, the non-ohmic front contact with ITO could explain the unusual shape of the JV curve under illumination.

5.4.4 Effect of annealing

I showed in the previous section the benefit of annealing a GaAs/ITO contact regarding its electrical properties. I also showed in Section 5.2 that the NW array planarized with BCB and contacted with ITO can withstand annealing temperatures up to 400 °C, above which the BCB degrades and cracks begin to appear. Consequently, the NW homojunction sample was annealed at 400 °C during 1 min in inert atmosphere.

The EQE after annealing is improved and yields a J_{sc} of $12.7\,\mathrm{mA\,cm^{-2}}$, compared to $12.1\,\mathrm{mA\,cm^{-2}}$ before (Figure 5.19). In particular, the EQE is improved between 400 nm and 670 nm, in very good agreement with the gain in transparency of ITO in this wavelength range after annealing (see Figure 5.12, page 189).

In Figure 5.20, the parameters extracted from the JV curves under illumination are plotted for about 20 diodes from the homojunction sample, before and after annealing. The slight increase in J_{sc} observed from the EQE is confirmed, while the V_{oc} has not significantly changed. The main improvement is on the FF, which increased from about 32 % to 42 %. I investigate this enhancement by analyzing the JV curve of one diode.

The JV curves after annealing of the previously studied diode are shown in Figure 5.21a. The curve under illumination has significantly improved below the V_{oc}, and not above. In particular, the slope of the curve at $V = V_{oc}$ has improved from $20\,\Omega\,\mathrm{cm^2}$ to $15\,\Omega\,\mathrm{cm^2}$, consistently with the improved ITO/GaAs JV characteristic upon annealing. The JV curve in the dark has not changed significantly below V_{oc}, but as can be seen in log scale (Figure 5.21b), the current

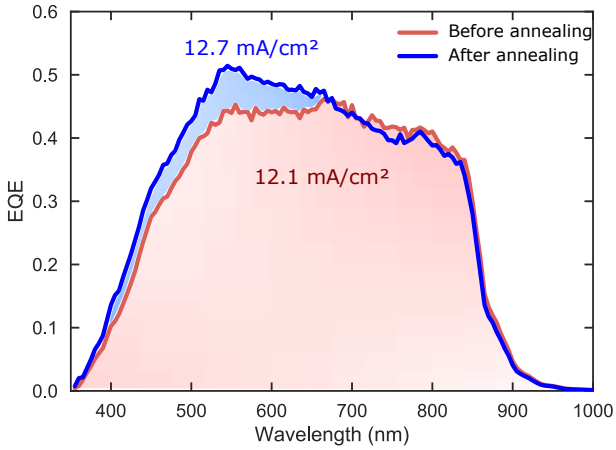

Figure 5.19: *EQE of the NW homojunction before and after a* 400 ℃ *annealing.* *[76838, A16_a]*

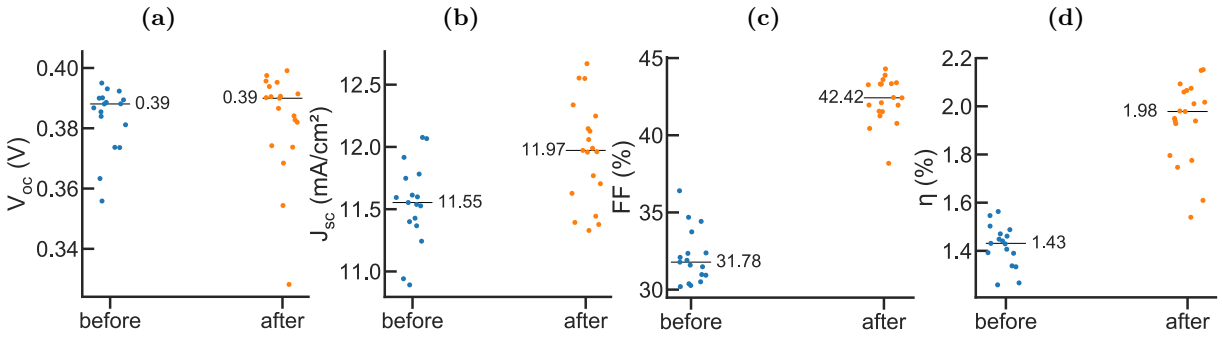

Figure 5.20: *Summary of the parameters extracted from the JV curves under illumination of the diodes from the homojunction sample, before and after a* 400 ℃ *annealing in inert atmosphere. The median value is indicated (black).*

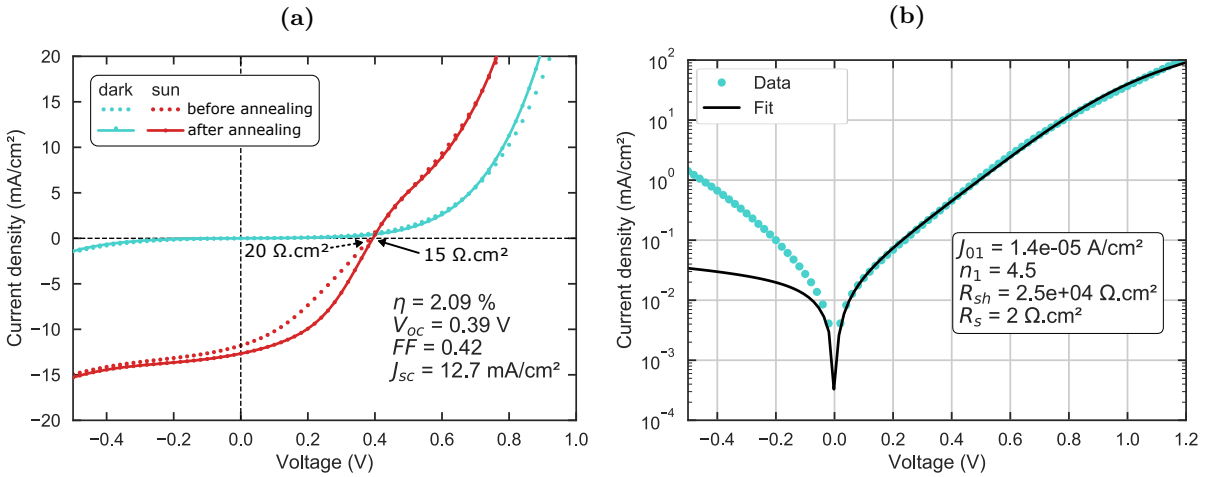

Figure 5.21: *JV curves of the NW homojunction solar cell after a* 400 ℃ *annealing during* 1 min *in inert atmosphere. (a) In the dark and under illumination, with the curves before annealing plotted with dots for comparison, and (b) in the dark in logarithmic scale, along with a one-diode fit.* *[76838, A16_a]*

at higher bias has changed: the ideality has decreased from 5 to 4.5 and the recombination parameter from 2.5×10^{-5} A cm^{-2} to 1.4×10^{-5} A cm^{-2}.

Overall, after annealing this diode exhibits a power conversion efficiency of 2.1 %, in the same range as other GaAs-NWs-on-Si solar cells in the literature with a comparable core-shell structure (3.3 % in [Boulanger et al. 2016], 4.1 % in [Dastjerdi et al. 2016], 0.7 % in [Mikulik et al. 2019]).

After 400 °C annealing, a better efficiency of 2.1 % is obtained, in part due to an improved J_{sc} but mostly due to a better FF, consistently with the improvement of the n-GaAs/ITO contact which becomes more ohmic after high temperature annealing.

5.4.5 Hyperspectral photoluminescence imaging

This sample was further investigated in a calibrated PL setup with spatial resolution, as introduced in Section 2.3, in order to quantitatively analyze its luminescence and the eventual spatial inhomogeneities. Its absolute luminescence can be related to the internal quasi-Fermi level splitting, whose comparison with V_{oc} might provide further information on the quality of interfaces.

The sample is illuminated using a green laser at 532 nm through a light scatterer to obtain a diffuse spot and illuminate the entire diode surface, and the light emitted in turn by the NW array is transmitted through the same objective, spectrally decomposed by a 3D Bragg grating, and collected by a Si CCD camera, with the spatial and spectral information stored in a hypercube.

A diode of size *e* was investigated (180 µm diameter), so that its entire surface fits the objective field of view (Figure 5.22a). A x50 objective with a long working distance (11 mm, NA = 0.6) is used to leave enough room to contact the front annular pad with an electrical probe. The sample is indeed connected to a Keithley 2635 source measure unit (SMU), so that the current and voltage can be simultaneously set and measured during the luminescence acquisition. The incident power was calibrated using the diode itself. JV measurements under the solar simulator illumination were made after the PL experiment to check that $I_{sc} = 3.4 \times 10^{-6}$ A. The laser light intensity resulting in the same current output is thus denoted as *1 sun illumination*, and higher intensities are expressed in suns as well. The spot profile is still not homogeneous, it is more intense at the middle of the diode and decreases towards the edge, which leads to the inhomogeneous intensity on the PL map (Figure 5.22b).

An absolute PL spectrum (Figure 5.22c) can be extracted from the hyperspectral image, averaged over the surface of the rectangle in Figure 5.22b. The main peak is attributed to the bandgap emission of GaAs, close to 1.43 eV. There is a low energy peak centered around 1.25 eV which was systematically present on the spectra of ITO-contacted NW arrays, but its origin is still unclear.

PL at short-circuit

For a faster mapping of the PL intensity, the spectrometer can be bypassed and an *order 0* map of the PL signal can be recorded, which displays the average PL intensity weighed by the spectral transmittance of the optical collection system, and the spectral sensitivity of the CCD detector (Figure 5.22d). Due to the low camera responsivity at low energies, it is assumed that only the main PL emission peak contribute to the light intensity measured by the CCD after dark subtraction, and that the spectral lineshape is conserved, so that variations of the intensity at the order 0 should be representative of the variation of the main PL emission peak.

The PL intensity at open-circuit (standard conditions for PL) can be compared to the PL intensity when the diode is placed in short-circuit (Figure 5.22e). Surprisingly, the intensity is

(a) *Dimensions.*

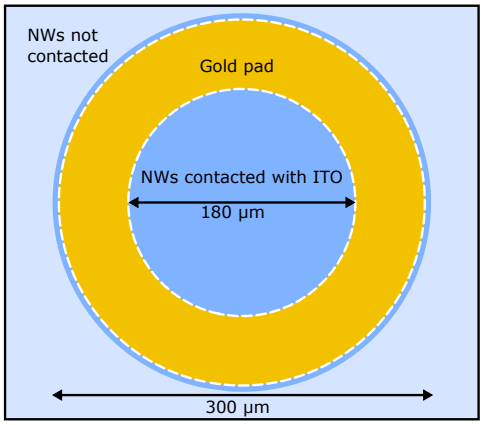

(b) *PL map at* 1.55 eV.

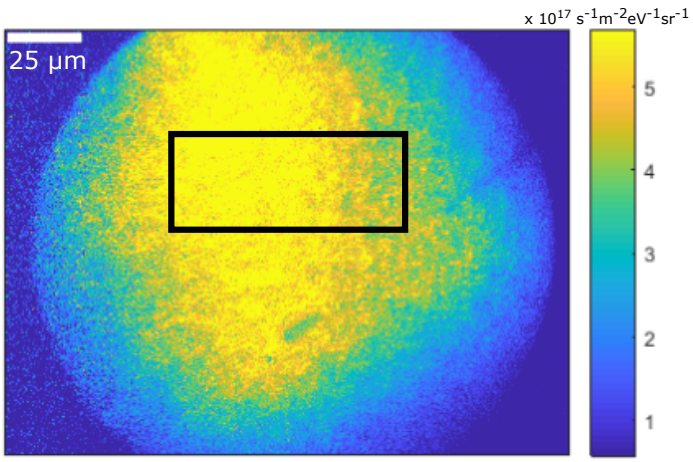

(c) *Average PL spectrum in rectangle.*

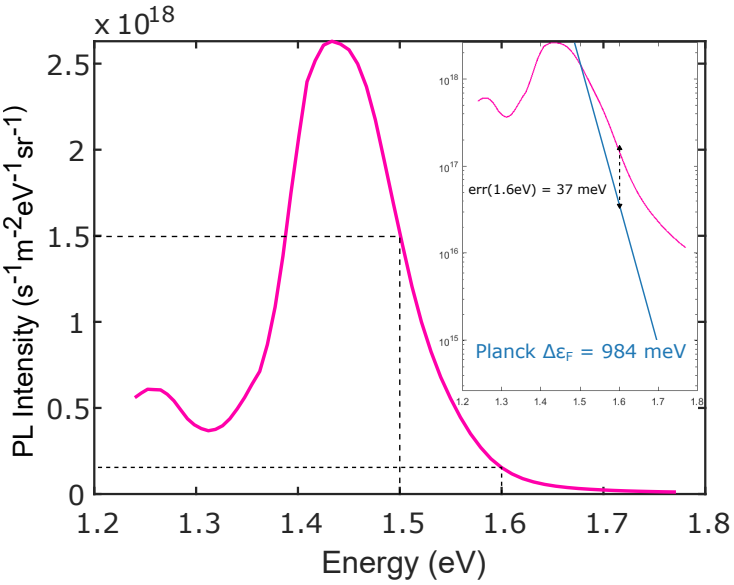

(d) *Open-circuit PL.*

(e) *Short-circuit PL.*

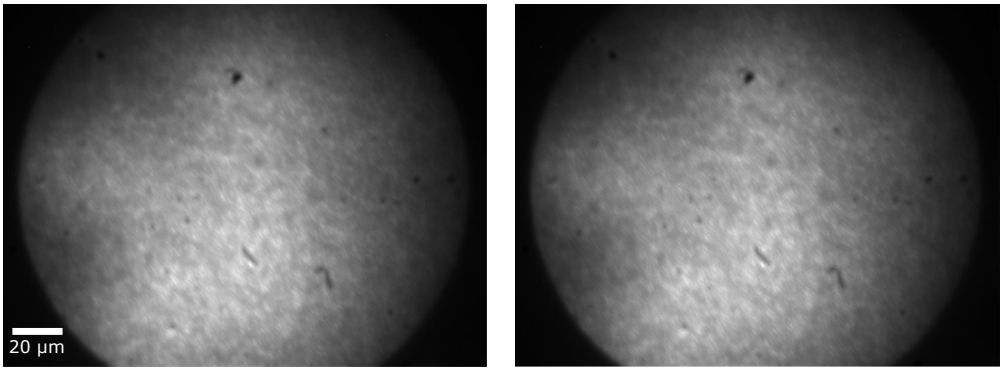

Figure 5.22: *(a) Top-view schematic of a NW diode of size* e. *(b) Absolute PL map of the NW diode under an excitation of* 82 sun *(*270 µA*), at* 1.55 eV. *(c) Average absolute PL spectrum in the zone identified with a rectangle. In inset the same spectrum is plotted in logarithmic scale, along with the generalized Planck law for a given value of* $\Delta\varepsilon_F$. *(d,e) PL maps of the NW diode under an excitation of* 80 sun, *acquired at the order 0 of the spectrometer and after subtraction of the background signal, in open-circuit and short-circuit conditions. The intensity is proportional to the PL intensity, weighed by the spectral sensitivity of the detector and the optics transmission. [76838, B8_e]*

the same in both conditions: the average pixel intensity differs by only 1 %. The expected J_{sc} was nonetheless measured by the SMU while in short-circuit, which confirms that a photogenerated current was indeed present.

A smaller quasi-Fermi level splitting was expected for the short-circuit condition. Indeed, the carrier concentrations in the band do not build up to their level in open-circuit, as they are extracted at the contacts in addition to other recombination effects. This suggests that the carriers are still partly confined inside the NW, likely due to the important barriers on the path of minority carriers (at the GaP foot and the GaAs/ITO front contact), despite a steady flow of extracted carriers which overcome these barriers toward their respective contacts.

Quasi-Fermi-level splitting estimation

Under sufficiently high excitation, the semiconductor luminescence varies with the exponential of the quasi-Fermi-level splitting ($\Delta\varepsilon_F = \varepsilon_{Fc} - \varepsilon_{Fv}$), through the generalized Planck law (Equation 2.9, page 40), which I rewrite here:

$$\phi(\hbar\omega) = A(\hbar\omega)\phi_{\mathrm{bb}}(\hbar\omega)\exp\left(\frac{\varepsilon_{Fc} - \varepsilon_{Fv}}{k_B T}\right)$$

This formula expresses the luminescence over a hemisphere, but the objective collects the light through a numerical aperture of 0.6, normal to the substrate. I lack information on the angular profile of absorption in this NW array, however, without dedicated optimization of the array and after embossing in BCB and ITO contact, the angular distribution of NW arrays was reported to be similar to planar layers [Cui et al. 2016]. Therefore, I assume a Lambertian emission profile, which leads to a luminescence in the normal direction, per steradian:

$$\mathrm{d}\phi(\hbar\omega) = \frac{\mathrm{d}\phi(\hbar\omega)}{d\Omega} = A(\hbar\omega)\frac{\phi_{\mathrm{bb}}}{\pi}(\hbar\omega)\exp\left(\frac{\varepsilon_{Fc} - \varepsilon_{Fv}}{k_B T}\right) \tag{5.9}$$

A second approximation consists in assuming a perfect absorption in the NW array, by neglecting the loss through reflection and transmission to the substrate. It is possible to estimate the final error on the quasi-Fermi level splitting value, due to this approximation. The EQE of this sample is already 40 % at 1.5 eV (827 nm), as shown in Figure 5.19. So the absorption is necessarily above 0.4, and probably closer to 1 if the EQE is hindered by poor carrier collection (*i.e.*, poor internal quantum efficiency) rather than poor absorption. So this assumption could result in a luminescence value overestimated by about a factor 2. Through Equation 5.9, it is equivalent to an overestimation of $\Delta\varepsilon_F$ by 18 mV, a very reasonable error compared to the expected values, above V_{oc} (0.4 V).

Then, by developing Φ_{bb} in Equation 5.9, the following relationship between the normalized luminescence of a pixel and the quasi-Fermi-level splitting $\Delta\varepsilon_F$ is obtained:

$$\mathrm{d}\phi(\hbar\omega) = \frac{(\hbar\omega)^2}{4\pi^3\hbar^3c^2}\exp\left(\frac{-\hbar\omega}{k_B T}\right) \times \exp\left(\frac{\Delta\varepsilon_F}{k_B T}\right) \tag{5.10}$$

The calibration of the PL setup and the accuracy of the method were verified by measuring the PL of GaAs solar cells for which the ε_F determined through Equation 5.10 above 1.45 eV equals the V_{oc}, as described in [Delamarre et al. 2012].

This relationship is evaluated at $\hbar\omega = 1.5\,\mathrm{eV}$ with the luminescence determined from the spectrum in Figure 5.22c : $\mathrm{d}\phi(\hbar\omega = 1.5\,\mathrm{eV}) = 1.5 \times 10^{18}\,\mathrm{s^{-1}\,m^{-2}\,eV^{-1}\,sr^{-1}}$. I find $\Delta\varepsilon_F = 0.984\,\mathrm{eV}$, in the NW junction under an illumination of 82 sun. The plot of Equation 5.10 in logarithmic scale alongside the PL spectrum does not accurately fit the high energy part of the PL peak (inset in Figure 5.22c). Such enlargement of the high-energy part unpredicted by the generalized Planck law might originate from more complex absorption in processed NW array, such as resonances or re-absorption by the ITO and results in a modified lineshape.

However, due to the logarithmic dependence of $\Delta\varepsilon_F$ on the luminescence intensity, the error on the determination of $\Delta\varepsilon_F$ is very small, only 37 meV at $\hbar\omega = 1.6$ eV. The order of magnitude of $\Delta\varepsilon_F$ is thus still accurate and its very high value is now compared with the actual voltage at the contacts (V_{oc}) under different excitation conditions.

Comparison with J_{sc}/V_{oc} characteristic

A power law of the quasi-Fermi-level splitting as a function of the excitation intensity can be obtained and compared with a J_{sc}/V_{oc} characteristic for the same diode.

To do so, PL maps at order 0 (Figure 5.22d) are acquired for different excitation levels. A higher photoexcitation should only result in the increase of $\exp\left(\frac{\Delta\varepsilon_F}{k_B R}\right)$ in Equation 5.10, and do not affect the spectrum lineshape. Therefore, the evolution of the PL intensity at order 0 is representative of the evolution of $d\phi(\hbar\omega)$. In Figure 5.23, $d\phi(\hbar\omega)$ is rescaled with the average intensity from the order 0 PL maps over the diode area for different excitation levels, using $d\phi(\hbar\omega)^{82\text{ sun}}$ as a reference, resulting in $\Delta\varepsilon_F$ for different excitation levels. In the same experiment, the value of J_{sc} and V_{oc} under the same excitation conditions were recorded and plotted along the previous curve.

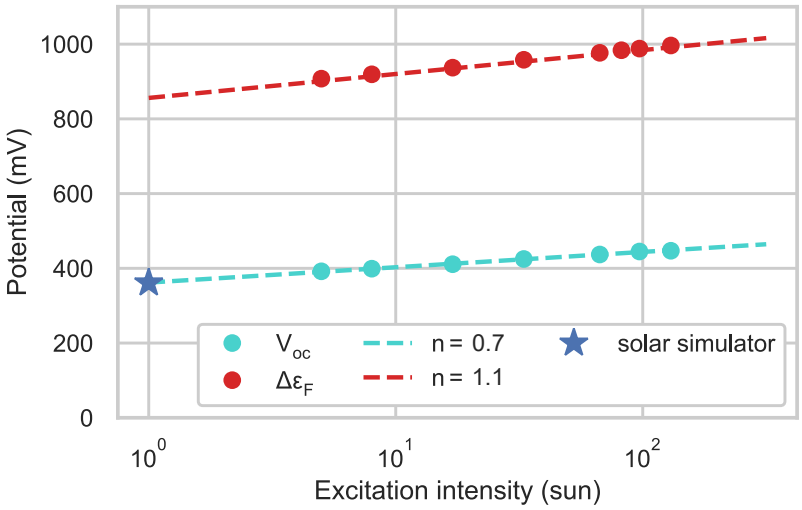

Figure 5.23: *Evolution of the V_{oc} and $\Delta\varepsilon_F$ with the excitation intensity. Each curve is fitted with a diode law (dashed lines).*

At all excitation levels, the quasi-Fermi level splitting is found to be much higher than the V_{oc}, by more than a factor 2. It reaches $\Delta\varepsilon_F = 1.0$ V at 130 sun, and $\Delta\varepsilon_F = 0.91$ V at 5 sun. The value at 1 sun is extrapolated as $\Delta\varepsilon_F = 0.86$ V. This high value compared to the V_{oc} is indicative of a sufficient material quality in the bulk of the NW, which is not deteriorated by a high concentration of defects. It also supports the idea that our device is hindered by collection issues, and that the carriers recombine at the contact interfaces.

The V_{oc} measured with the solar simulator at 1 sun is also indicated in Figure 5.23 with a blue marker, which falls exactly on the fitted V_{oc} (J_{sc}) curve which confirms that excitation with the green laser yields similar V_{oc} as with a simulated AM1.5G spectrum.

An ideality factor is calculated from the slope of the curves. For $\Delta\varepsilon_F(J_{sc})$, the ideality factor is 1.1, and for $V_{oc}(J_{sc})$, it is 0.7. These values are closer to expectation for GaAs, and much lower than previously determined by JV measurement ($n = 4.5$, Figure 5.17b). This again is consistent with the assumption that the high ideality of the JV curve is indicative of imperfect contacts and interfaces outside the GaAs junction. An ideality below 1 for $V_{oc}(J_{sc})$ could originate from a

decrease of the quasi-Fermi level splitting close to the contact interfaces at higher concentrations of photogenerated carriers, due to resistive contacts and surface recombination.

Using a calibrated setup, the absolute PL of a homojunction diode was investigated with spatial resolution. The PL is identical whether the diode is in short-circuit or not, which supports the likely presence of important carrier barriers. The quasi-Fermi-level splitting was estimated for different excitation levels and is found to be much higher than the V_{oc} measured in the same conditions, which suggests important contact issues. The ideality factor extracted from this curve is close to 1, as expected for GaAs material.

5.4.6 Conclusion

Section: Characterization of a GaAs core-shell homojunction solar cell

A GaAs core-shell homojunction NW solar cell (AlGaAs passivation) grown on Si was fully characterized.

The performances range from $\eta \approx 1.6\,\%$ to $\eta = 2.1\,\%$ across the sample surface, with more than half of the measured diodes over $1.9\,\%$ after annealing at $400\,°C$. The efficiency is mostly hindered by a low V_{oc} and a barrier for the carrier transport, possibly at the n-GaAs/ITO interface and responsible for a non-ideal *S-shape* in the JV curve, which slightly improves upon annealing. A very high ideality factor above 4 is attributed to the poor contacts and interfaces at the foot and top of the NWs.

Absolute PL maps were acquired using a hyperspectral imaging setup, and the quasi-Fermi-level splitting is found to be $984\,mV$ under an illumination of $80\,sun$ and extrapolated to $0.86\,V$ at $1\,sun$, more than twice the V_{oc}. Ideality factors of 1.1 and 0.7 are extracted from sun-$\Delta\varepsilon_F$ and sun-V_{oc} curves. These measurements are indicative of promising bulk GaAs properties, and confirm that the poor performances are due to unoptimized carrier separation and collection.

5.5 Characterization of GaAs/GaInP core-shell heterojunction solar cells

Another core-shell design consists in avoiding the n-GaAs:Si shell and to directly grow an n-GaInP shell around a p-GaAs core and a i-GaAs shell (Figure 5.24). Potential advantages compared to the previously shown homojunction are:

1. Removing the n-GaAs:Si shell which is known to be poorly doped (highly compensated), and prone to form rough sidewall surfaces and parasitic deposition on the mask.
2. Employing a GaInP barrier is beneficial to selectively repel holes from the n-contact, due to an important valence band offset with GaAs (at least 0.3 eV, depending on the composition and the degree of ordering in the InGaP shell [Adachi 2009]), resulting in a lower diode dark current and improved V_{oc}. The insertion of GaInP was in particular reported to reduce the dark current and improve V_{oc} in GaAs thin-films [Welser et al. 2009], or core-shell NWs [Gutsche et al. 2012] junction. The location of the GaInP shell inside the depletion region appears to play a role in limiting the recombination current assisted by tunneling [Liborius et al. 2019b].
3. A simplified structure could result from this design since the GaInP shell does not necessitate a GaAs capping layer. However, for the first sample presented here, an additional high-bandgap AlInP shell was employed to passivate the GaInP shell and collect carriers generated there.

The benefit of employing GaInP and not AlGaAs comes at the price of the potential presence of dislocations in the shell as shown in the previous chapter, and is discussed here.

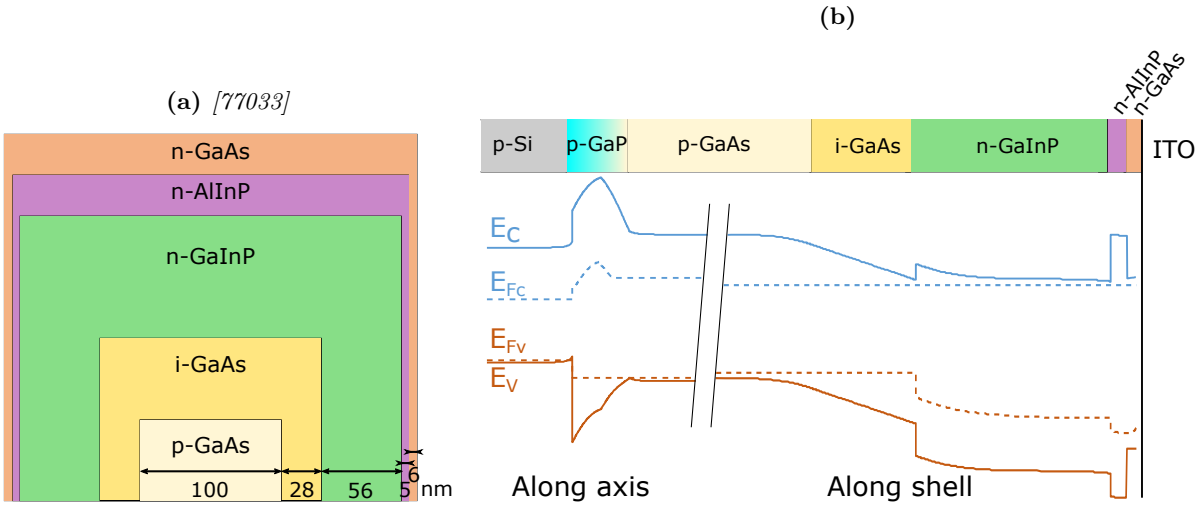

Figure 5.24: *(a) Schematic of the shell dimensions in the core-shell GaAs/GaInP heterojunction (sample 77033). (b) 1-D band structure along the axis and the shell of the NW. Calculated at the open-circuit voltage and for a constant photogeneration in all layers. Not at scale. The front contact between the n-GaAs cap and the ITO is represented with a recombining interface and a Schottky barrier for the electrons.*

5.5.1 Sample presentation

Nanowire growth

The growth took place at a different period and with a different epitaxier as compared to the previous sample, therefore key differences exist in the growth sequence.

In the Riber 32 MBE, after being held at (640 ± 10) °C in vacuum, the substrate temperature was stabilized to (600 ± 5) °C. The p-type NW core was initiated with a 2.33 min Ga pre-

deposition ($100\,ML_{GaAs(100)}$) under a Be flux of $1.5 \times 10^{11}\,cm^{-2}\,s^{-1}$.

The Ga flux during core growth is set to $2.0\,Å\,s^{-1}$ and a GaP:Be foot is grown during 20 s at a P/Ga flux ratio of 1.2. The main core segment is grown under an As/Ga flux ratio of 0.9 during 20 min. While the Be flux employed during core growth ($1.5 \times 10^{11}\,cm^{-2}\,s^{-1}$) is three times as low as for the core of the homojunction sample ($4.6 \times 10^{11}\,cm^{-2}\,s^{-1}$), this is in part compensated by the fact that dopants were also provided during the longer Ga pre-deposition, and that a lower V/III ratio (and thus, lower axial growth rate) and a longer core growth duration where used, which increase the relative average dopant concentration.

The temperature is then stabilized at 580 °C and droplet consumption is performed during 40 min by shutting down the Ga flux and using an As_4 flux at 19 % of its value during core growth. An intrinsic GaAs shell is then grown during 20 min at a Ga flux of $1.0\,Å\,s^{-1}$, under an excess of As_4. The substrate temperature is finally set to (425 ± 10) °C for the growth of a n-InGaP:Si shell during 40 min, aiming at an equivalent growth rate of $1.1\,Å\,s^{-1}$ and a planar composition of $Ga_{0.49}In_{0.51}P$ in thin-films, which, with the source cell angles of incidence in this MBE, rescales to $Ga_{0.51}In_{0.49}P$ on vertical facets. Although this nominal composition is lattice-matched to GaAs, I showed in the previous chapter that the NW sidewalls can be enriched in Ga.

The dopant flux employed during this shell growth is much higher than before, the resulting doping level in GaAs(100) thin-films would be $1.2 \times 10^{19}\,cm^{-3}$. The shell is terminated with a 5 min n-AlInP:Si shell (nominal planar growth rate of $1.0\,Å\,s^{-1}$ and composition $Al_{0.48}In_{52}P$) with an identical Si dopant flux. Finally, a GaAs capping shell is grown during 8 min at a Ga flux of $0.55\,Å\,s^{-1}$, and a very high Si dopant flux, which results in a planar doping level of $2.4 \times 10^{19}\,cm^{-3}$).

Dimensions and doping levels

In the patterns of pitch 500 nm, the NWs are typically 1900 nm long and 290 nm thick. As previously, the NW shell dimensions were roughly estimated considering the incident fluxes at the NW sidewalls, the actual NW diameter, and subtracting an estimated core diameter (105 nm) (Figure 5.24a).

Due to different growth conditions from the GaAs NWs characterized by CL in the previous chapter, and with the assumption that the doping mechanisms in GaAs NWs are the same in other materials, the doping levels can only be roughly estimated. In the core it is approximately $p = 1.5 \times 10^{18}\,cm^{-3}$, and below $10^{18}\,cm^{-3}$ in the InGaP, AlInP and GaAs shells.

Band structure

The 1-D band structure along the NW axis and through its shell is represented in Figure 5.24b with the previously estimated dimensions and doping levels, under illumination (constant photogeneration of $10\,mA\,cm^{-2}$) and for a bias $V = V_{oc}$.

The conduction-band alignment between GaAs and InGaP is more favorable for the transport of electrons compared to AlGaAs. The AlInP layer, if depleted, could however induce a barrier to their extraction.

Device fabrication and characterization

The sample was planarized with the SiO_x/BCB method described in the previous section, and a (630 ± 20) nm thick ITO layer was deposited, much thicker than for other samples. The ITO contact disks were not defined by lift-off, but by selective etching of the ITO outside the disks (positive photolithography), in a diluted HCl solution. Due to important underetch, part of the annular Ti/Au pads were lifted-off at the edge of the ITO contact disks (see Figure 5.25).

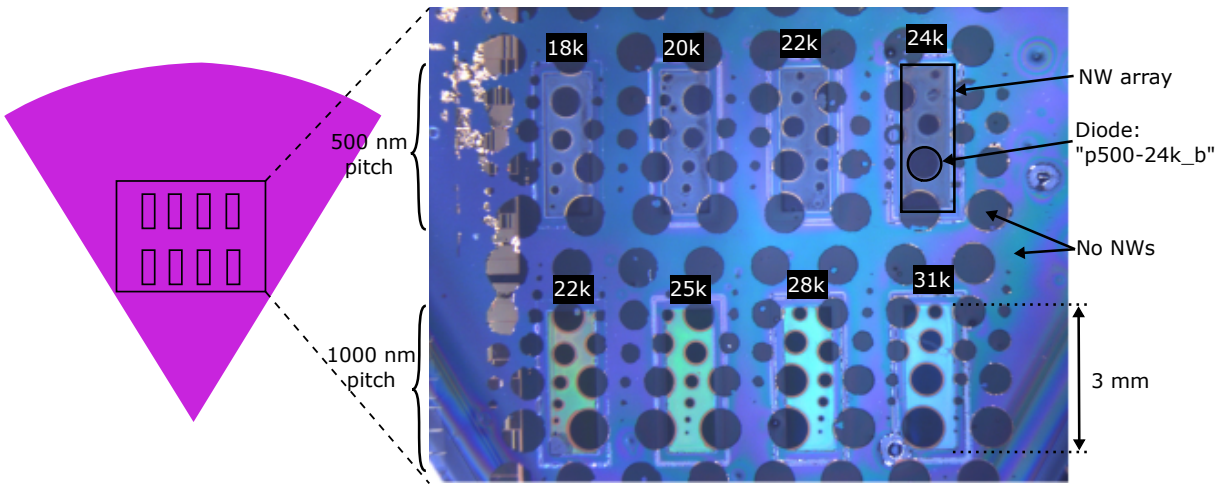

Figure 5.25: *Image of the fully processed NW heterojunction sample. 8 different rectangular zones are made of NW arrays with a given pitch (*500 nm *or* 1000 nm*) and a given EBL dose during the exposure of the resist (from* 18 000 μC cm^{-2} *to* 31 000 μC cm^{-2}*), which leads to holes of different sizes in the SiO_x mask, where the NWs selectively grow. [77033]*

A 1/6 2" patterned Si substrate was used for this sample instead of a full 2" wafer, which results in a slightly lower NW yield (up to 90 %), less room for making diodes, and higher chance of surface contamination or damage during the fabrication process.

A picture of the diode with the associated nomenclature is shown in Figure 5.25. Several patterns are present on this sample, but the analysis of the EQE and JV curves is realized on the best diode from the pattern of pitch 500 nm and dose 18k, in line with the previously characterized homojunction sample. However, the evolution of the JV parameters between different pattern is analyzed afterwards, as 22 diodes were measured on this sample.

5.5.2 External quantum efficiency

The EQE before annealing is very low overall (it amounts for $J_{sc} = 5.4\,\text{mA cm}^{-2}$) but it also presents a notable drop below 680 nm (Figure 5.26). The drop coincides with the presumed position of the $Ga_{0.5}In_{0.5}P$ bandgap (650 nm). Carriers may be photogenerated in the GaInP shell, or in the GaAs close to the interface with GaInP, as high energy photons have shorter penetration depths into GaAs. They could then recombine due to the likely presence of dislocations in the GaInP. [Mariani et al. 2013a] showed a low EQE in the short wavelength range of unpassivated GaAs NW solar cell, attributed to recombination of high energy photons at the surface states, alleviated by using an efficient passivation. It could also be due to absorption in the ITO, which is significant between 350 nm and 600 nm (about 30 % loss through a 200 nm thick layer, see Figure 5.12), and the ITO was especially thick for this sample (600 nm).

As for the fact that even at higher wavelengths, the EQE is limited below 30 %, similar to the homojunction sample, one can argue that it is due to carrier collection issues at the contacts. It could also be due to parasitic absorption in the GaAs capping layer, which was deposited around the AlInP shell. For comparison, 2 % and 1 % of the incident light is absorbed within 5 nm of a planar GaAs layer at 600 nm and 800 nm, respectively. In the NW structure, this might be even worse due to possible light resonance at the NW top shell edge, and also since a thicker layer is expected for the shell segment at the top due to the MBE geometry (26 nm).

After a 400 °C annealing (same conditions as for the homojunction sample), the EQE is higher below 700 nm and lower above (Figure 5.26). Overall, it results in an increased J_{sc} of 5.7 mA cm^{-2}. The enhancement at low wavelengths is likely to be caused by the improved ITO transparency after annealing, between 300 nm and 700 nm (Figure 5.12).

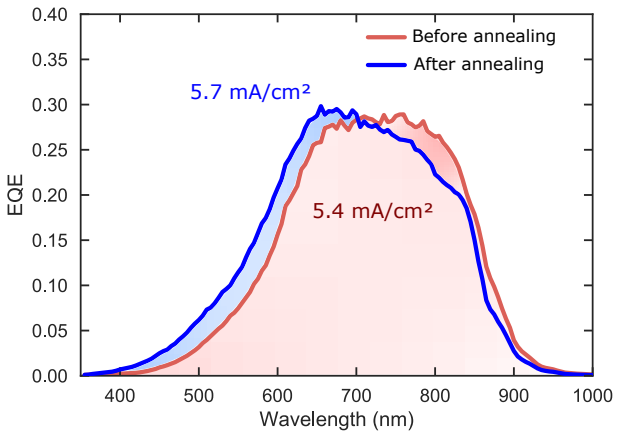

Figure 5.26: *EQE of the NW heterojunction before and after a* 400 °C *annealing. [77033, p500_18k_c]*

The EQE of the heterojunction sample is low overall, possibly due to collection issues and parasitic absorption in the GaAs capping shell. It presents a drop at lower wavelengths, which might be caused by absorption in the ITO or recombinations of carriers generated close to or in the GaInP shell. It is improved upon annealing.

5.5.3 Current-voltage characteristics

JV curves before and after annealing

Even before annealing, the JV characteristic of the heterojunction solar cell (Figure 5.27a) are much closer to the expected diode behavior than the homojunction sample. There is no *kink* or *S-shape* close to the V_{oc}, nor any sign of *roll-over* at higher voltage. The cross-over occurs at higher voltage bias (>0.6 V) than for the homojunction, and above this point the curve in the dark remains close to the curve under illumination.

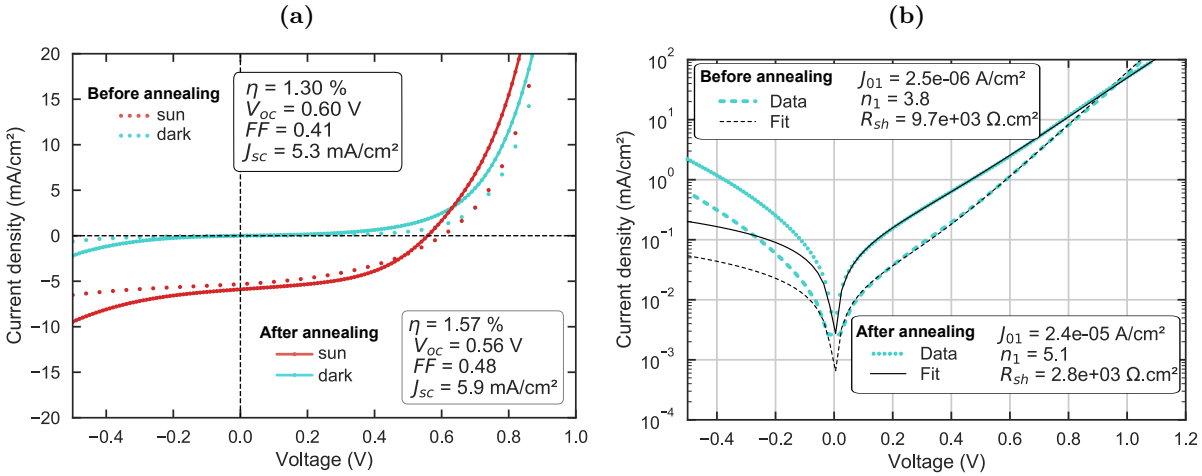

Figure 5.27: *JV curves of the NW heterojunction before and after a* 400 °C *annealing during* 1 min *in inert atmosphere. (a) In the dark and under illumination. (b) In the dark in logarithmic scale, along with a one-diode fit. [77033, p500_18k_c]*

There is still a high reverse current which cannot be fitted to the diode model (Figure 5.27b), although the shunt fitted on the positive voltage of the dark curve is high enough ($10^4\,\Omega\,cm^2$) to impact the fill-factor under illumination. However, there is again an important 'apparent shunt'

on the curve under illumination with a non-zero slope at $V = 0$, which indicates a variable photocurrent and possible carrier collection issues.

After annealing, the diode current is increased. The fitted recombination parameter is an order of magnitude higher than before annealing, though the ideality coefficient has also increased from 3.8 to 5.1, which is still not representative of a semiconductor junction in the SRH recombination model.

Improved JV characteristic

The regular shape of the JV curve under illumination may be due to an improved front n-GaAs/ITO contact.

While the GaInP/ITO contact was not found in the previous section to be more conductive than the GaAs/ITO for identical doping levels, the effective doping level in the n-GaInP:Si shells is still unknown. Indeed, CL spectroscopy was only performed on n-GaAs:Si shell to avoid the influence of eventual composition fluctuations on the luminescence lineshape. Si incorporation as donor in GaInP sidewall facets might be better than for GaAs due to growth kinetics effects, or due to a different exposure sequence to the fluxes in the MBE. In this case, a higher carrier concentration in the GaInP shell could also lead to a high electron concentration in the GaAs capping shell by diffusion, which would result in a better contact with ITO.

Another possibility is that many dopant-related defects help electrical transport at the interface. Indeed, a much higher dopant flux was used to dope the GaAs capping shell than for the homojunction sample (resulting in a planar doping of $2.4 \times 10^{19}\,\mathrm{cm}^{-3}$ versus $2 \times 10^{18}\,\mathrm{cm}^{-3}$). The electron concentrations measured by CL were limited to about $5 \times 10^{17}\,\mathrm{cm}^{-3}$ in this doping range, indicating that there is a high concentration of inactivated Si impurities, which may lead to the formation of defects such as $\mathrm{Si_{As}}$ acceptors, $\mathrm{Si_{As}}$–$\mathrm{V_{Ga}}$ acceptor-vacancy bonds, or Si clusters, characterized by deep level defects, as already mentioned in the doping section (Section 4.2). In turn, high densities of localized states distributed in energy across the bandgap provide a pathway for carrier transport (see Section 2.1 and [Brillson 2010], pp 493-494). The effective Schottky barrier height can be lowered by conduction through these localized states.

A Be flux was provided during the Ga droplet pre-deposition, which might load it with Be atoms prior to the NW nucleation, and thus increase the chance of obtaining a p-doped GaP foot as compared to the homojunction sample. Higher doping concentration in the GaP foot would help to avoid its depletion and lower its effective height and width.

However, the ideality factor in this device is still close to 5, which implies either:

- The presence of other junctions in series, as previously discussed for the ideality of the homojunction sample. This means that either the foot heterojunction or the GaAs/ITO contact still suffers from a barrier, and limits the current flow at high voltage.
- The mechanism leading to high idealities is actually intrinsic to the NW. In particular, high ideality factors associated with high reverse-bias leakage currents were observed in similar core-shell p-GaAs/n-InGaP single-NW samples, and were attributed to tunneling processes [Liborius et al. 2019a].

Improved $\mathbf{V_{oc}}$

The heterojunction sample performances are hindered by a low J_{sc}. However, the V_{oc} is remarkably high (0.6 V) compared to the previous homojunction sample (0.4 V), and to the rest of the GaAs NW-on-Si solar cells reported in the literature [Boulanger et al. 2016]; [Mikulik et al. 2019]; [Yao et al. 2015].

The origin of the enhanced V_{oc} is not fully clear. It might be attributed in part to a reduced J_0 as compared to the homojunction. However, due the high idealities obtained and the high reverse leakage currents, the J_0 values cannot be meaningfully compared.

Other p-i-n core-shell homojunctions were grown and fabricated (not shown), but with an InGaP passivation. Their V_{oc} reaches 0.47 V, which is an improvement from the 0.4 V of the AlGaAs-passivated homojunction presented before. This might indicate a benefit of replacing AlGaAs with GaInP, maybe through reduced recombinations at the heterointerface. Yet, this is not sufficient to close the gap toward 0.6 V. One may argue that the specific heterojunction architecture where the n-GaAs is removed is beneficial in some way to preserve the V_{oc}, although no such effect is expected purely from the band-structure, and electrical modeling simulations performed in our group have not revealed significant improvements [Petronio 2019].

Despite a lower J_{sc}, the JV characteristic is improved in the heterojunction sample, possibly due to an improved ITO/GaAs contact by doping or defect-assisted electrical transport, or to an improved GaP foot doping lowering the effective barrier at the p-Si/p-GaP/p-GaAs heterojunction. However, still high reverse-bias leakage current and ideality factor may indicate that other mechanisms are also present in these NW devices, such as tunneling current. The V_{oc} is improved from 0.4 V to 0.6 V, for reasons not yet elucidated.

5.5.4 Influence of the pattern

JV curves under illumination were acquired for 22 diodes from the patterns on this sample, differing by their pitch and the EBL exposure dose to pattern the holes (see Figure 5.25), and are summarized in Figure 5.28. Overall, the diodes on the patterns of pitch 500 nm perform better than the ones on 1000 nm pitch arrays. In particular, the V_{oc} and the FF are especially better in the 500 nm pitch arrays, while the trend is less clear for the J_{sc}. The FF improvement can be interpreted in term of improvement of the conduction at the front contact. The contact area between one nanowire and the transparent contact is not dependent on the pitch, whereas four times more current is expected to flow through each NW of the 1000 nm pitch arrays, if the overall current is similar to that in the 500 nm pitch arrays. This results in a larger voltage drop at this interface.

Some correlations can be found with the exposure dose as well, which is directly proportional to the size of the hole in which the Ga droplet is deposited and where each NW grows. The best V_{oc} are systematically found for the lowest exposure dose for each pith (Figure 5.28a). If the Si/GaP/GaAs interface concentrates many recombining defects, the V_{oc} might be lowered where this interface occupies a larger area, for larger holes. There might be a correlation with the FF for pitch 1000 nm arrays, and an anti-correlation for pitch 500 nm (Figure 5.28c), but variation of FF are more difficult to interpret since this parameter is mostly determined by the JV curve shape, which varies a lot in our case due to very low J_{sc} values. As for the J_{sc} (Figure 5.28b), surprisingly there seems to be an anti-correlation with the exposure dose, independently of the array pitch.

There are important variations of the JV parameters over the different patterns, in particular the 500 nm pitch arrays perform better than the 1000 nm pitch ones. The smallest exposure doses (smallest hole size in the mask) tend to yield the best device performances.

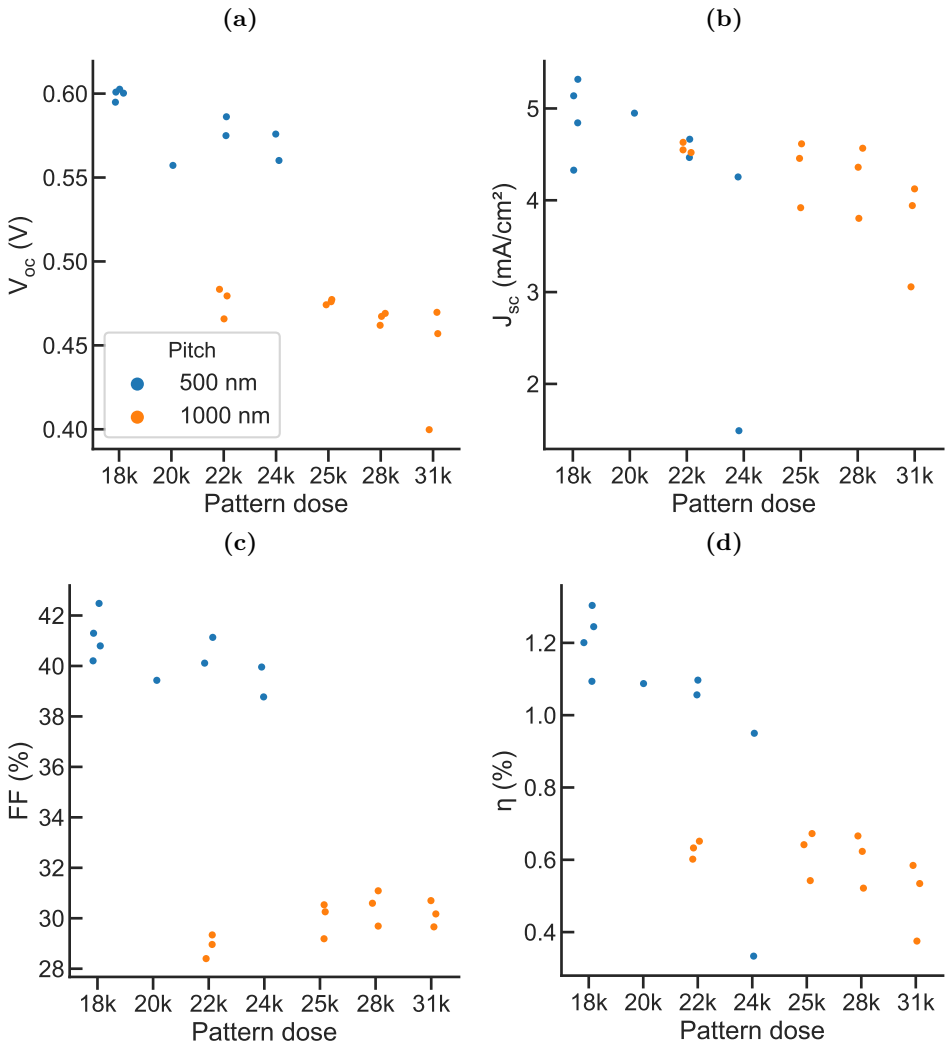

Figure 5.28: *Summary of the parameters extracted from the JV curves under illumination of the diodes from the heterojunction sample before annealing, at different patterns. The pitch is the inter-NW distance and the pattern dose corresponds to the amount of injected current inside each hole during the pattern mask EBL patterning. The hole size scales with the dose. [77033]*

5.5.5 Electroluminescence spatial inhomogeneities

The sample was characterized with the same hyperspectral PL imaging setup as the homojunction sample. The PL was not studied as a function of the excitation, thus there is no $\Delta\varepsilon_F(J_{sc})$ relationship for this sample. However, the diode showed a strong electroluminescence (EL) signal, which was further studied.

A diode of size e was characterized (Figure 5.29a), but as the annular contact is poorly defined on this sample, an electrical probe was placed directly on the ITO. The hyperspectral EL image is acquired at a forward bias of 1.4 V, and the luminescence is calibrated similarly to the PL experiments. Figure 5.29b shows the hyperspectral EL image averaged between 1.35 eV and 1.45 eV.

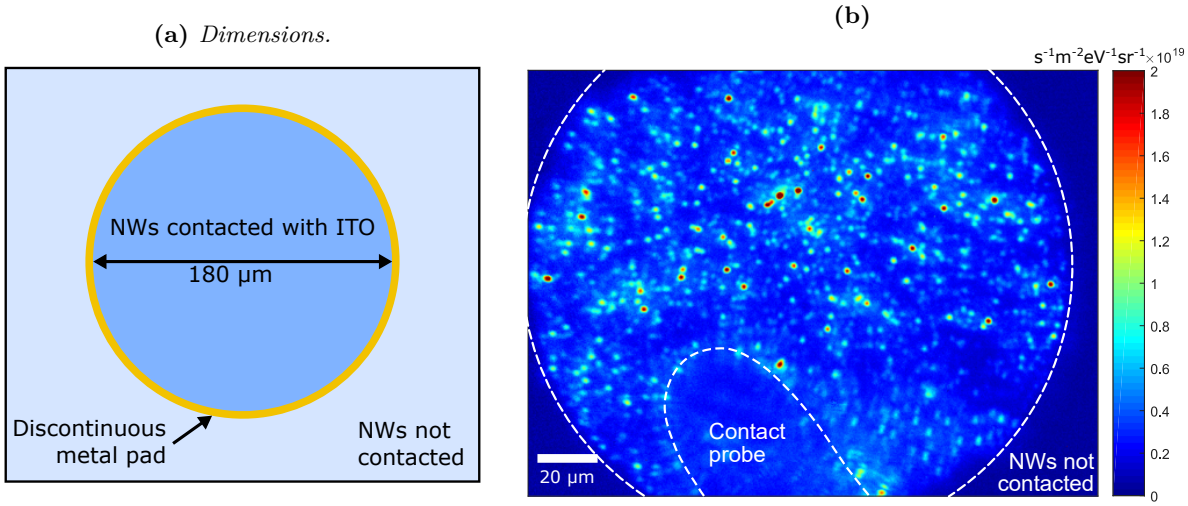

Figure 5.29: *(a) Schematic of a diode of size e on this sample. The ITO contour and annular metal pad are not well-defined. (b) EL map of a NW diode from the heterojunction sample, acquired at a bias of* 1.4 V*, and integrated between* 1.35 eV *and* 1.45 eV*. [77033, p500_18k_e]*

Important spatial inhomogeneities of the EL are visible over the surface of the diode. There seems to be localized emission from various point-like zones over the diode surface. One may wonder if the emission comes from single NWs, or if it corresponds to regions of higher vertical yield. To gain more insight on the origin of the inhomogeneities, I superimposed the EL map with a large-field, high-resolution SEM picture of the whole diode surface area (Figure 5.30). The positioning is realized using notable details on the diode contour seen on both the SEM and the optical image taken at the same position as the EL map, and the precision should be close to 1 µm.

The defective NWs are clearly identified as dark zones on the SEM image, and the yield does not vary at the scale of this image, whereas several localized spots of higher EL intensity are visible.

Each EL spot size is of the order of 2 µm wide, and increases with the spot intensity. The apparent NW size is already expected to be larger than its geometrical section (<300 nm), due to light scattering. Through Equation 5.11, the typical Airy disk diameter for a numerical aperture of 0.6 and at a wavelength of 532 nm is $D_{\text{Airy}} = 1080$ nm.

$$D_{\text{Airy}} = \frac{1.22\lambda}{NA} \tag{5.11}$$

Therefore, it is not ruled out that the spots may correspond to emission from single NWs. This does not necessarily implies that only few NWs are electrically active in the solar cell working conditions. Indeed, at the high voltage bias used for EL (1.4 V), the JV curve slope is very steep, and small voltage variations result in large changes to the current. If the ITO contact

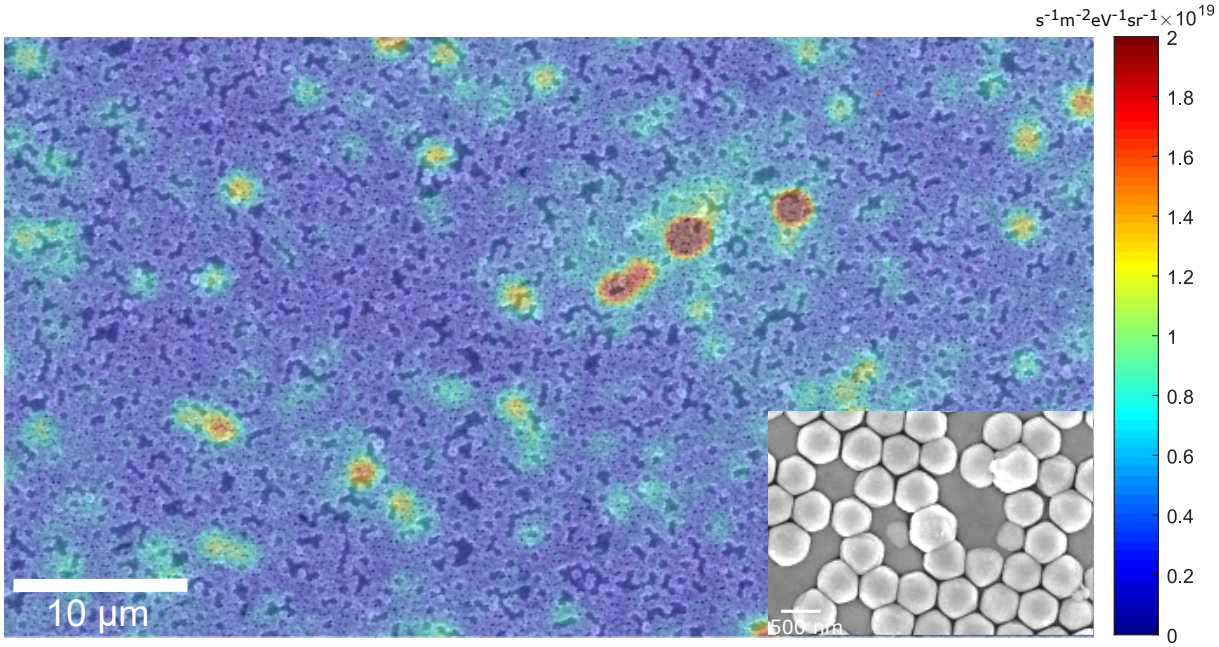

Figure 5.30: *EL mapping superimposed on a top-view SEM image of one diode of the heterojunction sample 77033. The EL hypermap is acquired at a bias of* 1.4 V*, and integrated between* 1.35 1 45*eV. The NW can be resolved from the SEM image, in particular the absence of NW appears as dark zones. The precision on the position of the images relative to each other is* ±1 µm*. Inset: Closer SEM top-view image of the ITO-contacted NW array.*

varies from NW to NW, for example when the contact surface area is larger on longer NWs, the voltage drop at the contact then also changes slightly and so does the bias across the NW junction, resulting in a large change of recombination current. This is consistent with the fact that the n-GaAs/ITO contact is not fully conductive.

Interestingly, there was no EL signal from the previous homojunction sample in similar conditions, even at forward voltage bias up to 2.6 V. This could be indicative of a very low internal bias in the NW homojunction, so that most of the voltage drop is at the n-GaAs/ITO interface. Therefore, there could have been an improvement of this interface on the heterojunction sample where EL signal was clearly visible, likely due to higher dopant concentration in the n-GaAs external shell.

Spatially resolved electroluminescence reveals important inhomogeneities over the diode surface. Localized emission spots could originate from individual NWs with above-average ITO contact. There was no EL signal on the previous homojunction sample, suggesting an improvement of the n-GaAs/ITO contact.

5.5.6 Characterization of a second-generation heterojunction

Following these first samples grown at C2N on a Riber32 setup, the growth process and fabrication process were transferred to IPVF equipment, starting in November 2018. After growth calibration studies, new devices were fabricated in February 2019 though due to an unexpected source cell failure followed by a long maintenance period and the move of the machine to from Riber factory to IPVF facilities, only one sample with good vertical yield was processed into a solar cell, later in 2019.

Here I present the characterization of this sample and the improvements from the previous heterojunction.

5.5.6.1 Sample presentation

Design changes

The design was slightly changed (Figure 5.31) compared to the previous sample. The AlInP shell was removed, to simplify the design and avoid parasitic light absorption in the GaAs capping shell. A thinner GaInP shell was aimed for, compared to the previous sample (from 35 nm to 56 nm), which was not sufficient to prevent the formation of dislocations due to uncontrolled GaInP composition (see Section 4.1, page 127, where NWs from this specific sample were characterized by TEM, and the presence of dislocations verified). The last nm of the n-GaInP:Si shell were more highly doped than the rest, in order to facilitate the electrical contact with ITO, while not introducing many defects close to the core.

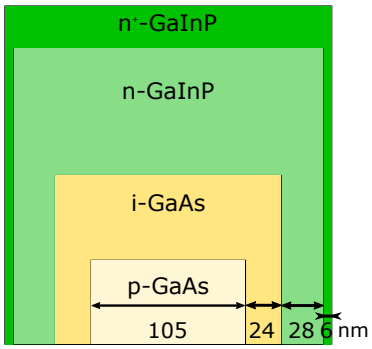

Figure 5.31: *Schematic of the core and shell dimensions for the heterojunction sample (second generation). [B276]*

Nanowire growth

A 1/6 2" sample was used. As the solar cell performances were previously found to be better on arrays of 500 nm pitch than on the ones of 1000 nm pitch, new arrays were designed with 360 nm and 500 nm pitch, with larger size so that more diodes can be processed inside each array, and with two different doses. This pattern design was described in Figure 3.24, page 93). The patterned substrates were fabricated in advance at C2N during summer 2018, but the last HF dip was performed the day before the growth, in the IPVF lab. After one night storage and transportation in a box filled with N_2, the samples were readily placed under vacuum in the MBE.

In the Compact21 MBE, after being held for 10 min at (690 ± 10) °C in vacuum, the substrate temperature was stabilized to 620 °C. The p-type NW core was initiated with a 1 min Ga predeposition ($42\,ML_{GaAs(100)}$) under a Be flux of $6 \times 10^{11}\,cm^{-2}\,s^{-1}$.

The Ga flux during core growth is set to $2.0\,Å\,s^{-1}$ and a GaP:Be foot is grown during 80 s (this sample was initially meant to characterize foot variations by TEM). After a 30 s graded transition from GaP to GaAs, the main core segment is grown under an As/Ga flux ratio of 1.2 during 12 min.

The droplet consumption is performed at the same temperature during 20 min by shutting down the Ga flux and using an As_4 flux at 16 % of its value during core growth. An intrinsic GaAs shell is then grown during 30 min at 590 °C with a Ga flux of $0.73\,Å\,s^{-1}$, under an excess of As_4. The substrate temperature is finally set to (470 ± 10) °C for the growth of a n-InGaP:Si shell, aiming at an equivalent growth rate of $1.1\,Å\,s^{-1}$ and a planar composition of $Ga_{0.58}In_{0.42}P$ in thin-films, which should be identical on vertical facets as all source cells are placed at the same angle in this MBE.

The GaInP:Si shell was grown in two steps. During the first 25 min, a flux of Si is provided during growth, that would yield a doping level $n = 6 \times 10^{18}\,cm^{-3}$ in planar layers. The last

nanometers were grown using the delta-doping technique, as described in Section 4.2.3.4. GaInP is grown during 32 s, after which the Ga flux is stopped and an increased Si flux is provided under excess As_4 during 32 s, resulting in a Si surface concentration of $1.4 \times 10^{12}\,cm^{-2}$ in one atomic plane. This cycle was repeated 10 times, which results in an equivalent GaInP layer grown during 5.35 min with an average Si concentration of $1.7 \times 10^{19}\,cm^{-3}$. To simplify the design, no extra passivation shell was employed after GaInP onto which the ITO contact is directly deposited.

The morphology of the NW array at the end of the growth is presented in Figure 5.32, and the STEM-EDX and TEM analyses of NWs from this sample were realized in Section 4.1, indicating fluctuations of the Ga content in the shell, and the presence of dislocations.

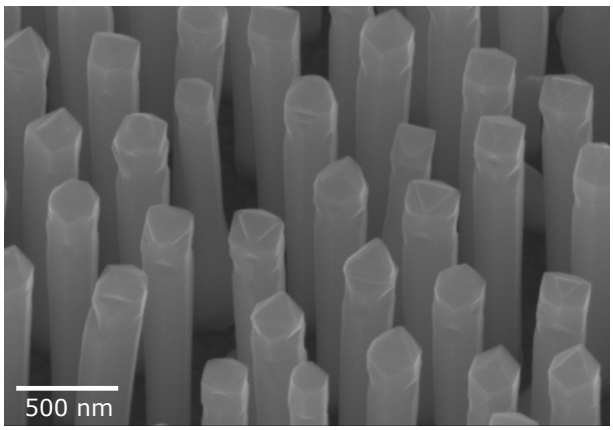

Figure 5.32: *SEM overview of the as-grown NW array, inside a pattern where the pitch is* 500 nm. *[B276]*

Dimensions and doping levels

In the patterns of pitch 500 nm, the NWs are typically 1900 nm long and (220 ± 20) nm thick. As previously, the NW shell dimensions were roughly estimated considering the incident fluxes at the NW sidewalls, the actual NW diameter, and subtracting the core diameter (100 nm) (Figure 5.31).

Due to different growth conditions from the NWs characterized by CL, and the different MBE setup, the doping levels can only be roughly estimated. In the GaAs core it is approximately $p = 10^{18}\,cm^{-3}$. In the shell, doping levels below $10^{18}\,cm^{-3}$ were determined by CL in delta-doped (with Si) GaAs shells (Section 4.2, page 155).

The 1-D band structure along the NW axis and through its shell is similar to the one of the previous heterojunction sample (Figure 5.24b, page 205), without the AlInP and GaAs outermost shells.

Device fabrication

The sample was planarized without SiO_x coating, only using BCB, and on the IPVF equipment where etching processes are not optimized. As a result, there is an important BCB thickness inhomogeneity on this sample, with some NWs remaining buried inside it, as shown in Figure 5.4a. A (155 ± 15) nm thick ITO layer was deposited, much thinner than the previous heterojunction sample, and comparable with the homojunction sample. However, due to unavailability of the MP600 sputtering tool used at IPVF for the study of ITO planar contacts, it was deposited with another tool at IPVF (MP500), under similar conditions but a lower voltage bias (60 V instead of 120 V).

A picture of the diode on the 1/6 2" patterned Si substrate, with the associated nomenclature, is shown in Figure 5.33. The *p500-14k* pattern presents a singular periodic inhomogeneity, as 4×6 subsquares can be seen inside the 2 mm × 3 mm rectangle. Inside each square the vertical yield is highly inhomogeneous with a gradient visible with naked eye, the darker zones exhibiting almost no growth. This is due to issues during EBL exposure which was not reproducible over the patterning of one subfield (corresponding to the square which can be patterned by the electron beam before the stage has to be moved). Consequently, some holes were not opened due to too low exposure dose.

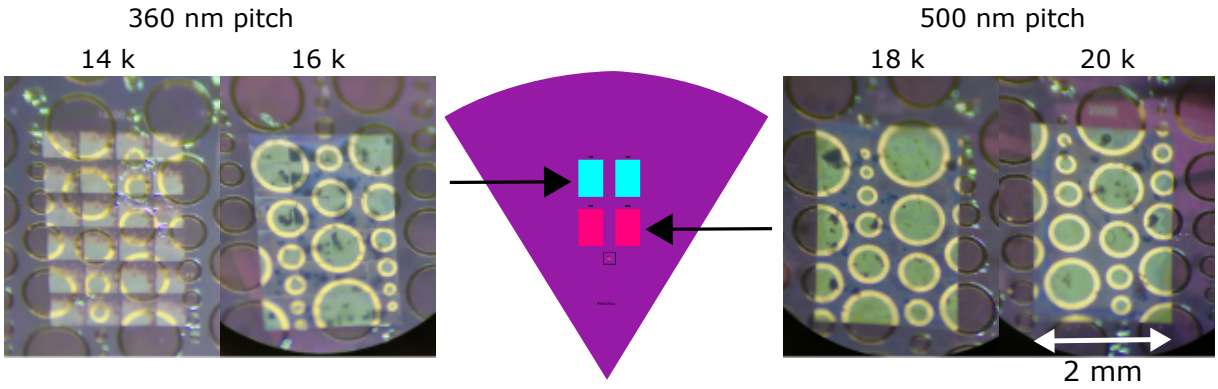

Figure 5.33: *Images of the fully processed heterojunction sample (second generation). 4 rectangular patterns differ by the pitch (*360 nm *and* 500 nm*) and the EBL exposure dose. [B276]*

The analysis of the EQE and JV curves is realized on the best diode from the pattern *p500-18k*, in line with the previously characterized samples.

5.5.6.2 Improved performances

The EQE is improved compared to the previous samples, and amounts to 14.2 mA cm^{-2}, about half of what is obtained in the best planar GaAs solar cells (Figure 5.34). In particular the EQE peaks at 60 % for wavelength between 700 nm and 800 nm. This improvement could be attributed to the absence of GaAs capping shell, or to the 3.5 times thinner ITO shell, both resulting in reduced parasitic light absorption. Lower collection losses due to a better n$^+$-GaInP/ITO contact could also contribute.

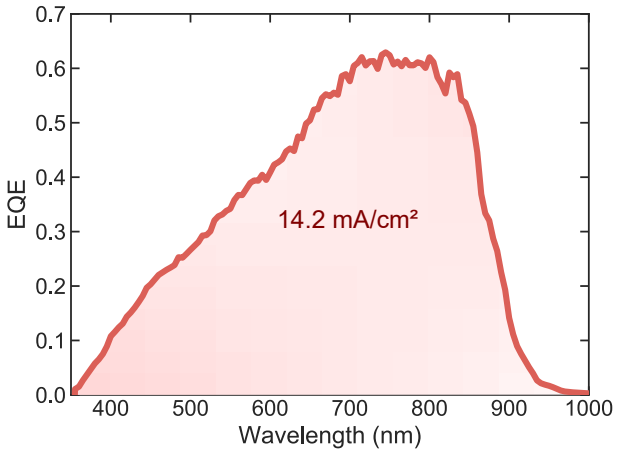

Figure 5.34: *EQE of the best diode from the second-generation NW sample heterojunction. [B276, p500_18k1_c]*

The shape, however, is still non ideal since the EQE drops below 700 nm, similar to the previous heterojunction sample. This time, the ITO is much thinner however ((155 ± 15) nm),

close to the thickness of the first homojunction sample for which the EQE did not suffer such drop. Therefore, the poor performance at low wavelengths might be mostly caused by collection losses inside the NWs, rather than parasitic absorption in the ITO layer. In particular, the presence of dislocations in the shells of several NWs from this sample was confirmed by TEM characterization (Figure 4.9b, page 127). High-energy photons are more likely to be absorbed in the GaInP shell or in the GaAs core close to the interface with GaInP. The carriers generated there have then more chance to reach a dislocation line and recombine without being collected.

In a future work, the GaInP composition and thickness could be further optimized to limit the lattice-mismatch and the occurrence of dislocations.

The JV curve in the dark and under illumination (Figure 5.35a) resembles the one of the previous heterojunction diode, with an exponential shape without *S-shape*, a cross-over happening at 0.7 V with a limited forward current enhancement, and an apparent shunt on the curve under illumination compared to the one in the dark (slope close to $V = 0$).

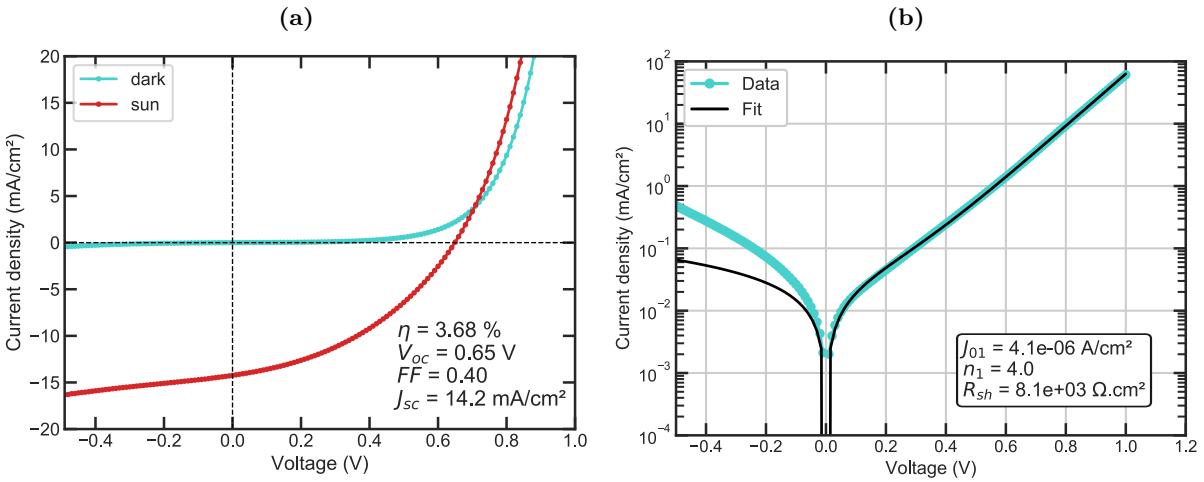

Figure 5.35: *JV curves of the second-generation NW heterojunction (a) in the dark and under illumination, and (b) in the dark in logarithmic scale, along with a one-diode fit. No annealing was performed on this sample. [B276, p500_18k1_c]*

The fit of the JV curve in the dark (Figure 5.35b) still reveals a high and unfittable reverse-current, a satisfying shunt resistance ($R_{sh} = 8 \times 10^3\,\Omega\,\mathrm{cm}^2 > 10^3\,\Omega\,\mathrm{cm}^2$), and a diode characteristic with similar parameters (ideality factor of 4.0, recombination parameter $J_0 = 4 \times 10^{-6}\,\mathrm{A\,cm}^{-2}$).

Compared to the previous heterojunction, the main improvement comes from the J_{sc}, but the V_{oc} has also increased from 0.6 , to 0.65 , and a power conversion efficiency of 3.7 % is reached. In this structure, the electron contact selectivity is ensured by the i-GaAs/n-GaInP heterojunction while the n^+-GaInP is there to promote an efficient electron extraction. By spatially separating these two functions, as in [Oener et al. 2018], we may have improved the contact while lowered the recombinations by using a lower dopant concentration in the bulk of the GaInP shell.

5.5.6.3 Influence of the pattern

Despite improved performances on the best diode, the performances were found to be inhomogeneous over the sample surface (Figure 5.36).

The samples on the 360 nm pitch patterns are mostly defective (Figure 5.36d), which is reasonable considering the poor array properties, with a very low average yield due to inhomogeneous hole definition by EBL (Figure 5.33). There is a wide spread of the JV parameters, in particular some diodes with very low V_{oc} and FF seem to suffer from shunt.

The diodes from 500 nm pitch patterns are more homogeneous but still lack consistency.

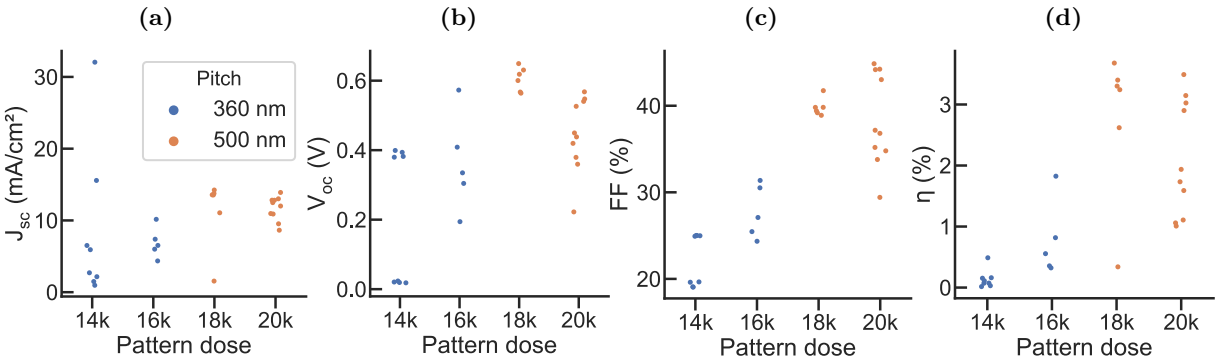

Figure 5.36: *Summary of the parameters extracted from the JV curves under illumination of the diodes from the homojunction sample, before and after a* 400 °C *annealing in inert atmosphere.*

This probably originates from the complicated fabrication process, this sample being part of the first batch being processed with IPVF means, and with an imperfect BCB etching procedure leading to many inhomogeneities.

However, the performances of the *p500-18k* diodes are more closely packed, and lead to efficiencies consistently above 3 % except for one (Figure 5.36d). The diodes from the pattern with higher dose (20k, larger holes), systematically present lower V_{oc} (Figure 5.36b) with more spread. The J_{sc} is also typically slightly lower than for 18k (Figure 5.36a). This is similar to what was previously observed on the other heterojunction sample (Figure 5.28), where the J_{sc} and V_{oc} were typically decreasing with the exposure dose within one pitch.

I have no clear explanation for this phenomenon which requires further investigation. The interface at the foot might suffer more from localized defect states than from a barrier limiting the current, and therefore the performances would improve with a decreasing interface area (hole size) rather than with an increase.

A new generation of NW heterojunction was grown in a new MBE setup and with a degraded fabrication process. The EQE may have benefited from the improved design ($J_{sc} = 14.2\,\mathrm{mA\,cm^{-2}}$), in particular the GaInP external shell doping, and efficiencies up to 3.7 % were measured, with record V_{oc} of 0.65 V.

Table 5.1: *JV characteristics for the best diode of each of the three NW solar cells presented in this thesis. The J_{sc} is determined from the EQE, and the efficiency is accordingly rescaled.*

Sample number	Design	J_{sc} ($\mathrm{mA\,cm^{-2}}$)	V_{oc} (V)	FF	Efficiency (%)
76838, A16_a	Homojunction	12.7	0.39	0.42	2.09
77033, p500_18k_c	Heterojunction	5.7	0.56	0.48	1.52
B276, p500_18k1_c	Heterojunction 2	14.2	0.65	0.40	3.68

5.5.7 Conclusion

Section: Characterization of GaAs/GaInP core-shell heterojunction solar cells

Three NW solar cells-on-Si from different growth and fabrication batches were presented and opto-electrically characterized.
I presented a sample with a novel core-shell GaAs/GaInP design, where the n-GaAs shell is removed. Its EQE is very low, probably hindered by absorption in the thick ITO contact layer, and by recombination due to the likely presence of dislocations in the shell. However, the V_{oc} is increased to 0.6 V, and the JV shape is improved, possibly due to a better interface with ITO, the dopant concentration in the outermost n-GaAs:Si shell being an order of magnitude higher than previously. The performances are worse on the arrays of larger pitch (1000 nm) and seem to depend on the hole size in the mask, for reasons yet unclear. The spatially resolved EL over the surface of one diode is highly inhomogeneous, localized emission could originate from fluctuation of the imperfect ITO/n-GaAs contact, resulting in different applied bias.

Finally, using a new MBE setup and realizing the fabrication at IPVF, a new generation of core-shell heterojunction was fabricated, with an improved design. The performances vary between patterns and over the sample surface, which I attribute in part to fabrication inconsistencies. The lowest pitch (360 nm) yields the worst performances, but the efficiency is consistently above 3 % on one pattern, and reaches 3.7 % for one diode, with a record V_{oc} of 0.65 V, despite the attested presence of dislocations in the GaInP shell. The J_{sc} is improved from the previous sample and reaches 14.2 mA cm^{-2}.

There are still collection issues in the device. The foot could be improved by optimizing the growth on more highly doped Si substrate, or by thinning the GaP stem and increasing its dopant concentration. The front contact with ITO is still mostly unknown despite the studies on planar GaInP, and whether a good electrical contact is formed on highly doped and possibly highly compensated GaInP:Si layers. There is also room for improvement for the NW crystal quality: the droplet consumption should be optimized for every sample growth condition, and the shell composition and thickness can be further optimized to avoid the presence of dislocations.

5.6 Summary of Chapter 5: Nanowire solar cell fabrication and characterization

In Section 5.1, after comparison of different structures employed in the literature, and in light of our previous studies on NW arrays, I choose to fabricate p-i-n core-shell junctions and to embed them inside a filling material to contact them with ITO at the top.

In Section 5.2, I present the development of a double-step planarization technique using SiO_x and BCB, which permits to successfully planarize NW arrays without residual stress. Standard thin-film fabrication techniques are then used, to localize conformal ITO transparent contacts deposited by sputtering and metal pads suited for electrical characterization with point-probes. I demonstrated the fabrication of several hundreds functional diodes over a $1.5 \times 1.5\,\mathrm{cm}$ NW array.

In Section 5.3, I investigated the contact between ITO and planar III-V layers. It is a Schottky contact for low doping that becomes conductive when the III-V layers are highly doped to $n = 1.5 \times 10^{19}\,\mathrm{cm}^{-3}$. The conductivity of the contact on moderately doped GaAs is found to improve after long annealing in air above 400 °C, contrary to GaInP. ITO deposited on glass is also more transparent after annealing. A reproducible annealing scheme is chosen to optimize a n-GaAs/ITO contact, using rapid thermal annealing in inert atmosphere. The contact resistivity was found to improve above 350 °C down to below $10^{-2}\,\Omega\,\mathrm{cm}^2$ at 500 °C. 400 °C is the maximum temperature compatible with BCB, at which the contact resistivity with ITO is fluctuating from $10^{-1}\,\Omega\,\mathrm{cm}^2$ to $10^{1}\,\Omega\,\mathrm{cm}^2$, and is expected to have a reduced but non-negligible impact on the performances of the NW solar cells.

NW solar cells-on-Si with two different architectures were grown and fabricated first in 2018, then in 2019. The first, presented in Section 5.4, is a GaAs core-shell homojunction passivated with AlGaAs, with a conversion efficiency up to $\eta = 2.1\,\%$, hindered by a low V_{oc} and a non-ideal *S-shape* in the JV curve, which slightly improves upon a 400 °C annealing. A very high ideality factor above 4 is attributed to the poor contacts and interfaces at the foot and top of the NWs, in particular, the contact with ITO. The absolute PL of this sample allows to extract the quasi-Fermi-level splitting, which reaches 0.984 V under 80 sun illumination, extrapolated to 0.86 V at 1 sun, indicating a good NW material quality. Sun-V_{oc} and sun-$\Delta\varepsilon_F$ characteristics yields $n = 0.7$, and $n = 1.1$, respectively, also lower than the one from the experimental JV curve, which confirms that collection issues and defective contacts are hindering the performances.

A second sample, presented in Section 5.5, follows a novel core-shell p-i-GaAs/n-GaInP heterojunction design, where the n-GaAs shell is removed. Its EQE is very low, probably hindered by absorption in the thick ITO contact layer, and to recombinations due to the likely presence of dislocation in the shell. However, the V_{oc} is increased to 0.6 V, and the JV shape is improved, possibly due to a better interface with ITO. Spatially resolved EL over the surface of one diode reveals localized emission which could originate from fluctuations of the voltage drop at the contact interfaces.
Using a new MBE setup, another heterojunction device was fabricated with a simplified structure and with a high Si concentration in the GaInP shell close to the ITO contact. Even with inhomogeneous performances attributed to the fabrication, the efficiency reaches 3.7 %, with a record V_{oc} of 0.65 V, despite the attested presence of dislocations in the GaInP shell. The J_{sc} is improved from the previous sample and reaches $14.2\,\mathrm{mA\,cm}^{-2}$.

Conclusion and perspectives

In this thesis, I have focused on a strategy to integrate III-V solar cells on silicon, using NW arrays grown by MBE, as a first step toward cost-efficient tandem solar cells with conversion efficiencies above 30 %. As introduced in Chapter 1, the NW geometry allows to directly grow them on a silicon substrate, avoiding degradation of the material quality due to material mismatch. High absorption is possible while using little material, thanks to light-trapping effects. Self-catalyzed VLS growth by MBE was thus elected, with a core-shell radial junction design, offering a high potential for solar cell operation. I focused on the NW top cell, the most critical part of a tandem device where it is combined with a planar Si bottom cell.

In the introduction, this objective was divided into 3 main challenges:

1. Control of the homogeneity and crystal quality during the growth of GaAs NWs by VLS on patterned Si substrate (Chapter 3).
2. Synthesis of core-shell NW structures, with high core and shell chemical and crystalline quality, and controlled doping levels (Chapter 4).
3. Development of a fabrication process for NW solar cells, and characterization of the fabricated devices (Chapter 5).

Before addressing these topics, theoretical concepts and experimental methods needed to be introduced (Chapter 2).

Chapter 2: Theory and Methods

I first focused on understanding some key concepts to separate and collect charge carriers in semiconductor solar cells, to help design and understand these complex nanoscopic solar cells: particle transport, recombination processes, p-i-n structure, and issues toward making ohmic contacts, with a particular focus on GaAs.

I also explained the basic principles of epitaxial growth by MBE, and described the setups used in this work. I presented two models for the NW growth by VLS, which relate the observed morphology and crystal structure to growth parameters, in particular through the droplet contact angle. I highlighted how the VLS growth could promote an efficient use of precursor materials. I then described the patterned substrate fabrication process, and the baseline procedure for the growth of core-shell NWs by MBE.

Finally, I presented several advanced characterization techniques employed in this thesis. Transmission electron microscopy and cathodoluminescence spectroscopy are used to investigate the properties of individual, as-grown NWs, in particular their crystal structure, composition, and carrier distribution. External quantum efficiency and hyperspectral photoluminescence imaging, on the other hand, allow to characterize fully processed solar cells.

Chapter 3: Growth of Defect-free GaAs NW Arrays on Si

Even using a regular template for the growth, it is a tough task to obtain an array with perfect homogeneity and vertical alignment of all NWs without optimization, and there is room for

improvement especially regarding the growth on Si. The state-of-the art of NW array growth was presented in Section 3.1 and different NW synthesis techniques were compared, showing current limitations in self-catalyzed growth on Si.

I investigated the occurrence of non-vertical growth in self-catalyzed GaAs NW arrays grown by MBE and highlighted different causes, in particular the importance of the polarity of the initial NW seed. I presented the optimization of the vertical NW yield on patterned Si substrates with specific design, growth conditions and substrate preparation. While there is a dependence of the yield of pure GaAs NWs on the Ga pre-deposition volume and on the V/III ratio, this simple growth scheme lacks homogeneity and robustness, as the vertical yield does not consistently reach 90 %. On the other hand, I showed that it is possible to achieve yields higher than **90 %** with reproducibility, through careful preparation of the wafer surface before mask processing, and by initiating the GaAs NW growth with a GaP stem. Other procedures are beneficial for the yield, such as using 2" substrates to limit edge effects or applying a high temperature *in situ* pre-treatment before initiating the growth. I demonstrated homogeneous and reproducible yield above 90 % in mm-wide patterns defined by single-shot EBL, and a yield of **100 %** was attained in 50 µm × 50 µm patterns defined by high resolution EBL.

In Section 3.3, I studied the crystal defects in NWs, in particular those formed during the Ga catalyst consumption, using TEM and atomic-resolution STEM. Consumption at low temperature under a high As flux leads to the formation of an extra WZ segment which is expected as the droplet contact angle diminishes during the droplet crystallization. An elaborate consumption scheme inspired from the literature was employed, which permits to limit the GaAs regrowth to a 50 nm segment with a total of 3 twin planes from the foot to the tip, when a moderate Be flux is provided during axial growth, whereas high Be fluxes lead to uncontrolled overgrowth at the tip. I have also shown that, in these conditions, the droplet consumption mechanism is very sensitive to growth parameter variations, leading to either unconsumed Ga staying at the tip, GaAs re-growth, or in the best cases, defect-free droplet consumption. The inclusion of GaAsP markers helped to evidence the dissolution of part of the GaAs:Be NWs during the droplet consumption. A significant amount of Ga is missing after the consumption, either through evaporation or through diffusion and crystallization at the sidewalls.

Overall, these combined results demonstrate the possibility to grow homogeneous GaAs NW arrays over 1.5 cm×1.5 cm on 2" Si substrates, without crystal defect above the foot and up to the tip after droplet consumption. Such NW arrays make a convenient platform to investigate core-shell structures for photovoltaic devices, which was the object of the next chapter.

Chapter 4: GaAs(P) Core-Shell Nanowire Structures

In the fourth chapter, I studied the fabrication of functional NW core-shell structures for practical use in solar cells: shell growth, doped junctions, specific alloy compositions.

I first introduced the method used to grow core-shell NWs by MBE, and I showed how the NW array morphology improves when growing GaAs shells at 580 °C instead of lower temperatures. I then compared possible materials to grow wide-bandgap passivating shells and chose to focus on AlGaAs and InGaP shells. The composition in InGaP shells was investigated by TEM and EDX and was found to differ from the nominal composition that would be obtained on planar layers, due to the unique growth mode of NW shells. The composition difference and its fluctuations lead to the presence of dislocations, in relative agreement with the predictions of previous experimental and theoretical work. According to the same sources, only small adjustments of the shell thickness and composition are needed to reach dislocation-free conditions.

In Section 4.2 I investigated the mechanisms of Si and Be dopant incorporation in NWs, in order to reach high carrier concentration, necessary for core-shell junctions. Cathodoluminescence (CL) was shown to be an adequate tool to evaluate carrier concentration with the necessary spatial resolution in these nanosized objects. Using a technique developed by our team at C2N, CL spectra are extracted from doped NWs and fitted to the generalized Planck law. Empirical relationships which relate features of the spectrum or fitted parameters to the doping level are established using reference GaAs thin-films, and applied to NWs. P-type doping of GaAs NWs with Be was found to be effective both in the core grown by VLS (up to $8 \times 10^{18}\,\mathrm{cm}^{-3}$) and in the shell grown by VS (up to $1.3 \times 10^{19}\,\mathrm{cm}^{-3}$), in agreement with previous literature. N-type doping with Si was only investigated for GaAs NW shells as previous literature showed incorporation as acceptor (p-type) in NWs grown by VLS. Signature of p-type or heavily compensated n-type GaAs was found for NW shells grown at 580 °C. At lower temperature (450 °C), the shells appear to be of n-type but strong compensation is still suspected as the measured carrier concentrations are lower than the estimated dopant concentrations by an order of magnitude. These unexpected compensation phenomena seem to be due to the NW geometry which minimized the local V/III ratio, although alternative growth schemes did not result in improvements of the electron concentration which remains limited to $5 \times 10^{17}\,\mathrm{cm}^{-3}$ in our conditions.

In Section 4.3 I investigated composition inhomogeneities in $GaAs_{1-x}P_x$ NWs, as such alloys can be tuned to a bandgap of 1.7 eV, optimal for tandem-on-Si. A specific NW design allowed to evidence the simultaneous growth of an As-rich shell during the core growth, which was characterized by STEM-EDX. The shell composition is shown to depend on the underlying core, but this effect cannot be used to completely match both compositions. However, the temperature was found to change the P content both in the core and in the shell, which allows to obtain GaAsP NWs with matching core and shell compositions, at 1.7 eV bandgap. There are still composition inhomogeneities in the NWs as a P-rich layer is always present at the interface between the core and the shell, for reasons not yet understood.

Overall, growing core-shell GaAs NWs with p-doped core and n-doped shell appears possible, although the doping is limited in the shell and there is a trade-off between the shell morphology and its effective n-type doping depending on the substrate temperature. GaInP shells seem promising to passivate NWs but require special optimization to tune their composition. Due to the required optimization to partially control the alloy homogeneity in GaAsP NWs, I decided to focus on GaAs NWs for the fabrication of NW solar cells.

Chapter 5: Nanowire Solar Cell Fabrication and Characterization

The last chapter is dedicated to the development of a fabrication process for NW solar cells, and to their opto-electrical characterization.

I have first elected a strategy for the solar cell fabrication, in light of previous literature works (Section 5.1). A planarization method was developed using SiO_x and BCB, to leave only the top of the NWs emerging, without residual stress in the array. Individual diodes are then processed using cleanroom techniques, like for a planar semiconductor solar cell. I demonstrated the fabrication of several hundreds of functional diodes over a 1.5×1.5 cm NW array.

In Section 5.3, I optimized the contact between n-III-V planar layers and localized ITO contacts, to then extrapolate my findings to ITO contacts deposited on NW arrays. Obtaining an ohmic contact at such interface is notoriously complicated as GaAs is prone to Fermi-level pinning. I showed that the contact between n-GaAs and ITO is a Schottky contact that becomes conductive when GaAs is doped to $n = 1.5 \times 10^{19}\,\mathrm{cm}^{-3}$. A reproducible annealing scheme is chosen to optimize a n-GaAs/ITO contact, using rapid thermal annealing in inert atmosphere. The contact resistivity was found to improve above 350 °C down to below $10^{-2}\,\Omega\,\mathrm{cm}^2$ at 500 °C.

The ITO transparency also improves upon annealing, especially at low wavelengths (<700 nm). 400 °C is the maximum temperature compatible with BCB, at which the contact resistivity with ITO is fluctuating from $10^{-1}\,\Omega\,cm^2$ to $10^{1}\,\Omega\,cm^2$, and is expected to have a reduced but non-negligible impact on the performances of the NW solar cells.

In Section 5.4, I fully characterized a NW solar cell based on a **GaAs core-shell homojunction**, passivated with AlGaAs. Its PCE (1.5 % and 2.1 %, before and after a 400 °C annealing, respectively) is hindered by a low V_{oc} (0.4 V) and a non-ideal JV curve (*S-shape*, cross-over). A very high ideality factor above 4 is attributed to the poor contacts and interfaces at the foot and top of the NWs, in particular, the contact with ITO. The absolute PL of this sample allows to extract a **quasi-Fermi-level splitting of 0.98 V under 82 sun illumination, extrapolated to 0.86 V at 1 sun**, indicating a sufficient NW bulk material quality. Sun-V_{oc} and sun-$\Delta\varepsilon_F$ characteristics yield $n = 0.7$, and $n = 1.1$, respectively, also lower than the one extracted from the experimental JV curve, which confirms that collection issues and defective contacts are hindering the performances.

In Section 5.5, in order to avoid the defective n-GaAs shell, prone to uneven thickness, and in the hope to enhance the Fermi-level splitting across the solar cell, a novel **p-i-GaAs/n-GaInP heterojunction** design is proposed, where the n-GaAs shell is removed. New solar cells show limited efficiencies (up to 1.3 % and 1.6 %, before and after a 400 °C annealing, respectively), due to a very low EQE ($Jsc = 5.9\,mA\,cm^{-2}$), probably hindered by absorption in the thick ITO contact layer, and to recombinations due to the likely presence of dislocation in the shell. However, **the V_{oc} is increased to 0.6 V**, and the JV shape is improved, possibly due to a better interface with ITO. Spatially resolved EL over the surface of one diode reveals localized emission at the NW scale, which could originate from fluctuations of the voltage drop at the contact interfaces.

Using a new MBE setup, another heterojunction device was fabricated with a simplified structure, targeting a high Si concentration in the GaInP shell close to the ITO contact, *via* delta-doping. **The efficiency now reaches 3.7 %**, with **a record V_{oc} of 0.65 V**, despite the attested presence of dislocations in the GaInP shell. The **J_{sc}** is improved from the previous sample and reaches **$14.2\,mA\,cm^{-2}$**.

Overall, a fabrication process was developed to fabricated core-shell NW solar cells, a front-contact was studied and optimized with temperature and doping constraints, and solar cells were fabricated and characterized. The solar cells exhibit limited performances, but strong luminescence, suggesting that contact issues are the current limitation. A new core-shell heterojunction design with a high dopant concentration near the contact showed improved performances and a record V_{oc} (0.65 V) among NW solar cells grown on Si.

Perspectives

In the short-term, the development of the standalone NW top cell appears to remain the priority towards a tandem-on-Si. The best device presented here is a 3.7 % cell, which is limited at least in part for process reasons: the vertical yield is only 80 % although I demonstrated reliable yields above 90 % and close to 100 % using high-resolution EBL patterning; many NWs are disconnected due to polymer thickness inhomogeneity; and the substrate fabrication and preparation was realized in a degraded environment with possible contaminations. Re-development of (1) a reliable substrate fabrication process, (2) NW growth in the new MBE setup, in particular the temperature control for defect-free droplet consumption, and (3) a robust solar cell fabrication process, are needed. Then, the next devices could be characterized using the tools and techniques used in this thesis: luminescence mapping to identify contacting issues, EQE and STEM-EDX to solve shell composition fluctuations and dislocations, PL mapping to compare the V_{oc} and

the Fermi-level splitting in the NWs. The issues hindering the performances could then be finely investigated without the interference of process-related degradation, to ultimately solve the question of whether fundamental issues prevent NW solar cell on Si to function properly, or not.

Further optimization could then be focused on particular subjects, as identified in the previous chapters, still focusing on binary compounds such as GaAs to reduce complexity, before transitioning to ternary alloys such as GaAsP, with a more optimal bandgap.

- Regarding the vertical yield, recently reported results suggest that SAE by MBE can lead to high yield, using specific *in situ* sequences to prepare the Si surface before initiating the growth [Ruhstorfer et al. 2020]. A similar sequence could be used to make a NW stem, and the growth could them resume to VLS, which still permits a better control of the crystal phase and quality.
- GaInP shell composition could be better controlled in arrays with high vertical yield, and the precise growth conditions leading to an average composition close to the one lattice-matched to GaAs could be determined, thus avoiding dislocations and possible recombination of carriers generated in or near this high-bandgap shell.
- Doping of the n-shell (GaAs) could be further investigated using CL measurement, with further studies involving the use of the concepts introduced at the end of Section 4.2: new cell geometries to promote high local V/III ratio at the NW sidewalls, extension of the technique to other materials such as GaInP. The comparison of the electron concentrations in planar GaAs:Si and GaInP:Si (110) layers grown in a given range of conditions, through measuring their electron concentration by Hall effect, might also give more insight on different dopant incorporation dynamics between both materials.
- The use of Te as an alternative n-type dopant might help to overcome the current limitation, about $5 \times 10^{17}\,\mathrm{cm}^{-3}$ in the shell. A study is underway in our team to characterize the doping in Te-doped NWs by CL, in collaboration with Tampere University (Finland).
- Eventual barriers for carrier collection are suspected at the heterointerfaces at the foot (p-Si/p-GaP/p-GaAs). They could also be further investigated, through using highly doped Si substrates, or higher doping concentration in the GaP for example. Similarly, the Schottky barrier at the NW top (n-GaAs/ITO) could benefit from the techniques hinted in this thesis to make better ohmic contacts: delta-doping for increased dopant activation, or introduction of dopants above the limit of incorporation, to purposefully introduce deep levels.
- The detrimental effect of the presence of twin planes and stacking faults is still debated, however their annihilation above the foot is possible as shown here. To remove them inside the foot, it could be useful to investigate a wider range of parameters (droplet predeposition volume and V/III ratio mainly) at the beginning of the growth, for fine control over the contact angle.

More generally, the different techniques and optimizations developed here for the growth of NW arrays and the fabrication of core-shell structures may serve other fields of applications involving self-catalyzed NWs, such as light-emitting diodes, lasers, or photodetectors.

NW arrays are also very similar in nature to polycrystalline thin-films. Indeed, grain boundaries in materials such as CIGS delimit microscopic domains of roughly cylindrical shape, with important surface recombinations, which are then connected in parallel into complete solar cells (Figure 5.37). The knowledge gained about contact processing, dopant incorporation, impact of surface recombinations, or spatially resolved characterization, could thus be helpful for the development of these technologies as well.

(a) *NW array solar cell.*

(b) *CIGS thin-film solar cell.*

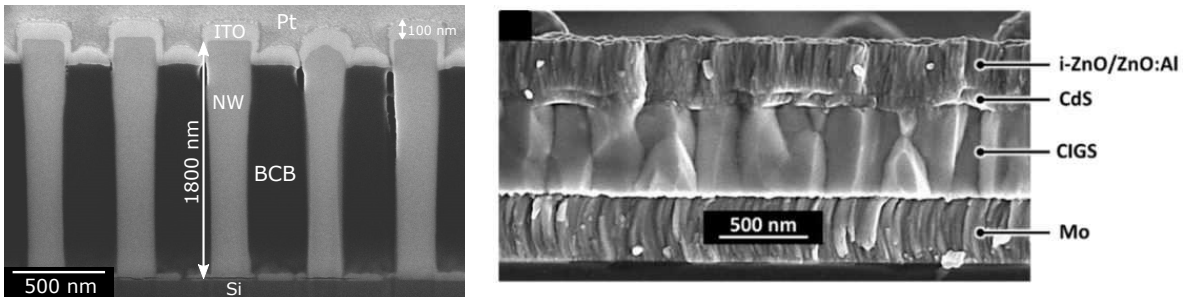

Figure 5.37: *Cross-section SEM view of complete NW solar cells illustrating the analogy between (a) NW arrays and (b) polycrystalline thin-films with vertical grains, from [Gouillart 2020].*

Summary in french

Introduction

En 2018, les énergies renouvelables ont assuré 26 % de la production globale d'électricité [REN21 2019], et l'on s'attend à ce que cette part augmente à 70–85 % en 2050 [IPCC 2018]. Cette croissance rapide est motivée par une prise de conscience généralisée de l'influence humaine sur le changement climatique, ainsi que par des prix de plus en plus compétitifs pour les énergies renouvelables face aux énergies fossiles, grâce à un développement technologique et industriel constant. La communauté internationale s'est engagée à limiter le réchauffement climatique à 1.5 °C par rapport à la température de l'ère pré-industrielle, en signant l'accord de Paris sur le climat.

L'utilisation de l'énergie solaire et en particulier le photovoltaïque (PV), occupe une place importante parmi les énergies renouvelables, car il s'agit d'exploiter une source d'énergie inépuisable: la lumière du soleil ; et ce avec de faibles émissions de gaz à effet de serre. Le marché du PV pour la production terrestre d'électricité est dominé par les technologies à base de plaquettes de silicium (Si), qui représentent 95 % des modules solaires fabriqués. Leur efficacité de conversion est proche de 20 % et leur prix n'a cessé de décroître ce qui permet aujourd'hui d'installer des systèmes PV de grande échelle avec un coût de l'électricité compétitif, sans besoin de subventions. Cependant, l'efficacité des cellules solaires en Si est fondamentalement limitée et restera toujours sous la barre des 30 %. Ainsi, de nouvelles technologies devraient les supplanter au cours des 10 prochaines années, en particulier celles combinant plusieurs cellules superposées les unes aux autres (cellules 'tandem'), et qui maximisent l'utilisation du spectres solaire. Ces technologies tandem devront *a priori* combiner un nouveau matériau avec des cellules en Si pour bénéficier de la maturité technologique et industrielle de ces dernières.

Les semiconducteurs III-V sont les matériaux les mieux adaptés pour réaliser des cellules solaires à très haute performance, notamment des tandems, même si leur application est limitée à la recherche ou au spatial à cause de leur coût élevé. Ils représentent néanmoins une excellente plate-forme pour l'exploration de nouveaux concepts de PV à haute efficacité: nanostructures pour améliorer le piégeage optique, procédés de synthèse innovants, compréhension de mécanismes fondamentaux comme les porteurs chauds, formation de contacts, de couches passivantes, *etc.* Les connaissances accumulées en étudiant des cellules solaires III-V qui implémentent ces concepts pourraient ensuite être transféré à d'autres domaines du PV, comme les technologies à base de couche mince, où la présence de joints de grain microscopiques les rend comparables à des matériaux nanostructurés.

Les III-V étant des matériaux cristallins, il est nécessaire de les synthétiser par *épitaxie*, en les faisant croître sur un substrat cristallin pré-existant. Une des manières de réaliser des cellules solaires tandem en III-V sur Si est d'utiliser un substrat III-V, de fabriquer une couche mince de quelques microns d'épaisseur (la cellule solaire) par épitaxie, puis de décoller cette couche pour la reporter ensuite sur une cellule Si et ainsi réaliser la tandem. Cette approche est complexe à cause de la technologie non triviale pour assembles les deux cellules, et surtout encore trop couteuse car le substrat de matériaux III-V, s'il peut être réutilisé pour la fabrication de plusieurs couches minces, n'en reste pas moins extrêmement cher. Les scénarios qui évaluent le cout d'une production industrielle de ce genre de cellule solaires prévoient des prix un ordre

de grandeur au dessus des technologies actuelles.

Pour éviter le surcoût du substrat III-V, une alternative serait de réaliser l'épitaxie de la cellule III-V directement sur la cellule Si, elle aussi cristalline. Malheureusement, les matériaux sont incompatibles en raisons de leur polarité (ou non), des dégradations de la cellule Si pendant l'épitaxie, mais surtout car leurs paramètres de maille sont différents, ce qui entraine la formation inévitable de dislocations dans la cellule III-V, limitant drastiquement ses performances. Le record d'efficacité de cellule tandem utilisant cette technologie est de 22.3 %.

Dans ce travail de thèse, j'étudie des nanofils (NF), des nanostructures qui présentent l'avantage, de par leur faible diamètre, de pouvoir relaxer les contraintes mécaniques sans générer de défauts. Ils peuvent ainsi être synthétisés par épitaxie directe sur substrat Si (voir Figure 38a), ce qui est notamment possible en utilisant le mécanisme de croissance vapeur-liquide-solide (VLS), la technique employée ici. Une goutte composée d'une des précurseurs du NF est située au sommet de celui-ci et y catalyse la croissance. Ce procédé permet une meilleure utilisation des éléments V par rapport à la croissance de couche mince, car les éléments sont dispensés en proportions proches de la stœchiométrie, ce qui ouvre des perspectives d'économie de matériaux. Une réduction de coûts serait aussi possible grâce aux propriétés de piégeage optique de nanofils en réseaux, qui permettent d'absorber efficacement la lumière incidente dans un faible volume de matériau.

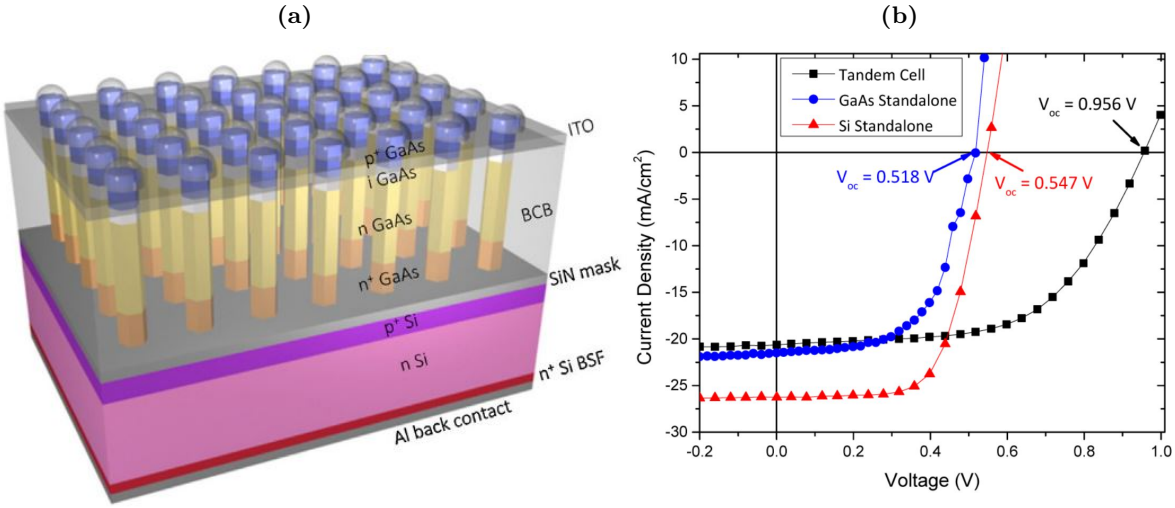

Figure 38: *(a) Représentation schématique et (b) caractéristique courant-tenstion (JV) d'une cellule soalire tandem en nanofils de GaAs crûs par SAE-MOCVD sur une cellule de base en Si. L'accord des courant et l'addition des tensions sont visibles. Extrait de [Yao et al. 2015].*

Les cellules solaires à nanofils permettent tout comme leurs équivalents planaires d'atteindre de hauts rendements (prédiction de 33 % en tandem sur Si [LaPierre 2011b]), et des cellules à base d'InP réalisées par gravure dans une cellule massif ont déjà montré une efficacité de conversion de 17.8 % [Dam et al. 2016]. Des cellules à 15.3 % d'efficacité en GaAs (arséniure de gallium) ont été réalisées par croissance VLS sur substrat GaAs, en utilisant un catalyseur en or [Aberg et al. 2016]. Ces preuves de concepts illustrent le potentiel des nanofils mais n'ont pas démontré la faisabilité d'une cellule sur Si, pour lesquelles en particulier un catalyseur en or n'est pas envisageable, en raison de sa diffusion dans le silicium et des défauts qu'il y génère. Pour l'instant, les démonstrations de cellules solaires par croissance de NFs sur Si culminent vers 4 % d'efficacité pour des NFs GaAs crûs par MBE en utilisant du gallium (Ga) comme catalyseur (croissance 'auto-catalysée') ([Dastjerdi et al. 2016]; [Boulanger et al. 2016]), et à 11.4 % pour une tandem Si (planaire)/GaAs (NF) crûe par croissance épitaxiale sélective, sans catalyseur (Figure 38). La croissance auto-catalysée via épitaxie par jet moléculaire (MBE) présente des avantages intéressants par rapport à la croissance sans catalyseur, pour le contrôle de la qualité

cristalline. En effet, il a été montré théoriquement ([Glas et al. 2007]) et expérimentalement ([Jacobsson et al. 2016]; [Panciera et al. 2020]) que l'angle de contact que forme la goutte avec le nanofil contrôle la phase cristalline formée.

Malgré ce potentiel et les nombreux travaux sur la croissance auto-catalysée sur Si, les performances sont encore limités par plusieurs aspects:

- La morphologie du réseau de nanofils est souvent dégradée, avec de nombreux fils non-verticaux souvent à cause de la nucléation imparfaite sur le Si.
- La qualité cristalline des nanofils, contrôlable en théorie, est contrainte par les conditions de croissances spécifiques à l'initiation et la terminaison du NF.
- Le dopage par addition contrôlée d'impureté dans les nanofils n'est pas maitrisé comme pour l'épitaxie de couches minces, à cause de leurs modes de croissance originaux. Il est en particulier difficile de mesurer avec précision la concentration des porteurs de charge dans ces nanostructures.
- La fabrication de cellules solaires à partir de millions de nanofils représente un défi technologique, en particulier en ce qui concerne le contact transparent en face avant.

Ainsi, après avoir introduit le contexte de cette recherche et l'objectif envisagé dans le chapitre 1, puis décrit les notions théoriques et méthodes expérimentales utilisées dans le projet dans le second chapitre, je présente dans les chapitres 3, 4 et 5 mes résultats expérimentaux vers la résolution des problèmes mentionnés ci-dessus, pour aboutir à la fabrication de cellules solaires complètes et à leur caractérisation.

Croissance de réseaux de nanofils en GaAs sur substrat silicium

La croissance d'un réseau de NFs en GaAs présentant des dimensions homogènes et une bonne qualité cristalline est un préliminaire à toute applications impliquant ces réseaux de NFs. Un premier objectif a été le contrôle de la croissance sélective de NFs en réseaux organisés, notamment en assurant un taux de verticalité supérieur à 90 %, voire de 95 % à 100 % sous certaines conditions.

Je présente tout d'abord un bref historique du développement de réseaux organisés de nanofils ainsi que l'état de l'art du contrôle de la verticalité. Il apparait que la croissance auto-catalysée sur Si résulte généralement en nanofils non verticaux, ce qui suggère que l'interface avec le Si et la nucléation des premières couches atomiques sont cruciales. Cette hypothèse est corroborée par l'observation systématique des orientations des nanofils que j'ai crûs par MBE auto-catalysée, qui suggère que les fils qui démarrent suivant la direction $\langle 111 \rangle B$ restent verticaux alors que ceux qui démarrent suivant $\langle 111 \rangle A$ se déstabilisent pour suivre une direction $\langle 111 \rangle B$ non verticale. Ce modèle peut expliquer la plupart des évènements de non-verticalité dans les réseaux étudiés ici, et d'autres phénomènes comme les macles 3D sont plus secondaires.

La première étude d'optimisation de la verticalité consiste à varier les paramètres de croissance. Cependant, si les NFs de GaAs présentent une dépendance à certains paramètres, le taux de verticalité reste généralement bas, inhomogène, et manque de reproductibilité, ce qui met en cause la robustesse de notre approche. En revanche, la combinaison de deux améliorations permet d'assurer des taux de verticalité robustes, supérieurs à 90 %: l'initiation de la croissance en GaP avant de la poursuivre en GaAs, et l'adoption d'une technique de nettoyage du substrat Si à base de cycles d'oxidation et de gravure sèche avant fabrication du masque sélectif (Figure 39). Une fois cette procédure robuste établie, je montre que le taux de verticalité est peu sensible aux paramètres de croissance (température du substrat et taille de goutte de Ga). D'autres paramètres permettent ensuite d'optimiser la verticalité jusque 95 %: la croissance au centre de substrat grande taille (2") pour une meilleure homogénéité, et une étape de traitement thermique *in situ* à 800 °C avant la croissance. L'utilisation de lithographie électronique haute résolution a même permis d'atteindre 100 % sur une zone de $50 \times 50\,\mu m$ (Figure 39c), mais

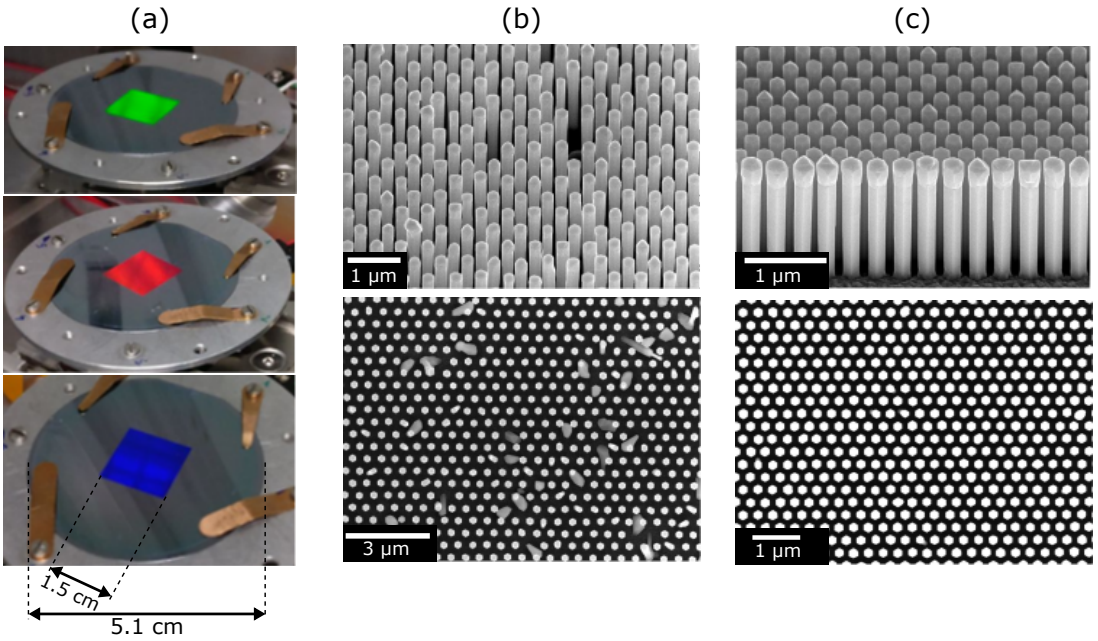

Figure 39: *(a) Photographie d'un substrat Si de 2" avec un réseau hexagonal de NFs sur une surface de* 1.5 cm×1.5 cm *au centre. La périodicité des NFs induit une diffraction de la lumière blanche du laboratoire à des angles et des couleurs précis. (b) Image au microscope électronique à balayage (SEM) du réseau de NFs après épitaxie, avec* 45° *d'angle de vue (haut) ou vu du dessus (bas). Le taux de verticalité dépasse* 90 %*. (c) Image d'un réseau donc le masque sélectif a été défini par lithographie électronique à haute résolution, 'pixel-par-pixel'. Le taux de verticalité est de* 100 %*. [76838]*

cette technique est trop lente pour pouvoir réaliser les réseaux de plusieurs mm^2 nécessaires à la fabrication de cellules solaires.

j'ai également étudié les défauts cristallins dans les NFs, en particulier les fautes d'empilement selon la direction $\langle 111 \rangle B$. Mis à part au niveau du pied, il est possible de choisir des conditions de croissances qui limitent leur présence à maximum 1 dans les premiers 1.5 µm de NFs GaAs, vraisemblablement grâce à un large angle de contact de la goutte dû à un faible ratio de flux V/III (1.4). Ma principale étude concerne les fautes formées lors de la consommation *in situ* de la goutte de Ga, en utilisant de la microscopie électronique en transmission à haute résolution (TEM et STEM) pour la caractérisation. La consommation de goutte à 500 °C sous flux d'arsenic (As) conduit à la formation d'un segment supplémentaire de GaAs en phase hexagonale Wurtzite (WZ), ce qui est attendu lorsque l'angle de contact de la goutte diminue au fur et à mesure de sa réduction.

Une technique de consommation de goutte inspirée de la littérature a été utilisé, et a permis de limiter la re-croissance de GaAs à un segment de 50 nm comprenant seulement 3 fautes d'empilement dont un segment WZ. L'apport d'un flux modéré de béryllium (Be) est nécessaire pour atteindre ce résultat, alors qu'un flux élevé de Be résulte en une excroissance latérale incontrôlée des têtes de NFs. Par optimisation des conditions pendant cette étape de consommation, des fils entièrement dépourvus de fautes dans leur partie supérieure ont été crûs. Je montre cependant que cette procédure de consommation est particulièrement sensible aux fluctuations des conditions de croissance, ce qui peut entrainer une consommation partielle de la goutte, ou une re-croissance de GaAs au sommet du fil plus importante (plusieurs centaines de nm). L'inclusion de marqueurs périodique de GaAsP dans les NFs a permis de mettre en évidence la dissolution d'une partie des NFs GaAs:Be au cours de la consommation de goutte. La majorité du Ga initialement présent dans la goutte n'est plus présent après la consommation, ce qui peut être attribué à de l'évaporation, ou de la diffusion puis cristallisation au niveau des facettes latérales des NFs.

Ces résultats, une fois combinés, montrent qu'il est possible de faire croître des réseaux de NFs GaAs homogènes au milieu de plaquettes de Si 2", sur des surfaces de 1.5 cm×1.5 cm, sans faute d'empilement à part proche du pied des NFs, grâce à une consommation de goutte optimisée. De tels réseaux de NFs constituent une base de référence pour étudier des structures plus élaborées comme des jonctions cœur-coquille pour des dispositifs PV, ce qui est l'object du chapitre suivant.

Structures cœur-coquille dans des nanofils GaAs(P)

Dans le quatrième chapitre, j'ai étudié la fabrication de structures cœur-coquille fonctionnelles pour les cellules solaires à NF. En particulier, il s'agit de contrôler la croissance de coquilles de GaAs ou d'autre alliage III-V, de réaliser des jonctions en dopant le cœur et la coquille, et d'étudier des alliages III-V spécifiques adaptés au PV.

J'ai tout d'abord introduit la méthode utilisée pour croitre des coquilles de NF par MBE, et montré que la morphologie de réseaux de NFs GaAs est meilleure quand les coquilles sont crûes à 580 °C et pas moins. J'ai ensuite comparé différents matériaux candidats pour réaliser des coquilles de passivation à grande largeur de bande interdite, et décidé de me concentrer sur AlGaAs et GaInP. AlGaAs, en accord de maille avec GaAs quelle que soit sa composition, présente l'avantage de la simplicité en dépit d'une propension à se déposer sur le masque. InGaP est moins sujet à ce défaut mais nécessite une composition précise pour être en accord de maille avec GaAs. La composition et la structure de coquilles GaInP autour de cœurs GaAs ont été analysés par TEM et par analyse dispersive en énergie de rayons X (EDX), ce qui a permis de mettre en évidence des fluctuations importantes de composition entre le sommet du fil et les facettes, attribuées à l'influence complexe des orientations des flux de matériaux en fonctions des effets d'ombrage et de ré-émission. Cet écart à la composition nominale induit la formation de dislocations, conformément à ce que prédisent des travaux théoriques et expérimentaux antécédents. Selon ces mêmes travaux, peu d'ajustement sont nécessaires en terme de contrôle de la composition et de l'épaisseur des coquilles GaInP pour atteindre un régime sans dislocations.

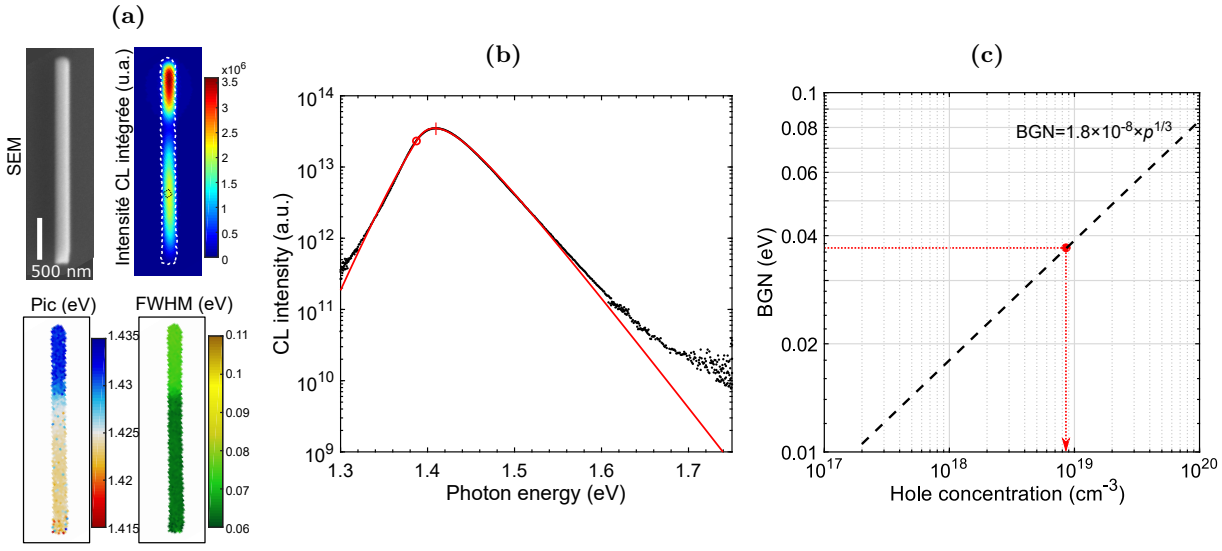

Figure 40: *(a) Cartographie de CL à température ambiante d'un NF au coeur GaAs dopé Be, passivé par une coquille AlGaAs:Be. Le spectre moyen est extrait des pixels encadrés en tirets noirs. [76847] (b) Spectre de CL à température ambiante. En rouge: ajustement à la loi de Planck généralisée. Les positions de la largeur de bande interdite (point) et du niveau de Fermi (trait vertical) sont indiqués. (c) Concentration de trous déduite du rétrécissemnt de la bande interdite (BGN), en utilsant la relation empirique d'Equation 4.9. Adapté de [Chen et al. 2020a]. [76741]*

Je me suis ensuite penché sur les mécanismes d'incorporation des dopants Si et Be dans les NFs de GaAs, afin d'atteindre de hautes concentrations de porteurs de charge, nécessaires pour réaliser des jonctions cœur-coquille. J'ai montré en quoi la cathodoluminescence (CL) est un outil adéquat pour évaluer les concentrations de porteur avec la précision spatiale nécessaire pour ces objet nanoscopiques (Figure 40a). En utilisant une technique développée par notre équipe au C2N, des spectres de CL de NFs dopés ont été analysés et ajustés à la loi de Planck généralisée (Figure 40b). Des relations empiriques permettant de relier des caractéristiques des spectres de luminescence aux concentrations de porteurs ont été établies en utilisant des couches minces de référence, puis appliquées aux NFs (Figure 40c). Je montre que le dopage de type p (Be) des NFs de GaAs est réalisable dans le cœur crû par VLS et dans la coquille crûe en régime vapeur-solide (VS), jusqu'à $p = 8 \times 10^{18}\,\mathrm{cm}^{-3}$, conformément à d'autres travaux de la littérature. Le dopage de type n (Si) a été étudié uniquement pour des coquilles de NFs GaAs, puisque des travaux antérieurs ont montré que Si, dopant amphotère pour les III-V, s'incorpore volontiers en tant qu'accepteur (type p) dans des nanofils de GaAs crûs par VLS. J'ai observé une signature de GaAs:Si de type p, ou de type n extrêmement compensé, en étudiant des coquilles crûes à haute température (580 °C). A plus basse température (450 °C), les coquilles semblent être de type n, mais une importante compensation est toujours soupçonnées puisque les concentrations d'électrons mesurées sont inférieures d'un ordre de grandeur aux concentrations de dopant estimées. Ces mécanismes de compensation ne sont pas attendus pour des couches planaires crûes dans les mêmes conditions, et semblent dûes à la géométrie particulière des NFs qui minimisent le ratio V/III localement. Cependant, des stratégies de croissances alternatives visant à atténuer ce problème n'ont pas démontré une hausse franche de la concentration d'électrons, qui reste limitée vers $5 \times 10^{17}\,\mathrm{cm}^{-3}$ dans nos conditions.

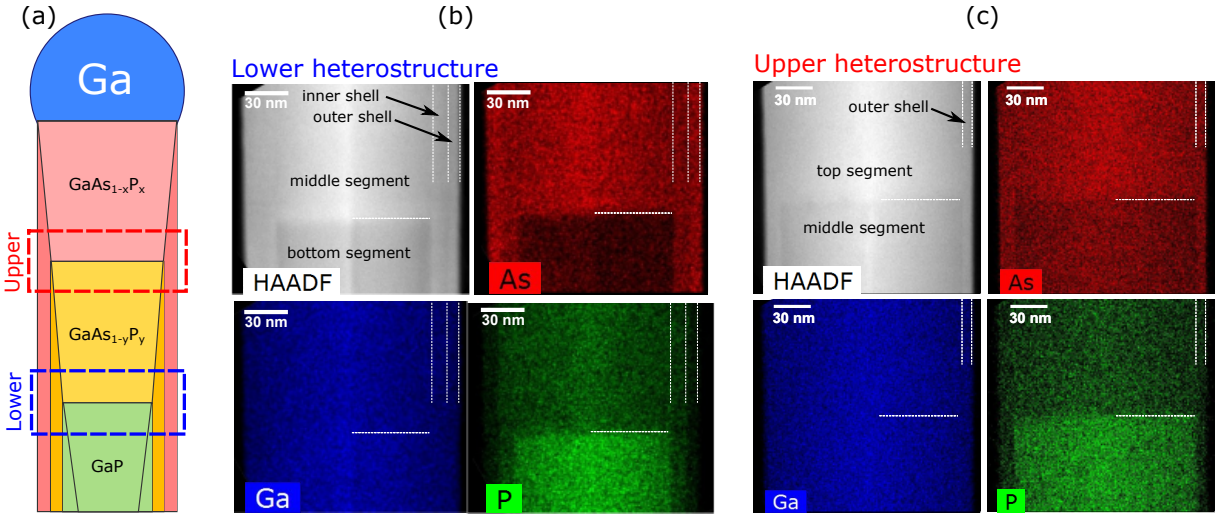

Figure 41: *(a) Schéma d'un nanofil incluant 3 étapes avec des compositions de $GaAs_{1-x}P_x$ différentes le long de l'axe. Une croissance radiale a également eu lieu durant la croissance axiale, ce qui résulte en plusieurs coquilles. (b),(c) Images TEM et EDX acquises suivant l'axe de zone $\langle 11\bar{2} \rangle$, et qui révèlent des structures cœur-coquille (a)simple et (b)double au niveau des deux transitions. Les coquilles sont toujours plus riches en As que le coeur correspondant. [76659]*

Enfin, je me suis attaché à l'étude des inhomogénéités de composition dans des NFs de $GaAs_{1-x}P_x$, car pour une certaine composition, ce matériau peut présenter une bande interdite de 1.7 eV, optimale pour une cellule solaire tandem sur Si. Une architecture de NF spécifique en 3 étages a permis de mettre en évidence la croissance simultanée et accidentelle d'une coquille pendant la croissance VLS du cœur, caractérisée par STEM-EDX (Figure 41). Je montre que la composition de cette coquille dépend de celle du cœur sur laquelle elle croît, mais cet effet ne peut pas être exploité pour rendre les deux composition identiques. En revanche, la température

a une influence sur la fraction de P dans le cœur et dans la coquille, ce qui permet, en l'adaptant, de croître des NFs $GaAs_{1-x}P_x$ de composition identique entre cœur et coquille, pour une bande interdite de 1.7 eV. Il reste néanmoins des inhomogénéités dans les NFs: une fine région de quelques monocouches atomiques est plus riche en P, à l'interface entre le cœur et la coquille, quelles que soient les conditions. L'origine de sa formation n'est pas encore établie.

Finalement, il est possible de croître des NFs GaAs avec un cœur dopé p et une coquille dopée n, même si le dopage est limitée dans la coquille, et qu'il y a un compromis entre la morphologie de la coquille et son dopage n efficace, selon la température du substrat. Les coquilles GaInP sont prometteuses pour passiver les NFs mais demandent une optimisation spécifique pour ajuster leur composition. A cause des contraintes requises pour contrôler partiellement l'homogénéité de la composition de NFs $GaAs_{1-x}P_x$, je décide de privilégier les nanofils GaAs pour la fabrication de cellules solaires.

Fabrication et caractérisation de cellules solaires en nanofils

Le dernier chapitre est consacré au développement d'un procédé de fabrication pour les cellules solaires à NF, puis à la caractérisation de dispositifs complets.

J'ai tout d'abord précisé l'architecture et la méthode de fabrication envisagées, au regard des résultats des chapitres précédents et de travaux antérieurs de la littérature. J'ai développé une méthode de planarisation des réseaux de NFs en combinant une première enduction de silice par dépôt chimique en phase vapeur assisté par plasma, puis une encapsulation dans une matrice de polymère (BCB), sans contrainte résiduelle apparente dans le réseau de fils. Le sommet des NFs est découvert par gravures successives pour permettre de les contacter électriquement. Des diodes individuelles sont ensuite définies par photolithographie, en utilisant des procédés standard de fabrication de dispositifs planaires III-V, notamment des dépôt de métaux et d'oxydes. Plusieurs centaines de diodes fonctionnelles ont ainsi été fabriquées à partir d'un échantillon comportant un réseau de NFs de 1.5×1.5 cm.

Le contact avant de la cellule solaire, entre les coquilles de type n des NFs et un oxyde transparent conducteur, est particulièrement complexe car le GaAs est sujet à un blocage du niveau de Fermi à ses surfaces libres et interfaces. J'ai donc étudié et optimisé le contact entre des couches minces de III-V de type n et des contacts localisés d'oxyde d'indium-étain (ITO: In_2O_3:SnO_2) pour ensuite extrapoler ces résultats aux contacts déposés sur les réseaux de NFs. Si le contact n-GaAs/ITO est de type Schottky à $n = 1.5 \times 10^{18}\,cm^{-3}$, il devient ohmique dès lors que le GaAs est dopé plus fortement à $n = 1.5 \times 10^{19}\,cm^{-3}$. Une méthode reproductible basée sur un recuit rapide sous atmosphère inerte est finalement choisie pour optimiser un contact n-GaAs/ITO. La température de recuit maximale compatible avec l'usage de BCB est 400 °C, à laquelle la résistivité du contact n-GaAs/ITO varie entre 10^{-1} et $10^{1}\,\Omega\,cm^2$, et pourrait donc avoir un impact non-négligeable sur les performances des cellules solaires. La transparence de l'ITO est également améliorée par un recuit, en particulier aux basses longueurs d'onde (la transmittance de l'ITO sur lame de verre à $\lambda = 400$ nm passe de 60 % à 80 %).

La première cellule solaire entièrement fabriquée et caractérisée est une homojonction cœur-coquille à base de GaAs, passivée par AlGaAs (Figure 42a). Son efficacité (1.5 % avant, et 2.1 % après un recuit à 400 °C) est limitée par une faible tension à circuit ouvert ($V_{oc} = 0.4$ V), et par une courbe courant-tension (JV) non idéale (forme en S, croisement). Un haut facteur d'idéalité supérieur à 4 est attribué aux contacts et interfaces non ohmiques, en particulier celui avec l'ITO. J'ai réalisé une mesure de la photoluminescence (PL) en unité absolue sur cet échantillon, qui permet d'extraire un écart des niveaux de Fermi de 0.98 V à 82 soleils d'illumination, ce qui indique une bonne qualité du matériau. Les courbes soleil-V_{oc} et soleil-$\Delta\varepsilon_F$ donnent $n = 0.7$, et $n = 1.1$, respectivement, valeurs plus faibles que celle de la courbe JV, ce qui confirme que

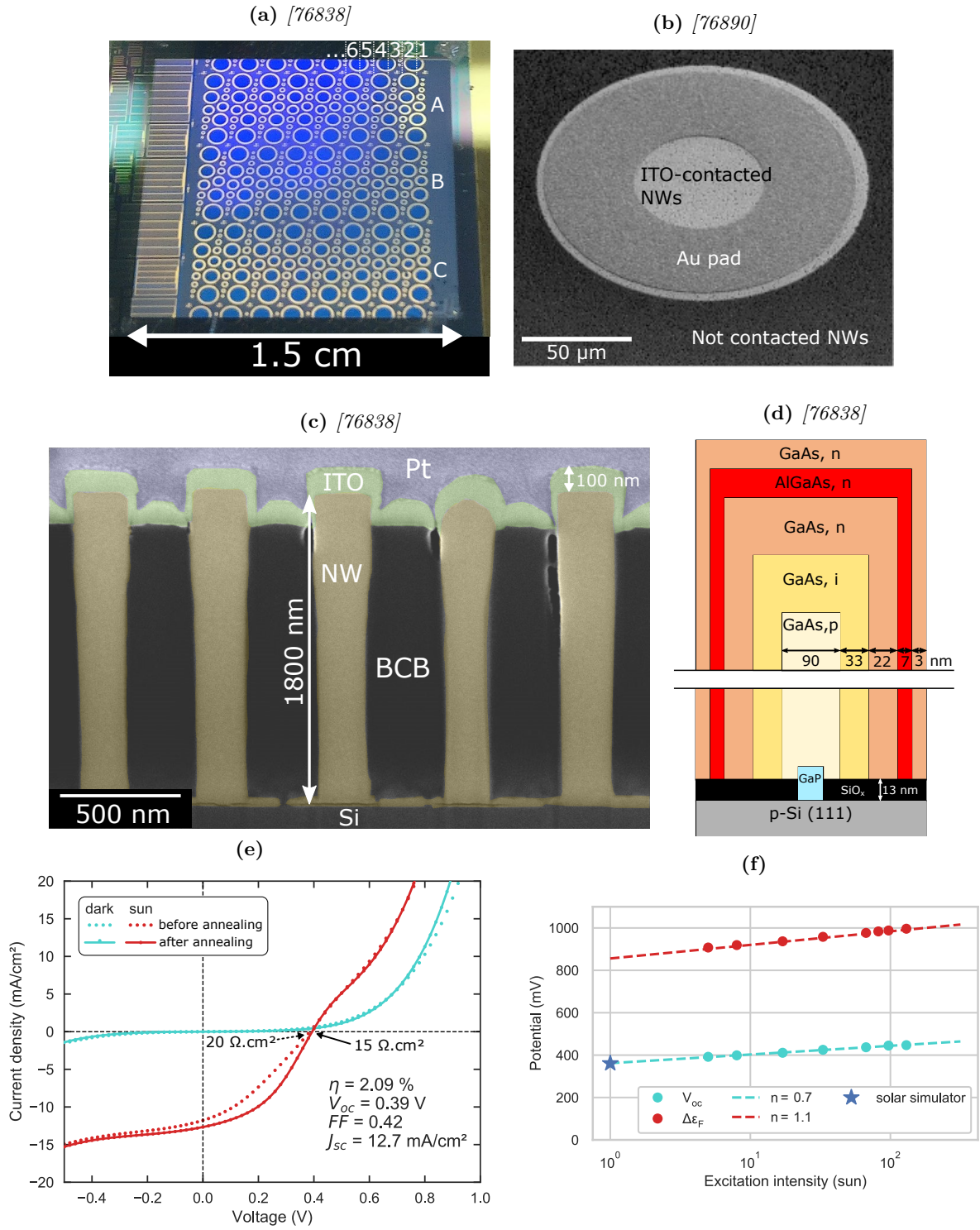

Figure 42: *(a) Photographie d'un réseau de NFs de* $1.5 \times 1.5\,\mathrm{cm}$*, sur lequel des cellules solaires ont été fabriquées (une diode = un cercle). (b) Image SEM d'une diode formée par un disque d'ITO et d'un anneau de métal (Ti/Au), déposés sur le réseau de NFs (c) Image en coupe d'une cellule solaire à NFs. La couche de platine (Pt) du dessus ne fait pas partie du dispositif mais a été déposée localement pour réaliser la coupe. (d) Schéma des dimensions d'une homojonction coeur-coquille GaAs passivée AlGaAs. (e) Courbes JV d'une cellule solaire homojonction avant et après recuit à* 400 °C *(*1 min*, sous atmosphère inerte). (g) Evolution du* V_{oc} *et de* $\Delta\varepsilon_F$ *avec l'intensité d'excitation. Chaque courbe est ajustée à une loi de diode (lignes tirettées).*

les performances sont limitées par des problèmes de collecte et par des contacts imparfaits, et non par la qualité intrinsèque du matériau dans le NF.

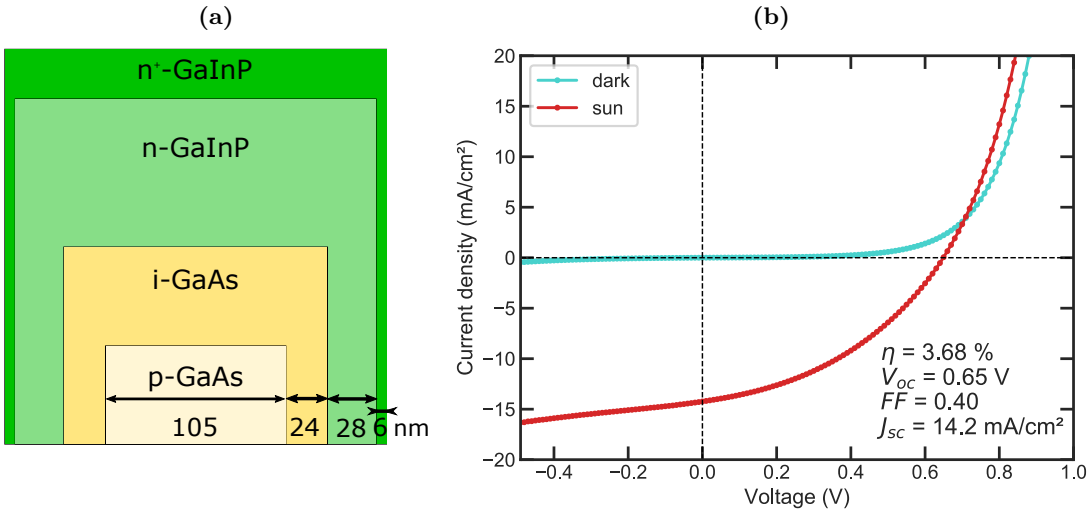

Figure 43: *(a) Schéma d'une heterojonction coeur-coquille de seconde génération. (b) Courbes JV correspondantes, dans le noir et sous illumination d'un soleil. Cet échantillon n'a pas subi de recuit. [B276, p500_18k1_c]*

Finalement, pour éviter la présence d'une coquille n-GaAs, d'épaisseur inégale, et dans la perspective d'améliorer la sélectivité des contacts, une nouvelle architecture est utilisée pour fabriquer les derniers dispositifs, une hétérojonction cœur-coquille p-i-GaAs/n-GaInP. Les nouvelles cellules ont une efficacité limitée (jusqu'à 1.3 % avant, et 1.6 % après un recuit à 400 °C), à cause d'une faible efficacité quantique externe (EQE. $Jsc = 5.9\,\mathrm{mA\,cm^{-2}}$), probablement due à de l'absorption parasite dans la couche d'ITO ainsi qu'à des recombinaisons à cause de la présence quasi-certaine de dislocations dans la coquille. Le V_{oc} (0.6 V) est pourtant supérieur à celui de la cellule précédente (0.4 V), et l'allure de la courbe JV est améliorée, possiblement grâce à une meilleure interface entre la coquille n^{++}-GaAs et l'ITO. Une cartographie d'électroluminescence (EL) de la surface de l'échantillon révèle une émission localisée à l'échelle des NFs, qui pourrait être causée par une chute de tension variable entre NFs à l'interface avec l'ITO.

En utilisant un nouveau bâti de MBE, une autre cellule solaire à hétérojonction a été fabriquée, avec une structure simplifiée (Figure 43a) et avec une importante concentration de dopants Si dans la coquille GaInP proche du contact. Les performances sont inhomogènes sur la surface de l'échantillon, ce qui est attribué à une fabrication en mode dégradé, ainsi qu'à un faible taux de verticalité (80 %) à cause d'un nouvel environnement de laboratoire, et de conditions de travail non optimales. Néanmoins, l'efficacité est alors de 3.7 %, avec un V_{oc} record de 0.65 V (Figure 43b), malgré la présence attestée de dislocations dans la coquille GaInP. Le J_{sc} atteint désormais $14.2\,\mathrm{mA/cm^{-2}}$, attribué à un meilleur contact pour l'extraction des électrons.

Conclusion

En résumé, cette thèse a traité de différents aspects conduisant à la fabrication de cellules solaires en NFs de GaAs crûs par MBE en réseaux organisés sur substrat Si. La croissance maitrisée d'ensemble de nanofils en réseaux périodiques a été démontrée avec plus de 90 % de verticalité de façon reproductible, ainsi qu'avec un nombre limité de fautes cristallines. Des jonctions cœur-coquille avec coquille grand gap, des dopages n et p maitrisés dans le cœur et la coquille, et le contrôle de la composition dans des nanofils GaAsP à grand gap ont été montrés. Grâce au développement d'un procédé de fabrication, des cellules solaires à NF ont été fabriquées et caractérisées. Leur efficacité de conversion ($\eta = 2.1\,\%$) est limitée par la collecte des

porteurs de charge, et non par des défauts intrinsèques aux NFs, qui exhibent une luminescence élevée. Une nouvelle architecture d'hétérojonction avec contact très dopé a permis d'améliorer les performances ($\eta = 3.7\,\%$), notamment $J_{sc} = 14.2\,\mathrm{mA\,cm^{-2}}$, et en particulier $V_{oc} = 0.65\,\mathrm{V}$, un record parmi les cellules solaires à NF crûes sur substrat Si.

A court terme, le développement de la cellule NF seule devrait demeurer une priorité, avant d'envisager l'intégration en tandem. la réalisation de cellules combinant tous les développements présentés dans ce manuscrit pourrait mener à un gain immédiat de performances, puisque la meilleure cellule présentée ici a été réalisée dans un environnement dégradé (déménagements de laboratoires, procédés à ré-optimiser). Les méthodes de caractérisation présentées dans cette thèse pourront ensuite permettre d'identifier plus finement les performances et éventuellement de répondre à la question de savoir si oui, ou non, il existe des limitations fondamentales aux performances et à la viabilité de cellules solaires en NFs III-V crûes sur Si.

Toujours est-il que les différentes techniques et optimisations développées ici pour la croissance de réseaux de NFs et pour la fabrication de structures cœur-coquille pourraient servir d'autres champs d'application qui impliquent des NFs auto-catalysés et leur intégration sur Si, notamment les diodes électroluminescentes, les lasers, ou les photodétecteurs.

Les réseaux de NFs sont similaires aux couches minces de matériaux polycristallins. En effet, les joints de grain dans des matériaux comme le CIGS délimitent des domaines microscopiques de taille à peu près cylindrique, avec d'importantes recombinaisons d'interface, et qui sont ensuite connectés en parallèle pour réaliser des cellules solaires. Les connaissances acquises en étudiant les problématiques des dispositifs à NFs (effets des surfaces décuplés, contact en parallèle de nano-objets, incorporation de dopants, méthodes de caractérisation avec haute résolution spatiale) pourraient aussi servir au développement de ces technologies.

Bibliography

Aberg, Ingvar et al. (Jan. 2016). "A GaAs Nanowire Array Solar Cell With 15.3% Efficiency at 1 Sun". In: *IEEE Journal of Photovoltaics* 6.1, pp. 185–190. DOI: 10.1109/JPHOTOV.2015.2484967 *Cited on pages 4, 24, 25, 30, 73, 74, 174, 176–178, 197, 228.*

Adachi, Sadao (2009). *Properties of Semiconductor Alloys: Group-IV, III–V and II–VI*. ISBN: 9780470743690 *Cited on pages 120, 194, 205.*

Agora-Energiewende and Sandbag (2020). *The European Power Sector in 2019*. URL: https://www.agora-energiewende.de/en/publications/the-european-power-sector-in-2019/ *Cited on page 8.*

Aifantis, K. E., A. L. Kolesnikova, and A. E. Romanov (2007). "Nucleation of misfit dislocations and plastic deformation in core/shell nanowires". In: *Philosophical Magazine* 87.30, pp. 4731–4757. DOI: 10.1080/14786430701589350 *Cited on page 128.*

Akimoto, K., M. Kamada, K. Taira, M. Arai, and N. Watanabe (1986). "Photoluminescence killer center in AlGaAs grown by molecular-beam epitaxy". In: *Journal of Applied Physics* 59.8, pp. 2833–2836. DOI: 10.1063/1.336938 *Cited on page 120.*

Algra, Rienk E., Marcel A. Verheijen, Magnus T. Borgström, Lou-Fé Feiner, George Immink, Willem J. P. van Enckevort, Elias Vlieg, and Erik P A M Bakkers (Nov. 2008). "Twinning superlattices in indium phosphide nanowires". In: *Nature* 456.7220, pp. 369–372. DOI: 10.1038/nature07570. arXiv: 0807.1423 *Cited on pages 99, 107.*

Amano, Chikara, Koshi Ando, and Masafumi Yamaguchi (1988). "The effect of oxygen on the properties of AlGaAs solar cells grown by molecular-beam epitaxy". In: *Journal of Applied Physics* 63.8, pp. 2853–2856. DOI: 10.1063/1.340938 *Cited on page 120.*

Ansara, I. et al. (Apr. 1994). "A binary database for III–V compound semiconductor systems". In: *Calphad* 18.2, pp. 177–222. DOI: 10.1016/0364-5916(94)90027-2 *Cited on page 167.*

Anttu, Nicklas (Mar. 2019a). "Absorption of light in a single vertical nanowire and a nanowire array". In: *Nanotechnology* 30.10, p. 104004. DOI: 10.1088/1361-6528/aafa5c *Cited on page 101.*

— (Feb. 2019b). "Physics and design for 20% and 25% efficiency nanowire array solar cells". In: *Nanotechnology* 30.7, p. 074002. DOI: 10.1088/1361-6528/aaf3f5 *Cited on pages 21, 31.*

Anttu, Nicklas and H. Q. Xu (2013). "Efficient light management in vertical nanowire arrays for photovoltaics". In: *Optics Express* 21.S3, A558. DOI: 10.1364/oe.21.00a558 *Cited on pages 21, 31.*

Arab, Shermin, Maoqing Yao, Chongwu Zhou, P. Daniel Dapkus, and Stephen B. Cronin (2016). "Doping concentration dependence of the photoluminescence spectra of n -type GaAs nanowires". In: *Applied Physics Letters* 108.18. DOI: 10.1063/1.4947504 *Cited on page 131.*

Arthur, J. R. and J. J. LePore (July 1969). "GaAs, GaP, and GaAsxP1-x Epitaxial Films Grown by Molecular Beam Deposition". In: *Journal of Vacuum Science and Technology* 6.4, pp. 545–548. DOI: 10.1116/1.1315677 *Cited on page 167.*

Aspnes, D.E. (Sept. 1983). "Recombination at semiconductor surfaces and interfaces". In: *Surface Science* 132.1-3, pp. 406–421. DOI: 10.1016/0039-6028(83)90550-2 *Cited on pages 41, 137.*

Assali, S. et al. (2013). "Direct band gap wurtzite gallium phosphide nanowires". In: *Nano Letters* 13.4, pp. 1559–1563. DOI: 10.1021/nl304723c *Cited on page 77.*

Azizur-Rahman, K. M. and R. R. LaPierre (2015). "Wavelength-selective absorptance in GaAs, InP and InAs nanowire arrays". In: *Nanotechnology* 26.29. DOI: 10.1088/0957-4484/26/29/295202 *Cited on page 21.*

Bachmann, K. J. et al. (May 1979). "Solar-cell characteristics and interfacial chemistry of indium-tin-oxide/indium phosphide and indium-tin-oxide/gallium arsenide junctions". In: *Journal of Applied Physics* 50.5, pp. 3441–3446. DOI: 10.1063/1.326337 *Cited on page 185.*

Bahrami, Danial, Seyed Mohammad Mostafavi Kashani, Ali Al Hassan, Arman Davtyan, and Ullrich Pietsch (Jan. 2020). "High yield of self-catalyzed GaAs nanowire growth on silicon (111) substrate templated by focused ion beam patterning". In: *Nanotechnology* May. DOI: 10.1088/1361-6528/ab6d99 *Cited on page 73.*

Balasubramanian, N. and A. Subrahmanyam (1990). "Schottky diode properties and the photovoltaic behaviour of indium tin oxide (ITO)/n-GaAs junctions-effect of arsenic deficient GaAs surface". In: *Semiconductor Science and Technology* 5.8, pp. 871–876. DOI: 10.1088/0268-1242/5/8/012 *Cited on pages 185, 188.*

Balestrieri, Matteo (2014). "Transparent conductive oxides with photon converting properties in view of photovoltaic applications : the cases of rare earth-doped zinc oxide and cerium oxide". PhD thesis. Université de Strasbourg *Cited on page 13.*

Bar-Sadan, Maya, Juri Barthel, Hadas Shtrikman, and Lothar Houben (May 2012). "Direct Imaging of Single Au Atoms Within GaAs Nanowires". In: *Nano Letters* 12.5, pp. 2352–2356. DOI: 10.1021/nl300314k *Cited on page 25.*

Barrigón, E., Olof Hultin, David Lindgren, Farnaz Yadegari, Martin H Magnusson, Lars Samuelson, L. I. M. Johansson, and Mikael T Björk (Feb. 2018). "GaAs Nanowire pn-Junctions Produced by Low-Cost and High-Throughput Aerotaxy". In: *Nano Letters* 18.2, pp. 1088–1092. DOI: 10.1021/acs.nanolett.7b04609 *Cited on page 25.*

Barrigón, Enrique, Magnus Heurlin, Zhaoxia Bi, Bo Monemar, and Lars Samuelson (2019). "Synthesis and Applications of III–V Nanowires". In: *Chemical Reviews* 119.15, pp. 9170–9220. DOI: 10.1021/acs.chemrev.9b00075 *Cited on pages 20, 23, 24, 27.*

Bauer, Benedikt, Andreas Rudolph, Marcello Soda, Anna Fontcuberta I Morral, Josef Zweck, Dieter Schuh, and Elisabeth Reiger (2010). "Position controlled self-catalyzed growth of GaAs nanowires by molecular beam epitaxy". In: *Nanotechnology* 21.43. DOI: 10.1088/0957-4484/21/43/435601 *Cited on pages 28, 76, 77.*

Bauhuis, G. J., P. Mulder, E. J. Haverkamp, J. C.C.M. Huijben, and J. J. Schermer (2009). "26.1% thin-film GaAs solar cell using epitaxial lift-off". In: *Solar Energy Materials and Solar Cells* 93.9, pp. 1488–1491. DOI: 10.1016/j.solmat.2009.03.027 *Cited on page 16.*

Becquerel, Edmond (1839). "Mémoire sur les effets électriques produits sous l'influence des rayons solaires". In: *Comptes rendus de l'académie des sciences* 9.19, p. 561 *Cited on page 7.*

Benali, Abdennacer et al. (2014). "Optical simulation of multijunction solar cells based on III-V nanowires on silicon". In: *Energy Procedia* 60.C, pp. 109–115. DOI: 10.1016/j.egypro.2014.12.351 *Cited on page 31.*

Bercegol, Adrien (2019). "Transport de charge dans le photovoltaïque par imagerie multidimensionnelle de luminescence". PhD thesis. PSL Université Paris *Cited on page 68.*

Berg, Alexander, Philippe Caroff, Naeem Shahid, Mark N. Lockrey, Xiaoming Yuan, Magnus T. Borgström, Hark Hoe Tan, and Chennupati Jagadish (2017). "Growth and optical properties of InxGa1-xP nanowires synthesized by selective-area epitaxy". In: *Nano Research* 10.2, pp. 672–682. DOI: 10.1007/s12274-016-1325-1 *Cited on page 75.*

Bett, A. W., F. Dimroth, G. Stollwerck, and O. V. Sulima (1999). "III-V compounds for solar cell applications". In: *Applied Physics A: Materials Science and Processing* 69.2, pp. 119–129. DOI: 10.1007/s003390050983 *Cited on pages 16, 33.*

Blakemore, J. S. (1982). "Semiconducting and other major propreties of GaAs". In: *Journal of Applied Physics* 53.10, R123 *Cited on page 135.*

Blömers, Ch, T. Grap, M. I. Lepsa, J. Moers, St Trellenkamp, D. Grützmacher, H. Lüth, and Th Schäpers (2012). "Hall effect measurements on InAs nanowires". In: *Applied Physics Letters* 101.15. DOI: 10.1063/1.4759124 *Cited on page 130.*

Boland, Jessica L. et al. (2015). "Modulation doping of GaAs/AlGaAs core-shell nanowires with effective defect passivation and high electron mobility". In: *Nano Letters* 15.2, pp. 1336–1342. DOI: 10.1021/nl504566t *Cited on page 157.*

Bologna, Nicolas et al. (2018). "Dopant-Induced Modifications of Ga xIn(1- x)P Nanowire-Based p-n Junctions Monolithically Integrated on Si(111)". In: *ACS Applied Materials and Interfaces* 10.38, pp. 32588–32596. DOI: 10.1021/acsami.8b10770 *Cited on pages 27, 76.*

Borgström, Magnus T. et al. (2018). "Towards Nanowire Tandem Junction Solar Cells on Silicon". In: *IEEE Journal of Photovoltaics* 8.3, pp. 733–740. DOI: 10.1109/JPHOTOV.2018.2816264 *Cited on pages 24, 25, 73.*

Boulanger, J. P., A. C.E. Chia, B. Wood, S. Yazdi, T. Kasama, M. Aagesen, and R. R. LaPierre (May 2016). "Characterization of a Ga-Assisted GaAs Nanowire Array Solar Cell on Si Substrate". In: *IEEE Journal of Photovoltaics* 6.3, pp. 661–667. DOI: 10.1109/JPHOTOV.2016.2537547 *Cited on pages 24, 27, 30, 131, 174, 177, 194, 197, 200, 209, 228.*

BP (2019). *Statistical Review of Global Energy*. URL: http://www.bp.com/statisticalreview *Cited on page 10.*

Breuer, Steffen, Carsten Pfüller, Timur Flissikowski, Oliver Brandt, Holger T. Grahn, Lutz Geelhaar, and Henning Riechert (2011). "Suitability of Au- and self-assisted GaAs nanowires for optoelectronic applications". In: *Nano Letters* 11.3, pp. 1276–1279. DOI: 10.1021/nl104316t *Cited on page 25.*

Brillson, Leonard J. (Mar. 2010). *Surfaces and Interfaces of Electronic Materials*. Weinheim, Germany: Wiley-VCH Verlag GmbH & Co. KGaA. ISBN: 9783527665709. DOI: 10.1002/9783527665709 *Cited on pages 41, 45–47, 209.*

Brown, Evan, Chunyang Sheng, Kohei Shimamura, Fuyuki Shimojo, and Aiichiro Nakano (2015). "Enhanced charge recombination due to surfaces and twin defects in GaAs nanostructures". In: *Journal of Applied Physics* 117.5. DOI: 10.1063/1.4907534 *Cited on page 99.*

Burgelman, Marc, Koen Decock, Samira Khelifi, and Aimi Abass (May 2013). "Advanced electrical simulation of thin film solar cells". In: *Thin Solid Films* 535, pp. 296–301. DOI: 10.1016/j.tsf.2012.10.032 *Cited on page 194.*

Burstein, Elias (Feb. 1954). "Anomalous Optical Absorption Limit in InSb". In: *Physical Review* 93.3, pp. 632–633. DOI: 10.1103/PhysRev.93.632 *Cited on page 135.*

Cariou, Romain et al. (Apr. 2018). "III–V-on-silicon solar cells reaching 33% photoconversion efficiency in two-terminal configuration". In: *Nature Energy* 3.4, pp. 326–333. DOI: 10.1038/s41560-018-0125-0 *Cited on pages 17–19.*

Caroff, P., K. A. Dick, J. Johansson, M. E. Messing, K. Deppert, and L. Samuelson (2009). "Controlled polytypic and twin-plane superlattices in III-V nanowires". In: *Nature Nanotechnology* 4.1, pp. 50–55. DOI: 10.1038/nnano.2008.359 *Cited on page 99.*

Casadei, Alberto et al. (2013). "Doping incorporation paths in catalyst-free Be-doped GaAs nanowires". In: *Applied Physics Letters* 102.1. DOI: 10.1063/1.4772020. arXiv: 1210.1670 *Cited on pages 28, 130, 141.*

Casey, H. C., J. Muth, S. Krishnankutty, and J. M. Zavada (1996). "Dominance of tunneling current and band filling in InGaN/AlGaN double heterostructure blue light-emitting diodes". In: *Applied Physics Letters* 68.20, pp. 2867–2869. DOI: 10.1063/1.116351 *Cited on page 197.*

Casey, H. C. and Frank Stern (1976). "Concentration-dependent absorption and spontaneous emission of heavily doped GaAs". In: *Journal of Applied Physics* 47.2, pp. 631–643. DOI: 10.1063/1.322626 *Cited on page 134.*

Chai, Y. G., R. Chow, and C. E. C. Wood (Nov. 1981). "The effect of growth conditions on Si incorporation in molecular beam epitaxial GaAs". In: *Applied Physics Letters* 39.10, pp. 800–803. DOI: 10.1063/1.92562 *Cited on page 149.*

Chang, Chia Chi et al. (2012). "Electrical and optical characterization of surface passivation in GaAs nanowires". In: *Nano Letters* 12.9, pp. 4484–4489. DOI: 10.1021/nl301391h *Cited on page 99.*

Chatillon, Christian and Dominique Chatain (1995). "Congruent vaporization of GaAs(s) and stability of Ga(l) droplets at the GaAs(s) surface". In: *Journal of Crystal Growth* 151.1-2, pp. 91–101. DOI: 10.1016/0022-0248(95)00044-5 *Cited on page 112.*

Chen, Chen, Shyemaa Shehata, Cécile Fradin, Ray LaPierre, Christophe Couteau, and Gregor Weihs (2007). "Self-directed growth of AlGaAs core-shell nanowires for visible light applications". In: *Nano Letters* 7.9, pp. 2584–2589. DOI: 10.1021/nl070874k. arXiv: 0710.0518 *Cited on page 160.*

Chen, Hung-ling (2018). "Ultrathin and nanowire-based GaAs solar cells". PhD thesis. Université Paris-Saclay, Université Paris-Sud *Cited on pages 12, 21, 31, 45, 99, 101, 132, 175.*

Chen, Hung-Ling, Romaric De Lépinau, Andrea Scaccabarozzi, Fabrice Oehler, Jean-Christophe Harmand, Andrea Cattoni, and Stéphane Collin (Sept. 2020a). "Quantitative Assessment of Carrier Density by Cathodoluminescence (2): GaAs nanowires". In: *submitted*. arXiv: 1909.05602 *Cited on pages 102, 132, 139, 140, 148, 231.*

Chen, Hung-Ling, Andrea Scaccabarozzi, Romaric De Lépinau, Fabrice Oehler, Aristide Lemaître, Jean-Christophe Harmand, Andrea Cattoni, and Stéphane Collin (Sept. 2020b). "Quantitative Assessment of Carrier Density by Cathodoluminescence (1): GaAs thin films and modeling". In: *submitted*. arXiv: 1909.05598 *Cited on pages 132, 134–137, 153.*

Chen, Hung-Ling et al. (Nov. 2017). "Determination of n-Type Doping Level in Single GaAs Nanowires by Cathodoluminescence". In: *Nano Letters* 17.11, pp. 6667–6675. DOI: 10.1021/acs.nanolett.7b02620 *Cited on pages 30, 132.*

Chen, Hung-Ling et al. (Sept. 2019). "A 19.9%-efficient ultrathin solar cell based on a 205-nm-thick GaAs absorber and a silver nanostructured back mirror". In: *Nature Energy* 4.9, pp. 761–767. DOI: 10.1038/s41560-019-0434-y *Cited on pages 17, 193, 195, 196.*

Chen, Wanghua and Pere Roca i Cabarrocas (Jan. 2019). "Rational design of nanowire solar cells: from single nanowire to nanowire arrays". In: *Nanotechnology*. DOI: 10.1088/1361-6528/aaff8d *Cited on page 23.*

Chia, A. C E, J. P. Boulanger, and R. R. Lapierre (2013). "Unlocking doping and compositional profiles of nanowire ensembles using SIMS". In: *Nanotechnology* 24.4. DOI: 10.1088/0957-4484/24/4/045701 *Cited on page 27.*

Chia, A. C.E., N. Dhindsa, J. P. Boulanger, B. A. Wood, S. S. Saini, and R. R. LaPierre (2015). "Nanowire dopant measurement using secondary ion mass spectrometry". In: *Journal of Applied Physics* 118.11. DOI: 10.1063/1.4931148 *Cited on pages 27, 131.*

Chia, A. C.E. and R. R. Lapierre (2013). "Electrostatic model of radial pn junction nanowires". In: *Journal of Applied Physics* 114.7. DOI: 10.1063/1.4818958 *Cited on pages 27, 131.*

Chia, Andrew C E and Ray R. Lapierre (2012). "Analytical model of surface depletion in GaAs nanowires". In: *Journal of Applied Physics* 112.6. DOI: 10.1063/1.4752873 *Cited on pages 27, 30, 137.*

Cho, Kee et al. (2011). "Molecular monolayers for conformal, nanoscale doping of InP nanopillar photovoltaics". In: *Applied Physics Letters* 98.20, pp. 12–15. DOI: 10.1063/1.3585138 *Cited on page 24.*

Chopra, K. L., S. Major, and D. K. Pandya (1983). "Transparent conductors-A status review". In: *Thin Solid Films* 102.1, pp. 1–46. DOI: 10.1016/0040-6090(83)90256-0 *Cited on page 185.*

Christesen, Joseph D., Xing Zhang, Christopher W. Pinion, Thomas A. Celano, Cory J. Flynn, and James F. Cahoon (2012). "Design principles for photovoltaic devices based on Si nanowires with axial or radial p-n junctions". In: *Nano Letters* 12.11, pp. 6024–6029. DOI: 10.1021/nl303610m *Cited on page 30.*

Cirlin, G. E., V. G. Dubrovskii, I. P. Soshnikov, N. V. Sibirev, Yu B. Samsonenko, A. D. Bouravleuv, J. C. Harmand, and F. Glas (2009). "Critical diameters and temperature domains for MBE growth of III-V nanowires on lattice mismatched substrates". In: *Physica Status Solidi - Rapid Research Letters* 3.4, pp. 112–114. DOI: 10.1002/pssr.200903057 *Cited on page 21.*

Colombo, C., M. Heiß, M. Grätzel, and A. Fontcuberta I Morral (2009). "Gallium arsenide p-i-n radial structures for photovoltaic applications". In: *Applied Physics Letters* 94.17, pp. 2007–2010. DOI: 10.1063/1.3125435 *Cited on pages 28, 142, 149.*

Colombo, C., D. Spirkoska, M. Frimmer, G. Abstreiter, and A. Fontcuberta I Morral (2008). "Ga-assisted catalyst-free growth mechanism of GaAs nanowires by molecular beam epitaxy". In: *Physical Review B - Condensed Matter and Materials Physics* 77.15, pp. 2–6. DOI: 10.1103/PhysRevB.77.155326 *Cited on pages 28, 160.*

Conesa-Boj, Sònia, Dominik Kriegner, Xiang-Lei Han, Sébastien Plissard, Xavier Wallart, Julian Stangl, Anna Fontcuberta i Morral, and Philippe Caroff (Jan. 2014). "Gold-Free Ternary III–V Antimonide Nanowire Arrays on Silicon: Twin-Free down to the First Bilayer". In: *Nano Letters* 14.1, pp. 326–332. DOI: 10.1021/nl404085a *Cited on pages 28, 160.*

Connell, Justin G., Kunho Yoon, Daniel E. Perea, Edwin J. Schwalbach, Peter W. Voorhees, and Lincoln J. Lauhon (2013). "Identification of an intrinsic source of doping inhomogeneity in vapor-liquid-solid-grown nanowires". In: *Nano Letters* 13.1, pp. 199–206. DOI: 10.1021/nl3038695 *Cited on pages 131, 168.*

Cop, Pascal, Sosuke Kitano, Kota Niinuma, Bernd Smarsly, and Hiromitsu Kozuka (2018). "In-Plane Stress Development in Mesoporous Thin Films". In: *Nanoscale*. DOI: 10.1039/C8NR00793D *Cited on page 177.*

Cui, Y, D. van Dam, S A Mann, N. J. J. van Hoof, P. J. van Veldhoven, E C Garnett, E P A M Bakkers, and J E M Haverkort (Oct. 2016). "Boosting Solar Cell Photovoltage via Nanophotonic Engineering". In: *Nano Letters* 16.10, pp. 6467–6471. DOI: 10.1021/acs.nanolett.6b02971 *Cited on pages 24, 202.*

Cui, Yingchao et al. (Sept. 2013). "Efficiency Enhancement of InP Nanowire Solar Cells by Surface Cleaning". In: *Nano Letters* 13.9, pp. 4113–4117. DOI: 10.1021/nl4016182 *Cited on pages 174, 177.*

Czaban, Josef A., David A. Thompson, and Ray R. LaPierre (2009). "GaAs core-shell nanowires for photovoltaic applications". In: *Nano Letters* 9.1, pp. 148–154. DOI: 10.1021/nl802700u *Cited on pages 27, 141, 150.*

Dai, Xing, Agnes Messanvi, Hezhi Zhang, Christophe Durand, Joël Eymery, Catherine Bougerol, François H. Julien, and Maria Tchernycheva (2015). "Flexible Light-Emitting Diodes Based on Vertical Nitride Nanowires". In: *Nano Letters* 15.10, pp. 6958–6964. DOI: 10.1021/acs.nanolett.5b02900 *Cited on page 176.*

Dalacu, Dan, Alicia Kam, D Guy Austing, Xiaohua Wu, Jean Lapointe, Geof C Aers, and Philip J Poole (Sept. 2009). "Selective-area vapour–liquid–solid growth of InP nanowires". In: *Nanotechnology* 20.39, p. 395602. DOI: 10.1088/0957-4484/20/39/395602 *Cited on page 164.*

Dam, Dick van, Niels J. J. van Hoof, Yingchao Cui, Peter J. van Veldhoven, Erik P A M Bakkers, Jaime Gómez Rivas, and Jos E M Haverkort (Dec. 2016). "High-Efficiency Nanowire Solar Cells with Omnidirectionally Enhanced Absorption Due to Self-Aligned Indium–Tin–Oxide Mie Scatterers". In: *ACS Nano* 10.12, pp. 11414–11419. DOI: 10.1021/acsnano.6b06874 *Cited on pages 4, 21, 24, 73, 176, 228.*

Darbandi, Ali, James C. McNeil, Azadeh Akhtari-Zavareh, Simon P. Watkins, and Karen L. Kavanagh (2016). "Direct measurement of the electrical abruptness of a nanowire p-n junction". In: *Nano Letters* 16.7, pp. 3982–3988. DOI: 10.1021/acs.nanolett.6b00289 *Cited on page 131.*

Dasgupta, Neil P. et al. (2014). "25th anniversary article: Semiconductor nanowires - Synthesis, characterization, and applications". In: *Advanced Materials* 26.14, pp. 2137–2183. DOI: 10.1002/adma.201305929 *Cited on page 20.*

Dastjerdi, M H T, J P Boulanger, P Kuyanov, Martin Aagesen, and R R LaPierre (2016). "Methods of Ga droplet consumption for improved GaAs nanowire solar cell efficiency". In: *Nanotechnology* 27.47, p. 475403. DOI: 10.1088/0957-4484/27/47/475403 *Cited on pages 4, 24, 27, 104, 107, 200, 228.*

Dastjerdi, M. H. T., E M Fiordaliso, E D Leshchenko, A Akhtari-Zavareh, T Kasama, M Aagesen, V G Dubrovskii, and R R LaPierre (Oct. 2017). "Three-fold Symmetric Doping Mechanism in GaAs Nanowires". In: *Nano Letters* 17.10, pp. 5875–5882. DOI: 10.1021/acs.nanolett.7b00794 *Cited on pages 27, 28, 131, 141, 142, 145.*

Dayeh, Shadi A. et al. (2013). "Direct measurement of coherency limits for strain relaxation in heteroepitaxial core/shell nanowires". In: *Nano Letters* 13.5, pp. 1869–1876. DOI: 10.1021/nl3022434 *Cited on page 126.*

De Wild-Scholten, M. J. (2013). "Energy payback time and carbon footprint of commercial photovoltaic systems". In: *Solar Energy Materials and Solar Cells* 119, pp. 296–305. DOI: 10.1016/j.solmat.2013.08.037 *Cited on page 15.*

Delamarre, Amaury, Laurent Lombez, and Jean Franois Guillemoles (2012). "Contactless mapping of saturation currents of solar cells by photoluminescence". In: *Applied Physics Letters* 100.13, pp. 8–11. DOI: 10.1063/1.3697704 *Cited on page 202.*

Den Hertog, Martien I. et al. (2009). "Mapping active dopants in single silicon nanowires using off-axis electron holography". In: *Nano Letters* 9.11, pp. 3837–3843. DOI: 10.1021/nl902024h *Cited on page 131.*

Detz, Hermann et al. (2017). "Lithography-free positioned GaAs nanowire growth with focused ion beam implantation of Ga". In: *Journal of Vacuum Science & Technology B, Nanotechnology and Microelectronics: Materials, Processing, Measurement, and Phenomena* 35.1, p. 011803. DOI: 10.1116/1.4973340 *Cited on page 73.*

Diedenhofen, Silke L., Olaf T. A. Janssen, Grzegorz Grzela, Erik P. A. M. Bakkers, and Jaime Gómez Rivas (Mar. 2011). "Strong Geometrical Dependence of the Absorption of Light in Arrays of Semiconductor Nanowires". In: *ACS Nano* 5.3, pp. 2316–2323. DOI: 10.1021/nn103596n *Cited on pages 21, 24.*

Dimakis, Emmanouil, Manfred Ramsteiner, Abbes Tahraoui, Henning Riechert, and Lutz Geelhaar (Nov. 2012). "Shell-doping of GaAs nanowires with Si for n-type conductivity". In: *Nano Research* 5.11, pp. 796–804. DOI: 10.1007/s12274-012-0263-9 *Cited on pages 30, 131, 149, 177.*

Dimroth, Frank et al. (2014). "Comparison of direct growth and wafer bonding for the fabrication of GaInP/GaAs dual-junction solar cells on silicon". In: *IEEE Journal of Photovoltaics* 4.2, pp. 620–625. DOI: 10.1109/JPHOTOV.2014.2299406 *Cited on page 20.*

Domke, C., Ph. Ebert, M. Heinrich, and K. Urban (Oct. 1996). "Microscopic identification of the compensation mechanisms in Si-doped GaAs". In: *Physical Review B* 54.15, pp. 10288–10291. DOI: 10.1103/PhysRevB.54.10288 *Cited on page 149.*

Drouin, Dominique, Alexandre Réal Couture, Dany Joly, Xavier Tastet, Vincent Aimez, and Raynald Gauvin (May 2007). "CASINO V2.42—A Fast and Easy-to-use Modeling Tool for Scanning Electron Microscopy and Microanalysis Users". In: *Scanning* 29.3, pp. 92–101. DOI: 10.1002/sca.20000 *Cited on page 65.*

Dubrovskii, V. G. (Nov. 2017). "Understanding the vapor–liquid–solid growth and composition of ternary III–V nanowires and nanowire heterostructures". In: *Journal of Physics D: Applied Physics* 50.45, p. 453001. DOI: 10.1088/1361-6463/aa87a7 *Cited on page 167.*

Dufouleur, Joseph, Carlo Colombo, Tonko Garma, Bernt Ketterer, Emanuele Uccelli, Marco Nicotra, and Anna Fontcuberta i Morral (May 2010). "P-Doping Mechanisms in Catalyst-Free Gallium Arsenide Nanowires". In: *Nano Letters* 10.5, pp. 1734–1740. DOI: 10.1021/nl100157w *Cited on pages 28, 130, 142, 149.*

Dumin, D. J. and G. L. Pearson (Nov. 1965). "Properties of Gallium Arsenide Diodes between 4.2° and 300°K". In: *Journal of Applied Physics* 36.11, pp. 3418–3426. DOI: 10.1063/1.1703009 *Cited on page 197.*

Enquist, P., G. W. Wicks, L. F. Eastman, and C. Hitzman (1985). "Anomalous redistribution of beryllium in GaAs grown by molecular beam epitaxy". In: *Journal of Applied Physics* 58.11, pp. 4130–4134. DOI: 10.1063/1.335543 *Cited on pages 142, 145, 148.*

Essig, Stephanie et al. (Aug. 2017). "Raising the one-sun conversion efficiency of III–V/Si solar cells to 32.8% for two junctions and 35.9% for three junctions". In: *Nature Energy* 2.9, p. 17144. DOI: 10.1038/nenergy.2017.144 *Cited on pages 17–19.*

Fan, Hong Jin, Peter Werner, and Margit Zacharias (2006). "Semiconductor nanowires: From self-organization to patterned growth". In: *Small* 2.6, pp. 700–717. DOI: 10.1002/smll.200500495 *Cited on page 73.*

Farrell, Alan C., Wook Jae Lee, Pradeep Senanayake, Michael A. Haddad, Sergey V. Prikhodko, and Diana L. Huffaker (2015). "High-Quality InAsSb Nanowires Grown by Catalyst-Free Selective-Area Metal-Organic Chemical Vapor Deposition". In: *Nano Letters* 15.10, pp. 6614–6619. DOI: 10.1021/acs.nanolett.5b02389 *Cited on page 75.*

Fave, Alain, Jean François Lelièvre, Thibaut Gallet, Qiaoyu Su, and Mustapha Lemiti (2017). "Fabrication of Si tunnel diodes for c-Si based tandem solar cells using proximity rapid thermal diffusion". In: *Energy Procedia* 124, pp. 577–583. DOI: 10.1016/j.egypro.2017.09.281 *Cited on page 34.*

Feifel, Markus et al. (Nov. 2018). "Direct Growth of III–V/Silicon Triple-Junction Solar Cells With 19.7% Efficiency". In: *IEEE Journal of Photovoltaics* 8.6, pp. 1590–1595. DOI: 10.1109/JPHOTOV.2018.2868015 *Cited on page 20.*

Fontcuberta I Morral, A., C. Colombo, G. Abstreiter, J. Arbiol, and J. R. Morante (2008). "Nucleation mechanism of gallium-assisted molecular beam epitaxy growth of gallium arsenide nanowires". In: *Applied Physics Letters* 92.6, pp. 2008–2010. DOI: 10.1063/1.2837191 *Cited on pages 28, 77, 82.*

Fountaine, Katherine T., Christian G. Kendall, and Harry A. Atwater (2014). "Near-unity broadband absorption designs for semiconducting nanowire arrays via localized radial mode excitation". In: *Optics Express* 22.S3, A930. DOI: 10.1364/oe.22.00a930 *Cited on page 31.*

Foxon, C.T., B.A. Joyce, and M.T. Norris (May 1980). "Composition effects in the growth of Ga(In)AsyP1-y alloys by MBE". In: *Journal of Crystal Growth* 49.1, pp. 132–140. DOI: 10.1016/0022-0248(80)90073-1 *Cited on pages 154, 167.*

Freeouf, J. L. and J. M. Woodall (1981). "Schottky barriers: An effective work function model". In: *Applied Physics Letters* 39.9, pp. 727–729. DOI: 10.1063/1.92863 *Cited on page 41.*

Fuhrmann, Bodo, Hartmut S. Leipner, Hans Reiner Höche, Luise Schubert, Peter Werner, and Ulrich Gösele (2005). "Ordered arrays of silicon nanowires produced by nanosphere lithography and molecular beam epitaxy". In: *Nano Letters* 5.12, pp. 2524–2527. DOI: 10.1021/nl051856a *Cited on page 73.*

Gamalski, A. D., C. Ducati, and S. Hofmann (2011). "Cyclic supersaturation and triple phase boundary dynamics in germanium nanowire growth". In: *Journal of Physical Chemistry C* 115.11, pp. 4413–4417. DOI: 10.1021/jp1095882 *Cited on page 57.*

Gao, Qian et al. (2019). "Axial p-n junction design and characterization for InP nanowire array solar cells". In: *Progress in Photovoltaics: Research and Applications* 27.3, pp. 237–244. DOI: 10.1002/pip.3083 *Cited on page 24.*

Garnett, Erik C., Mark L. Brongersma, Yi Cui, and Michael D. McGehee (Aug. 2011). "Nanowire Solar Cells". In: *Annual Review of Materials Research* 41.1, pp. 269–295. DOI: 10.1146/annurev-matsci-062910-100434 *Cited on pages 20, 23.*

Garnett, Erik and Peidong Yang (2010). "Light trapping in silicon nanowire solar cells". In: *Nano Letters* 10.3, pp. 1082–1087. DOI: 10.1021/nl100161z *Cited on pages 21, 24.*

Ghahfarokhi, Omid Madani, Nicklas Anttu, Lars Samuelson, and Ingvar Åberg (2016). "Performance of GaAs Nanowire Array Solar Cells for Varying Incidence Angles". In: *IEEE Journal of Photovoltaics* 6.6, pp. 1502–1508. DOI: 10.1109/JPHOTOV.2016.2604564 *Cited on page 21.*

Ghalamestani, Sepideh Gorji, Sofia Johansson, B. Mattias Borg, Erik Lind, Kimberly A. Dick, and Lars Erik Wernersson (2012). "Uniform and position-controlled InAs nanowires on 2" Si substrates for transistor applications". In: *Nanotechnology* 23.1. DOI: 10.1088/0957-4484/23/1/015302 *Cited on page 75.*

Gibson, Sandra J., Brad van Kasteren, Burak Tekcan, Yingchao Cui, Dick van Dam, Jos E.M. Haverkort, Erik P.A.M. Bakkers, and Michael E. Reimer (2019). "Tapered InP nanowire arrays for efficient broadband high-speed single-photon detection". In: *Nature Nanotechnology*. DOI: 10.1038/s41565-019-0393-2 *Cited on pages 31, 177.*

Gibson, Sandra J, Jonathan P Boulanger, and Ray R Lapierre (2013). "Opportunities and pitfalls in patterned self-catalyzed GaAs nanowire growth on silicon". In: *Semicond. Sci. Technol* 28, pp. 105025–9. DOI: 10.1088/0268-1242/28/10/105025 *Cited on pages 27, 77.*

Gibson, Sandra J and Ray R LaPierre (Oct. 2014). "Model of patterned self-assisted nanowire growth". In: *Nanotechnology* 25.41, p. 415304. DOI: 10.1088/0957-4484/25/41/415304 *Cited on pages 27, 164.*

Gibson, Sandra and Ray Lapierre (2013). "Study of radial growth in patterned self-catalyzed GaAs nanowire arrays by gas source molecular beam epitaxy". In: *Physica Status Solidi - Rapid Research Letters* 7.10, pp. 845–849. DOI: 10.1002/pssr.201307142 *Cited on pages 27, 77, 160.*

Glas, Frank (2015). "Strain in Nanowires and Nanowire Heterostructures". In: *Semiconductors and Semimetals*. Ed. by Anna Fontcuberta I. Morral, Chennupati Jagadish, and Shadi A. Dayeh. Vol. 93. Burlington: Academic Press. Chap. Strain in, pp. 79–123. ISBN: 9780128030271. DOI: 10.1016/bs.semsem.2015.09.004 *Cited on pages 126–128, 165.*

Glas, Frank, Jean-Christophe Harmand, and Gilles Patriarche (Oct. 2007). "Why Does Wurtzite Form in Nanowires of III-V Zinc Blende Semiconductors?" In: *Physical Review Letters* 99.14, p. 146101. DOI: 10.1103/PhysRevLett.99.146101 *Cited on pages 55, 229.*

— (Mar. 2010). "Nucleation Antibunching in Catalyst-Assisted Nanowire Growth". In: *Physical Review Letters* 104.13, p. 135501. DOI: 10.1103/PhysRevLett.104.135501 *Cited on page 160.*

Glas, Frank, Mohammed Reda Ramdani, Gilles Patriarche, and Jean Christophe Harmand (2013). "Predictive modeling of self-catalyzed III-V nanowire growth". In: *Physical Review B - Condensed Matter and Materials Physics* 88.19, pp. 1–14. DOI: 10.1103/PhysRevB.88.195304 *Cited on pages 58, 88, 104, 167.*

Goktas, N. Isik, E. M. Fiordaliso, and R. R. Lapierre (2018). "Doping assessment in GaAs nanowires". In: *Nanotechnology* 29.23. DOI: 10.1088/1361-6528/aab6f1 *Cited on pages 27, 30, 131.*

Gomyo, A., K. Kobayashi, S. Kawata, I. Hino, T. Suzuki, and T. Yuasa (Sept. 1986). "Studies of GaxIn1-xP layers grown by metalorganic vapor phase epitaxy; Effects of V/III ratio and growth temperature". In: *Journal of Crystal Growth* 77.1-3, pp. 367–373. DOI: 10.1016/0022-0248(86)90325-8. arXiv: JournalofCrystalGrowth77(1986)367âĂŤ373 *Cited on page 121.*

Goto, Hajime, Katsutoshi Nosaki, Katsuhiro Tomioka, Shinjiro Hara, Kenji Hiruma, Junichi Motohisa, and Takashi Fukui (2009). "Growth of core-shell inP nanowires for photovoltaic application by selective-area metal organic vapor phase epitaxy". In: *Applied Physics Express* 2.3. DOI: 10.1143/APEX.2.035004 *Cited on page 26.*

Gott, James A., Richard Beanland, H. Aruni Fonseka, Jonathan J.P. Peters, Yunyan Zhang, Huiyun Liu, and Ana M. Sanchez (2019). "Defect Dynamics in Self-Catalyzed III-V Semiconductor Nanowires". In: *Nano Letters* 19.111, pp. 4574–4580. DOI: 10.1021/acs.nanolett.9b01508 *Cited on page 28.*

Gouillart, Louis (2020). "Development of ultrathin Cu(In,Ga)Se2–based solar cells with reflective back contacts". PhD thesis. Université Paris-Saclay *Cited on page 226.*

Grassman, T. J., M. R. Brenner, S. Rajagopalan, R. Unocic, R. Dehoff, M. Mills, H. Fraser, and S. A. Ringel (2009). "Control and elimination of nucleation-related defects in GaP/Si(001) heteroepitaxy". In: *Applied Physics Letters* 94.23. DOI: 10.1063/1.3154548 *Cited on page 19.*

Grassman, T. J., J. A. Carlin, B. Galiana, L. M. Yang, F. Yang, M. J. Mills, and S. A. Ringel (2013). "Nucleation-related defect-free GaP/Si(100) heteroepitaxy via metal-organic chemical vapor deposition". In: *Applied Physics Letters* 102.14. DOI: 10.1063/1.4801498 *Cited on page 19.*

Green, Martin A., Ewan D. Dunlop, Jochen Hohl-Ebinger, Masahiro Yoshita, Nikos Kopidakis, and Anita W.Y. Ho-Baillie (2020). "Solar cell efficiency tables (Version 55)". In: *Progress in Photovoltaics: Research and Applications* 28.1, pp. 3–15. DOI: 10.1002/pip.3228 *Cited on pages 18, 20.*

Green, Martin A., Ewan D. Dunlop, Dean H. Levi, Jochen Hohl-Ebinger, Masahiro Yoshita, and Anita W.Y. Ho-Baillie (2019). "Solar cell efficiency tables (version 54)". In: *Progress in Photovoltaics: Research and Applications* 27.7, pp. 565–575. DOI: 10.1002/pip.3171 *Cited on pages 16, 195, 196.*

Guillemoles, Jean-Francois, Thomas Kirchartz, David Cahen, and Uwe Rau (2019). "Guide for the perplexed to the Shockley–Queisser model for solar cells". In: *Nature Photonics* 13.8, pp. 501–505. DOI: 10.1038/s41566-019-0479-2 *Cited on page 12.*

Guo, Ya Nan et al. (2013). "Phase separation induced by Au catalysts in ternary InGaAs nanowires". In: *Nano Letters* 13.2, pp. 643–650. DOI: 10.1021/nl304237b *Cited on page 160.*

Gutsche, Christoph, Ingo Regolin, Kai Blekker, Andrey Lysov, Werner Prost, and Franz J. Tegude (Jan. 2009). "Controllable p-type doping of GaAs nanowires during vapor-liquid-solid growth". In: *Journal of Applied Physics* 105.2, p. 024305. DOI: 10.1063/1.3065536 *Cited on page 130.*

Gutsche, Christoph et al. (2012). "N-GaAs/InGaP/p-GaAs core-multishell nanowire diodes for efficient light-to-current conversion". In: *Advanced Functional Materials* 22.5, pp. 929–936. DOI: 10.1002/adfm.201101759 *Cited on page 205.*

Haapamaki, C. M., J. Baugh, and R. R. Lapierre (2012). "Critical shell thickness for InAs-AlxIn1-xAs(P) core-shell nanowires". In: *Journal of Applied Physics* 112.12. DOI: 10.1063/1.4769735 *Cited on pages 127, 128.*

Haas, F. et al. (2013). "Nanoimprint and selective-area MOVPE for growth of GaAs/InAs core/shell nanowires". In: *Nanotechnology* 24.8. DOI: 10.1088/0957-4484/24/8/085603 *Cited on pages 27, 75.*

Hakkarainen, Teemu et al. (Aug. 2019). "Te incorporation and activation as n-type dopant in self-catalyzed GaAs nanowires". In: *Physical Review Materials* 3.8, p. 086001. DOI: 10.1103/PhysRevMaterials.3.086001 *Cited on pages 150, 174.*

Hamano, Tetsuko, Hideki Hirayama, and Yoshinobu Aoyagi (Mar. 1997). "New Technique for Fabrication of Two-Dimensional Photonic Bandgap Crystals by Selective Epitaxy". In: *Japanese Journal of Applied Physics* 36.Part 2, No. 3A, pp. L286–L288. DOI: 10.1143/JJAP.36.L286 *Cited on page 75.*

Harmand, Jean Christophe, Gilles Patriarche, Frank Glas, Federico Panciera, Ileana Florea, Jean Luc Maurice, Laurent Travers, and Yannick Ollivier (2018). "Atomic Step Flow on a Nanofacet". In: *Physical Review Letters* 121.16, p. 166101. DOI: 10.1103/PhysRevLett.121.166101 *Cited on page 57.*

Harris, J.J., J.B. Clegg, R.B. Beall, J. Castagné, K. Woodbridge, and C. Roberts (May 1991). "Delta-doping of GaAs and Al0.33Ga0.67As with Sn, Si and Be: a comparative study". In: *Journal of Crystal Growth* 111.1-4, pp. 239–245. DOI: 10.1016/0022-0248(91)90978-E *Cited on page 107.*

Heiss, Martin et al. (2011). "Direct correlation of crystal structure and optical properties in wurtzite/zinc-blende GaAs nanowire heterostructures". In: *Physical Review B - Condensed Matter and Materials Physics* 83.4, pp. 1–10. DOI: 10.1103/PhysRevB.83.045303. arXiv: 1011.5165 *Cited on pages 28, 99.*

Heon Kim, Young, Dong Woo Park, and Sang Jun Lee (2012). "Gallium-droplet behaviors of self-catalyzed GaAs nanowires: A transmission electron microscopy study". In: *Applied Physics Letters* 100.3. DOI: 10.1063/1.3678185 *Cited on pages 104, 109.*

Hertenberger, S., D. Rudolph, M. Bichler, J. J. Finley, G. Abstreiter, and G. Koblmüller (Dec. 2010). "Growth kinetics in position-controlled and catalyst-free InAs nanowire arrays on Si(111) grown by selective area molecular beam epitaxy". In: *Journal of Applied Physics* 108.11, p. 114316. DOI: 10.1063/1.3525610 *Cited on page 76.*

Hertenberger, S. et al. (2012). "High compositional homogeneity in In-rich InGaAs nanowire arrays on nanoimprinted SiO 2/Si (111)". In: *Applied Physics Letters* 101.4. DOI: 10.1063/1.4738769 *Cited on pages 75, 76.*

Hestroffer, K. et al. (Oct. 2010). "The structural properties of GaN/AlN core–shell nanocolumn heterostructures". In: *Nanotechnology* 21.41, p. 415702. DOI: 10.1088/0957-4484/21/41/415702 *Cited on page 165.*

Heurlin, Magnus, Nicklas Anttu, Christian Camus, Lars Samuelson, and Magnus T. Borgström (May 2015). "In Situ Characterization of Nanowire Dimensions and Growth Dynamics by Optical Reflectance". In: *Nano Letters* 15.5, pp. 3597–3602. DOI: 10.1021/acs.nanolett.5b01107 *Cited on page 75.*

Heurlin, Magnus, David Lindgren, Knut Deppert, Lars Samuelson, Martin H. Magnusson, Martin L. Ek, and Reine Wallenberg (2012). "Continuous gas-phase synthesis of nanowires with tunable properties". In: *Nature* 492.7427, pp. 90–94. DOI: 10.1038/nature11652 *Cited on page 25.*

Heyn, Ch and D. E. Jesson (2015). "Congruent evaporation temperature of molecular beam epitaxy grown GaAs (001) determined by local droplet etching". In: *Applied Physics Letters* 107.16. DOI: 10.1063/1.4934218 *Cited on page 112.*

Heyn, Ch, A. Stemmann, and W. Hansen (2009). "Dynamics of self-assembled droplet etching". In: *Applied Physics Letters* 95.17. DOI: 10.1063/1.3254216 *Cited on page 112.*

Heyn, Christian, Thorben Bartsch, Stefano Sanguinetti, David Jesson, and Wolfgang Hansen (2015). "Dynamics of mass transport during nanohole drilling by local droplet etching". In: *Nanoscale Research Letters* 10.1. DOI: 10.1186/s11671-015-0779-5 *Cited on page 112.*

Hilse, M, M Ramsteiner, S Breuer, L Geelhaar, and H Riechert (May 2010). "Incorporation of the dopants Si and Be into GaAs nanowires". In: *Applied Physics Letters* 96.19, p. 193104. DOI: 10.1063/1.3428358 *Cited on pages 30, 106, 107, 131, 141, 149, 168.*

Himwas, C. et al. (Dec. 2017). "In situ passivation of GaAsP nanowires". In: *Nanotechnology* 28.49, p. 495707. DOI: 10.1088/1361-6528/aa9533 *Cited on pages 33, 121, 160, 163.*

Himwas, Chalermchai et al. (2019). "Correlated optical and structural analyses of individual GaAsP/GaP core-shell nanowires". In: *Nanotechnology*. DOI: 10.1088/1361-6528/ab1760 *Cited on pages 64, 160, 163.*

Hiruma, K., M. Yazawa, T. Katsuyama, K. Ogawa, K. Haraguchi, M. Koguchi, and H. Kakibayashi (1995). "Growth and optical properties of nanometer-scale GaAs and InAs whiskers".

In: *Journal of Applied Physics* 77.2, pp. 447–462. DOI: 10.1063/1.359026 *Cited on pages 82, 83.*

Holland, M. C. and C. R. Stanley (1996). "Comparison of (Al,Ga)As(110) grown by molecular beam epitaxy with As2 and As4". In: *Journal of Vacuum Science and Technology B: Microelectronics and Nanometer Structures* 14.3, pp. 2305–2308. DOI: 10.1116/1.588926 *Cited on pages 149, 154.*

Holm, Jeppe V, Henrik I Jørgensen, Peter Krogstrup, Jesper Nygård, Huiyun Liu, and Martin Aagesen (Feb. 2013). "Surface-passivated GaAsP single-nanowire solar cells exceeding 10% efficiency grown on silicon". In: *Nature Communications* 4, p. 1498. DOI: 10.1038/ncomms2510 *Cited on page 160.*

Horowitz, Kelsey A W, Timothy Remo, Brittany Smith, Aaron Ptak, Kelsey A W Horowitz, Timothy Remo, Brittany Smith, and Aaron Ptak (2018). *A Techno-Economic Analysis and Cost Reduction Roadmap for III-V Solar Cells A Techno-Economic Analysis and Cost Reduction Roadmap for III-V Solar Cells*. URL: https://www.nrel.gov/docs/fy19osti/72103.pdf *Cited on page 17.*

Hou, H. Q., B. W. Liang, T. P. Chin, and C. W. Tu (July 1991). "In situ determination of phosphorus composition in GaAs 1- x P x grown by gas-source molecular beam epitaxy". In: *Applied Physics Letters* 59.3, pp. 292–294. DOI: 10.1063/1.105601 *Cited on page 167.*

Hu, Y., R. R. Lapierre, M. Li, K. Chen, and J. J. He (2012). "Optical characteristics of GaAs nanowire solar cells". In: *Journal of Applied Physics* 112.10. DOI: 10.1063/1.4764927 *Cited on pages 25, 27.*

Huang, Ningfeng, Chenxi Lin, and Michelle L. Povinelli (2012). "Broadband absorption of semiconductor nanowire arrays for photovoltaic applications". In: *Journal of Optics* 14.2. DOI: 10.1088/2040-8978/14/2/024004 *Cited on page 21.*

Hurle, D. T. J. (May 1999). "A comprehensive thermodynamic analysis of native point defect and dopant solubilities in gallium arsenide". In: *Journal of Applied Physics* 85.10, p. 6957. DOI: 10.1063/1.370506 *Cited on page 149.*

IEA PVPS, International Energy Agency Photovoltaic Power Systems Programme (2019). *Trends in photovoltaic applications 2019*. URL: http://www.iea-pvps.org/index.php?id=trends *Cited on pages 10, 11.*

Ilegems, M. (Mar. 1977). "Beryllium doping and diffusion in molecular-beam epitaxy of GaAs and Al x Ga 1- x As". In: *Journal of Applied Physics* 48.3, pp. 1278–1287. DOI: 10.1063/1.323772 *Cited on pages 142, 149.*

Ilkiv, Igor, Demid Kirilenko, Konstantin Kotlyar, and Alexey Bouravleuv (Jan. 2020). "Thermal decomposition of GaAs nanowires". In: *Nanotechnology* 31.5, p. 055701. DOI: 10.1088/1361-6528/ab4e27 *Cited on page 112.*

IPCC (2018). *Summary for Policymakers*. URL: https://www.ipcc.ch/sr15/ *Cited on pages 3, 8, 9, 227.*

Irber, Dominik M. et al. (2017). "Quantum Transport and Sub-Band Structure of Modulation-Doped GaAs/AlAs Core-Superlattice Nanowires". In: *Nano Letters* 17.8, pp. 4886–4893. DOI: 10.1021/acs.nanolett.7b01732 *Cited on page 157.*

ISE, Fraunhofer (2015). *Current Status of Concentrator Photovoltaik Technology*. URL: https://www.ise.fraunhofer.de/en/renewable-energy-data.html *Cited on page 17.*

— (2019). *Photovoltaics Report*. URL: https://www.ise.fraunhofer.de/en/publications/studies/photovoltaics-report.html *Cited on pages 10, 11, 15.*

Ivanov, S. V., P. S. Kop'ev, and N. N. Ledentsov (1991). "Interplay of beryllium segregation and diffusion in heavily doped GaAs and AlGaAs grown by molecular beam epitaxy (thermodynamic analysis)". In: *Journal of Crystal Growth* 108.3-4, pp. 661–669. DOI: 10.1016/0022-0248(91)90246-2 *Cited on pages 145, 148.*

Jabeen, Fauzia, Vincenzo Grillo, Silvia Rubini, and Faustino Martelli (2008). "Self-catalyzed growth of GaAs nanowires on cleaved Si by molecular beam epitaxy". In: *Nanotechnology* 19.27. DOI: 10.1088/0957-4484/19/27/275711 *Cited on pages 77, 100.*

Jacobsson, Daniel, Federico Panciera, Jerry Tersoff, Mark C. Reuter, Sebastian Lehmann, Stephan Hofmann, Kimberly A. Dick, and Frances M. Ross (2016). "Interface dynamics and crystal phase switching in GaAs nanowires". In: *Nature* 531.7594, pp. 317–322. DOI: 10.1038/nature17148 *Cited on pages 57, 141, 229.*

Jensen, Linus E., Mikael T. Björk, Sören Jeppesen, Ann I. Persson, B. Jonas Ohlsson, and Lars Samuelson (2004). "Role of surface diffusion in chemical beam epitaxy of InAs nanowires". In: *Nano Letters* 4.10, pp. 1961–1964. DOI: 10.1021/nl048825k *Cited on page 74.*

Jiang, N. et al. (2013). "Enhanced minority carrier lifetimes in GaAs/AlGaAs core-shell nanowires through shell growth optimization". In: *Nano Letters* 13.11, pp. 5135–5140. DOI: 10.1021/nl4023385 *Cited on page 25.*

Joyce, Hannah J., Callum J. Docherty, Qiang Gao, H. Hoe Tan, Chennupati Jagadish, James Lloyd-Hughes, Laura M. Herz, and Michael B. Johnston (2013). "Electronic properties of GaAs, InAs and InP nanowires studied by terahertz spectroscopy". In: *Nanotechnology* 24.21. DOI: 10.1088/0957-4484/24/21/214006 *Cited on page 174.*

Joyce, Hannah J. et al. (2014). "Electron mobilities approaching bulk limits in "surface-free" GaAs nanowires". In: *Nano Letters* 14.10, pp. 5989–5994. DOI: 10.1021/nl503043p *Cited on page 25.*

Kauppinen, Christoffer et al. (2016). "A technique for large-area position-controlled growth of GaAs nanowire arrays". In: *Nanotechnology* 27.13. DOI: 10.1088/0957-4484/27/13/135601 *Cited on page 73.*

Kayes, Brendan M., Harry A. Atwater, and Nathan S. Lewis (2005). "Comparison of the device physics principles of planar and radial p-n junction nanorod solar cells". In: *Journal of Applied Physics* 97.11. DOI: 10.1063/1.1901835 *Cited on pages 29, 32.*

Kayes, Brendan M., Hui Nie, Rose Twist, Sylvia G. Spruytte, Frank Reinhardt, Isik C. Kizilyalli, and Gregg S. Higashi (2011). "27.6% Conversion efficiency, a new record for single-junction solar cells under 1 sun illumination". In: *Conference Record of the IEEE Photovoltaic Specialists Conference*, pp. 000004–000008. DOI: 10.1109/PVSC.2011.6185831 *Cited on pages 24, 195, 196.*

Kelrich, A, Y Calahorra, Y Greenberg, A Gavrilov, S Cohen, and D Ritter (Nov. 2013). "Shadowing and mask opening effects during selective-area vapor–liquid–solid growth of InP nanowires by metalorganic molecular beam epitaxy". In: *Nanotechnology* 24.47, p. 475302. DOI: 10.1088/0957-4484/24/47/475302 *Cited on page 164.*

Ketterer, B, E Mikheev, E Uccelli, and A. Fontcuberta i Morral (Nov. 2010). "Compensation mechanism in silicon-doped gallium arsenide nanowires". In: *Applied Physics Letters* 97.22, p. 223103. DOI: 10.1063/1.3517254 *Cited on pages 28, 142, 149.*

Ketterer, Bernt, Martin Heiss, Emanuele Uccelli, Jordi Arbiol, and Anna Fontcuberta I Morral (2011). "Untangling the electronic band structure of wurtzite GaAs nanowires by resonant Raman spectroscopy". In: *ACS Nano* 5.9, pp. 7585–7592. DOI: 10.1021/nn202585j *Cited on page 99.*

Ketterer, Bernt, Emanuele Uccelli, and Anna Fontcuberta i Morral (2012). "Mobility and carrier density in p-type GaAs nanowires measured by transmission Raman spectroscopy". In: *Nanoscale* 4.5, p. 1789. DOI: 10.1039/c2nr11910b *Cited on pages 28, 131.*

Kim, Wonjong et al. (Jan. 2018). "Bistability of Contact Angle and Its Role in Achieving Quantum-Thin Self-Assisted GaAs nanowires". In: *Nano Letters* 18.1, pp. 49–57. DOI: 10.1021/acs.nanolett.7b03126 *Cited on pages 57, 109.*

King, Richard R. et al. (2006). "Advanced III-V multijunction cells for space". In: *Conference Record of the 2006 IEEE 4th World Conference on Photovoltaic Energy Conversion, WCPEC-4* 2, pp. 1757–1762. DOI: 10.1109/WCPEC.2006.279831 *Cited on page 16.*

Koblmueller, Gregor and Gerhard Abstreiter (2013). "Growth an d properties of InGaAs nanowires on sili c on". In: *Phys. Status Solidi RRL* 8.1, pp. 11–30. DOI: 10.1002/pssr.v7.10 *Cited on page 177.*

Köhler, K., P. Ganser, and M. Maier (1993). "Comparison of Si δ-doping with homogeneous doping in GaAs". In: *Journal of Crystal Growth* 127.1-4, pp. 720–723. DOI: 10.1016/0022-0248(93)90719-D *Cited on page 149.*

Kressel, H., J. U. Dunse, H. Nelson, and F. Z. Hawrylo (Mar. 1968). "Luminescence in Silicon-Doped GaAs Grown by Liquid-Phase Epitaxy". In: *Journal of Applied Physics* 39.4, pp. 2006–2011. DOI: 10.1063/1.1656480 *Cited on page 150.*

Kroemer, Herbert (1987). "Polar-on-nonpolar epitaxy". In: *Journal of Crystal Growth* 81.1-4, pp. 193–204. DOI: 10.1016/0022-0248(87)90391-5 *Cited on page 19.*

Krogstrup, Peter, Henrik Ingerslev Jørgensen, Martin Heiss, Olivier Demichel, Jeppe V. Holm, Martin Aagesen, Jesper Nygard, and Anna Fontcuberta i Morral (Mar. 2013). "Single-nanowire solar cells beyond the Shockley–Queisser limit". In: *Nature Photonics* 7.4, pp. 306–310. DOI: 10.1038/nphoton.2013.32. arXiv: 1301.1068 *Cited on pages 21, 28.*

Krogstrup, Peter, Ronit Popovitz-Biro, Erik Johnson, Morten Hannibal Madsen, Jesper Nygård, and Hadas Shtrikman (2010). "Structural phase control in self-catalyzed growth of GaAs nanowires on silicon (111)". In: *Nano Letters* 10.11, pp. 4475–4482. DOI: 10.1021/nl102308k *Cited on page 100.*

Kupec, J. and B. Witzigmann (2009). "Dispersion, Wave Propagation and Efficiency Analysis of Nanowire Solar Cells". In: *Optics Express* 17.12, p. 10399. DOI: 10.1364/oe.17.010399 *Cited on page 21.*

Küpers, Hanno, Ryan B. Lewis, Abbes Tahraoui, Mathias Matalla, Olaf Krüger, Faebian Bastiman, Henning Riechert, and Lutz Geelhaar (2018). "Diameter evolution of selective area grown Ga-assisted GaAs nanowires". In: *Nano Research* 11.5, pp. 2885–2893. DOI: 10.1007/s12274-018-1984-1. arXiv: 1708.05596 *Cited on pages 77, 78, 90, 160.*

Kuyanov, P., J. Boulanger, and R.R. LaPierre (Mar. 2017). "Control of GaP nanowire morphology by group V flux in gas source molecular beam epitaxy". In: *Journal of Crystal Growth* 462, pp. 29–34. DOI: 10.1016/j.jcrysgro.2017.01.025 *Cited on page 79.*

Ky, Nguyen Hong and F. K. Reinhart (1998). "Amphoteric native defect reactions in Si-doped GaAs". In: *Journal of Applied Physics* 83.2, pp. 718–724. DOI: 10.1063/1.366743 *Cited on page 152.*

Lapierre, R R et al. (2013). "III-V nanowire photovoltaics: Review of design for high efficiency". In: *Physica Status Solidi - Rapid Research Letters* 7.10, pp. 815–830. DOI: 10.1002/pssr.201307109 *Cited on pages 20, 23, 24.*

LaPierre, R. R. (Feb. 2011a). "Numerical model of current-voltage characteristics and efficiency of GaAs nanowire solar cells". In: *Journal of Applied Physics* 109.3, p. 034311. DOI: 10.1063/1.3544486 *Cited on pages 22, 27, 30, 160, 174.*

— (July 2011b). "Theoretical conversion efficiency of a two-junction III-V nanowire on Si solar cell". In: *Journal of Applied Physics* 110.1, p. 014310. DOI: 10.1063/1.3603029 *Cited on pages 27, 30, 228.*

LaPierre, R. R., B. J. Robinson, and D. A. Thompson (Mar. 1996). "Group V incorporation in InGaAsP grown on InP by gas source molecular beam epitaxy". In: *Journal of Applied Physics* 79.6, pp. 3021–3027. DOI: 10.1063/1.361241 *Cited on page 167.*

Lee, Ching Ting, Ching Hung Fu, Chang Da Tsai, and Wei Lin (1998). "Performance characterization of InGaP schottky contact with ITO transparent electrodes". In: *Journal of Electronic Materials* 27.9, pp. 1017–1021. DOI: 10.1007/s11664-998-0155-7 *Cited on pages 185, 190.*

Lépinau, Romaric de, Andrea Scaccabarozzi, Gilles Patriarche, Laurent Travers, Stéphane Collin, Andrea Cattoni, and Fabrice Oehler (July 2019). "Evidence and control of unintentional As-rich shells in GaAs 1– x P x nanowires". In: *Nanotechnology* 30.29, p. 294003. DOI: 10.1088/1361-6528/ab14c1 *Cited on page 160.*

Liang, Dong, Yangsen Kang, Yijie Huo, Yusi Chen, Yi Cui, and James S. Harris (2013). "High-efficiency nanostructured window GaAs solar cells". In: *Nano Letters* 13.10, pp. 4850–4856. DOI: 10.1021/nl402680g *Cited on page 30.*

Liborius, Lisa, Jan Bieniek, Andreas Nägelein, Franz Josef Tegude, Werner Prost, Thomas Hannappel, Artur Poloczek, and Nils Weimann (2019a). "n-Doped InGaP Nanowire Shells in GaAs/InGaP Core–Shell p–n Junctions". In: *Physica Status Solidi (B) Basic Research* September. DOI: 10.1002/pssb.201900358 *Cited on page 209.*

Liborius, Lisa, Fabian Heyer, Khaled Arzi, Claudia Speich, Werner Prost, Franz Josef Tegude, Nils Weimann, and Artur Poloczek (2019b). "Toward Nanowire HBT: Reverse Current Reduction in Coaxial GaAs/InGaP n(i)p and n(i)pn Core-Multishell Nanowires". In: *Physica Status Solidi (A) Applications and Materials Science* 216.1, pp. 1–6. DOI: 10.1002/pssa.201800562 *Cited on page 205.*

Lim, Sung K., Michael J. Tambe, Megan M. Brewster, and Silvija Gradečak (2008). "Controlled growth of ternary alloy nanowires using metalorganic chemical vapor deposition". In: *Nano Letters* 8.5, pp. 1386–1392. DOI: 10.1021/nl080129n *Cited on page 160.*

Loiko, Natalia A., Alexander A. Miskevich, and Valery A. Loiko (2018). "Incoherent component of light scattered by a monolayer of spherical particles: analysis of angular distribution and absorption of light". In: *Journal of the Optical Society of America A* 35.1, p. 108. DOI: 10.1364/josaa.35.000108 *Cited on page 73.*

Lucci, I. et al. (2018). "Universal description of III-V/Si epitaxial growth processes". In: *Physical Review Materials* 2.6, pp. 1–6. DOI: 10.1103/PhysRevMaterials.2.060401 *Cited on page 19.*

Madaria, Anuj R. et al. (2012). "Toward optimized light utilization in nanowire arrays using scalable nanosphere lithography and selected area growth". In: *Nano Letters* 12.6, pp. 2839–2845. DOI: 10.1021/nl300341v *Cited on pages 27, 73, 92.*

Maguire, J., R. Murray, R. C. Newman, R. B. Beall, and J. J. Harris (Mar. 1987). "Mechanism of compensation in heavily silicon-doped gallium arsenide grown by molecular beam epitaxy". In: *Applied Physics Letters* 50.9, pp. 516–518. DOI: 10.1063/1.98265 *Cited on page 149.*

Makita, Kikuo et al. (2020). "III-V//Si multijunction solar cells with 30% efficiency using smart stack technology with Pd nanoparticle array". In: *Progress in Photovoltaics: Research and Applications* 28.1, pp. 16–24. DOI: 10.1002/pip.3200 *Cited on page 19.*

Mancini, L. et al. (Dec. 2014). "Three-dimensional nanoscale study of Al segregation and quantum dot formation in GaAs/AlGaAs core-shell nanowires". In: *Applied Physics Letters* 105.24, p. 243106. DOI: 10.1063/1.4904952 *Cited on page 160.*

Mandl, Bernhard et al. (2006). "Au-free epitaxial growth of InAs nanowires". In: *Nano Letters* 6.8, pp. 1817–1821. DOI: 10.1021/nl060452v *Cited on page 76.*

Mandl, Bernhard et al. (2010). "Growth mechanism of self-catalyzed group III-V nanowires". In: *Nano Letters* 10.11, pp. 4443–4449. DOI: 10.1021/nl1022699 *Cited on pages 73, 76.*

Mariani, Giacomo, Adam C Scofield, Chung-Hong Hung, and Diana L Huffaker (Feb. 2013a). "GaAs nanopillar-array solar cells employing in situ surface passivation". In: *Nature Communications* 4, p. 1497. DOI: 10.1038/ncomms2509 *Cited on pages 31, 32, 174, 176, 197, 207.*

Mariani, Giacomo, Ping-Show Wong, Aaron M Katzenmeyer, Francois L Eonard, Joshua Shapiro, and Diana L Huffaker (2011). "Patterned Radial GaAs Nanopillar Solar Cells". In: DOI: 10.1021/nl200965j *Cited on page 176.*

Mariani, Giacomo, Zhengliu Zhou, Adam Scofield, and Diana L Huffaker (Apr. 2013b). "Direct-Bandgap Epitaxial Core–Multishell Nanopillar Photovoltaics Featuring Subwavelength Optical Concentrators". In: *Nano Letters* 13.4, pp. 1632–1637. DOI: 10.1021/nl400083g *Cited on pages 24, 26, 30, 176, 177.*

Mårtensson, Thomas et al. (2004). "Epitaxial III - V Nanowires on Silicon". In: *Nano Letters* 4.10, pp. 1987–1990. DOI: 10.1088/0957-4484/17/11/S07 *Cited on page 74.*

Masu, Kazuya, Makoto Konagai, and Kiyoshi Takahashi (1983). "Diffusion of beryllium into GaAs during liquid phase epitaxial growth of p- Ga 0.2 Al 0.8 As Diffusion of beryllium into GaAs during liquid phase epitaxial growth of p-Ga O . 2 Al o . 8 As". In: *Journal of Applied Physics Applied Physics Letters* 54.102, pp. 1574–13117. DOI: 10.1063/1.4772020 *Cited on pages 141, 142.*

Matsushima, Yuichi and Shun-ichi Gonda (Nov. 1976). "Molecular Beam Epitaxy of GaP and GaAs(1-x)P(x)". In: *Japanese Journal of Applied Physics* 15.11, pp. 2093–2101. DOI: 10.1143/JJAP.15.2093 *Cited on page 167.*

Matteini, Federico, Gözde Tütüncüoglu, Dmitry Mikulik, Jelena Vukajlovic-Plestina, Heidi Potts, Jean-Baptiste Leran, W. Craig Carter, and Anna Fontcuberta i Morral (Oct. 2016). "Impact of the Ga Droplet Wetting, Morphology, and Pinholes on the Orientation of GaAs Nanowires". In: *Crystal Growth & Design* 16.10, pp. 5781–5786. DOI: 10.1021/acs.cgd.6b00858 *Cited on pages 23, 79, 88.*

Matteini, Federico, Gözde Tütüncüoglu, Daniel Rüffer, Esther Alarcón-Lladó, and Anna Fontcuberta I Morral (2014). "Ga-assisted growth of GaAs nanowires on silicon, comparison of surface SiOx of different nature". In: *Journal of Crystal Growth* 404, pp. 246–255. DOI: 10.1016/j.jcrysgro.2014.07.034 *Cited on pages 23, 28.*

Mattila, M., T. Hakkarainen, and H. Lipsanen (2007). "Catalyst-free fabrication of InP and InP(N) nanowires by metalorganic vapor phase epitaxy". In: *Journal of Crystal Growth* 298.SPEC. ISS, pp. 640–643. DOI: 10.1016/j.jcrysgro.2006.10.084 *Cited on page 76.*

Metaferia, Wondwosen et al. (2016). "GaAsP Nanowires Grown by Aerotaxy". In: *Nano Letters* 16.9, pp. 5701–5707. DOI: 10.1021/acs.nanolett.6b02367 *Cited on pages 25, 160.*

Mikulik, Dmitry, Mikhail Mintairov, Ian Nachemson, Valery Evstropov, Pablo Romero-Gomez, Maxim Shvarts, and Anna Fontcuberta I Morral (2019). "Extraction of p-n junction properties and series resistance in GaAs nanowire-based solar cells using light concentration". In: *Nanotechnology* 30.9. DOI: 10.1088/1361-6528/aaf67c *Cited on pages 23, 24, 28, 200, 209.*

Misra, Soumyadeep, Linwei Yu, Martin Foldyna, and Pere Roca Cabarrocas (2013). "High efficiency and stable hydrogenated amorphous silicon radial junction solar cells built on VLS-grown silicon nanowires". In: *Solar Energy Materials and Solar Cells* 118, pp. 90–95. DOI: 10.1016/j.solmat.2013.07.036 *Cited on page 23.*

Mohan, Premila, Junichi Motohisa, and Takashi Fukui (2005). "Controlled growth of highly uniform, axial/radial direction-defined, individually addressable InP nanowire arrays". In: *Nanotechnology* 16.12, pp. 2903–2907. DOI: 10.1088/0957-4484/16/12/029 *Cited on page 75.*

— (2006). "Fabrication of InPInAsInP core-multishell heterostructure nanowires by selective area metalorganic vapor phase epitaxy". In: *Applied Physics Letters* 88.13, pp. 1–4. DOI: 10.1063/1.2189203 *Cited on page 75.*

Mohseni, P K, C Maunders, G A Botton, and R R LaPierre (Nov. 2007). "GaP/GaAsP/GaP core–multishell nanowire heterostructures on (111) silicon". In: *Nanotechnology* 18.44, p. 445304. DOI: 10.1088/0957-4484/18/44/445304 *Cited on pages 27, 160.*

Mohseni, P. K., A. D. Rodrigues, J. C. Galzerani, Y. A. Pusep, and R. R. LaPierre (Dec. 2009). "Structural and optical analysis of GaAsP/GaP core-shell nanowires". In: *Journal of Applied Physics* 106.12, p. 124306. DOI: 10.1063/1.3269724 *Cited on pages 160, 163.*

Mohseni, Parsian K., Ashkan Behnam, Joshua D. Wood, Christopher D. English, Joseph W. Lyding, Eric Pop, and Xiuling Li (Mar. 2013). "In x Ga 1– x As Nanowire Growth on Graphene: van der Waals Epitaxy Induced Phase Segregation". In: *Nano Letters* 13.3, pp. 1153–1161. DOI: 10.1021/nl304569d *Cited on page 160.*

Mohseni, Parsian K and Ray R Lapierre (2009). "A growth interruption technique for stacking fault-free nanowire superlattices". In: DOI: 10.1088/0957-4484/20/2/025610 *Cited on page 160.*

Molière, T. et al. (2017). "GaAs microcrystals selectively grown on silicon: Intrinsic carbon doping during chemical beam epitaxy with trimethylgallium". In: *Journal of Applied Physics* 121.3. DOI: 10.1063/1.4974538 *Cited on page 76.*

Moore, James E., Sourabh Dongaonkar, Raghu Vamsi Krishna Chavali, Muhammad Ashraful Alam, and Mark S. Lundstrom (July 2014). "Correlation of Built-In Potential and I–V Crossover in Thin-Film Solar Cells". In: *IEEE Journal of Photovoltaics* 4.4, pp. 1138–1148. DOI: 10.1109/JPHOTOV.2014.2316364 *Cited on page 196.*

Morgan, D. V., Y. Aliyu, and R. W. Bunce (1992). "The Thermal Stability of Indium-Tin-Oxide/n-GaAs Schottky Contacts". In: *Physica Status Solidi (a)* 133.1, pp. 77–93. DOI: 10.1002/pssa.2211330110 *Cited on pages 185, 188.*

Morkötter, S. et al. (2015). "Demonstration of confined electron gas and steep-slope behavior in delta-doped GaAs-AlGaAs core-shell nanowire transistors". In: *Nano Letters* 15.5, pp. 3295–3302. DOI: 10.1021/acs.nanolett.5b00518 *Cited on page 157.*

Mosberg, A. B., S. Myklebost, D. Ren, H. Weman, B. O. Fimland, and A. T.J. Van Helvoort (2017). "Evaluating focused ion beam patterning for position-controlled nanowire growth using computer vision". In: *Journal of Physics: Conference Series* 902.1. DOI: 10.1088/1742-6596/902/1/012020 *Cited on page 73.*

Moss, T. S. (1954). "The interpretation of the properties of indium antimonide". In: *Proceedings of the Physical Society. Section B* 67.10, pp. 775–782. DOI: 10.1088/0370-1301/67/10/306 *Cited on page 135.*

Munshi, Abdul Mazid et al. (Feb. 2014). "Position-Controlled Uniform GaAs Nanowires on Silicon using Nanoimprint Lithography". In: *Nano Letters* 14.2, pp. 960–966. DOI: 10.1021/nl404376m *Cited on pages 77–79, 90, 160.*

Nakai, Eiji, Muyi Chen, Masatoshi Yoshimura, Katsuhiro Tomioka, and Takashi Fukui (Jan. 2015). "InGaAs axial-junction nanowire-array solar cells". In: *Japanese Journal of Applied Physics* 54.1, p. 015201. DOI: 10.7567/JJAP.54.015201 *Cited on pages 26, 76, 176, 177.*

Nakai, Eiji, Masatoshi Yoshimura, Katsuhiro Tomioka, and Takashi Fukui (2013). "GaAs / InGaP Core – Multishell Nanowire-Array- Based Solar Cells". In: *Cited on page 26.*

Nelson, R. J. and R. G. Sobers (1978). "Minority-carrier lifetimes and internal quantum efficiency of surface-free GaAs". In: *Journal of Applied Physics* 49.12, pp. 6103–6108. DOI: 10.1063/1.324530 *Cited on page 40.*

Noborisaka, Jinichiro, Junichi Motohisa, and Takashi Fukui (2005). "Catalyst-free growth of GaAs nanowires by selective-area metalorganic vapor-phase epitaxy". In: *Applied Physics Letters* 86.21, pp. 1–3. DOI: 10.1063/1.1935038 *Cited on page 75.*

Nomura, Takashi, Hiroshi Ogasawara, Masahiro Miyao, and Minoru Hagino (May 1991). "Composition control of GaAsP grown by molecular beam epitaxy". In: *Journal of Crystal Growth* 111.1-4, pp. 61–64. DOI: 10.1016/0022-0248(91)90947-4 *Cited on page 167.*

Novotny, Clint J. and Paul K. L. Yu (Nov. 2005). "Vertically aligned, catalyst-free InP nanowires grown by metalorganic chemical vapor deposition". In: *Applied Physics Letters* 87.20, p. 203111. DOI: 10.1063/1.2131182 *Cited on page 76.*

NSM (Ioffe) (2019). *Semiconductors on NSM*. URL: http://www.ioffe.ru/SVA/NSM/Semicond/ (visited on 12/01/2019) *Cited on page 59.*

Oehler, Fabrice, Andrea Cattoni, Andrea Scaccabarozzi, Gilles Patriarche, Frank Glas, and Jean-Christophe Harmand (Feb. 2018). "Measuring and Modeling the Growth Dynamics of Self-Catalyzed GaP Nanowire Arrays". In: *Nano Letters* 18.2, pp. 701–708. DOI: 10.1021/acs.nanolett.7b03695 *Cited on pages 59, 61, 79, 88, 118, 119, 160, 163, 164.*

Oener, Sebastian Z., Alessandro Cavalli, Hongyu Sun, Jos E. M. Haverkort, Erik P. A. M. Bakkers, and Erik C. Garnett (Dec. 2018). "Charge carrier-selective contacts for nanowire solar cells". In: *Nature Communications* 9.1, p. 3248. DOI: 10.1038/s41467-018-05453-5 *Cited on pages 176, 217.*

Ohlsson, B. J., M. T. Björk, M. H. Magnusson, K. Deppert, L. Samuelson, and L. R. Wallenberg (2001). "Size-, shape-, and position-controlled GaAs nano-whiskers". In: *Applied Physics Letters* 79.20, pp. 3335–3337. DOI: 10.1063/1.1418446 *Cited on pages 23, 74.*

Olson, J. M., R. K. Ahrenkiel, D. J. Dunlavy, Brian Keyes, and A. E. Kibbler (Sept. 1989). "Ultralow recombination velocity at Ga 0.5 In 0.5 P/GaAs heterointerfaces". In: *Applied Physics Letters* 55.12, pp. 1208–1210. DOI: 10.1063/1.101656 *Cited on page 120.*

Orrù, Marta et al. (2016). "A Roadmap for Controlled and Efficient n-Type Doping of Self-Assisted GaAs Nanowires Grown by Molecular Beam Epitaxy". In: *Advanced Functional Materials* 26.17, pp. 2836–2845. DOI: 10.1002/adfm.201504853 *Cited on page 149.*

Orton, J. W. (John Wilfred) and Tom Foxon (2015). *Molecular beam epitaxy : a short history*, p. 516. ISBN: 0191061166 *Cited on pages 50, 53, 119, 120, 149, 154.*

Otnes, Gaute and Magnus T Borgström (2017). "Towards high efficiency nanowire solar cells". In: *Nano Today* 12, pp. 31–45. DOI: 10.1016/j.nantod.2016.10.007 *Cited on pages 20, 23, 24, 26, 29, 30, 176.*

Otnes, Gaute, Magnus Heurlin, Mariusz Graczyk, Jesper Wallentin, Daniel Jacobsson, Alexander Berg, Ivan Maximov, and Magnus T. Borgström (2016). "Strategies to obtain pattern fidelity in nanowire growth from large-area surfaces patterned using nanoimprint lithography". In: *Nano Research* 9.10, pp. 2852–2861. DOI: 10.1007/s12274-016-1165-z *Cited on page 74.*

Otnes, Gaute et al. (2018). "Understanding InP Nanowire Array Solar Cell Performance by Nanoprobe-Enabled Single Nanowire Measurements". In: *Nano Letters* 18.5, pp. 3038–3046. DOI: 10.1021/acs.nanolett.8b00494 *Cited on pages 24, 30, 175, 185.*

Panciera, Federico, Zhaslan Baraissov, Gilles Patriarche, Vladimir G Dubrovskii, Frank Glas, Laurent Travers, Utkur Mirsaidov, and Jean-christophe Harmand (Feb. 2020). "Phase selection in self-catalysed GaAs nanowires". In: *Nano Letters*. DOI: 10.1021/acs.nanolett.9b04808 *Cited on pages 57, 58, 112, 229.*

Panish, Morton B. (May 1969). "The Ga/GaAs/GaP system: Phase chemistry and solution growth of GaAsχP1-χ". In: *Journal of Physics and Chemistry of Solids* 30.5, pp. 1083–1090. DOI: 10.1016/0022-3697(69)90364-3 *Cited on page 167.*

Parker, D. G (1987). "On the formation of near ideal quasi-Schottky barriers between indium tin oxide and gallium arsenide". In: *GEC journal of research* 5.2, pp. 116–123 *Cited on page 185.*

Parkinson, Patrick et al. (2009). "Carrier lifetime and mobility enhancement in nearly defect-free core-shell nanowires measured using time-resolved terahertz spectroscopy". In: *Nano Letters* 9.9, pp. 3349–3353. DOI: 10.1021/nl9016336 *Cited on page 99.*

Pavesi, L., Nguyen Hong Ky, J. D. Ganière, F. K. Reinhart, N. Baba-Ali, I. Harrison, B. Tuck, and M. Henini (1992). "Role of point defects in the silicon diffusion in GaAs and Al 0.3Ga0.7As and in the related superlattice disordering". In: *Journal of Applied Physics* 71.5, pp. 2225–2237. DOI: 10.1063/1.351120 *Cited on pages 149, 152.*

Pavesi, L., F. Piazza, M. Henini, and I. Harrison (1993). "Orientation dependence of the Si doping of GaAs grown by molecular beam epitaxy". In: *Semiconductor Science and Technology* 8.2, pp. 167–171. DOI: 10.1088/0268-1242/8/2/004 *Cited on page 149.*

Perea, Daniel E., Jonathan E. Allen, Steven J. May, Bruce W. Wessels, David N. Seidman, and Lincoln J. Lauhon (2006). "Three-dimensional nanoscale composition mapping of semiconductor nanowires". In: *Nano Letters* 6.2, pp. 181–185. DOI: 10.1021/nl051602p *Cited on page 25.*

Perillat-Merceroz, G., R. Thierry, P. H. Jouneau, P. Ferret, and G. Feuillet (2012). "Strain relaxation by dislocation glide in ZnO/ZnMgO core-shell nanowires". In: *Applied Physics Letters* 100.17. DOI: 10.1063/1.4704927 *Cited on page 126.*

Petronio, Federico (2019). "Modelling of GaAs nanowires based solar cells". Master's thesis. Politecnico di Milano *Cited on page 210.*

Piccin, M. et al. (2007). "Growth by molecular beam epitaxy and electrical characterization of GaAs nanowires". In: *Physica E: Low-Dimensional Systems and Nanostructures* 37.1-2, pp. 134–137. DOI: 10.1016/j.physe.2006.07.002 *Cited on page 82.*

Plissard, S., G Larrieu, X Wallart, and P Caroff (2011). "High yield of self-catalyzed GaAs nanowire arrays grown on silicon via gallium droplet positioning". In: *Nanotechnology* 22.27, p. 275602. DOI: 10.1088/0957-4484/22/27/275602 *Cited on pages 59, 61, 77–79, 88, 118.*

Plissard, Sébastien, Kimberly A Dick, Guilhem Larrieu, Sylvie Godey, Ahmed Addad, Xavier Wallart, and Philippe Caroff (2010). "Gold-free growth of GaAs nanowires on silicon: arrays and polytypism". In: *Nanotechnology* 21.38, p. 385602. DOI: 10.1088/0957-4484/21/38/385602 *Cited on page 77.*

Ploog, Klaus (Feb. 1987). "Delta- (°-) doping in MBE-grown GaAs: Concept and device application". In: *Journal of Crystal Growth* 81.1-4, pp. 304–313. DOI: 10.1016/0022-0248(87)90409-X *Cited on page 157.*

Priante, G., S. Ambrosini, V. G. Dubrovskii, A. Franciosi, and S. Rubini (Sept. 2013). "Stopping and Resuming at Will the Growth of GaAs Nanowires". In: *Crystal Growth & Design* 13.9, pp. 3976–3984. DOI: 10.1021/cg400701w *Cited on pages 56, 104, 109.*

Priante, Giacomo, Gilles Patriarche, Fabrice Oehler, Frank Glas, and Jean Christophe Harmand (2015). "Abrupt GaP/GaAs Interfaces in Self-Catalyzed Nanowires". In: *Nano Letters* 15.9, pp. 6036–6041. DOI: 10.1021/acs.nanolett.5b02224 *Cited on page 161.*

Qian, Xiaofeng, Mitsumoto Kawai, Hajime Goto, and Ju Li (2015). "Effect of twin boundaries and structural polytypes on electron transport in GaAs". In: *Computational Materials Science* 108, pp. 258–263. DOI: 10.1016/j.commatsci.2015.06.011 *Cited on page 99.*

Ramdani, M. R. et al. (2010). "Fast growth synthesis of GaAs nanowires with exceptional length". In: *Nano Letters* 10.5, pp. 1836–1841. DOI: 10.1021/nl100557d *Cited on page 22.*

Ramdani, Mohammed Reda, Jean Christophe Harmand, Frank Glas, Gilles Patriarche, and Laurent Travers (2013). "Arsenic pathways in self-catalyzed growth of GaAs nanowires". In: *Crystal Growth and Design* 13.1, pp. 91–96. DOI: 10.1021/cg301167g *Cited on pages 54, 58, 119, 163.*

Raychaudhuri, S. and E. T. Yu (2006). "Critical dimensions in coherently strained coaxial nanowire heterostructures". In: *Journal of Applied Physics* 99.11. DOI: 10.1063/1.2202697 *Cited on pages 126–128.*

Ren, Dingkun, Alan C. Farrell, Benjamin S. Williams, and Diana L. Huffaker (2017). "Seeding layer assisted selective-area growth of As-rich InAsP nanowires on InP substrates". In: *Nanoscale* 9.24, pp. 8220–8228. DOI: 10.1039/C7NR00948H *Cited on page 75.*

REN21 (2019). *Global Status Report*. URL: https://www.ren21.net/reports/global-status-report/ *Cited on pages 3, 8, 10, 227.*

Richter, Armin, Martin Hermle, and Stefan W Glunz (Oct. 2013). "Reassessment of the Limiting Efficiency for Crystalline Silicon Solar Cells". In: *IEEE Journal of Photovoltaics* 3.4, pp. 1184–1191. DOI: 10.1109/JPHOTOV.2013.2270351 *Cited on page 14.*

Rideout, V.L. (1975). "A review of the theory and technology for ohmic contacts to group III–V compound semiconductors". In: *Solid-State Electronics*. DOI: 10.1016/0038-1101(75)90031-3 *Cited on pages 45, 46.*

Ringel, S. A. et al. (2013). "Ideal GaP/Si heterostructures grown by MOCVD: III-V/active-Si subcells, multijuntions, and MBE-to-MOCVD III-V/Si interface science". In: *Conference Record of the IEEE Photovoltaic Specialists Conference*, pp. 3383–3388. DOI: 10.1109/PVSC.2013.6745175 *Cited on page 20.*

Rizzo Piton, Marcelo et al. (Aug. 2019). "Gradients of Be-dopant concentration in self-catalyzed GaAs nanowires". In: *Nanotechnology* 30.33, p. 335709. DOI: 10.1088/1361-6528/ab1a97 *Cited on pages 107, 130, 131, 141.*

Roest, Aarnoud L, Marcel A Verheijen, Olaf Wunnicke, Stacey Serafin, Harry Wondergem, and Erik P A M Bakkers (2006). "Position-controlled epitaxial III–V nanowires on silicon". In: DOI: 10.1088/0957-4484/17/11/S07 *Cited on page 74.*

Rudolph, D. et al. (2014). "Effect of interwire separation on growth kinetics and properties of site-selective GaAs nanowires". In: *Applied Physics Letters* 105.3. DOI: 10.1063/1.4891427 *Cited on page 31.*

Rudolph, Daniel et al. (2011). "Direct observation of a noncatalytic growth regime for GaAs nanowires". In: *Nano Letters* 11.9, pp. 3848–3854. DOI: 10.1021/nl2019382 *Cited on page 76.*

Rudolph, Daniel et al. (Apr. 2013). "Spontaneous alloy composition ordering in GaAs-AlGaAs core-shell nanowires". In: *Nano Letters* 13.4, pp. 1522–1527. DOI: 10.1021/nl3046816 *Cited on page 160.*

Ruhstorfer, Daniel, Simon Mejia, Manfred Ramsteiner, Markus Döblinger, Hubert Riedl, Jonathan J Finley, and Gregor Koblmüller (Feb. 2020). "Demonstration of n -type behavior in catalyst-free Si-doped GaAs nanowires grown by molecular beam epitaxy". In: *Applied Physics Letters* 116.5, p. 052101. DOI: 10.1063/1.5134687 *Cited on pages 27, 76, 225.*

Russo-Averchi, Eleonora et al. (May 2015). "High Yield of GaAs Nanowire Arrays on Si Mediated by the Pinning and Contact Angle of Ga". In: *Nano Letters* 15.5, pp. 2869–2874. DOI: 10.1021/nl504437v *Cited on pages 28, 77–79.*

Salehzadeh, O., K. L. Kavanagh, and S. P. Watkins (2013). "Geometric limits of coherent III-V core/shell nanowires". In: *Journal of Applied Physics* 114.5. DOI: 10.1063/1.4816460 *Cited on pages 127, 128.*

Sanchez, A. M., J. A. Gott, H. A. Fonseka, Y. Zhang, Huiyun Liu, and R. Beanland (May 2018). "Stable Defects in Semiconductor Nanowires". In: *Nano Letters* 18.5, pp. 3081–3087. DOI: 10.1021/acs.nanolett.8b00620 *Cited on page 28.*

Sanchez, Ana M., Yunyan Zhang, Edward W. Tait, Nicholas D.M. Hine, Huiyun Liu, and Richard Beanland (2017). "Nonradiative Step Facets in Semiconductor Nanowires". In: *Nano Letters* 17.4, pp. 2454–2459. DOI: 10.1021/acs.nanolett.7b00123 *Cited on pages 28, 99.*

Sartel, C., D.L. Dheeraj, F. Jabeen, and J.C. Harmand (July 2010). "Effect of arsenic species on the kinetics of GaAs nanowires growth by molecular beam epitaxy". In: *Journal of Crystal Growth* 312.14, pp. 2073–2077. DOI: 10.1016/J.JCRYSGRO.2010.04.027 *Cited on pages 59, 154, 160.*

Sato, T., K. Hiruma, M. Shirai, K. Tominaga, K. Haraguchi, T. Katsuyama, and T. Shimada (1995). "Site-controlled growth of nanowhiskers". In: *Applied Physics Letters* 66.2, pp. 159–161. DOI: 10.1063/1.113549 *Cited on pages 74, 82.*

Scaccabarozzi, Andrea, Andrea Cattoni, Gilles Patriarche, Laurent Travers, Stéphane Collin, Jean-Cristophe Harmand, Frank Glas, and Fabrice Oehler (2020). "High yield of vertical GaP and GaAs nanowires on patterned silicon using In catalyst". In: *submitted* *Cited on pages 32, 79, 80.*

Scarpellini, David, Alexey Fedorov, Claudio Somaschini, Cesare Frigeri, Monica Bollani, Sergio Bietti, Richard N etzel, and Stefano Sanguinetti (2017). "Ga crystallization dynamics during annealing of self-assisted GaAs nanowires". In: *Nanotechnology* 28.4. DOI: 10.1088/1361-6528/28/4/045605 *Cited on page 104.*

Scheer, Roland and Hw Schock (2011). *Chalcogenide photovoltaics*, p. 368. ISBN: 9783527633708. DOI: 10.1002/9783527633708 *Cited on pages 196, 197.*

Schneider, Caroline A, Wayne S Rasband, and Kevin W Eliceiri (July 2012). "NIH Image to ImageJ: 25 years of image analysis". In: *Nature Methods* 9.7, pp. 671–675. DOI: 10.1038/nmeth.2089 *Cited on page 86.*

Schroth, Philipp et al. (2019). "Impact of the shadowing effect on crystal structure of patterned self-catalyzed GaAs nanowires". In: *Nano Letters*, acs.nanolett.9b00380. DOI: 10.1021/acs.nanolett.9b00380 *Cited on pages 100, 163.*

Senanayake, Pradeep et al. (2010). "Photoconductive gain in patterned nanopillar photodetector arrays". In: *Applied Physics Letters* 97.20, pp. 19–22. DOI: 10.1063/1.3517491 *Cited on page 177.*

Shah, Jay M., Y.-L. Li, Th Gessmann, and E. F. Schubert (Aug. 2003). "Experimental analysis and theoretical model for anomalously high ideality factors (n>>2.0) in AlGaN/GaN p-n junction diodes". In: *Journal of Applied Physics* 94.4, pp. 2627–2630. DOI: 10.1063/1.1593218 *Cited on page 197.*

De-Sheng, Jiang, Y. Makita, K. Ploog, and H. J. Queisser (Feb. 1982). "Electrical properties and photoluminescence of Te-doped GaAs grown by molecular beam epitaxy". In: *Journal of Applied Physics* 53.2, pp. 999–1006. DOI: 10.1063/1.330581 *Cited on page 136.*

Shimamura, Kohei, Zaoshi Yuan, Fuyuki Shimojo, and Aiichiro Nakano (2013). "Effects of twins on the electronic properties of GaAs". In: *Applied Physics Letters* 103.2, pp. 1–5. DOI: 10.1063/1.4811746 *Cited on page 99.*

Shin, Jae Cheol et al. (2013). "Wafer-scale production of uniform InAs y P 1-y nanowire array on silicon for heterogeneous integration". In: *ACS Nano* 7.6, pp. 5463–5471. DOI: 10.1021/nn4014774 *Cited on page 177.*

Shockley, William and Hans J. Queisser (1961). "Detailed balance limit of efficiency of p-n junction solar cells". In: *Journal of Applied Physics* 32.3, pp. 510–519. DOI: 10.1063/1.1736034. arXiv: 9809069v1 [arXiv:gr-qc] *Cited on pages 12, 14.*

Shu-Dong, Wu, GUO Li-Wei, Wang Wen-Xin, Li Zhi-Hua, NIU Ping-Juan, Huang Qi, and Zhou Jun-Ming (Apr. 2005). "Incorporation Behaviour of Arsenic and Phosphorus in GaAsP/GaAs Grown by Solid Source Molecular Beam Epitaxy with a GaP Decomposition Source". In: *Chinese Physics Letters* 22.4, pp. 960–962. DOI: 10.1088/0256-307X/22/4/050 *Cited on page 167.*

Silverman, Timothy J, Michael G Deceglie, Bill Marion, Sam Cowley, Brendan Kayes, and Sarah Kurtz (June 2013). "Outdoor performance of a thin-film gallium-arsenide photovoltaic module". In: *2013 IEEE 39th Photovoltaic Specialists Conference (PVSC)*. IEEE, pp. 0103–0108. ISBN: 978-1-4799-3299-3. DOI: 10.1109/PVSC.2013.6744109 *Cited on page 16.*

Sköld, Niklas, Jakob B. Wagner, Gunnel Karlsson, Tania Hernán, Werner Seifert, Mats-Erik Pistol, and Lars Samuelson (Dec. 2006). "Phase Segregation in AlInP Shells on GaAs Nanowires". In: *Nano Letters* 6.12, pp. 2743–2747. DOI: 10.1021/nl061692d *Cited on page 160.*

Sladek, K., V. Klinger, J. Wensorra, M. Akabori, H. Hardtdegen, and D. Grützmacher (2010). "MOVPE of n-doped GaAs and modulation doped GaAs/AlGaAs nanowires". In: *Journal of Crystal Growth* 312.5, pp. 635–640. DOI: 10.1016/j.jcrysgro.2009.11.026 *Cited on page 157.*

Soga, Tetsuo, Mingju Yang, Takashi Jimbo, and Masayoshi Umeno (1996). "High-efficiency monolithic three-terminal GaAs/Si tandem solar cells fabricated by metalorganic chemical vapor deposition". In: *Japanese Journal of Applied Physics, Part 1: Regular Papers and Short Notes and Review Papers* 35.2 SUPPL. B, pp. 1401–1404. DOI: 10.1143/jjap.35.1401 *Cited on page 20.*

Sørensen, C. B., H. Gislason, D. Birkedal, and J. M. Hvam (1995). "MBE growth and characterization of high purity GaAs/AlGaAs on the (110) surface of GaAs". In: *Microelectronics Journal* 26.8, pp. 767–773. DOI: 10.1016/0026-2692(95)00035-6 *Cited on page 154.*

Spicer, W. E., P. W. Chye, P. R. Skeath, C. Y. Su, and I. Lindau (Sept. 1979). "New and unified model for Schottky barrier and III–V insulator interface states formation". In: *Journal of Vacuum Science and Technology* 16.5, pp. 1422–1433. DOI: 10.1116/1.570215 *Cited on page 137.*

Spicer, W. E., I. Lindau, P. Skeath, C. Y. Su, and Patrick Chye (Feb. 1980). "Unified Mechanism for Schottky-Barrier Formation and III-V Oxide Interface States". In: *Physical Review Letters* 44.6, pp. 420–423. DOI: 10.1103/PhysRevLett.44.420 *Cited on page 41.*

Spirina, A. A., A. G. Nastovjak, and N. L. Shwartz (2018). "Influence of GaAs substrate properties on the congruent evaporation temperature". In: *Journal of Physics: Conference Series* 993.1. DOI: 10.1088/1742-6596/993/1/012011 *Cited on page 112.*

Spirkoska, Dance, Anna Fontcuberta i Morral, Joseph Dufouleur, Qiushi Xie, and Gerhard Abstreiter (2011). "Free standing modulation doped core-shell GaAs/AlGaAs hetero-nanowires". In: *Physica Status Solidi - Rapid Research Letters* 5.9, pp. 353–355. DOI: 10.1002/pssr.201105338 *Cited on pages 28, 157.*

Spirkoska, D et al. (Dec. 2009). "Structural and optical properties of high quality zinc-blende/wurtzite GaAs nanowire heterostructures". In: *Physical Review B* 80.24, p. 245325. DOI: 10.1103/PhysRevB.80.245325 *Cited on page 28.*

Storm, Kristian, Filip Halvardsson, Magnus Heurlin, David Lindgren, Anders Gustafsson, Phillip M. Wu, Bo Monemar, and Lars Samuelson (2012). "Spatially resolved Hall effect measurement in a single semiconductor nanowire". In: *Nature Nanotechnology* 7.11, pp. 718–722. DOI: 10.1038/nnano.2012.190 *Cited on page 130.*

Stringfellow, G. B. (1972). "The importance of lattice mismatch in the growth of GaxIn1-xP epitaxial crystals". In: *Journal of Applied Physics* 43.8, pp. 3455–3460. DOI: 10.1063/1.1661737 *Cited on page 164.*

Sturmberg, Björn C.P., Kokou B. Dossou, Lindsay C. Botten, Ara A. Asatryan, Christopher G. Poulton, Ross C. McPhedran, and C. Martijn De Sterke (2014). "Optimizing Photovoltaic Charge Generation of Nanowire Arrays: A Simple Semi-Analytic Approach". In: *ACS Photonics* 1.8, pp. 683–689. DOI: 10.1021/ph500212y. arXiv: 1412.5224 *Cited on page 31.*

Sun, Wen et al. (2015). "Spontaneous formation of core-shell GaAsP nanowires and their enhanced electrical conductivity". In: *Journal of Materials Chemistry C* 3.8, pp. 1745–1750. DOI: 10.1039/c4tc02305f *Cited on pages 33, 160.*

Suomalainen, S., T. V. Hakkarainen, T. Salminen, R. Koskinen, M. Honkanen, E. Luna, and Mircea Guina (2015). "Te-doping of self-catalyzed GaAs nanowires". In: *Applied Physics Letters* 107.1, pp. 1–5. DOI: 10.1063/1.4926494 *Cited on page 150.*

Sze, S.M. and Kwok K. Ng (Oct. 2006). *Physics of Semiconductor Devices*. Hoboken, NJ, USA: John Wiley & Sons, Inc. ISBN: 9780470068328. DOI: 10.1002/0470068329 *Cited on pages 38, 188.*

Tajik, N, Z Peng, P Kuyanov, and R R Lapierre (2011). "Sulfur passivation and contact methods for GaAs nanowire solar cells". In: DOI: 10.1088/0957-4484/22/22/225402 *Cited on pages 27, 174, 175.*

Tchernycheva, M et al. (July 2012). "Photovoltaic properties of GaAsP core–shell nanowires on Si(001) substrate". In: *Nanotechnology* 23.26, p. 265402. DOI: 10.1088/0957-4484/23/26/265402 *Cited on page 160.*

Tejwani, M. J., H. Kanber, B. M. Paine, and J. M. Whelan (Dec. 1988). "Growth and diffusion of abrupt beryllium-doped profiles in gallium arsenide by organometallic vapor phase epitaxy". In: *Applied Physics Letters* 53.24, pp. 2411–2413. DOI: 10.1063/1.100412 *Cited on page 142.*

Tersoff, J., D. E. Jesson, and W. X. Tang (Apr. 2009). "Running Droplets of Gallium from Evaporation of Gallium Arsenide". In: *Science* 324.5924, pp. 236–238. DOI: 10.1126/science.1169546 *Cited on page 112.*

Thelander, Claes, Philippe Caroff, Sébastien Plissard, Anil W. Dey, and Kimberly A. Dick (2011). "Effects of crystal phase mixing on the electrical properties of InAs nanowires". In: *Nano Letters* 11.6, pp. 2424–2429. DOI: 10.1021/nl2008339 *Cited on page 99.*

Togonal, Aliénor Svietlana et al. (2016). "Core-Shell Heterojunction Solar Cells Based on Disordered Silicon Nanowire Arrays". In: *Journal of Physical Chemistry C* 120.5, pp. 2962–2972. DOI: 10.1021/acs.jpcc.5b09618 *Cited on pages 23, 24.*

Tok, E S, J H Neave, M J Ashwin, B A Joyce, and T S Jones (Apr. 1998). "Growth of Si-doped GaAs(110) thin films by molecular beam epitaxy; Si site occupation and the role of arsenic".

In: *Journal of Applied Physics* 83.8, pp. 4160–4167. DOI: 10.1063/1.367169 *Cited on pages 54, 149, 152, 154.*

Tomioka, K., P. Mohan, J. Noborisaka, S. Hara, J. Motohisa, and T. Fukui (Jan. 2007). "Growth of highly uniform InAs nanowire arrays by selective-area MOVPE". In: *Journal of Crystal Growth* 298.SPEC. ISS, pp. 644–647. DOI: 10.1016/j.jcrysgro.2006.10.183 *Cited on page 75.*

Tomioka, Katsuhiro, Junichi Motohisa, Shinjiroh Hara, and Takashi Fukui (2008). "Control of InAs nanowire growth directions on Si". In: *Nano Letters* 8.10, pp. 3475–3480. DOI: 10.1021/nl802398j *Cited on pages 27, 75, 83, 86.*

Uccelli, Emanuele et al. (2011). "Three-dimensional multiple-order twinning of self-catalyzed GaAs nanowires on Si substrates". In: *Nano Letters* 11.9, pp. 3827–3832. DOI: 10.1021/nl201902w *Cited on pages 28, 84, 85.*

Umeno, Masayoshi, Tetsuo Soga, Krishnan Baskar, and Takashi Jimbo (Jan. 1998). "Heteroepitaxial technologies on Si for high-efficiency solar cells". In: *Solar Energy Materials and Solar Cells* 50.1-4, pp. 203–212. DOI: 10.1016/S0927-0248(96)00149-3 *Cited on page 20.*

Vainorius, Neimantas, Daniel Jacobsson, Sebastian Lehmann, Anders Gustafsson, Kimberly A. Dick, Lars Samuelson, and Mats Erik Pistol (2014). "Observation of type-II recombination in single wurtzite/zinc-blende GaAs heterojunction nanowires". In: *Physical Review B - Condensed Matter and Materials Physics* 89.16, pp. 1–8. DOI: 10.1103/PhysRevB.89.165423 *Cited on page 99.*

Vainorius, Neimantas, Sebastian Lehmann, Daniel Jacobsson, Lars Samuelson, Kimberly A. Dick, and Mats-Erik Pistol (Apr. 2015). "Confinement in Thickness-Controlled GaAs Polytype Nanodots". In: *Nano Letters* 15.4, pp. 2652–2656. DOI: 10.1021/acs.nanolett.5b00253 *Cited on pages 99, 100.*

Van der Pauw, L.J. (1958). *A method of measuring specific resistivity and Hall effect of discs of arbitrary shape* *Cited on page 54.*

VanSant, Kaitlyn T. et al. (Apr. 2019). "Toward Low-Cost 4-Terminal GaAs//Si Tandem Solar Cells". In: *ACS Applied Energy Materials* 2.4, pp. 2375–2380. DOI: 10.1021/acsaem.9b00018 *Cited on page 17.*

Vettori, Marco et al. (2018). "Growth optimization and characterization of regular arrays of GaAs/AlGaAs core/shell nanowires for tandem solar cells on silicon". In: *Nanotechnology*. DOI: 10.1088/1361-6528/aaf3fe *Cited on pages 32, 77, 78, 88, 89, 120.*

Vukajlovic-Plestina, J. et al. (2019). "Fundamental aspects to localize self-catalyzed III-V nanowires on silicon". In: *Nature Communications* 10.1, p. 869. DOI: 10.1038/s41467-019-08807-9 *Cited on pages 28, 77, 78.*

Wagner, Jakob B., Niklas Sköld, L. Reine Wallenberg, and Lars Samuelson (May 2010). "Growth and segregation of GaAs–AlxIn1-xP core-shell nanowires". In: *Journal of Crystal Growth* 312.10, pp. 1755–1760. DOI: 10.1016/j.jcrysgro.2010.02.009 *Cited on page 160.*

Wagner, R. S. and W. C. Ellis (1964). "Vapor-liquid-solid mechanism of single crystal growth". In: *Applied Physics Letters* 4.5, pp. 89–90. DOI: 10.1063/1.1753975 *Cited on page 55.*

Wagner, R. S., W. C. Ellis, K. A. Jackson, and S. M. Arnold (1964). "Study of the filamentary growth of silicon crystals from the vapor". In: *Journal of Applied Physics* 35.10, pp. 2993–3000. DOI: 10.1063/1.1713143 *Cited on page 21.*

Wallentin, Jesper and Magnus T. Borgström (2011). "Doping of semiconductor nanowires". In: *Journal of Materials Research* 26.17, pp. 2142–2156. DOI: 10.1557/jmr.2011.214 *Cited on pages 130, 142.*

Wallentin, Jesper et al. (Mar. 2013). "InP Nanowire Array Solar Cells Achieving 13.8% Efficiency by Exceeding the Ray Optics Limit". In: *Science* 339.6123, pp. 1057–1060. DOI: 10.1126/science.1230969. arXiv: 20 *Cited on pages 24, 30, 73, 174, 175.*

Wang, Fan et al. (2015). "Spatially resolved doping concentration and nonradiative lifetime profiles in single Si-Doped InP nanowires using photoluminescence mapping". In: *Nano Letters* 15.5, pp. 3017–3023. DOI: 10.1021/nl504929n *Cited on page 131.*

Wang, Jia, Sébastien R. Plissard, Marcel A. Verheijen, Lou-Fé Feiner, Alessandro Cavalli, and Erik P A M Bakkers (Aug. 2013). "Reversible Switching of InP Nanowire Growth Direction by Catalyst Engineering". In: *Nano Letters* 13.8, pp. 3802–3806. DOI: 10.1021/nl401767b. arXiv: 1204.4131 *Cited on page 83.*

Wang, Zh M., B. L. Liang, K. A. Sablon, and G. J. Salamo (2007). "Nanoholes fabricated by self-assembled gallium nanodrill on GaAs(100)". In: *Applied Physics Letters* 90.11. DOI: 10.1063/1.2713745 *Cited on page 112.*

Ward, J. Scott, Timothy Remo, Kelsey Horowitz, Michael Woodhouse, Bhushan Sopori, Kaitlyn VanSant, and Paul Basore (Sept. 2016). "Techno-economic analysis of three different substrate removal and reuse strategies for III-V solar cells". In: *Progress in Photovoltaics: Research and Applications* 24.9, pp. 1284–1292. DOI: 10.1002/pip.2776 *Cited on page 17.*

Welser, Roger E., Mark Chaplin, and Van Un (2009). "Demonstration of quantum solar cell concepts in InGaP barrier structures". In: *Conference Record of the IEEE Photovoltaic Specialists Conference* V, pp. 000857–000860. DOI: 10.1109/PVSC.2009.5411153 *Cited on page 205.*

Wen, C.-Y, J Tersoff, K Hillerich, M C Reuter, J H Park, S Kodambaka, E A Stach, and F M Ross (July 2011). "Periodically Changing Morphology of the Growth Interface in Si, Ge, and GaP Nanowires". In: *Physical Review Letters* 107.2, p. 025503. DOI: 10.1103/PhysRevLett.107.025503 *Cited on page 57.*

Wen, C.-Y, J Tersoff, M C Reuter, E A Stach, and F M Ross (Nov. 2010). "Step-Flow Kinetics in Nanowire Growth". In: *Physical Review Letters* 105.19, p. 195502. DOI: 10.1103/PhysRevLett.105.195502 *Cited on page 57.*

Wood, Brendan A., Paul Kuyanov, Martin Aagesen, and Ray R. LaPierre (Dec. 2017). "GaAsP nanowire-on-Si tandem solar cell". In: *Journal of Photonics for Energy* 7.04, p. 1. DOI: 10.1117/1.JPE.7.042502 *Cited on pages 24, 34, 160, 174.*

Woodbridge, K, J.P. Gowers, and B.A. Joyce (Nov. 1982). "Structural properties and composition control of GaAsyP1-y grown by MBE on VPE GaAs0.63P0.37 substrates". In: *Journal of Crystal Growth* 60.1, pp. 21–28. DOI: 10.1016/0022-0248(82)90168-3 *Cited on page 167.*

Wright, Steve and Herbert Kroemer (1980). "Reduction of oxides on silicon by heating in a gallium molecular beam at 800??Ca)". In: *Applied Physics Letters* 36.3, pp. 210–211. DOI: 10.1063/1.91428 *Cited on page 89.*

Wu, Jiang et al. (2014). "Wafer-scale fabrication of self-catalyzed 1.7 eV GaAsP core-shell nanowire photocathode on silicon substrates". In: *Nano Letters* 14.4, pp. 2013–2018. DOI: 10.1021/nl500170m *Cited on page 160.*

Wu, Z. H., X. Y. Mei, D. Kim, M. Blumin, and H. E. Ruda (2002). "Growth of Au-catalyzed ordered GaAs nanowire arrays by molecular-beam epitaxy". In: *Applied Physics Letters* 81.27, pp. 5177–5179. DOI: 10.1063/1.1532772 *Cited on page 74.*

Wurfel, P (1982). "The chemical potential of radiation". In: *Journal of Physics C: Solid State Physics* 15.18, pp. 3967–3985. DOI: 10.1088/0022-3719/15/18/012 *Cited on page 132.*

Würfel, Peter and Uli Würfel (Jan. 2016). *Physics of Solar Cells*. 3rd editio. Wiley. ISBN: 978-3-527-41312-6 *Cited on pages 38–41.*

Xiong, Qihua, J. Wang, and P. C. Eklund (2006). "Coherent twinning phenomena: Towards twinning superlattices in III-V semiconducting nanowires". In: *Nano Letters* 6.12, pp. 2736–2742. DOI: 10.1021/nl0616983 *Cited on page 99.*

Xu, Tao et al. (Mar. 2012). "Faceting, composition and crystal phase evolution in III–V antimonide nanowire heterostructures revealed by combining microscopy techniques". In: *Nan-*

otechnology 23.9, p. 095702. DOI: 10.1088/0957-4484/23/9/095702 *Cited on page 160.*

Yao, Maoqing et al. (June 2014). "GaAs Nanowire Array Solar Cells with Axial p–i–n Junctions". In: *Nano Letters* 14.6, pp. 3293–3303. DOI: 10.1021/nl500704r *Cited on pages 24, 26, 177.*

Yao, Maoqing et al. (Nov. 2015). "Tandem Solar Cells Using GaAs Nanowires on Si: Design, Fabrication, and Observation of Voltage Addition". In: *Nano Letters* 15.11, pp. 7217–7224. DOI: 10.1021/acs.nanolett.5b03890 *Cited on pages 4, 24, 26, 76, 174, 177, 187, 197, 209, 228.*

Yastrebova, Natalya V (2007). "High-efficiency multi-junction solar cells : Current status and future potential". In: *Centre for Research in Photonics, University of Ottawa* April *Cited on page 17.*

Ye, Han and Zhongyuan Yu (2014). "Plastic relaxation of mixed dislocation in axial nanowire heterostructures using Peach-Koehler approach". In: *Physica Status Solidi - Rapid Research Letters* 8.5, pp. 445–448. DOI: 10.1002/pssr.201409072 *Cited on page 21.*

Yee, R. J., S. J. Gibson, V. G. Dubrovskii, and R. R. Lapierre (2012). "Effects of Be doping on InP nanowire growth mechanisms". In: *Applied Physics Letters* 101.26. DOI: 10.1063/1.4773206 *Cited on page 27.*

Yoshikawa, Kunta et al. (2017). "Silicon heterojunction solar cell with interdigitated back contacts for a photoconversion efficiency over 26%". In: *Nature Energy* 2.5, p. 17032. DOI: 10.1038/nenergy.2017.32 *Cited on pages 14, 15.*

Yoshimura, Masatoshi, Eiji Nakai, Katsuhiro Tomioka, and Takashi Fukui (2013). "Indium phosphide core-shell nanowire array solar cells with lattice-mismatched window layer". In: *Applied Physics Express* 6.5. DOI: 10.7567/APEX.6.052301 *Cited on pages 24, 26, 30.*

Yuan, Xiaoming, Philippe Caroff, Jennifer Wong-Leung, Lan Fu, Hark Hoe Tan, and Chennupati Jagadish (2015). "Tunable Polarity in a III-V Nanowire by Droplet Wetting and Surface Energy Engineering". In: *Advanced Materials* 27.40, pp. 6096–6103. DOI: 10.1002/adma.201503540 *Cited on page 83.*

Zamani, Mahdi et al. (2018). "Optimizing the yield of A-polar GaAs nanowires to achieve defect-free zinc blende structure and enhanced optical functionality". In: *Nanoscale*. DOI: 10.1039/C8NR05787G *Cited on pages 28, 87.*

Zardo, I, S Conesa-Boj, F Peiro, J R Morante, J Arbiol, E Uccelli, G Abstreiter, and A. Fontcuberta i Morral (Dec. 2009). "Raman spectroscopy of wurtzite and zinc-blende GaAs nanowires: Polarization dependence, selection rules, and strain effects". In: *Physical Review B* 80.24, p. 245324. DOI: 10.1103/PhysRevB.80.245324 *Cited on page 28.*

Zhang, J, A C E Chia, and R R LaPierre (May 2014a). "Low resistance indium tin oxide contact to n-GaAs nanowires". In: *Semiconductor Science and Technology* 29.5, p. 054002. DOI: 10.1088/0268-1242/29/5/054002 *Cited on pages 176, 186.*

Zhang, Yunyan, Martin Aagesen, Ana M. Sanchez, Richard Beanland, Jiang Wu, and Huiyun Liu (Jan. 2017a). "GaAsP nanowires and nanowire devices grown on silicon substrates". In: ed. by Manijeh Razeghi. Vol. 10111, p. 101110X. DOI: 10.1117/12.2250588 *Cited on pages 106, 107.*

Zhang, Yunyan, Ana M. Sanchez, Jiang Wu, Martin Aagesen, Jeppe V. Holm, Richard Beanland, Thomas Ward, and Huiyun Liu (2015). "Polarity-driven quasi-3-fold composition symmetry of self-catalyzed III-V-V ternary core-shell nanowires". In: *Nano Letters* 15.5, pp. 3128–3133. DOI: 10.1021/acs.nanolett.5b00188 *Cited on pages 28, 160, 163.*

Zhang, Yunyan, Jiang Wu, Martin Aagesen, Jeppe Holm, Sabina Hatch, Mingchu Tang, Suguo Huo, and Huiyun Liu (Aug. 2014b). "Self-Catalyzed Ternary Core–Shell GaAsP Nanowire Arrays Grown on Patterned Si Substrates by Molecular Beam Epitaxy". In: *Nano Letters* 14.8, pp. 4542–4547. DOI: 10.1021/nl501565b *Cited on pages 27, 28, 77, 78, 89, 160.*

Zhang, Yunyan et al. (Aug. 2013). "Self-Catalyzed GaAsP Nanowires Grown on Silicon Substrates by Solid-Source Molecular Beam Epitaxy". In: *Nano Letters* 13.8, pp. 3897–3902. DOI: 10.1021/nl401981u *Cited on pages 28, 33.*

Zhang, Yunyan et al. (2016). "Influence of Droplet Size on the Growth of Self-Catalyzed Ternary GaAsP Nanowires". In: *Nano Letters* 16.2, pp. 1237–1243. DOI: 10.1021/acs.nanolett.5b04554 *Cited on pages 28, 160.*

Zhang, Yunyan et al. (Aug. 2017b). "Growth of Pure Zinc-Blende GaAs(P) Core–Shell Nanowires with Highly Regular Morphology". In: *Nano Letters* 17.8, pp. 4946–4950. DOI: 10.1021/acs.nanolett.7b02063 *Cited on pages 28, 99, 160.*

Zhang, Yunyan et al. (Jan. 2018). "Doping of Self-Catalyzed Nanowires under the Influence of Droplets". In: *Nano Letters* 18.1, pp. 81–87. DOI: 10.1021/acs.nanolett.7b03366 *Cited on pages 28, 107, 131, 141.*

Zhong, Zhiqin et al. (2016). "Efficiency enhancement of axial junction InP single nanowire solar cells by dielectric coating". In: *Nano Energy* 28, pp. 106–114. DOI: 10.1016/j.nanoen.2016.08.032 *Cited on page 75.*

université PARIS-SACLAY
ÉCOLE DOCTORALE
Physique et ingénierie : Electrons, Photons, Sciences du vivant (EOBE)

Titre : Cellules solaires en GaAs sur Si à base de réseaux de nanofils épitaxiés par jets moléculaires

Mots clés : Photovoltaïque, nanofils, III-V, nanotechnologie, épitaxie par jets moléculaires

Résumé : Les nanofils (NF) épitaxiés sur substrat Si sont des absorbeurs optiques efficaces et permettent d'intégrer des matériaux III-V de haute qualité sur Si en évitant les défauts généralement induits par le désaccord de maille entre ces deux matériaux, ce qui permettrait de fabriquer des cellules solaires tandem III-V/Si de plus de 30% d'efficacité. L'objectif de cette thèse est de développer des cellules solaires à NFs III-V, crûes sur substrat Si. Un premier objectif a été le contrôle de la croissance sélective de NFs en réseaux organisés, avec des taux de verticalité reproductibles supérieurs à 90% et atteignant 100%. A partir de caractérisation au microscope électronique en transmission, les conditions de croissance ont été optimisées pour améliorer la qualité cristalline en réduisant le nombre de fautes d'empilement, pour étudier des NFs de GaAsP avec un bandgap optimal, et pour étudier des hétérostructures cœur-coquille. En déterminant la concentration de porteurs dans les NFs par cathodoluminescence, je montre que le dopage du cœur ou de la coquille à un niveau p=8E18 cm^{-3} est possible en utilisant du Be, mais que le dopant Si est amphotère et ne permet d'atteindre que n=5E17 cm^{-3} dans les coquilles. Un procédé de fabrication de cellules a été développé pour contacter des jonctions de NFs cœur-coquille. Un dispositif de première génération basé sur une homojonction GaAs présente une efficacité de 2.1%, limitée par des problèmes de collection des porteurs, alors que la séparation des niveaux de Fermi estimée d'après des mesures de photoluminescence atteint une valeur prometteuse de 0.98 V à 82 soleils, extrapolée à 0.86 V à 1 soleil. Une nouvelle hétérojonction p-i-GaAs/n-GaInP présente une efficacité de 3.7% et un V_{oc} record de 0.65 V. Ces démonstrations de cellules solaires à nanofils ouvrent la voie vers des cellules tandem à haute efficacité.

Title : GaAs-on-Si solar cells based on nanowire arrays grown by molecular beam epitaxy

Keywords : Photovoltaics, nanowires, III-V, nanotechnology, molecular beam epitaxy

Abstract : Nanowires (NW) epitaxially grown on Si substrate are efficient light absorbers and allow to integrate high-quality III-V materials on Si by preventing defects induced by the lattice-mismatch between both materials. They provide a way to fabricate tandem III-V/Si solar cells above 30% efficiency. The goal of this thesis is to develop III-V NW solar cells grown on Si substrates. First, the control of the selective NW growth in ordered arrays on Si was addressed, and vertical yields consistently above 90% and up to 100% were demonstrated. Using transmission electron microscope characterization, the growth conditions were optimized to improve the crystal quality by reducing the number of stacking faults, to investigate GaAsP NWs with the optimal bandgap for tandem, and to study core-shell heterostructures. Using cathodoluminescence to determine the carrier concentrations in NWs, it was shown that the core and the shell can be doped with Be up to p=8E18 cm^{-3}, while Si is an amphoteric dopant, resulting in shell doping limited to n=5E17 cm^{-3}. A solar cell fabrication process was developed to contact NW core-shell junctions. A first-generation GaAs homojunction device shows efficiencies up to 2.1%, limited by carrier collection issues, whereas the quasi-Fermi level splitting, estimated from PL measurements, reaches a promising value of 0.98 V at 82 sun, extrapolated to 0.86 V at 1 sun. A new core-shell p-i-GaAs/n-GaInP heterojunction exhibits efficiencies up to 3.7%, with a record V_{oc}=0.65 V. These GaAs-based NW top-cells directly grown on Si pave the way toward high-efficiency tandem solar cells.

Université Paris-Saclay
Espace Technologique / Immeuble Discovery
Route de l'Orme aux Merisiers RD 128 / 91190 Saint-Aubin, France